

CHARACTERIZATION AND MODELING OF LIGHTNING PROCESSES WITH
EMPHASIS ON COMPACT INTRACLOUD DISCHARGES

By

AMITABH NAG

A DISSERTATION PRESENTED TO THE GRADUATE SCHOOL
OF THE UNIVERSITY OF FLORIDA IN PARTIAL FULFILLMENT
OF THE REQUIREMENTS FOR THE DEGREE OF
DOCTOR OF PHILOSOPHY

UNIVERSITY OF FLORIDA

2010

© 2010 Amitabh Nag

To my parents and *Gurudev*

ACKNOWLEDGMENTS

I would like to thank my advisor, Dr. Vladimir Rakov, for his patient guidance and support over the course of my graduate study. I am grateful for the comments and suggestions that I received from Dr. Martin Uman, Dr. Douglas Jordan, and Dr. Robert Moore. I would like to acknowledge the help and cooperation of my colleagues and members of the University of Florida, Lightning Research Group. Dimitris Tsalikis, Dr. Joseph Howard, Christopher Biagi, Dustin Hill, Michael Stapleton, and Keith Rambo have all contributed in various ways toward the completion of this study.

Finally, I would like to thank my parents whose sacrifices, support, and blessings will always be the reason behind whatever I achieve in life. They have motivated me and helped me stay focused over the past four years.

TABLE OF CONTENTS

	<u>page</u>
ACKNOWLEDGMENTS	4
LIST OF TABLES	10
LIST OF FIGURES	14
ABSTRACT	31
CHAPTER	
1 INTRODUCTION	33
2 LITERATURE REVIEW	36
2.1 Role of Lightning in the Global Electric Circuit.....	36
2.2 Lightning Discharge Processes	37
2.2.1 Cloud-to-Ground Discharges	38
2.2.1.1 Preliminary breakdown in ground discharges	43
2.2.1.2 Electric and magnetic field waveforms from natural negative first strokes	46
2.2.2 Cloud Discharges	50
2.2.2.1 General information.....	50
2.2.2.2 Initial breakdown in cloud discharges	52
2.3 Lightning Initiation Mechanisms	56
2.3.1 Conventional Breakdown.....	57
2.3.2 Runaway Breakdown	58
2.4 Rocket-Triggered Lightning.....	58
2.5 Compact Intracloud Discharges	62
3 EXPERIMENTAL SETUP	67
3.1 The Lightning Observatory in Gainesville.....	67
3.2 Overview of Experiments	68
3.2.1 Single-Station Experiment	68
3.2.2 Two-Station Experiment	70
3.2.3 Equipment	72
3.2.3.1 Fiber optic links	72
3.2.3.2 Digital storage oscilloscopes	75
3.2.3.3 GPS time-stamping system.....	80
3.2.3.4 Dedicated phone line	81
3.3 Wideband Electric Field Measurements	82
3.3.1 Theory	82
3.3.2 Antenna	83
3.3.3 Electric Field Measuring System for the Two-Station Experiment (E1).....	84

3.3.4	Electric Field Measuring System for the Single-Station Experiment (E2)	86
3.4	Electric Field Derivative Measurements	89
3.4.1	Theory	89
3.4.2	Antenna	89
3.4.3	dE/dt Measuring System for the Two-Station Experiment (dE1)	90
3.4.4	dE/dt Measuring System for the Single-Station Experiment (dE2)	91
3.5	Magnetic Field Derivative Measuring System	92
3.5.1	Theory	92
3.5.2	Antenna	93
3.5.3	dB/dt Measuring System for the Single-Station and Two-Station Experiments (dB)	95
3.6	Narrowband HF Measuring System	96
3.7	Narrowband VHF measuring system	97
3.8	Amplitude Calibration of Measuring Systems	100
3.9	Time Delays Between Measurements	102
3.10	Details of the Two-Station Experiment Configuration	103
4	COMPACT INTRACLOUD LIGHTNING DISCHARGES	109
4.1	Phenomenology	109
4.1.1	Experimental Data and Methodology	109
4.1.2	Relation of Compact Intracloud Discharges to Other Types of Lightning	113
4.1.3	Different Types of Electric Field Waveforms	115
4.1.4	Source Heights	120
4.1.5	Electric Field Waveform Characteristics	123
4.2	Conceptual Mechanism and Modeling	127
4.2.1	Evidence of Reflections in CID Electromagnetic Field Signatures	128
4.2.2	Bouncing-Wave Mechanism	133
4.2.3	Bouncing-Wave Model: Current Distribution along the Channel	140
4.2.4	Bouncing-Wave Model: Electric Fields at 2 and 200 km	143
4.2.5	Hertzian Dipole Approximation	146
4.2.6	Equivalent Current Sources to Represent Multiple Traveling Waves in the Bouncing-Wave Model	147
4.2.7	Bouncing-Wave Model: Allowed Ranges of Variation of Input Parameters	152
4.2.7.1	Reflection coefficients	152
4.2.7.2	Propagation speed (v) and channel length (Δh)	155
4.2.7.3	Source height	161
4.2.7.4	Distance	161
4.2.7.5	Current waveshape	162
4.2.8	Testing the Validity of Bouncing-Wave Model and Hertzian-Dipole Approximation Using Electric Fields Simultaneously Measured at Near and Far Distances by <i>Eack</i> [2004]	169
4.2.8.1	Bouncing-wave model	169
4.2.8.2	Hertzian dipole approximation	170
4.2.8.3	Discussion	171
4.2.9	Discussion and Summary	172
4.3	Estimation of Electrical Parameters	177

4.3.1	The Hertzian Dipole Approximation Approach.....	178
4.3.2	Limits of Validity of the Hertzian Dipole Approximation.....	182
4.3.3	Electrical Parameters of CIDs.....	190
4.3.4	Upper Bound on Electric Field Prior to CID.....	194
4.3.5	Total Energy Dissipated by CIDs.....	203
4.3.6	Discussion.....	207
4.4	Summary.....	213
5	PRELIMINARY BREAKDOWN PULSE TRAINS IN NEGATIVE CLOUD-TO-GROUND LIGHTNING AND IN ATTEMPTED LEADERS.....	219
5.1	Characterization of Microsecond- and Submicrosecond-Scale Electric Field Pulses Prior to First Return-Stroke Waveforms.....	219
5.2	Attempted Leaders.....	230
5.3	Some Inferences on the Role of Lower Positive Charge Region in Facilitating Different Types of Lightning.....	233
5.3.1	Introduction.....	233
5.3.2	Analysis and Discussion.....	241
5.3.2.1	Generation of preliminary breakdown pulse train.....	241
5.3.2.2	Variations in occurrence of preliminary breakdown pulse train.....	242
5.3.2.3	Type of discharge versus magnitude of lower positive charge region.....	244
5.4	Summary.....	247
6	TWO-STATION MEASUREMENTS OF CLOUD-TO-GROUND LIGHTNING ELECTRIC FIELDS.....	251
6.1	Introduction.....	251
6.2	Measured Electric Field Waveforms.....	253
6.3	Transmission Line Model.....	277
6.3.1	Channel-Base Current without Pronounced Slow Front.....	280
6.3.2	Electric Fields Computed Using the Original Transmission Line Model.....	280
6.3.3	Electric Fields Computed Using the Two-Wave Transmission Line Model.....	281
6.3.4	Electric Fields Computed Using the Three-Wave Transmission Line Model.....	282
6.3.5	Channel-Base Current with Pronounced Slow Front and Computed Electric Fields.....	283
6.4	Discussion.....	299
6.5	Summary.....	303
7	CHARACTERIZATION OF POSITIVE CLOUD-TO-GROUND LIGHTNING.....	311
7.1	Multiplicity.....	311
7.2	Parameters of Return Stroke Electric Field and Field Derivative Waveforms.....	318
7.2.1	Distance-Normalized Electric Field Peaks.....	318
7.2.2	Risetime.....	319
7.2.3	Slow Front and Fast Transition.....	328

7.2.4	Zero Crossing Time	329
7.2.5	dE/dt Waveform Characteristics	337
7.3	Peak Current.....	346
7.3.1	Peak Current Estimated by the National Lightning Detection Network (NLDN).....	346
7.3.2	Linear Regression Equations Relating NLDN Currents and Distance-Normalized Fields	346
7.3.3	Peak Currents Inferred from Measured Electric Field Peaks Using the Transmission Line Model	351
7.4	Charge Transferred by Return Strokes.....	359
7.5	Ratio of Electric and Magnetic Field Peaks.....	365
7.6	Leader Stepping	365
7.7	Preliminary Breakdown Pulse Trains.....	367
7.8	Bipolar Lightning Discharges	369
7.9	Summary	373
8	FIRST VERSUS SUBSEQUENT RETURN-STROKE CURRENT AND FIELD PEAKS IN NEGATIVE CLOUD-TO-GROUND LIGHTNING DISCHARGES	386
8.1	Introduction.....	386
8.2	Methodology	386
8.3	Instrumentation and Data.....	388
8.3.1	Electric Field Measurements in Gainesville, Florida.....	388
8.3.2	Electric Field Measurements in Austria.....	390
8.3.3	Electric Field Measurements in Brazil.....	390
8.3.4	Electric Field Measurements in Sweden.....	391
8.3.5	Currents Estimated by Lightning Locating Systems.....	391
8.4	Analysis and Discussion	392
8.5	Summary	400
9	SUMMARY OF RESULTS AND RECOMMENDATIONS FOR FUTURE RESEARCH	404
9.1	Summary of Results.....	404
9.1.1	Compact Intracloud Discharges.....	404
9.1.2	Preliminary Breakdown in Cloud-to-Ground Flashes and in Attempted Leaders	407
9.1.3	First Return Strokes in Negative Cloud-to-Ground Lightning	408
9.1.4	Positive Cloud-to-Ground Lightning	409
9.1.5	Ratio of First versus Subsequent Return Stroke Intensities in Negative Cloud-to-Ground Discharges.....	410
9.2	Recommendations for Future Research.....	411
APPENDIX		
A	INVENTORY TABLE AND CATALOG OF 48 COMPACT INTRACLOUD DISCHARGE WAVEFORMS.....	413

B	ELECTRIC FIELD DERIVATIVE WAVEFORMS OF 27 POSITIVE RETURN STROKES.....	464
C	NLDN RESPONSES TO ROCKET-TRIGGERED LIGHTNING AT CAMP BLANDING, FLORIDA, IN 2004, 2005, AND 2007	478
C.1	Introduction.....	478
C.2	Data and Methodology.....	479
C.3	Results and Discussion.....	480
C.3.1	Flash and Stroke Detection Efficiencies	480
C.3.2	Location Accuracy	483
C.3.3	Peak Current Estimates	487
C.4	Summary	491
	LIST OF REFERENCES	495
	BIOGRAPHICAL SKETCH	508

LIST OF TABLES

<u>Table</u>	<u>page</u>
2-1	Characteristics of narrow bipolar electric field pulses and associated HF (3-30 MHz) radiation.65
3-1	A list of LOG sensors (see Figure 3-3) used in two-station and single-station experiments.71
3-2	Digital storage oscilloscope used at the LOG prior to April 2008.76
3-3	Digital storage oscilloscopes used at the LOG after April 2008.78
3-4	Characterization and calibration factors of measuring systems at the LOG prior to April 2008 (Benton Hall).103
3-5	Characterization and calibration factors of electric field and dE/dt measuring systems at the LOG after April, 2008 (Engineering Building).....104
3-6	Characterization and calibration factors of dB/dt measuring systems at the LOG after April, 2008 (Engineering Building).105
3-7	GPS locations, accurate to ± 2 m, of all antennas on the roof of the Engineering Building in 2008.105
4-1	Number of NLDN-located CIDs in different horizontal distance ranges.111
4-2	Influence of source height on the ratio of initial electric field peak to opposite polarity overshoot of CID electric fields.161
4-3	Influence of distance on the ratio of initial electric field peak to opposite polarity overshoot of CID electric fields.163
4-4	Parameters β and k in Equation 4-9 yielding different values of current risetime (t_1). ...163
4-5	Combinations of reflection coefficients, propagation speeds, and channel lengths that produce distant CID electric fields that are consistent with experimental data for current risetime of 3 μ s.165
4-6	Combinations of propagation speeds and channel lengths that produce distant CID electric fields that are consistent with experimental data for $\rho = 0$ and current risetime of 2 μ s.165
4-7	CID parameters for which electric fields at close and far distances that are based on the bouncing-wave model and Hertzian dipole approximation best fit the fields measured by <i>Eack</i> in New Mexico.172

4-8	Comparison of electric fields based on the Hertzian dipole approximation and bouncing-wave model for a current risetime of 6 μs for different combinations of reflection coefficients, current wave speeds, and channel lengths.	187
4-9	Comparison of electric fields based on the Hertzian dipole approximation and bouncing wave model for a current risetime of 3 μs for different combinations of reflection coefficients, current wave speeds, and channel lengths.	188
4-10	Comparison of electric fields based on the Hertzian dipole approximation and bouncing wave model for a current risetime of 8.5 μs for different combinations of reflection coefficients, current wave speeds, and channel lengths.	188
4-11	Parameters of nine located CIDs with channel lengths estimated using reflections in dE/dt waveforms and assumed propagation speed of 2.5×10^8 m/s.	192
4-12	Peak current and charge transfer at 5 μs scaled to different channel lengths that were inferred for 9 CIDs using reflections in measured dE/dt waveforms and assumed propagation speeds.	193
4-13	Peak current and charge transfer at 5 μs scaled to different channel lengths for 39 CIDs.	193
4-14	The maximum electric field at the surface of each of the two oppositely charged spheres separated by a zero net charge region (Figure 4-42a) for different combinations of charge transfer and assumed volume charge density.	204
5-1	Categorization of pulses according to normalized amplitude.	220
5-2	Summary of occurrence of smaller and narrower pulses observed in the 12 cloud-to-ground discharges.	227
6-1	Summary of natural lightning fields simultaneously measured at Camp Blanding and in Gainesville, Florida.	255
6-2	Characteristics of electric field waveforms produced by negative first return strokes measured at near (Camp Blanding) and far (Gainesville) stations.	257
6-3	Initial (radiation) electric field peaks for each stroke in four flashes recorded at near (Camp Blanding) and far (Gainesville) stations.	259
6-4.	The values of the parameters m , I_0 , η , n , τ_1 , and τ_2 for different values of k , reproduced from Table II of <i>De Conti and Visacro</i> , used in Equation 6-9 to produce current waveform shown in Figure 6-35.	295
7-1	Summary of the positive and bipolar cloud-to-ground lightning data (a total of 54 flashes) recorded at the LOG. Data recorded is indicated by "Y" and not recorded by "N".	315

7-2	Interstroke interval, distance between first and second strokes, and semi-major axis (SMA) length of NLDN 50% location error ellipse for each stroke of 8 two-stroke positive flashes.....	318
7-3	Parameters of electric field waveforms produced by first and subsequent return strokes in positive lightning.....	320
7-4	Number of positive return strokes in different distance ranges and corresponding GM electric field peaks normalized to 100 km.....	320
7-5	Risetimes of return stroke electric field waveforms in different regions and in different seasons.....	326
7-6	Characteristics of the slow front and fast transition in positive and negative returns strokes in different regions.....	336
7-7	Zero-crossing time and opposite polarity overshoot relative to peak of the return stroke electric field waveform for different seasons in Florida and Japan.....	342
7-8	Number of positive return strokes in different distance ranges and corresponding GM current peaks.....	347
7-9	Number of negative return strokes in different distance ranges and corresponding GM current peaks.....	352
7-10	Summary of electric field change (ΔE), charge transfer (ΔQ), and average current ($\Delta Q/\Delta t$) at different times (Δt) after the beginning of the return stroke field change for 17 first and 2 subsequent positive return strokes.....	362
7-11	Ratio of electric and magnetic field peaks for the seven positive return strokes.....	365
8-1	Summary of first to subsequent stroke electric field or current peak ratios estimated from different studies.....	397
8-2	Summary of first to subsequent stroke electric field or current peak ratios for subsequent strokes following a previously-formed channel.....	398
8-3	Summary of first to subsequent stroke electric field or current peak ratios for multiple-stroke flashes only.....	399
8-4	Summary of subsequent to first stroke electric field or current peak ratio estimated from different studies.....	401
8-5	Summary of multiple-stroke flash characteristics reported in different studies.....	402
A-1	Summary of horizontal distance (r), measured electric (E_p) and magnetic (B_p) field peaks, height (h), elevation angle (α), inclined distance (R), and normalized electric field (E_N) for 48 CIDs recorded at the LOG in 2008.....	413

C-1 Summary of flashes and strokes recorded at Camp Blanding during summers of 2004, 2005, and 2007, along with the corresponding NLDN detection efficiencies.....479

LIST OF FIGURES

<u>Figure</u>	<u>page</u>
2-1	The left panel shows a simplified illustration of the global electric circuit. The right panel shows the Earth-atmosphere lossy capacitor system (not to scale).....37
2-2	Different types of lightning discharges.....39
2-3	Four types of cloud-to-ground lightning discharge..40
2-4	Various processes comprising a negative cloud-to-ground lightning flash.....41
2-5	Examples of electric field pulse waveforms characteristic of (a) preliminary breakdown in negative ground flashes, (b) the active stage (initial breakdown) in cloud flashes.....44
2-6	Histogram of the ratio of preliminary breakdown to first return stroke field peaks for individual flashes.46
2-7	Typical vertical electric field intensity (left column) and azimuthal magnetic flux density (right column) waveforms for first (solid line) and subsequent (broken line) return strokes.....47
2-8	Electric field waveforms of (a) a first return stroke, (b) a subsequent stroke initiated by a dart-stepped leader, and (c) a subsequent return stroke initiated by a dart leader, showing the fine structure both before and after the initial field peak..48
2-9	Occurrence statistics of electric field pulses in a cloud discharge.....53
2-10	Electric field record of cloud flash 05/24/06_299.55
2-11	Examples of (a) “classical” and (b) “narrow” pulses in the early stage of cloud discharges.....55
2-12	Histogram of total duration of unipolar and bipolar pulses in 12 selected cloud discharges.....56
2-13	Submicrosecond-scale pulses that occurred in a cloud discharge..59
2-14	Sequence of events in classical triggered lightning. The upward positive leader and initial continuous current constitute the initial stage..60
2-15	Narrow bipolar pulses recorded by the Los Alamos Sferic Array (LASA).....65
3-1	The Lightning Observatory on the roof of the Engineering Building on the University of Florida campus at Gainesville.68
3-2	Google Earth image of the LOG in 2008.....69

3-3	Schematic showing positions of the different sensors at the LOG in 2008.	71
3-4	Block diagram of the single-station experiment.	73
3-5	Block diagram of the two-station experiment.....	74
3-6	Frequency response of an Opticomm MMV-120C fiber-optic link used at the LOG.	75
3-7	Digitizing oscilloscopes inside the glass cupola at the LOG in August, 2008.	77
3-8	The GPS antenna used at the LOG.	80
3-9	An electric field antenna system.	82
3-10	An elevated flat plate antenna used for measuring wideband electric field at the LOG.	85
3-11	Electronics inside a Hoffman enclosure used in electric field measuring system (E1) at the LOG.....	87
3-12	Schematic of the high input-impedance amplifier used in electric field measuring system (E1) at the LOG.	87
3-13	Frequency response of the high input-impedance amplifier used in electric field measuring system (E1) at the LOG.....	88
3-14	Frequency response of the high input-impedance amplifier used in electric field measuring system (E2) at the LOG.....	88
3-15	An electric field derivative antenna system.....	89
3-16	Schematic of the amplifier used in dE/dt measuring systems (dE1 and dE2) at the LOG.	91
3-17	Frequency response of the amplifiers used in dE/dt measuring systems (dE1 and dE2) at the LOG.....	92
3-18	A single-ended output coaxial loop antenna with both ends of the cable terminated in 50 Ω	94
3-19	Two loops (oriented north-south and east-west) of the magnetic field derivative antenna used at the LOG.....	96
3-20	Frequency response of the amplifiers used in dB/dt measuring systems, dB (N-S) and dB (E-W), at the LOG.....	97
3-21	Block diagram of the HF measuring system. The HF receiver had an overall gain of 31 (30 dB) at center frequency (5 MHz).....	98

3-22	Frequency response of the HF receiver used at the LOG.	98
3-23	Whip antenna used for the narrowband VHF measurement at the LOG.	99
3-24	Block diagram of the VHF measuring system. The VHF receiver had an overall gain of 27 (29 dB) at the center frequency (36 MHz).	99
3-25	Frequency response of the VHF receiver used at the LOG.	100
3-26	The histogram of the ratio of electric to magnetic field peaks for 43 first return strokes in negative cloud-to-ground lightning, recorded in 2008 in Gainesville, Florida.	102
3-27	OR gate used to generate trigger pulses at Camp Blanding.	107
3-28	Functional diagram of a one-shot circuit implemented using a CD74HC221 (monostable multivibrator) used to generate a 5 V, 462 μ s rectangular pulse which is fed into the telephone line.	107
3-29	Trigger pulse from Camp Blanding received at Gainesville via the AT&T BellSouth analog conditioned telephone line.	108
3-30	A block diagram schematically showing the two-station experiment.	108
4-1	Electromagnetic signatures produced by a CID in Gainesville, Florida.	110
4-2	Geometrical parameters and equations used in estimating radiation source heights. See text for details.	112
4-3	Electric field and VHF (36 MHz) radiation from a CID that was followed by a "normal" IC (from another experiment in Gainesville, Florida).	114
4-4	A CID that occurred during an eight-stroke negative CG, within horizontal distances of 7 to 8 km of all the CG strokes. (a) Wideband electric field and VHF (36 MHz) radiation. (b) Plan view of NLDN-estimated relative positions of the CID (hollow circle) and return strokes (numbered solid circles) of CG flash.	117
4-5	Wideband electric field record (top) showing two CIDs that occurred 66 ms apart at a horizontal distance of 24 km from each other. Individual CID signatures (bottom) displayed on expanded (10 and 5 μ s per division for CID 1 and CID 2, respectively) time scales.	119
4-6	Occurrence context of CIDs.	120
4-7	Three types of CID electric field waveforms exhibiting (a) only radiation, (b) radiation and static field components (induction component is not apparent), and (c) only induction and static field components.	121
4-8	Histograms of radiation source heights for 48 CIDs.	123

4-9	Histograms of electric fields peaks normalized to $R = 100$ km and $\alpha = 0^\circ$ for 48 CIDs.....	125
4-10	Electric field waveform characteristics for 48 CIDs.....	126
4-11	Signatures of a CID that transferred negative charge downward (or positive charge upward), recorded in Gainesville, Florida..	130
4-12	Signatures of a CID that transferred negative charge upward (or positive charge downward), recorded in Gainesville, Florida.	131
4-13	Characteristics of 5 MHz HF radiation signature for 31 CIDs.	135
4-14	Characteristics of 36 MHz VHF radiation signature for 52 CIDs.	136
4-15	Histograms of the starting-time of (a) HF and (b) VHF radiation signatures relative to the onset-time of the corresponding electric field waveform.	137
4-16	Illustration of the bouncing-wave mechanism for a CID current pulse with a peak of 50 kA and propagation speed $v = 2 \times 10^8$ m/s injected at the bottom of a 100 m long vertical conducting channel at $t = 0$	138
4-17	Currents associated with the bouncing-wave model.....	144
4-18	Geometrical parameters used in calculating the electric field at observation point P on perfectly conducting ground at horizontal distance r from the vertical CID channel extending between heights h_1 and h_2	145
4-19	Electric fields predicted by the bouncing-wave model.....	148
4-20	Electric fields at (a) 2 km and (b) 200 km computed using the Hertzian dipole approximation for a CID with a channel length of 100 m at a height of 15 km, excited by current waveform shown in Figure 4-17a for $z = h_1 + \Delta h/2$ (in the middle of the channel).....	149
4-21	Currents, electric fields, electric field derivatives, and their components.	153
4-22	Currents, electric fields, electric field derivatives, and their components.	154
4-23	Illustration of the reversal distance for electrostatic and induction field components. Inset shows the direction of the far ($\alpha < 35.3^\circ$) electric field vector for different combinations of charge polarity and direction of charge motion.	155
4-24	Combinations of propagation speed and channel length for which the ratio of initial electric field peak to opposite polarity overshoot of model-predicted electric fields at 200 km attains 2.5 (the lowest value found in the experimental data) and 3.0 for a current risetime of 6 μ s and for (a) $\rho = 0$ and (b) $\rho = -0.5$	158

4-25	Bouncing-wave model predicted electric fields at 200 km for different combinations of propagation speed and channel length for a current risetime of 6 μs and for (a) $\rho = 0$ and (b) $\rho = -0.5$	159
4-26	Currents and corresponding electric fields for the same total current duration (30 μs) and peak (50 kA), but different risetimes of 3, 6 and 9 μs for $\rho = 0$, $\Delta h = 100$ m, and $v = 2 \times 10^8$ m/s.....	166
4-27	Electric field waveforms at 200 km for different propagation speeds and channel lengths of (a) 100 m and (b) 500 m, for a current risetime of 2 μs and $\rho = 0$	167
4-28	Electric field waveforms at 200 km for different combinations of propagation speed and channel length for a current risetime of 8.5 μs and for (a) $\rho = 0$ and (b) $\rho = -0.5$	168
4-29	Electric fields computed using the bouncing-wave model (in red) overlaid with the fields measured by <i>Eack</i> (in blue) at (a) near and (b) far distances.....	173
4-30	Electric fields computed using the Hertzian dipole approximation (in red) overlaid with the fields measured by <i>Eack</i> (in blue) at (a) near and (b) far distances.....	173
4-31	Bouncing-wave model-predicted electric field for a CID and current waveforms obtained by solving Equation 4-13 (blue line) and using the radiation field approximation (red line)..	181
4-32	Vertical electric fields for the bouncing-wave model (solid line) for $\rho = 0$, $v = 2 \times 10^8$ m/s, RT = 6 μs , and channel lengths of (a) 100, (b) 350, and (c) 700 m versus those for the Hertzian dipole approximation (dashed line).....	184
4-33	Same as Figure 4-32, but for $\rho = -0.5$ and channel lengths of (a) 100 and (b) 350 m, for both of which the Hertzian dipole approximation is acceptable.....	185
4-34	Comparison of the Hertzian dipole validity domain (combinations of propagation speed and channel length) with the "allowed" one for RT = 6 μs and $\rho = 0$	186
4-35	Measured electric field and electric field derivative, and inferred electrical parameters, each as a function of time, for a CID.....	189
4-36	Histogram of peak currents for 48 CIDs.....	195
4-37	Histogram of zero-to-peak current risetimes for 48 CIDs.....	196
4-38	Histogram of 10-to-90% current risetimes for 48 CIDs.....	197
4-39	Histogram of charge transferred at 5 μs for 48 CIDs.....	198
4-40	Histogram of peak radiated power for 48 CIDs.....	199
4-41	Histogram of radiated energy at 5 μs for 48 CIDs.....	200

4-42	Simplified charge configuration and electric field intensity profile giving rise to a CID.....	205
4-43	Ranges of dissipated energy and channel length for typical first strokes in cloud-to-ground flashes, regular intracloud flashes, and CIDs.	214
4-44	NLDN-reported peak current versus peak current estimated using the transmission line model with $v = 1.8 \times 10^8$ m/s for 48 CIDs.	214
4-45	NLDN-reported peak current versus peak current estimated using the Hertzian dipole (HD) approximation for 48 CIDs.....	215
5-1	Electric field record of cloud-to-ground flash 05/24/06_1078 showing preliminary breakdown pulse train followed by two return strokes.....	221
5-2	Examples of (a) “classical” and (b) “narrow” preliminary breakdown pulses in cloud-to-ground discharges analyzed in this study.	223
5-3	Occurrence of pulses of different amplitude prior to the first stroke of cloud-to-ground flash whose electric field record is shown in Figure 5-1.....	224
5-4	Occurrence of pulses of different total duration prior to the first stroke of cloud-to-ground flash whose electric field record is shown in Figure 5-1.....	224
5-5	Histogram of pulse amplitude for four different types of pulses in cloud-to-ground flash whose electric field record is shown in Figure 5-1.	225
5-6	Histogram of total pulse duration for four different types of pulses in cloud-to-ground flash whose electric field record is shown in Figure 5-1.....	225
5-7	Histogram of total duration of unipolar and bipolar pulses in 12 cloud-to-ground discharges.....	226
5-8	Occurrence of pulses of different total duration in different parts (four quarters) of the preliminary breakdown pulse train for all 12 cloud-to-ground flashes combined.....	226
5-9	Histogram of the total duration of preliminary breakdown pulse trains for 12 cloud-to-ground flashes.....	228
5-10	Ranges of variation (vertical bars) and mean values (diamonds) of pulse duration in individual preliminary breakdown pulse trains.....	229
5-11	Ranges of variation (vertical bars) and mean values (diamonds) of interpulse interval in individual preliminary breakdown pulse trains.	229
5-12	Electric field record of an attempted leader with no pulse activity following the preliminary breakdown pulse train..	231

5-13	Typical (a) “classical” and (b) “narrow” pulses of a preliminary breakdown (PB) pulse train of an attempted leader.	234
5-14	Histogram of preliminary breakdown pulse train duration for attempted leaders. Note that a total of 35 preliminary breakdown pulse trains were found in 33 electric field records.	235
5-15	Ranges of variation (vertical bars) and mean values (diamonds) of pulse duration in individual preliminary breakdown pulse trains of attempted leaders.	235
5-16	Ranges of variation (vertical bars) and mean values (diamonds) of interpulse interval in individual preliminary breakdown pulse trains of attempted leaders.	236
5-17	The electric field record of the PB pulse train of a negative cloud-to-ground discharge that occurred on August 1, 2008 in Gainesville, Florida at a distance of 28 km from the measuring station.	240
5-18	A schematic illustration (left) of electric field enhancement and reduction effects of the lower positive charge region (+Q _{LP}) below the main negative charge region (-Q _N). Schematic representation of preliminary breakdown stepping process (right, top) in negative ground flashes. A sketch of expected electric field record (right, bottom) of resultant wideband PB pulse train.	242
5-19	Percentage of flashes with detectable PB pulse train and altitudes of the upper cloud boundary (UCB), the main negative charge region (assumed to be between the 0°C and -15°C isotherms), and the lower cloud boundary (LCB), each as a function of latitude.	245
5-20	Schematic representation of four types of lightning, A–D, that may arise depending upon the magnitude of the LPCR.	248
6-1	The electric field waveforms of three-stroke flash 073107_1252, measured at the near (top panel) and far (bottom panel) stations both shown on a 140 ms time scale.	260
6-2	The electric field waveforms of single-stroke flash 100407_360, measured at the near (top panel) and far (bottom panel) stations both shown on a 100 ms time scale.	261
6-3	The electric field waveforms of a two-stroke flash 070508_008, measured at the near (top panel) and far (bottom panel) stations shown on a 15 ms time scale.	262
6-4	The electric field waveform of six-stroke flash 070608_020, measured at the near (top panel) station shown on a 450 ms time scale.	263
6-5	The electric field waveforms of the first return stroke of flash 073107_1252, measured at the near (top panel) and far (bottom panel) stations shown on a 1 ms time scale.	264

6-6	The electric field waveforms of the first return stroke of flash 100407_360, measured at the near (top panel) and far (bottom panel) stations shown on a 1 ms time scale.	265
6-7	The electric field waveforms of the first return stroke of flash 070508_008, measured at the near (top panel) and far (bottom panel) stations shown on a 2.5 ms time scale. ...	266
6-8	The electric field waveforms of the first return stroke of flash 070608_020, measured at the near (top panel) and far (bottom panel) stations shown on a 2 ms time scale.	267
6-9	The initial rising portion of the first strokes of flash 073107_1252 at the near (blue line) and far (red line) stations overlaid for direct comparison, shown on a 30 μ s time scale.....	268
6-10	The initial rising portion of the first strokes of flash 100407_360 at the near (blue line) and far (red line) stations overlaid for direct comparison, shown on a 50 μ s time scale.....	268
6-11	The initial rising portion of the first strokes of flash 070508_008 at the near (blue line) and far (red line) stations overlaid for direct comparison, shown on a 50 μ s time scale.....	269
6-12	The initial rising portion of the first strokes of flash 070608_020 at the near (blue line) and far (red line) stations overlaid for direct comparison, shown on a 100 μ s time scale.	269
6-13	The initial rising portion of the first stroke of flash 073107_1252 at the near (blue line, top panel) and far (red line, bottom) stations each shown on a 30 μ s time scale. ...	270
6-14	The initial rising portion of the first stroke of flash 100407_360 at the near (blue line, top panel) and far (red line, bottom) stations each shown on a 20 μ s time scale.	271
6-15	The initial rising portion of the first stroke of flash 070508_008 at the near (blue line, top panel) and far (red line, bottom) stations each shown on a 40 μ s time scale.	272
6-16	The initial rising portion of the first stroke of flash 070608_020 at the near (blue line, top panel) and far (red line, bottom) stations each shown on a 50 μ s time scale.	273
6-17	First positive stroke electric and magnetic field waveforms measured at 825 and 288 m at Camp Blanding, Florida, by <i>Jerauld et al.</i> [2009] on a 40-ms timescale.	274
6-18	Electric field of the first positive stroke measured in Gainesville, at a distance of 45 km by the Los Alamos Sferic Array (LASA)..	275
6-19	Magnetic field measured at 288 m by <i>Jerauld et al.</i> [2009], overlaid with the electric field measured a distance of 45 km from the first positive stroke.	276

6-20	Ratio of near and far initial (radiation) field peaks versus inverse ratio of near and far field distances for 8 negative return strokes recorded at Camp Blanding and in Gainesville.	276
6-21	NLDN-estimated peak current versus initial (radiation) field peak normalized to 100 km for 8 negative return strokes recorded at Camp Blanding (near station) and in Gainesville (far station).....	277
6-22	Geometrical parameters used in calculating the electric field at observation point P on perfectly conducting ground at horizontal distance r from the vertical return-stroke channel extending between ground and height H.	281
6-23	The channel-base current waveform given by Equation 6-8 used to calculate return stroke electric fields for the one-wave, two-wave and three-wave models.	282
6-24	Electrostatic (red), induction (green), and radiation (blue) components of electric field and the total electric field (magenta) up to 10 μ s at (a) 500 m and (b) 100 km from the lightning channel computed using the original, one-wave TL model for an assumed current-wave propagation speed of 0.5×10^8 m/s and channel length of 4 km.	284
6-25	Electrostatic (red), induction (green), and radiation (blue) components of electric field and the total electric field (magenta) up to 10 μ s at (a) 500 m and (b) 100 km from the lightning channel computed using the original, one-wave TL model for an assumed current-wave propagation speed of 1×10^8 m/s and channel length of 4 km. ...	285
6-26	Electrostatic (red), induction (green), and radiation (blue) components of electric field and the total electric field (magenta) up to 10 μ s at (a) 500 m and (b) 100 km from the lightning channel computed using the original, one-wave TL model for an assumed current-wave propagation speed of 2×10^8 m/s and channel length of 4 km. ...	286
6-27	Electrostatic (red), induction (green), and radiation (blue) components of electric field and the total electric field (magenta) up to 10 μ s at (a) 500 m and (b) 100 km from the lightning channel computed using the two-wave model for an assumed current-wave propagation speed of 0.5×10^8 m/s and channel length of 4 km.	287
6-28	Electrostatic (red), induction (green), and radiation (blue) components of electric field and the total electric field (magenta) up to 10 μ s at (a) 500 m and (b) 100 km from the lightning channel computed using the two-wave model for an assumed current-wave propagation speed of 1×10^8 m/s and channel length of 4 km.	288
6-29	Electrostatic (red), induction (green), and radiation (blue) components of electric field and the total electric field (magenta) up to 10 μ s at (a) 500 m and (b) 100 km from the lightning channel computed using the two-wave model for an assumed current-wave propagation speed of 2×10^8 m/s and channel length of 4 km.	289
6-30	Electric field components E_u and E_d due to the upward and downward moving current waves, respectively, along with the total electric field ($E_u + E_d$) at 500 m for	

	current propagation speeds of (a) 0.5×10^8 , (b) 1×10^8 , and (c) 2×10^8 for the two-wave model.	290
6-31	Electrostatic (red), induction (green), and radiation (blue) components of electric field and the total electric field (magenta) up to $10 \mu\text{s}$ at (a) 500 m and (b) 100 km from the lightning channel computed using the three-wave model for an assumed current-wave propagation speed of 0.5×10^8 m/s and channel length of 4 km.	291
6-32	Electrostatic (red), induction (green), and radiation (blue) components of electric field and the total electric field (magenta) up to $10 \mu\text{s}$ at (a) 500 m and (b) 100 km from the lightning channel computed using the three-wave model for an assumed current-wave propagation speed of 1×10^8 m/s and channel length of 4 km.	292
6-33	Electrostatic (red), induction (green), and radiation (blue) components of electric field and the total electric field (magenta) up to $10 \mu\text{s}$ at (a) 500 m and (b) 100 km from the lightning channel computed using the three-wave model for an assumed current-wave propagation speed of 2×10^8 m/s and channel length of 4 km.	293
6-34	Electric field components E_u , E_d , and E_r due to the two incident current waves (upward and downward moving), and the ground reflected current wave, respectively, along with the total electric field ($E_u + E_d + E_r$) at 500 m for current propagation speeds of (a) 0.5×10^8 , (b) 1×10^8 , and (c) 2×10^8 for the three-wave model.	294
6-35	Current waveform represented by Equation 6-9 with parameters given in Table 6-4.	295
6-36	Electrostatic (red), induction (green), and radiation (blue) components of electric field and the total electric field (magenta) up to $10 \mu\text{s}$ at (a) 500 m and (b) 100 km computed using the one-wave model.	296
6-37	Electrostatic (red), induction (green), and radiation (blue) components of electric field and the total electric field (magenta) up to $10 \mu\text{s}$ at (a) 500 m and (b) 100 km computed using the two-wave model.	297
6-38	Electrostatic (red), induction (green), and radiation (blue) components of electric field and the total electric field (magenta) up to $10 \mu\text{s}$ at (a) 500 m and (b) 100 km computed using the three-wave model.	298
6-39	Total electric fields at (a) 500 m and (b) 100 km for the one-wave (red line), two-wave (green line), and three-wave (blue line) models for $v = 10^8$ m/s overlaid for direct comparison.	305
6-40	The return stroke electric fields at 100 km for the (a) two-wave and (b) three-wave models when the height of the junction point is 20 m (red line) and 100 m (blue line) above ground.	306
6-41	Contributions from upward (dotted curve) and downward (solid gray curve) waves to the model-predicted dE/dt waveform at 30 m calculated by <i>Jerauld et al.</i> [2007]	

	using the two-wave model with dI/dt as input and current originating at a height of 6.5 m.	307
6-42	Electric fields at 100 km calculated by <i>Jerauld et al.</i> [2007] using the single- and two-wave models, assuming propagation over a perfectly conducting ground.	308
6-43	Total electric fields at (a) 500 m and (b) 100 km for the one-wave (red line), two-wave (green line), and three-wave (blue line) models for $v = 10^8$ m/s overlaid for direct comparison.	309
6-44	Electrostatic (red), induction (green), and radiation (blue) components of electric field and the total electric field (magenta) up to 10 μ s at (a) 500 m and (b) 100 km computed using the three-wave model.	310
7-1	Histogram of the number of strokes per flash for 52 positive cloud-to-ground flashes in Florida.	312
7-2	Electric field record of a multiple-stroke positive cloud-to-ground flash in Florida with three return strokes (RS) shown on a 75-ms time scale.	317
7-3	Histogram of the initial electric field peak normalized to 100 km for 48 positive return strokes.	321
7-4	Distance-normalized electric field peak versus distance from the measuring station for 48 positive return strokes.	322
7-5	Histogram of the zero-to-peak risetime for 62 positive return strokes.	324
7-6	Histogram of the 10-90% risetime for 62 positive return strokes.	325
7-7	Zero-to-peak risetime time versus the distance from the measuring station for 48 positive return strokes.	327
7-8	10-to-90% risetime time versus the distance from the measuring station for 48 positive return strokes.	327
7-9	A typical slow front-fast transition sequence in a positive return stroke electric field waveform recorded on June 1, 2008 in Gainesville, Florida, shown on a 70 μ s time scale.	330
7-10	Histogram of the slow front duration for 62 positive return strokes. Statistics given are arithmetic mean (AM), geometric mean (GM), minimum (min), and maximum (max) values for first and subsequent strokes, as well as for all data combined.	331
7-11	Histogram of the slow front amplitude relative to peak for 62 positive return strokes. ...	332
7-12	Histogram of the fast transition 10-to-90% risetime for 62 positive return strokes.	333

7-13	Slow front duration versus the distance from the measuring station for 48 positive return strokes.....	334
7-14	Slow front amplitude relative to peak versus the distance from the measuring station for 48 positive return strokes.	334
7-15	Fast transition 10-to-90% risetime time versus the distance from the measuring station for 48 positive return strokes.....	335
7-16	The electric field waveform of a positive return stroke that occurred at a distance of 157 km on May 5, 2008 in Gainesville, Florida, shown on a 2.5 ms time scale.	339
7-17	Histogram of the zero crossing time for 41 positive return strokes.....	340
7-18	Zero crossing time versus distance from the measuring station for 34 positive return strokes.	340
7-19	Histogram of the opposite polarity overshoot relative to peak for 31 positive return strokes.....	341
7-20	Opposite polarity overshoot relative to peak versus distance from the measuring station for 27 positive return strokes.....	342
7-21	A typical electric field derivative (dE/dt) waveform of a positive return stroke in the dataset presented here shown on a 23 μ s time scale.	343
7-22	Histogram of the peak electric field derivative normalized to 100 km for 27 positive return strokes.....	344
7-23	Peak dE/dt normalized to 100 km versus distance from the measuring station for 27 positive return strokes.	344
7-24	Histogram of the width of the dE/dt pulse at half peak value for 37 positive return strokes.	345
7-25	dE/dt half-peak width versus the distance from measuring station for 27 (out of 37) located positive return strokes.	345
7-26	Histogram of the NLDN-estimated peak currents for 48 positive return strokes. Statistics given are arithmetic mean (AM), geometric mean (GM), minimum (min), and maximum (max) values for first and subsequent strokes, as well as for all data combined.....	347
7-27	NLDN-estimated peak current versus distance from the measuring station for 48 positive return strokes.....	348
7-28	NLDN-estimated peak current versus normalized electric field peak for 48 positive return strokes.....	349

7-29	NLDN-estimated peak current versus peak current estimated using Equation 7-2 (with E being negative).....	352
7-30	Normalized electric field peak versus distance from the measuring station for 116 negative return strokes.....	352
7-31	NLDN-estimated peak current versus distance-normalized electric field peak for 116 first and subsequent negative return strokes.....	353
7-32	NLDN-estimated peak current versus measured electric field peak for 48 positive and 116 negative return strokes.....	354
7-33	The NLDN-estimated peak currents versus peak currents estimated using the transmission line model for assumed return-stroke speeds of (a) 10^8 m/s, (b) 1.5×10^8 m/s, (c) 1.8×10^8 m/s, and (d) 3×10^8 m/s for 75 negative subsequent return strokes.....	356
7-34	The NLDN-estimated peak currents versus peak currents estimated using the transmission line model for assumed return-stroke speed of 1.8×10^8 m/s for (a) 41 negative first return strokes and (b) 48 positive return strokes.....	358
7-35	Measurements of electric field changes (ΔE) at times $\Delta t = 0.5$ ms, 1.0 ms, and 1.5 ms after the beginning of the return stroke.....	361
7-36	Histograms of charge transfer within (a) 0.5 ms, (b) 1 ms, and (c) 1.5 ms of the beginning of the return stroke field change.....	363
7-37	Charge transfer at 1.5 ms versus the distance from the measuring station for 19 positive return strokes.....	364
7-38	Electric field (integrated dE/dt) signature of the return stroke of a single-stroke positive flash that apparently involved a stepped leader shown on a 600- μ s time scale.....	367
7-39	Electric field signature of preliminary breakdown (PB) pulse train having the same initial polarity as the following return stroke (RS) of a positive flash on a 20-ms time scale.....	369
7-40	Electric field signature of preliminary breakdown pulse train having initial polarity opposite to that of the following return stroke of a positive flash on a 65-ms time scale.....	370
7-41	Electric field record of bipolar flash composed of three negative strokes followed by a positive stroke and then by a negative one, recorded in Gainesville, Florida, on October 5, 2007.....	372
7-42	Electric field waveforms of individual return strokes of the five-stroke bipolar flash shown in Figure 7-41.....	373

7-43	Electric field record of a three-stroke bipolar cloud-to-ground flash with two negative and one positive return strokes (RS), shown on a 404-ms time scale.	374
7-44	Electric field waveforms of the first (top panel) and second (bottom panel) return strokes of a two-stroke flash, each shown on a 300 μ s time scale. The interstroke interval was 19 ms.	378
7-45	Electric field waveforms of the first (top panel) and second (bottom panel) return strokes of a two-stroke flash, each shown on a 500 μ s time scale. The interstroke interval was 79 ms.	379
7-46	Electric field waveforms of the first (top panel) and second (bottom panel) return strokes of a two-stroke flash, each shown on a 300 μ s time scale. The interstroke interval was 8.5 ms.	380
7-47	Electric field waveforms of the first (top panel) and second (bottom panel) return strokes of a two-stroke flash, each shown on a 300 μ s time scale.	381
7-48	Electric field waveforms of the first (top panel) and second (bottom panel) return strokes of a two-stroke flash, each shown on a 300 μ s time scale.	382
7-49	Electric field waveforms of the first (top panel) and second (bottom panel) return strokes of a two-stroke flash, each shown on a 200 μ s time scale.	383
7-50	Electric field waveforms of the first (top panel) and second (bottom panel) return strokes of a two-stroke flash, each shown on a 300 μ s time scale.	384
7-51	Electric field waveforms of the first (top panel) and second (bottom panel) return strokes of a two-stroke flash, each shown on a 250 μ s time scale.	385
8-1	Typical electric field record of a multiple-stroke negative cloud-to-ground flash in Florida with three return strokes	389
8-2	Histogram of the ratio of the first-to-subsequent-return-stroke electric field peak for multiple stroke negative cloud-to-ground lightning flashes in (a) Florida, (b) Austria, (c) Brazil, and (d) Sweden.	392
8-3	Histogram of the ratio of the subsequent-to-first-return-stroke electric field peak for multiple stroke negative cloud-to-ground lightning flashes in (a) Florida, (b) Austria, (c) Brazil, and (d) Sweden.	393
8-4	Geometric mean (GM) electric field peaks for strokes of different order estimated from different studies, labeled A, B, C, D, E, and F.	394
B-1	Electric field derivative waveform of a positive return stroke that occurred on December 16, 2007, at 06:50:27 (UTC) at a distance of 38 km, shown on a 30- μ s time scale.	464

B-2	Electric field derivative waveform of a positive return stroke that occurred on December 16, 2007, at 06:55:35 (UTC) at a distance of 7.8 km, shown on a 30- μ s time scale.	464
B-3	Electric field derivative waveform of a positive return stroke that occurred on December 16, 2007, at 07:02:55 (UTC) at a distance of 8.5 km, shown on a 25- μ s time scale.	465
B-4	Electric field derivative waveform of the (a) first return stroke and (b) second return stroke (of a two-stroke positive flash) that occurred on January 22, 2008, at 23:55:10 (UTC), shown on a 30- μ s time scale.	465
B-5	Electric field derivative waveform of a positive return stroke that occurred on January 23, 2008, at 02:35:47 (UTC) at a distance of 8.4 km, shown on a 20- μ s time scale.	466
B-6	Electric field derivative waveform of a positive return stroke that occurred on January 23, 2008, at 02:56:28 (UTC) at a distance of 64 km, shown on a 35- μ s time scale.	467
B-7	Electric field derivative waveform of a positive return stroke that occurred on April 26, 2008, at 22:16:22 (UTC) at a distance of 98 km, shown on a 40- μ s time scale.	467
B-8	Electric field derivative waveform of a positive return stroke that occurred on April 26, 2008, at 22:26:10 (UTC) at a distance of 94 km, shown on a 35- μ s time scale.	468
B-9	Electric field derivative waveform of a positive return stroke that occurred on May 18, 2008, at 17:27:12 (UTC) at a distance of 84 km, shown on a 40- μ s time scale.	468
B-10	Electric field derivative waveform of a positive return stroke that occurred on May 18, 2008, at 19:07:38 (UTC) at a distance of 72 km, shown on a 30- μ s time scale.	469
B-11	Electric field derivative waveform of a positive return stroke that occurred on May 18, 2008, at 21:25:29 (UTC) at a distance of 49 km, shown on a 40- μ s time scale.	469
B-12	Electric field derivative waveform of a positive return stroke that occurred on June 1, 2008, at 19:35:47 (UTC) at a distance of 72 km, shown on a 30- μ s time scale.	470
B-13	Electric field derivative waveform of a positive return stroke that occurred on June 1, 2008, at 21:23:41 (UTC) at a distance of 31 km, shown on a 30- μ s time scale.	470
B-14	Electric field derivative waveform of the (a) first return stroke and (b) second return stroke (of a two-stroke positive flash), that occurred on June 2, 2008, at 23:06:25 (UTC), shown on a 50- μ s time scale.	471
B-15	Electric field derivative waveform of a positive return stroke that occurred on June 9, 2008, at 20:27:05 (UTC) at a distance of 101 km, shown on a 30- μ s time scale.	472

B-16	Electric field derivative waveform of a positive return stroke that occurred on August 13, 2008, at 21:23:59 (UTC) at a distance of 20 km, shown on a 40- μ s time scale.	472
B-17	Electric field derivative waveform of a positive return stroke that occurred on August 13, 2008, at 22:08:10 (UTC) at a distance of 23 km, shown on a 30- μ s time scale.	473
B-18	Electric field derivative waveform of a positive return stroke that occurred on August 13, 2008, at 22:11:17 (UTC) at a distance of 28 km, shown on a 40- μ s time scale.	473
B-19	Electric field derivative waveform of a positive return stroke that occurred on August 14, 2008, at 12:52:06 (UTC) at a distance of 42 km, shown on a 60- μ s time scale.	474
B-20	Electric field derivative waveform of a positive return stroke that occurred on August 14, 2008, at 13:27:12 (UTC) at a distance of 25 km, shown on a 40- μ s time scale.	474
B-21	Electric field derivative waveform of a positive return stroke that occurred on August 23, 2008, at 20:47:43 (UTC) at a distance of 42 km, shown on a 50- μ s time scale.	475
B-22	Electric field derivative waveform of a positive return stroke that occurred on August 23, 2008, at 21:01:46 (UTC) at a distance of 42 km, shown on a 40- μ s time scale.	475
B-23	Electric field derivative waveform of a positive return stroke that occurred on August 24, 2008, at 21:53:34 (UTC) at a distance of 35 km, shown on a 40- μ s time scale.	476
B-24	Electric field derivative waveform of the (a) first return stroke and (b) second return stroke (of a two-stroke positive flash), that occurred on November 30, 2008, at 16:03:52 (UTC) at a distance of 41 km, shown on a 30- μ s time scale.	476
C-1	Histogram of Camp Blanding triggered lightning return-stroke peak currents, I , for 2004, 2005, and 2007.	481
C-2	NLDN stroke detection efficiency as a function of peak current measured at Camp Blanding.	482
C-3	Plot of NLDN stroke locations for 18 strokes in 10 flashes triggered during 2004, 2005, and 2007 at Camp Blanding.	484
C-4	Histogram of the NLDN absolute location errors. Corresponding statistics are also given.	485
C-5	NLDN absolute location error versus Camp Blanding peak current.	488
C-6	NLDN absolute location error versus the number of reporting NLDN sensors.	488
C-7	NLDN 50% error ellipse semi-major axis length versus Camp Blanding peak current.	489
C-8	NLDN absolute location error plotted versus NLDN 50% error ellipse semi-major axis length.	490

C-9	NLDN-reported peak current versus peak current directly measured at Camp Blanding.....	491
C-10	Histograms of (a) signed and (b) absolute NLDN peak current estimation errors, given as a percentage of the directly measured Camp Blanding current ($\Delta I\% = 100\Delta I/I_{CB}$, where $\Delta I = I_{NLDN} - I_{CB}$).	493
C-11	Number of reporting NLDN sensors versus Camp Blanding peak current for 18 strokes detected by multiple sensors and 5 strokes detected by a single (Ocala) sensor.	494

Abstract of Dissertation Presented to the Graduate School
of the University of Florida in Partial Fulfillment of the
Requirements for the Degree of Doctor of Philosophy

CHARACTERIZATION AND MODELING OF LIGHTNING PROCESSES WITH
EMPHASIS ON COMPACT INTRACLOUD DISCHARGES

By

Amitabh Nag

May 2010

Chair: Vladimir A. Rakov
Cochair: Martin A. Uman
Major: Electrical and Computer Engineering

Electromagnetic signatures of different lightning processes in Florida are acquired and examined with emphasis on compact intracloud discharges (CIDs).

CIDs are the strongest natural producers of HF-VHF radiation, and they are considered the prime candidate for proposed satellite-based VHF global lightning monitors. Based on experimental evidence of reflections in electric field and dE/dt records and modeling, we infer that CID is essentially a bouncing-wave phenomenon. A transmission line model of CIDs including multiple reflections is developed and used for testing the applicability of Hertzian (electrically short) dipole approximation to CIDs. The latter approximation was used to estimate electrical parameters of CIDs. CID peak currents were found to be comparable to those of first return strokes.

The occurrence of preliminary breakdown pulse trains in different geographical locations and the role of the lower positive charge region (LPCR) in facilitating different types of lightning are examined. While the LPCR may serve to enhance the electric field at the bottom of the negative charge region and thereby facilitate the launching of a negatively-charged leader toward

ground, presence of excessive LPCR may prevent the occurrence of negative cloud-to-ground flashes by “blocking” the progression of descending negative leader from reaching ground.

Natural lightning electric field waveforms simultaneously measured at Camp Blanding and in Gainesville (45 km apart) are examined. It is shown, via modeling, that the slow front in electric field at far distances is primarily due to the radiation field component, while at near distances it is composed of more or less equal contributions from all three components of electric field. For both experimental and model-predicted waveforms, the duration of the slow front appears to be similar at near and far distances from the lightning channel.

Various features of positive lightning discharges, which are considerably less understood than their negative counterparts, are analyzed. Relative magnitudes of first and subsequent return-stroke current and field peaks in negative cloud-to-ground lightning are examined. The performance characteristics of the U.S. National Lightning Detection Network (NLDN) are evaluated using rocket-triggered lightning data.

CHAPTER 1 INTRODUCTION

Lightning is a transient, high-current electrical discharge that transfers charge between the atmosphere and the Earth or between different parts of the atmosphere. The primary sources of lightning are clouds termed cumulonimbus, commonly referred to as thunderclouds [Uman, 1987]. Lightning was present on Earth long before human life evolved and it may even have played a crucial role in the evolution of life on our planet. Each year some 25 million cloud-to-ground lightning discharges occur in the United States alone. Lightning strikes involve the formation of channels carrying tens of kiloamperes of electric current with channel peak temperatures of the order of 30,000 K. Thus, lightning strikes have far-reaching and often disastrous consequences affecting essential services such as aviation, power transmission and distribution, communication, as well as the day-to-day human life. It has been recently established that the rate of lightning incidence (and the global electric circuit in general) can be significantly influenced by changes in Earth's climate. On the other hand, lightning activity may have important consequences to life on Earth, for example, via changing the global balance of NO_x (nitrogen oxides, mainly nitric oxide, NO , and nitrogen dioxide, NO_2) which largely controls the amount of ozone in the atmosphere [Rakov and Uman, 2003].

Lightning is the second most effective weather-related killer in the United States. According to the US National Oceanographic and Atmospheric Administration (NOAA) publication Storm Data, the annual average number of lightning-related deaths in the United States between 1965-95 is 85. Also, about 300 individuals are injured by lightning each year in the United States. The recent Sago coal-mine explosion in West Virginia leading to the death of 12 miners in January 2006 and many California wildfires causing immense damage to property and wildlife are believed to have been caused by lightning. Lightning and other effects of

thunderstorms have been a major concern for the aviation industry. A typical commercial plane is struck by lightning once a year on average [Rakov and Uman, 2003, Ch. 10]. There were two well documented cases where lightning was initiated by large rockets launched from Earth, the Saturn V vehicle of NASA's Apollo 12 and US Air Force's Atlas-Centaur 67. The latter suffered damage that led to the loss of the vehicle and its payload. More recently, in 2006 the launch of NASA's Atlantis had to be delayed due to lightning strike to the launch pad. According to the Electric Power Research Institute (EPRI), lightning is a major cause (40-50%) of electric service interruptions, resulting in \$50 million per year in damage and restoration expenses. Lightning is involved in 5% of all US residential-property-damage insurance claims, including those from tens of thousands of home fires, with total claims of over one billion dollars annually.

Over the years, a large number of studies have been conducted to measure and model various features and effects of lightning discharges, which served to improve our understanding of the physics of the lightning processes and the role of lightning in the global circuit. Lightning Locating Systems (LLSs) such as the North American Lightning Detection Network (NALDN), monitor, report, and archive the occurrence of lightning on continental and regional scales. The information available from the LLSs can be used to study the occurrence of lightning discharges and examine the existence of any trend in its long-term variation. In fact, LLSs (along with satellites) have become an indispensable tool in studying global lightning activity. However, LLSs are still evolving via the incorporation of newly acquired knowledge about lightning [e.g. Cummins *et al.*, 2006].

Different types of lightning discharges produce unique electromagnetic signatures that can be measured and studied to obtain insight into the processes involved in the discharges. Many of these processes remain poorly understood. The purpose of this dissertation is to examine

measured electromagnetic signatures of different lightning processes with an aim to improve our understanding of the physical processes involved, infer various parameters of these processes, and develop models that can be used to describe their salient properties. Chapter 2 gives a review of the existing literature concerning lightning that is relevant to this dissertation. Chapter 3 gives a detailed description of the experiments and instrumentation at the International Center for Lightning Research and Testing (ICLRT) with emphasis on the Lightning Observatory in Gainesville (LOG). The main goals of this dissertation are listed below.

- Discuss the phenomenology, newly proposed-mechanism, models, and electrical parameters of Compact Intracloud Discharges.
- Characterize preliminary breakdown pulse trains in negative cloud-to-ground lightning and in attempted leaders and qualitatively examine the inferred dependence of lightning type on the magnitude of the lower positive charge region.
- Examine the fine structure of electric field waveforms produced by first return strokes in negative cloud-to-ground lightning in experimental data and via modeling.
- Characterize in detail various features of positive and bipolar cloud-to-ground lightning discharge.
- Examine the relative magnitudes of first and subsequent return stroke electric field and current peaks in negative cloud-to-ground lightning.

The atmospheric electricity sign convention according to which a downward-directed electric field (or field change) vector is considered to be positive is used throughout this dissertation except in Sections 4.2 and 4.3. The physics sign convention according to which a downward-directed electric field (or field change) vector is considered to be negative is used in these two Sections.

CHAPTER 2 LITERATURE REVIEW

This chapter presents a review of the existing literature concerning lightning that is relevant to this dissertation. Section 2.1 presents a brief introduction to the physics of natural lightning, both cloud and cloud-to-ground types. Section 2.2 presents a brief review of the mechanism of lightning initiation in thunderclouds. Rocket-triggered lightning and the Compact Intracloud Discharge are discussed, respectively, in Sections 2.3 and 2.4.

2.1 Role of Lightning in the Global Electric Circuit

The conductivity of atmosphere at sea level is 10^{-14} S/m and it increases rapidly with altitude. In the region of the atmosphere 60 km or so above the sea level, free electrons are major contributors to the conductivity. This region is sometimes referred to as the electrosphere [e.g., *Chalmers*, 1967]. It is usually assumed that under quasi-static conditions, the electrosphere is conductive enough to consider it an equipotential region. The potential of the electrosphere is positive with respect to the Earth, its magnitude being about 300 kV. According to the "classical" view of atmospheric electricity, the Earth-atmosphere system can be crudely modeled as a lossy spherical capacitor [e.g., *Uman*, 1974], with the inner and outer shells consisting of the Earth's surface and the electrosphere, respectively (see Figure 2-1). According to this model, the Earth's surface is negatively charged, having a total magnitude of roughly 5×10^5 C, while an equal positive charge is distributed throughout the atmosphere [*Rakov and Uman*, 2003]. The capacitor is lossy because the atmosphere is weakly-conducting. The charge on the Earth's surface would thus disappear (if not re-supplied) in about 10 minutes. Thunderstorms (lightning discharges), which primarily transfer negative charge to Earth, therefore, serve to recharge the Earth. There are, on average, 2000 thunderstorms in progress at any time over about 10% of the Earth's

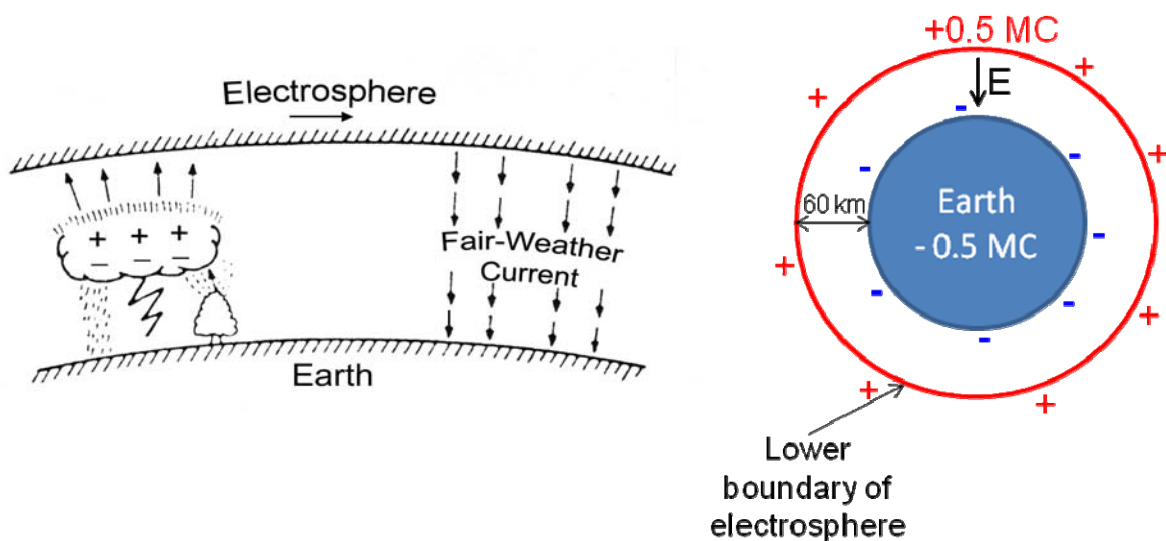


Figure 2-1. The left panel shows a simplified illustration of the global electric circuit. Adapted from *Pierce* [1974]. The right panel shows the Earth-atmosphere lossy capacitor system (not to scale).

surface. There are other contributors to the global electric circuit [see, for example, *Rakov and Uman*, 2003] that are not considered here.

2.2 Lightning Discharge Processes

Uman [1987] defines lightning as a transient, high-current electrical discharge that transfers charge between the atmosphere and the Earth or between different parts of the atmosphere. The most common sources of lightning are the electric charge regions located in ordinary thunderstorm (cumulonimbus) clouds.

The charge structure of a cumulonimbus can be approximated as a vertical tripole consisting of three charge centers, main positive at the top, main negative in the middle, and an additional smaller positive at the bottom. The two upper charges, located respectively at heights of about 12 and 7 km for Florida [*Krehbiel*, 1986], are usually specified to be equal in magnitude (typically some tens of coulombs) and therefore form a dipole. The magnitude of the lower positive charge (probably about 10 C or less), located approximately at a height of about 2 km, is

significantly smaller than that of the dipole charges. These cloud charge locations (which vary from one geographical region to another) and magnitudes have been estimated by a variety of remote [e.g., *Krehbiel*, 1986] and in situ methods [e.g., *Simpson and Scrase*, 1937]. Two primary mechanisms that attempt to explain the cloud electrification process are the convection mechanism and the graupel-ice mechanism. In the convection mechanism the electric charges are supplied by external sources such as fair-weather space charge and corona near ground and cosmic rays at the cloud top. Organized convection provides large-scale charge separation. There is no role for precipitation in forming the dipole charge structure. This mechanism was supported by *Vonnegut* [1953, 1994], *Wilson* [1956], and *Moore and Vonnegut* [1977] among others. The graupel-ice mechanism explains the process of cloud electrification by collisions between precipitation particles (graupel) and cloud particles (small ice crystals). The presence of water droplets is necessary for significant charge transfer [*Reynolds et al.*, 1957, *Takahashi*, 1978, *Jayaratne et al.*, 1983]. The large-scale separation of charged particles is provided by the action of gravity.

Around 75% of lightning discharges occur within the cloud and include intracloud, intercloud and cloud-to-air discharges. Cloud discharges are often referred to as ICs. Lightning discharges involving charge transfer to the ground constitute around 25% of all lightning discharges and are called cloud-to-ground discharges, often referred to as CGs. Figure 2-2 shows the various types of lightning discharges.

2.2.1 Cloud-to-Ground Discharges

Cloud-to-ground discharges or CGs, as the name suggests, involve charge transfer between cloud and ground via a high conductivity channel. The overall cloud-to-ground lightning discharge, often termed ground flash, consists of typically three to five component strokes or just

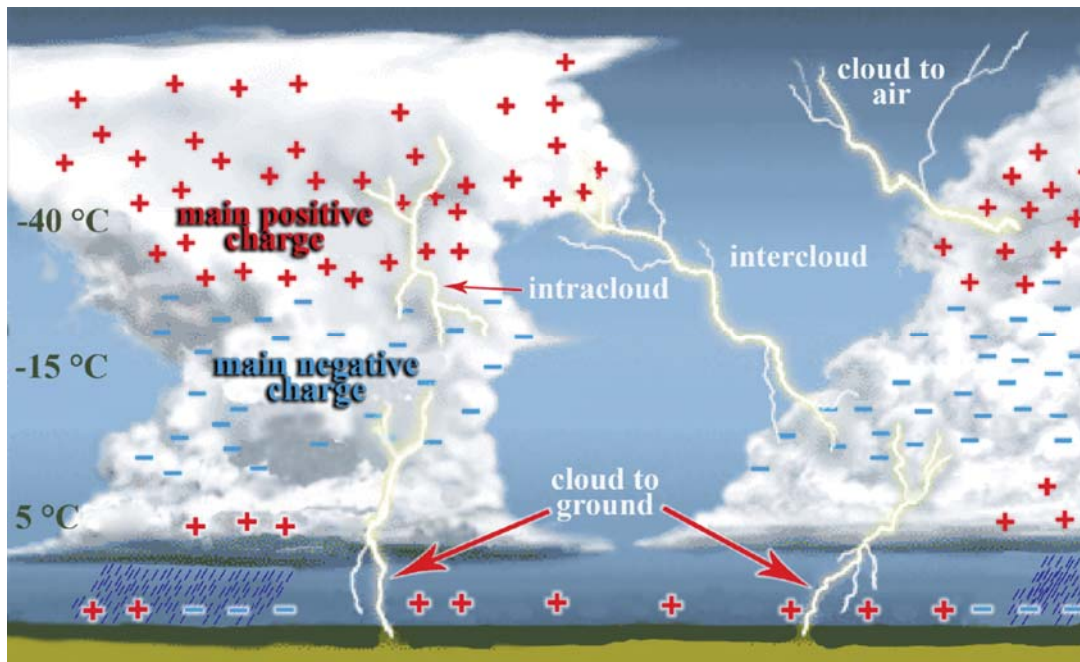


Figure 2-2. Different types of lightning discharges. Taken from *Schoene* [2007].

strokes [*Rakov and Uman*, 2003]. Each stroke is composed of a leader/return stroke sequence.

Cloud-to-ground discharges can be classified into four types (Figure 2-3) according to the polarity of the charge transferred to ground and the direction of propagation of the initial leader. Types (a) and (b) effectively lower negative charge to ground, while types (c) and (d) effectively lower positive charge to ground. Downward negative lightning comprises about 90% of all cloud-to-ground flashes, while downward positive lightning accounts for only about 10% of cloud-to-ground discharges. Upward negative and positive lightning is relatively rare as compared to the other two categories and are usually observed on tall structures or short structures on mountain tops.

The various processes associated with a negative cloud-to-ground lightning flash are shown in Figure 2-4. A downward-negative cloud-to-ground stroke is composed of a downward-moving leader and an upward-moving return stroke. Leader initiating the first stroke in a flash exhibits stepping and is preceded by the initial or preliminary breakdown, which can be defined as the in-cloud process that initiates or leads to the initiation of the downward-moving stepped

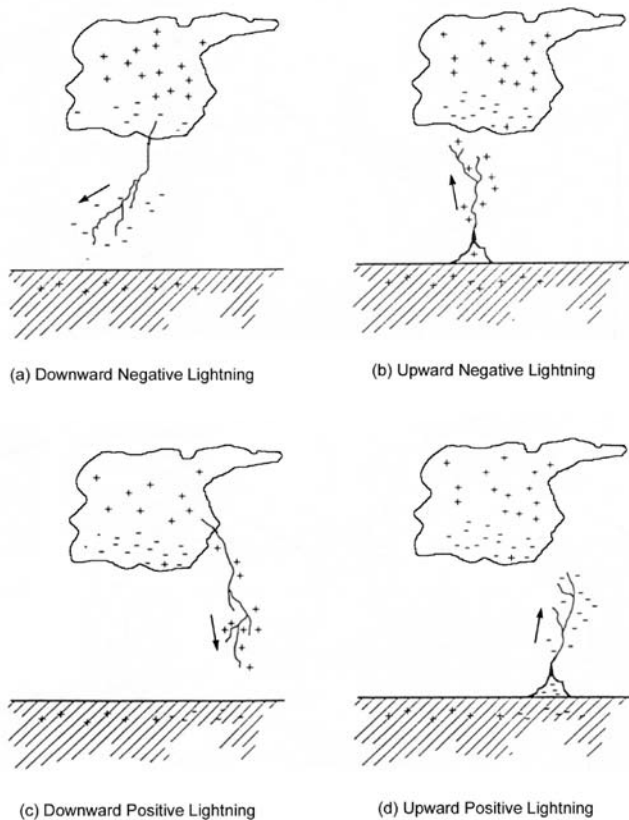


Figure 2-3. Four types of cloud-to-ground lightning discharge. Taken from *Rakov and Uman* [2003].

leader. The stepped leader serves to form a negatively charged plasma channel extending from the cloud toward the ground at an average speed of 2×10^5 m/s. As the leader approaches ground, one or several upward leaders, having positive charge, are initiated from the ground or from grounded objects (e.g., trees or other structures) and one of these upward leaders attaches to a branch of the downward-moving stepped leader at tens of meters above the ground surface. Once the two leaders have connected, a large surge of current, known as the first return stroke, travels at about one third to one half the speed of light (with speed generally decreasing with increasing height) from the ground toward the cloud charge source along the plasma channel neutralizing the negative leader charge. When the first-return stroke reaches the cloud, in-cloud discharge activity known as J (for junction) and K-processes occur in the cloud. The J-processes

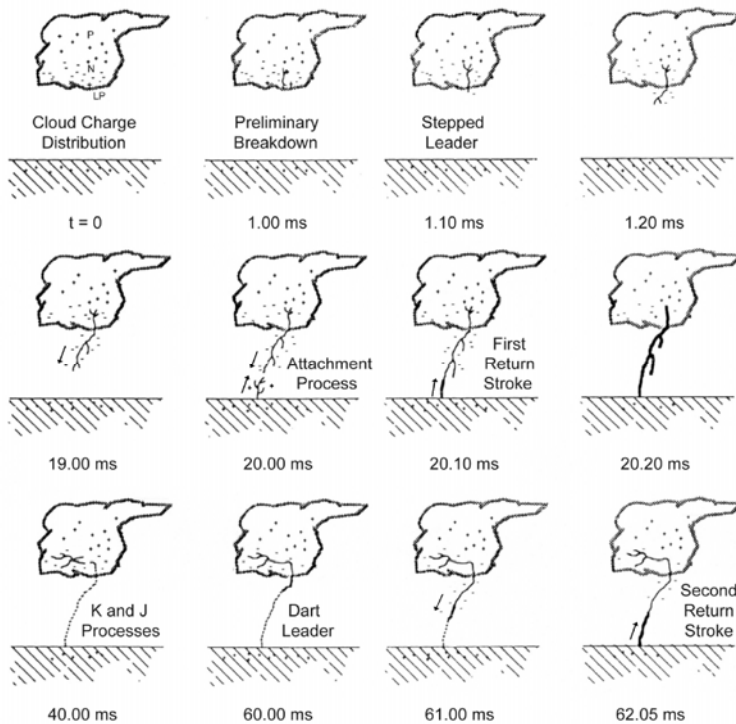


Figure 2-4. Various processes comprising a negative cloud-to-ground lightning flash. Adapted from *Uman* [1987].

result in redistribution of cloud charge in response to the preceding return-stroke and lasts for tens of milliseconds. K-processes are transients that occur during the slower J-process.

Following this in-cloud activity, often a new leader, known as a dart or dart-stepped leader, follows the path of the previous leader channel at an average speed of 10^6 - 10^7 m/s and does not exhibit stepping. As the dart or dart-stepped leader approaches ground, an attachment process similar to that for the first stroke takes place. However, the attachment process for subsequent strokes occurs over a shorter distance, takes less time and typically occurs when the upward leader is less than 10 meters in height. This is followed by the subsequent return-stroke wave that again neutralizes the leader charge deposited along the channel. The peak currents associated with the first and subsequent return strokes are about 30 kA and 15 kA, respectively.

Downward-positive flashes (type c), accounting for roughly 10% of the total cloud-to-ground discharges, transport positive charge from cloud to ground. The leader/return stroke process in downward positive discharges is similar to that of negative flashes. However, the peak currents and charge transfers associated with positive first strokes can be much higher than for negative first strokes. The highest directly measured lightning currents and the largest charge transfers to ground are thought to be associated with positive lightning [*Goto and Narita, 1995*]. Also, single-stroke positive flashes are much more common than single-stroke negative flashes. Positive lightning has been found to be related to sprites which occur in the middle atmosphere [*Boccippio et al., 1995*]. Positive lightning can be the dominant type of lightning during the dissipating stage of thunderstorms and during the cold season. Positive lightning discharges are characterized in Chapter 7 of this dissertation.

Upward lightning discharges (types b and d) are thought to occur only from tall objects (higher than 100 m or so) or from objects of moderate height on mountain tops. The initiation mechanism involved in an upward discharge is completely different from that in a downward flash. The first leader in an upward flash is initiated from the ground-based object and moves towards the cloud. This upward directed leader bridges the gap between the object and the cloud charge source or in-cloud discharge channel, forming a continuous path to ground through which a current, with a magnitude of typically several hundred amperes lasting for several hundred milliseconds called the initial continuous current (ICC), flows. This process is followed by subsequent dart leader/return stroke sequences which are similar to subsequent strokes of downward flashes. It may be mentioned here that rocket-triggered lightning (discussed in Section 2.4) is similar in phenomenology to the upward lightning discharge initiated from tall grounded objects.

Lightning discharges (flashes) that transfer to ground both positive and negative charges are termed bipolar lightning discharges. These discharges have not been well studied. The sparse data on bipolar lightning indicate that the majority of bipolar flashes is initiated by upward leaders from tall objects, events called "natural upward lightning" [Berger, 1978]. In the data of Berger [1978], obtained between 1963 and 1973 at Mount San Salvatore in Switzerland, bipolar flashes accounted for 72 out of 1196 observed flashes (6 percent). Rakov [2005], based on a review of literature, states that bipolar flashes may not occur less often than positive flashes, at least when tall objects are involved, with bipolar flashes constituting 6 to 14% of summer lightning in Europe and the United States and 3 to 33% of winter lightning in Japan. Jerauld *et al.* [2009] examined one unusual lightning flash, producing two channel terminations on ground and containing two strokes that lowered positive charge followed by four strokes that lowered negative charge. That bipolar lightning flash is the first well documented description of a natural downward bipolar lightning flash. Bipolar lightning discharges are examined in Chapter 7 of this dissertation.

2.2.1.1 Preliminary breakdown in ground discharges

In the electric field records of some cloud-to-ground discharges, a bipolar pulse train with pulses having the same initial polarity as the following return-stroke, durations of the order of tens of microseconds and preceding the first-return stroke pulse typically by tens of milliseconds is commonly attributed to preliminary breakdown.

The preliminary breakdown involves the formation of one or more channels in the cloud. In the latter case, the channels extend in seemingly random directions from the cloud charge source, with one of them evolving into the stepped leader that bridges the cloud charge source and the ground [e.g., Rakov and Uman, 2003, Ch. 4]. The preliminary breakdown process in ground flashes sometimes produces a train of relatively large microsecond-scale electric field

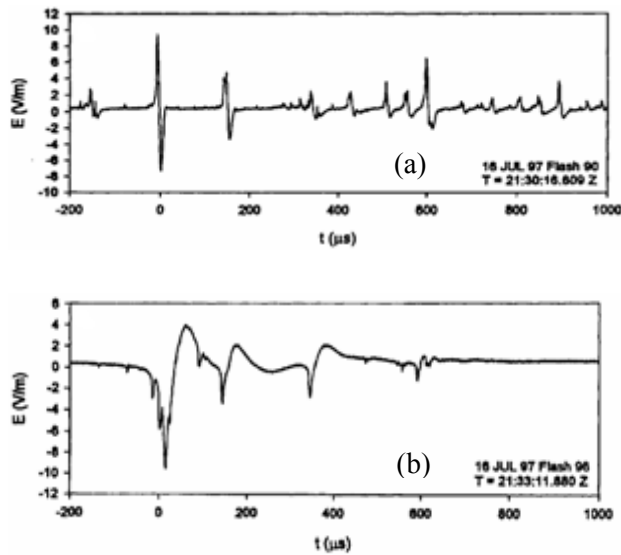


Figure 2-5. Examples of electric field pulse waveforms characteristic of (a) preliminary breakdown in negative ground flashes, (b) the active stage (initial breakdown) in cloud flashes. The waveforms have been recorded, from a distant storm, by D.E. Crawford at Camp Blanding, Florida. Adapted from *Rakov* [1999].

pulses, as illustrated in Figure 2-5a. The pulses are typically bipolar with the polarity of the initial half-cycle being the same as that of the following return-stroke pulse. The characteristic features of preliminary-breakdown pulse trains in negative cloud-to-ground flashes (based on information found in the literature) are as follows:

- Duration of the pulse train: The entire duration of the preliminary-breakdown pulse train is of the order of 1 ms [e.g., *Rakov*, 1999].
- Regularity of pulses in a train: This is a subjective feature, but it has been noted by many researchers. According to *Kitagawa and Brook* [1960] and *Weidman and Krider* [1979], regularity of preliminary-breakdown pulses and uniformity of time intervals between them in the case of cloud-to-ground flashes is higher than for cloud flashes.
- Overall pulse shape: Individual preliminary-breakdown pulses in the train are bipolar, as reported by many investigators [e.g., *Kitagawa*, 1957; *Clarence and Malan*, 1957; *Kitagawa and Kobayashi*, 1959; *Kitagawa and Brook*, 1960; *Krider and Radda*, 1975; *Weidman and Krider*, 1979; *Beasley et al.*, 1982; *Gomes et al.*, 1998; *Rakov*, 1999].
- Polarity of the initial half cycle: The initial polarity of bipolar pulses in the train of a negative cloud-to-ground flash is the same as that of negative return-stroke pulses [e.g., *Weidman and Krider*, 1979]. For the atmospheric electricity sign convention [e.g., *Rakov and Uman*, 2003, pp. 8-9] this polarity is positive. In contrast, for the initial breakdown in

cloud flashes, the dominant polarity of the initial half cycle of individual pulses is negative [e.g., *Rakov*, 1999].

- Overall pulse duration: According to *Rakov et al.* [1996], the typical total duration of individual pulses in the train is in the range of 20 to 40 μs . In contrast, for the preliminary breakdown in cloud flashes the typical total pulse duration is 50 to 80 μs .
- Interpulse interval: The typical time interval between individual pulses in the train is 70 to 130 μs , versus 600 to 800 μs for initial breakdown in cloud flashes [*Rakov et al.*, 1996].

The percentage of flashes exhibiting detectable preliminary breakdown pulse trains varies from less than 20% to 100% [e.g., *Clarence and Malan*, 1957; *Gomes et al.*, 1998; *Nag and Rakov*, 2008]. The time interval between the pulse train and the return-stroke waveform is typically a few tens of milliseconds. The amplitude of the preliminary breakdown pulses can be comparable to, or even exceed, that of the first return stroke pulse, which makes them capable of producing significant electromagnetic interference to the functioning of various airborne and ground-based circuits. The statistical distribution of the ratios of electric field peaks of the initial half-cycle of the largest preliminary breakdown pulse in a train and the corresponding first return-stroke pulse for 59 flashes analyzed by *Nag* [2007] is shown in Figure 2-6. (Those flashes occurred at distance ranging from a few to about 100 km.) The geometric and arithmetic means of the ratio are 0.45 and 0.62, respectively, with minimum and maximum values being 0.16 and 5.1, respectively. About 19% of the 59 preliminary breakdown pulse trains contain pulses whose peaks are greater than those of the corresponding first return strokes, although this percentage might be somewhat influenced by local noise level.

Nag and Rakov [2008] identified and examined lightning events exhibiting pulse trains that are characteristic of preliminary breakdown in negative cloud-to-ground discharges, but are not followed by return stroke waveforms. They referred to these events as "attempted first cloud-to-ground leaders". Preliminary breakdown in negative cloud-to-ground lightning and attempted leaders are examined in detail in Chapter 5 of this dissertation.

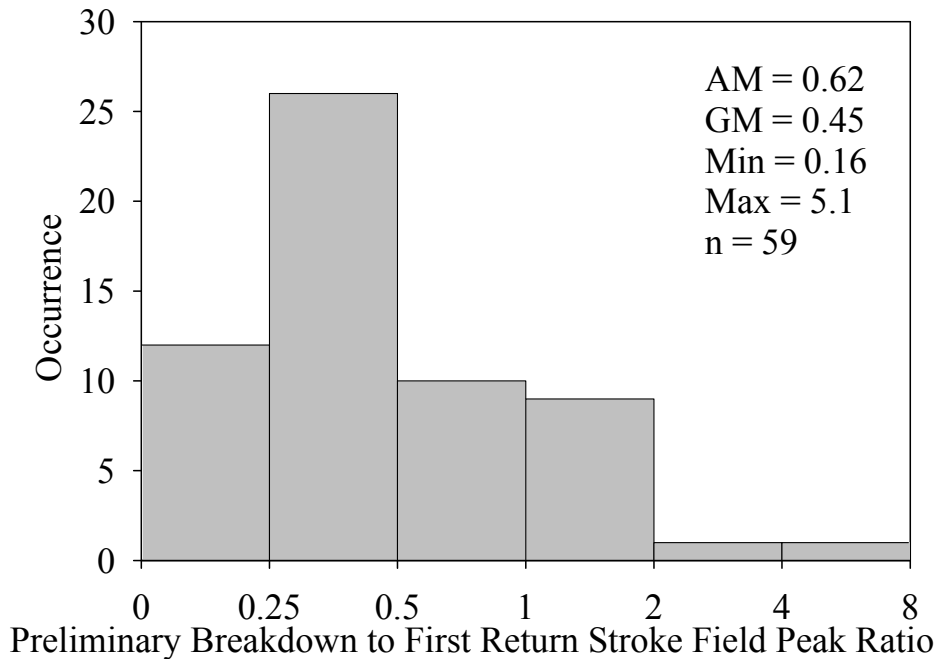


Figure 2-6. Histogram of the ratio of preliminary breakdown to first return stroke field peaks for individual flashes. Adapted from Nag [2007].

2.2.1.2 Electric and magnetic field waveforms from natural negative first strokes

Several studies have been conducted to examine first stroke electric fields in the range of tens to hundreds of kilometers [e.g. *Weidman and Krider*, 1978 in Florida and Arizona and *Cooray and Lundquist*, 1982 in Sweden]. Figure 2-7 shows “typical” electric and magnetic fields at distances ranging from 1 to 200 km from negative return strokes, published by *Lin et al.* [1979], which are drawings based upon many measurements obtained in Florida. The initial peak (when discernible) of the fields at each distance is essentially due to the radiation component and decreases inversely with distance in the absence of significant propagation effects [*Lin et al.*, 1980]. After some tens of microseconds, the electric and magnetic fields within a few kilometers are dominated by the electrostatic and magnetic induction components, respectively. Beyond 50 km or so, the both the electric and magnetic field waveshapes are bipolar and dominated by their respective radiation components.

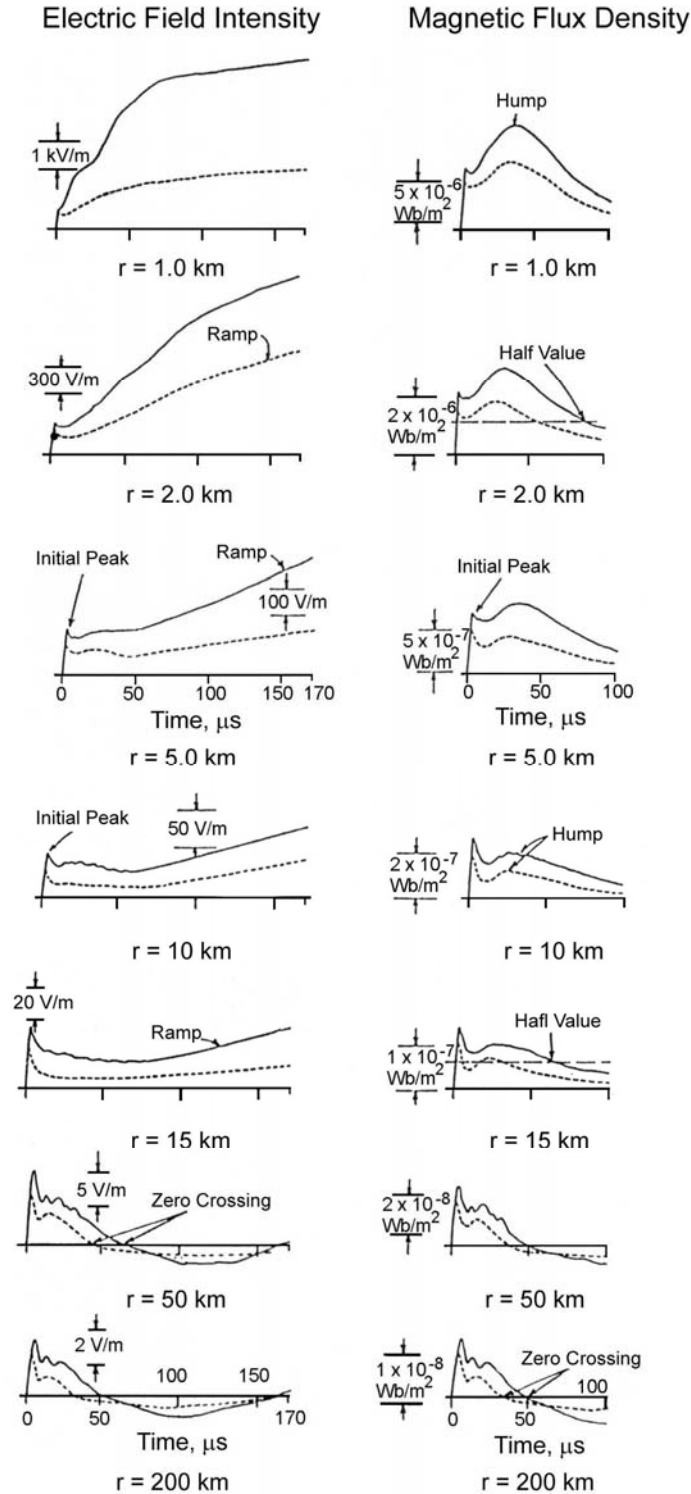


Figure 2-7. Typical vertical electric field intensity (left column) and azimuthal magnetic flux density (right column) waveforms for first (solid line) and subsequent (broken line) return strokes (leader waveforms not shown) at distances of 1, 2, 5, 10, 15, 50, and 200 km. Adapted from *Lin et al.* [1979].

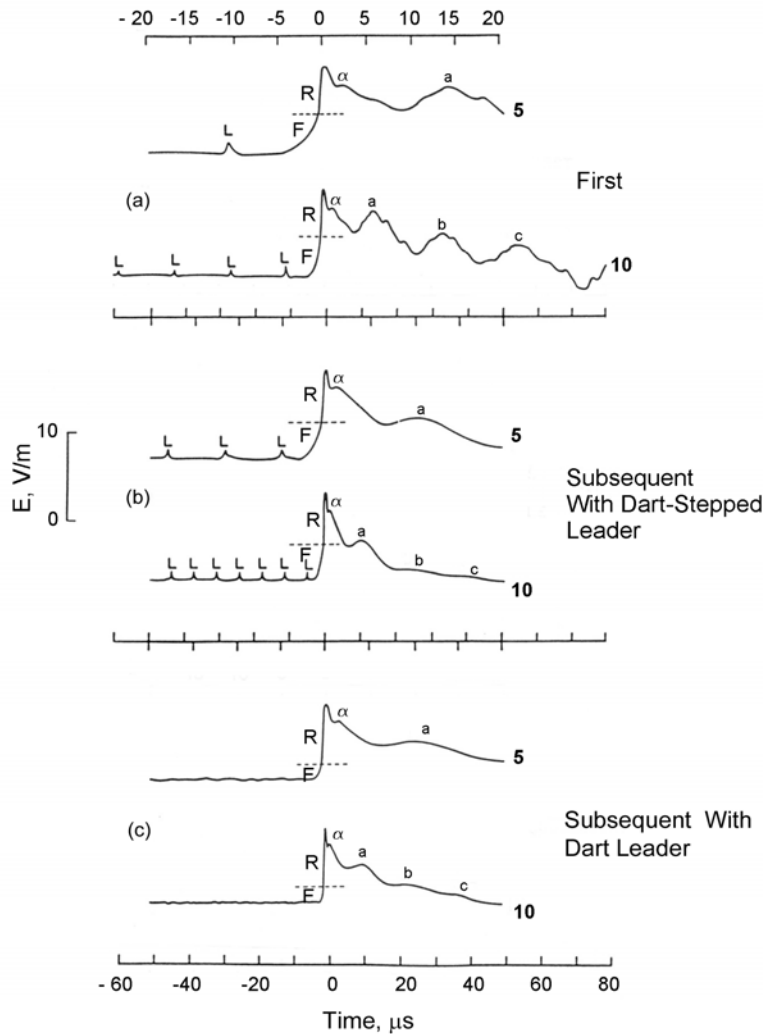


Figure 2-8. Electric field waveforms of (a) a first return stroke, (b) a subsequent stroke initiated by a dart-stepped leader, and (c) a subsequent return stroke initiated by a dart leader, showing the fine structure both before and after the initial field peak. Each waveform is shown on two time scales, 5 μs per division (labelled 5) and 10 μs per division (labeled 10). The fields are normalized to a distance of 100 km. Leader pulses (L), slow front (F), and fast transition (R) are indicated. Adapted from *Weidman and Krider* [1978].

The fine structure in the electric field waveforms of first and subsequent return strokes (Figure 2-8), was examined by *Weidman and Krider* [1978]. First-stroke fields can be separated temporally into two phases. The first one is the so-called “initial slow front,” or simply “slow front,” described by *Weidman and Krider* [1978] as an initial portion or front which rises slowly for 2–8 μs to about half the peak field amplitude. The second part which follows the slow front is

an abrupt transition to peak, typically referred to as the “fast transition,” having a 10-90% rise time of 0.2 μs or less when the field propagation was over seawater, according to *Weidman and Krider* [1978]. [*Weidman and Krider*, 1980 give a 10-90% rise time of 0.1 μs over seawater]. The shape of the slow front is typically concave, although *Weidman and Krider* [1978] do report some convex shaped fronts. The relative amplitude of the slow front and total peak field for first strokes is reported by *Weidman and Krider* [1978] to be 0.4-0.5, while *Cooray and Lundquist* [1982] and *Master et al.* [1984] give ratios of about 0.4 and 0.3, respectively. The corresponding first-stroke slow front durations are 4, 2.9, and 5 μs , respectively.

Weidman and Krider [1978] report that subsequent return strokes preceded by dart leaders also exhibit slow fronts, although they are generally smaller than those of first strokes, with the front amplitude to total field peak ratio being about 0.2. These subsequent return stroke field fronts are also of shorter duration, having a mean of 0.6–0.9 μs . Interestingly, subsequent return strokes preceded by dart leaders were reported to have fast transitions to peak field similar to those of first strokes, indicating that the primary distinction between first and these subsequent return strokes fields is the slow front. Finally, slow fronts from subsequent strokes preceded by dart-stepped leaders are also reported by *Weidman and Krider* [1978] to have front amplitude to peak field ratios similar to those of first strokes, but a mean duration of 2.1 μs , in between those of first (mean of 4 μs) and subsequent return strokes preceded by dart leaders (mean of 0.6–0.9 μs).

The origin of the slow-front current in first strokes has long been a matter of discussion. It has often been attributed to the presence of an upward connecting leader [e.g., *Rakov and Uman*, 2003, p. 144]. *Weidman and Krider* [1978] noted that “the shapes and relative amplitudes of the fronts and fast transitions in the current waveforms are surprisingly similar to those in the

radiated fields'' (currents and fields being measured in different studies). On the other hand, there are experimental data [Willett *et al.*, 1989a], although for triggered-lightning strokes, which suggest that radiation field waveforms can exhibit pronounced slow fronts without similar features in corresponding current waveforms. Other mechanisms of slow-front production have been considered by Weidman and Krider [1978], Thottappillil and Uman [1993], and Cooray *et al.* [2004]. According to Jerould *et al.* [2007] the source of the slow fronts observed in the currents and in the distant radiation fields of natural first strokes is likely to be a pair of microsecond-scale current waves, each having a peak of up to some tens of kiloamperes, propagating in opposite directions from the junction of the descending and upward connecting leaders at a speed on the order of 10^8 m/s.

In Chapter 6 of this dissertation results of the two-station measurements of natural and triggered lightning discharges are described. Return-stroke waveforms measured simultaneously at close (less than 1 km from the lightning channel) and distant (about 45 km from the lightning channel) stations are examined in order to gain additional insights into the origin of the slow front in return-stroke field waveforms.

2.2.2 Cloud Discharges

2.2.2.1 General information

Cloud discharges or ICs, constituting approximately three-quarters of all lightning discharges, do not contact ground. ICs have been less well studied than CGs because of the difficulty of securing photographic records of in-cloud channels and inability to obtain direct measurements of currents and charge transfers associated with ICs. Ground-based single- and multiple-station electric field measurements, as well as VHF lightning-channel imaging have been the primary means of studying ICs.

In general, cloud discharges are most likely to begin in the high electric field region near the upper boundary of the main negative charge, bridging the main negative and upper positive charge regions. However, they have been found to occur between the main negative charge region and the lower positive charge region (sometimes in hybrid flashes), in which case they are referred to as inverted intracloud discharges [*Qie et al.* 2005, *Tassendorf et al.*, 2007]. Cloud discharges can be viewed as being composed of an early or active stage and a late or final stage. The beginning of a cloud discharge is typically marked by the largest microsecond scale pulses in its wideband electric field record. According to *Villanueva et al.* [1994], the larger pulses tend to occur early in a flash and presumably are related to the flash initiating breakdown process. These early stage pulses are often referred to as initial-breakdown pulses. The transition from the early stage to the late stage of a cloud discharge is thought to be related to the disintegration of the channel existing between the main negative and upper positive charge regions.

The late stage, also called the J-stage, is physically similar to the J-process (junction process) in ground discharges. In the late stage, charge transport supposedly takes place from remote sources in the main negative charge region to the partially (or completely) neutralized negative charge center from where the negative channel originated during the initial stage. Various transient processes occurring during the late stage are referred to as K-processes.

Kitagawa and Brook [1960] portrayed the electric field signature of cloud lightning discharges as being composed of three stages, initial, very active and final. However, the three-stage structure was later replaced by the presently accepted two-stage model (described above) proposed by *Villanueva et al.* [1994]. *Villanueva et al.* analyzed microsecond-scale pulses in wideband electric field records of cloud flashes in Florida and New Mexico acquired using a 12-bit digitizing system with a 500 ns sampling interval. The average of the peak-to-peak amplitude

of the five largest pulses in a flash was found. All pulses with peak-to-peak amplitude greater than 50% of the average amplitude were labeled “large pulses”, pulses with amplitudes between 25% and 50% of the average amplitude were labeled “medium pulses”, and pulses between 12.5% and 25% of the average amplitude were labeled “small pulses”. The results of the analysis showed that about 60% and 50% of the large pulses occurred within the first 20 ms and 5 ms, respectively, of the flash suggesting that the large pulses were associated with the initial-breakdown process. Occurrence statistics of pulses in one of the electric field records in this study is shown in Figure 2-9. *Bodhika et al.* [2006] conducted a similar study of cloud flashes recorded in Sri Lanka and reported that about 80% of electric field pulses occurred in the early stage of the flash thus supporting the two stage structure of cloud discharges proposed by *Villanueva et al.* [1994]. However, in both the above cited studies, pulses that were smaller than 12.5% of the average amplitude [“in some flashes there were hundreds of them”, *Villanueva et al.*, 1994] were not included.

2.2.2.2 Initial breakdown in cloud discharges

Preliminary breakdown, often called initial breakdown, may be viewed as an in-cloud process that precedes and leads to the initiation of both cloud discharges and downward cloud-to-ground discharges. Cloud discharges can be viewed as being composed of an early (or active) stage having a duration of some tens to a few hundreds of milliseconds and a late (or final) stage that constitutes the remainder of the flash. In general, cloud discharges are most likely to begin with a negatively charged channel extending in an intermittent manner with an average speed of the order of 10^5 m/s. Overall, the early-stage processes in cloud lightning are probably similar to the initial breakdown and stepped leader processes in negative cloud-to-ground lightning.

The largest microsecond-scale electric field pulses tend to occur at the beginning of a cloud discharge [*Villanueva et al.*, 1994]. These pulses, in analogy to the preliminary breakdown

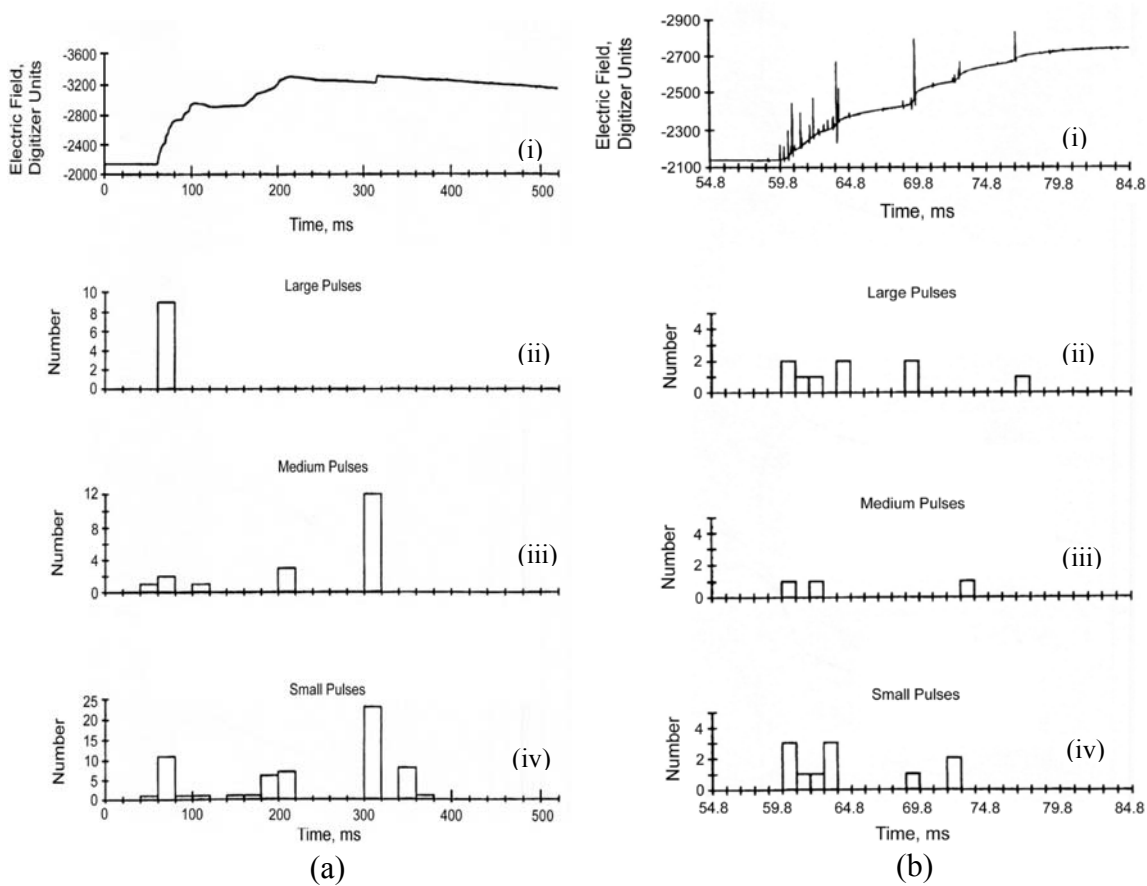


Figure 2-9. Occurrence statistics of electric field pulses in a cloud discharge. a. (i) Overall electric field record and histograms of occurrence of (ii) large, (iii) medium, and (iv) small electric field pulses in different parts of this record for cloud flash 64 on day 231 in 1991 at Kennedy Space Center, Florida. b. Same as (a) but for the first 25 ms of the flash. Adapted from *Villanueva et al.* [1994].

pulses in ground flashes (described in Section 2.2.1.1), are usually referred to as initial or preliminary breakdown pulses. These pulses are either relatively slow-rising, wide bipolar waveforms with several small pulses superimposed on the initial half cycle or relatively narrow or smooth singly-peaked or multiply-peaked bipolar waveforms [*Rakov, 2006*] as illustrated in Figure 2-5b. The initial polarity of the bipolar electric field pulses in cloud discharges is usually opposite to that of the preliminary-breakdown pulses in negative cloud-to-ground discharges, the latter pulses being usually of the same polarity as that of the following return-stroke pulse. Individual pulses in the early stage of cloud discharges are characterized by a typical total

duration of 50-80 μs and the typical time interval between pulses is 600-800 μs [Rakov *et al.*, 1996]. Kitagawa and Brook [1960] reported that cloud-flash pulses appeared in groups separated by intervals ranging from 0.3 to 10 ms.

Nag *et al.* [2009] examined microsecond- and submicrosecond-scale pulses in electric field records of cloud discharges acquired in summer 2006, in Gainesville, Florida and included all detectable pulses, including the smaller pulses ignored by Villanueva *et al.* [1994] and Bodhika *et al.* [2006], in the initial stage of cloud discharges. Figure 2-10 shows an example of the measured electric field waveform of a cloud discharge in their data set. In addition to “classical” initial breakdown pulses (see Figure 2-11a) having durations of the order of tens of microseconds, “narrow” pulses, having durations equal to or less than 4 μs (see Figure 2-11b), were also observed. Nag *et al.* [2009] found that the majority of pulses in the early stage of cloud discharges are typically small in both amplitude and duration. Further, they found that the amplitudes of these most common pulses are 50% or less than that of the largest pulse, and their durations are less than or equal to 4 μs . In contrast, total durations of “classical” initial breakdown pulses in cloud flashes are thought to be considerably longer, typically some tens of microseconds. Figure 2-12 shows the distribution of total durations of pulses in their 12 cloud flashes. One can see from this Figure that 85% (1125 out of 1323) of the pulses had durations less than or equal to 4 μs , of which 70% (783 out of 1125) were bipolar, and that 26% (338 out of 1323) of the pulses had durations less than 1 μs . The arithmetic mean pulse duration was 3.5 μs , which is outside the 50–80 μs range of typical durations usually given for “classical” initial breakdown pulses in cloud discharges [e.g., Rakov and Uman, 2003]. The discrepancy is apparently due to the inclusion of smaller pulses by Nag *et al.* [2009] that were ignored in

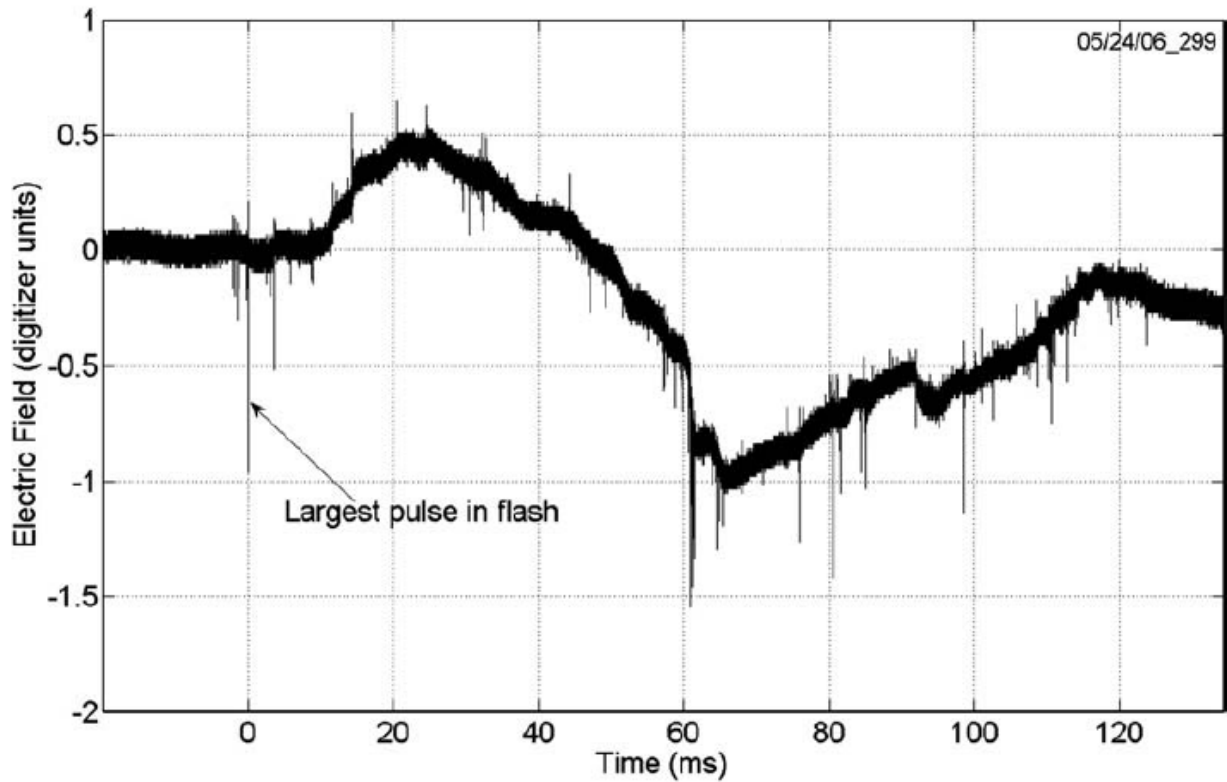


Figure 2-10. Electric field record of cloud flash 05/24/06_299. Taken from Nag *et al.* [2009].

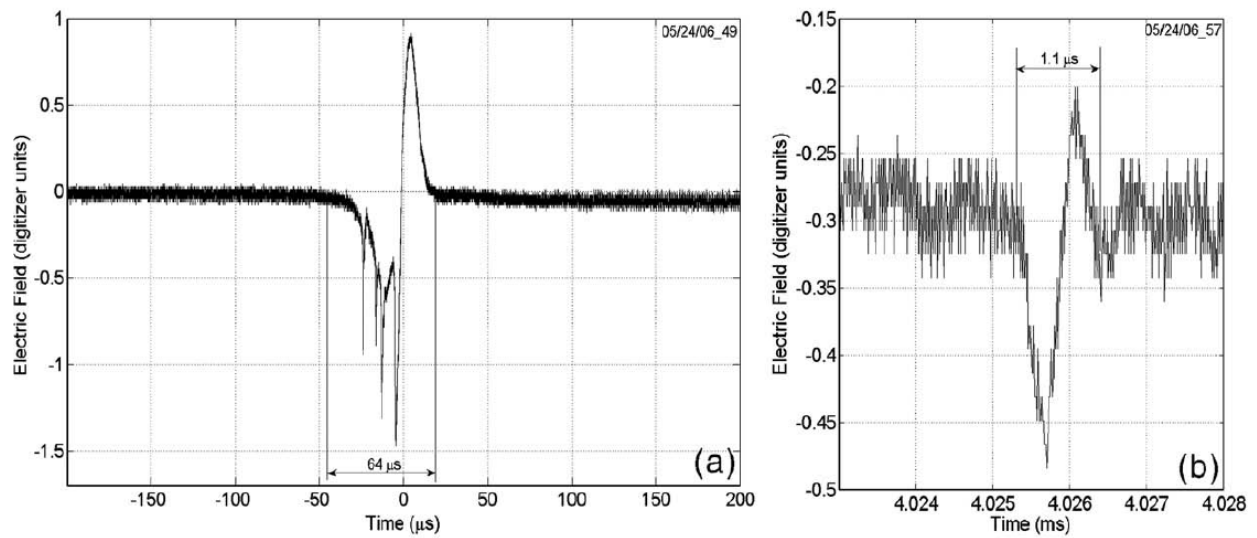


Figure 2-11. Examples of (a) “classical” and (b) “narrow” pulses in the early stage of cloud discharges. Taken from Nag *et al.* [2009].

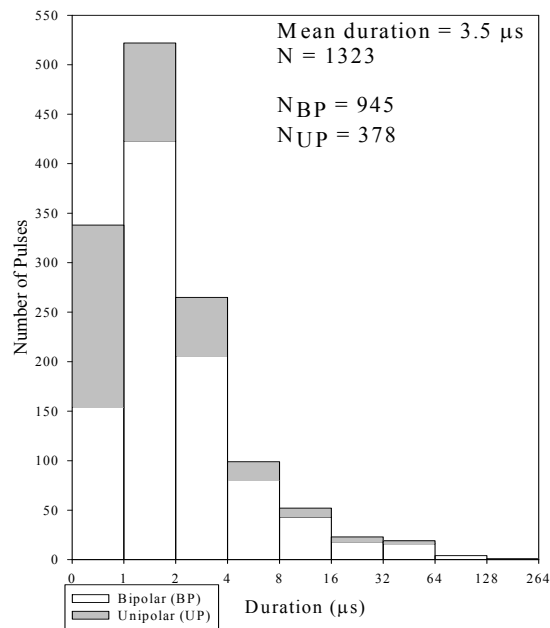


Figure 2-12. Histogram of total duration of unipolar and bipolar pulses in 12 selected cloud discharges. Adapted from Nag *et al.* [2009].

previous studies. In Weidman and Krider's [1979] study only a few (2 out of 137) negative pulses had durations less than 10 μs.

2.3 Lightning Initiation Mechanisms

One of the less understood areas in lightning research is the initiation mechanism of a downward lightning discharge. This is mainly because of the fact that the maximum electric fields typically measured in thunderclouds are 1 to 2 x 10⁵ V/m, which is an order of magnitude lower than the expected air breakdown field of the order of 10⁶ V/m. Also, there is a lack of optical records due to the in-cloud nature of this process. The detailed physics involved in the initiation of lightning is not yet understood. It may be thought of as a process which results in the formation of the first plasma channel within the cloud that may lead to either a cloud or a ground discharge depending on the configurations of charges involved and region of the cloud in which the breakdown is taking place.

Over the years a number of theories have been proposed in order to explain the physics behind the initiation mechanism of lightning. In this section, a brief review of the proposed lightning initiation mechanisms that involve either conventional or runaway air breakdown is presented. Both of these two mechanisms attempt to explain the formation of an ionized region, sometimes referred to as lightning seed, in the cloud that is capable of locally enhancing the electric field at its extremities thus leading to the formation of a self-propagating leader channel.

2.3.1 Conventional Breakdown

According to the conventional breakdown mechanism, lightning is initiated via the emission of positive corona from the surface of precipitation particles, highly deformed by strong electric fields in the case of raindrops, coupled with some mechanism whereby the electric field is locally enhanced to support the propagation of corona streamers. The most detailed hypothetical scenario of lightning initiation via conventional breakdown is described by *Griffiths and Phelps* [1976b] who consider a system of positive streamers developing from a point on a hydrometeor where the electric field exceeds the corona onset value of 2.5 to 9.5 x 10⁵ V/m (2.5 to 9.5 kV/cm). The developing streamers are assumed to form a conical volume that grows longitudinally. The ambient electric field in the thundercloud required to support the propagation of corona streamers, E_0 , was found by *Griffiths and Phelps* [1976a] from laboratory experiments to be 1.5 x 10⁵ V/m (1.5 kV/cm) at about 6.5 km and 2.5 x 10⁵ V/m (2.5 kV/cm) at about 3.5 km. If the ambient electric field is higher than E_0 , the streamer system will intensify, carrying an increasing amount of positive charge on the propagating base of the cone and depositing an equally increasing amount of negative charge in the conical volume. As a result, an asymmetric conical dipole is formed, which presumably can serve to enhance the existing electric field at the cone apex [*Rakov*, 2006].

Another hypothetical mechanism proposed by *Nguyen and Michnowski* [1996] involves a bidirectional streamer development assisted by a chain of precipitation particles, as opposed to the propagation of positive streamers alone.

2.3.2 Runaway Breakdown

Gurevich et al. [1999] suggested that runaway electrons may play an important role in lightning initiation. Energy gained by a runaway electron from the electric field between collisions with air particles, must be more than it loses in a collision. The runaway breakdown mechanism is associated with a current pulse having an amplitude of 100-200 A leading to the formation of a field-enhancing ionized region (“lightning seed”) by a cosmic ray particle with an energy of 10^{16} eV [*Gurevich et al.*, 2003]. The current pulse is predicted to generate a bipolar electric field pulse with a characteristic full width of 0.2-0.4 μ s [*Gurevich et al.*, 2002] which is more than an order of magnitude shorter than the shortest preliminary breakdown pulses, including so-called narrow bipolar pulses [e.g., *Rakov*, 2006] (see Section 2.5) that have characteristic full widths of a few tens of microseconds.

Submicrosecond-scale electric field pulses somewhat similar to the “lightning initiation pulses” predicted by *Gurevich et al.* [2002, 2003] have been observed as a part of preliminary breakdown in cloud and ground discharges by *Gurevich et al.* [2003] and by the University of Florida Lightning Research Group (see Figure 2-13) [*Rakov and DeCarlo*, 2005; *Rakov*, 2006]. However, the relation between the runaway breakdown mechanism proposed by *Gurevich et al.* [1999] and the occurrence of multiple submicrosecond-scale pulses is still unclear.

2.4 Rocket-Triggered Lightning

The rocket-and-wire technique is a method of artificially initiating a cloud-to-ground lightning flash. The technique involves launching a small rocket that extends upward a thin conducting wire, which can be grounded or ungrounded. If the wire is grounded, the flash is

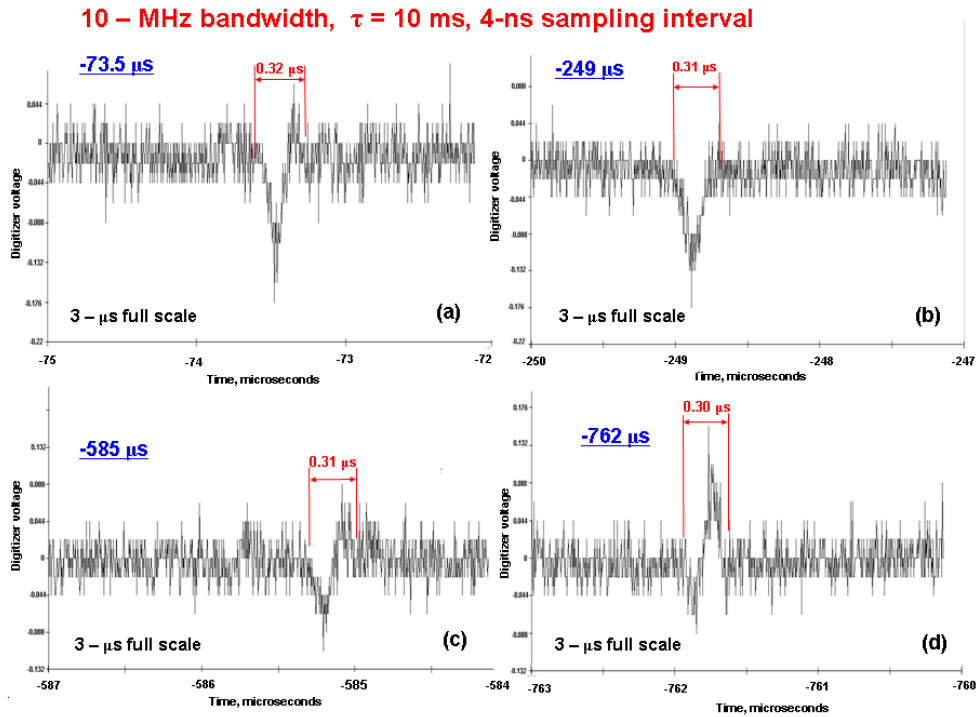


Figure 2-13. Submicrosecond-scale pulses that occurred in a cloud discharge. Taken from *Rakov and DeCarlo* [2005] and *Rakov* [2006].

usually referred to as “classical” triggered lightning. The primary distinction between natural cloud-to-ground lightning (described in Section 2.2.1) and classical rocket-triggered lightning is that the stepped-leader/first-return-stroke sequence in natural lightning is replaced by initial stage (the upward positive leader, involving destruction of the triggering wire, and initial continuous current) in classical triggered lightning. In fact, the phenomenology of classical triggered lightning is similar to that of upward lightning initiated by tall grounded objects [*Rakov and Uman*, 2003, Ch. 6].

The rocket is typically constructed from fiberglass or plastic and is about 1 m in length. The triggering wire is Kevlar-reinforced copper or steel of diameter about 0.2 mm and the spool can be mounted on either the rocket or the ground. The rocket is launched when thunderstorm conditions are deemed adequate, although these conditions may vary by region. The sequence of

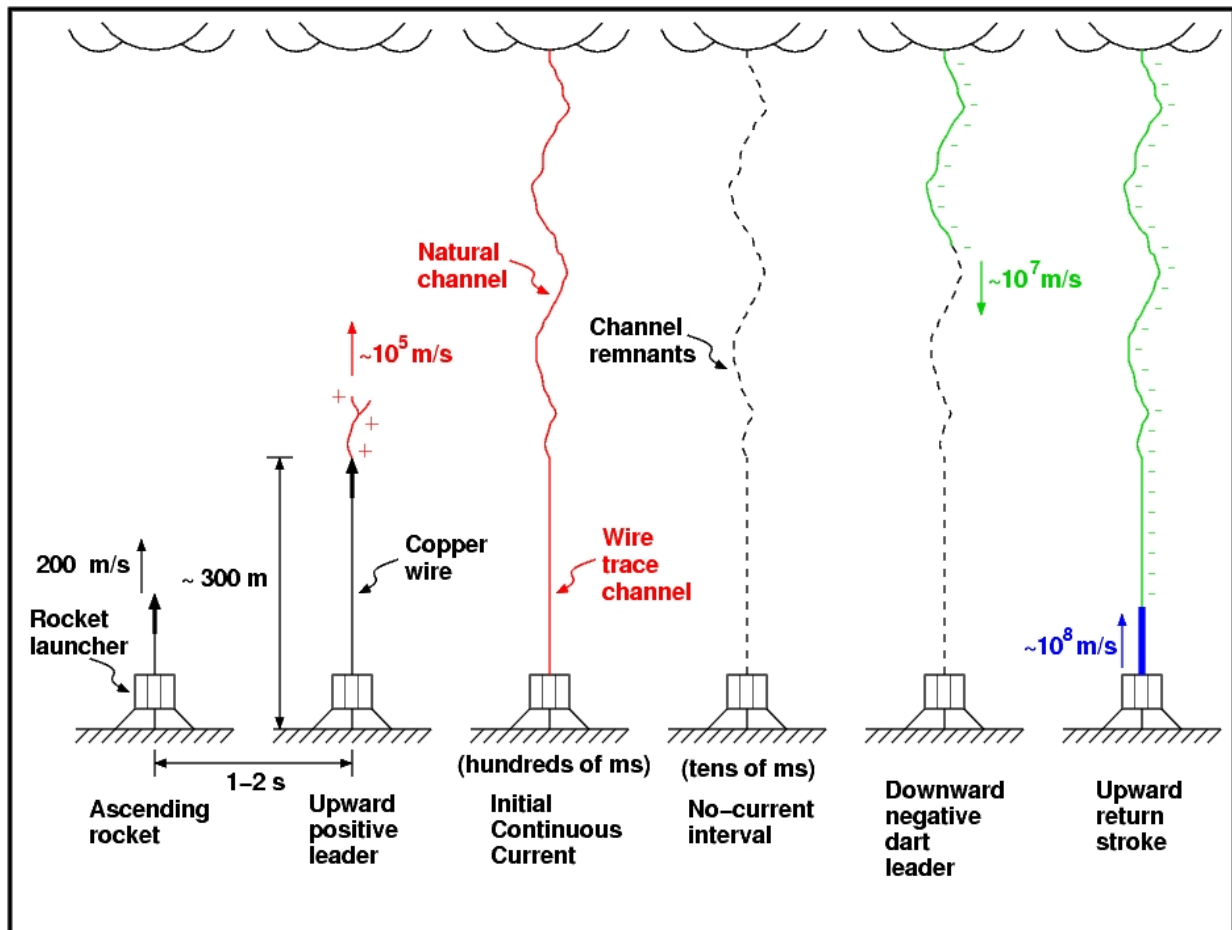


Figure 2-14. Sequence of events in classical triggered lightning. The upward positive leader and initial continuous current constitute the initial stage. Adapted from *Rakov et al.* [1998].

events in classical triggered lightning is shown in Figure 2-14. Under favorable conditions, i.e., when the measured static electric field on ground is sufficiently high (less than -5 kV/m for negative charge overhead), a rocket trailing a wire is launched. The average speed of the rocket is about 200 m/s , and when the rocket reaches about 300 m , a positively-charged upward leader (assuming a negative cloud charge source overhead) is initiated from the upper end of the wire. This leader has an average speed of about 10^5 m/s . The upward leader current vaporizes the triggering wire and the gap between the bottom of the leader and the ground is bridged by a plasma channel. The upward leader leads to establishing the initial continuous current (ICC)

which has a duration of some hundreds of milliseconds. The combined upward-leader and ICC processes are referred to as the initial stage (IS) of rocket-triggered lightning, which is similar to the initial stage in upward flashes initiated from tall towers [Miki *et al.*, 2005]. After a no-current interval of some tens of milliseconds, a downward-propagating negatively-charged dart leader may traverse the gap between cloud and ground at an average speed of about 10^7 m/s. When this dart leader makes contact with ground, an upward return stroke wave propagates up towards the cloud at a speed of the order of 10^8 m/s. After an interval of typically some tens of milliseconds, more strokes may follow. These leader/return-stroke sequence are thought to be very similar to subsequent dart-leader/return-stroke sequences in natural negative lightning [e.g., Fisher *et al.*, 1993].

Triggering with an ungrounded wire, having a gap of some hundreds of meters or more between the bottom of the conducting wire and ground, is usually referred to as “altitude” triggered lightning. In cases where the gap is only a few meters or less, it is typically not referred to as altitude triggering. The primary difference between classical and altitude triggered lightning techniques is that the latter is capable, to a degree, of reproducing a stepped leader followed by a first return stroke, whereas the classical method is not. In both cases, usually negative cloud charge is lowered towards ground. In altitude triggering, the bottom of the conducting triggering wire is typically isolated from a grounded “intercepting wire” by insulating Kevlar cable. The grounded intercepting wire and insulating Kevlar cable typically have lengths on the order of some tens and hundreds of meters, respectively. Unintentional altitude triggering can also occur as a result of accidental breakage of the wire during classical triggering. Since the triggering wire is ungrounded, the presence of a strong electric field (due to the overhead cloud charge source) results in the initiation of a bidirectional (positive charge up and negative charge down) leader

from opposite ends of the wire. When contact is made between the downward-stepped and upward-connecting leaders, the return stroke is initiated. However, this return stroke is dissimilar from both natural first and subsequent strokes, as well as strokes in classical-triggered lightning. The current waveform measured at ground appears to be “chopped” soon after reaching its peak value, and its width is appreciably smaller than that of the following return strokes. This phenomenon is presumably due to the return stroke front (having a speed on the order of 10^8 m/s) catching up with the upward-moving leader tip (which is still propagating towards the cloud at a speed of about 10^5 m/s) after $10\ \mu\text{s}$ or so, producing an opposite-polarity downward-moving reflected current wave that “chops” the current waveform measured at ground. This return stroke is referred to as an “initial-stage” return stroke [Rakov and Uman, 2003]. The leader/return-stroke sequences that follow this initial-stage stroke are thought to be similar those in classical triggered lightning. Although the altitude-triggering technique reproduces some features observed in natural stepped leaders and first return strokes, the complexity of the triggering process (e.g. the bidirectional leader and the reflected initial-stage return stroke wave) often makes it difficult to interpret the resulting data. Details of observations from altitude-triggered lightning can be found in *Laroche et al.* [1991], *Lalande et al.* [1998], *Rakov et al.* [1998], *Chen et al.* [2003], and *Saba et al.* [2005].

2.5 Compact Intracloud Discharges

Cloud lightning discharges that produce both (1) single, usually solitary bipolar electric field pulses having typical full widths of 10 to $30\ \mu\text{s}$ and (2) intense HF-VHF radiation bursts (much more intense than those from any other cloud-to-ground or “normal” cloud discharge process) are referred to as Compact Intracloud Discharges (CIDs). These discharges were first reported by *Le Vine* [1980] and later characterized by *Willett et al.* [1989b] and *Smith et al.* [1999, 2004], among others. Most of the reported electric field signatures of these discharges are

produced by distant (tens to hundreds of kilometers) events and hence are essentially radiation. The radiation field pulses produced by CIDs are referred to as Narrow Bipolar Pulses (NBPs). Close waveforms that are dominated by the induction and electrostatic field components were reported before this study only once [Eack, 2004]. Both polarities of the initial half-cycle of the NBPs have been observed, with negative polarity (atmospheric electricity sign convention, according to which a downward-directed electric field vector is assumed to be positive) being more frequent. The term "CID" was coined by *Smith et al.* [1999] who inferred that the spatial extent of these discharges must be relatively small, 300 to 1000 m. CIDs tend to occur at relatively large altitudes, typically more than 10 km [Smith et al., 2004], while *Light and Jacobson* [2002] reported that CIDs often produced no optical emission observable by FORTE satellite. A recent summary of ground-based and space observations of CIDs is given by *Hamlin et al.* [2009].

Le Vine [1980], who used an electric field measuring system triggered when the associated HF-VHF signal, in the range from 3 to 300 MHz, exceeded a relatively high threshold level, reported observations of narrow bipolar electric field pulses that have been recorded in conjunction with their associated HF-VHF radiation. The initial polarity of the bipolar pulses was negative (atmospheric electricity sign convention), that is, opposite to that of electric field pulses due to return strokes in negative cloud-to-ground lightning. The pulse amplitudes were of the order of one-third those of the return stroke peaks recorded at about the same time. *Le Vine* [1980] attributed the observed narrow bipolar pulses accompanied by strong HF-VHF radiation to K processes, a hypothesis not confirmed by subsequent studies.

Willett et al. [1989b], working at KSC in 1985 and 1987, obtained recordings of both electric field (E) and electric field derivative (dE/dt) for narrow bipolar pulses. Their measuring

system was triggered by the output of an HF receiver that could be tuned to any center frequency between 3 and 18 MHz. Both polarities of the initial half-cycle of the narrow bipolar pulses were observed, with negative polarity (atmospheric electricity sign convention) being more frequent. For 18 waveforms, *Willett et al.* [1989b] estimated arithmetic mean values of E and dE/dt peaks normalized to 100 km of 8 V/m and 20 V/m/ μ s, respectively. Both values are comparable to their counterparts for first return strokes observed in the same experiment. The overall pulse width was 20 to 30 μ s. Spectral analysis indicated that the sources of the narrow bipolar pulses radiated much more strongly than first return strokes at frequencies from 10 to at least 50 MHz. At 18 MHz the energy-spectral density (measured in $(\text{V m}^{-1} \text{ Hz}^{-1})^2$) for these pulses was nearly 16 dB higher than that for first return strokes at the same distance.

Smith et al. [1999], who used a multiple-station electric field change measuring system in concert with an HF (3 to 30 MHz) time-of-arrival (TOA) lightning locating system, presented a detailed characterization of the narrow bipolar pulses in three thunderstorms at distances greater than 80 km in New Mexico and west Texas, including locations of their sources in the cloud. The characteristics of the 24 narrow bipolar electric field pulses (see for example, Figure 2-15) and associated HF (3 to 30 MHz) radiation studied by *Smith et al.* [1999] are summarized in Table 2-1. *Smith et al.* [1999] reported that the pulse peaks were comparable to those of return-stroke waveforms. Nearly all pulses studied by *Smith et al.* [1999] were the only events within the field record having a length of typically 4 to 10 ms. The HF (3 to 30 MHz) emissions associated with narrow bipolar pulses had a duration of only a few microseconds and were typically 10 times more powerful than the HF emissions from “normal lightning discharges.”

CIDs have recently attracted considerable attention because (a) they are likely to be the strongest natural producers of HF-VHF radiation [e.g., *Thomas et al.*, 2001], (b) they are

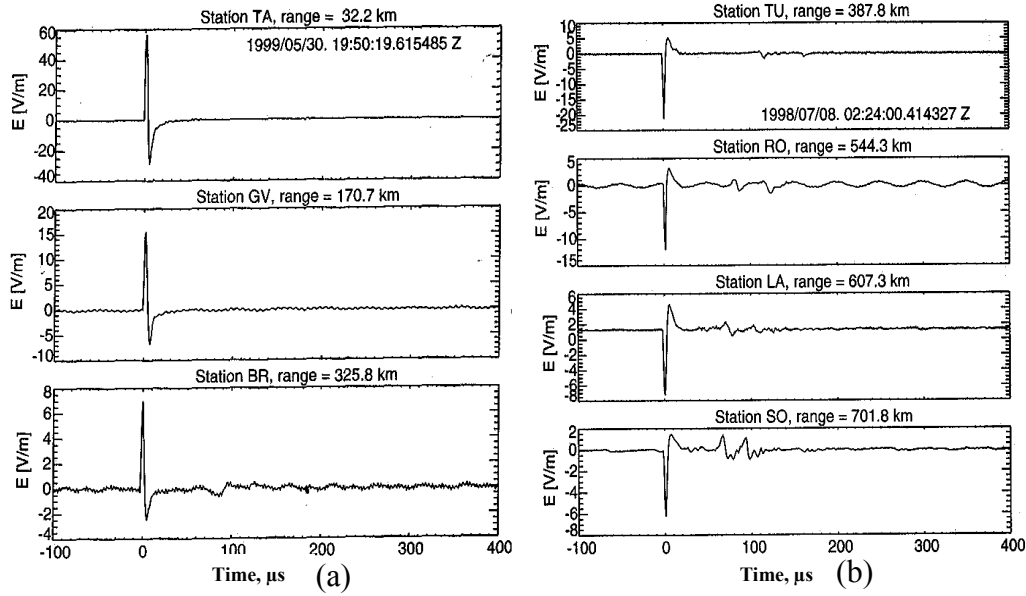


Figure 2-15. Narrow bipolar pulses recorded by the Los Alamos Sferic Array (LASA). (a) Narrow positive bipolar pulses (positive NBPs) from a discharge that occurred 32 km northwest of Tampa, Florida. Physics sign convention is used here. (b) Narrow negative bipolar pulses (negative NBPs) from a discharge that occurred in Oklahoma. Adapted from *Smith et al.* [2002].

Table 2-1. Characteristics of narrow bipolar electric field pulses and associated HF (3-30 MHz) radiation reported by *Smith et al.* [1999].

Electric Field Pulse Characteristics	Mean \pm Std. Dev.
Risetime (10-90 percent)	$2.3 \pm 0.8 \mu\text{s}$
Half-peak width	$4.7 \pm 1.3 \mu\text{s}$
Pulse duration	$25.8 \pm 4.9 \mu\text{s}$
Initial peak ^a	$9.5 \pm 3.6 \text{ V m}^{-1}$
Opposite polarity overshoot ^a	$-3.9 \pm 1.6 \text{ V m}^{-1}$
Ratio of initial peak to opposite polarity overshoot	2.7
Ratio of peaks for narrow bipolar pulses and return-stroke pulses	0.71
Ratio of peaks for narrow bipolar pulses and cloud-flash pulses	2.6
HF Radiation Characteristics	Mean \pm Std. Dev.
Duration	$2.8 \pm 0.8 \mu\text{s}$
Peak ^b	$2.4 \pm 1.1 \text{ mV m}^{-1}$
Ratio of peaks for narrow bipolar pulses and return-stroke pulses	9.9
Ratio of peaks for narrow bipolar pulses and cloud-flash pulses	29

^a Normalized to 100 km; physics sign convention.

^b Normalized to 10 km and 1 kHz bandwidth.

considered the prime candidate for proposed satellite-based VHF global lightning monitors [e.g., *Wiens et al.*, 2008] and (c) they are thought to involve the runaway electron breakdown [e.g., *Gurevich and Zybin*, 2004; *Gurevich et al.*, 2004; *Tierney et al.*, 2005].

Watson and Marshall [2007] used the original transmission line (TL) model [*Uman et al.*, 1975] and a modified TL model with an exponentially increasing current along the channel to compute electric field signatures at horizontal distances of a few and 200 km and compare them with corresponding measured waveforms reported by *Eack* [2004]. Both models can successfully match the two-station field measurements. The exponentially increasing current was assumed by *Watson and Marshall* to correspond to the runaway breakdown process. The original TL model was also employed by *Le Vine* [1980].

In Chapter 4 of this dissertation, new experimental data that are needed for testing the validity of various models of CID are presented. Further, we propose a conceptual mechanism for this phenomenon and present a model based on this mechanism for computing electromagnetic field signatures of CIDs. Electrical parameters of CIDs are also inferred.

CHAPTER 3 EXPERIMENTAL SETUP

3.1 The Lightning Observatory in Gainesville

Measurements of electromagnetic signals from lightning discharges have been performed in Gainesville, on the University of Florida campus, since 2004. Over the years the experimental setup has undergone upgrades, modifications, expansions, and relocation. From 2004 to 2007 the instrumentation was located on the roof and in a closet on the third floor of Benton Hall ($29^{\circ} 38' 37.77''$ N, $82^{\circ} 20' 50.00''$ W), a three-storey building on the University of Florida campus. In 2004, the experimental setup was operated by Brian DeCarlo. The experimental setup in 2005-2007 is described in detail in *Nag* [2007]. In 2004 and 2005, the system included only wideband electric field measurements. In 2006 and 2007, the measurement station was gradually expanded to include, in addition to wideband electric field, electric field derivative (dE/dt), narrowband high frequency (HF) and very high frequency (VHF) measurements. In March 2008 the experimental setup was relocated to the roof of the five-storey New Engineering Building (Building # 33) on the University of Florida campus and named the Lightning Observatory in Gainesville (LOG) ($29^{\circ} 38' 32.27''$ N $82^{\circ} 20' 49.70''$ W). The Lightning Observatory (see Figure 3-1), where all instrumentation is presently located, includes a glass cupola providing over a 180 degree unobstructed view of the horizon. The cupola houses digitizing oscilloscopes, with the sensors being located nearby on the roof. In April-May 2008, additional electric field and dE/dt antennas, a new magnetic field derivative (dB/dt) antenna, and an x-ray sensor were added to the existing experimental setup. Figure 3-2 shows the Google Earth image of the LOG in 2008. Approximate locations of different sensors are shown with different symbols on the image.



Figure 3-1. The Lightning Observatory on the roof of the Engineering Building on the University of Florida campus at Gainesville.

3.2 Overview of Experiments

3.2.1 Single-Station Experiment

The purpose of this experiment was to obtain correlated wideband electric field, electric field derivative, magnetic field derivative, and narrowband very high frequency signatures (labeled E2, dE2, dB, and VHF, respectively, in Figures 3-2 and 3-3) of cloud and ground lightning discharges. Note that prior to April 2008, a narrowband high frequency (HF) measurement system was also a part of this experimental setup. It is not shown in Figures 3-2 and 3-3, which are for post-April 2008. The measuring system settings allowed one to detect

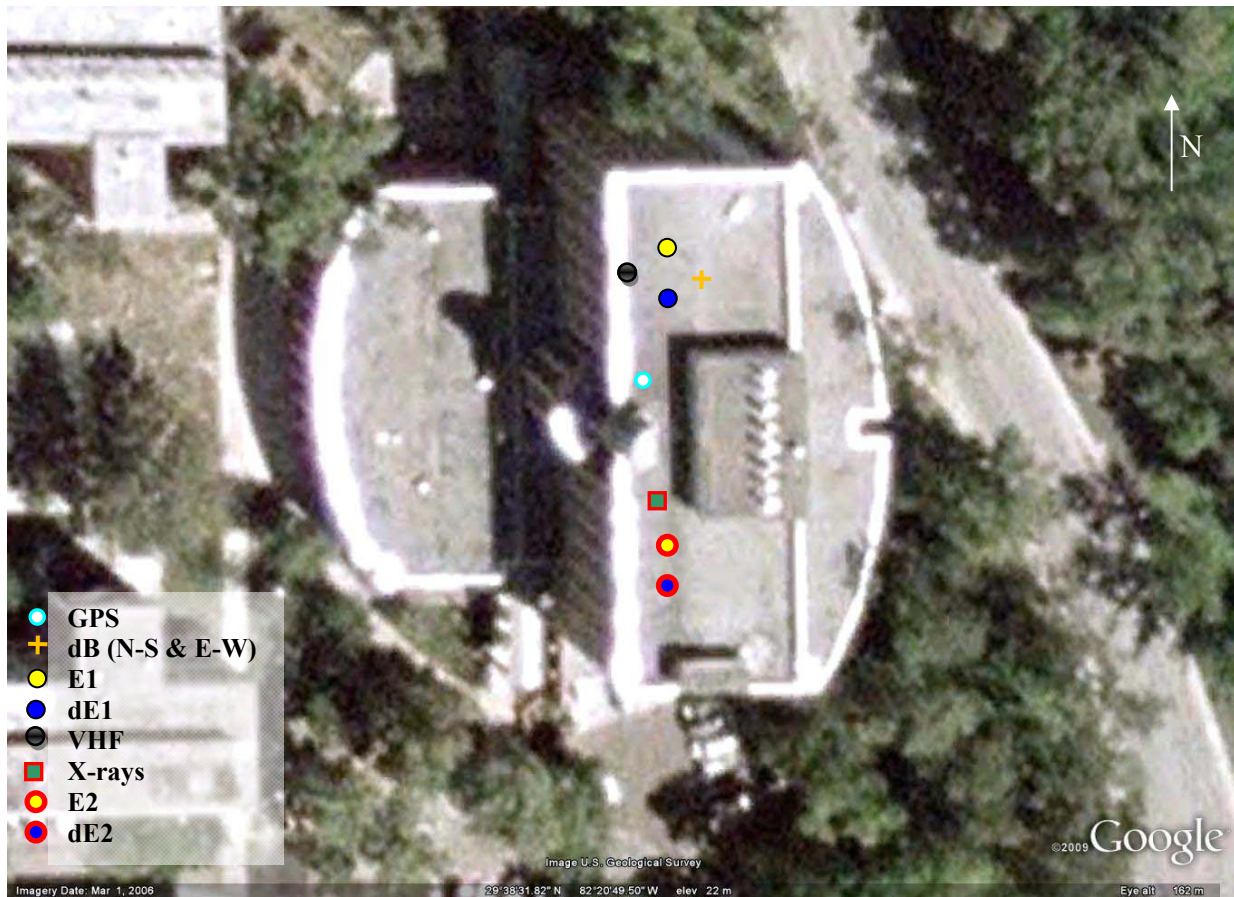


Figure 3-2. Google Earth image of the LOG in 2008. Approximate locations of different sensors are shown with different symbols on the image. E1, E2, dE1, dE2, dB, VHF, and X-ray are the electric field (two-station experiment), electric field (single-station experiment), electric field derivative (two-station experiment), electric field derivative (single-station experiment), magnetic field derivative (both experiments), VHF (single-station experiment) and x-rays (single-station experiment) sensor, respectively. Also shown is the location of the GPS antenna.

electromagnetic signals from lightning discharges occurring at distances ranging from a few to about 100 km from the measuring station. The primary focus was on studying preliminary breakdown pulse trains in negative cloud-to-ground discharges and compact intracloud discharges (CIDs). In addition, correlated wideband electric field, and electric and magnetic field derivative measurements of positive, bipolar, and negative cloud-to-ground lightning from thunderstorms in and around Gainesville were also acquired. In May 2008, an x-ray sensor provided by Dr. J. Dwyer of the Florida Institute of Technology was installed for measuring

high-energy radiation from close (within 1 km) cloud-to-ground lightning. X-ray measurements (none were acquired as of November 2008) are outside the scope of this dissertation and will not be further discussed here.

Figure 3-3 schematically shows positions of the different sensors used in this experiment. These sensors, grouped by experiment, are listed in the Table 3-1. Figure 3-4 shows the block diagram of the single-station experiment.

3.2.2 Two-Station Experiment

This experiment was designed to measure field waveforms (primarily radiation) at the Gainesville station due to natural and rocket-triggered lightning at Camp Blanding, Florida. The Gainesville and Camp Blanding measuring stations are 45 km apart. The measuring system at Gainesville is externally triggered in synchronization with the triggering of the Camp Blanding system. An AT&T BellSouth analog conditioned telephone line was used to transmit a trigger pulse generated at Camp Blanding (near station) in response to lightning strikes on-site or in its immediate vicinity, to Gainesville (distant station). The transmission time of the trigger pulse from Camp Blanding to Gainesville was measured in 2007 (when the measuring station was located at Benton Hall) and in 2008 (after relocation to the Engineering Building) and was found to be approximately 29 ms in both cases. This means that the lightning event producing the trigger at Camp Blanding triggers the system in Gainesville with a 29-ms delay. The effect of the transmission delay of the trigger pulse is countered by choosing the pretrigger time of the oscilloscope to be greater than this transmission delay.

This experiment enables simultaneous measurements of near (hundreds of meters from lightning channel) and distant (about 45 km from lightning channel) fields from the same cloud-to-ground discharge. A detailed description of the configuration of the two-station experiment is given in Section 3.14. The experimental setup included electric field, electric field derivative,

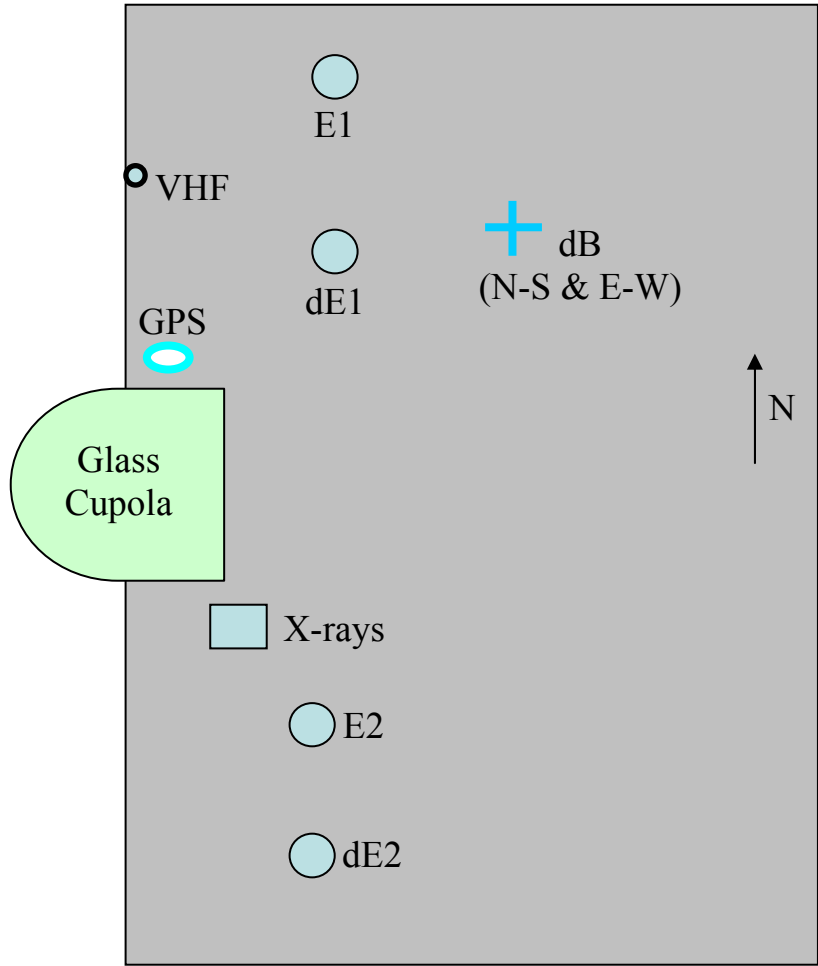


Figure 3-3. Schematic showing positions of the different sensors at the LOG in 2008. The use of sensors in different experiments is indicated in Table 3-1.

Table 3-1. A list of LOG sensors (see Figure 3-3) used in two-station and single-station experiments.

Two-station experiment	Single-station experiment (stand-alone mode)	Remarks
1. E1	1. E2	Wideband vertical electric field
2. dE1	2. dE2	Electric field derivative
3. dB (N-S)	3. dB (N-S)	Magnetic field derivative (north-south component)
4. dB (E-W)	4. dB (E-W)	Magnetic field derivative (east-west component)
	5. VHF	Narrowband (36 MHz) VHF radiation
	6. X rays	NaI x-ray detector

and magnetic field derivative measurements labeled E2, dE2, and dB, respectively, in Figures 3-2 and 3-3, which show positions of the corresponding sensors. These sensors are listed in Table 3-1. Figure 3-5 shows the block diagram of the two-station experiment.

3.2.3 Equipment

The equipment used in the two experiments discussed in Sections 3.2.1 and 3.2.2, included sensors, fiber optic links, digital storage oscilloscopes, GPS time stamping system, and a dedicated phone line. The sensors used for each measurement are described in Sections 3.3 to 3.7. The characteristics of the other equipment used are described in the following subsections.

3.2.3.1 Fiber optic links

Opticomm MMV-120C fiber-optic links are being used at the LOG. The Opticomm MMV-120C fiber-optic links utilize frequency modulation (FM) with a carrier frequency of 70 MHz and operate at an optical wavelength of 1310 nm. The Opticomm links were intended by the manufacturer to be used as video fiber-optic links and therefore had an input and output resistance of 75 Ω (the standard resistance for video equipment). However, they were modified to match the performance characteristics (impedance and bandwidth) required for lightning experiments at the ICLRT at Camp Blanding, Florida. The transmitter has an input impedance of 68 k Ω and the receiver has an output impedance of 50 Ω . The bandwidth (-3 dB) of the link is from DC to 30 MHz, as specified by the manufacturer. The manufacturer lists the signal-to-noise ratio to be about 67 dB, however this value is acquired using the short-haul RS-250C standard in which the signal is low-pass filtered with a cut-off frequency of about 5 MHz. Thus, 67 dB may not be an accurate representation of the true signal-to-noise ratio over entire bandwidth. In practice, the signal-to-noise ratio over the entire bandwidth is several dB lower than the value obtained under the short-haul RS-250C standard.

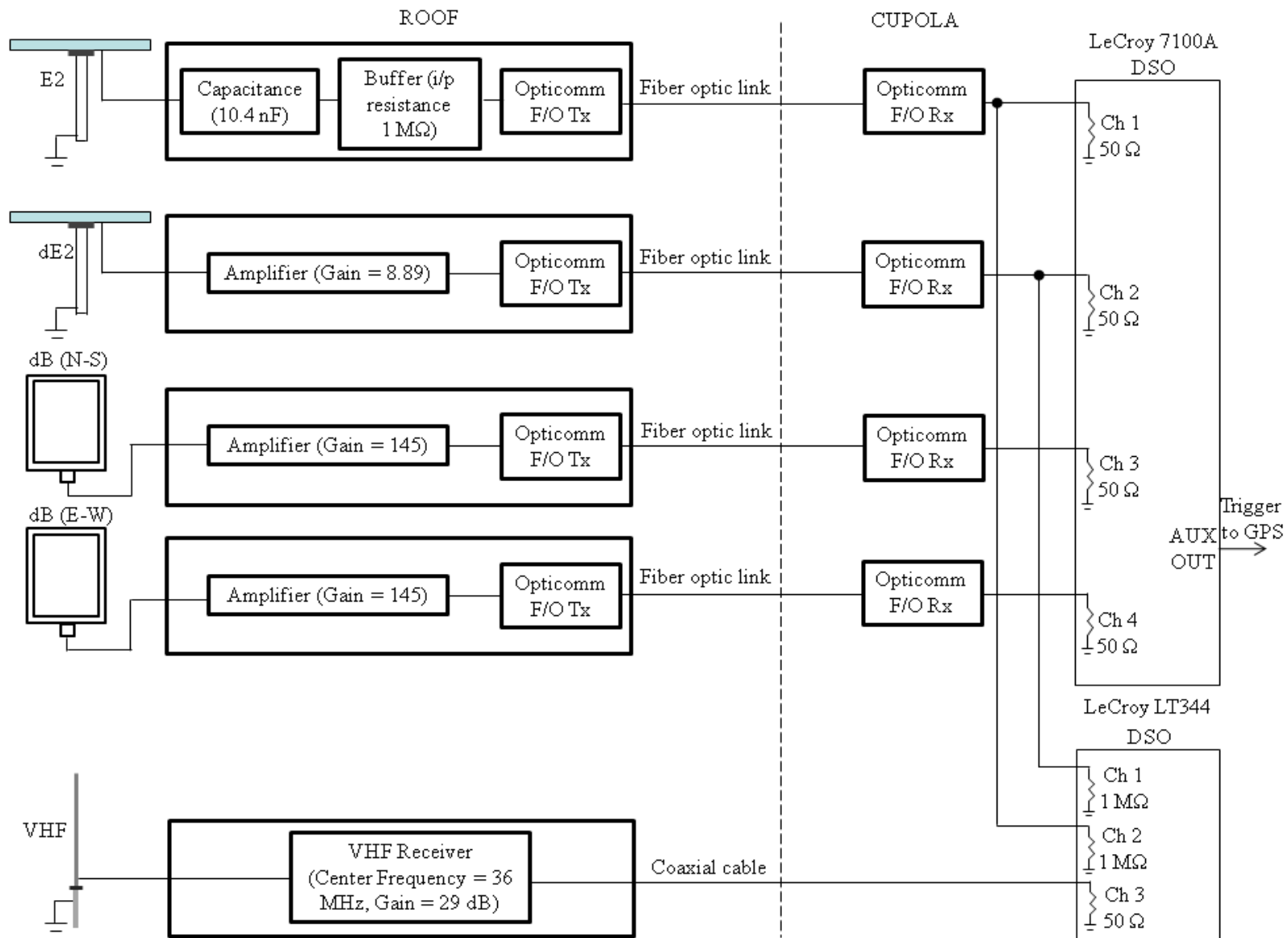


Figure 3-4. Block diagram of the single-station experiment.

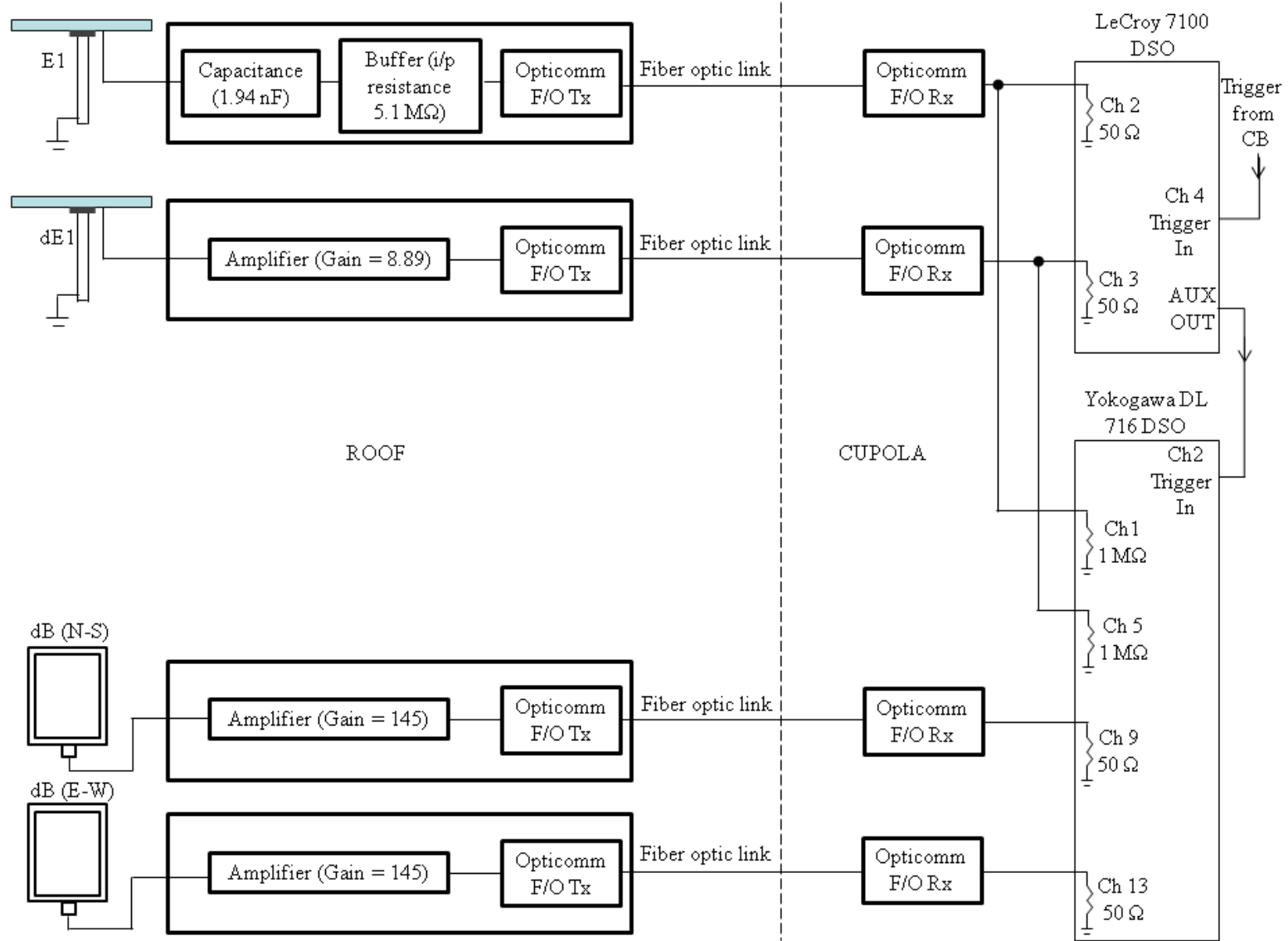


Figure 3-5. Block diagram of the two-station experiment.

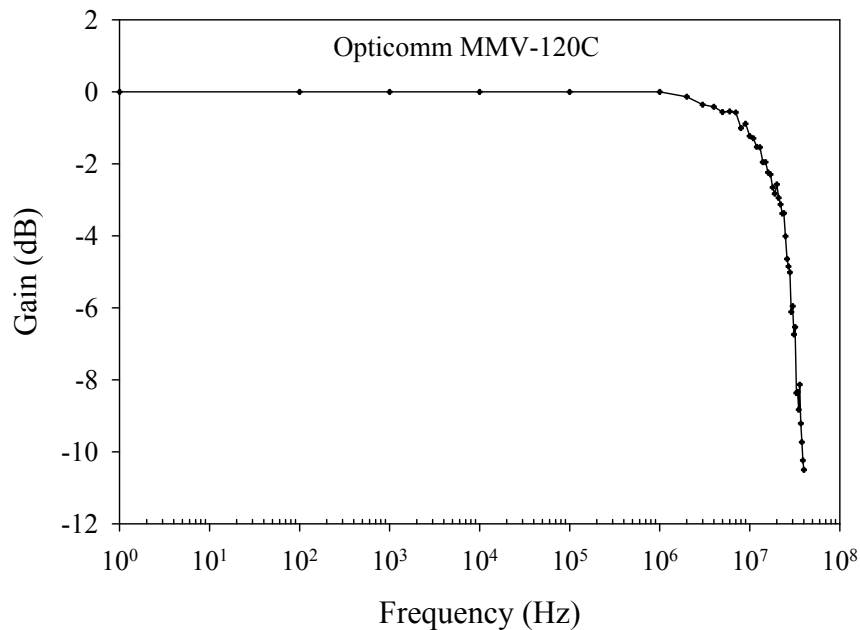


Figure 3-6. Frequency response of an Opticomm MMV-120C fiber-optic link used at the LOG.

The Opticomm links utilize 62.5/125 μm (core/cladding) graded index multi-mode fiber-optic cable with ST connectors purchased from Fiber Instrument Sales, Inc. Figure 3-6 shows the measured frequency response for an Opticomm MMV-120C fiber-optic link (with a 50 m long fiber) used at the LOG. The Opticomm links were calibrated using a 100 Hz, 1 V peak-to-peak square wave.

3.2.3.2 Digital storage oscilloscopes

Four digital storage oscilloscopes (shown in Figure 3-7) were used at the LOG in 2008. The various characteristics of each of the oscilloscopes are given below. Specific oscilloscope configurations are given in Tables 3-2 and 3-3.

LeCroy WavePro 7100: The LeCroy WavePro 7100 is a four-channel DSO with a maximum bandwidth of 1 GHz at a maximum sampling rate of 10 GHz with an 8-bit vertical resolution. The maximum sampling rate is 20 GHz when operating in the 2-channel mode. The WavePro 7100 is capable of recording 24 megabyte per channel when all four channels are in use. Hence

Table 3-2. Digital storage oscilloscope used at the LOG prior to April 2008.

DSO Type	Experiment	Measurements	Record length (ms)	Pre-trigger time (ms)	Sampling rate (MHz)	Trigger mode and input	Comment
LeCroy 7100	Single-station/Two-station experiment	E, dE/dt, HF, VHF	480	100	100	Threshold trigger on E/Threshold trigger on signal from Camp Blanding	Used for both experiments, manually switched between triggering modes

with an 8-bit resolution (that is one byte required to store each sample) the total record length is 24 megasamples for each of the 4 channels. At a maximum sampling rate of 10 GHz, the maximum record length is 2.4 ms. The WavePro 7100 uses the Microsoft Windows 2000 Professional (SP 4) operating system and has a flat panel touch-screen display. The processor memory is 1024 MB and the processor speed is 1.7 GHz. The recorded data can either be stored on the internal hard drive of the oscilloscope or on an external hard disk via USB port.

LeCroy WavePro 7100A: The LeCroy WavePro 7100A is an advanced version of the LeCroy WavePro 7100 with an extended memory option. Like the WavePro 7100, the WavePro 7100A is a four-channel DSO with a maximum bandwidth of 1 GHz at a maximum sampling rate of 10 GHz with an 8-bit vertical resolution. The maximum sampling rate is 20 GHz when operating in the 2-channel mode. The WavePro 7100 is capable of recording 50 megabytes per channel when all four channels are in use. Hence with an 8-bit resolution the total record length is 50 megasamples for each of the 4 channels. At a maximum sampling rate of 10 GHz, the maximum record length is 5 ms. The WavePro 7100A uses the Microsoft Windows XP Professional (SP 2) operating system and has a flat panel touch-screen display. The processor memory is 1.98 GB and the processor speed is 2.8 GHz. The recorded data can either be stored on the internal hard drive of the oscilloscope or on an external hard disk via USB port.



Figure 3-7. Digitizing oscilloscopes inside the glass cupola at the LOG in August, 2008.

LeCroy LT344Waverunner: The LeCroy LT344 is a four channel DSO with a maximum bandwidth of 500 MHz at a maximum sampling rate of 500 MHz with 8-bit vertical resolution. The LT344 is capable of a maximum record length of one megabyte per channel when all four channels are in use. Since a sample is recorded with 8-bit resolution, one byte is required to store each sample; hence the total record length is one megasample per channel. At the maximum

Table 3-3. Digital storage oscilloscopes used at the LOG after April 2008.

DSO Type	Experiment	Measurements	Record length (ms)	Pre-trigger time (ms)	Sampling rate (MHz)	Trigger mode and input	Comment
Lecroy LT344	Single-station experiment	E, dE/dt, VHF	10	4	100	Threshold trigger on E or VHF	Used after April, 2008
LeCroy 7100	Two-station experiment	E, dE/dt	480	100	100	Width trigger on signal from CB	Used also for the single-station experiment prior to August, 2008
LeCroy 7100A	Single-station experiment	E, dE/dt, dB/dt (two components), VHF	240/500	80/100	100	Threshold trigger on E or VHF	Added in August, 2008
Yokogawa DL716	Two-station experiment	E, dE/dt, dB/dt (two components)	3206	1280	10	Threshold trigger on LeCroy 7100 trigger-out	Used after May, 2008

sampling rate of 500 MHz, the maximum record length is 2 ms. Typically the LT344 is not used to acquire a single continuous record but rather is used in segmented memory mode. In segmented memory mode, the acquisition memory is divided into multiple segments and a separate trigger is required to record each segment. For example, if five segments are used, the acquisition memory is divided into 200 kilosamples per segment per channel. Segmented memory mode is useful when acquisition memory is limited and multiple events are to be recorded with the duration of each event being very small relative to the time between events. Segmented memory mode is ideal for recording the electric and magnetic field waveforms (or their time-derivatives) from individual return strokes. The input resistance of each LT344 channel can be set to 50 Ω or 1 M Ω , either AC or DC coupled. Each channel can be set from 2 mV per division to 10 V per division with a maximum RMS input voltage of 5 V and 280 V

when 50 Ω and 1 M Ω input resistances are used, respectively. In addition, each channel can be individually configured with an internal low pass filter of 25 MHz or 200 MHz (-3 dB). The LT344 is equipped with a PCMCIA Type III slot, which is used to add storage such as a hard drive or a compact flash card which come in a variety of sizes. A 128 MB compact flash card was used in the LT344; hence a maximum of 32 waveforms could be stored if one megabyte was used per channel and all four channels were in use for each acquisition. Waveforms can be moved to and from the DSO over a 10Base-T Ethernet connection or the GPIB bus using LeCroy *Scope Explorer* software.

Yokogawa DL716: The Yokogawa DL716 is a 16 channel DSO with a maximum bandwidth of 4 MHz (-3 dB) and a maximum sampling rate of 10 MHz, with 12-bit vertical resolution. The DL716 is capable of a maximum record length of 16 megasamples per channel when all 16 channels are used simultaneously. At the maximum sampling rate of 10 MHz, the maximum record length is 1.6 s when all 16 channels are used. Therefore, the DL716 is ideal for recording a continuous full-flash record of lightning electric and magnetic fields. Each DL716 channel can be set from 5 mV per division to 20 V per division with a maximum peak-to-peak input voltage range of 250 V. The input resistance of each channel is 1 M Ω shunted with 30 pF of input capacitance, either AC or DC coupled. In addition, each channel can be individually configured with an internal low-pass filter having a -3 dB cutoff at 500 Hz, 5 kHz, 50 kHz, or 500 kHz.

The DL716 is equipped with 9.2 GB of internal storage and many acquired waveforms can be stored in the digitizer itself. The DL716 is also equipped with an external SCSI hard disk connector so that more storage can be added. Waveforms can be moved to and from the DL716 over a 10Base-T Ethernet connection using the File Transfer Protocol (FTP).



Figure 3-8. The GPS antenna used at the LOG.

The DL716 can be triggered by any of the 16 channels or by an external TTL level trigger input. One major disadvantage of the DL716 is that, for long records (several hundred milliseconds or more), it takes up to 15 minutes to write the data from memory to disk. During this interval, the digitizer cannot trigger and hence no new lightning data can be recorded.

3.2.3.3 GPS time-stamping system

This system consisted of a GPS antenna (shown in Figure 3-8), the GPS-ACU/2K manufactured by Trimble and a PC card, the bc627-AT manufactured by Datum Inc. The antenna and card tracked the GPS time in UTC format which was displayed on a PC via a software interface. The bc627-AT was connected to the trigger out of an oscilloscope. Any lightning event recorded by the oscilloscope generated an output trigger, causing the GPS card to trigger at the same instant and produce a timestamp.

As stated in Section 1, prior to March 2008, the instrumentation was located on the third floor and roof of Benton Hall. At that time, the GPS system PC was housed inside an electrical closet alongside electrical and communication junction boxes of the building. Spurious signals, probably from these junction boxes, often coupled to the GPS system producing timestamps that did not correspond to lightning flashes. In fact, timestamps were produced even when there was no nearby thunderstorms. However, since relocation of the instrumentation to the Engineering Building in March 2008, spurious timestamps have no longer been generated. The GPS timestamps generated by our system were compared with those generated by the National Lightning Detection Network (NLDN) for the same lightning events and it was found that for 43% of the events, NLDN times were within 10-ms of our GPS time stamps, for 71% they were within 40 ms and for 99% within 80 ms. The correctness of our event matching with NLDN data was verified using inter-stroke intervals in multiple stroke CGs and intervals between individual pulses produced by ICs.

3.2.3.4 Dedicated phone line

A dedicated phone line, a conditioned line provided by AT&T/Bellsouth, is being used to provide a link between Camp Blanding and Gainesville. This link is a four-wire line that enables transmission of a trigger pulse from Camp Blanding to Gainesville and vice versa. The line has a characteristic impedance of 600 Ω and a frequency bandwidth from 300 Hz to 3 KHz. Currently, the link is being used to transmit trigger pulses generated at Camp Blanding in response to rocket-triggered or natural on-site events to Gainesville. The transmission delay of a pulse from Camp Blanding to Gainesville (45 km apart) is about 29 ms. The link is being used in the two-station experiment.

3.3 Wideband Electric Field Measurements

The various measurements in the experiments discussed in Section 3.2 are described in the following sections.

3.3.1 Theory

Lightning discharges, both cloud and cloud-to-ground, have durations that may extend to a second or more. However, the individual physical processes in a particular discharge can vary on microsecond and even submicrosecond time scales. Lightning processes can produce electromagnetic signatures in the range from a few hertz (long continuing currents) to 10^{20} Hz (hard x-rays) [Rakov, 2008].

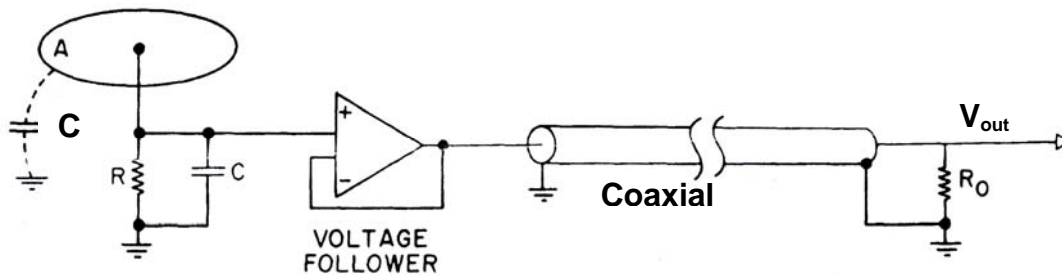


Figure 3-9. An electric field antenna system. Adapted from *Uman* [1987].

A sensor that is commonly used to measure the lightning wideband electric field is a metallic flat plate antenna. Figure 3-9 shows an example of flat plate antenna system. C_a is the capacitance between the antenna plate and the ground, and R_0 terminates the coaxial cable in its characteristic impedance. C is the integrating capacitor and R is the relatively large resistor (usually input resistance of associated electronics) that provides a discharge path for the capacitor C , so that the output voltage in response to a step-function excitation decays exponentially with a time constant $\tau = RC$. The value of τ should be chosen such that it is much larger than the variation time of the signal of interest.

In order to satisfy boundary conditions on the surface of a perfect conductor, the electric field vector on the surface of sensing plate will only have a vertical component. The charge Q induced on the antenna plate having a surface area A is given by Equation 3-1, which follows from the boundary condition on the normal component of electric field on the surface of a good conductor ($|\epsilon_0 \vec{E}| = \rho_s$ where ρ_s is the surface charge density assumed to be constant).

$$Q(t) = \epsilon_0 A E(t) \quad (3-1)$$

Any change in the vertical electric field E on the antenna plate will cause a change in Q . The resultant short-circuit current I is given by:

$$I(t) = \frac{dQ(t)}{dt} = \epsilon_0 A \frac{dE(t)}{dt} \quad (3-2)$$

Therefore, the voltage across the resistor R and capacitor C in Figure 3-9 (assuming that $R \gg 1/\omega C$ and $C_a \ll C$) and hence the output voltage (V_{out}) is given by Equation 3-3.

$$V_{out} = \frac{1}{C} \int_0^t I(t) d\tau = \frac{\epsilon_0 A E(t)}{C} \quad (3-3)$$

Thus, the output voltage is directly proportional to the vertical component of electric field at the position of the antenna (assuming that the antenna does not significantly distort the electric field to be measured).

3.3.2 Antenna

Circular flat plate antennas such as the one shown in Figure 3-10 were used to measure wideband electric field at the LOG. The sensing plate of each antenna (made of aluminum) was raised above the roof of the building by mounting it on a vertical metallic (galvanized iron) pole. The sensing plate and the vertical pole were separated by a 1.5 cm long PVC insulator. The pole was fastened to a metallic (aluminum) base which was connected to a nearby conductor of the

lightning protective system of the building. Signal from the antenna (voltage between the sensing plate and grounded pole) was relayed via a double-shielded and sleeved RG-223 coaxial cable to the electronics inside a Hoffman box (a shielding metallic enclosure) placed at the antenna base. Raising the flat plate enhances the electric field relative to that in the absence of the antenna. This field enhancement (geometrical "gain") along with any electronic gain increases the sensitivity of the system for the same area of the flat plate. All elevated flat plate antennas used at the LOG were calibrated with respect to a standard flat-plate antenna placed essentially flush with ground (roof surface). Additional field enhancement factor due to presence of the building was also taken into account.

3.3.3 Electric Field Measuring System for the Two-Station Experiment (E1)

This electric field measuring system included a circular flat plate antenna which had a diameter of 44.6 cm and an area of 0.156 m². The flat plate was mounted on a metallic pole, so that it was at a height of 1.71 m above the roof of the building. The antenna was followed by an integrating capacitor (1.94 nF) and a unity gain high input impedance amplifier placed inside a Hoffman box (see Figure 3-11). The signal from the antenna and associated electronics was transmitted to a LeCroy digitizing oscilloscope which sampled at a rate of 100 MHz and a Yokogawa digitizing oscilloscope which sampled at a rate of 10 MHz. The -3 dB bandwidth of the electric field measuring system was from 16 Hz (determined by the RC time constant of 9.89 ms of the integrator) to 13 MHz (determined by the -3 dB upper frequency response of the amplifier) or from 16 Hz to 4 MHz (the latter determined by the -3 dB upper frequency response of the Yokogawa oscilloscope). An Opticomm fiber optic transmitter-receiver pair along with a 51 m long 62.5 μ m multi-mode fiber with ST connectors was used to transmit the signal from the antenna and associated electronics to the digitizing oscilloscopes.

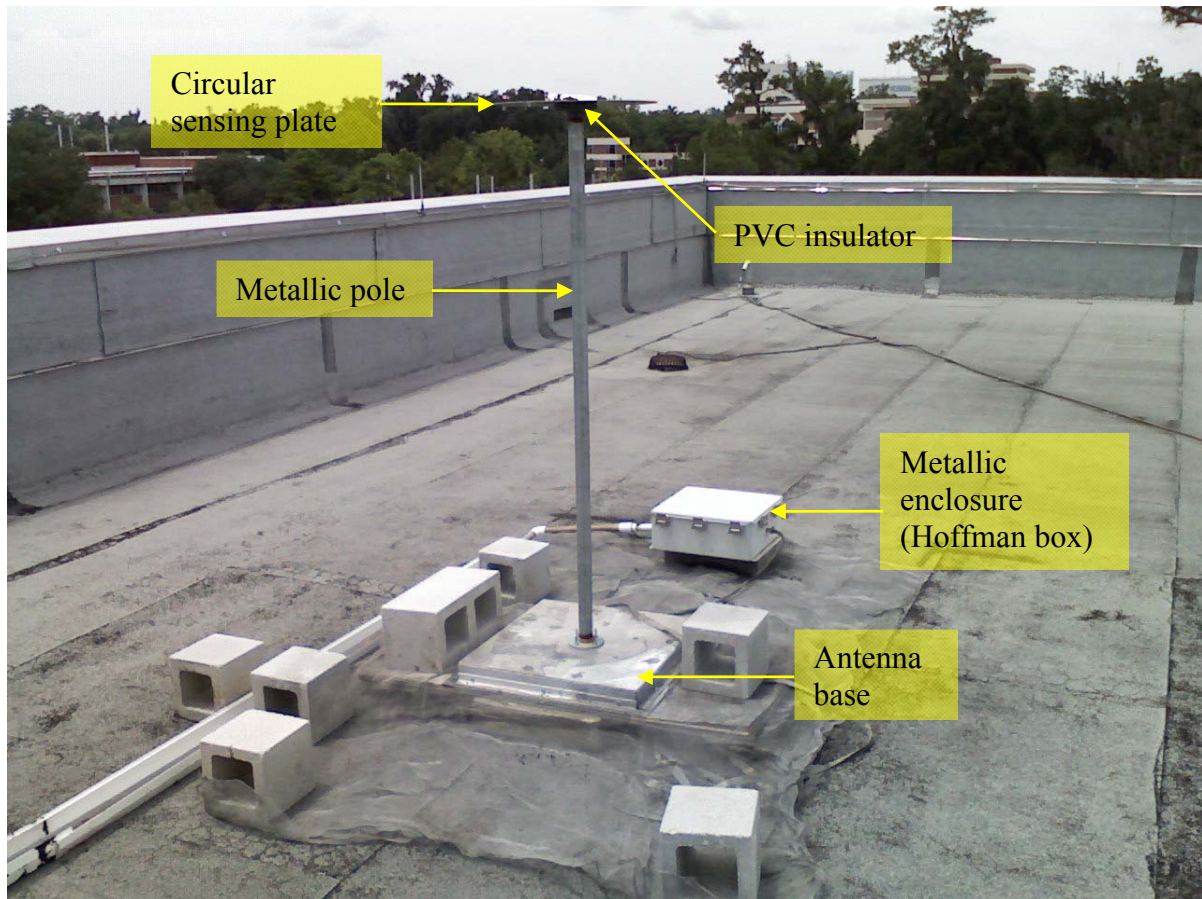


Figure 3-10. An elevated flat plate antenna used for measuring wideband electric field at the LOG. Similar antennas were used for the dE/dt and narrowband HF measurements.

Figure 3-12 shows a schematic of the unity gain high input impedance amplifier circuit. It consisted of an AD825 operational amplifier which was used to implement a voltage follower. The input impedance of the amplifier was $5.1\text{ M}\Omega$ and the output impedance of the feedback circuit, and hence of the amplifier, was a fraction of an Ohm. The RC time constant of the antenna system was equal to 9.89 ms. The output of the amplifier was connected to the input of an Opticomm MMV-120C transmitter terminated in $50\ \Omega$. Two 12 V batteries (placed inside the Hoffman box) were used, one to power the Opticomm MMV-120C transmitter, and the other to power the amplifier. The amplifier ground was at 6 V above the negative battery terminal in order to bias the AD825 operational amplifier with $\pm 6\text{ V}$. Since the amplifier ground was 6 V

above the common ground, a separate 12 V battery was required to power it. The relay circuit of the amplifier block was however powered by the same 12 V battery as the Opticomm MMV-120C transmitter. The frequency response of the amplifier with a 50 Ω load is shown in Figure 3-13. In order to eliminate ground loops, all electronic components were isolated from each other and the metal box by pieces of plastic and Styrofoam.

3.3.4 Electric Field Measuring System for the Single-Station Experiment (E2)

The electric field measuring system used for this experiment was similar to the one used in the two-station experiment. However, a 10.4 nF integrating capacitor followed by a unity gain amplifier (based on an AD825 operational amplifier) with an input impedance of 1 M Ω was used. The frequency response of the amplifier with a 50 Ω load is shown in Figure 3-14. The -3 dB bandwidth of the electric field measuring system was from 15 Hz (determined by the RC time constant of 10.4 ms of the integrator) to 12 MHz (determined by the -3 dB upper frequency response of the amplifier). The circular flat plate electric field antenna had a diameter of 50.3 cm and an area of 0.199 m². The flat plate was mounted on a metallic pole, so that it was at a height of 1.62 m above the roof of the building. An Opticomm fiber optic transmitter-receiver pair along with a 51 m long 62.5 μ m multi-mode fiber was used to transmit the signal from the antenna and associated electronics to LeCroy digitizing oscilloscopes sampling at a rate of 100 MHz.

Note that while the electric field measuring systems at the LOG did not have any electronic gain, there were geometrical gains due to the antennas being located on top of a building and because the sensing plates were elevated above the roof level. Amplitude calibration of the measuring systems is discussed in Section 3.12. Tables 3-4 and 3-5 summarize the characteristics of the electric field measuring systems along with their calibration factors.

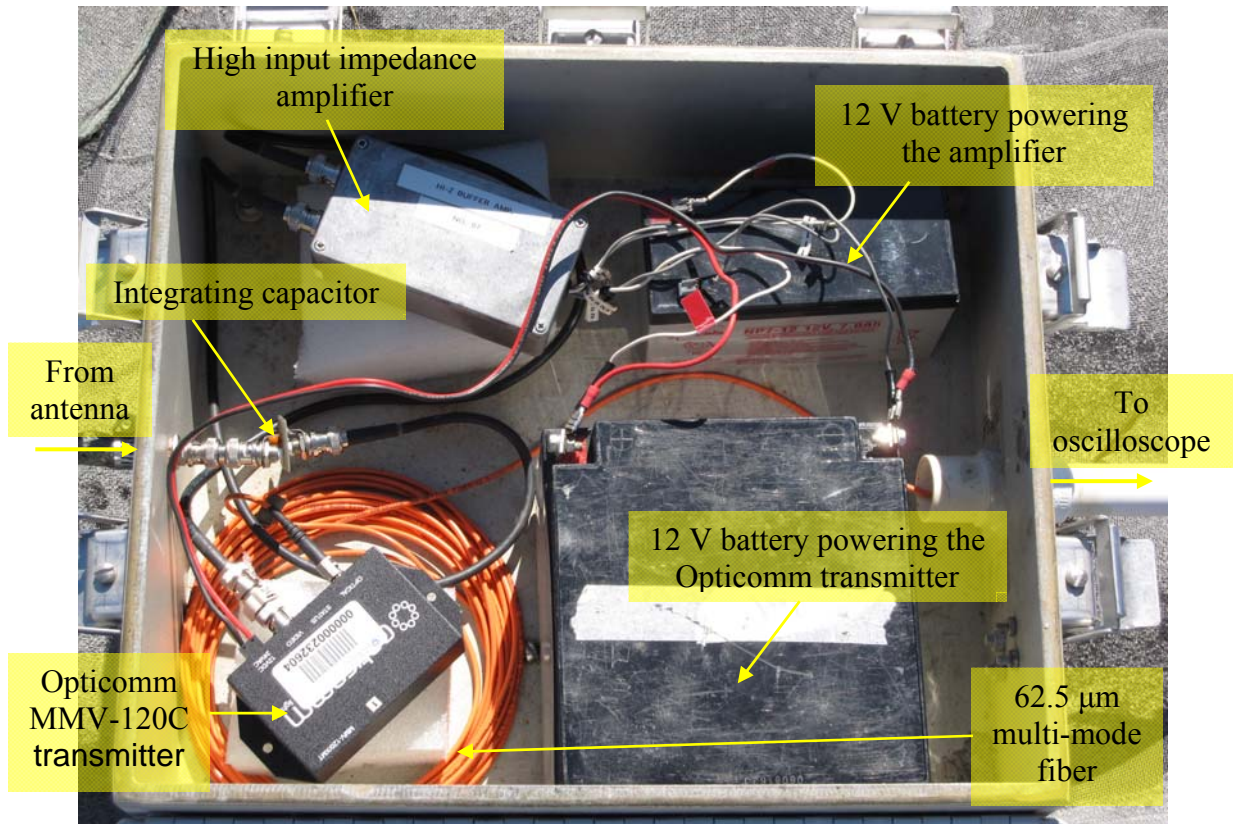


Figure 3-11. Electronics inside a Hoffman enclosure used in electric field measuring system (E1) at the LOG.

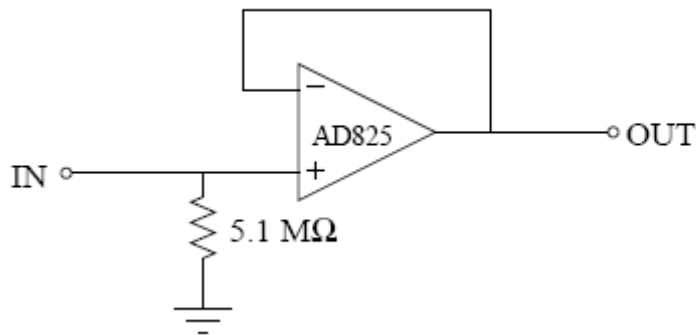


Figure 3-12. Schematic of the high input-impedance amplifier used in electric field measuring system (E1) at the LOG.

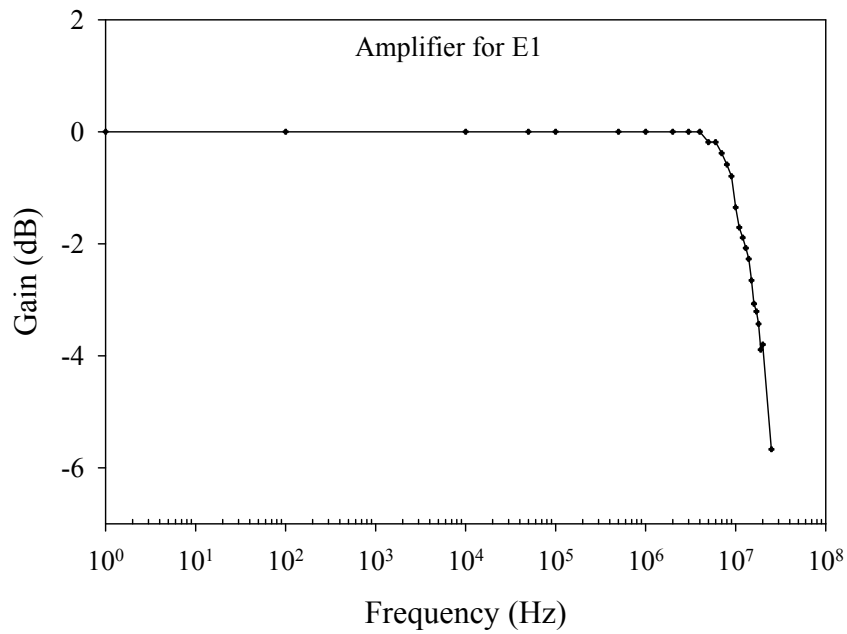


Figure 3-13. Frequency response of the high input-impedance amplifier used in electric field measuring system (E1) at the LOG.

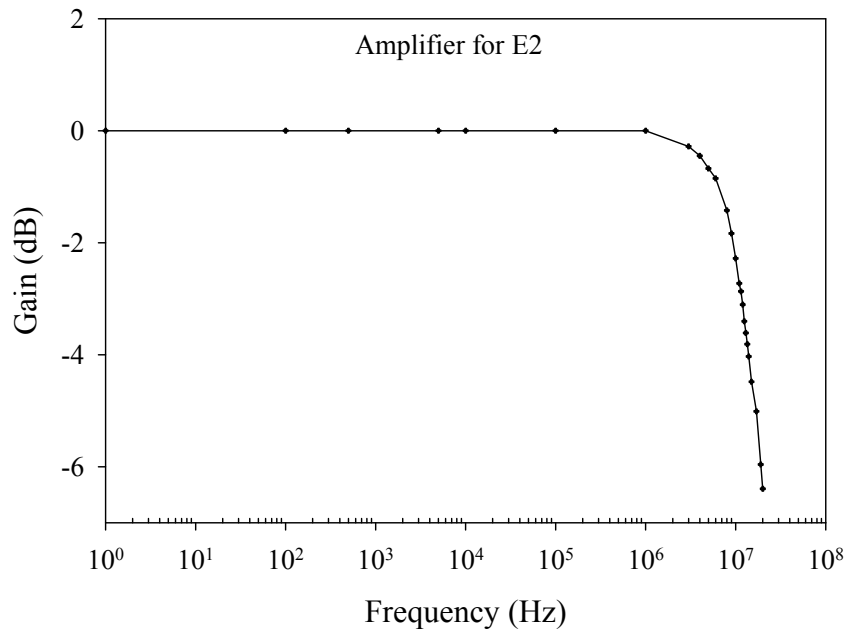


Figure 3-14. Frequency response of the high input-impedance amplifier used in electric field measuring system (E2) at the LOG.

3.4 Electric Field Derivative Measurements

3.4.1 Theory

Figure 3-15 shows the configuration for a flat plate antenna system acting as an electric field derivative (dE/dt) sensor. In this case, it follows from Equation 3-2 that the output voltage across the resistor R is given by Equation 3-4.

$$V_{out} = IR = \epsilon_0 AR \frac{dE(t)}{dt} \quad (3-4)$$

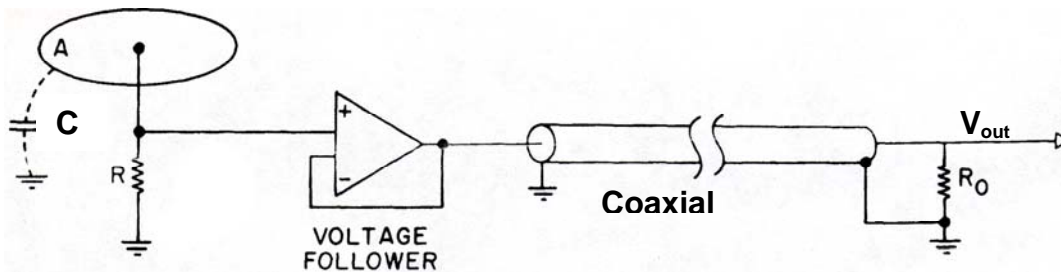


Figure 3-15. An electric field derivative antenna system. Adapted from *Uman* [1987].

Equation 3-4 represents the ideal time domain response of a flat plate dE/dt antenna. The output voltage of the antenna is directly proportional to the vertical component of the electric field derivative at ground. Further, the output voltage is directly proportional to the area of the antenna and the resistance between the antenna plate and ground. The antenna capacitance C_a [of about 80 pF, *Jerauld*, 2007] does not affect the amplitude of the output voltage of the ideal ($R \ll 1/\omega C_a$ or $f \ll 1/(2\pi RC_a)$, where $f = \omega/2\pi$) dE/dt measuring system. For dE/dt measurement systems at the LOG, $R = 50 \Omega$, so that the limiting frequency $f \ll 40$ MHz.

3.4.2 Antenna

Circular flat plate antennas similar to the one described in Section 3.3.2 and shown in Figure 3-10 were used to measure electric field derivative at the LOG. Specific dimensions are given in Sections 3.4.3 and 3.4.4.

3.4.3 dE/dt Measuring System for the Two-Station Experiment (dE1)

This dE/dt measuring system included a circular flat plate antenna having a diameter of 46.5 cm and an area of 0.170 m². The flat plate was mounted on a metallic pole, so that it was at a height of 1.33 m above the roof of the building. The antenna was followed by an amplifier with a gain (ratio of output to input voltage) of 8.89 placed inside a Hoffman box. The signal from the antenna and associated electronics was transmitted to a LeCroy digitizing oscilloscope which sampled at a rate of 100 MHz and a Yokogawa digitizing oscilloscope which sampled at a rate of 10 MHz. The upper limit of the frequency bandwidth of the dE/dt measuring system was 17 MHz (determined by the -3 dB upper frequency response of the amplifier) or 4 MHz (determined by the -3 dB upper frequency response of the Yokogawa oscilloscope). An Opticomm fiber optic transmitter-receiver pair along with a 51 m long 62.5 μm single-mode fiber with ST connectors was used to transmit the signal from the antenna and associated electronics to the digitizing oscilloscope.

Figure 3-16 shows a schematic of the amplifier circuit. It consisted of a THS4215, an ultra-low-distortion, high-speed operational amplifier which was used to implement a non-inverting amplifier. The input and output impedances of the amplifier were equal to 50 Ω. The amplifier was powered by a 12 V battery placed inside the Hoffman box. The frequency response of the amplifier with a 50 Ω load is shown in Figure 3-17. The output of the amplifier is connected to the input of an Opticomm MMV-120C transmitter terminated in 50 Ω. Note that the THS4215 has a closed loop output resistance of a fraction of an Ohm. Hence the total output resistance of the amplifier circuit as shown in Figure 3-16 is approximately 50 Ω. The load impedance for this circuit is the input impedance of the Opticomm transmitter (50 Ω shunt resistance). The output resistance of the amplifier and the input resistance of the Opticomm form a voltage divider that

reduces the overall gain of the amplifier by half. Hence, the overall gain of the amplifier circuit loaded by the $50\ \Omega$ input impedance of the Opticomm is 8.89, as stated in the previous paragraph. In order to eliminate ground loops, all electronic components in the Hoffman box were isolated from each other and the metal box by pieces of plastic and Styrofoam.

3.4.4 dE/dt Measuring System for the Single-Station Experiment (dE2)

With the exception of the antenna, all aspects of the dE/dt measuring system used for this experiment (including amplifier characteristics) were the same as those used in the two-station

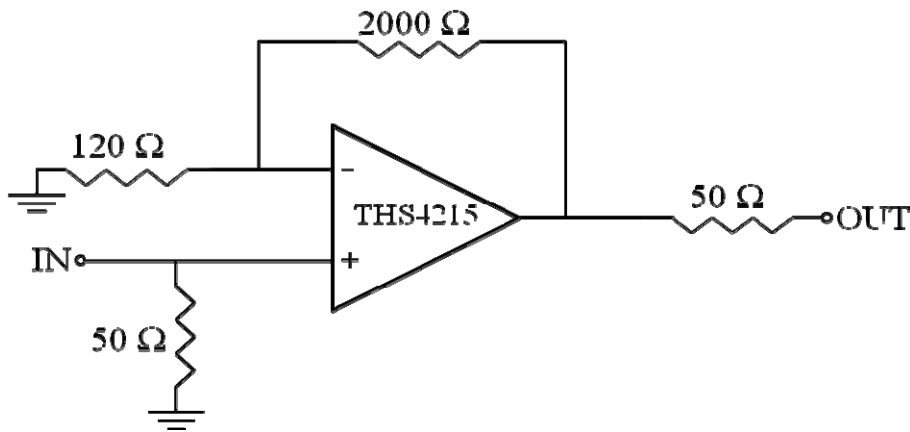


Figure 3-16. Schematic of the amplifier used in dE/dt measuring systems (dE1 and dE2) at the LOG. Note that the overall gain of the amplifier circuit loaded by the $50\ \Omega$ input impedance of the Opticomm is 8.89.

experiment. In the single-station experiment, the circular flat plate dE/dt field antenna had a diameter of 50.3 cm and an area of $0.199\ \text{m}^2$. The flat plate was mounted on a metallic pole, so that it was at a height of 1.7 m above the roof of the building. The upper limit of the frequency bandwidth of the dE/dt measurement was 17 MHz which was determined by the -3 dB upper frequency response of the amplifier.

Note that in addition to the electronic gain of 8.89, the dE/dt measuring systems at the LOG had geometrical gains (field enhancements) due to the antennas being located on top of a building and because the sensing plates were elevated above the roof level. The amplitude

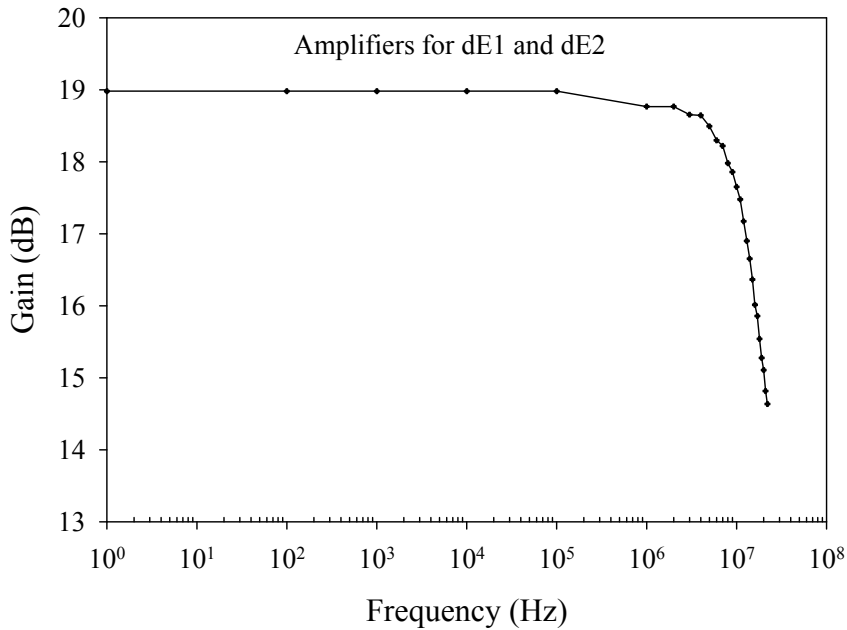


Figure 3-17. Frequency response of the amplifiers used in dE/dt measuring systems (dE1 and dE2) at the LOG.

calibration of the measuring systems is discussed in Section 3.12. Tables 3-4 and 3-5 summarize the characteristics of the dE/dt measuring systems along with their calibration factors.

3.5 Magnetic Field Derivative Measuring System

3.5.1 Theory

To measure the magnetic field from lightning a loop of wire can be used as an antenna. According to Faraday's law a changing magnetic field passing through an open circuited loop of wire will induce a voltage at the terminals of the wire. The voltage magnitude at the terminals of the wire is given by Equation 3-5.

$$V_{out} = A \frac{dB_n(t)}{dt} \quad (3-5)$$

where A is the area of the loop and $B_n(t)$ is the normal component of magnetic flux density passing through the loop, $B_n = B \cos \alpha$, where B is the total magnetic flux density and α is the angle between the B vector and the normal to the loop. The output voltage is proportional to the

time derivative of the magnetic field passing through the loop ($\frac{dB_n(t)}{dt}$). In the following the subscript "n" in B_n is dropped to simplify notation.

3.5.2 Antenna

At the LOG, we used a square coaxial-cable loop antenna with a single-ended output, which means that the output voltage is taken from only one end of the cable. The antenna was developed by George Schnetzer [Jerauld, 2007]. Each end of the cable was terminated in its characteristic impedance of 50 Ω . Figure 3-18 shows (a) the diagram and (b) equivalent circuit of a single-ended output coaxial-cable loop antenna with both ends of the cable terminated in 50 Ω . The 50 Ω termination on the end of the cable at which the output voltage is measured is physically the input resistance of an amplifier. The other end of the cable is terminated by soldering a 50 Ω resistor between the inner conductor and the outer shield. This soldering is located at the base of the antenna. Note that current is induced on both the inner conductor and the outer shield by either an external electric or magnetic field. Due to the current induced in the shield, unwanted magnetic field will necessarily be induced perpendicular to the loop. This induced magnetic field will distort the external magnetic field to be measured. Therefore, a small gap is placed in the shield to inhibit any shield current and hence prevent any unwanted magnetic fields from the shield. This gap is placed at the top of the loop, as shown in Figure 3-18. The expressions for the ideal time-domain output voltage, V_{out} , and -3 dB upper frequency response, ω_0 , of a single ended coaxial-cable loop antenna are given by Equations 3-6 and 3-7.

$$V_{out} = -\frac{1}{2} \frac{R_{load} A}{R_{loop} + R_{load}} \frac{dB(t)}{dt} \quad (3-6)$$

$$\omega_0 = \frac{R_{loop} + R_{load}}{L_{loop}} \quad (3-7)$$

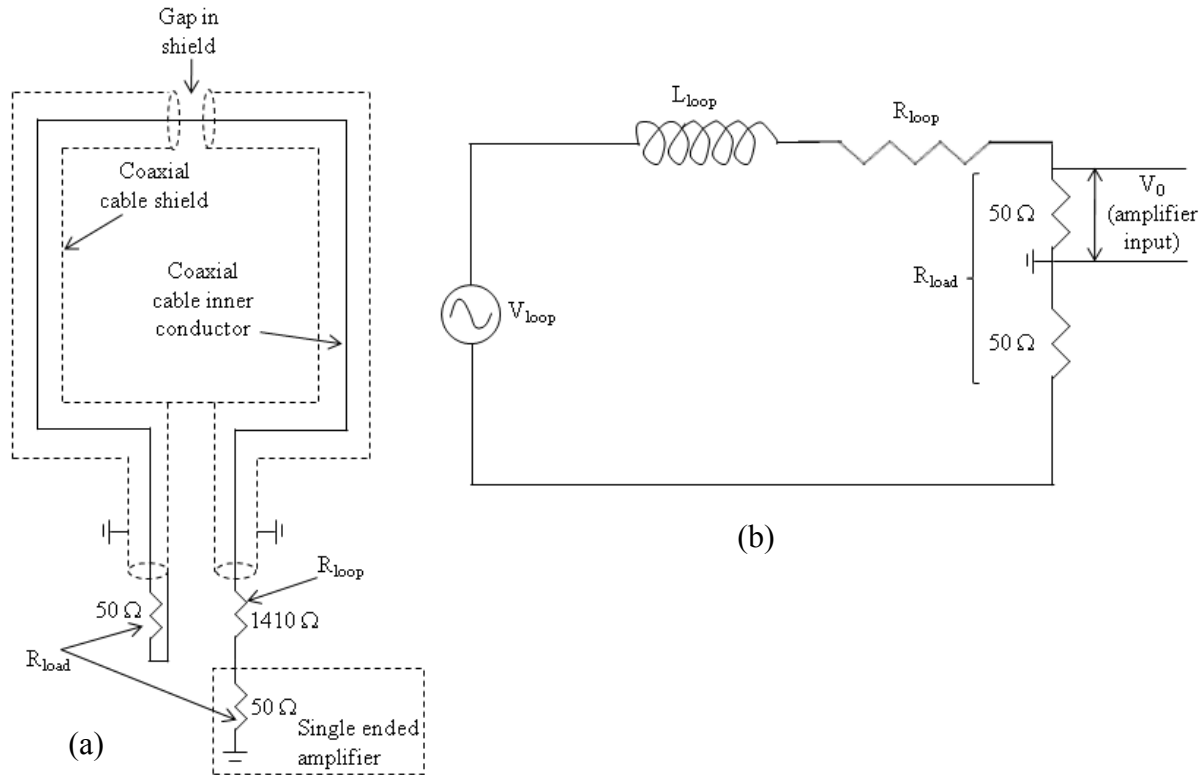


Figure 3–18. (a) Diagram and (b) equivalent circuit of a single-ended output coaxial loop antenna with both ends of the cable terminated in $50\ \Omega$. Adapted from *Jerauld* [2007].

For a loop terminated in $50\ \Omega$ at both ends, R_{load} is $100\ \Omega$. L_{loop} is the inductance of the loop, which is determined by the geometry of the antenna. R_{loop} is the total resistance of the loop antenna including the inherent resistance of the inner conductor and any externally added resistance. R_{loop} affects both the gain and the bandwidth of the antenna and is determined by the desired characteristics of the antenna. If no external resistance is added to the antenna, R_{loop} is the resistance of the inner conductor of the cable, which is nearly zero (can be neglected).

At the LOG, two square single-ended coaxial-cable loop antennas of area $0.533\ \text{m}^2$ terminated in $50\ \Omega$ were used to measure dB/dt. The antennas were arranged in an orthogonal crossed-loop pair (as shown in Figure 3-19) individual antenna planes being oriented in north-south and east-west directions and labeled dB (N-S) and dB (E-W), respectively. An external

resistance (R_{loop}) of 1410 Ω was used. R_{load} , as stated previously, was 100 Ω due to the 50 Ω terminations at each end of the cable. The inductance of this loop (L_{loop}) is approximately 4 μH [Jerauld, 2007]. The upper limit of the frequency bandwidth of the antenna was calculated using Equation 3-7 to be about 61 MHz.

3.5.3 dB/dt Measuring System for the Single-Station and Two-Station Experiments (dB)

The output of each antenna loop was connected to an amplifier with 50 Ω input resistance and a gain of 145. The amplifiers were implemented using OPA657, which is a low noise operational amplifier. The frequency response of one such amplifier with a 50 Ω load is shown in Figure 3-20. The signals from the two loops and associated electronics placed inside a Hoffman box were transmitted to two channels of a LeCroy digitizing oscilloscope, which sampled at a rate of 100 MHz, and a Yokogawa digitizing oscilloscope, which sampled at a rate of 10 MHz. In order to eliminate ground loops, all electronic components were isolated from each other and the metal box by pieces of plastic and Styrofoam. Note that the magnetic field measuring systems, dB (N-S) and dB (E-W), were used in both experiments discussed in Section 3.2. The upper limit of the frequency bandwidth of the dB/dt measurements was 15 MHz (determined by the -3 dB upper frequency response of the amplifier in case of the single-station experiment) or 4 MHz (determined by the -3 dB upper frequency response of the Yokogawa oscilloscope in case of the two-station experiment). Opticomm fiber optic transmitter-receiver pair along with a 51 m long 62.5 μm multi-mode fibers with ST connectors is used to transmit the signal from the antenna and associated electronics to the digitizing oscilloscopes. Table 3-6 summarizes the characteristics of the dB/dt measuring systems along with the associated amplitude calibration factors determined using Equation 3-6.

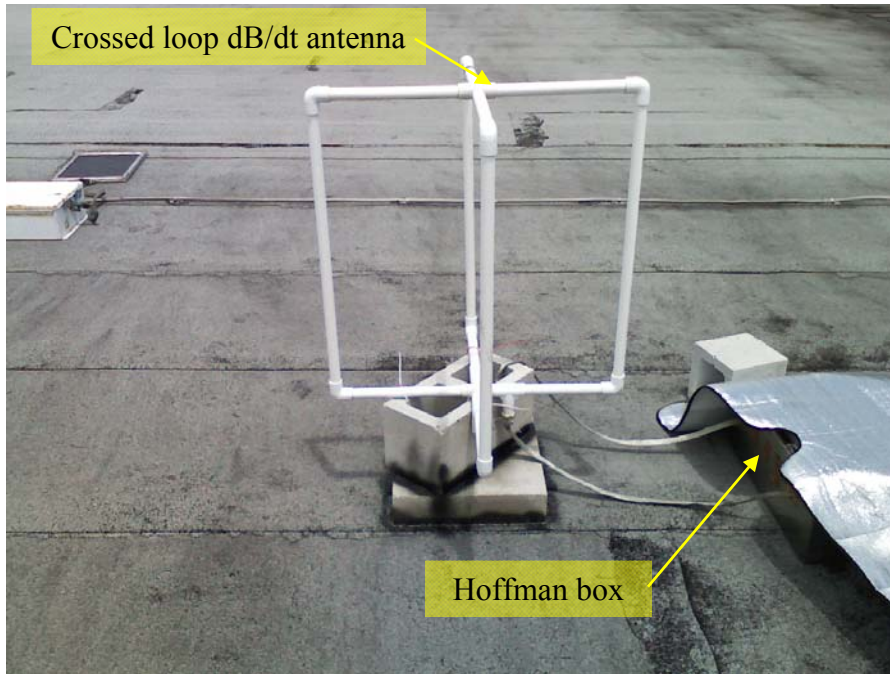


Figure 3-19. Two loops (oriented north-south and east-west) of the magnetic field derivative antenna used at the LOG.

3.6 Narrowband HF Measuring System

The narrowband HF measuring system included an elevated flat plate antenna, similar to the one described in Section 3.7.2, followed by an HF receiver having center frequency at 5 MHz (with a -3 dB bandwidth of 4.7 MHz to 5.4 MHz) and an overall gain (ratio of output to input voltage) of 31. The electronics were placed inside a Hoffman box at the base of the antenna. The signal from the antenna and associated electronics was transmitted to a LeCroy digitizing oscilloscope which sampled at a rate of 100 MHz. An Opticomm fiber optic transmitter-receiver pair along with a 51 m long 62.5 μm single-mode fiber with ST connectors was used to transmit the signal from the antenna and associated electronics to the digitizing oscilloscope. Figure 3-21 shows the block diagram of the HF measuring system. The HF receiver consisted of two single stage amplifiers and a passive bandpass filter. The amplifiers were implemented using the THS4211 operational amplifier and were powered by two 12 V batteries placed inside the

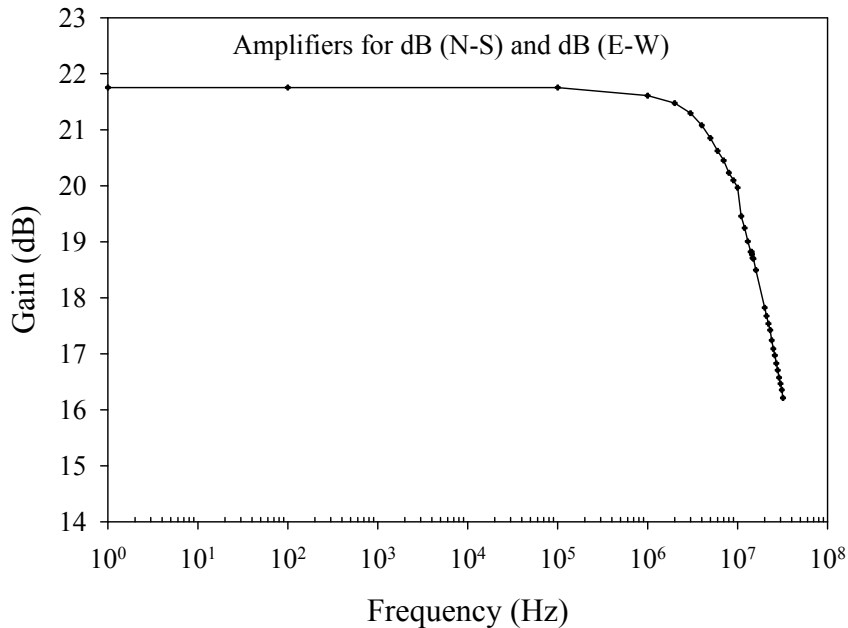


Figure 3-20. Frequency response of the amplifiers used in dB/dt measuring systems, dB (N-S) and dB (E-W), at the LOG.

Hoffman box. The filter circuit was connected between the two amplifier blocks in order to reduce DC offset that is introduced by the high gain amplifiers. The frequency response of the HF receiver (amplifier-filter-amplifier configuration) is shown in Figure 3-22.

The sensing circular flat plate of the HF measuring system had a diameter of 50.3 cm and an area of 0.199 m². The plate was elevated, so that it was at height of 1.62 m above the roof of the building. No absolute amplitude calibration for the narrowband HF measuring system was attempted, since it was not essential for the purpose of this experiment.

3.7 Narrowband VHF measuring system

The narrowband VHF measuring system included a whip antenna, followed by a VHF receiver having center frequency at 36 MHz (with a -3 dB bandwidth of 34 MHz to 38 MHz) and an overall gain (ratio of output to input voltage) of 27. The whip antenna had a length of 67 cm

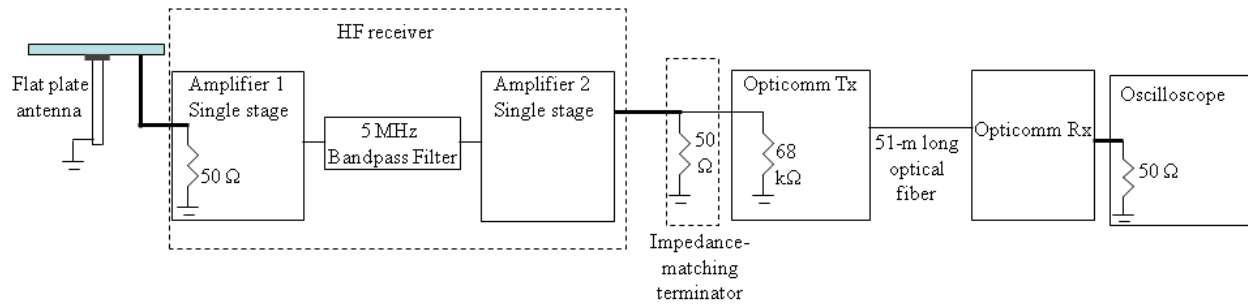


Figure 3-21. Block diagram of the HF measuring system. The HF receiver had an overall gain of 31 (30 dB) at center frequency (5 MHz).

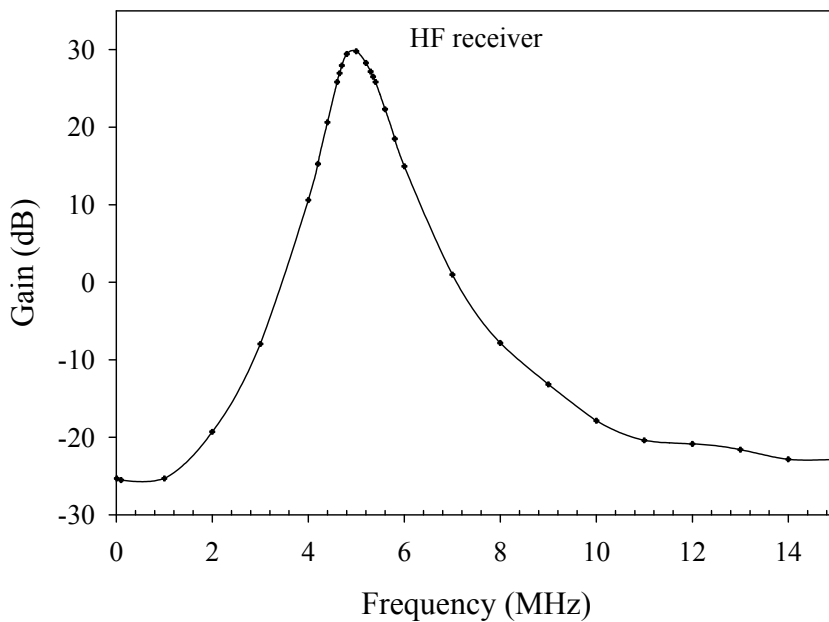


Figure 3-22. Frequency response of the HF receiver used at the LOG.

and was mounted on top of a 3.26 m tall metallic pole attached to the parapet on the western side of the roof, as shown in Figure 3-23, so that the tip of the antenna was at a height of about 4 m above the roof level. The sensing section of the whip was insulated by a thin plastic disc from the grounded section (portion below the insulator in Figure 3-23). The electronics were placed in a Hoffman box located on the roof surface near the antenna. The signal was transmitted from the antenna and associated electronics via 42 meters of double shielded and sleeved RG-223 coaxial cables to a LeCroy digitizing oscilloscope which sampled at a rate of 100 MHz. Figure 3-24

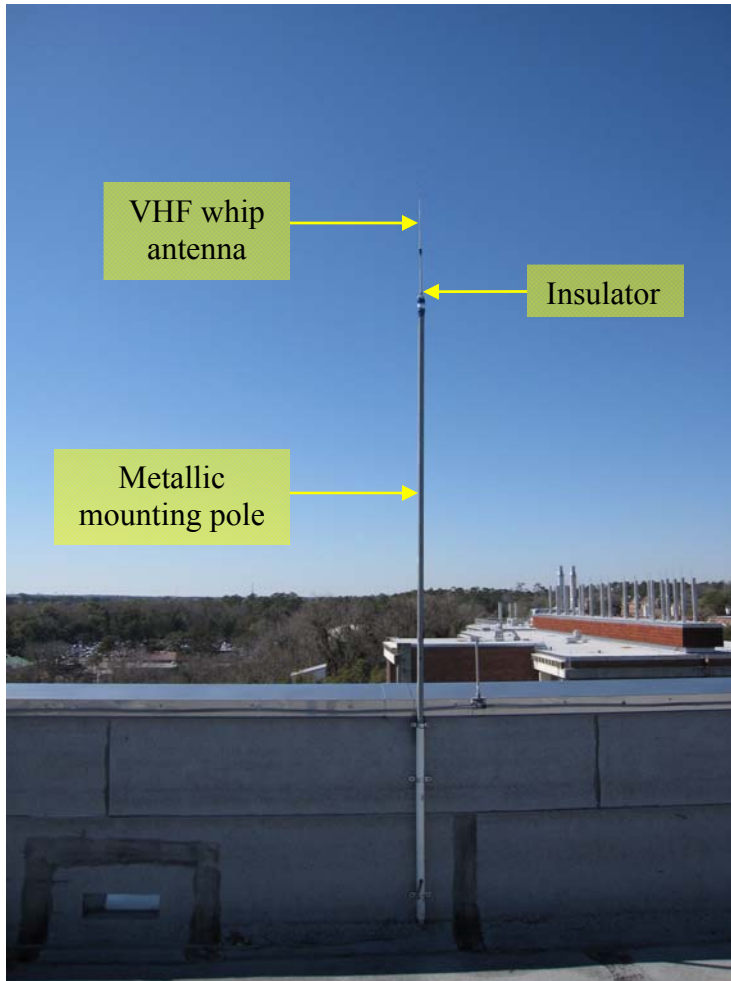


Figure 3-23. Whip antenna used for the narrowband VHF measurement at the LOG.

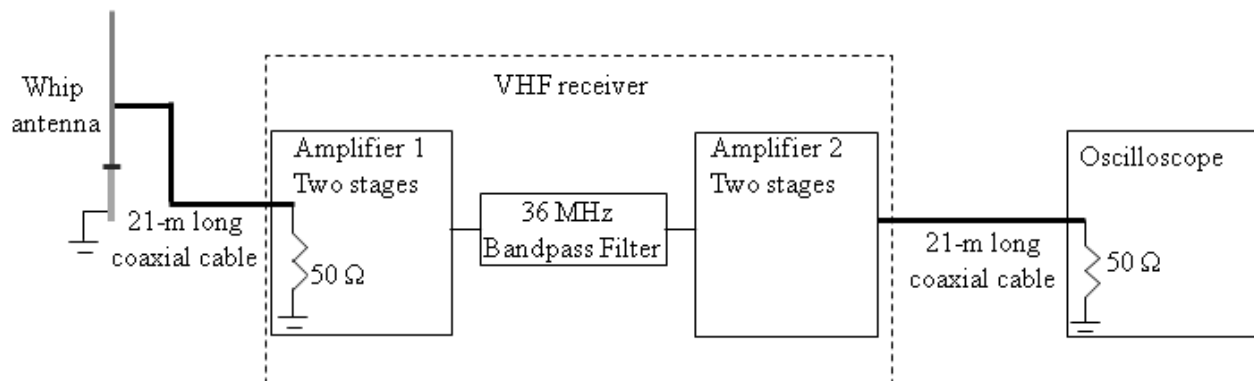


Figure 3-24. Block diagram of the VHF measuring system. The VHF receiver had an overall gain of 27 (29 dB) at the center frequency (36 MHz).

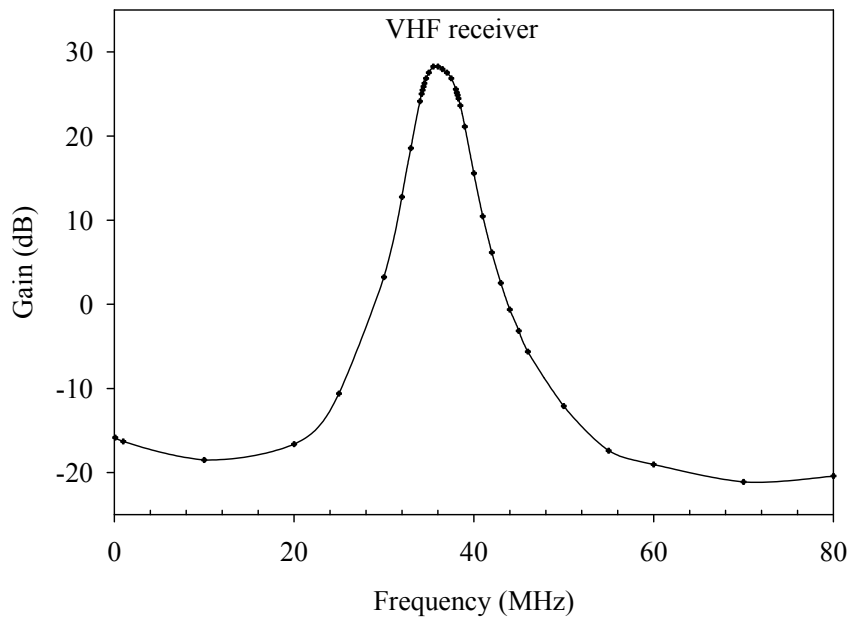


Figure 3-25. Frequency response of the VHF receiver used at the LOG.

shows the block diagram of the VHF measuring system. The VHF receiver consisted of two dual stage amplifiers and passive bandpass filters. Each amplifier consisted of two THS4211 operational amplifiers and was powered by a 12 V battery placed in the Hoffman box. The filter circuit was connected between the two amplifier blocks in order to reduce DC offset that is introduced by the high gain amplifiers. The frequency response of the VHF receiver (amplifier-filter-amplifier configuration) is shown in Figure 3-25. No absolute amplitude calibration of the narrowband VHF measuring system was attempted, since it was not essential to the purpose of this work.

3.8 Amplitude Calibration of Measuring Systems

As stated in section 3-1, the antennas of the LOG were located on the roof of Benton Hall (a 12 m tall building) from 2004-2007. In 2008, the antennas were relocated to the roof of the five-storey Engineering Building, which is 23 m tall. Further, the sensing plate of each electric field and dE/dt antenna was elevated above the roof surface. Both these factors, that is, the height

of the building and the elevation of the antenna sensing plates serve to enhance the measured electric field and, in effect, introduce an additional gain in the system. The enhancement of electric field due to the presence of the building was estimated using results of finite difference time domain (FDTD) calculations of *Baba and Rakov* [2007] and *Baba* [personal communication, 2009]. The enhancement factor for Benton Hall is about 1.2 and that for the Engineering Building is about 1.4.

Each of the elevated flat plate antennas used at the LOG was calibrated experimentally (using simultaneously measured lightning electric fields) with respect to another flat plate antenna placed essentially flush with the roof surface. The enhancement factors for all electric field and dE/dt antennas along with overall calibration factors for different measurements at the LOG in 2008 are listed in Tables 3-4 and 3-5. Note that the gains due to the building height, elevation of sensing plates, and electronic amplifiers (if any) are all multiplicative factors to the measured fields. The presence of tall building has essentially no effect on the gain of the dB/dt measuring system, the amplitude calibration factor for which was estimated using Equation 3-6. Table 3-7 gives the GPS locations, accurate to ± 2 m, of all antennas on the roof of the Engineering Building in 2008.

In order to check the calibration of the measuring systems, we computed the ratio of the electric to magnetic field peaks for 43 first return strokes in negative lightning at distances ranging from 8 to 67 km. The return-stroke initial field peaks (essentially radiation) are produced by sources near ground (typically within 100 m), so that the elevation angle, $\alpha \approx 0$, and the expected ratio of electric to magnetic field peaks is the speed of light. (This method is described in Chapter 4.) Figure 3-26 shows the histogram of the ratio of electric to magnetic field peaks for

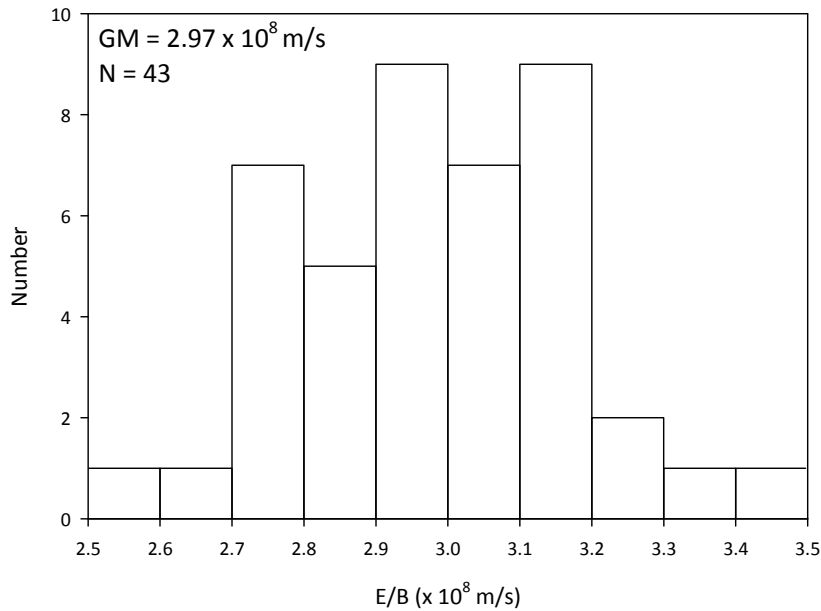


Figure 3-26. The histogram of the ratio of electric to magnetic field peaks for 43 first return strokes in negative cloud-to-ground lightning, recorded in 2008 in Gainesville, Florida.

43 first return strokes in negative cloud-to-ground lightning. We found that the 43 ratios were within $\pm 16\%$ of the speed of light with the arithmetic mean being $0.99c$, which gives us confidence in our electric and magnetic field measurements.

3.9 Time Delays Between Measurements

For all measuring systems (with the exception of the narrowband VHF system) at the LOG, equal length (51 m) optical fiber cables of the same specification and manufacturer were used. Hence time delays between various measurements were negligible (less than a few nanoseconds). For the VHF measuring system, on the other hand, a 42.7-m long double-shielded and sleeved coaxial cable was used. The end-to-end (from the input of the electronics at the antenna to the oscilloscope input) traversal time for a VHF signal was measured to be $0.31 \mu\text{s}$. Traversal time through a 51 m long optical fiber at the speed of light was $0.17 \mu\text{s}$. The end-to-end traversal time through a fiber optic link and associated electronics for the electric field

Table 3-4. Characterization and calibration factors of measuring systems at the LOG prior to April 2008 (Benton Hall).

Measuring system	E1	dE1
Experiment	Both	Both
Antenna Description	Elevated flat plate	Elevated flat plate
Elevation of sensing plate above the roof (m)	1.71 m	1.33 m
Diameter of plate (cm)	44.6	46.5
Antenna plate area, A, (m ²)	0.156	0.170
Integrating capacitance, C, (nF)	1.94	-
Resistance, R	5.1 MΩ (see Figure 3-12)	50 Ω (see Figure 3-16)
Gain due to elevation of sensing plate, G_p	15.3	9.1
Electronic gain, G_e	1	8.89
Relationship between measured voltage and field ($Field = K \times V_{out}$)	$E(t) = \frac{CV_{out}}{G_p G_e \epsilon_0 A}$ V/m	$\frac{dE(t)}{dt} = \frac{V_{out}}{G_p G_e \epsilon_0 AR}$ V/m/μs
Calibration factor without building enhancement effect, K	91.8 m ⁻¹	164.2 m ⁻¹ μs ⁻¹
Gain due to presence of building, G_b	1.2	1.2
Overall calibration factor, $K_t = K/G_b$	76.5 m ⁻¹	136.9 m ⁻¹ μs ⁻¹

measuring system (E2) was measured to be 0.3 μs. Hence, the time delay between the VHF signal and electric field signal (E2) was 10 ns (the narrowband VHF signal lagged the electric field signal by 10 ns).

3.10 Details of the Two-Station Experiment Configuration

As discussed in Section 3.2.2, this experiment was designed to measure distant field waveforms at the LOG and close ones at Camp Blanding due to natural and rocket-triggered lightning at Camp Blanding. An AT&T BellSouth analog conditioned telephone line was used to transmit a trigger pulse generated at Camp Blanding (near station) in response to lightning strikes on-site or in its immediate vicinity to Gainesville (distant station). The frequency bandwidth of this line, according to the provider specifications was from 300 Hz to 3 kHz and its characteristic impedance was 600 Ω. In case of lightning on-site (either natural or rocket-triggered), a trigger pulse is generated in the Launch Control at Camp Blanding via an OR gate. There are two inputs to the OR gate, trigger pulse due to detected optical signals (in case of on-site natural lightning),

Table 3-5. Characterization and calibration factors of electric field and dE/dt measuring systems at the LOG after April, 2008 (Engineering Building).

Measuring system	E1	dE1	E2	dE2
Experiment	Two-station	Two-station	Single-station	Single-station
Antenna Description	Elevated flat plate	Elevated flat plate	Elevated flat plate	Elevated flat plate
Elevation of sensing plate above the roof (m)	1.71	1.33	1.62	1.70
Diameter of plate (cm)	44.6	46.5	50.3	50.3
Antenna area, A, (m ²)	0.156	0.170	0.199	0.199
Integrating capacitance, C, (nF)	1.94	-	10.4	-
Resistances	5.1 MΩ (see Figure 3-10)	50 Ω (see Figure 3-13)	1 MΩ (see Section 3.7.4)	50 Ω (see Figure 3-13)
Gain due to elevation of sensing plate, G_p	15.3	9.1	11	13.1
Electronic gain, G_e	1	8.89	1	8.89
Relationship between measured voltage and field ($Field = K \times V_{out}$)	$E(t) = \frac{CV_{out}}{G_p G_e \epsilon_0 A}$ V/m	$\frac{dE(t)}{dt} = \frac{V_{out}}{G_p G_e \epsilon_0 AR}$ V/m/μs	$E(t) = \frac{CV_{out}}{G_p G_e \epsilon_0 A}$ V/m	$\frac{dE(t)}{dt} = \frac{V_{out}}{G_p G_e \epsilon_0 AR}$ V/m/μs
Calibration factor without building enhancement effect, K	91.8 m ⁻¹	164.2 m ⁻¹ μs ⁻¹	536.7 m ⁻¹	97.5 m ⁻¹ μs ⁻¹
Gain due to presence of building, G_b	1.4	1.4	1.4	1.4
Overall calibration factor, $K_t = K/G_b$	65.6 m ⁻¹	117.3 m ⁻¹ μs ⁻¹	383.3 ^a m ⁻¹	69.6 m ⁻¹ μs ⁻¹

^a From 08/19/08 to 11/30/08, G_e for E2 was 1.4, and the overall calibration factor K_t was 273.8 m⁻¹.

Table 3-6. Characterization and calibration factors of dB/dt measuring systems at the LOG after April, 2008 (Engineering Building).

Measuring system	dB (N-S)	dB (E-W)
Experiment	Both	Both
Antenna Description	Loop	Loop
Antenna area, A , (m ²)	0.533	0.533
Resistances	$R_{load} = 100 \Omega$ $R_{loop} = 1410 \Omega$ (see Figure 3-15)	$R_{load} = 100 \Omega$ $R_{loop} = 1410 \Omega$ (see Figure 3-15)
Electronic gain, G_e	145	145
Relationship between measured voltage and field ($Field = K \times V_{out}$)	$\frac{dB(t)}{dt} = \frac{2V_{out}(R_{loop} + R_{load})}{G_e R_{load} A} \text{ T/s}$	$\frac{dB(t)}{dt} = \frac{2V_{out}(R_{loop} + R_{load})}{G_e R_{load} A} \text{ T/s}$
Calibration factor without building enhancement effect, K	0.391 m ⁻²	0.391 m ⁻²
Gain due to presence of building, G_b	-	-
Overall calibration factor, ($K_t = K/G_b$)	0.391 m ⁻²	0.391 m ⁻²

Table 3-7. GPS locations, accurate to ± 2 m, of all antennas on the roof of the Engineering Building in 2008.

Measurement	Antenna GPS location (2008)
E1	29.64248 N -82.34714 W
dE1	29.64244 N -82.34714 W
E2	29.64214 N -82.34715 W
dE2	29.64209 N -82.34714 W
dB (N-S) and dB (E-W)	29.64246 N -82.34711 W
VHF	29.64234 N -82.34715 W

and trigger pulse due to current sensed by the current-viewing resistor (shunt) at the base of the launcher (in case of rocket-triggered lightning), as shown in Figure 3-27. The output of the OR gate is a 3.15 V, 200 μ s TTL pulse. This pulse is transmitted via a fiber optic link to the Office Trailer at Camp Blanding where it triggers a one-shot monostable circuit. The one-shot circuit is implemented using the CD74HC221, which is a high-speed CMOS logic dual monostable multivibrator whose schematic is shown in Figure 3-28. The output of the one-shot circuit is a 5 V, 462 μ s rectangular pulse. This pulse is fed into the Camp Blanding end of the AT&T BellSouth analog conditioned telephone line terminated in its characteristic impedance (600 Ω). This pulse undergoes some distortion due to the characteristics of the phone line (see Figure 3-29) and arrives at Gainesville (receiving) end in about 29 ms. The phone line is terminated in its characteristic impedance at the Gainesville end. This pulse was used to trigger the measuring systems at the LOG. The transmission delay of the trigger pulse from Camp Blanding to Gainesville was estimated by measuring the round trip time of a test pulse from Camp Blanding to Gainesville and back. The one way transmission delay is half the round trip time. A block diagram of the two-station experiment is shown in Figure 3-30.

During thunderstorms near both Gainesville and Camp Blanding, it was found that higher frequency noise pulses were often coupled to the phone line causing it to generate spurious triggers. In order to alleviate this problem two steps were taken. Firstly, a low pass filter with a -3 dB cut-off frequency of 1.5 kHz was installed at the Gainesville end of the line. Secondly, instead of triggering the LeCroy oscilloscope on a rising pulse edge (level trigger), a more selective pulse-width trigger was chosen. The oscilloscope triggered only when it sensed at its input a pulse whose width is greater than 350 μ s at a voltage level of 702 mV, which is a characteristic feature of the actual trigger pulse received at Gainesville (see Figure 3-29). These

steps have reduced the problem of spurious triggers greatly, however, on rare occasions some spurious pulses did trigger the measuring systems of the two-station experiment at the LOG.

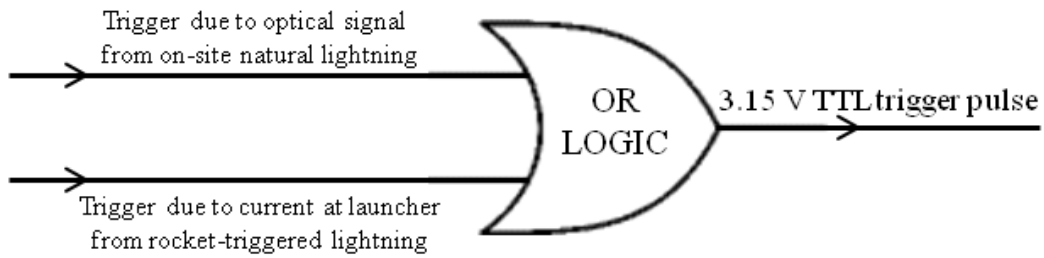


Figure 3-27. OR gate used to generate trigger pulses at Camp Blanding.

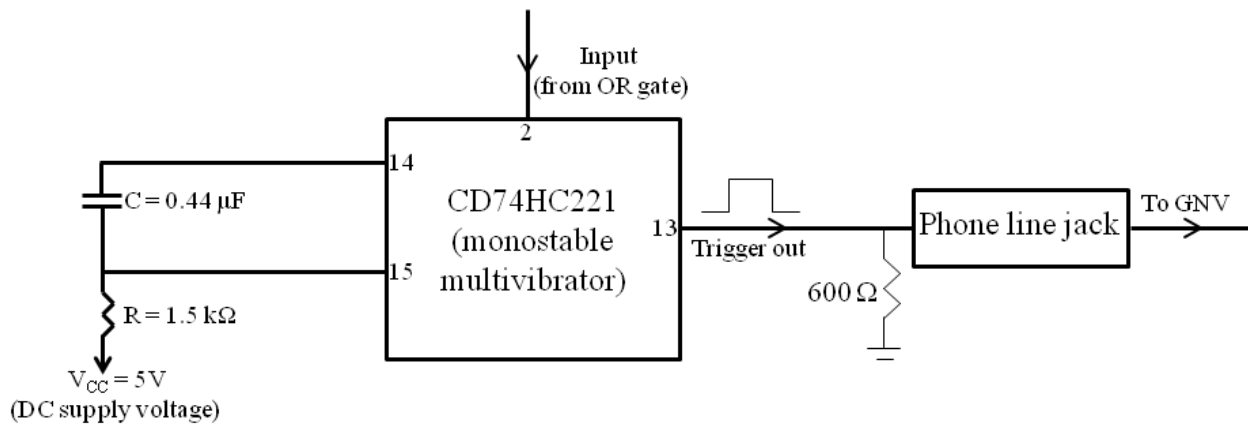


Figure 3-28. Functional diagram of a one-shot circuit implemented using a CD74HC221 (monostable multivibrator) used to generate a 5 V, 462 μs rectangular pulse which is fed into the telephone line.

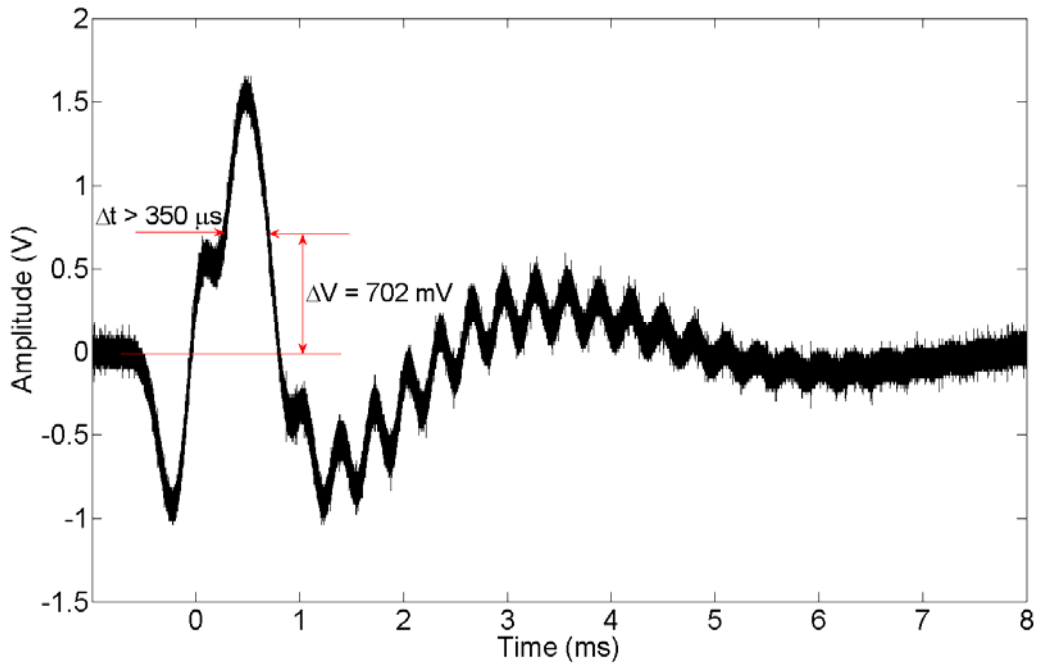


Figure 3-29. Trigger pulse from Camp Blanding received at Gainesville via the AT&T BellSouth analog conditioned telephone line.

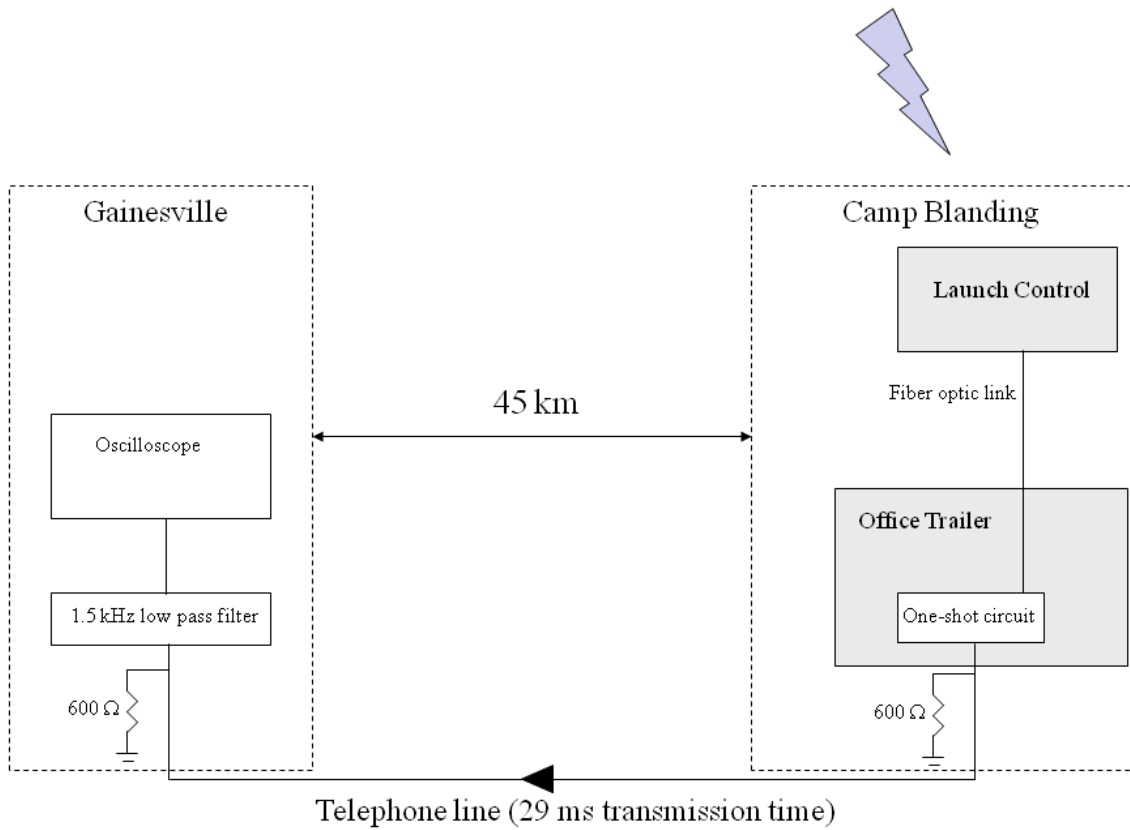


Figure 3-30. A block diagram schematically showing the two-station experiment.

CHAPTER 4 COMPACT INTRACLOUD LIGHTNING DISCHARGES

Cloud lightning discharges that produce both (1) single, usually solitary bipolar electric field pulses having typical full widths of 10 to 30 μs and (2) intense HF-VHF radiation bursts (much more intense than those from any other cloud-to-ground or “normal” cloud discharge process) are referred to as Compact Intracloud Discharges (CIDs). These discharges were first reported by *Le Vine* [1980] and later characterized by *Willett et al.* [1989b] and *Smith et al.* [1999, 2004], among others as discussed in Chapter 2 (Section 2.5). In this Chapter, we present and characterize new experimental data, propose a conceptual mechanism for this phenomenon, and present a model based on this mechanism for computing electromagnetic field signatures of CIDs. Electrical parameters of CIDs are also inferred.

4.1 Phenomenology

In this Section, we present new experimental data that are needed for testing the validity of various models of this phenomenon. Electric field waveform characteristics, source heights, and context of occurrence of CIDs are examined. The atmospheric electricity sign convention according to which a downward-directed electric field (or field change) vector is considered to be positive is used in this Section.

4.1.1 Experimental Data and Methodology

We examine wideband electric fields, electric field derivatives (dE/dt), magnetic field derivatives (dB/dt), and narrowband VHF (36 MHz) radiation bursts produced by 157 CIDs. The initial polarity of distant (essentially radiation) wideband electric field pulses produced by 156 of these CIDs was negative (opposite to that of negative return strokes). One relatively close waveform did not exhibit the radiation field pulse, with only induction and static field components being evident (see Figure 4-7c). All the 157 events transported negative charge

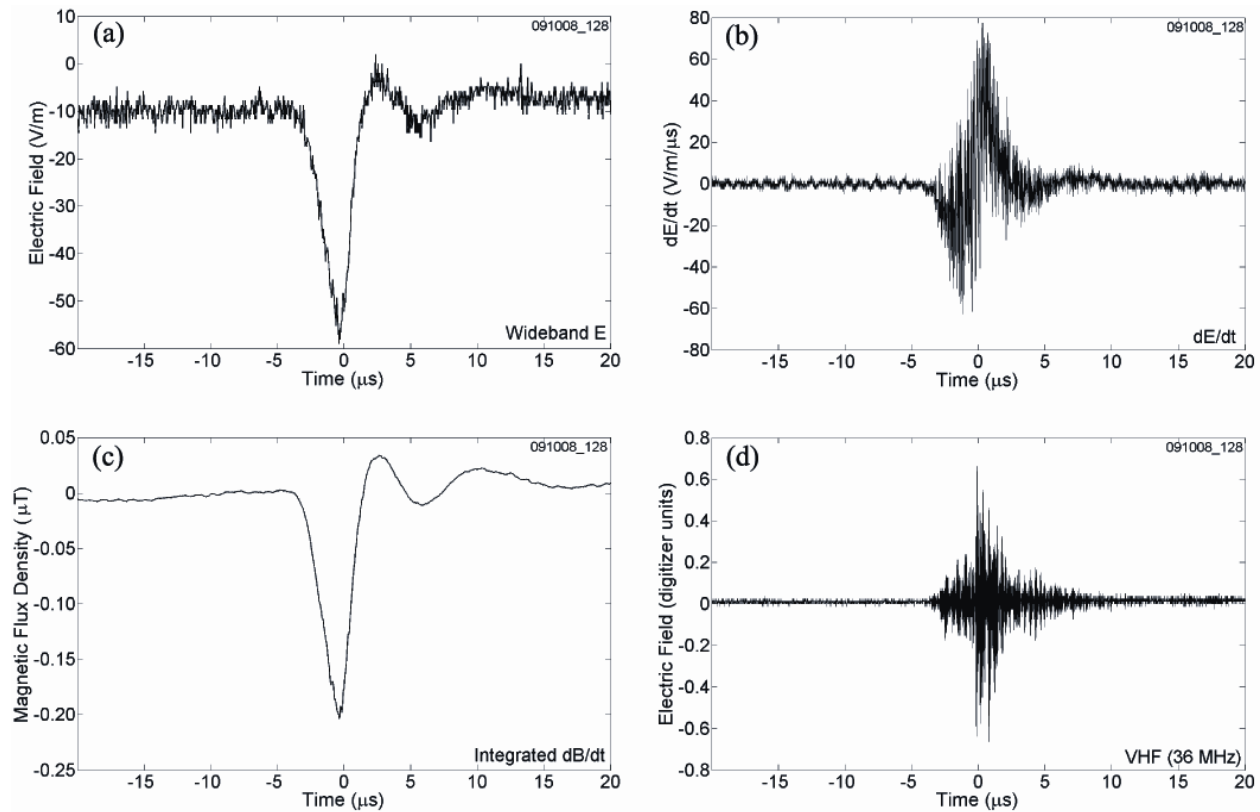


Figure 4-1. (a) Wideband electric field, (b) electric field derivative (dE/dt), (c) integrated magnetic field derivative (dB/dt), and (d) narrowband VHF (36 MHz) radiation burst produced by a CID in Gainesville, Florida. From $E_z/B_\phi = 2.24 \times 10^8$ m/s, and $r = 17.2$ km, the source height $h = 15$ km.

upward (or lowered positive charge). The data were acquired in August-September, 2008 at the LOG using instrumentation described in Chapter 3. Typical measured waveforms for one CID are shown in Figure 4-1. We also recorded, over the same time period, 4 CIDs whose distant electric field waveforms had initial positive polarity. These four transported negative charge downward (or raised positive charge) and are not further considered in this Section.

CIDs were identified by their intense VHF radiation signature and characteristic wideband field (NBP or, in one case, its close-range counterpart) and field derivative waveforms. Different triggering schemes were employed in acquiring the data analyzed in this Chapter. For 80 events the system was triggered on VHF only. The trigger threshold was empirically set at a relatively high level so as to minimize triggers on cloud-to-ground lightning (those were less

Table 4-1. Number of NLDN-located CIDs in different horizontal distance ranges.

Distance Range (km)	0-10	10-20	20-30	30-40	40-50	50-60	60-70	70-135	0-135
Number of events	5	20	21	24	18	36	13	13	150 ^a
Number of events used in Sections 4.1.4 and 4.1.5	0	14	8	10	6	3	6	1	48

^a149 events were identified by the NLDN as cloud discharges and 1 event as positive CG.

than 6% of all triggers). For 77 events the system could also trigger on wideband electric field, but the VHF threshold was always exceeded. Thus, we assume that for all the 157 events analyzed here our measuring system was triggered on VHF. The sample of 157 was formed by manually searching all our strong-VHF records for characteristic CID wideband field and field derivative signatures (see Figure 4-1) and accepting only those with electric field peaks greater than 1.5 times the background noise level. There were many strong VHF producers that did not satisfy the latter criterion, which probably introduced some amplitude bias, as discussed in Section 4.1.5.

GPS timestamps were used to obtain NLDN-estimated locations for selected events. Out of 157 CIDs, 149 (95%) were correctly identified as cloud discharges and located by the NLDN. The distances of these events from the measurement station ranged from 5 to 132 km. One CID was misidentified by the NLDN as a positive CG at 38 km with an estimated peak current of 24 kA. Seven CIDs were not detected by the NLDN. Table 4-1 gives the number of located events in different distance ranges.

Simultaneous measurements of electric and magnetic radiation field pulses produced by CIDs and NLDN-reported horizontal distances to these discharges can be used to obtain estimates of source heights. For a vertical source above perfectly conducting ground (see Figure 4-2), the ratio of the vertical component of electric field intensity (E_z) and the azimuthal component of magnetic flux density (B_ϕ) on the ground surface is given by [e.g., *Baum*, 2008]

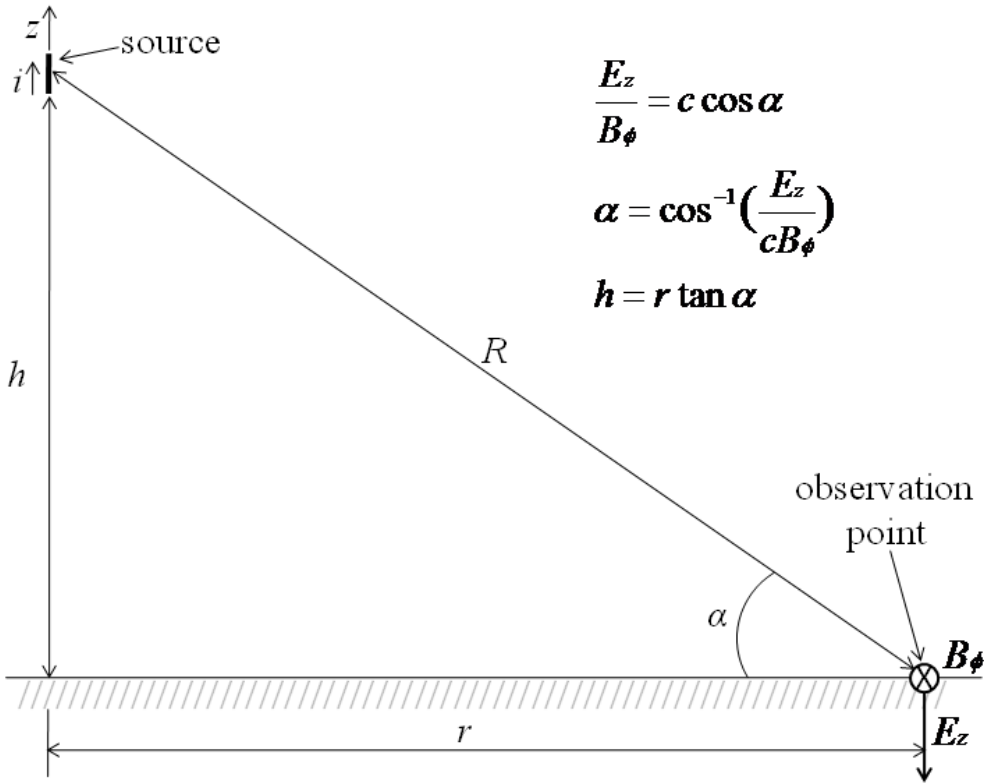


Figure 4-2. Geometrical parameters and equations used in estimating radiation source heights. See text for details.

$$\frac{E_z}{B_\phi} = c \cos \alpha \quad (4-1)$$

where c is the speed of light, so that the elevation angle α can be found as $\alpha = \cos^{-1}\left(\frac{E_z}{cB_\phi}\right)$.

The source height can be estimated as $h = r \tan \alpha$, where r is the horizontal distance of the source from the field measuring station. This approach is valid for a vertical radiator and for early-time field measurements for which $\Delta t \ll R/c$ [Baum, 2008], where R is the inclined distance from the measuring station to the source, this distance being given by $R = \sqrt{h^2 + r^2}$. For $R = 15 - 30$ km, $R/c = 50 - 100 \mu\text{s}$, while Δt (NBP risetime) is typically a few microseconds. In order to check if our height-estimation method is influenced by calibration of our field measuring systems, we computed E_z/B_ϕ ratios for 43 first return strokes in negative lightning at distances ranging from 8 to 67 km. The return-stroke initial field peaks (essentially radiation) are produced

by sources near ground (typically within 100 m), so that $\alpha \approx 0$ and expected ratio $E_z/B_\phi \approx c$. We found that the 43 ratios were within $\pm 16\%$ of the speed of light with the arithmetic mean being $0.99c$, which gives us confidence in our electric and magnetic field measurements.

For estimating source heights we selected 48 CIDs with NLDN-reported distances ranging from 12 to 89 km, whose electric field peaks were greater than 2.5 times the background noise level (in order to reduce the peak-measurement error). Each of these 48 CIDs was reported by 4 to 22 (11 on average) NLDN sensors with a length of the semi-major axis of 50% location error ellipse ranging from 400 m to 4.9 km (mostly 400 m, so that the median was as small as 400 m). Measured waveforms including electric field, dE/dt , dB/dt , and narrowband VHF (36 MHz) for these 48 CIDs are shown in Appendix A.

4.1.2 Relation of Compact Intracloud Discharges to Other Types of Lightning

It is generally thought that CIDs occur in isolation (within several hundred microseconds to a few milliseconds) or at the beginning of ordinary cloud discharges [e.g., *Smith et al.*, 2004]. *Krehbiel et al.* [2008] reported a CID that occurred 800 ms prior to a gigantic jet.

The majority (72%; actually 72.6%, but set at 72% to assure that all the percentages add to 100%) of CIDs examined here appeared to occur in isolation; that is, there was no other lightning process occurring prior to or following the CIDs within the length of the record (500 ms with a 100 ms pretrigger). About 24% of CIDs were found to occur prior to, during, or following cloud-to-ground (CG) or “normal” IC lightning discharges. Specifically, 18% (28 out of 157) of CIDs accompanied ordinary cloud discharges. NLDN locations were available for 8 IC flashes in all of which CIDs preceded IC impulsive processes. Five CIDs preceded IC impulsive processes by 5.3 to 67 ms with horizontal separation distances being 1 km or less. Seven CIDs were within 10 km of ICs, and one beyond 25 km. An example of wideband electric field and VHF radiation from a CID followed by a cloud (IC) flash is shown in Figure 4-3. Further, 6% (9 out of 157) of the

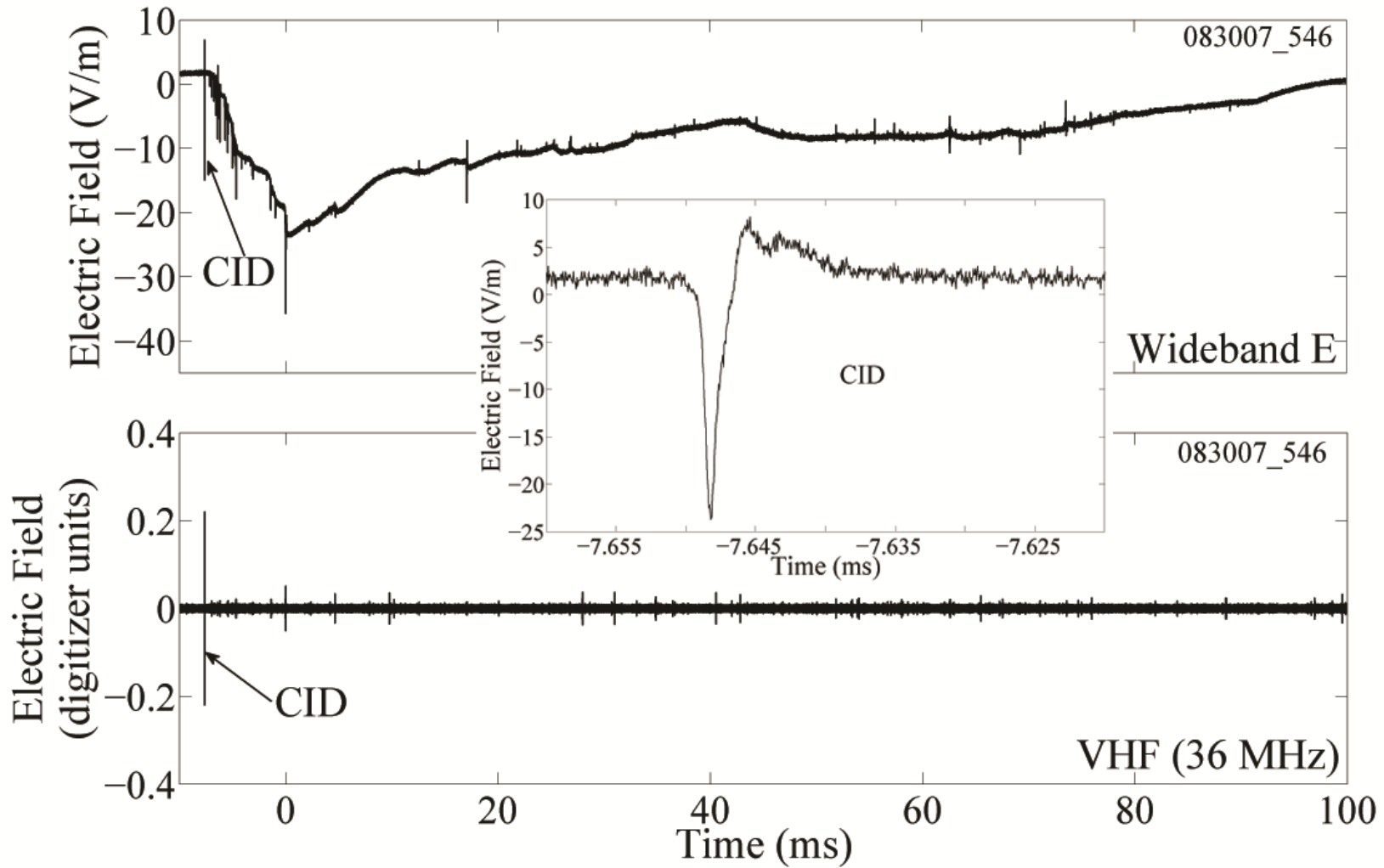


Figure 4-3. Electric field and VHF (36 MHz) radiation from a CID that was followed by a "normal" IC (from another experiment in Gainesville, Florida). Inset shows the CID signature on an expanded (5 μ s per division) time scale. No NLDN locations are available.

CIDs appeared to occur in association with CG flashes. NLDN locations were available for 7 CG flashes. In three cases, CIDs were found to precede CGs by 72 to 233 ms, while in four cases, they occurred during or after CGs. In three cases, CIDs were found to occur within 5 km of CG strokes and in seven cases they were within 20 km. Figure 4-4a shows the wideband electric field and VHF radiation from an eight-stroke CG (only the second through seventh strokes were recorded by our system), with a CID occurring between the third and fourth strokes at horizontal distances of 7 to 8 km from all strokes of this flash. Plan view of NLDN locations of this CID and the CG strokes is shown in Figure 4-4b. Interestingly, locations of seven out of eight strokes are within less than 1 km of each other, while one stroke (of order 4), which was immediately preceded by the CID, created a new termination on ground, about 3 km away from other strokes of the flash.

We also observed (for the first time) three sequences of two CIDs (4% of all CIDs analyzed here), with time intervals within the pairs being 43, 66, and 181 ms. These intervals are comparable to interstroke intervals in CG flashes. The horizontal separation distances were 16, 24, and 11 km, respectively. The CIDs in the first pair were found to occur successively at heights of 18 and 15 km. Electric field record of one of the "multiple" CID events (the second pair) is shown in Figure 4-5.

The occurrence context of CIDs is summarized in Figure 4-6. It is presently not clear how CIDs influence (if at all) the ordinary lightning processes.

4.1.3 Different Types of Electric Field Waveforms

The electric field associated with lightning discharges is often viewed as being composed of the electrostatic, induction, and radiation field components. At larger distances (beyond several tens of kilometers) and at early times the radiation component is generally the dominant one. As distance decreases, relative contributions of the other two components increase. Most of

the CID waveforms found in the literature are essentially radiation (NBP pulses), with closer waveforms that exhibit both radiation and electrostatic field components being exceedingly rare. Only seven were recorded within 15 km and five within 10 km [Eack, 2004]. Only one waveform [Eack, 2004, Figure 4-1] dominated by induction and electrostatic field components (no radiation field component is discernible) is found in the literature.

In Figures 4-7a-c, we present three types of CID electric field waveforms recorded in Gainesville, Florida. CID that produced the essentially radiation field signature, shown in Figure 4-7a, was located at a horizontal distance of 40 km, and for the event shown in Figure 4-7b the distance was 9.4 km. In the latter case, note an electrostatic field change of about 6 V/m after the radiation pulse (induction field component might be significant too, but is difficult to identify). NLDN did not detect the CID whose electric field signature is shown in Figure 4-7c, but its parent thunderstorm was observed to be overhead. For this event, the static and induction components are dominant and the radiation component is undetectable (negligible). Results presented in Figures 4-7a-c are consistent with experimental [Eack, 2004] and model-predicted [Watson and Marshall, 2007] waveforms found in the literature, with the type of waveform shown in Figure 4-7c being previously observed, as noted above, only once. Note that for a short vertical dipole at relatively large elevation angle α above ground (see Figure 4-2) the radiation field peak on the one hand and induction and static field changes on the other hand are expected to have opposite polarities. Specifically, it follows from equation (A.38) of Uman [1987, p. 329] for the electric field at perfectly conducting ground due to a differential vertical dipole that the opposite polarities are expected for $\alpha > 35.3^\circ$, which translates to $r < 21$ km if source height $h = 15$ km.

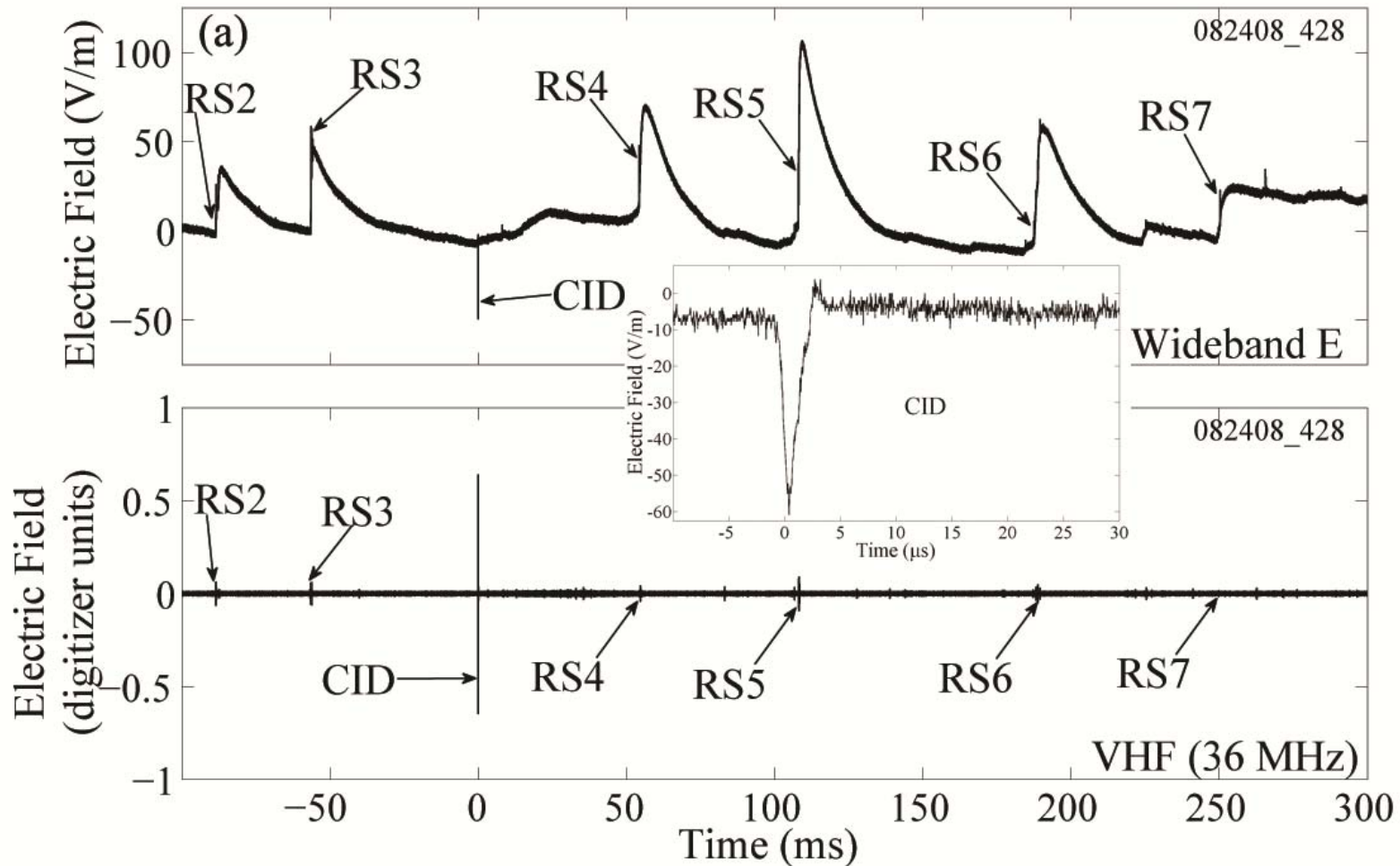


Figure 4-4a. Wideband electric field and VHF (36 MHz) radiation from a CID that occurred during an eight-stroke negative CG, within horizontal distances of 7 to 8 km of all the CG strokes. Only the second through seventh strokes were recorded by our measurement system. The CID height above ground was estimated to be about 14 km. Note that the VHF radiation produced by the CID is much larger than that produced by the CG strokes (RS2 to RS7). Inset shows the CID wideband electric field signature on an expanded time scale.

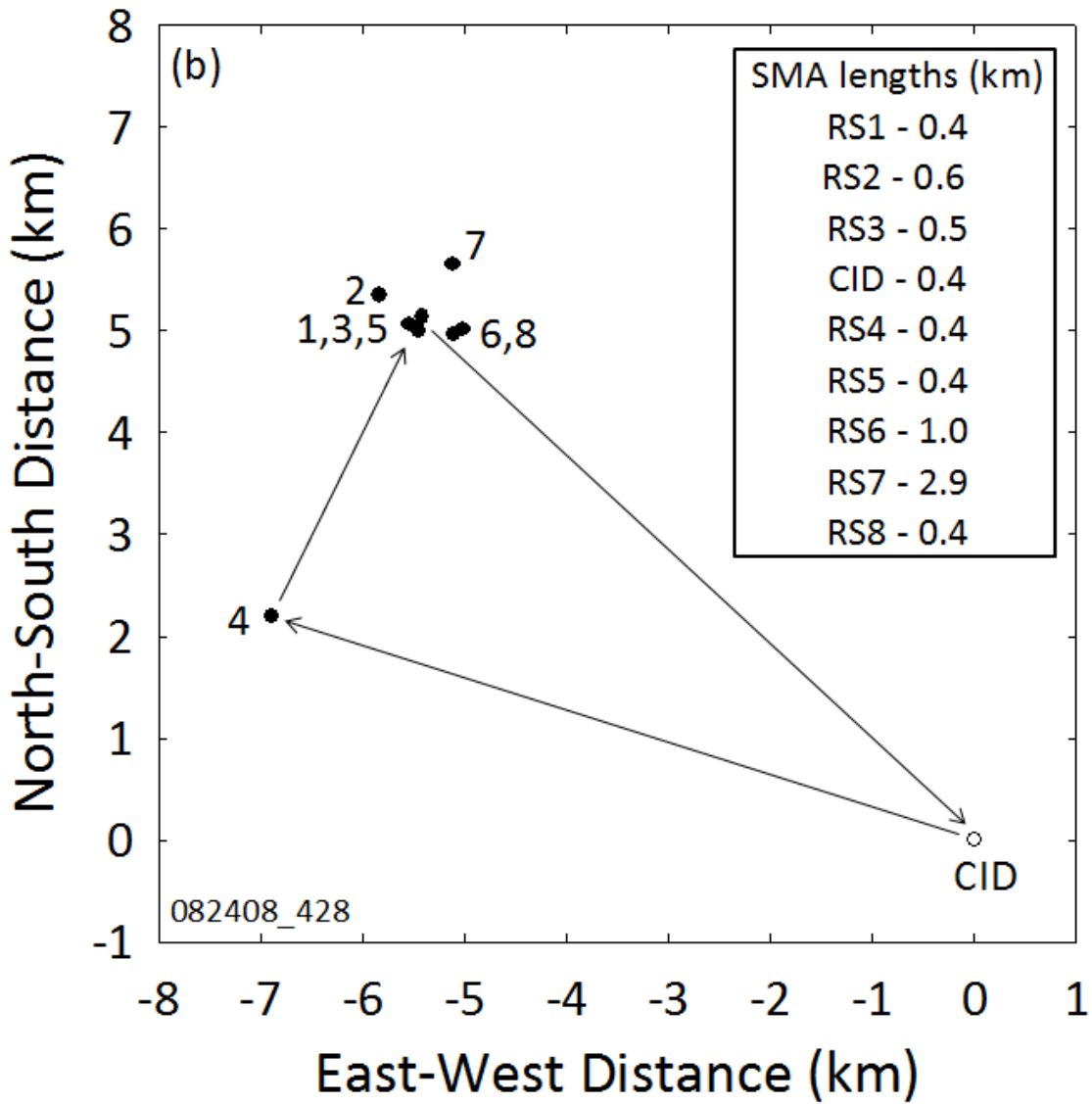


Figure 4-4b. Plan view of NLDN-estimated relative positions of the CID (hollow circle) and return strokes (numbered solid circles) of CG flash whose wideband and VHF signatures are shown in Figure 4-4a. The semi-major axis (SMA) lengths of NLDN-reported 50% location error ellipses for each of the return strokes and the CID are also given. Strokes 1 to 3 occurred before the CID and strokes 4 to 8 after it. Arrows indicate changes in plan-view location from strokes 1-3 to the CID, then to stroke 4 (new termination on ground), and to strokes 5-8.

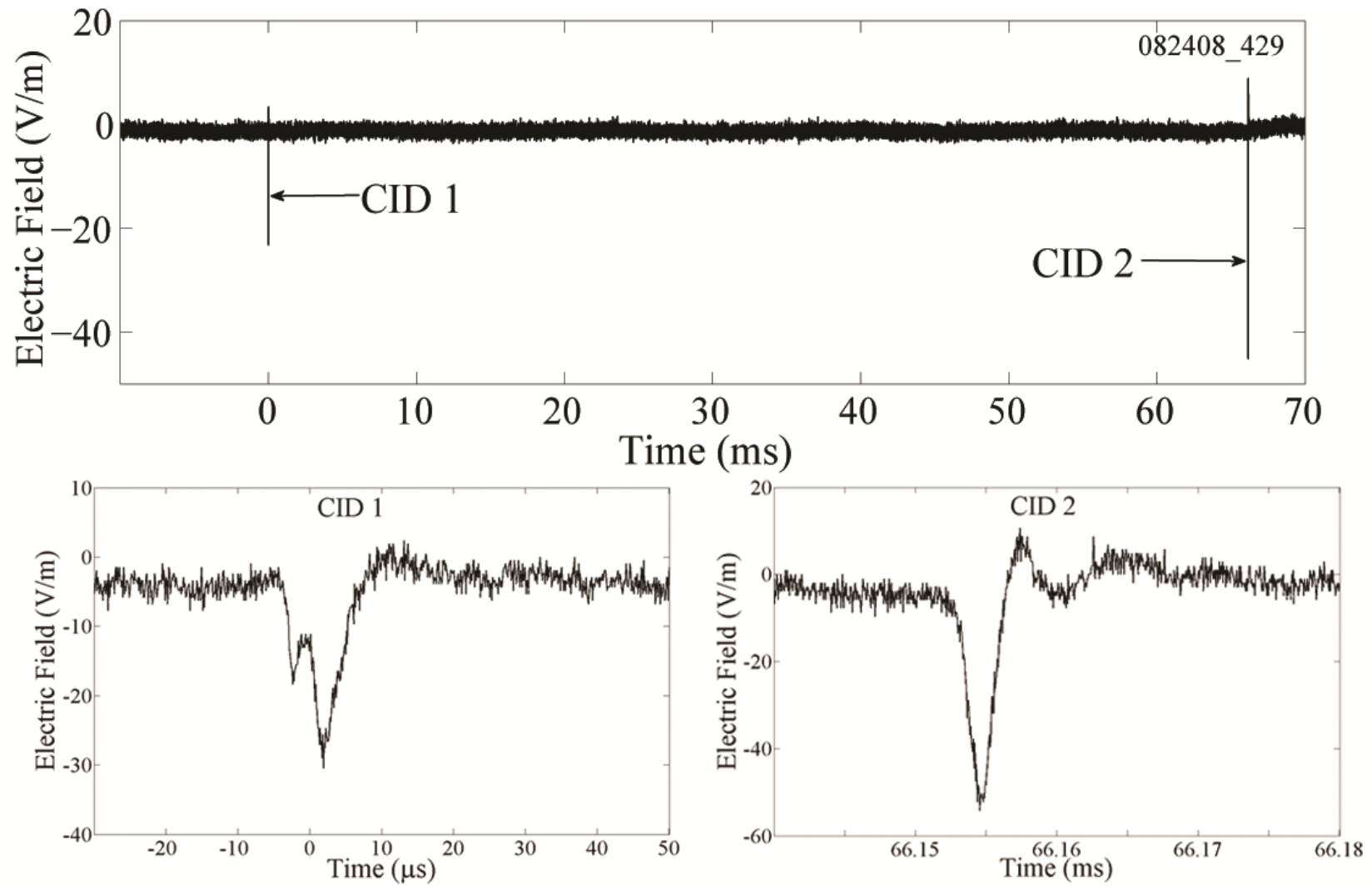


Figure 4-5. (top) Wideband electric field record showing two CIDs that occurred 66 ms apart at a horizontal distance of 24 km from each other. The height of CID 2 above ground was estimated to be about 17 km, while the height of CID 1 is unknown. (bottom) Individual CID signatures displayed on expanded (10 and 5 μ s per division for CID 1 and CID 2, respectively) time scales.

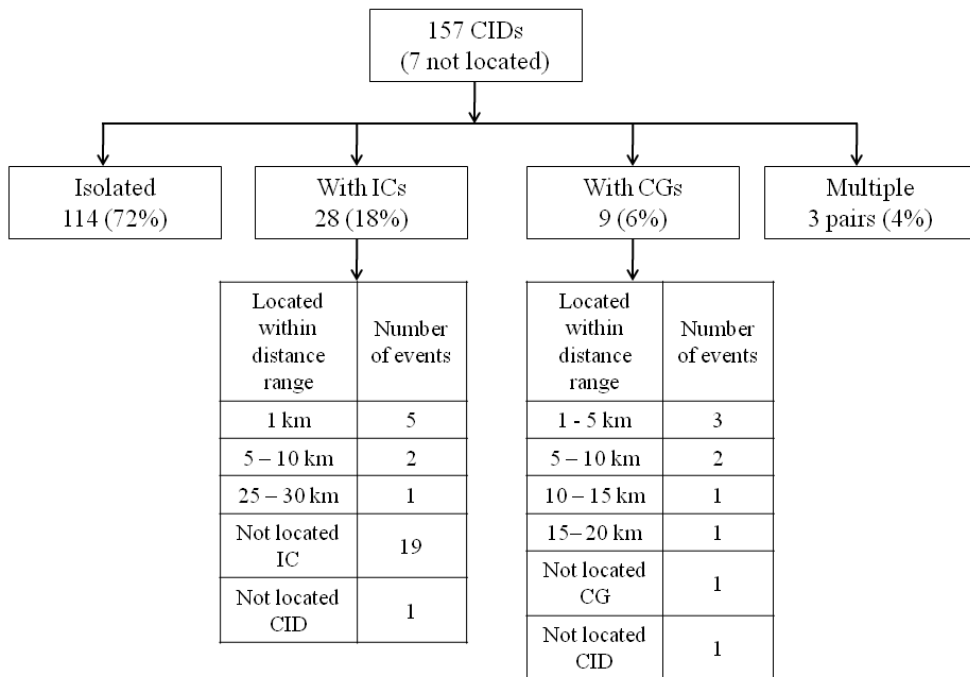


Figure 4-6. Occurrence context of CIDs.

Of the 157 CID signatures examined here, 151 were of type (a), 5 of type (b), and 1 of type (c), where (a), (b), and (c) are the three parts of Figure 4-7. Unfortunately, no source heights could be estimated for waveforms of types (b) and (c).

4.1.4 Source Heights

Smith et al. [2004] used two methods to estimate CID heights above ground. One was based on measuring delays of ionosphere and ground-ionosphere reflections with respect to direct-path wave in VLF/LF ground-based (LASA) field records. The other one employed FORTE satellite VHF records showing direct-path and ground-reflection signals. The ground-based estimates were on average 1 km higher than the satellite estimates, the latter being considered by *Smith et al.* as more accurate.

The distribution of source heights for 48 CIDs inferred here using the method described in Section 4.1.1 is shown in Figure 4-8. Table A-1 in Appendix A gives the horizontal distance and

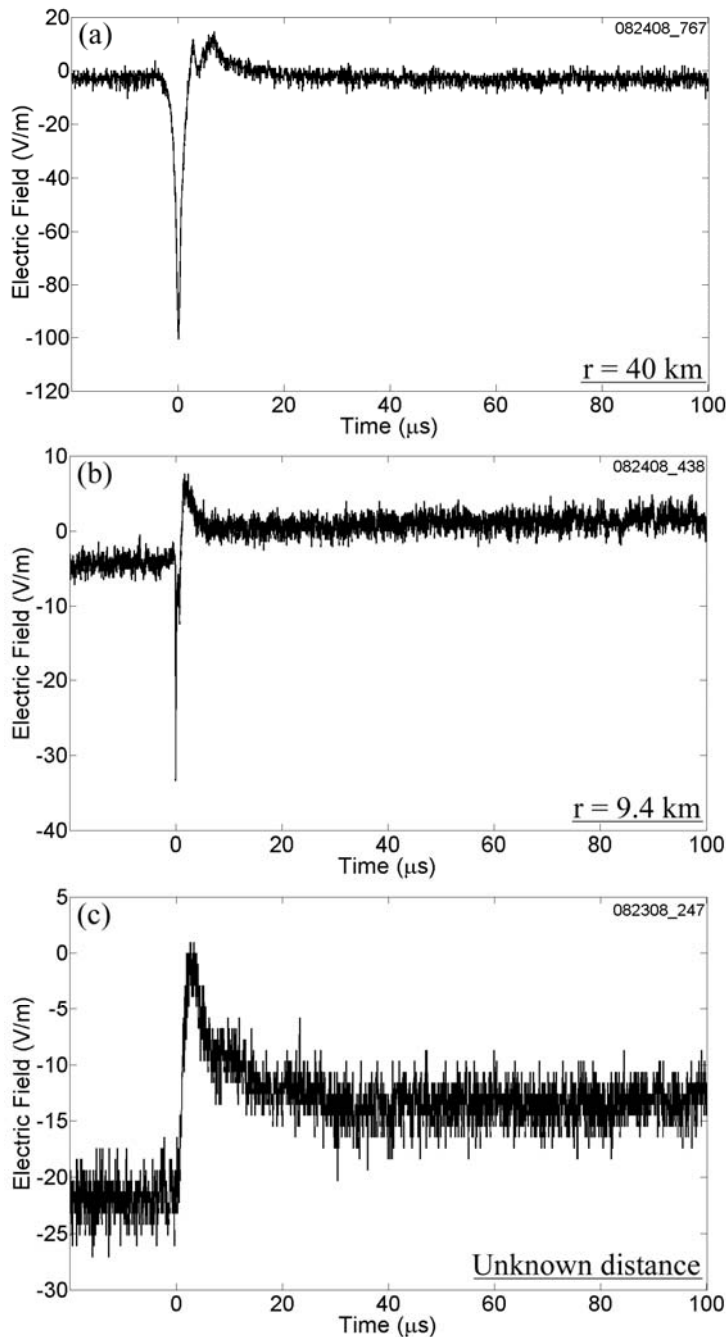


Figure 4-7. Three types of CID electric field waveforms exhibiting (a) only radiation, (b) radiation and static field components (induction component is not apparent), and (c) only induction and static field components. Note that for the geometry shown in Figure 4-2, the radiation field peak on the one hand and induction and static field changes on the other are expected to have opposite polarities when $\alpha > 35.3^\circ$. Assuming a source height of 15 km and using NLDN-estimated distances, we found $\alpha = 21^\circ$ and 58° for (a) and (b), respectively. Of 157 CID signatures, 151 were of type (a), 5 of type (b), and 1 of type (c).

height information for each of these 48 CIDs. The minimum and maximum source heights were 8.8 and 29 km, respectively. The geometric mean was 16 km and median was 15 km, the latter being similar to the median source height of 13 km reported for the same NBP initial polarity by *Smith et al.* [2004]. The majority of height values in *Smith et al.*'s study (based mostly on events in the vicinity of Florida) were between 3 and 20 km, although some heights were as large as about 30 km. Note that the heights larger than 15 to 20 km are likely to be above the upper cloud boundary and therefore appear unrealistic. There are two primary sources of error in our estimated source height: elevation angle error and distance error. The angle error is primarily due to inaccuracies in the measurement of the electric field peak because of the presence of background noise. The distance error can be estimated using NLDN-reported 50% location error ellipses. As these two types of errors are uncorrelated, the total height error for each of the 48 CIDs may be taken as the square root of the sum of the squares of the two individual error components. The median height error was estimated to be $\pm 14\%$ (error range was from 5 to 23%), which does not explain the apparently unrealistic source heights. There are nine CIDs whose estimated heights are greater than 20 km in our dataset. We found them unremarkable in all respects, except for their height. All nine were isolated and occurred at horizontal distances ranging from 32 to 63 km.

Jacobson and Heavner [2005] found that less than 20% of their CIDs observed in Florida were at altitudes ranging from 15 to 20 km, and very few occurred above 20 km. They stated that their altitude measurement uncertainties were less than 2 km, so it is likely that at least some of their events were truly occurring above the nominal tropopause, whose altitude they estimated to be about 15 km. It is possible that the CIDs observed at heights greater than 20 km were associated with convective surges overshooting the tropopause and penetrating deep into the

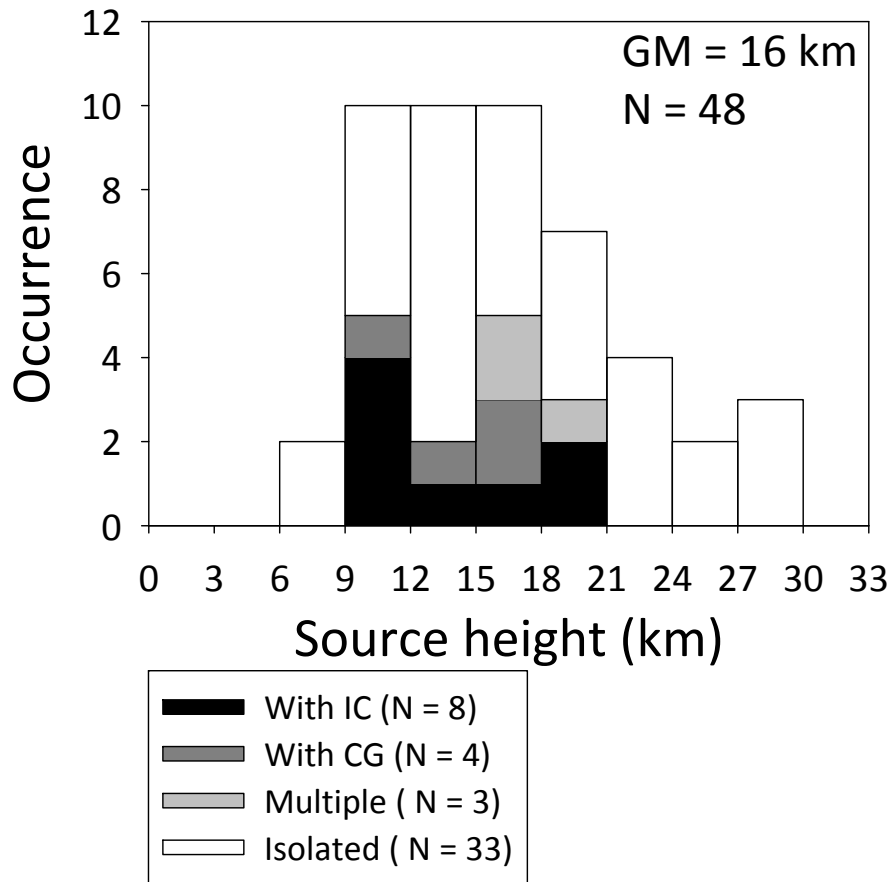


Figure 4-8. Histograms of radiation source heights for 48 CIDs.

stratosphere [e.g., *Romps and Kuang, 2009*]. *Darrah [1978]* observed tropopause overshoots up to 5 km in severe storms.

We wonder if at least some of the CIDs inferred to occur well above the cloud top (in the stratosphere) could be associated with gigantic jets. *Krehbiel et al. [2008]* described gigantic jets as resembling negative upward leaders exhibiting impulsive rebrightening and extending from cloud tops to the ionosphere.

4.1.5 Electric Field Waveform Characteristics

For the subset of 48 CIDs, we estimated electric field peaks normalized, assuming inverse distance dependence, to $R = 100$ km and to $\alpha = 0^\circ$ as

$$E_N = E \left(\frac{R}{100} \right) \frac{\cos 0^\circ}{\cos \alpha} \quad (4-2)$$

Normalization to $\alpha = 0^\circ$ corresponds to $h = 0$, but at 100 km the result is essentially the same for median $h = 15$ km. The distribution of normalized electric field peaks is shown in Figure 4-9. The geometric mean is 20 V/m, which is considerably larger than the initial electric field peak at 100 km for negative first return strokes (6 V/m in Florida [Rakov and Uman, 2003]). We found that the normalized electric field peak tends to increase with horizontal distance (determination coefficient = 0.59). This suggests that our sample is biased toward larger peaks, with the bias increasing with increasing distance. Indeed, the geometric mean normalized electric field peak for horizontal distance ranges of 10-30 km, 30-50 km, and 50-70 km were found to be 15 V/m (N = 22), 23 V/m (N = 16), and 31 V/m (N = 9), respectively. One CID that occurred at 89 km had a normalized electric field peak of 35 V/m. This amplitude bias was apparently introduced by the requirement to have sufficiently pronounced field signatures for estimating source heights. Note that even for the smallest distances, 10 to 30 km, the source strength (15 V/m) is considerably higher than that for first return strokes in negative CGs (6 V/m).

Willett *et al.* [1989b] reported an arithmetic mean distance-normalized NBP initial peak of 8.0 ± 5.3 V/m at 100 km for 18 Florida CIDs that occurred in a storm at a distance of 45 km (no distances for individual events were available). Further, Smith *et al.* [1999] found a mean of 9.5 ± 3.6 V/m at 100 km for 24 CIDs at horizontal distances ranging from 82 to 454 km (there might have been significant propagation effects) in New Mexico and West Texas. Our arithmetic mean (\pm standard division) is 21 ± 8.9 V/m at 100 km for all the 48 events and 15 ± 3.4 V/m for 22 events within 10-30 km.

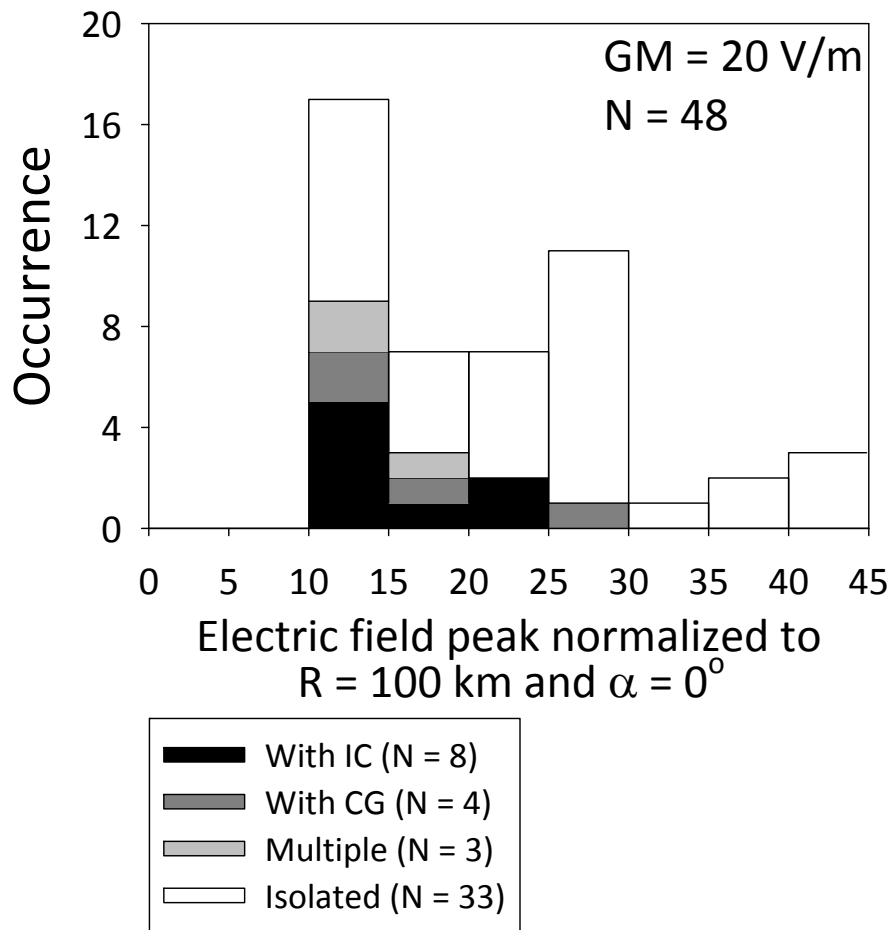


Figure 4-9. Histograms of electric fields peaks normalized to $R = 100$ km and $\alpha = 0^\circ$ for 48 CIDs.

Figure 4-10a and 10b show distributions of the total pulse duration (including the overshoot) and the total width of the initial half-cycle, respectively, for the 48 CIDs. The total durations range from 9.6 to 38 μs with arithmetic and geometric means of 24 and 23 μs , respectively. The total width of the initial half-cycle ranges from 2.8 to 13 μs with arithmetic and geometric means being 6.1 and 5.7 μs , respectively. *Smith et al.* [1999] found the arithmetic mean total pulse duration to be 26 ± 4.9 μs , which is similar to our estimate.

Figure 4-10c shows the distribution of the ratio of initial electric field peak to opposite polarity overshoot for the 48 CIDs. The ratio ranges from 3.5 to 17 with arithmetic and

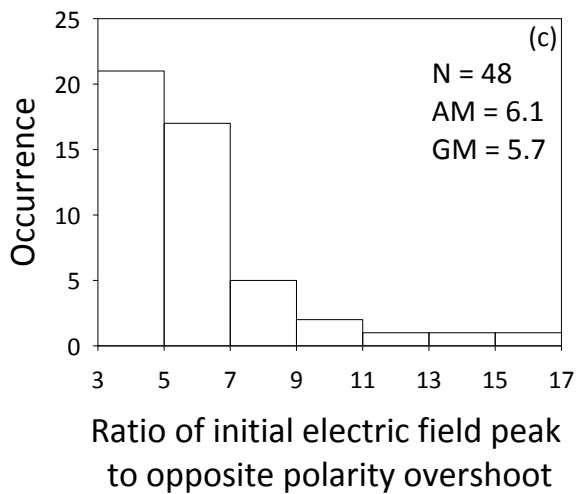
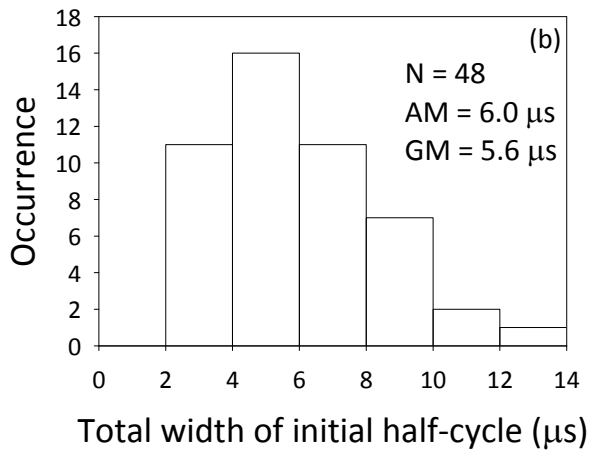
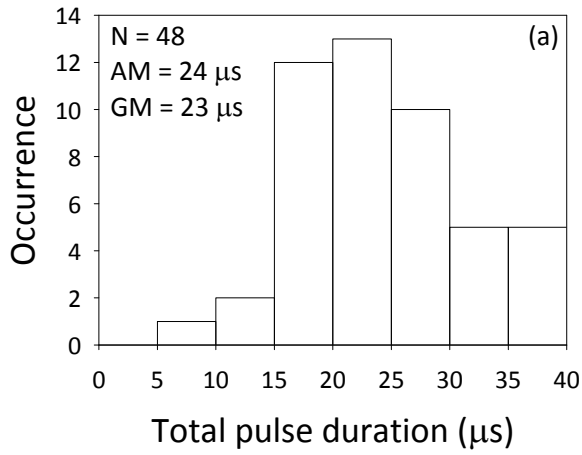


Figure 4-10. (a) Total pulse duration including overshoot, (b) total width of initial half-cycle, and (c) ratio of initial electric field peak to opposite polarity overshoot for 48 CIDs.

geometric means being 6.1 and 5.7, respectively. *Willett et al.* [1989b] reported the arithmetic mean ratio to be 8.8 ± 5.2 for 18 events and 9.1 ± 2.0 for 6 events in two different storms in Florida, while *Smith et al.* [1999] found the arithmetic mean ratio to be 2.7 for 24 CIDs in New Mexico and West Texas. Our estimate is between the previously reported values.

4.2 Conceptual Mechanism and Modeling

As discussed in Chapter 2, *Watson and Marshall* [2007] used the original transmission line (TL) model [*Uman et al.*, 1975] and a modified TL model with an exponentially increasing current along the channel to compute electric field signatures at horizontal distances of a few and 200 km and compare them with corresponding measured waveforms reported by *Eack* [2004]. Both models can successfully match the two-station field measurements. The exponentially increasing current was assumed by *Watson and Marshall* to correspond to the runaway electron breakdown process. The original TL model was also employed by *Le Vine* [1980]. In all the modeling studies to date the TL was assumed to be energized at one end with the other end being terminated in its characteristic impedance, so that the travelling wave is totally absorbed there. A good agreement with measurements was achieved for currents and speeds comparable to those of return strokes in cloud-to-ground lightning; that is, for current peaks of some tens of kiloamperes, durations of some tens of microseconds, and speeds of the order of 10^8 m/s.

In this Section, we propose a conceptual mechanism for the CID phenomenon and present a model based on this mechanism for computing electromagnetic field signatures of CIDs. The model is used to determine "allowed" (consistent with experimental data) ranges of effective current reflection coefficients at channel ends, propagation speed, channel length, and current risetime. Additionally, the Hertzian dipole approximation and testing model validity against two-station measurements of *Eack* [2004] are considered. The physics sign convention according to

which a downward-directed electric field (or field change) vector is considered to be negative is used in this Section and in Section 4.3.

The data used in this Section were acquired in summers of 2007 and 2008 in Gainesville, Florida (at the LOG), and include wideband electric fields, electric field derivatives (dE/dt), magnetic field derivatives (dB/dt), and narrowband VHF (36 MHz) radiation bursts produced by CIDs. For some events we also have narrowband HF (5 MHz) radiation records. A total of 220 CIDs (including 212 dE/dt signatures) were examined in this Section. The instrumentation used to acquire the data is described in Chapter 3. Phenomenological characteristics of 157 CIDs acquired in August-September of 2008 at the LOG are discussed in Section 4.1.

4.2.1 Evidence of Reflections in CID Electromagnetic Field Signatures

Hamlin et al. [2007] reported that 12% of their CIDs each showed evidence of one current-pulse reflection, which appeared as a secondary pulse after the initial peak in their distant electric field waveforms. They interpreted the secondary pulse as a signature of reflection of the current pulse off the "far end" of the CID channel and used this feature to estimate CID channel lengths. The average time interval between the primary and secondary electric field peaks was 6.7 μs with a standard deviation of 2.7 μs . The upper bound on the channel length (determined assuming that the current wave travelled at the speed of light) was found to be about 2 km. In the following, we will present experimental evidence of multiple (up to 7) reflections from both ends of the CID channel. Our pulse detection efficiency was considerably higher than *Hamlin et al.'s*, because, in addition to electric fields, we used our dE/dt records. We found that *Hamlin et al.'s* secondary peak is actually a higher-order one and therefore would result in an overestimate if used for calculating radiator length. Also, electric field peaks of the same polarity as that of the main pulse occur at the time when the current front is in the middle of the channel, in contrast

with *Hamlin et al.*'s [2007] assumption that they occur at the time of first reflection at the far end of the channel.

In Figure 4-11 we present (a) electric field, (b) dE/dt , and (c) VHF radiation burst produced by one of the CIDs in our data set. For this event, the initial polarity of NBP (see Figure 4-11a) is the same as that of negative return strokes and consistent with motion of positive charge upward (or negative charge downward). The duration, about 16 μs , is typical for NBPs (10 to 30 μs on average). A superposition of electric field, dE/dt , and VHF signatures is shown in Figure 4-11d. A typical event with initial polarity consistent with motion of negative charge upward is shown in a similar format in Figure 4-12, with HF signature additionally presented in Figure 4-12c. Both events occurred at unknown distances, but their fields are clearly dominated by the radiation field component.

At least one secondary peak (labeled S4) having the same polarity as the primary peak and multiple shoulders (labeled S1-S3 and S5) are seen in Figure 4-11a. We observed one or more secondary peaks in 34 (15%) of 220 CID electric field records, while in 186 (85%) cases no secondary peak could be identified. Following *Hamlin et al.* [2007], we measured time intervals between the primary and first clear secondary peak (S4 in Figure 4-11a) of the same polarity in electric field records of 34 CIDs. They ranged between 1.0 μs to 5.8 μs with a mean of 3.2 μs . The latter is about a factor of two shorter than *Hamlin et al.*'s mean of 6.7 μs .

In dE/dt signatures, secondary peaks (see Figure 4-11b) appear as pronounced oscillations after the initial opposite polarity (negative) overshoot. There are five pronounced cycles in Figure 4-11b, whose positive half-cycles are labeled S1 to S5. The first three of them correspond to shoulders S1 to S3 and the following one to the secondary peak S4 in Figure 4-11a. Note that peaks in electric field waveform correspond to local "zeros" in dE/dt waveform (and vice versa),

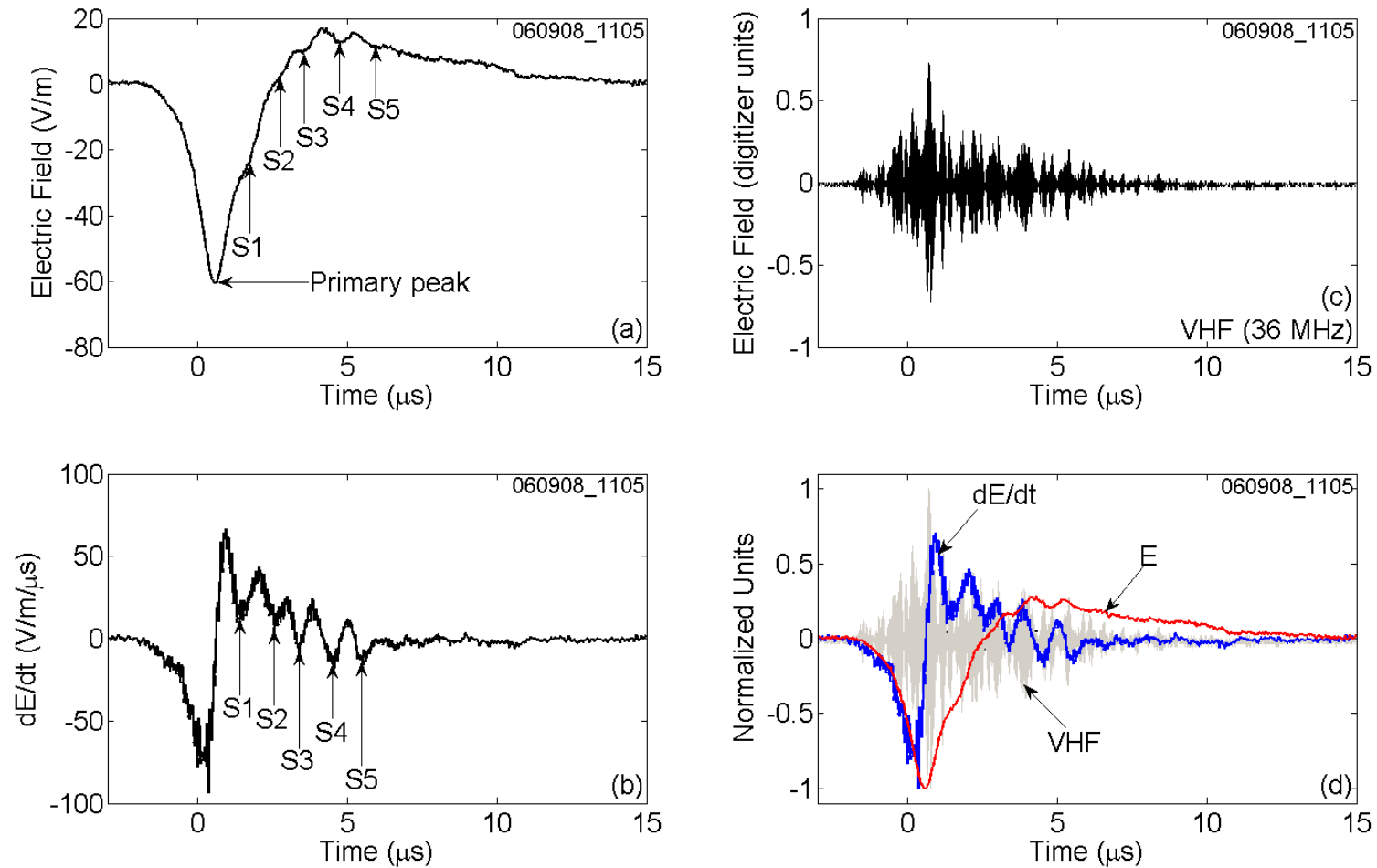


Figure 4-11. (a) Electric field, (b) dE/dt , and (c) VHF radiation signatures of a CID that transferred negative charge downward (or positive charge upward), recorded in Gainesville, Florida. The event occurred at an unknown distance. The three signatures are overlaid in (d) for direct comparison. S1-S5 are five secondary peaks appearing as pronounced oscillations in (b) and mostly as shoulders in (a). Electric field and dE/dt waveforms have been low-pass filtered to accentuate reflection signatures.

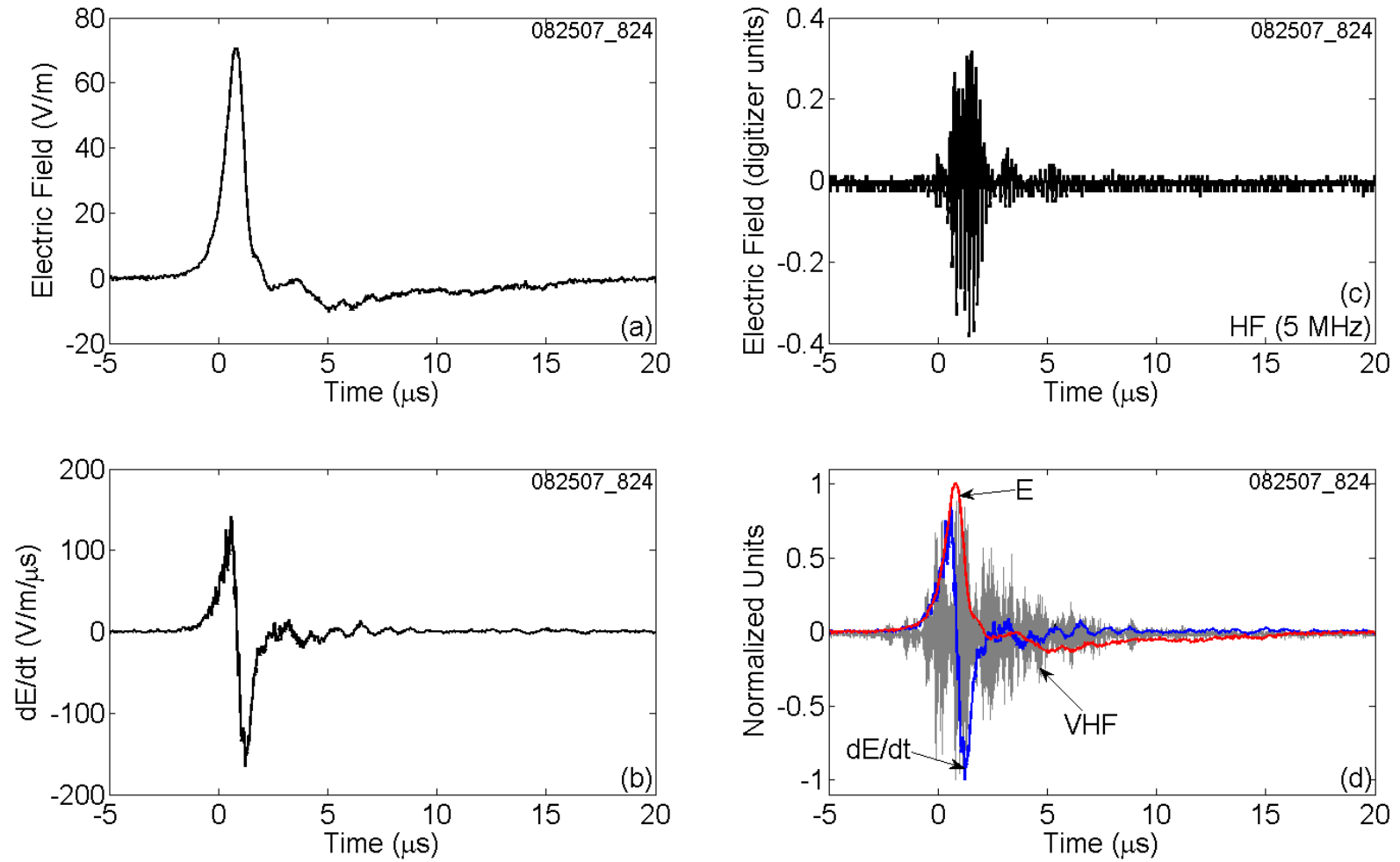


Figure 4-12. (a) Electric field, (b) dE/dt , and (c) HF of a CID that transferred negative charge upward (or positive charge downward), recorded in Gainesville, Florida. The event occurred at an unknown distance. The electric field, dE/dt , and VHF signatures are overlaid in (d) for direct comparison.

as seen in Figure 4-11d where the two waveforms (as well as the VHF radiation signature) are superimposed. We found multiple secondary peaks (oscillations) in 32 (15%) of 212 dE/dt records. Factors that can make reflections undetectable in the remaining 85% include a relatively small magnitude of the incident wave, relatively long radiating channel, relatively large losses along the channel, and a relatively small (in absolute value) current reflection coefficients at channel ends. It is important to note that lower-order reflections (during the primary portion of the overall electric field or dE/dt waveform), while being undetectable, do influence the magnitude of the overall waveform (see Figure 4-22b). It is likely that the 15% of waveforms showing pronounced reflections correspond to shortest CID channels. The average time interval between consecutive peaks of the same polarity in dE/dt signatures ranged from 0.84 to 1.8 μs (with a mean of 1.2 μs). We will show later, via modeling, that the multiple peaks (oscillations) in dE/dt waveforms are due to reflections at either end of CID channel, with time interval between consecutive peaks (oscillation period) being equal to the roundtrip time along the channel. One-half of the period is the channel traversal time. Interestingly, the period of oscillations remains more or less constant (see Figure 4-11b), implying that the radiator length remains fixed during the bouncing-wave process. A round trip time of 1 μs corresponds, for example, to a propagation speed of 2×10^8 m/s and a channel length of 100 m.

Figures 4-13a and 4-13b show the histogram of the total duration of 5 MHz HF radiation signature in our dataset and the scatter plot of the total duration of HF radiation signature versus total duration of the corresponding electric field waveform of 31 CIDs, respectively. The AM and GM durations of the 5 MHz HF radiation burst are 5.8 and 5.3 μs , respectively. Figures 4-14a and 4-14b show the histogram of the total duration of 36 MHz VHF radiation signature in our dataset and the scatter plot of the total duration of VHF radiation signature versus total

duration of the corresponding electric field waveform of 52 CIDs, respectively. The AM and GM durations of the 36 MHz VHF radiation signature are both 11 μs . In our data, the VHF signature usually begins at about the same time as the electric field and dE/dt signatures, and all three have comparable durations. In contrast, the corresponding HF signature in our data (see Figure 4-12c) began, on average, 1.7 μs after the electric field, dE/dt , and VHF signatures did. Figures 4-15a and 4-15b, respectively, show histograms of the starting-time of HF and VHF radiation signatures relative to the onset-time of the corresponding electric field waveform. An apparent delay in the onset of HF relative to VHF may be related to the production of longer streamers (associated with lower frequency fields) at later times. There appears to be some structure in the VHF radiation waveforms in Figures 4-11c and 4-12d, but we could not uniquely relate this structure to features of corresponding electric field or dE/dt waveforms.

4.2.2 Bouncing-Wave Mechanism

Based on the evidence of multiple reflections, we postulate that the compact intracloud discharge is essentially a bouncing-wave phenomenon. It can be viewed as beginning with injection of current pulse at one end of a relatively short conducting channel (this channel could be created by the runaway electron breakdown process [e.g., Tierney *et al.*, 2005, Gurevich and Zybin, 2004, Gurevich *et al.*, 2004]), which is reflected multiple times successively at either end of the channel until it is attenuated and absorbed, depending upon the conditions along the channel and boundary conditions at channel ends, respectively. The concept is illustrated by four schematic snapshots in Figure 4-16.

Figure 4-16a shows a CID current pulse (similar to that inferred by *Watson and Marshal* [2007]) with a peak current of 50 kA, total duration of 30 μs (much longer than expected time needed to traverse the channel), and risetime of 6 μs (somewhat shorter than 9 μs in *Watson and Marshal's* pulse, but more consistent with experimental data, as shown in Section 4.2.7), injected

at the bottom of a 100 m long vertical conducting channel at $t = 0$. The pulse (i_0) travels upward at an assumed speed of 2×10^8 m/s (similar to that inferred by *Watson and Marshal* [2007]), so that the front of this pulse will reach the top of the channel at $t = 0.5 \mu\text{s}$. The instant just before the pulse hits the top is schematically shown in part A of Figure 4-16b. At the top of the channel, the current pulse in general will "see" an impedance discontinuity and hence will be partly reflected. The front of the current pulse (scaled according to the reflection coefficient at the top of the channel) will move downward. This is shown in part B of Figure 4-16b. The downward motion of the current pulse front will continue till $t = 1 \mu\text{s}$ at which time it will hit the bottom of the channel where it will be reflected again and begin travelling upward (C in Figure 4-12b). The second reflection at the top and resultant downward moving wave are depicted in part D of Figure 4-16b. Note that while the initial parts of the current pulse front have already experienced multiple reflections at the top and bottom of the channel, later portions of the front (total front duration is $6 \mu\text{s}$) are still making their first trip upward, or did not even enter the bottom of the channel. At $t = 30.5 \mu\text{s}$, the last point on the tail of the originally injected current pulse will reach the top. After $t = 0.5 \mu\text{s}$, in addition to the upward-moving incident wave (i_0), different portions of the pulse will be travelling either downward or upward after being reflected from the top or the bottom of the channel, respectively. However, with each successive reflection and traversal of the channel, the current pulse will be diminished due to partial absorption at the channel end and attenuation along the channel. The multiple current reflections are illustrated in Figure 4-16c where reflection coefficients at the top (ρ_t) and bottom (ρ_b) of the channel were assumed to be equal to -1.

One of the features of CIDs is very strong HF-VHF radiation. It is generally thought that HF-VHF radiation is produced due to electrical breakdown of virgin air. The CID mechanism

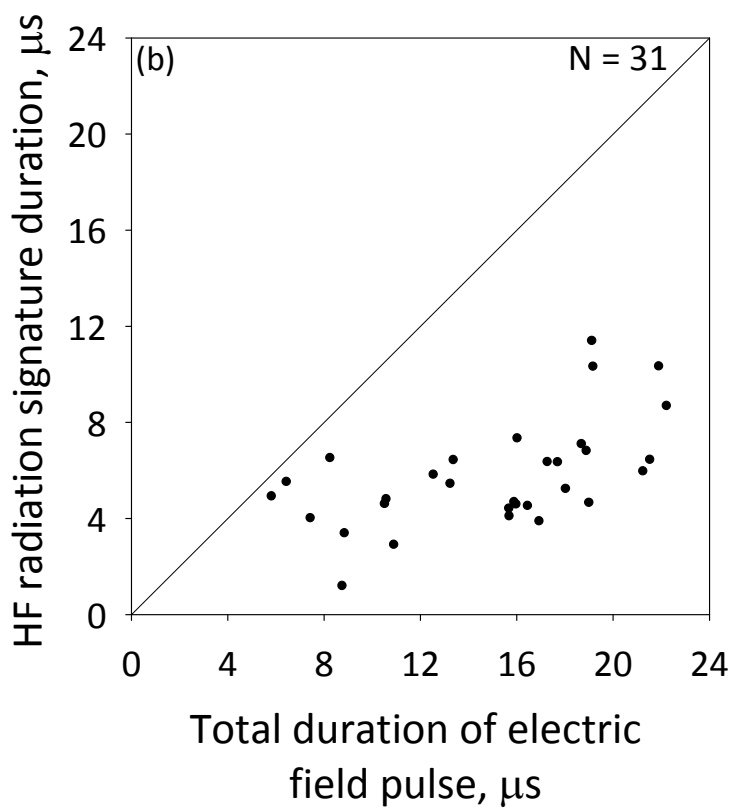
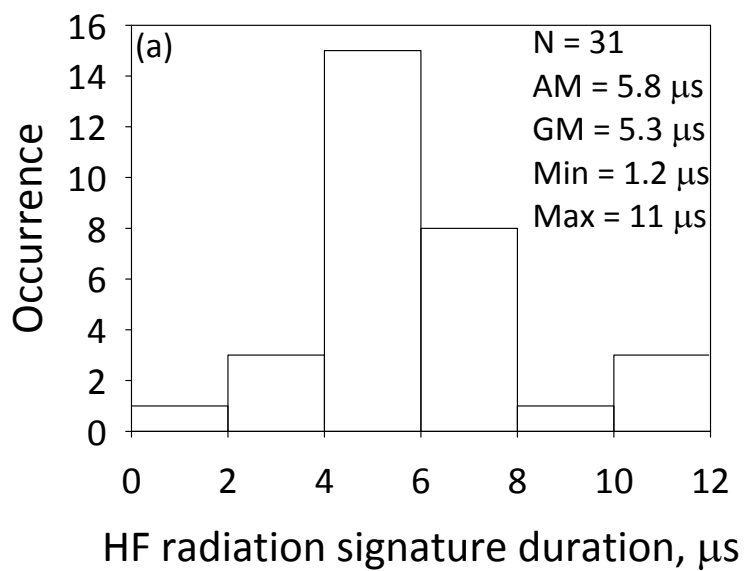


Figure 4-13. (a) Histogram of the total duration of 5 MHz HF radiation signature and (b) total duration of HF radiation signature versus total duration of the corresponding electric field waveform for 31 CIDs.

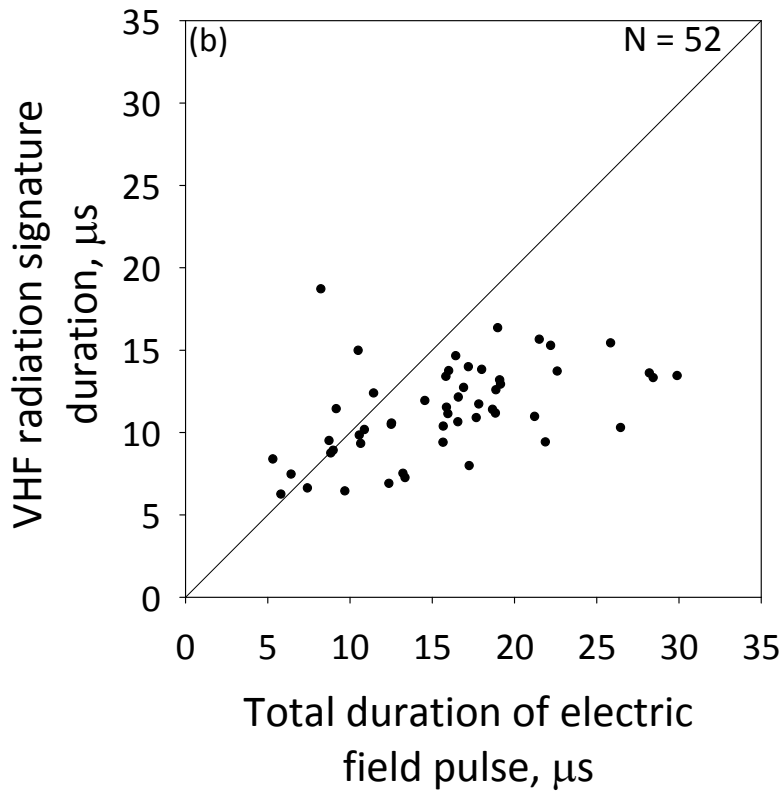
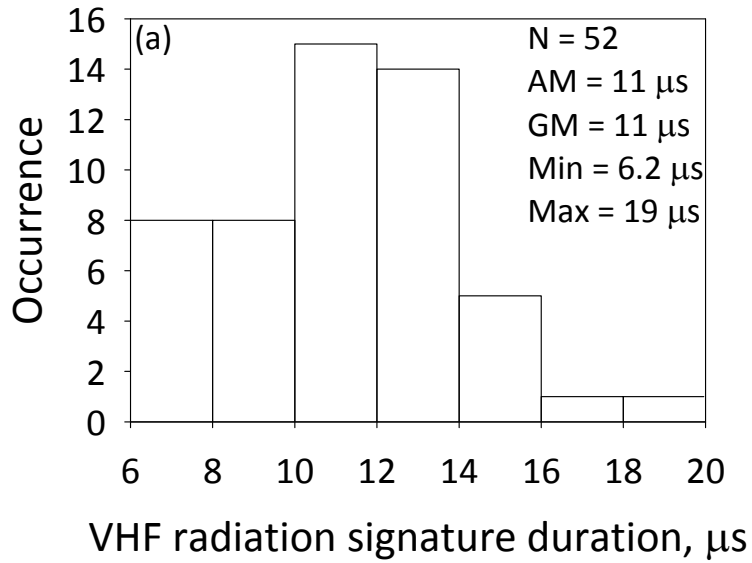


Figure 4-14. (a) Histogram of the total duration of 36 MHz VHF radiation signature and (b) total duration of HF radiation signature versus total duration of the corresponding electric field waveform for 52 CIDs.

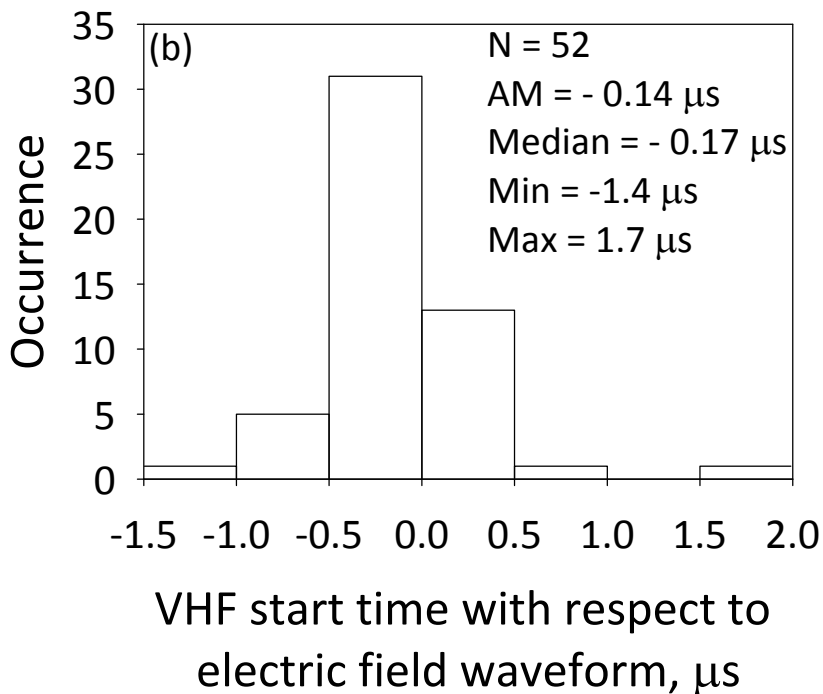
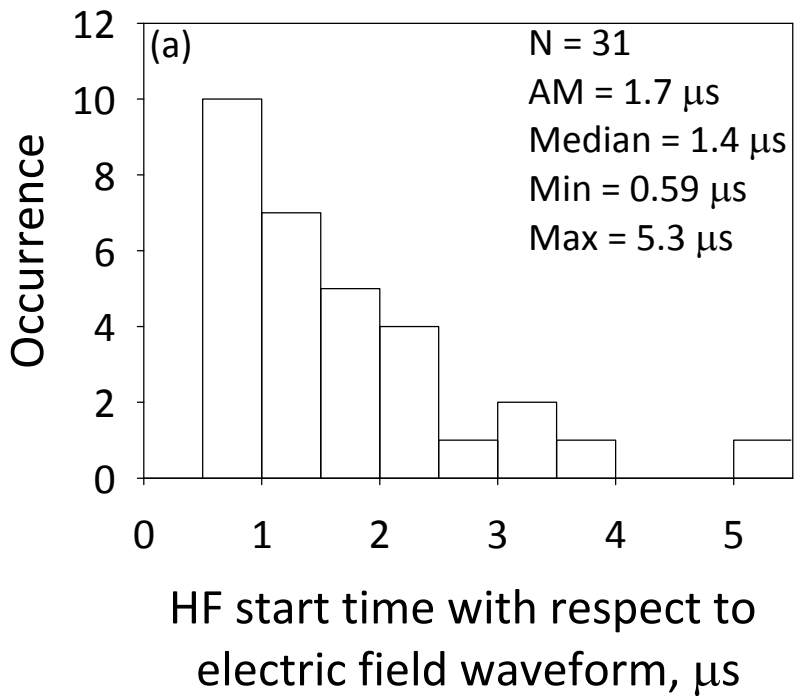


Figure 4-15. Histograms of the starting-time of (a) HF and (b) VHF radiation signatures relative to the onset-time of the corresponding electric field waveform.

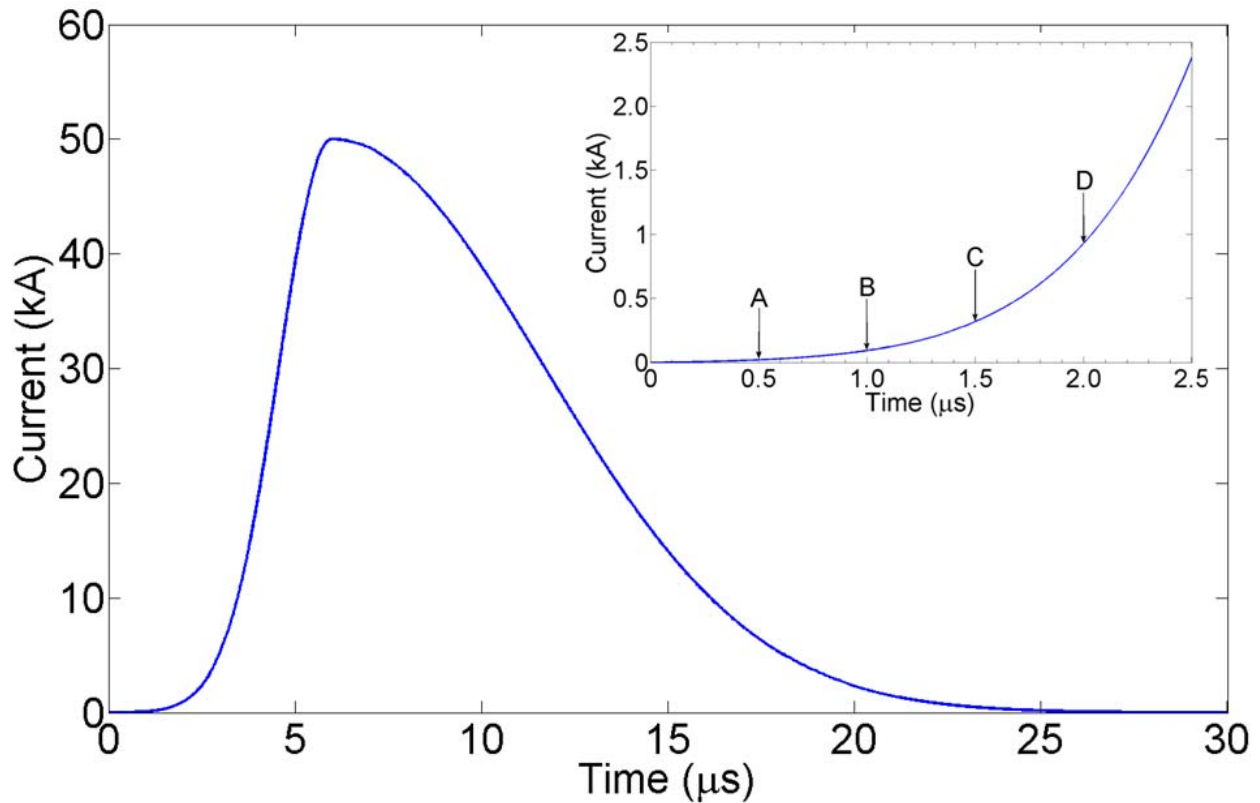


Figure 4-16a. A CID current pulse with a peak of 50 kA, total duration of 30 μs and zero-to-peak risetime of 6 μs , injected at the bottom of a 100 m long vertical conducting channel at $t = 0$. The inset shows the initial 2.5 μs of the incident current waveform and first four reflections occurring at A, B, C, and D. Vertical arrows indicate times at which reflections begin. The wave makes two round trips (experiences four reflections) during initial 2 μs , six round trips (12 reflections) during the current risetime (6 μs), and 30 round trips (60 reflections) during the entire current duration (30 μs). In practice, due to attenuation along the channel and absorption at channel ends, higher-order reflections will be progressively less pronounced, so that less than 10 reflections are expected to be detectable in the dE/dt waveforms and even less in electric field signatures.

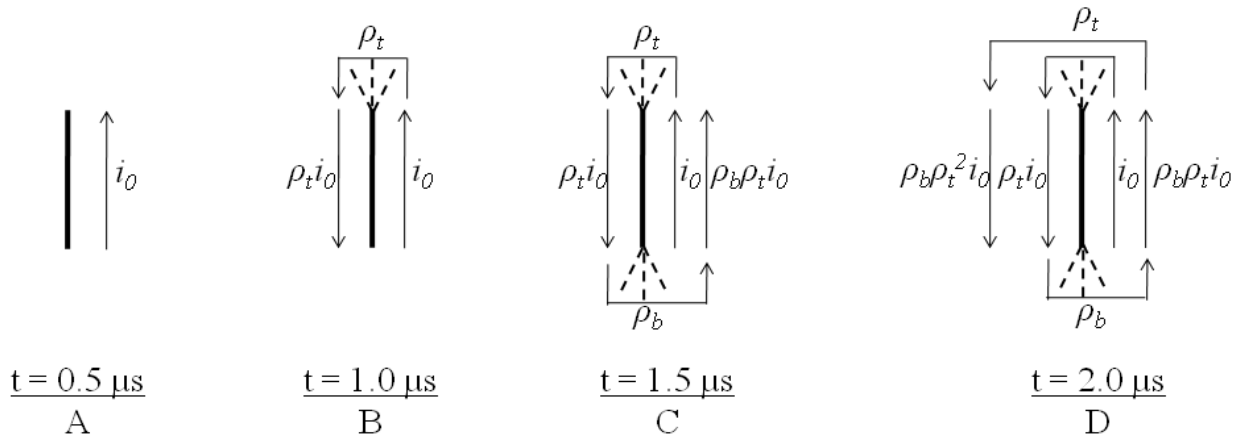


Figure 4-16b. Schematic representation of the bouncing-wave mechanism of CID for channel length $\Delta h = 100$ m and propagation speed $v = 2 \times 10^8$ m/s. Current-wave duration is much longer than the channel traversal time. Straight arrows represent current waves on CID channel and bracket-shaped arrows represent the process of wave reflection at the ends. If $\rho_b = \rho_t = 1$ (short-circuit conditions), it is the same wave bouncing between the ends. If $\rho_b = \rho_t = -1$ (open-circuit conditions), the wave changes polarity each time it hits the end. If $\rho_b = \rho_t = -0.5$, the current wave changes polarity and is reduced in magnitude by a factor of 2 at each end. If $\rho_t = 0$, the wave is fully absorbed at the top end. For $|\rho_t| < 1$ and $|\rho_b| < 1$ partial absorption takes place at the top and bottom, respectively. It is expected that reflected current waves will reduce current at each end, while corresponding voltage will be enhanced there. As a result, corona-like electrical breakdown (shown by broken lines) may occur at the channel ends. Breakdown associated with the incident wave, i_0 , is not shown here.

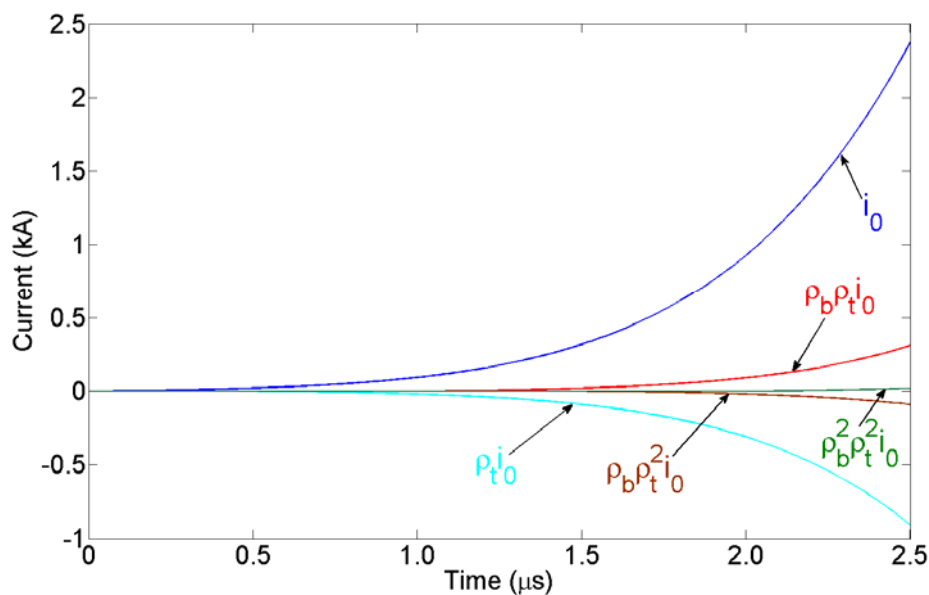


Figure 4-16c. Illustration of the multiple current reflections with reflection coefficients at the top (ρ_t) and bottom (ρ_b) of the channel assumed to be equal to -1.

described above implies that HF-VHF radiation will be produced (1) when the front of current pulse moves upward along the channel for the first time (actually creates that channel) and (2) at either end of the channel when current reflections are produced there. Reflections of different portions of current pulse may result in corona-like electrical breakdown (represented by broken lines in Figure 4-16b) at channel extremities, because a reduction of current is accompanied by an increase of line charge density and associated voltage (voltage doubles at an open circuit end and increases by a factor of 1.5 if the current reflection coefficient $\rho = -0.5$). This breakdown at both channel ends is likely to produce an intense burst of HF-VHF radiation which is a characteristic feature of CIDs (see Figure 4-11c). The proposed scenario also helps explain the "noisiness" of dE/dt waveforms compared to corresponding electric field waveforms, a CID feature first noticed by *Willett et al.* [1989].

4.2.3 Bouncing-Wave Model: Current Distribution along the Channel

We consider a vertical channel whose bottom and top ends are at heights of h_1 and h_2 , respectively. The assumption that the CID channel is generally vertical is supported by large magnitudes of the vertical component of electric field measured at ground level [see, for example, *Willett et al.*, 1989; *Smith et al.*, 1999, and Section 4.1] that are comparable with or exceeding those of first return strokes. The larger the deviation of the channel from vertical, the smaller the vertical component of electric field at ground level. For a horizontally oriented channel this field component at ground level is close to zero. Additionally, the observed occurrence of CIDs between horizontally extensive charge layers [e.g., *Rison et al.*, 1999] and their relatively short channels are probably consistent with more or less vertical orientation. We do not consider here the process of creation of the CID channel. The presence of conducting channel in the cloud is evidenced by pronounced VLF/LF field waveforms. We assume that the channel is energized by injection of a current wave at its bottom end. The transmission line (TL)

model that relates the longitudinal current $i(z,t)$ at any height z and any time t to the current at the channel origin (which in our case is at h_1) is given by:

$$i(z,t) = i(h_1, t - \frac{z - h_1}{v}) \quad (4-3)$$

In order to account for the multiple reflections that take place at the channel ends (as described in Section 4.2.2) we specify two equivalent current sources, $i_u(h_1,t)$ and $i_d(h_2,t)$ (see Section 4.2.6, Equations 4-7 and 4-8), connected at the bottom and at the top of the channel, respectively. $i_u(h_1,t)$ accounts for the incident wave and all reflections at h_1 ; it propagates upward. $i_d(h_2,t)$ accounts for all reflections at h_2 and propagates downward. One can compute partial electric fields at observation point P due to each of these two currents. The total electric field at P due to a current wave originating at h_1 and undergoing multiple reflections at both channel ends is given by the superposition of these two electric field components (see Section 4.2.6).

Let us consider the event illustrated in Figure 4-16. A current pulse with a peak of 50 kA, total duration of 30 μ s, and risetime of 6 μ s (see Figure 4-16a), is injected at the bottom of a 100 m long vertical channel. We assume that the bottom of the channel is at an altitude of 15 km and that negative charge is transferred upward. The pulse travels upwards at an assumed speed of 2×10^8 m/s. The round-trip time for the current pulse along the channel from bottom to top and back is 1 μ s. Let the current reflection coefficients at the bottom and the at top of the channel be equal to -0.5. Note that in our model the reflection coefficients, for simplicity, account for both absorption at channel ends and attenuation along the channel. So, they should be viewed as effective reflection coefficients.

Figure 4-17a shows the currents computed using Equations 4-7 and 4-8 (Section 4.2.6), at the bottom ($z = h_1$), middle ($z = h_1 + \Delta h/2$) and top ($z = h_2$) of the 100 m long channel. Peak

currents at these heights are 40, 34, and 32 kA, respectively. They are not much different from each other (currents at the ends are within less than 20% of the current in the middle). A three-dimensional plot of current as a function of both time and height is shown in Figure 4-17b. Note that the incident current wave peak is 50 kA, while the equivalent current distribution along the channel peaks at 32 to 40 kA, due to reflections (absorption at the ends). Further, the overall current waveshapes at these three positions along the channel are similar. Half-peak widths are 7.0 μs , 8.2 μs , and 8.6 μs , respectively, although the waveforms in the middle and at the top are shifted by 0.25 and 0.5 μs , respectively, from the waveform at the bottom. Figure 4-17c shows the total current (including reflections, if any) along the channel at $t = 0.5, 4, 8,$ and 16 μs after the incident current wave starts moving upwards from the bottom of the channel. Note that at $t = 8 \mu\text{s}$ (not far from the current peak) the distribution of current along the channel is essentially uniform.

The current distribution along the CID channel is not much different from uniform, as expected for a Hertzian (electrically short) dipole, because of relatively short channel length, relatively long current waveforms, and relatively high propagation speed. In Section 4.3, we will show that at least some CIDs can be approximated by vertical Hertzian dipoles. This approximation will enable us to simplify the field equations and use measured fields to infer various electrical parameters of CIDs (within this approximation, the propagation speed and reflection coefficients are not input parameters and the current waveshape is the same as that of the time integral of NBP). In Section 4.2.5, we compute CID electric field waveforms using the Hertzian dipole approximation and compare them with their counterparts computed using the bouncing-wave model in Section 4.2.4.

4.2.4 Bouncing-Wave Model: Electric Fields at 2 and 200 km

The general time-domain equation for computing the vertical electric field dE_z due to a vertical differential current element idz (vertical dipole of length dz carrying a uniform current $i(t)$) at a height h above a perfectly conducting ground plane for the case of an observation point P on the plane at a horizontal distance r from the dipole is given by [e.g., *Uman*, 1987]:

$$dE_z(r, t) = \frac{1}{2\pi\epsilon_0} \left[\frac{(2h^2 - r^2)}{R^5(z)} dz \int_0^t i(z, \tau - \frac{R(z)}{c}) d\tau + \frac{(2h^2 - r^2)}{cR^4(z)} i(z, t - \frac{R(z)}{c}) dz - \frac{r^2}{c^2 R^3(z)} \frac{di(z, t - \frac{R(z)}{c})}{dt} dz \right] \quad (4-4)$$

where ϵ_0 is the electric permittivity of free space, R is the inclined distance from the dipole to the observation point, which is given by $R = \sqrt{z^2 + r^2}$.

From Equation 4-4 for the geometry shown in Figure 4-18, the total electric field at the observation point for a finite-length channel whose lower and upper ends are at altitudes of h_1 and h_2 , respectively, is given by:

$$E_z(r, t) = \frac{1}{2\pi\epsilon_0} \int_{h_1}^{h_2} dz \left[\frac{(2h^2 - r^2)}{R^5(z)} \int_0^t i(z, \tau - \frac{R(z)}{c}) d\tau + \frac{(2h^2 - r^2)}{cR^4(z)} i(z, t - \frac{R(z)}{c}) dz - \frac{r^2}{c^2 R^3(z)} \frac{di(z, t - \frac{R(z)}{c})}{dt} dz \right] \quad (4-5)$$

Where h_2 is a function of time during the first traversal of the channel.

Figure 4-19a shows the electrostatic, induction, radiation electric field components, and total electric field predicted by our model at a horizontal distance of 2 km. Current distribution shown in Figure 4-17 was used in the calculations. As expected, the static and induction components are dominant at 2 km (radiation nearly along the axis of the vertical dipole is negligible). Figure 4-19b shows the total electric field (essentially the same as its radiation

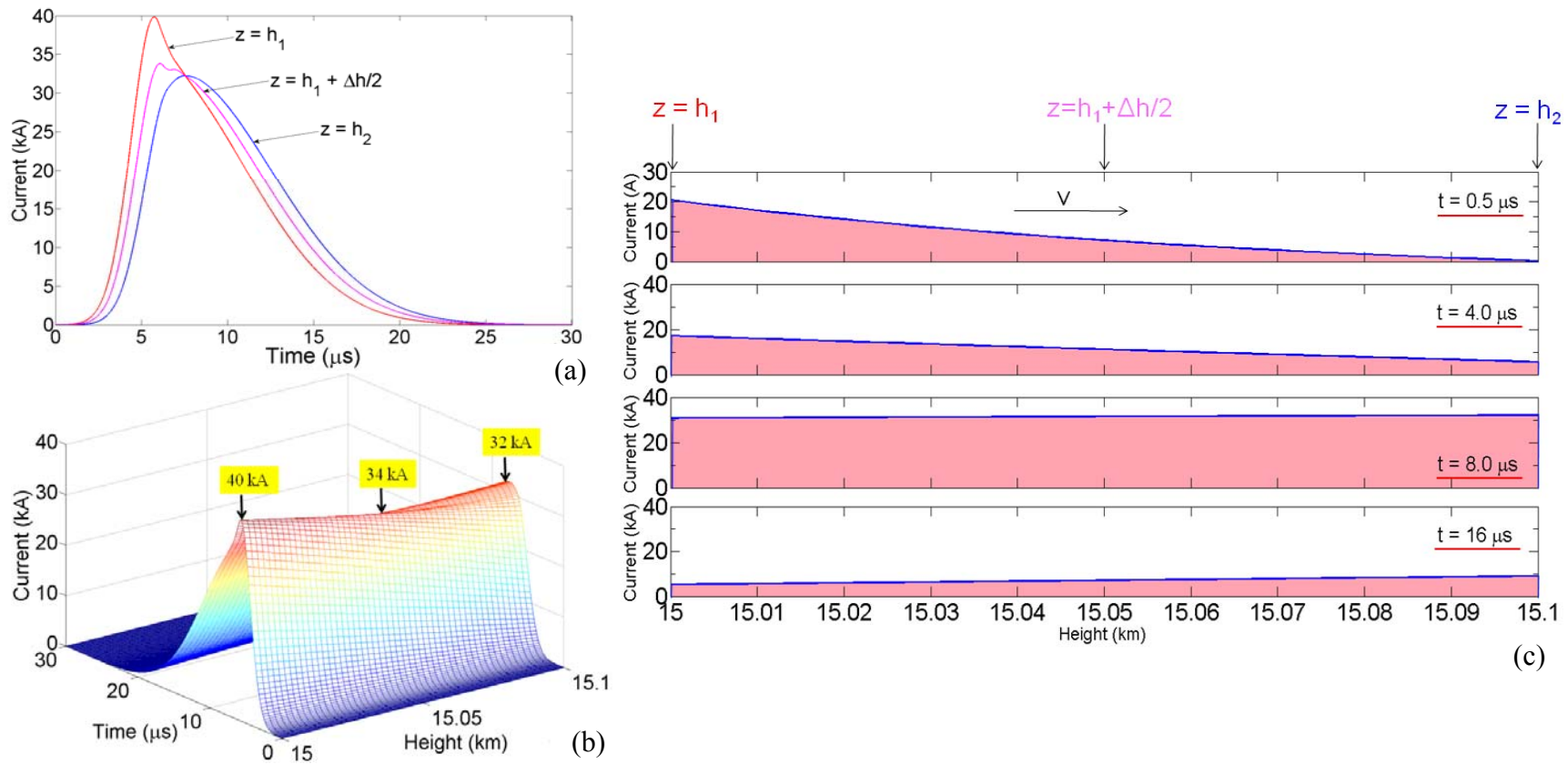


Figure 4-17. (a) Currents computed using Equations 4-7 and 4-8 (Section 4.2.6), at the bottom ($z = h_1$), middle ($z = h_1 + \Delta h/2$) and top ($z = h_2$) of the channel for a CID characterized by $h_1 = 15$ km, $\Delta h = 100$ m, $v = 2 \times 10^8$ m/s, $\rho_t = \rho_b = -0.5$, $I_p = 50$ kA, and current risetime = 6 μs . Peak currents at these three heights are 40, 34, and 32 kA, respectively. They are not much different from each other (currents at the ends are within less than 20% of the current in the middle). (b) A three-dimensional plot of current as a function of both time and height. Note that the incident current wave peak is 50 kA (as shown in Figure 3a), while the equivalent current distribution along the channel peaks at 32 to 40 kA, due to reflections (absorption at the ends). (c) The total current (including reflections, if any) along the channel at $t = 0.5$, 4, 8, and 16 μs after the incident current wave starts moving upwards from the bottom of the channel. Note that at $t = 8 \mu\text{s}$ (not far from the current peak) the distribution of current along the channel is essentially uniform.

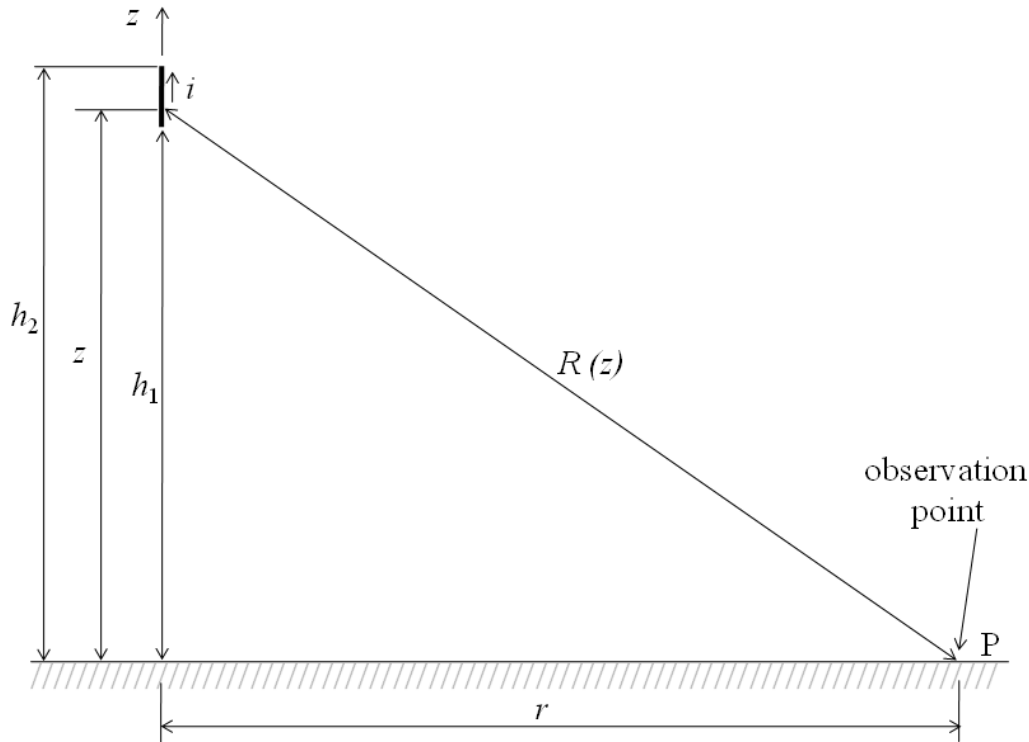


Figure 4-18. Geometrical parameters used in calculating the electric field at observation point P on perfectly conducting ground at horizontal distance r from the vertical CID channel extending between heights h_1 and h_2 . See text for details.

component) at a horizontal distance of 200 km. At least two secondary peaks can be seen in the electric field waveform shown in Figure 4-19b. Figure 4-19c shows the electric field derivative at 200 km, in which one can discern four cycles of oscillations after the primary cycle. The time interval between consecutive maxima in the dE/dt signature is $1 \mu\text{s}$ which corresponds to the round trip time of the current pulse along the channel, that is, from bottom to top and back. The half period ($0.5 \mu\text{s}$) is the travel time of the current pulse in one direction.

In Section 4.2.7, we used our bouncing-wave model to compute distant electric field waveforms and compare them with measurements. We varied model parameters, such as current wave propagation speed, channel length, current reflection coefficients, and current risetime, in order to examine effects of these variations on fields predicted by our model. We found that that model-predicted fields are consistent with experimental data only for relatively narrow ranges of

these parameters. Specifically, we estimated that the effective current reflection coefficients (assumed to be the same) at channel ends should be approximately in the range of 0 to -0.5, the wave propagation speed ranges from about 0.3 to 3×10^8 m/s, and the channel length is less than about 1000 m. The lower bound on channel length was assumed to be about 100 m, based on observed reflection signatures in dE/dt records. Influence of current risetime on field waveforms was also examined, and it was found to be typically in the range from about 2 to 8.5 μ s. We also determined the "allowed" combinations of parameters.

In Section 4.2.8, we test the validity of the bouncing-wave model using electric fields simultaneously measured at near and far distances by *Eack* [2004]. A good match between model-predicted fields and the experimental data is obtained for a peak current of 75 kA, current risetime of 5.2 μ s, propagation speed of 1.4×10^8 m/s, channel length of 650 m, and current reflection coefficients at channel ends equal to zero.

4.2.5 Hertzian Dipole Approximation

Equation 4-4 also applies to a vertical dipole of finite length Δh , provided that Δh is very short compared to the shortest significant wavelength λ (Hertzian dipole approximation). For a vertical Hertzian dipole we can replace dz with Δh in (2) to get:

$$E_z(r, t) = \frac{1}{2\pi\epsilon_0} \left[\frac{(2h^2 - r^2)\Delta h}{R^5} \int_0^t i(\tau - R/c) d\tau + \frac{(2h^2 - r^2)\Delta h}{cR^4} i(t - R/c) - \frac{r^2\Delta h}{c^2R^3} \frac{di(t - R/c)}{dt} \right] \quad (4-6)$$

Note that the current in Equation 4-6 is the same everywhere along the dipole (independent of z). In Figures 4-20a and b we compare electric field waveforms at $r = 2$ km and $r = 200$ km, respectively, computed using the Hertzian dipole approximation (Equation 4-6) with their counterparts computed using the bouncing-wave model. The Hertzian dipole, assumed to be 100 m in length and located at a height of 15 km above ground, was excited by the current found for the middle of the channel ($z = h_l + \Delta h/2$) using the bouncing wave model (see Figure 4-17a).

Figure 4-20c shows the dE/dt waveforms computed using the Hertzian dipole approximation and the bouncing wave model. Clearly, the fields computed using the Hertzian dipole approximation closely match those based on the bouncing-wave model. Note, however, that for longer channels, slower speeds, and shorter current risetimes, the Hertzian dipole approximation may not be applicable. Limits of validity of the Hertzian dipole approximation in terms of these parameters are discussed in Section 4.3.

In Section 4.2.8, we test the validity of the Hertzian dipole approximation using electric fields simultaneously measured at near and far distances by *Eack* [2004]. A good match between model-predicted fields and the experimental data is obtained for a peak current of 74 kA, current risetime of 9 μ s, and channel length of 500 m. The CID parameters providing a good match with the experimental data for the Hertzian dipole approximation are not much different (particularly the peak current) from those for the bouncing-wave model (see Section 4.2.4).

4.2.6 Equivalent Current Sources to Represent Multiple Traveling Waves in the Bouncing-Wave Model

An elevated vertical lightning channel is modeled as a transmission line with impedance mismatch at either end. As a result, reflections are produced when the travelling current pulse hits channel ends. We assume that the line is uniform and that any losses along the line are accounted for in the reflection coefficients at the ends. So, the reflection coefficients used in this Chapter are effective reflection coefficients. Although there will likely be a corona-like discharge (a nonlinear process) at either end of the line, we assume the effective reflection coefficients to be constant. The distribution of current along the channel can be expressed in terms of the incident current, $i_0(t)$, channel length, Δh , current wave speed, v , and effective current reflection coefficients at the top, ρ_t , and the bottom, ρ_b , of the channel. The initial part

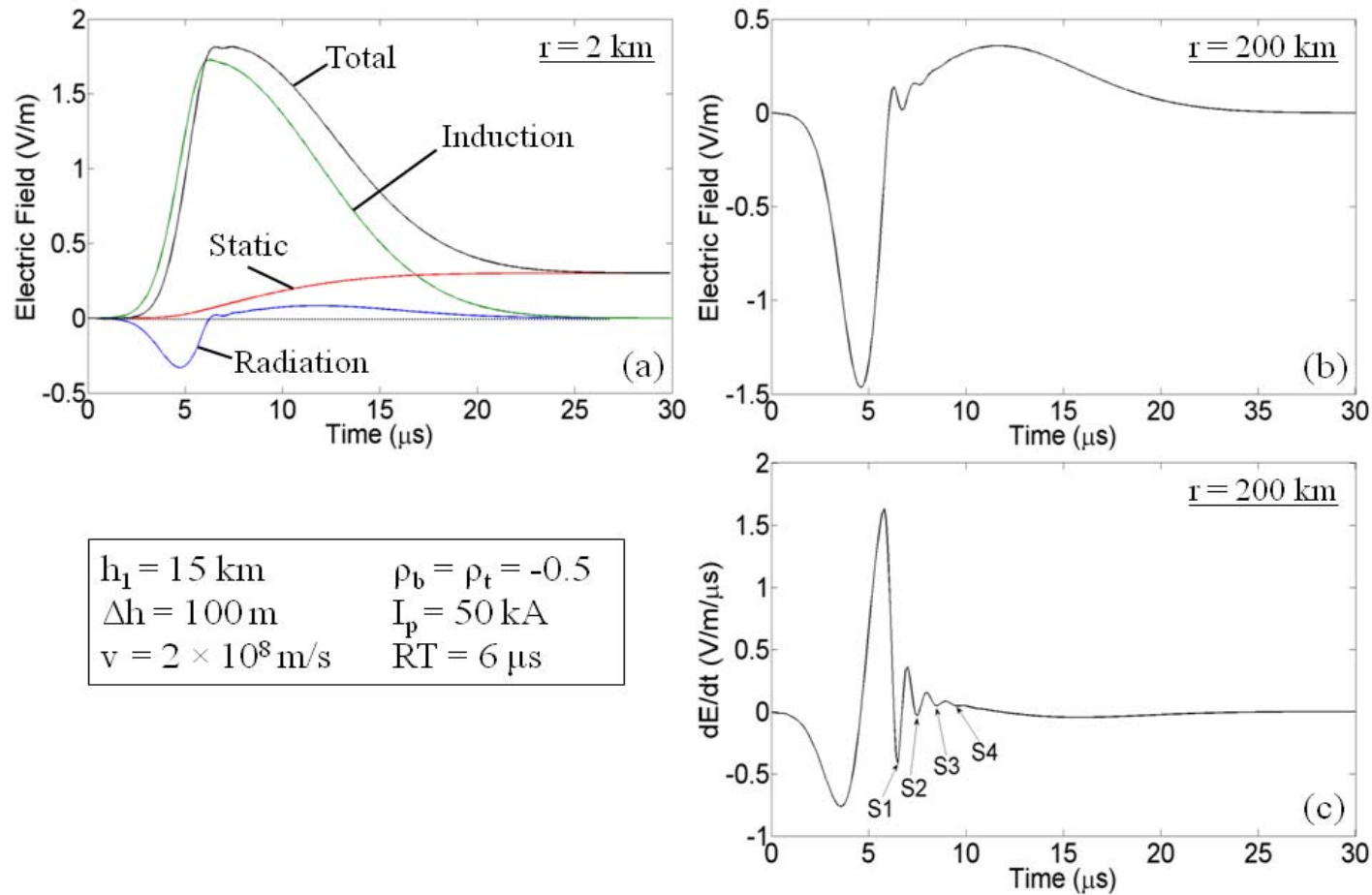


Figure 4-19. (a) Electrostatic, induction, radiation electric field components, and total electric field predicted by the bouncing-wave model at a horizontal distance of 2 km. As expected, the static and induction components are dominant at this distance. (b) Total electric field (essentially the same as its radiation component) at a horizontal distance of 200 km. At least two secondary peaks can be seen in the electric field waveform. (c) The electric field derivative at 200 km, in which one can discern four cycles of oscillations after the primary cycle. The time interval between consecutive maxima in the dE/dt signature is 1 μs which corresponds to the round trip time of the current pulse along the channel, that is, from bottom to top and back. The half period (0.5 μs) is the travel time of the current pulse in one direction.

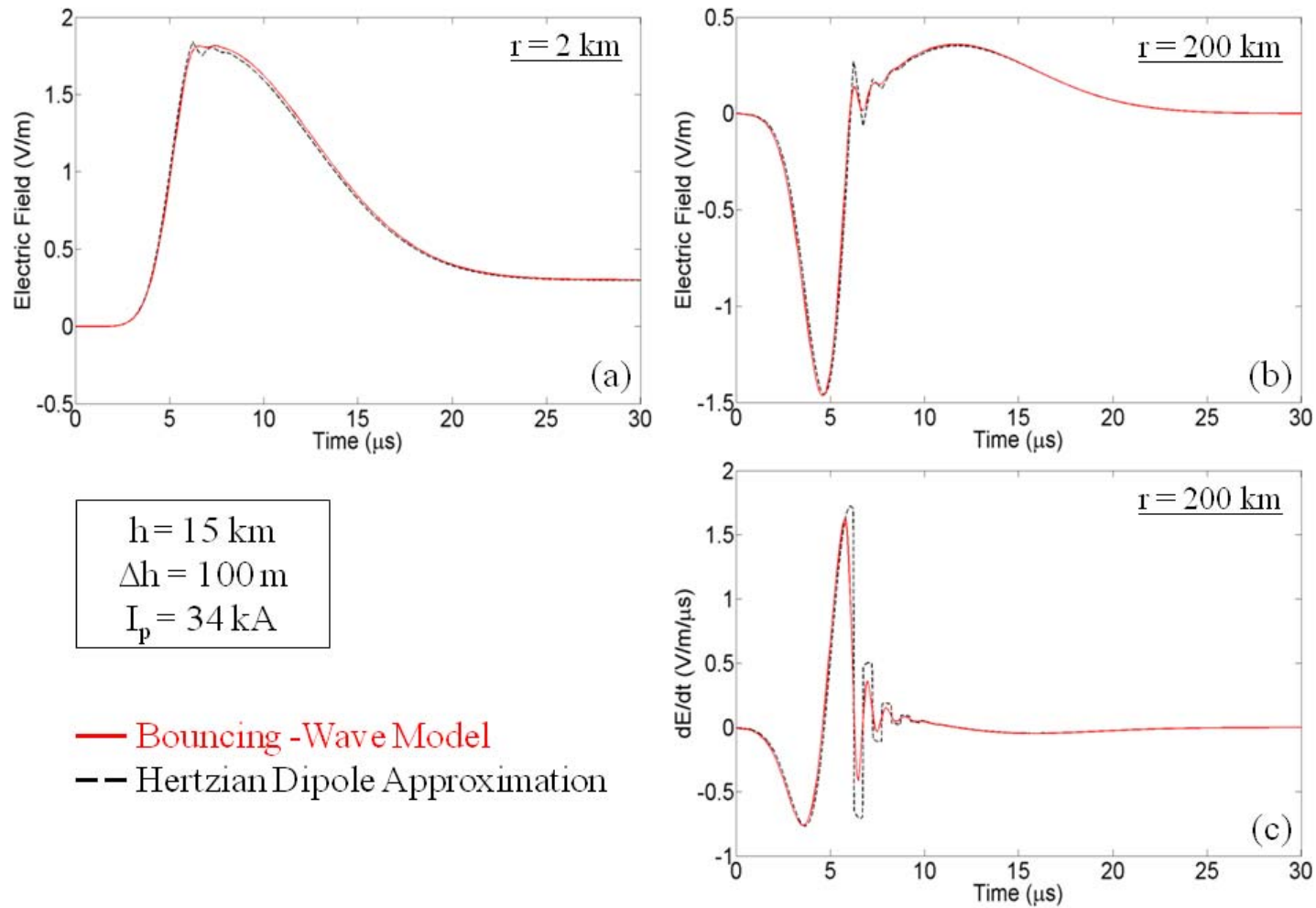


Figure 4-20. Electric fields at (a) 2 km and (b) 200 km computed using the Hertzian dipole approximation for a CID with a channel length of 100 m at a height of 15 km, excited by current waveform shown in Figure 4-17a for $z = h_1 + \Delta h/2$ (in the middle of the channel). The current peak, I_p , is 34 kA. The dE/dt signature is shown in (c). Electric fields and dE/dt computed using the bouncing wave model and presented in Figure 4-19 are also shown for direct comparison. A good match is evident in each of the three panels.

(first half a microsecond for, say, $\Delta h = 100$ m and $v = 2 \times 10^8$ m/s) of the incident current is associated with the creation of CID channel (probably via runaway electron breakdown [e.g., Tierney *et al.*, 2005; Gurevich and Zybin, 2004, Gurevich *et al.*, 2004]) and the later part with the polarization of the created channel in the cloud electric field. In the model considered here we assume that the channel is already created and an incident current $i_0(t)$ is injected at the bottom of the channel. Then the sum of upward-travelling current waves (incident wave and all reflections from the bottom) is given by:

$$i_u(h_1, t) = i_0(h_1, t) + \rho_t \rho_b i_0(h_1, t - \frac{2\Delta h}{v}) + \rho_t^2 \rho_b^2 i_0(h_1, t - \frac{4\Delta h}{v}) + \dots = \sum_{n=1,3,5,\dots}^{\infty} \rho_t^{\frac{n-1}{2}} \rho_b^{\frac{n-1}{2}} i_0(h_1, t - \frac{(n-1)\Delta h}{v}) \quad (4-7)$$

Similarly, for the sum of downward-travelling current waves (all reflections from the top) we have

$$i_d(h_2, t) = \sum_{n=2,4,6,\dots}^{\infty} \rho_t^{\frac{n}{2}} \rho_b^{\frac{n}{2}-1} i_0(h_2, t - \frac{(n-1)\Delta h}{v}) \quad (4-8)$$

These two expressions specify equivalent current sources connected at the channel ends. The two sources launch current waves toward each other and the total current at any position z along the channel can be obtained by appropriately shifting and combining $i_u(h_1, t)$ and $i_d(h_2, t)$.

For example, at $z = h_1 + \frac{\Delta h}{2} = h_2 - \frac{\Delta h}{2}$, $i(h_1 + \frac{\Delta h}{2}) = i_u(h_1, t - \frac{\Delta h}{2v}) + i_d(h_2, t - \frac{\Delta h}{2v})$. The total

current and its two components in the middle of the channel are shown in Figure 4-21a.

Additionally, in Figure 4-22b we show the incident current (i_0), the sum of all reflections (i_r), and the total current (i_{total}) in the middle of the channel. Note that while the incident current moves upward along the channel, the sum of all the reflections contains both upward and downward moving components. Field components and total fields at 200 km corresponding to currents

shown in Figures 4-21a and 4-22a are presented in Figures 4-21b and 4-22b and field derivatives are shown in Figures 4-21c and 4-22c. For computing the currents and fields shown in Figures 4-21 and 4-22 we used $\Delta h = 100$ m, $v = 2 \times 10^8$ m/s, and $\rho = -0.5$.

We now introduce sign conventions used in this study. As noted in Section 4.1, for a short vertical dipole at relatively large elevation angle α above ground (see Figure 4-23) the radiation field peak on the one hand and induction and static field changes on the other hand are expected to have opposite polarities. Specifically, it follows from equation (A.38) of *Uman* [1987, p. 329] for the electric field at perfectly conducting ground due to a differential vertical dipole that the opposite polarities are expected for $\alpha > 35.3^\circ$, which translates to $r < 21$ km if source height $h = 15$ km. The horizontal distance r at which the static and induction components change direction is equivalent to the well known [e.g., *Rakov and Uman*, 2003; Ch. 3] reversal distance for the electrostatic field due to an elevated finite-length vertical dipole. We assume that a positive charge moving in the positive z direction (vertically upward) constitutes a positive current. After the first reflection from the top of the channel, the current is flipped in polarity (due to negative current reflection coefficient). After the next reflection from the bottom of the channel, the polarity will be flipped again. Hence, i_u , the sum of upward-travelling current waves (incident wave and all reflections from the bottom), is positive, while i_d , the sum of downward-travelling current waves (all reflections from the top), is negative.

At far distances (for $\alpha < 35.3^\circ$), the electric field change is essentially equal to its radiation field component. Motion of positive charge upward (or negative charge moving downward) produces a radiation electric field change (initial peak) directed downward as shown in Figure 4-23 (inset). The opposite is true, that is the radiation electric field is directed upward, for motion of positive charge downward (or negative charge moving upward). At close distances (for $\alpha >$

35.3°), motion of positive charge upward (or negative charge moving downward) produces electrostatic and induction field changes directed upward and radiation electric field change directed downward.

According to the physics sign convention [e.g., *Rakov and Uman*, 2003; Ch. 1], a downward directed electric field vector is assumed to be negative. We use the physics sign convention in Sections 4.2 and 4.3.

4.2.7 Bouncing-Wave Model: Allowed Ranges of Variation of Input Parameters

We have used our bouncing-wave model to compute distant electric field waveforms and compare them with measurements. The model input parameters, current wave propagation speed, channel length, effective current reflection coefficients, source height, and current risetime were allowed to vary. We found that model-predicted fields are consistent with experimental data only for relatively narrow ranges of these parameters.

4.2.7.1 Reflection coefficients

The current reflection coefficient at either channel end is expected to be between -1 and 0. Positive reflection coefficients imply that the equivalent impedance of surrounding medium is lower than the characteristic impedance of current-carrying channel, which is physically unreasonable. As the magnitude of the reflection coefficient increases the amplitudes of the secondary peaks in the electric field waveform become larger. As a result, the number of secondary peaks discernible in the electric field waveform increases with increasing the reflection coefficient magnitude. If we limit the number of secondary peaks detectable in the electric field waveform to three, then effective current reflection coefficients (for simplicity accounting for both absorption at the ends and attenuation along the channel) should be in the range from -0.5 to 0. Note that in our dataset, 85% of the electric field waveforms do not exhibit any secondary peaks and in the remaining 15% typically only one secondary peak is observed. It

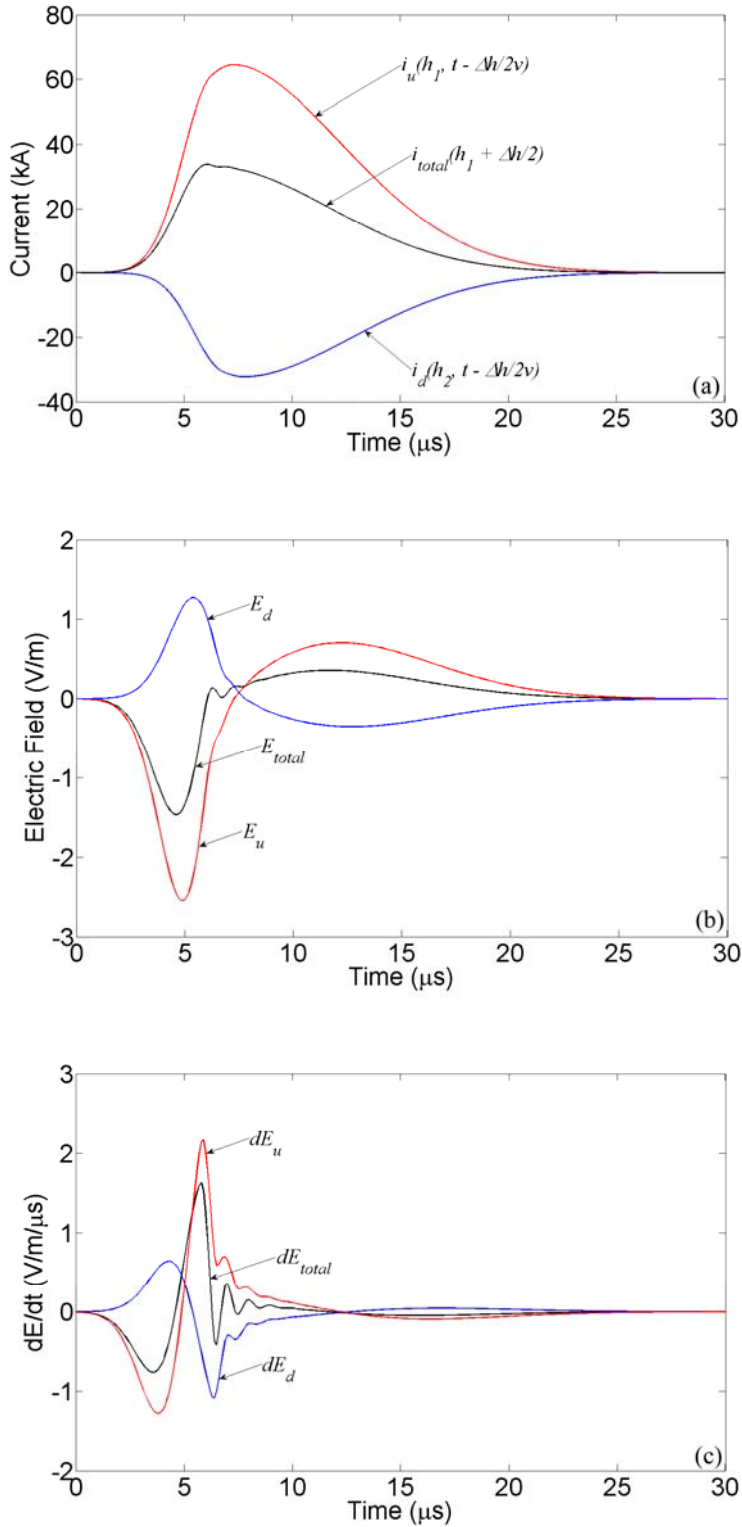


Figure 4-21. (a) The total current (i_{total}) and its upward (i_u) and downward (i_d) components in the middle of the channel, (b) the total electric field and its components corresponding to currents shown in (a), and (c) corresponding electric field derivatives.

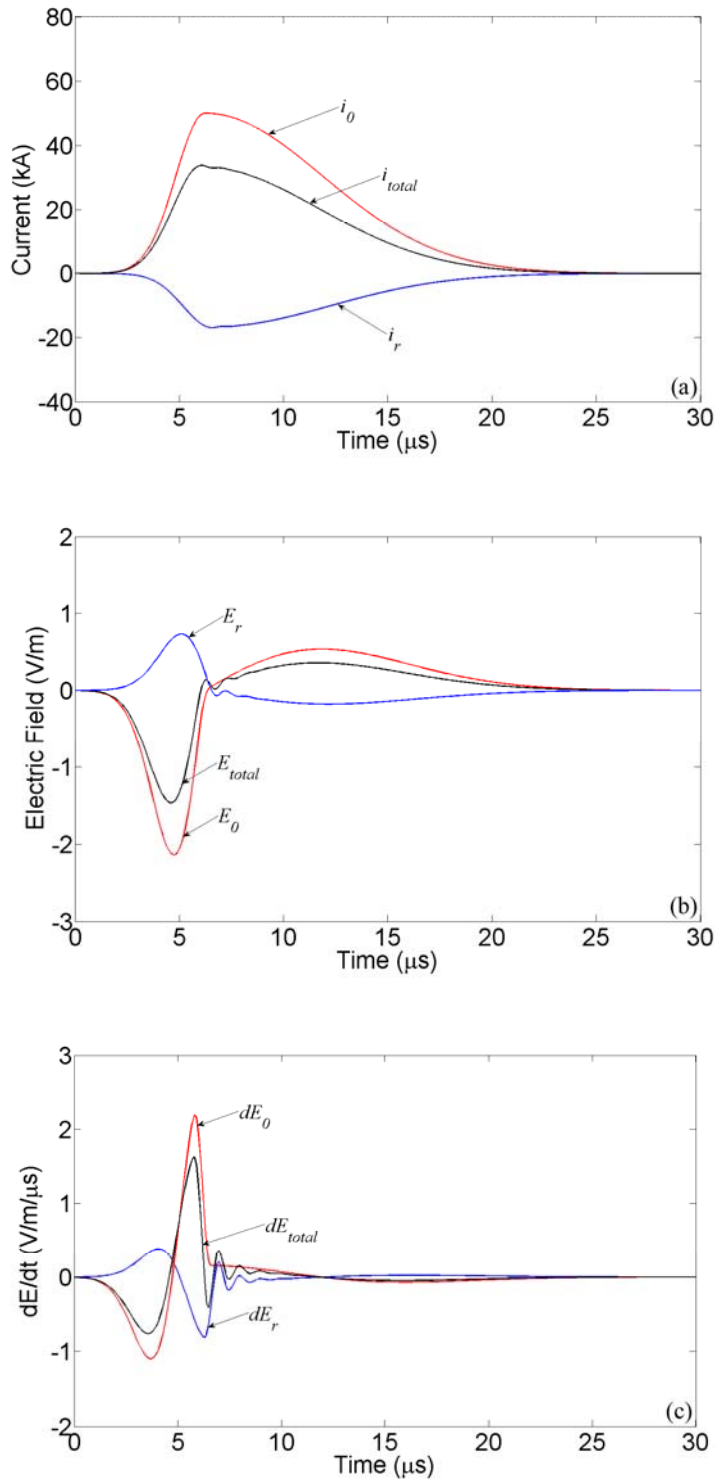


Figure 4-22. (a) The incident current (i_0), the sum of all reflections (i_r), and the total current (i_{total}) in the middle of the channel, (b) the electric field components and the total field corresponding to currents shown in (a), and (c) corresponding electric field derivatives. Note that while the incident current moves upward along the channel, the sum of all the reflections contains both upward and downward moving components.

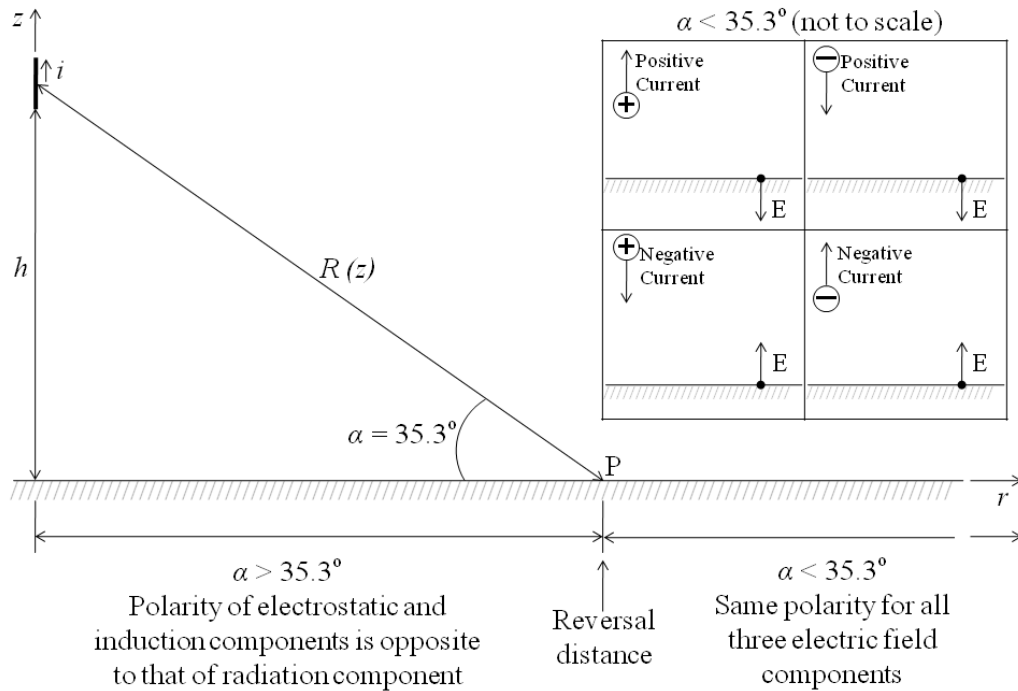


Figure 4-23. Illustration of the reversal distance for electrostatic and induction field components. Inset shows the direction of the far ($\alpha < 35.3^\circ$) electric field vector for different combinations of charge polarity and direction of charge motion. In case of bipolar electric field signature (dominated by its radiation component) the direction of electric field vector refers to the initial half cycle.

is likely that actual current reflection coefficients are close to -1, while the effective values are lower in absolute value due to our lumping of losses along the channel at the channel ends and combining those losses with absorption there. It is important to note that reflections do influence the overall field waveform, even when they are not detectable. All the field calculations presented in this Appendix were performed for two values of ρ (assumed to be the same at both channel ends), 0 and -0.5.

4.2.7.2 Propagation speed (v) and channel length (Δh)

The ratio of initial electric field peak to opposite polarity overshoot for distant CID electric field waveforms ranges from 2.5 to 14 in studies of *Willett et al.* [1989, Table 1] and *Smith et al.* [1999, Table 2]. In our data the ratio varies from 3.5 to 17 (see Section 4.1.5). Either decreasing

the current wave speed or increasing the channel length serves to decrease this ratio. Hence the smallest observed ratio (2.5) can be used to establish a lower bound for propagation speed and an upper bound for channel length; that is, "allowed" combinations of these two parameters. We additionally show results for the ratio equal to 3.

The upper bound for speed is the speed of light, and the lower bound for channel length was set to be about 100 m. In Section 4.3 it is shown that for 9 located CIDs for which we were able to estimate (assuming a speed of 2.5×10^8 m/s) channel lengths using oscillations in their measured dE/dt signatures, CID channel lengths range from 108 to 142 m. For a longer channel, the current wave will generally be more attenuated while traversing it, and hence the reflected wave will be less pronounced. Thus it is logical to assume that the 9 events with most pronounced reflections are associated with the shortest channels. Note that, for all 32 CIDs (discussed in Section 4.2.1), including the 9 located ones, whose dE/dt signatures showed multiple secondary peaks (oscillations), CID channel lengths range from 84 to 181 m, for an assumed speed of 2×10^8 m/s. The latter speed was considered to be the lower bound for the events with measured channel traversal times, since for lower speeds the channel length would become unreasonably small.

We first present field calculations that were performed using the incident current wave shown in Figure 4-16a. Its zero-to-peak risetime is 6 μ s and its total duration is 30 μ s. Influence of current risetime will be examined later in this Appendix. Figures 4-24a and b, show for $\rho = 0$ and $\rho = -0.5$, respectively, different combinations of propagation speed and channel length for which the ratio of initial electric field peak to opposite polarity overshoot of model-predicted electric fields at 200 km attains 2.5 (the lowest value found in the experimental data) and 3.0 (included for comparison). It can be seen from Figure 4-24a that the largest allowed (within our

model) value of channel length Δh for $\rho = 0$ is about 1000 m. A larger Δh would result in a speed greater than 3×10^8 m/s, which is not allowed. For the ratio equal to 3, the largest allowed $\Delta h = 750$ m. For $\rho = -0.5$, one can see from Figure 4-24b that the upper bound for channel length is about 500 m (not much different for ratios of 2.5 and 3). Also, it can be seen from Figures 4-24a and b that for the lowest assumed value of channel length (100 m), the lowest allowed values of propagation speed are about 0.3×10^8 m/s and 0.7×10^8 m/s for $\rho = 0$ and $\rho = -0.5$, respectively.

Allowed channel lengths for different values of propagation speed are tabulated in Figures 4-24a and b. The overall upper bounds on Δh for $\rho = 0$ and for $\rho = -0.5$ are 1000 and 500 m, respectively. Note that $\Delta h/v$ (channel traversal time), which yields the ratio = 2.5, is almost constant and equal to about $3.6 \mu\text{s}$ and $1.7 \mu\text{s}$ for $\rho = 0$ and $\rho = -0.5$, respectively. These longest allowed traversal times are about 0.6 and 0.3 times the current zero-to-peak risetime of $6 \mu\text{s}$.

Transformations of distant electric field waveforms in response to variations in Δh and v are illustrated in Figure 4-24 for a current risetime of $6 \mu\text{s}$. In each panel of this figure, the fields are shown for fixed values of ρ and Δh and variable v . Figures 4-25a and b show, for $\rho = 0$ and $\rho = -0.5$, respectively, the model predicted electric fields at 200 km (the source current is described in Section 4.2.3 and shown in Figure 4-16a) for four different propagation speeds and for two values of Δh . The latter are the assumed absolute lower bound (100 m) and the upper bound for each of the values of ρ (see Figure 4-24). For both values of reflection coefficient and for $\Delta h = 100$ m, one can see that electric field waveforms for all four propagation speeds appear to be consistent with experimental data (ratio ≥ 2.5). However, the electric field waveforms for the upper bounds of channel lengths ($\Delta h = 500$ m for $\rho = -0.5$ and $\Delta h = 1000$ m for $\rho = 0$) are inconsistent with experimental data (the ratio ≥ 2.5 condition is not satisfied), except for the upper bound on the propagation speed (3×10^8 m/s).

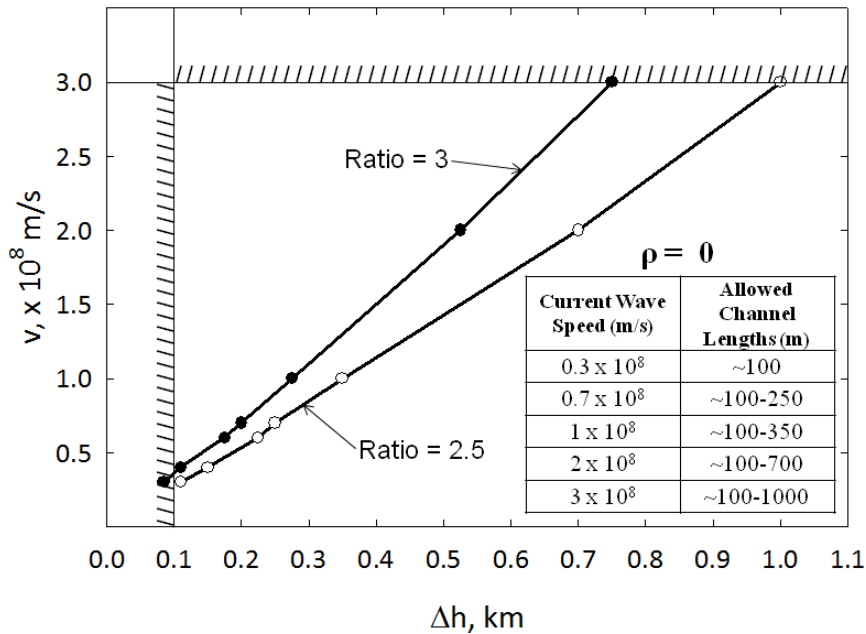


Figure 4-24a. Combinations of propagation speed and channel length for which the ratio of initial electric field peak to opposite polarity overshoot of model-predicted electric fields at 200 km attains 2.5 (the lowest value found in the experimental data) and 3.0 for a current risetime of $6 \mu\text{s}$ and $\rho = 0$. The area limited by the $v = 3 \times 10^8 \text{ m/s}$, $\Delta h = 0.1 \text{ km}$, and Ratio = 2.5 lines defines the domain of "allowed" combinations of v and Δh .

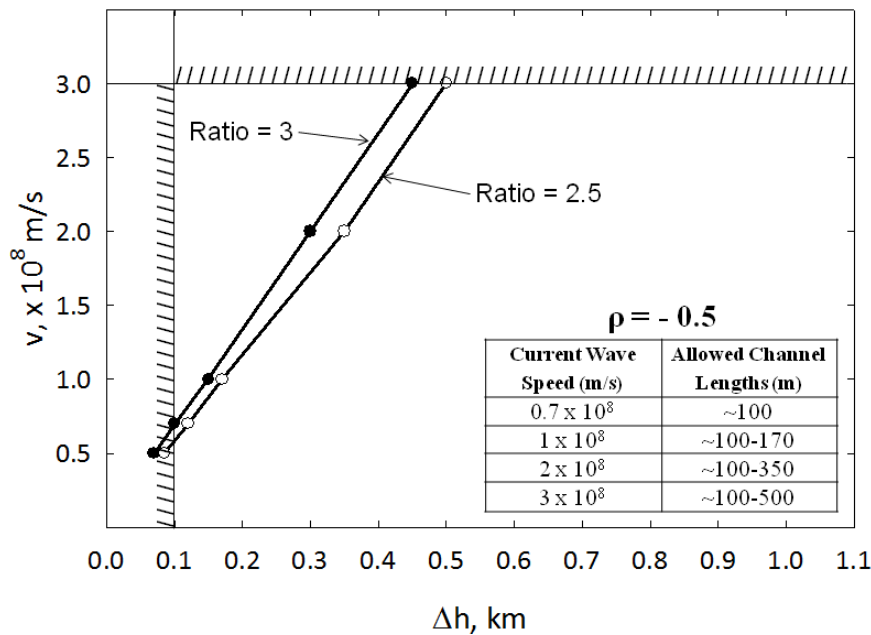


Figure 4-24b. Same as Figure 4-24a, but for $\rho = -0.5$.

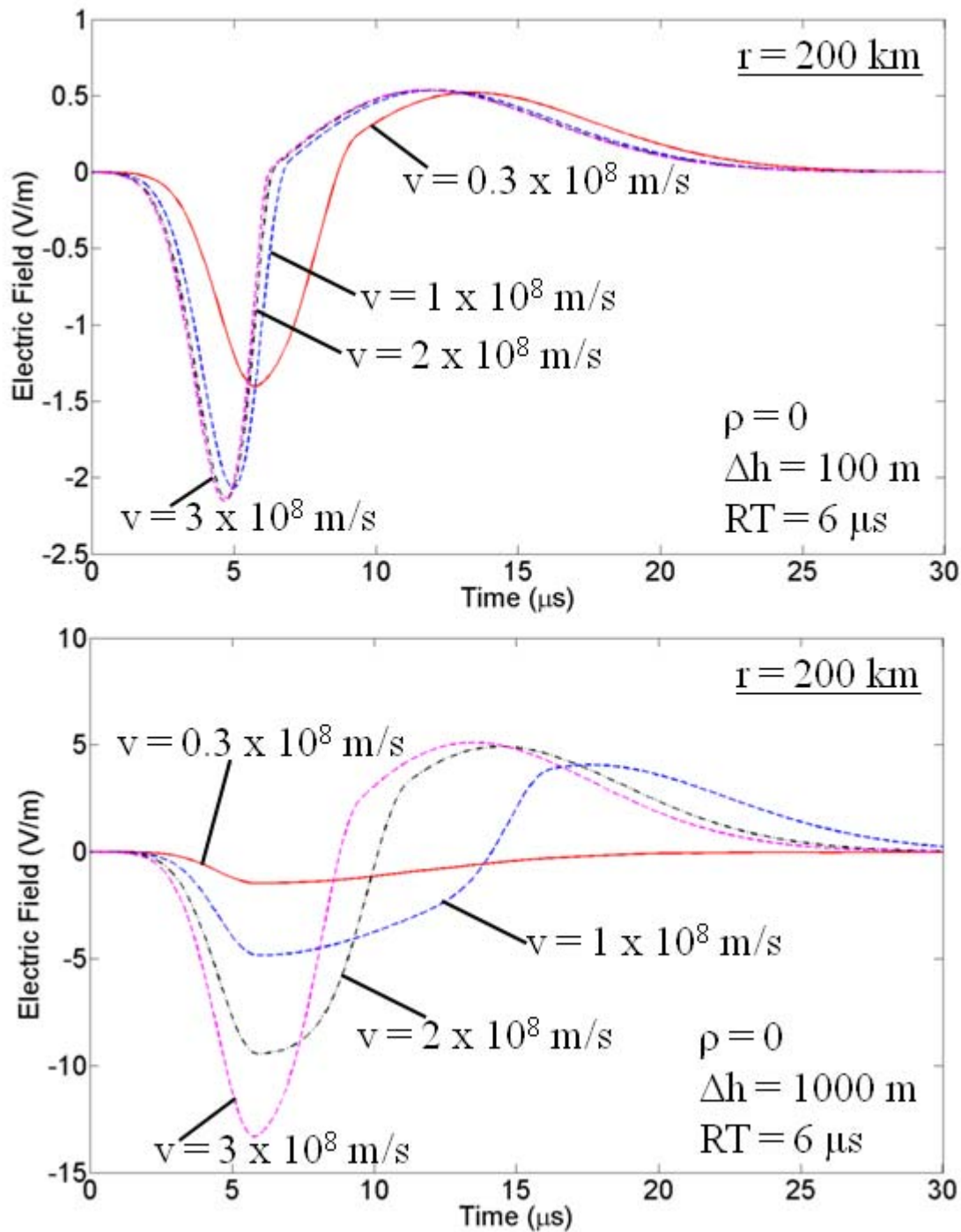


Figure 4-25a. Bouncing-wave model predicted electric fields at 200 km for different combinations of propagation speed and channel length for a current risetime of 6 μs (the source current is described in Section 4.2.3 and shown in Figure 4-16a) and $\rho = 0$.

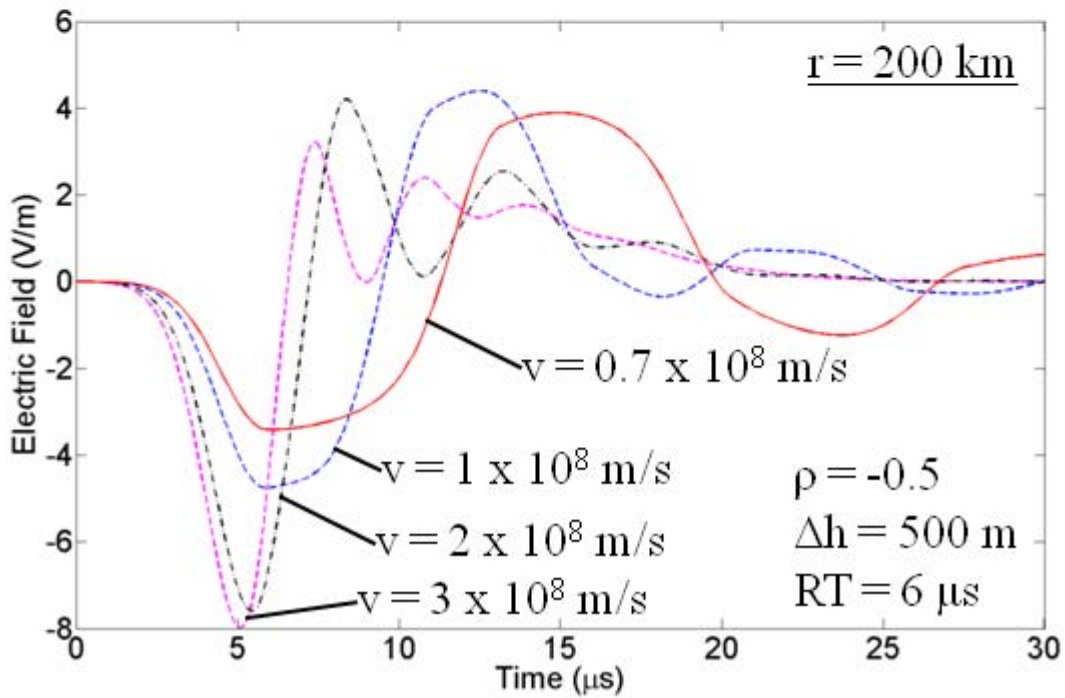
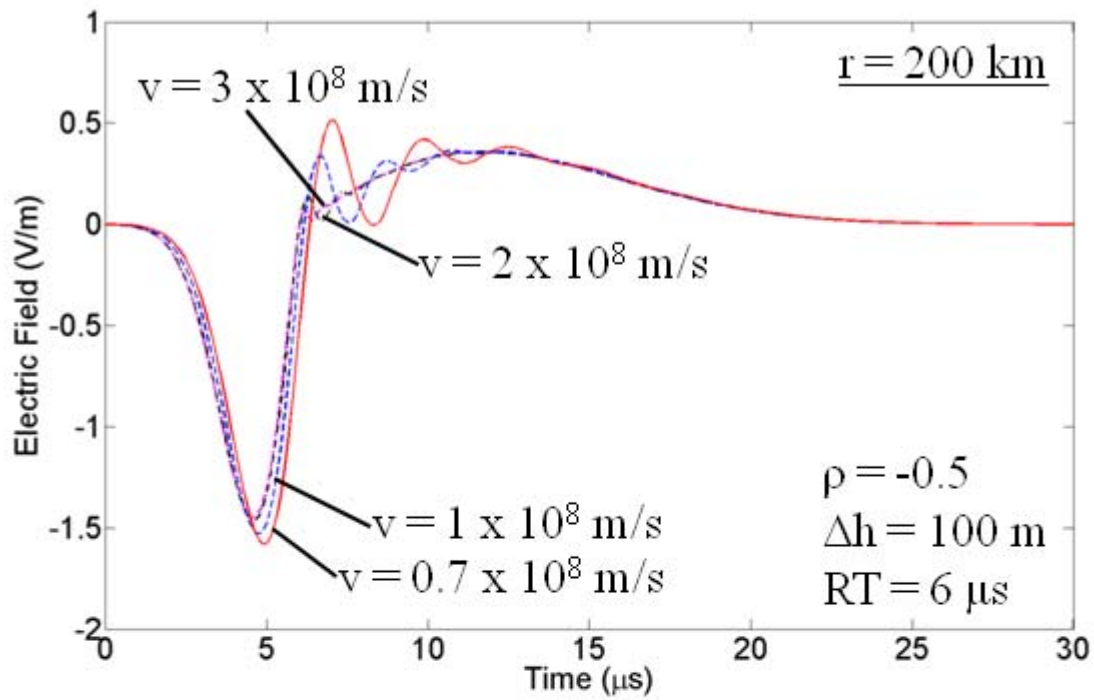


Figure 4-25b. Same as Figure 4-25a, but for $\rho = -0.5$.

Table 4-2. Influence of source height on the ratio of initial electric field peak to opposite polarity overshoot of CID electric fields. The fields were calculated using the bouncing-wave model for $r = 200$ km and current risetime of $6 \mu\text{s}$.

Reflection Coefficient	Current Wave Speed (m/s)	Channel Length (m)	Source Height (km)	Ratio
$\rho = -0.5$	0.7×10^8	100	5	3.0
			15	3.1
			25	3.1
	3×10^8	500	5	2.4
			15	2.5
			25	2.6
$\rho = 0$	0.3×10^8	100	5	2.7
			15	2.7
			25	2.7
	3×10^8	1000	5	2.7
			15	2.6
			25	2.5

4.2.7.3 Source height

Smith et al. [2004] reported the median CID source heights to be 13 km and 15 km, respectively (see also Section 4.1). The range of variation in our data is from 8.8 to 29 km. In our calculations we assumed a typical source height of 15 km. The ratio of the initial peak to the opposite polarity overshoot of the model-predicted waveforms of CIDs at a particular distance changes with altitude (as shown in Table 4-2) However, the changes are relatively small and the upper bounds on channel length at different speeds remain essentially the same for different altitudes. For example, all other parameters remaining constant, the upper bounds on channel length at a distance of 200 km, for $\rho = 0$ and $v = 3 \times 10^8$ m/s is about 1100 m for an altitude of 5 km, and about 1000 m for both 15 and 25 km.

4.2.7.4 Distance

The ratio of the initial peak to the opposite polarity overshoot of the model predicted waveforms of CIDs at a particular height changes with distance (as shown in Table 4-3). This, in turn, would change the upper bound on channel length at different speeds. However, these

changes are relatively small. For example, all other parameters remaining constant, the upper bounds on channel length for a source height (altitude) of 15 km, $\rho = 0$ and $v = 3 \times 10^8$ m/s are 900, 1000, and 1100 m for distances of 50, 200, and 400 km, respectively. Similarly, for $\rho = -0.5$ and $v = 3 \times 10^8$ m/s, the upper bounds on channel length is about 600 m for 50 km and about 500 m for both 200 and 400 km.

4.2.7.5 Current waveshape

The expression for the current injected at the bottom end of the CID channel used in all our computations is an asymmetric Gaussian pulse with total duration t_2 and zero-to-peak risetime of t_1 . The expression for $i_0(t)$ is given by:

$$i_0(t) = \begin{cases} A e^{-\beta(t-t_1)^2} & t \leq t_1 \\ A e^{-\beta(t-t_1)/k} & t > t_1 \end{cases} \quad (4-9)$$

where $k=(t_2-t_1)/t_1$, and β is a parameter that, along with k , controls the shape of the Gaussian pulse and causes current to approach zero at $t = 0$ and $t = t_2$. In computing electric fields we have used a current pulse with a peak (A) of 50 kA and total duration (t_2) of 30 μ s. In the following, we will examine the influence of current risetime (t_1), assuming that the total duration (t_2) of current pulse remains the same at 30 μ s. The values of the parameters β and k yielding different values of t_1 are given in Table 4-4.

In our model, for shorter lengths and higher speeds, the total width of the initial half-cycle of the CID electric field signature tends to become equal to the risetime of the incident current pulse. This is clearly seen in Figure 4-25a where all field waveforms were computed for the same current risetime of 6 μ s. Electric field signatures produced by currents having the same total duration (30 μ s) and peak (50 kA), but different risetimes, 3, 6 and 9 μ s, are shown in Figure 4-26, for $\rho = 0$, $\Delta h = 100$ m and $v = 2 \times 10^8$ m/s. The total width of the initial half-cycles of the electric field signatures are 3.4, 6.4, and 9.3 μ s, respectively. In our experimental data, the

Table 4-3. Influence of distance on the ratio of initial electric field peak to opposite polarity overshoot of CID electric fields. The fields were calculated using the bouncing-wave model for $h = 15$ km and current risetime of $6 \mu\text{s}$.

Reflection Coefficient	Current Wave Speed (m/s)	Channel Length (m)	Distance (km)	Ratio
$\rho = -0.5$	0.7×10^8	100	50	3.2
			200	3.1
			400	3.0
	3×10^8	500	50	3.0
			200	2.5
			400	2.4
$\rho = 0$	0.3×10^8	100	50	2.7
			200	2.7
			400	2.7
	3×10^8	1000	50	2.3
			200	2.6
			400	2.6

Table 4-4. Parameters β and k in Equation 4-9 yielding different values of current risetime (t_1). The total duration of current pulse t_2 remains the same and equal to $30 \mu\text{s}$.

Current Risetime (μs)	β	$k = (t_2 - t_1)/t_1$
2	$50/t_2$	14
3	$32/t_2$	9
6	$15/t_2$	4
8.5	$10/t_2$	2.53
9	$10/t_2$	2.33

total width of the initial half cycle ranged from 2.8 to $13 \mu\text{s}$ with a geometric mean of $5.6 \mu\text{s}$. We assumed that the initial half-cycle duration is unlikely to be less than $2.5 \mu\text{s}$ and used this as an additional criterion in determining allowed combinations of Δh and v .

From Figure 4-26 one can see that the ratio of the initial field peak to the opposite polarity overshoot decreases with increasing current risetime. The ratios for current risetimes of 3 , 6 and $9 \mu\text{s}$ are 8.5 , 4.0 , and 2.3 , respectively. For a current risetime of $8.5 \mu\text{s}$ the ratio is 2.5 , which is the minimum allowed value assumed in our study. Since we assume that the lower bound on channel length is 100 m, and increasing the channel length causes a decrease in the ratio (Figure

4-24), a current risetime longer than 8.5 μs would result in an electric field waveform that is inconsistent with experimental data for any channel length equal to or greater than the lower bound, when the propagation speed is 2×10^8 m/s. In fact, for propagation speeds of 0.7×10^8 m/s to 3×10^8 m/s, the ratio remains approximately 2.5 (varies from 2.47 to 2.55), when the current risetime is 8.5 μs . Tables 4-5 and 4-6 list the allowed combinations of reflection coefficients, propagation speeds, and channel lengths that produce distant field waveforms that are consistent with experimental data for current risetimes of 2 and 3 μs . The following criteria were used in determining allowed combinations: (1) the ratio of initial peak to opposite polarity overshoot is equal to or greater than about 2.5 (2) the total width of initial half cycle is equal to or greater than about 2.5 μs , and (3) the overall shape of the initial half cycle is consistent with observed ones. For longer risetimes, the range of allowed Δh - v combinations was determined by the ratio (criterion 1). For short risetimes and shorter channel lengths, the range of allowed Δh - v combinations was determined by the total width of the initial half cycle (criterion 2). Criterion 3 was the primary one for short risetimes and longer channel lengths. In this latter case, the initial half cycle exhibited flattening (see Figure 4-27b) that is not consistent with experimental data, for all speeds other than the speed of light. Note that for a current risetime of 2 μs and $\rho = -0.5$, no combination of parameters produced waveforms consistent with experimental data.

Transformations of distant electric field waveforms due to variations in Δh and v are illustrated in Figure 4-27 and 4-28 for current risetimes of 2 and 8.5 μs , respectively. Figures 4-27a and b show, for $\Delta h = 100$ m (the lower bound on channel length, see Table 4-6) and $\Delta h = 500$ m (the upper bound on channel length, see Table 4-6), respectively, the model predicted electric fields at 200 km (the source current is described in Section 4.2.3 and shown in Figure 4-16a) for different propagation speeds and $\rho = 0$. For $\Delta h = 100$ m, one can see that electric field

waveforms for all propagation speeds, except for 3×10^8 m/s (which violates criterion 1 described above), appear to be consistent with experimental data. However, the electric field waveforms for the upper bound on channel length ($\Delta h = 500$ m) are inconsistent with experimental data (violate criterion 3) for all propagation speeds, except for 3×10^8 m/s. For a current risetime of $8.5 \mu\text{s}$, electric field waveforms for $\rho = 0$ (Figure 4-28a) and -0.5 (Figure 4-28b) appear to be consistent with experimental data for propagation speeds ranging from about 10^8 to 3×10^8 m/s only for $\Delta h = 100$ m.

Table 4-5. Combinations of reflection coefficients, propagation speeds, and channel lengths that produce distant CID electric fields that are consistent with experimental data for current risetime of $3 \mu\text{s}$.

Reflection Coefficient	Current Wave Speed (m/s)	Channel Length (m)
$\rho = -0.5$	1.1×10^8	~100
	2×10^8	~100-175
	3×10^8	~100-275
$\rho = 0$	0.4×10^8	~100
	0.7×10^8	~100-200
	1×10^8	~100-250
	2×10^8	~100-500
	3×10^8	~100-800

Table 4-6. Combinations of propagation speeds and channel lengths that produce distant CID electric fields that are consistent with experimental data for $\rho = 0$ and current risetime of $2 \mu\text{s}$. No combination produced waveforms consistent with experimental data for $\rho = -0.5$.

Reflection Coefficient	Current Wave Speed (m/s)	Channel Length (m)
$\rho = 0$	0.6×10^8	~100
	0.7×10^8	~100-125
	1×10^8	~100-200
	2×10^8	~100-300
	3×10^8	~200-500

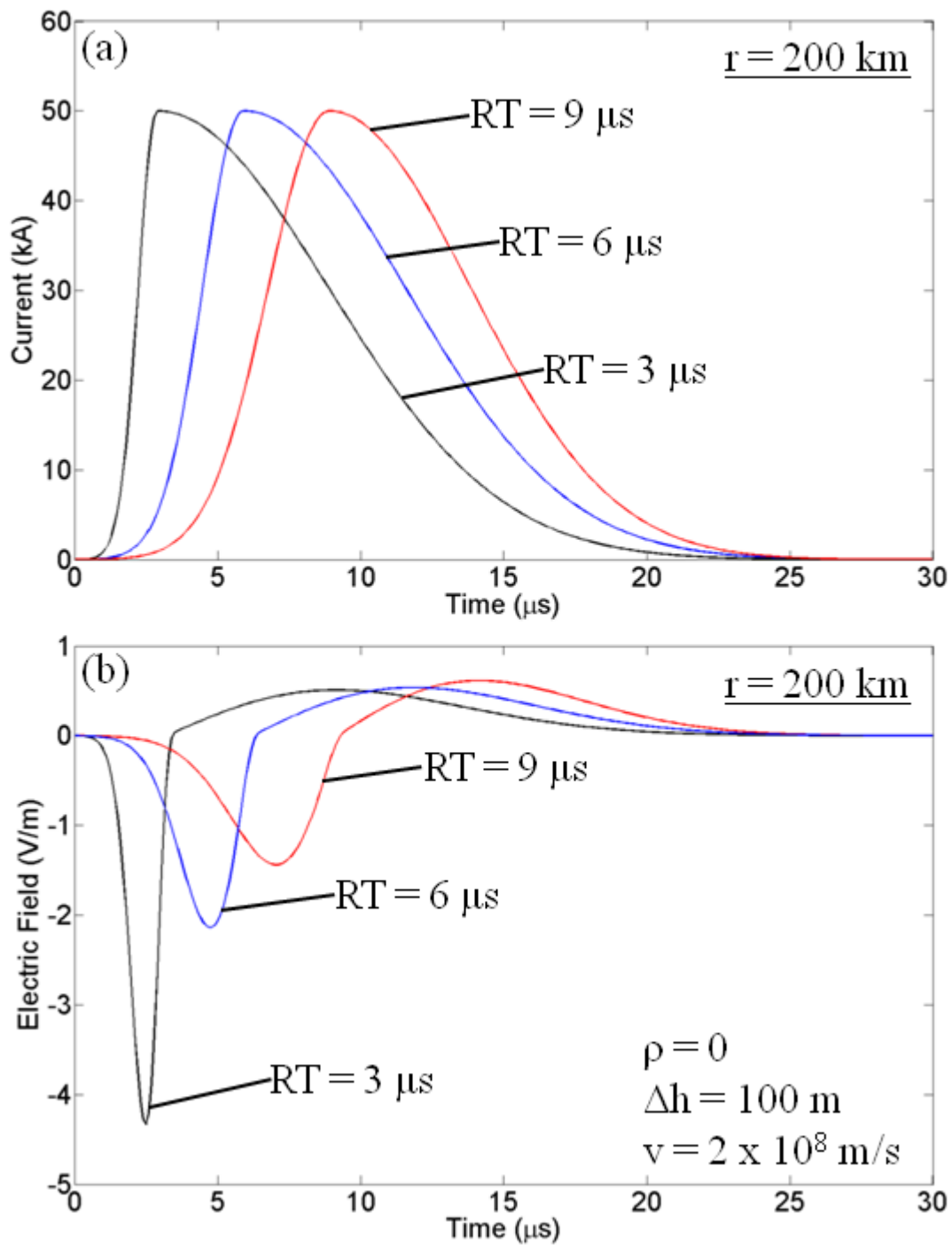


Figure 4-26. Currents (a) and corresponding electric fields (b) for the same total current duration (30 μs) and peak (50 kA), but different risetimes of 3, 6 and 9 μs for $\rho = 0$, $\Delta h = 100 \text{ m}$, and $v = 2 \times 10^8 \text{ m/s}$.

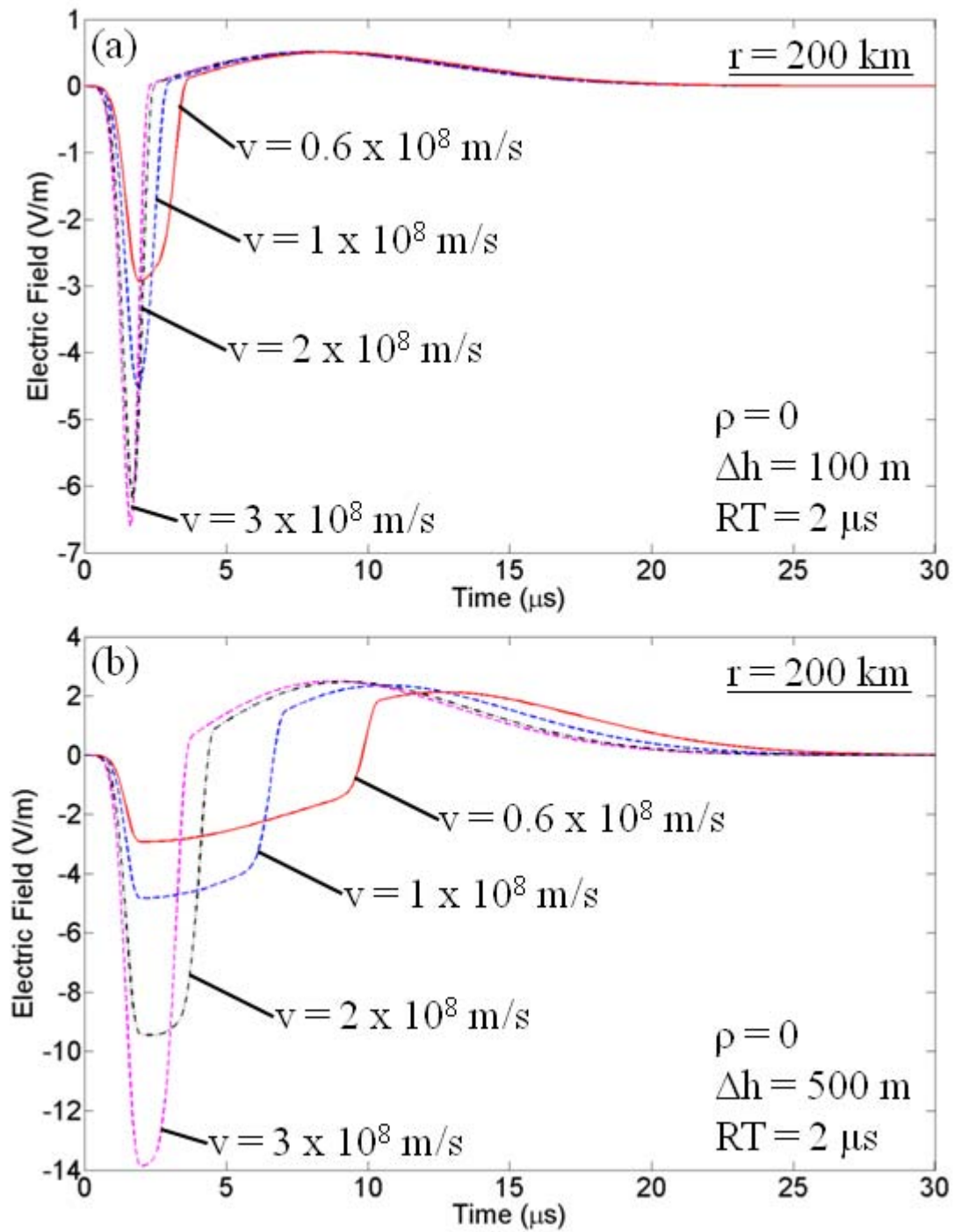


Figure 4-27. Electric field waveforms at 200 km for different propagation speeds and channel lengths of (a) 100 m and (b) 500 m, for a current risetime of 2 μs and $\rho = 0$.

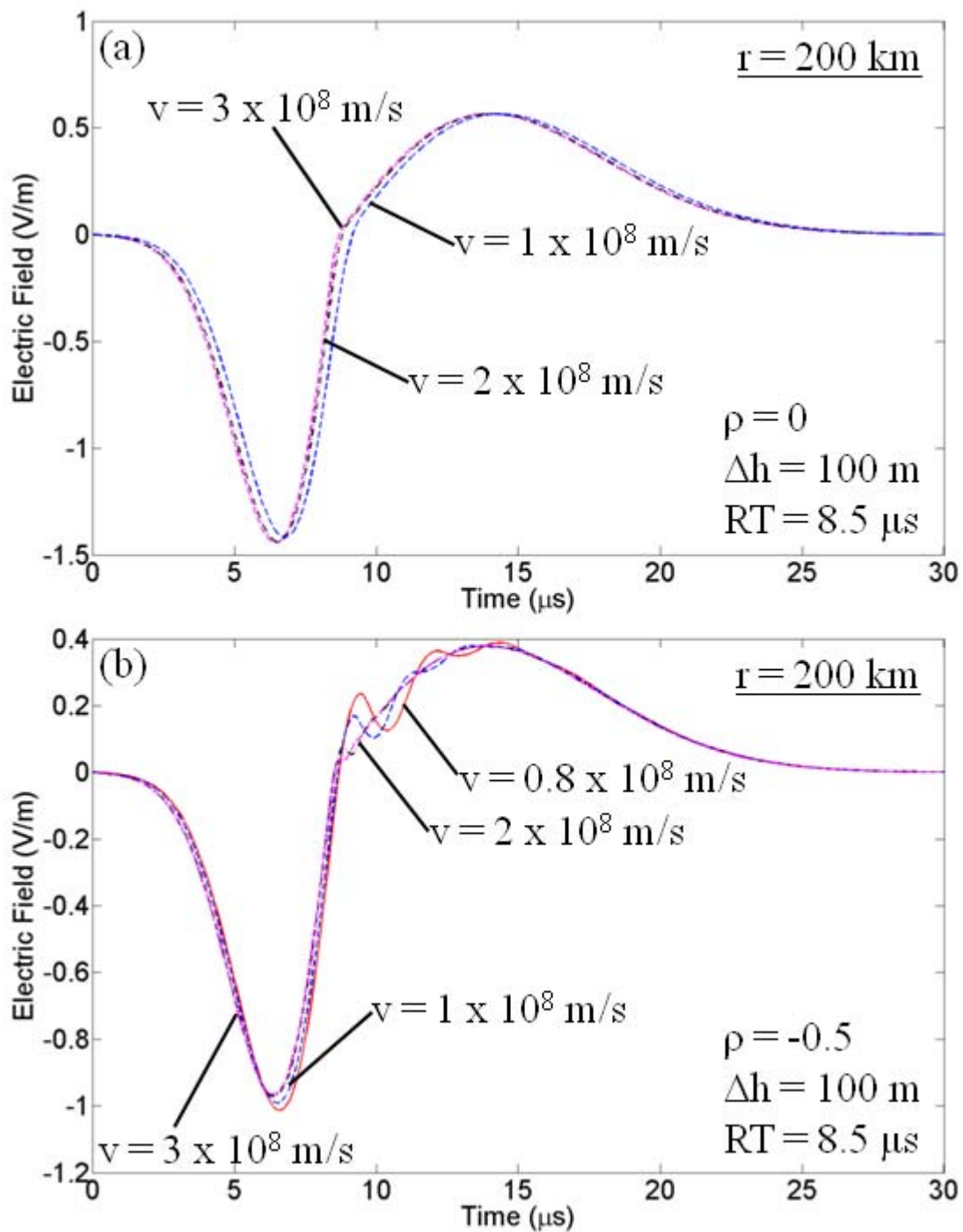


Figure 4-28. (a) Electric field waveforms at 200 km for different combinations of propagation speed and channel length for a current risetime of $8.5 \mu\text{s}$ and $\rho = 0$. (b) Same as in (a), but for $\rho = -0.5$.

4.2.8 Testing the Validity of Bouncing-Wave Model and Hertzian-Dipole Approximation Using Electric Fields Simultaneously Measured at Near and Far Distances by *Eack* [2004]

4.2.8.1 Bouncing-wave model

Here, we use the simultaneously measured near and far electric field signatures of one CID reported by *Eack* [2004] to test the validity of bouncing-wave model. This same event was previously used for testing the validity of other models by *Watson and Marshal* [2007]. The CID transferred negative charge upward (or positive charge downward). We use the trial and error approach to determine a combination of CID parameters, including the current peak, the current zero-to-peak risetime (RT), the propagation speed (v), current reflection coefficient (ρ), and the channel length (Δh), for which the bouncing-wave model predicted electric fields best match the measured electric fields at both near and far distances from the discharge. The CID channel was assumed to be vertical.

Electric field signatures of this CID, measured at Los Alamos (near station) and Socorro (far station), New Mexico, are shown in Figure 1 of *Eack* [2004] and reproduced in Figure 4-29 of this Chapter. Horizontal distances were estimated, using Los Alamos Sferic Array (LASA) measurements and a time-of-arrival (TOA) method, to be 2.8 km from the Los Alamos station and about 200 km from the Socorro station with a stated error of ± 2 km. The CID height was estimated to be of 11.6 km above mean sea level. The height above local terrain should be smaller by about 2 km [*Smith et al.*, 2004]; that is, about 9.6 km. The CID height was estimated by measuring delays of ionosphere and ground-ionosphere reflections with respect to direct-path wave in VLF/LF ground-based (LASA) field records. *Smith et al.* [2004] estimated errors of this method relative to another, more accurate method that employed FORTE satellite VHF records showing direct-path and ground-reflection signals. The ground-based estimates were on average 1 km higher than the satellite estimates. After removal of the 1-km bias, the LASA height

estimates were within ± 1 km of satellite estimates. Thus, the height of the CID in question is $9.6 - 1 = 8.6$ km with a random error of ± 1 km. In summary, uncertainties in distance of the CID in question are 0.8 to 4.8 km and 198 to 202 km from the Los Alamos and Socorro station, respectively, and uncertainties in height are 7.6 to 9.6 km above ground level. We include these uncertainties in our search for CID parameters that provide best match between model-predicted and measured electric field waveforms at both near and far distances.

Figures 4-29a and b show the model predicted electric fields overlaid with the measured ones at near and far distances, respectively. A reasonably good match between calculated and measured fields was obtained for a peak current of 75 kA, $RT = 5.2 \mu\text{s}$, $v = 1.4 \times 10^8$ m/s, $\rho = 0$, $\Delta h = 650$ m, horizontal distances of 2.3 and 200 km from the near and far stations, respectively, and the height of the bottom of the CID channel of 7.8 km above ground level. The CID current pulse was assumed to be injected at the bottom end of the CID channel and to travel upward. The expression for the current waveform is given in Section 4.2.7 (Equation 4-9). The values of β and k (parameters that control the shape of the Gaussian current pulse) along with the best-fit values of peak current, RT , v , ρ , and Δh are given in Table 4-7.

4.2.8.2 Hertzian dipole approximation

Here, we use the two-station data of *Eack* [2004] to test the validity of the vertical Hertzian dipole approximation. In contrast with the bouncing-wave model, v and ρ are not parameters of the Hertzian dipole approximation. The testing procedure used here is similar to that described above for the bouncing -wave model.

Figure 4-30 shows electric fields based on the Hertzian dipole approximation overlaid with the experimental data at near and far distances. A reasonably good match between calculated and measured fields was obtained for a peak current of 74 kA, $RT = 9 \mu\text{s}$, $\Delta h = 500$ m, horizontal distances of 2.4 and 200 km from the near and far stations, respectively, and the height of CID

channel of 7.2 km above ground level. The expression for the current waveform injected is given in Section 4.2.7 (Equation 4-9), with the values of β and k along with the best-fit peak current, RT , and Δh being given in Table 4-7.

4.2.8.3 Discussion

The Gaussian current pulse that we used for testing the Hertzian dipole approximation is the same as that employed by *Watson and Marshall* [2007] for modeling the same CID. They were unable to obtain a good match with *Eack's* near field data using the transmission line model and assuming that the stated horizontal distance, 2.8 km, is exact. As shown in this Appendix, both the close and distant fields can be reasonably well reproduced by the bouncing-wave model (which for $\rho = 0$ reduces to the transmission line model used by *Watson and Marshall* [2007]) when the uncertainties in the estimated horizontal distances and source height are taken into account.

We now compare, with reference to Table 4-7, parameters for which predictions of the bouncing-wave model and Hertzian dipole approximation best fit the two-station data of *Eack* [2004]. The channel lengths that fit *Eack's* two-station data for the bouncing-wave model and Hertzian dipole approximation are similar, 650 m and 500 m, respectively, and both are within the corresponding allowed ranges. The peak currents predicted by both models are almost the same (75 kA for the bouncing-wave model and 74 kA for the Hertzian dipole approximation). Note that our peak-current estimates of 74-75 kA are similar to that (74 kA) of *Watson and Marshall* (based on the TL model) and appreciably higher than that (29 kA) of *Eack* (based on the assumption that the near field peak is due to induction field component only). Our predicted zero-to-peak current risetime of 9 μ s for the Hertzian dipole approximation is larger than that (5.2 μ s) for the bouncing-wave model and is close to the upper limit (8.5 μ s) of the range of allowed values. The source heights for which a reasonably good match with two-station data is

obtained for the bouncing-wave model and Hertzian dipole approximation are similar, 7.8 and 7.2 km, respectively, although the latter is slightly outside the range of uncertainty (7.6 - 9.6 km) in this parameter.

Table 4-7. CID parameters for which electric fields at close and far distances that are based on the bouncing-wave model and Hertzian dipole approximation best fit the fields measured by *Eack* [2004].

Parameters	Bouncing-Wave Model		Hertzian Dipole Approximation	
	Best-fit value	Allowed range	Best-fit value	Allowed range
Peak current, kA	75	-	74	-
Zero-to-peak current risetime, μ s	5.2	2.5 - 8.5	9	2.5 - 8.5
Total Current duration (t_2), μ s	36	-	36	-
β (see Equation 4-9)	$18.1/t_2$	-	$10.25/t_2$	-
k (see Equation 4-9)	5.92	-	3	-
Propagation speed, m/s	1.4×10^8	$0.3 - 3 \times 10^8$	-	-
Current reflection coefficient	0	-0.5 - 0	-	-
Channel length, m	650	100 - 1000	500	100 - 550
Distance from near station, km	2.3	0.8 - 4.8	2.4	0.8 - 4.8
Distance from far station, km	200	198 - 202	200	198 - 202
Height of the channel above ground, km	7.8 (lower end)	7.6 - 9.6	7.2	7.6 - 9.6

4.2.9 Discussion and Summary

Smith et al. [1999] estimated the CID channel lengths to range from 300 to 1000 m. In estimating the lower bound, they considered two oppositely charged spherical regions, immediately adjacent to each other, with the CID channel extending between the centers of the two spheres (see Section 4.3 for more details). The lower bound on channel length was found by comparing the maximum electric field (at the point of contact of the spheres), for the average charge estimated from observations, with the conventional breakdown electric field in the cloud

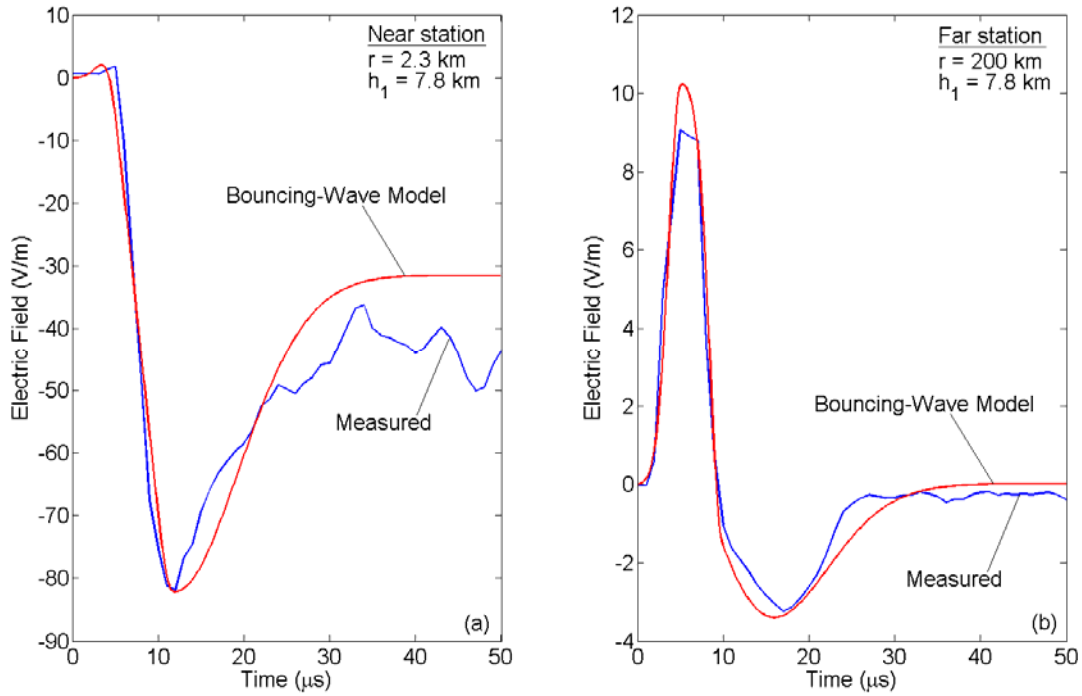


Figure 4-29. Electric fields computed using the bouncing-wave model (in red) overlaid with the fields measured by *Eack* [2004, Figure 1] (in blue) at (a) near and (b) far distances.

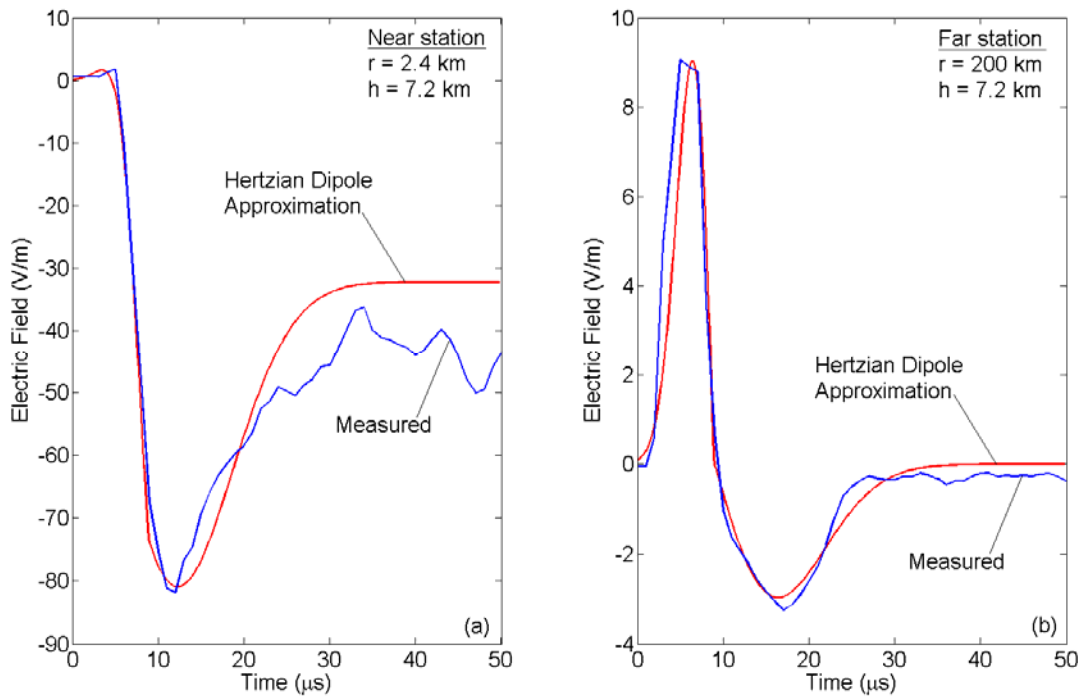


Figure 4-30. Electric fields computed using the Hertzian dipole approximation (in red) overlaid with the fields measured by *Eack* [2004, Figure 1] (in blue) at (a) near and (b) far distances.

(of the order 10^6 V/m). The upper bound on channel length of 1000 m was apparently based on the median duration of 3.2 μ s of HF radiation produced by CIDs [Smith, 1998] and the upper limit for the propagation speed of 3×10^8 m/s. Our channel lengths estimated from channel traversal times measured in dE/dt records are smaller than *Smith et al.*'s lower bound of 300 m, with the corresponding charge configuration being discussed in Section 4.3. The upper bound on CID channel length estimated in this study (see Section 4.2.7) by comparing bouncing-wave model predicted electric fields to experimental data is the same as that of *Smith et al.* [1999].

Using the upper bound on channel length and the mean duration (10-to-90%) of 13.7 μ s of CID dipole moment change, *Smith et al.* [1999] calculated the propagation speed of the current wave to be 7.3×10^7 m/s. According to the bouncing-wave mechanism proposed in this Chapter, the average propagation speed inferred by *Smith et al.* [1999], who essentially assumed that the total duration of the CID electric field pulse is equal to one channel traversal time, must be an underestimate, although it is within the range of allowed values (see Section 4.2.7).

Eack [2004] erroneously used the dipole approximation to infer the propagation speed for CIDs from his two-station electric field measurements. In doing so, he estimated the dipole moment change, Δp , from a close field record, which at later times is dominated by the electrostatic field component. From the electrostatic field change, ΔE_{es} , measured at distance r , the dipole moment change is

$$\Delta p = 4\pi\epsilon_0\Delta E_{es}r^3 \quad (4-10)$$

This step is fine, but then *Eack* substituted the resultant Δp value into the equation for dipole moment change in terms of the radiation electric field change, ΔE_r , at distance r (much larger than r in Equation 4-10),

$$\Delta p = 4\pi\epsilon_0c^2r \int \int \Delta E_r(t)dt dt, \quad (4-11)$$

where c is the speed of light (speed at which an electromagnetic wave propagates from the source to the observer), which he labeled as " v " and misinterpreted as the propagation speed of the CID current wave along the channel. The propagation speed along the channel is not a parameter of the dipole approximation and, hence, it cannot be derived from this approximation. In fact, solving Equation 4-11 for c should yield 3×10^8 m/s, and any deviation from this value (*Eack* computed 1.5×10^8 m/s, on average) should be viewed as being due to inadequacy of employed model and/or measurement errors. Further, *Eack* used his misinterpreted propagation speed and the total duration of the CID electric field pulse to estimate the CID channel length. The resultant (incorrect) average channel length for seven CIDs was 3.2 km (larger than the upper bound estimated in Section 4.2.7).

Hamlin et al. [2007] inferred that the secondary peak (of the same polarity as the preceding primary peak) in CID electric field signatures was due to reflection of the current wave from the far end of the channel. They used an assumed propagation speed of 3×10^8 m/s and the time difference between the primary and secondary peaks to estimate the upper bound on channel length, which was found to be 2 km. However, as found from modeling (see Section 4.2.4), the secondary peaks observed by *Hamlin et al.* [2007] actually occur at the time when the current front is in the middle of the channel, after being reflected from its far end. More importantly, the secondary peak, occurring several microseconds after the primary peak, results from one of the higher-order reflections from the far end of the channel, as evident from comparison of electric field and dE/dt signatures in Figure 4-11. It follows that *Hamlin et al.*'s channel lengths are overestimates. In Section 4.2.7, we estimated the upper bound on channel length to be about 1000 m. Longer channels would result in distant electric field waveforms that are inconsistent with experimental data.

Watson and Marshall [2007] used the original transmission line (TL) model [*Uman et al.*, 1975] and a modified TL model with an exponentially increasing current along the channel to compute electric field signatures at horizontal distances of 2.8 and 200 km and compare them with corresponding measured waveforms reported by *Eack* [2004]. Both models can, in principle, successfully match the two-station field measurements (for the TL model after a slight change in distance from the close station). The exponentially increasing current was assumed by *Watson and Marshall* to correspond to the runaway electron breakdown process. They estimated the propagation speed and channel length to be 6×10^7 m/s and 630 m, respectively, for the exponentially increasing current model. For the TL model (constant amplitude of current wave) they estimated a speed of 2×10^8 m/s and a channel length of 500 m. *Watson and Marshall's* estimates of propagation speed and channel length are within the range of allowed values found in Section 4.2.7.

In this study, we assume that the shortest CID channel length is about 100 m and show, via comparison of bouncing-wave model predictions with measurements, that the upper bound on channel length is approximately 1000 m. Thus, compact intracloud discharges are indeed "compact". The uniqueness of CIDs is apparently related to the fact that a short conducting channel (its length is primarily determined by the spatial extent of high-field region) is created faster (on a submicrosecond time scale) than the cloud electric field can polarize this channel (make it nearly equipotential). This mismatch results in a transient, bouncing-wave process in the channel. The polarization rate should be primarily determined by the conductivity of the channel, which for a "lightning seed" created via a runaway electron breakdown process is expected to be of the order of 10^{-4} S/m [*Solomon et al.*, 2001]. It is possible that the bouncing waves serve to maintain channel conductivity. As evidenced by a more or less constant period of oscillations

(see Figure 4-11b), the channel length remains constant in the later part of the discharge. This short and fixed channel length property (although there should be corona-like streamers developing from channel ends) implies that CIDs cannot pervade large cloud volumes and tap remote charge reservoirs, which is consistent with the fact that the majority CIDs tend to occur in isolation from any other lightning activity. On the other hand, CIDs apparently can and do cause charge redistribution in the cloud, which may facilitate or contribute to initiation of "normal" IC discharges or influence development of CG discharges [e.g., *Rison et al.*, 1999; *Thomas et al.*, 2001; *Krehbiel et al.*, 2008; Section 4.1].

4.3 Estimation of Electrical Parameters

In Section 4.2 we showed that the current distribution along the CID channel is often not much different from uniform, because of relatively short channel length, Δh , relatively long current waveform, and relatively high propagation speed, v . This observation suggests that at least for some "allowed" combinations of v and Δh , we can reasonably approximate the CID channel by a vertical Hertzian dipole. This approximation will enable us to simplify the field equations and use measured fields to infer various parameters of CIDs. Within the Hertzian dipole approximation, the propagation speed is not an input parameter and the current waveshape is the same as that of the time integral of CID radiation field signature, which is often referred to as the narrow bipolar pulse or NBP.

In this Section, we determine the limits of validity of the Hertzian dipole approximation as applied to CIDs, and use this approximation to infer the peak current, current risetime, charge transfer, radiated power, and radiated energy for the 48 located CIDs studied in Section 4.1. Additionally, we estimate the upper bound on cloud electric field prior to CID and total energy dissipated by this type of lightning. The physics sign convention according to which a

downward-directed electric field (or field change) vector is considered to be negative is used in this Section.

4.3.1 The Hertzian Dipole Approximation Approach

Equation 4-4 also applies to a vertical dipole of finite length $\Delta h = h_2 - h_1$, provided that Δh is very short compared to the shortest significant wavelength λ (Hertzian or electrically short dipole approximation). For example, for a dipole of length, $\Delta h = 500$ m can be considered Hertzian if $\lambda \gg 500$ m. This means that the above approximation is valid for frequencies $f \ll 600$ kHz. From Equation 4-4 for the geometry shown in Figure 4-18, the total electric field at the observation point for a vertical Hertzian dipole we can write:

$$E_z(r, t) = \frac{1}{2\pi\epsilon_0} \left[\frac{(2h^2 - r^2)\Delta h}{R^5} \int_0^t i(\tau - R/c) d\tau + \frac{(2h^2 - r^2)\Delta h}{cR^4} i(t - R/c) - \frac{r^2\Delta h}{c^2R^3} \frac{di(t - R/c)}{dt} \right] \quad (4-12)$$

where $R = \sqrt{h^2 + r^2}$. Note that current i in Equation (3) varies only as a function of time, with all the geometrical parameters being fixed.

In Section 4.3.2, we will show that the vertical Hertzian dipole approximation is consistent with the CID bouncing-wave model for a reasonably large subset of "allowed" combinations (established in Section 4.2.7) of v and Δh .

Equation 4-12 can be expressed as a second order differential equation:

$$\frac{dE_z}{dt} = \frac{\Delta h}{2\pi\epsilon_0} \left[\frac{(2h^2 - r^2)}{R^5} i + \frac{(2h^2 - r^2)}{cR^4} \frac{di}{dt} - \frac{r^2}{c^2R^3} \frac{d^2i}{dt^2} \right] \quad (4-13)$$

where arguments of E_z and i have been dropped to simplify notation. For known E_z and the geometrical parameters (Δh , h , and r) this equation can be numerically solved for i .

We employed the Runge-Kutta method of order three (with four stages and an embedded second-order method, also known as the Bogacki–Shampine method [*Bogacki and Shampine*, 1989]) to solve Equation (4) for i using measured electric fields E_z (which had a better signal-to-

noise ratio than the measured electric field derivative waveforms) of 48 located CIDs that occurred at horizontal distances r ranging from 12 to 89 km and heights h ranging from 8.8 to 29 km (Section 4.1). The initial and final values of current used to solve Equation 4 were required to be zero, and the error tolerance of the numerical solution was set to 10^{-6} . Channel lengths Δh for 9 CIDs were estimated from reflections in electric field derivative (dE/dt) waveforms and assumed propagation speeds covering the entire range of their allowed values (see Section 4.2). For the remaining 39 CIDs there were no reflection signatures observed, and a reasonable value of $\Delta h = 350$ m was assumed. This value is consistent with the Hertzian dipole approximations for speeds in the range of 2 to 3×10^8 m/s. We also considered other values of Δh , which are consistent with the Hertzian dipole approximation. Note that for E_z measured at far distances, the peak current can also be estimated analytically using the radiation field approximation, given by:

$$\frac{dE_z}{dt} = \frac{\Delta h}{2\pi\epsilon_0} \left(-\frac{r^2}{c^2 R^3} \frac{d^2 i}{dt^2} \right) \quad (4-14)$$

In order to illustrate this, an electric field waveform (shown in Figure 4-31a) computed using the current waveform shown in Figure 4-31b (black line) and the bouncing-wave model for a CID occurring at a height of 15 km and a horizontal distance of 200 km was used in both Equation 4-13 and the radiation field approximation (Equation 4-14) to solve for current. Results are presented in Figure 4-31b, along with the current used compute the electric field shown in Figure 2a. One can see from Figure 4-31b that the three current waveforms are very similar to each other. For the 9 CIDs with reflection signatures in dE/dt waveforms, occurring at horizontal distances ranging from 19 to 89 km, the radiation field approximation estimated current peaks were, on average, 17% greater than those obtained by numerically solving Equation 4-13. The differences in peak ranged from 7% to 21% for 8 CIDs and for one CID with a poor signal-to-noise ratio it was 47%.

The charge transferred up to time t can be obtained by integrating the current with respect to time:

$$Q = \int_0^t i(\tau) d\tau \quad (4-15)$$

Further, the source current can be used to find the radiation components of E_θ and H_ϕ and hence the Poynting vector, total radiated power, and energy. The magnitude of the Poynting vector, which has the meaning of the radiated power density, can be obtained as:

$$|\vec{S}| = |\vec{E}_\theta \times \vec{H}_\phi| \quad (4-16)$$

where $E_\theta = \frac{\Delta h}{4\pi\epsilon_0} \sin\theta \frac{1}{c^2 R} \frac{di}{dt}$ and $H_\phi = \frac{\Delta h}{4\pi} \sin\theta \frac{1}{cR} \frac{di}{dt}$ [e.g., *Uman*, 1987]. After substituting the latter two field expressions in Equation 4-16 we get

$$|\vec{S}| = \frac{1}{\epsilon_0 c^3} \left(\frac{\Delta h \sin\theta}{4\pi R} \frac{di}{dt} \right)^2 \quad (4-17)$$

The total radiated power, obtained by integrating Equation 4-17 over a spherical surface of radius R whose center is at the position of the dipole, is (presence of ground is not taken into account):

$$P_{rad} = \int_{\phi=0}^{2\pi} \int_{\theta=0}^{\pi} |\vec{S}| R^2 \sin\theta d\theta d\phi = \frac{\Delta h^2}{6\pi\epsilon_0 c^3} \left(\frac{di}{dt} \right)^2 \quad (4-18)$$

where θ and ϕ are the polar and azimuthal angles of the spherical coordinate system. The total energy dissipated up to time t can be obtained by integrating the radiated power with respect to time:

$$W = \int_0^t P_{rad}(\tau) d\tau \quad (4-19)$$

Note that since $\frac{di}{dt}$ is inversely proportional to Δh , $|\vec{S}|$, P_{rad} , and W are each independent of Δh .

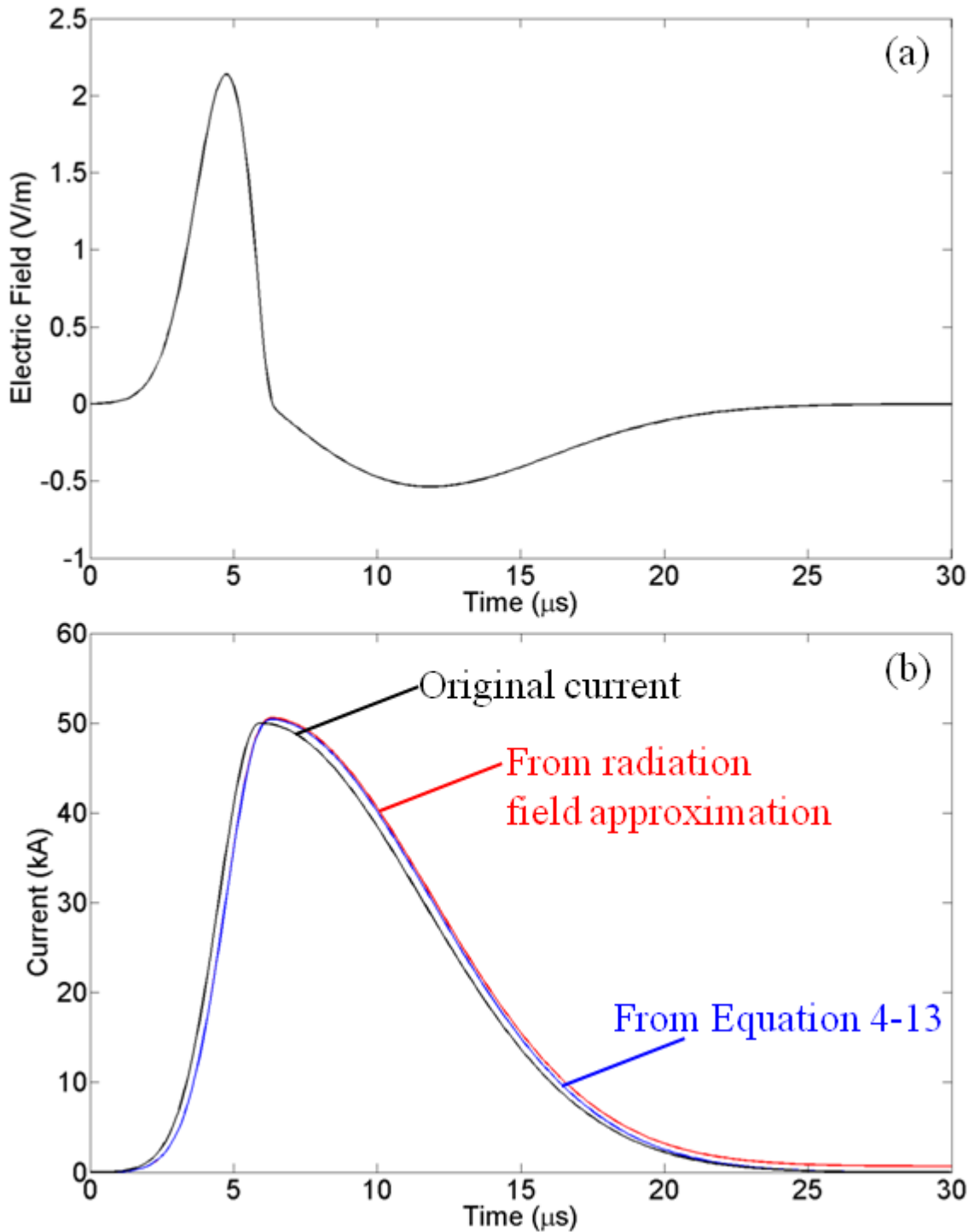


Figure 4-31. (a) Bouncing-wave model-predicted electric field for a CID occurring at a height of 15 km and a horizontal distance of 200 km ($\Delta h = 100$ m, $v = 2 \times 10^8$ m/s, $\rho = 0$) and (b) current waveforms obtained by solving Equation 4-13 (blue line) and using the radiation field approximation (red line) with the electric field shown in (a) as an input. Also shown is the current waveform (black line) used to compute the electric field in (a).

4.3.2 Limits of Validity of the Hertzian Dipole Approximation

In this Section, we compared electric fields produced at 200 km by a typical CID at a height of 15 km having a current zero-to-peak risetime RT of 6 μ s computed using the vertical Hertzian dipole approximation with their counterparts predicted by the bouncing-wave CID model (see Section 4.2). Calculations were performed for different combinations of effective current reflection coefficients at channel ends, channel lengths, and propagation speeds, each within the bounds ("allowed" ranges) established in Section 4.2.7. The Hertzian dipole was excited by the current found for the middle of the channel ($z = h_l + \Delta h/2$) using the bouncing wave model (see Equations 4-7 to 4-9 and Table 4-4 of Section 4.2). The bouncing-wave model predicted waveforms were used as the ground-truth, and electric field waveforms based on the Hertzian dipole approximation with initial peaks within about 15% of ground-truth peaks were considered as confirming the validity of the approximation. The influence of RT was also considered.

Figure 4-32 shows the electric fields for the Hertzian dipole approximation (dashed line) and bouncing-wave model (solid line) for $\rho = 0$, $v = 2 \times 10^8$ m/s, RT = 6 μ s, and channel lengths of 100, 350, and 700 m. While the Hertzian dipole approximation is acceptable for the lengths in the range of 100-350 m, it is not for 700 m. Figure 4-33 shows the electric fields for the Hertzian dipole approximation (dashed line) and bouncing-wave model (solid line) for $\rho = -0.5$, $v = 2 \times 10^8$ m/s, RT = 6 μ s, and channel lengths of 100 and 350 m. In both cases the Hertzian dipole approximation is acceptable. The results are summarized and compared with the "allowed" ranges of variation of v and Δh in Figure 4-34, from which one can see that the Hertzian dipole approximation is consistent with the bouncing-wave model for a reasonably large subset of "allowed" combinations of propagation speed and channel length. Specifically, it can be seen from Figure 4-34 that for $\rho = 0$ the Hertzian dipole approximation is valid for Δh ranging from

about 100 to 550 m and for speeds ranging from about 0.7×10^8 m/s to 3×10^8 m/s, while the "allowed" ranges are from about 100 to 1000 m for Δh and from about 0.3×10^8 m/s to 3×10^8 m/s for v . For $\rho = -0.5$, the Hertzian dipole approximation is valid for the entire "allowed" domain (from about 100 to 500 m for Δh and about from 0.7×10^8 m/s to 3×10^8 m/s for v ; see Figure 4-24b of Section 4.2.7). Note that for $RT = 6 \mu\text{s}$ $\Delta h/v$ (channel traversal time), for which the Hertzian dipole approximation is acceptable, is almost constant and equal to about $1.9 \mu\text{s}$ and $1.7 \mu\text{s}$ for $\rho = 0$ and $\rho = -0.5$, respectively.

Channel length values for which the Hertzian dipole approximation is valid (initial peaks within about 15% of bouncing-wave model predicted peaks) for different values of propagation speed and for $RT = 6 \mu\text{s}$ are given in Table 4-8. Note that the errors for the opposite polarity overshoot were larger, so the Hertzian dipole approximation may be invalid at later times after the initial half cycle, whose duration in our data set varies from 2.8 to $13 \mu\text{s}$ with a GM of $5.6 \mu\text{s}$. Since the errors at later times (during the NBP opposite polarity overshoot) are larger, the waveforms for the various parameters shown in Figure 4-35 (and discussed in Section 4.3.3) may be invalid at those times. Additionally, for some of the electric field waveforms after the initial half cycle and particularly towards the tail of the opposite polarity overshoot the signal-to-noise ratio was poor. This is why, we limited our estimates of charge transfer and energy to the initial $5 \mu\text{s}$ of the process. Note that the peak current, current risetimes, and peak power are generally unaffected by the uncertainties encountered at later times.

We now consider the influence of zero-to-peak risetime, RT . In Section 4.2 it was determined that the CID current risetime is likely to be in the range from about 2 to $8.5 \mu\text{s}$. For $RT = 2 \mu\text{s}$, the Hertzian dipole approximation is not valid for any allowed combination of parameters. For $RT = 3 \mu\text{s}$, the approximation is valid when $v = 2$ to 3×10^8 m/s and $\Delta h = 100$ to

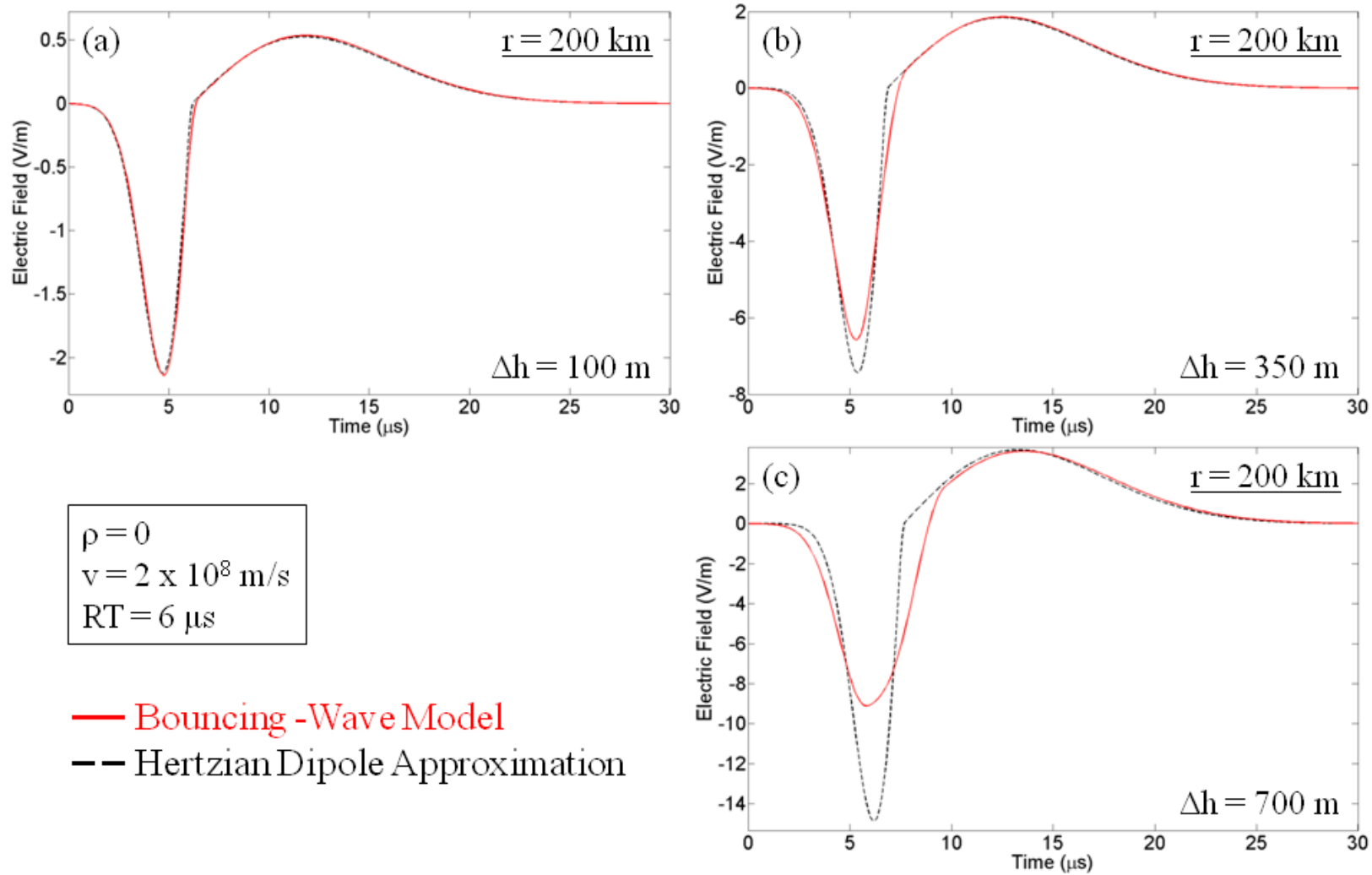


Figure 4-32. Vertical electric fields for the bouncing-wave model (solid line) for $\rho = 0$, $v = 2 \times 10^8$ m/s, $RT = 6 \mu\text{s}$, and channel lengths of (a) 100, (b) 350, and (c) 700 m versus those for the Hertzian dipole approximation (dashed line). The Hertzian dipole approximation is acceptable for channel lengths in the range of 100-350 m, but not for 700 m.

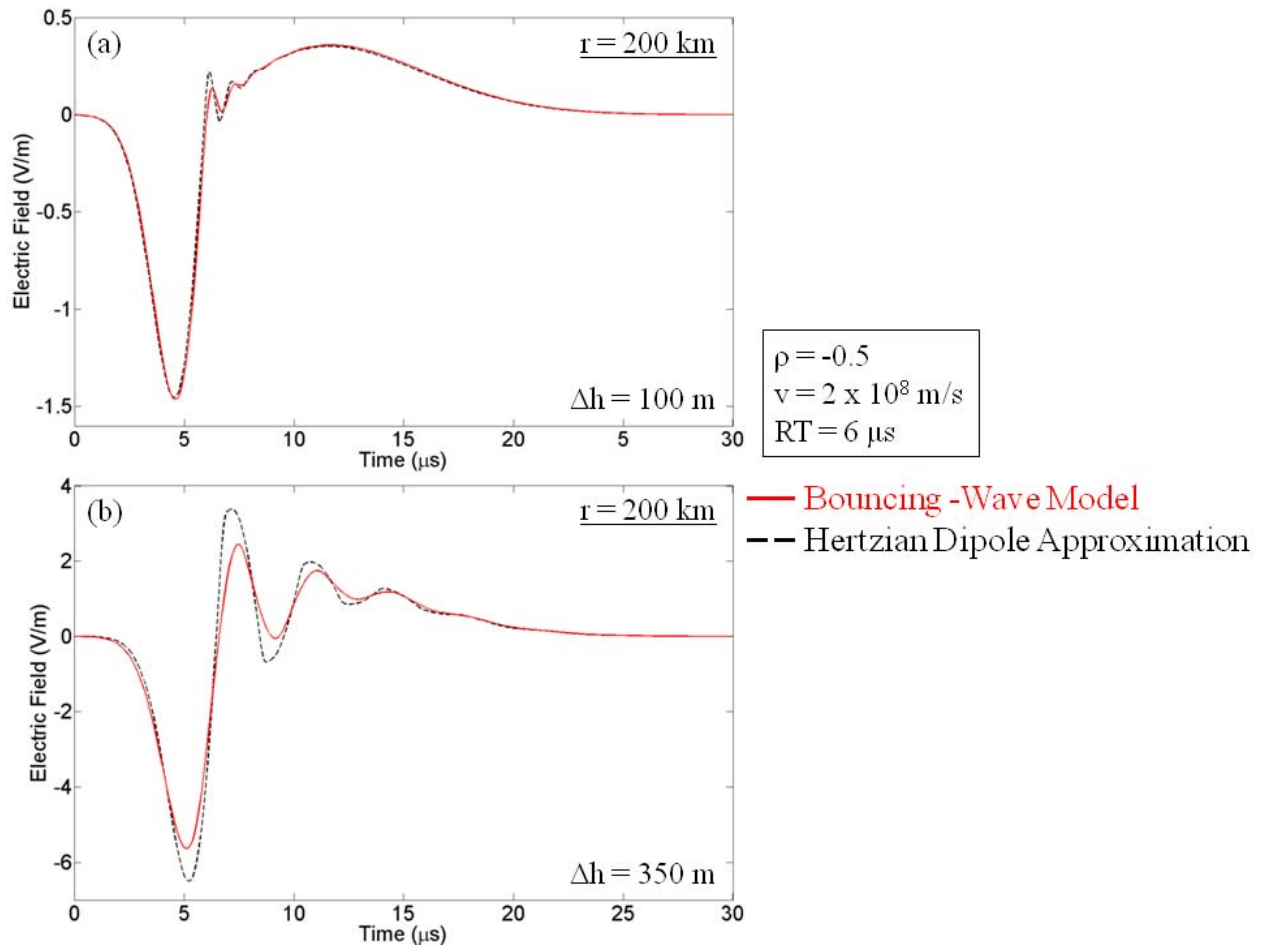


Figure 4-33. Same as Figure 4-32, but for $\rho = -0.5$ and channel lengths of (a) 100 and (b) 350 m, for both of which the Hertzian dipole approximation is acceptable.

200 m (channel traversal time, $\Delta h/v = 0.3$ to $1 \mu\text{s}$) for both $\rho = 0$ and $\rho = -0.5$. For $RT = 8.5 \mu\text{s}$, the approximation is valid for $\Delta h = 100 \text{ m}$ and for $v = 1$ to $3 \times 10^8 \text{ m/s}$ (channel traversal time, $\Delta h/v = 0.3$ to $1 \mu\text{s}$), which cover the entire range of "allowed" values for both $\rho = 0$ and $\rho = -0.5$. Channel length values for which the Hertzian dipole approximation is valid (initial peaks are within about 15% of bouncing-wave model predicted peaks) for different values of propagation speed are given in Table 4-9 for $RT = 3 \mu\text{s}$ and in Table 4-10 for $RT = 8.5 \mu\text{s}$. In summary, the shorter the current risetime, the smaller the Hertzian dipole domain relative to the allowed one, as expected.

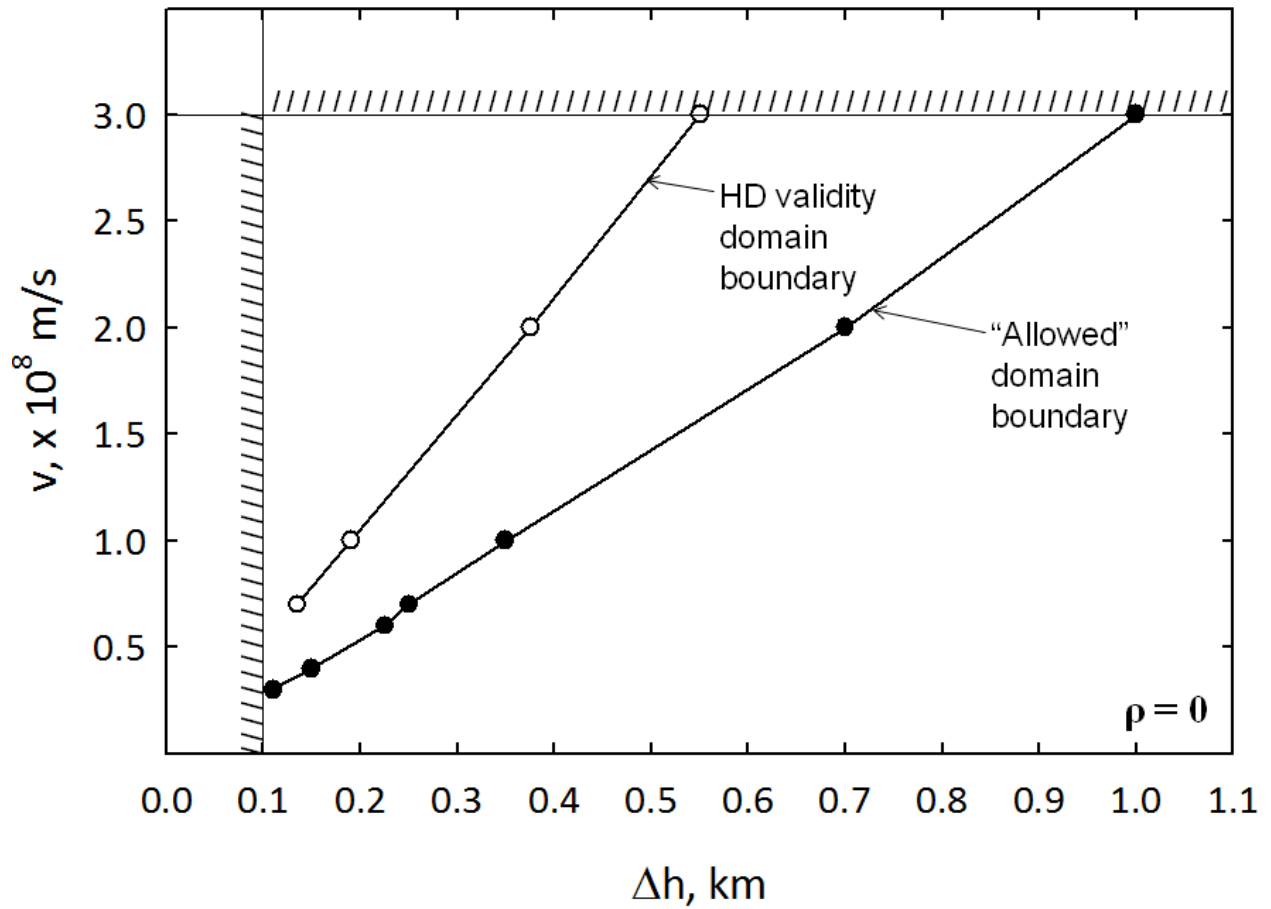


Figure 4-34. Comparison of the Hertzian dipole validity domain (combinations of propagation speed and channel length) with the "allowed" one for $RT = 6 \mu\text{s}$ and $\rho = 0$. See text for details.

Table 4-8. Comparison of electric fields based on the Hertzian dipole approximation and bouncing-wave model for a current risetime of 6 μs for different combinations of reflection coefficients, current wave speeds, and channel lengths. Combinations of speed and channel length in *italics* are considered to be consistent with the Hertzian dipole approximation.

Reflection Coefficients	Current Wave Speed (m/s)	Channel Length (m)	Difference in initial peak (%)	Difference in opposite polarity overshoot (%)	
$\rho = -0.5$	<i>0.7 x 10⁸</i>	<i>100</i>	8.7	58	
		<i>125</i>	15	37	
	<i>1 x 10⁸</i>	<i>100</i>	3.2	48	
		<i>170</i>	13	39	
	<i>2 x 10⁸</i>	<i>100</i>	-0.76	-1.9	
		<i>350</i>	15	39	
	<i>3 x 10⁸</i>	<i>100</i>	-1.3	-1.9	
		<i>500</i>	14	45	
	$\rho = 0$	<i>0.3 x 10⁸</i>	<i>100</i>	51	1.1
			<i>100</i>	7.4	-1.4
<i>0.7 x 10⁸</i>		<i>135</i>	15	-0.77	
		<i>250</i>	61	1.6	
<i>1 x 10⁸</i>		<i>100</i>	2.7	-1.7	
		<i>170</i>	11	-0.7	
<i>190</i>		<i>15</i>	-0.3		
		<i>350</i>	60	1.6	
<i>100</i>		<i>-0.62</i>	-1.9		
		<i>350</i>	13	-1.0	
<i>2 x 10⁸</i>		<i>375</i>	15	-0.9	
		<i>700</i>	63	1.8	
<i>100</i>		<i>-1.3</i>	-1.9		
		<i>500</i>	12	-1.1	
<i>3 x 10⁸</i>		<i>550</i>	15	-0.89	
	<i>1000</i>	60	1.6		

Table 4-9. Comparison of electric fields based on the Hertzian dipole approximation and bouncing wave model for a current risetime of 3 μs for different combinations of reflection coefficients, current wave speeds, and channel lengths. Combinations of speed and channel length in *italics* are considered to be consistent with the Hertzian dipole approximation.

Reflection Coefficients (ρ)	Current Wave Speed (m/s)	Channel Length (m)	Difference in initial peak (%)	Difference in opposite polarity overshoot (%)
$\rho = -0.5$	1.1×10^8	100	19	52
	2×10^8	<i>100</i>	4.4	66
		<i>150</i>	14	56
		175	21	51
	3×10^8	<i>100</i>	0.49	44
		225	14	56
275		21	61	
$\rho = 0$	0.4×10^8	100	127	-0.5
	0.7×10^8	100	42	-1.4
		200	164	1.0
	1×10^8	100	20	-1.7
		250	127	0.60
	2×10^8	<i>100</i>	2.5	-2.4
		<i>175</i>	15	-1.2
<i>100</i>		0.09	-2.4	
		<i>250</i>	15	-0.58

Table 4-10. Comparison of electric fields based on the Hertzian dipole approximation and bouncing wave model for a current risetime of 8.5 μs for different combinations of reflection coefficients, current wave speeds, and channel lengths. Combinations of speed and channel length in *italics* are considered to be consistent with the Hertzian dipole approximation.

Reflection Coefficients (ρ)	Current Wave Speed (m/s)	Channel Length (m)	Difference in initial peak (%)	Difference in opposite polarity overshoot (%)
$\rho = -0.5$	1×10^8	<i>100</i>	0.17	-1.4
	2×10^8	<i>100</i>	-1.4	-1.9
	3×10^8	<i>100</i>	-1.7	-1.9
$\rho = 0$	1×10^8	<i>100</i>	0.07	-1.6
	2×10^8	<i>100</i>	-1.4	-1.9
	3×10^8	<i>100</i>	-1.6	-1.9

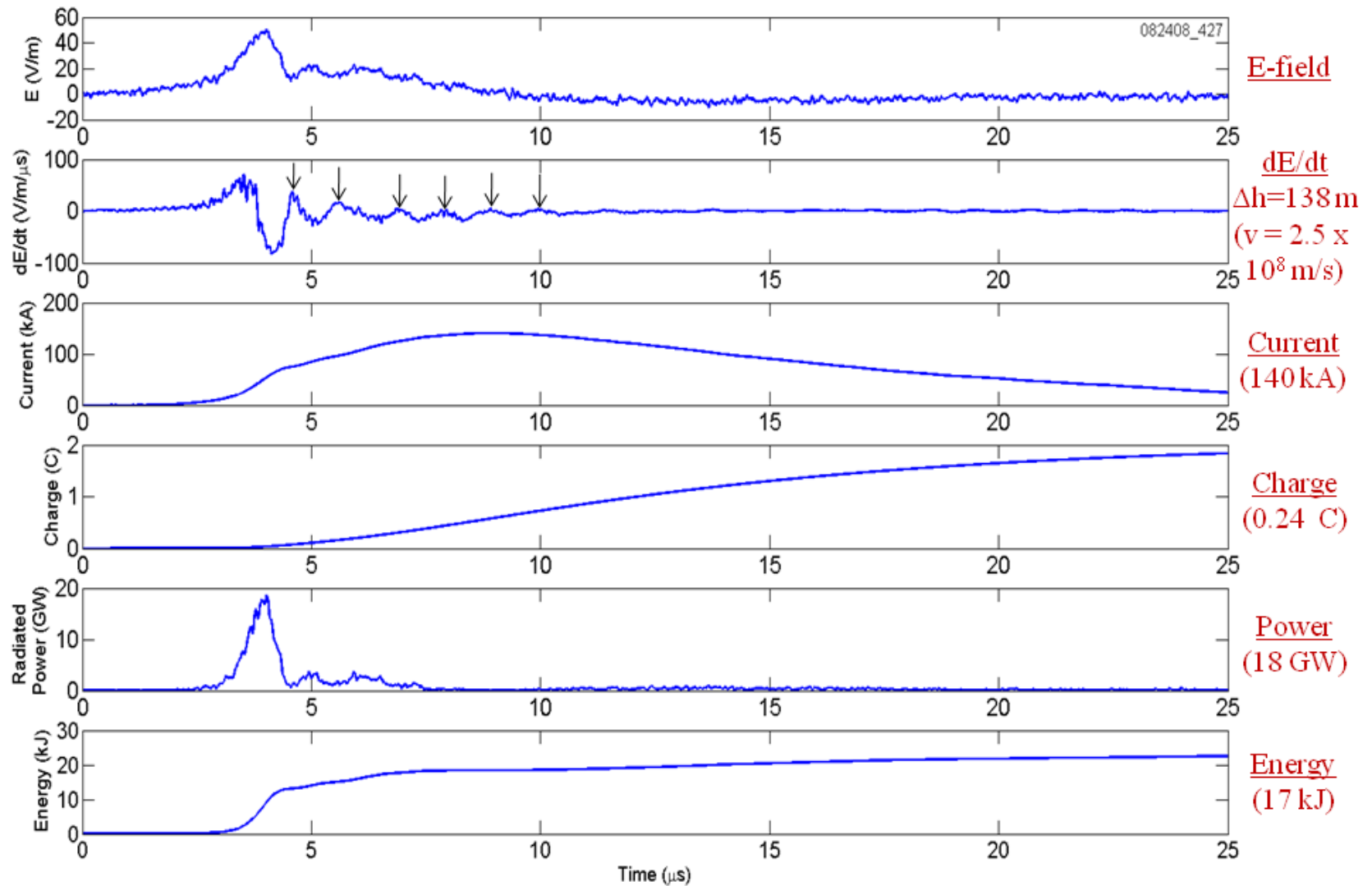


Figure 4-35. (a) Measured electric field, (b) measured electric field derivative, (c) inferred current, (d) inferred charge transferred, (e) inferred radiated power, and, (f) inferred radiated energy, each as a function of time, for a CID that occurred at a horizontal distance of 50 km, at an inferred height of 16 km, and had an inferred channel length of 103 m ($v = 2.5 \times 10^8 \text{ m/s}$).

4.3.3 Electrical Parameters of CIDs

Of the 48 located CIDs studied in Section 4.1, for 9 events, we were able to estimate channel lengths using reflection signatures in their measured dE/dt signatures and assumed speeds within their limiting values of 2×10^8 and 3×10^8 m/s. Speeds lower than 2×10^8 m/s are not considered, since for measured traversal times they would result in unreasonably small radiator lengths. For $v = 2.5 \times 10^8$ m/s (average speed value), the channel lengths for the nine events range from 108 to 142 m. These events occurred at horizontal distances of 30 to 89 km and estimated heights of 8.8 to 19 km, and had electric field peaks normalized to 100 km ranging from 14 to 35 V/m. Figure 4-35 shows the measured electric field and electric field derivative along with the inferred current, charge transferred, and radiated power and energy, each as a function of time, for one such event. Vertical arrows indicate reflection signatures in the dE/dt waveform. The estimated channel length (for $v = 2.5 \times 10^8$ m/s) was 138 m. Table 4-11 summarizes the estimated parameters for all the 9 events. The geometric mean (GM) peak current is 143 kA with a range 87 to 259 kA. The current zero-to-peak risetimes range from 3.0 to 9.5 μ s with a GM of 5.4 μ s. Note that one out of nine values of RT, 9.5 μ s, is larger than the estimated upper limit of 8.5 μ s. The charge transfer for the first 5 μ s ranges from 79 to 496 mC with the GM being 303 mC. The GM peak radiated power and energy radiated for the first 5 μ s are 29 GW (ranging from 12 to 70 GW) and 24 kJ (ranging from 7.5 to 52 kJ), respectively.

We now discuss uncertainties in estimated parameters for the 9 events. For the lower bound on speed (2×10^8 m/s), all radiator lengths (86 to 114 m) are near the assumed lower bound, 100 m (Section 4.2.7), which is expected because reflection signatures should be pronounced only for the shortest channels. For the upper bound on speed (3×10^8 m/s), the channel lengths would increase by a factor of 1.5 to range from 129 to 171 m. Since the inferred peak current and charge transfer are inversely proportional to channel length within the Hertzian

dipole approximation (see Section 4.3.1), these two parameters would decrease by a factor of 1.5. Thus, the uncertainty in our current and charge transfer estimates for the 9 events is $\leq 25\%$ for the assumed $v = 2.5 \times 10^8$ m/s. The current risetimes, peak power, and energy values, on the other hand, are independent of channel length (and hence of assumed speed) and will remain the same as those for 2.5×10^8 m/s. Table 4-12 summarizes the peak current and charge transfer at 5 μ s each scaled to different channel lengths (inferred using measured channel traversal times and different assumed propagation speeds) for the 9 CIDs.

Note that since all Δh values are less than 200 m (even for $v = 3 \times 10^8$ m/s), all nine events can be reasonable approximated by Hertzian dipoles for almost the entire "allowed" range of current zero-to-peak risetimes (about 2 to 8.5 μ s). As a result, the inferred current risetimes (ranging from 3 to 9.5 μ s with the GM being 5.4 μ s) should be close to their true values, confirming our assumed typical zero-to-peak risetime of 6 μ s.

For the remaining 39 events, which did not exhibit reflection signatures, the electrical parameters were estimated for three assumed values of channel length, 170, 350, and 500 m, for which the Hertzian dipole approximation is valid (for $RT = 6 \mu$ s) if the implied propagation speeds are $\geq 10^8$, $\geq 2 \times 10^8$, and 3×10^8 m/s, respectively. CID electrical parameters for $\Delta h = 170$ m, 350 m, and 500 m are compared in Table 4-13. The geometric mean values of peak current for the assumed channel length values of $\Delta h = 170$ m, 350 m, and 500 m were 132, 64, and 45 kA, respectively. The corresponding geometric mean charge transfers at 5 μ s were 293, 142, and 100 mC. Note that for the 39 events the Hertzian dipole validity domain is smaller than the "allowed" domain. As a result, we cannot assign any specific uncertainty to the estimated parameters in this case.

Table 4-11. Parameters of nine located CIDs with channel lengths estimated using reflections in dE/dt waveforms and assumed propagation speed of 2.5×10^8 m/s.

Event ID	Distance (km)	Radiator Height (km)	Electric Field at 100 km (V/m)	Radiator Length (m)	Peak Current (kA)	Zero-to-Peak Current Risetime (μ s)	10-90% Current Risetime (μ s)	Charge Transfer at 5 μ s (mC)	Peak Power (GW)	Energy at 5 μ s (kJ)
082408_427	19	15	14	138	140	7.9	3.9	243	18	17
083008_09	89	19	35	108	197	3.8	1.5	496	70	52
083008_31	52	16	28	138	259	5.9	3.4	441	28	39
083008_45	50	16	30	128	142	3.4	1.5	412	50	40
083008_52	50	17	30	139	148	3.0	1.4	493	59	50
091008_138	33	16	14	134	118	9.5	4.9	79	12	9.1
091008_140	36	13	22	142	104	4.7	1.6	272	28	23
091008_161	30	10	21	123	157	6.9	3.6	412	36	25
091008_176	43	8.8	16	113	87	7.0	3.9	230	12	7.5
AM	45	14	24	129	150	5.8	2.9	342	35	29
GM	41	14	22	129	143	5.4	2.6	303	29	24
Min	19	8.8	14	108	87	3.0	1.4	79	12	7.5
Max	89	19	35	142	259	9.5	4.9	496	70	52

Table 4-12. Peak current and charge transfer at 5 μ s scaled to different channel lengths that were inferred for 9 CIDs using reflections in measured dE/dt waveforms and assumed propagation speeds.

v, m/s	Δh , m				Peak current, kA				Charge Transfer at 5 μ s, mC			
	AM	GM	Min	Max	AM	GM	Min	Max	AM	GM	Min	Max
2 x 10 ⁸ (lower bound)	103	103	86	114	188	179	108	324	427	379	98	621
3 x 10 ⁸ (upper bound)	155	154	129	171	125	119	72	216	285	253	65	414
2.5 x 10 ⁸ (average)	129	129	108	142	150	143	87	259	342	303	79	496

Table 4-13. Peak current and charge transfer at 5 μ s scaled to different channel lengths for 39 CIDs.

Δh , m	v (allowed) m/s	Peak current, kA				Charge Transfer at 5 μ s, mC			
		AM	GM	Min	Max	AM	GM	Min	Max
170	$\geq 10^8$	142	132	68	328	327	293	45	706
350	$\geq 2 \times 10^8$	69	64	33	160	159	142	22	343
500	3×10^8	48	45	23	112	111	100	15	240

Figures 4-36 to 4-41 show histograms for the peak current, zero-to-peak current risetime, 10-to-90% current risetime, charge transfer at 5 μ s, peak radiated power, and energy at 5 μ s, respectively, for all 48 events, including 9 events with channel lengths estimated from reflection signatures (for an assumed propagation speed of 2.5 x 10⁸ m/s) and 39 events with an assumed channel length of 350 m (implied v $\geq 2 \times 10^8$ m/s). The minimum, maximum, arithmetic, and geometric mean values for each parameter are given for the 9 and 39 events individually and for all 48 events combined. As noted earlier, current risetimes, peak radiated power and radiated energy are independent of channel length, while peak current and charge transfer can be scaled to other channel lengths, provided that they are consistent with the Hertzian dipole approximation.

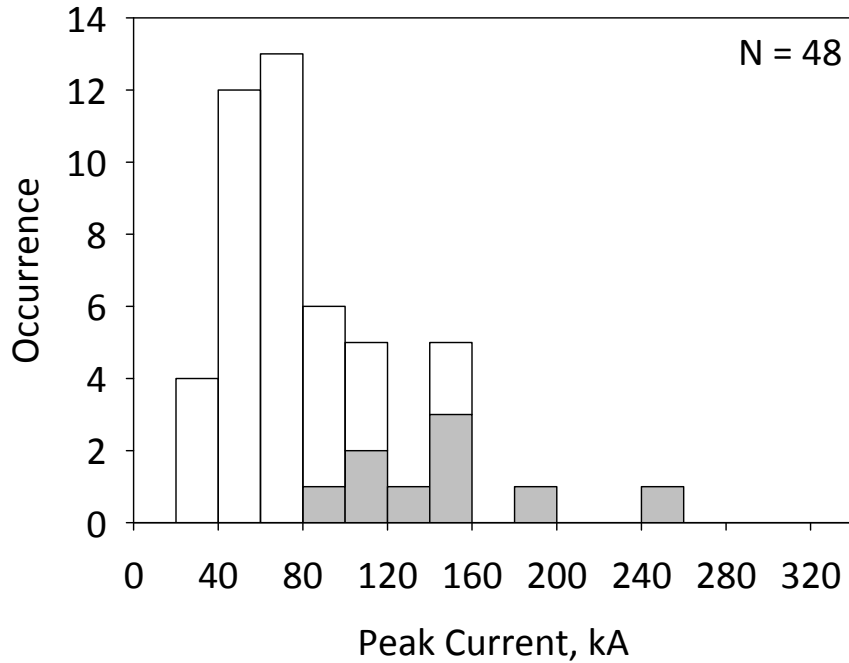
For the 39 CIDs, the geometric mean values of current zero-to-peak risetime and 10-to-90% current risetime are 4.9 and 2.5 μ s, respectively. The geometric mean peak radiated power,

and energy radiated for the first 5 μs are 28 GW and 32 kJ, respectively. For all 48 events, GM values of peak current, zero-to-peak current risetime, 10-to-90% current risetime, and charge transfer for the first 5 μs are 74 kA, 5.0 μs , 2.5 μs , and 164 mC, respectively. The corresponding geometric mean peak radiated power, and energy radiated for the first 5 μs are 29 GW and 31 kJ. Note that in the distributions of peak current and charge transfer at 5 μs (Figures 4-36 and 4-39, respectively) the 9 CIDs with reflection signatures constitute the tail of the histogram, which is related to their shorter inferred channel lengths. Overall, the CID current parameters are comparable to their counterparts for first return strokes in cloud-to-ground lightning, while their peak radiated electromagnetic power appears to be considerably higher.

4.3.4 Upper Bound on Electric Field Prior to CID

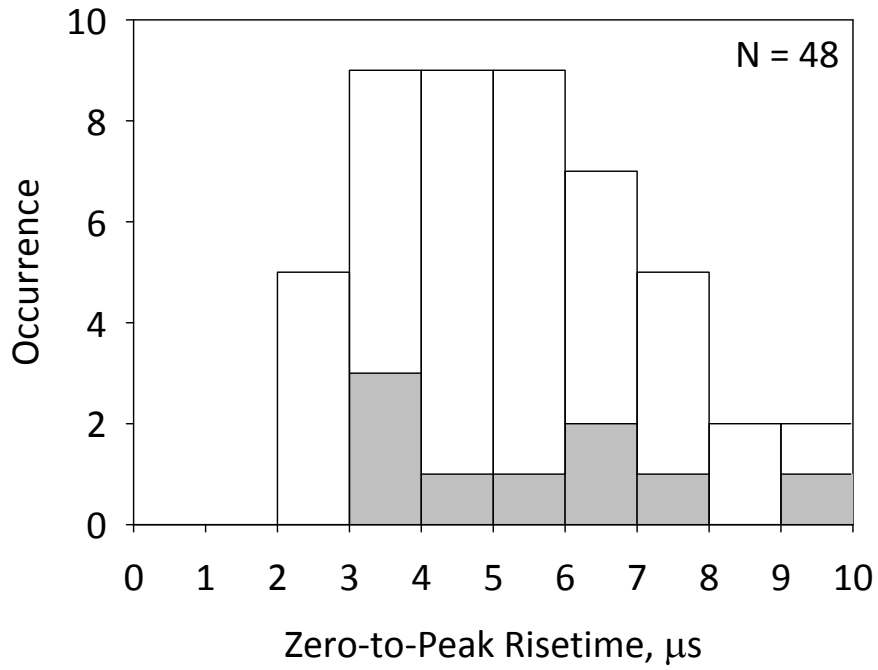
In this Section, we will consider the CID as a discharge between two spherical charge regions. Such simplified configuration is similar to that employed by *Cooray* [1997] for studying regular cloud discharges. For a CID current pulse with a peak current of 50 kA, total duration of 30 μs , and zero-to-peak risetime of 6 μs [see Section 4.2.3] the total CID charge transfer (which is the time integral of current), Q , is 0.44 C. Let us consider two spherical volumes, one containing +0.44 C of charge and the other -0.44 C of charge, each with a uniform volume charge density, ρ_v , of 20 nC/m³ (absolute value) [e.g., *Rakov and Uman*, 2003; Section 3.2.5].

Then, from $Q = \frac{4}{3}\pi b^3 \rho_v$, the radius, b , of each sphere is 174 m. Let us assume that the vertical distance between the surfaces of these spherical volumes is 100 m (assumed to be approximately equal to the shortest CID channel length), as shown in Figure 4-42a, and that the medium outside the charged spheres contains zero net charge. Presence of ground and other charges in the cloud is neglected. The 100-m assumption allows us to obtain the upper bound on electric field (all



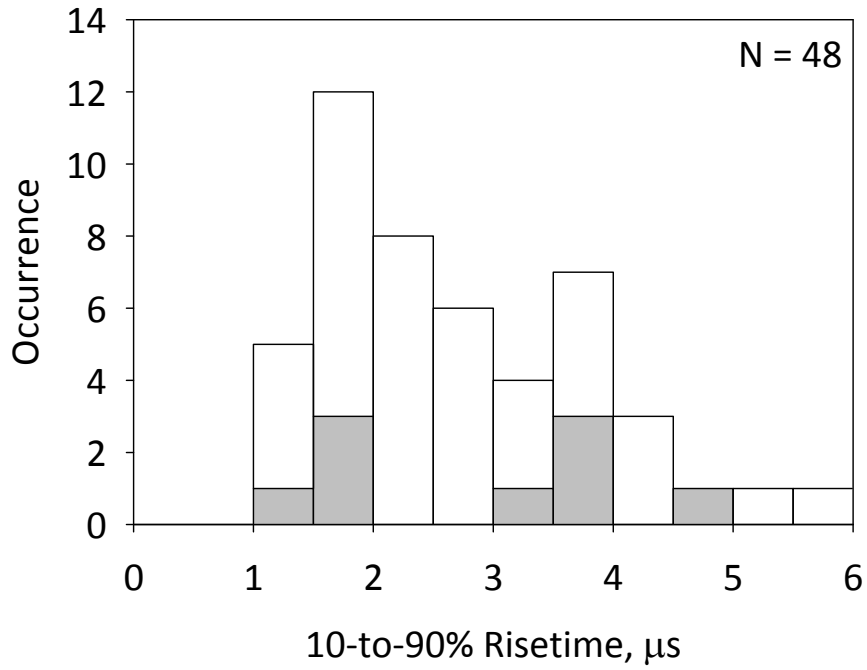
	CIDs with reflection signatures	CIDs without reflection signatures	All CIDs
AM, kA	150	69	84
GM, kA	143	64	74
Min, kA	87	33	33
Max, kA	259	160	259
N	9	39	48

Figure 4-36. Histogram of peak currents for 48 CIDs. For 9 events with reflection signatures, channel lengths were inferred using channel traversal times measured in dE/dt waveforms and assumed propagation speed of 2.5×10^8 m/s. For the other 39 events an assumed channel length of 350 m (implied $v \geq 2 \times 10^8$ m/s) was used. Statistics given are the arithmetic mean (AM), geometric mean (GM), minimum value (min), and maximum value (max) for the 9 and 39 events individually and for all data combined.



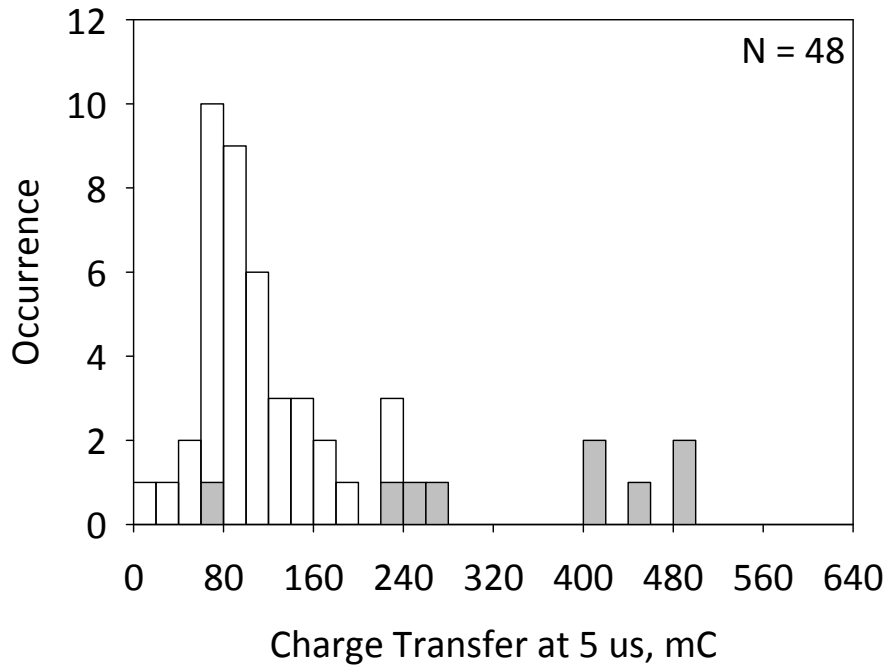
	CIDs with reflection signatures	CIDs without reflection signatures	All CIDs
AM, μs	5.8	5.2	5.3
GM, μs	5.4	4.9	5.0
Min, μs	3.0	2.3	2.3
Max, μs	9.5	9.5	9.5
N	9	39	48

Figure 4-37. Histogram of zero-to-peak current risetimes for 48 CIDs. See also caption of Figure 4-36.



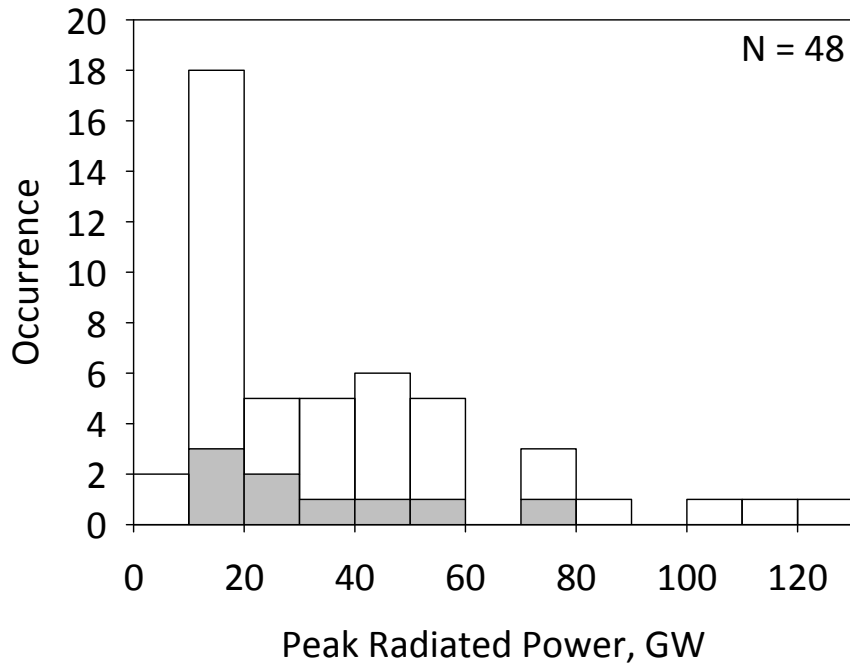
	CIDs with reflection signatures	CIDs without reflection signatures	All CIDs
AM, μs	2.9	2.7	2.7
GM, μs	2.6	2.5	2.5
Min, μs	1.4	1.1	1.1
Max, μs	4.9	5.7	5.7
N	9	39	48

Figure 4-38. Histogram of 10-to-90% current risetimes for 48 CIDs. See also caption of Figure 4-36.



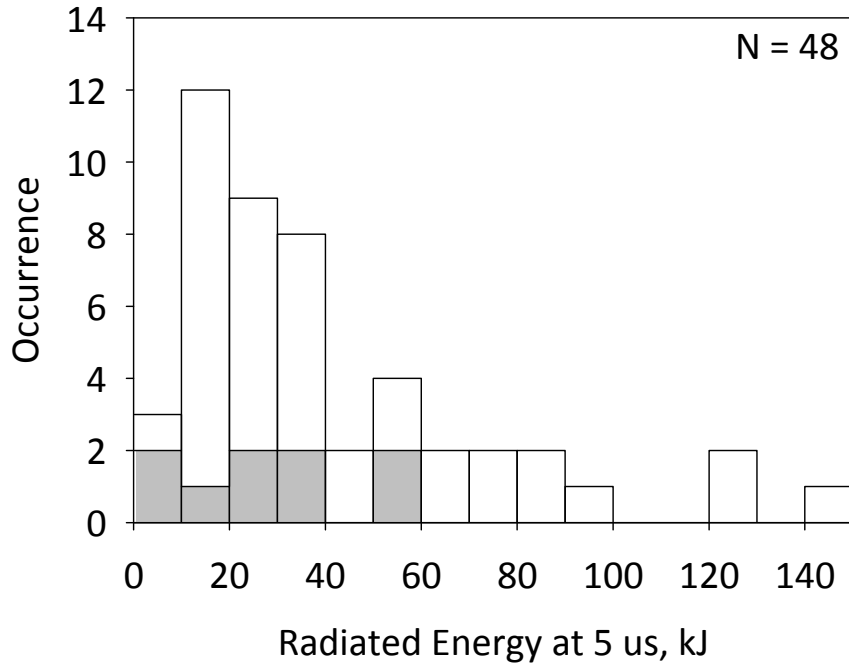
	CIDs with reflection signatures	CIDs without reflection signatures	All CIDs
AM, mC	342	159	193
GM, mC	303	142	164
Min, mC	79	22	22
Max, mC	496	343	496
N	9	39	48

Figure 4-39. Histogram of charge transferred at 5 μ s for 48 CIDs. See also caption of Figure 4-36.



	CIDs with reflection signatures	CIDs without reflection signatures	All CIDs
AM, GW	35	38	37
GM, GW	29	28	29
Min, GW	12	9.6	9.6
Max, GW	70	124	124
N	9	39	48

Figure 4-40. Histogram of peak radiated power for 48 CIDs. See also caption of Figure 4-36.



	CIDs with reflection signatures	CIDs without reflection signatures	All CIDs
AM, kJ	29	43	40
GM, kJ	24	32	31
Min, kJ	7.5	4.0	4.0
Max, kJ	52	146	146
N	9	39	48

Figure 4-41. Histogram of radiated energy at 5 μs for 48 CIDs. See also caption of Figure 4-36.

other conditions being the same, larger separations between the spheres will result in lower electric fields).

For each sphere, the electric field intensity at any point at a distance r from the center of the sphere can be obtained using Gauss's law as

$$E = \begin{cases} \frac{r\rho_v}{3\epsilon_0} & r \leq b \\ \frac{b^3\rho_v}{3\epsilon_0r^2} & r \geq b \end{cases} \quad (4-20)$$

For the positively charged sphere ρ_v is positive and the electric field is directed radially outward, while for the negatively charged one it is negative and directed radially inward. For the configuration shown in Figure 4-42a, the total electric field at any point along the line joining the centers of the two spheres is given by superposition of the field contributions (both directed upward) from the two spheres. The total electric field intensity profile (solid line) and contributions from the individual spheres (broken line) are shown in Figure 4-42b. Inside each of the charged spheres, the electric field intensity increases almost linearly with distance from 2×10^4 V/m at the center to a maximum of 1.8×10^5 V/m at the surface. Outside the charged spheres, the electric field intensity is minimum (1.6×10^5 V/m) at a point equidistant from the two spheres. A CID channel is likely to be formed primarily between the two spherical volumes of charge, where the net electric charge is assumed to be zero and the electric field intensity is near its highest values.

We will now examine dependence of electric field profile on charge transfer and volume charge density by using the peak currents for the nine events summarized in Table 4-11, but keeping the same current waveshape (risetime of 6 μ s and total duration of 30 μ s). In Section 4.3.3, we estimated the channel lengths for the nine located CIDs using channel traversal times measured in dE/dt waveforms and assumed propagation speed of 2.5×10^8 m/s to range from 108 to 142 m. The inferred peak currents ranged from 87 kA to 259 kA, with the geometric mean being 143 kA. The total charge transferred (over 30- μ s current duration) for peak currents of 87, 143, and 259 kA are 0.77 C, 1.3 C, and 2.3 C, respectively. For a total charge transfer of 1.3 C and assumed volume charge densities of 2 nC/m³, 20 nC/m³, and 200 nC/m³, the radii of the spherical charge regions are 533 m, 247 m, and 115 m, respectively. The maximum electric field intensities (occurring between the spheres, on their surfaces) are 6.9×10^4 , 2.8×10^5 , and $1.1 \times$

10^6 V/m, respectively. The maximum electric field values for different combinations of charge transfer and assumed charge density are summarized in Table 4-14. Additionally given are minimum and average electric fields between the spherical charge regions and estimated electric potential difference between them. Except for the probably unrealistically high $\rho_v = 200$ nC/m³ cases (for which maximum fields range from 7.3×10^5 V/m to 1.4×10^6 V/m), the maximum electric field for all combinations of Q and ρ_v considered does not exceed 3.5×10^5 V/m, which is less than the conventional breakdown electric field in the cloud (of the order 10^6 V/m) and is generally of the order of 10^4 to 10^5 V/m. These maximum electric field estimates are for $\Delta h = 100$ m. All other conditions being the same, the maximum electric field will decrease with increasing Δh .

If the two spherical charge regions were in direct contact ($\Delta h = 0$) the total electric field profile would have maximum at the point of contact that is given by

$$E_{\max} = \frac{2b\rho_v}{3\varepsilon_0} = \frac{2Q}{4\pi\varepsilon_0 b^2} = \frac{\Delta p}{4\pi\varepsilon_0 b^3} \quad (4-21)$$

where $\Delta p = 2Qb$ is the dipole moment change for charge transfer Q over a distance of $2b$. *Smith et al.* [1999] used such a configuration to impose a lower bound on CID channel length, which they assumed to extend between the centers of the charged spheres. In doing so, they computed E_{\max} for their average measured dipole moment change, $\Delta p = 0.38$ C km, and different b and compared those field values with electric fields measured in thunderclouds. For $b = 50$ m (corresponds to their channel length of 100 m), they found $E_{\max} = 2.7 \times 10^7$ V/m, which is about an order of magnitude greater than the conventional breakdown electric field in the cloud, and concluded that such a short channel was physically unrealistic. Our estimated CID channel lengths of the order of 100 m suggest that *Smith et al.'s* configuration, in which two oppositely charged regions are in direct contact, is inconsistent with at least some experimental data. In

order to explain such short channel lengths, the charged regions should be separated by a region of essentially zero net charge (which can be created due to mixing) or by a region of very low charge density compared to the charged regions.

4.3.5 Total Energy Dissipated by CIDs

In this Section, we estimate the total energy dissipated by a CID with reference to the charge configuration shown in Figure 4-42a. If we assume that a CID neutralizes all the charge in each of the two spherical regions, the total energy dissipated will be equal to the total electrostatic energy stored in this charge configuration. One can find the total electrostatic energy as the sum of the electrostatic energies required to individually assemble the two uniformly charged spheres (self electrostatic energy [*Cooray*, 1997]) and the electrostatic energy due the two spherical charge regions being placed in relatively close proximity to each other (mutual electrostatic energy).

The self electrostatic energy, W_1 , of a uniformly charged sphere of radius b containing charge Q can be readily found as [*Cheng*, 1993]:

$$W_1 = \frac{3Q^2}{20\pi\epsilon_0 b} \quad (4-22)$$

This equation can be obtained by integrating the electrostatic energy density, $W_e = \frac{\epsilon_0 E^2}{2}$, where E is given by Equation 4-20 for $r \leq b$, over the spherical volume. Estimation of the mutual electrostatic energy, W_2 , is more complicated and requires additional simplifying assumptions. We will replace the two spherical charge regions with their equivalent point charges of magnitude $+Q$ and $-Q$ located at corresponding sphere centers, so that they are separated by distance $(2b + \Delta h)$. This approximation is similar to that employed by *Cooray* [1997] for

Table 4-14. The maximum electric field at the surface of each of the two oppositely charged spheres separated by a zero net charge region (see Figure 4-42a) for different combinations of charge transfer and assumed volume charge density. The distance Δh between the surfaces of charged spheres is assumed to be 100 m. Also given are the minimum and average electric fields, potential difference between the spheres, the total electrostatic energy and its components. See text for details.

Peak Current, kA	Total Charge Transfer (Q), C	Volume Charge Density (ρ_v), nC/m ³	Radius of Spherical Charge Regions (b), m	Maximum Electric Field Between Spheres (E_{max}), V/m	Minimum Electric Field Between Spheres (E_{min}), V/m	Average Electric Field, $E_{av} = (E_{max} + E_{min})/2$, V/m	Potential Difference Between Spheres, $\Delta V \approx E_{av}\Delta h$, (V)	External Energy, (Q ΔV), J	Self (\approx Internal) Electrostatic Energy (W_1), J	Mutual Electrostatic Energy (W_2), J	Total Energy (W = 2W ₁ + W ₂), J	Total Energy (W = 2W ₁ + Q ΔV), J
50	0.44	2	375	4.6×10^4	4.4×10^4	4.5×10^4	4.5×10^6	2.0×10^6	2.8×10^6	2.1×10^6	7.7×10^6	7.6×10^6
		20	174	1.8×10^5	1.6×10^5	1.7×10^5	1.7×10^7	0.7×10^7	6.1×10^6	3.9×10^6	1.6×10^7	1.9×10^7
		200	81	7.3×10^5	4.7×10^5	6.0×10^5	6.0×10^7	2.6×10^7	1.3×10^7	6.7×10^6	3.3×10^7	5.2×10^7
87 (Min)	0.77	2	451	5.7×10^4	5.5×10^4	5.6×10^4	5.6×10^6	4.3×10^6	7.1×10^6	5.3×10^6	2.0×10^7	1.9×10^7
		20	210	2.3×10^5	2.1×10^5	2.2×10^5	2.2×10^7	1.7×10^7	1.5×10^7	1.0×10^7	4.1×10^7	4.7×10^7
		200	97	9.1×10^5	6.4×10^5	7.8×10^5	7.8×10^7	6.0×10^7	3.3×10^7	1.8×10^7	8.4×10^7	1.3×10^8
143 (GM)	1.3	2	533	6.9×10^4	6.7×10^4	6.8×10^4	6.8×10^6	8.8×10^6	1.6×10^7	1.2×10^7	4.5×10^7	4.1×10^7
		20	247	2.8×10^5	2.6×10^5	2.7×10^5	2.7×10^7	3.5×10^7	3.5×10^7	2.4×10^7	9.4×10^7	1.1×10^8
		200	115	1.1×10^6	8.4×10^5	1.0×10^6	1.0×10^8	1.3×10^8	7.5×10^7	4.4×10^7	1.9×10^8	2.8×10^8
259 (Max)	2.3	2	649	8.6×10^4	8.4×10^4	8.5×10^4	8.5×10^6	2.0×10^7	4.4×10^7	3.4×10^7	1.2×10^8	1.1×10^8
		20	301	3.5×10^5	3.3×10^5	3.4×10^5	3.4×10^7	7.8×10^7	9.4×10^7	6.7×10^7	2.6×10^8	2.7×10^8
		200	140	1.4×10^6	1.1×10^6	1.3×10^6	1.3×10^8	3.0×10^8	2.0×10^8	1.2×10^8	5.3×10^8	7.0×10^8

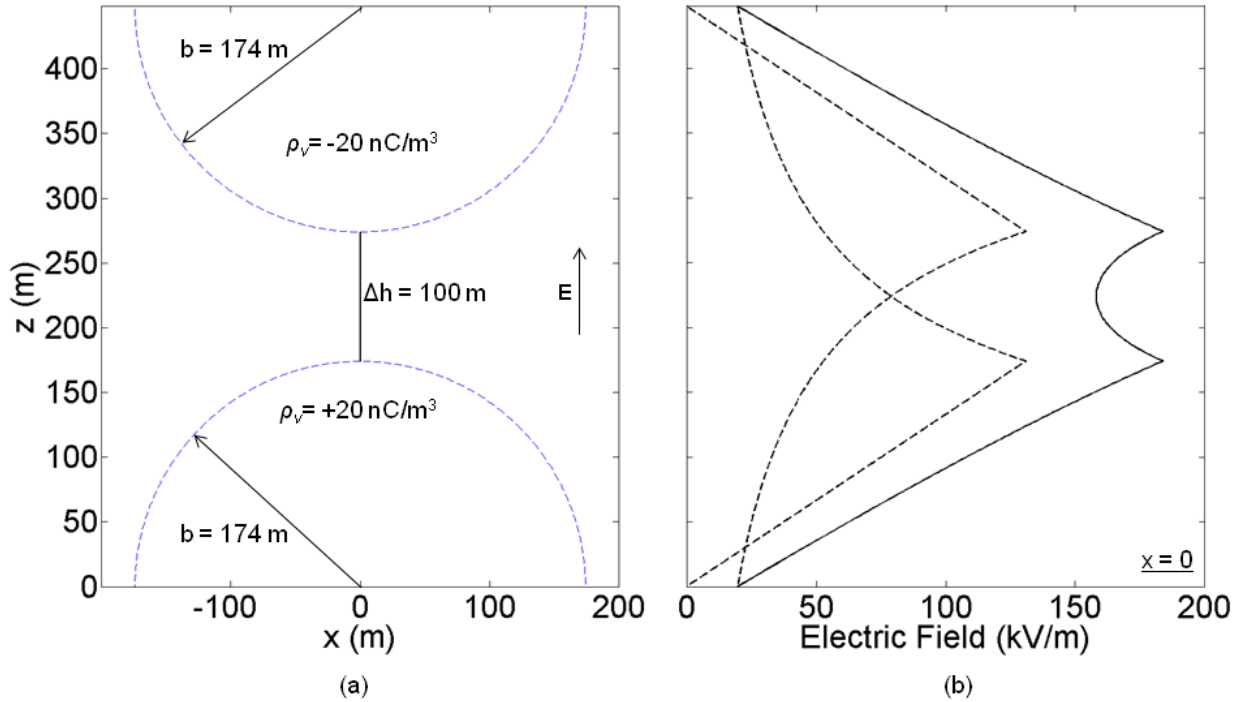


Figure 4-42. (a) Simplified charge configuration giving rise to a CID. The CID channel length, $\Delta h = 100$ m, is assumed to be approximately equal to the distance between the two charged regions. The electric field vector points upward and is assumed to be positive. (b) The electric field intensity as a function of z for $x = 0$ that is produced by each of the two charged regions (broken line) shown in (a) and the total electric field profile (solid line). Field and electrostatic energy values for this and other configurations are given in Table 4-14.

studying the energy dissipated by regular cloud discharges. The mutual electrostatic energy W_2 of these two point charges is given by [Cheng, 1993]:

$$W_2 = \frac{Q^2}{4\pi\epsilon_0(2b + \Delta h)} \quad (4-23)$$

Thus, the total electrostatic energy W of the overall charge configuration, and hence the energy dissipated by a resultant CID can be found as

$$W = 2W_1 + W_2 \quad (4-24)$$

Estimates of energy dissipated by a CID having a 100 m long channel for different values of total charge transfer Q (estimated for a fixed current waveshape and different peak currents)

and volume charge density ρ_v are given in Table 4-14. The assumed volume charge density ρ_v is used to compute b in Equation 4-22 for a given Q . For a charge transfer of 0.44 C (peak current of 50 kA), the total dissipated energy values are 7.7×10^6 , 1.6×10^7 , and 3.3×10^7 J for charge densities of 2, 20, and 200 nC/m³, respectively. For a charge density of 20 nC/m³ and charge transfers ranging from 0.44 C to 2.3 C the energy values range from 1.6×10^7 to 2.6×10^8 J. The corresponding energy per unit length ranges from 1.6×10^5 to 2.6×10^6 J/m.

It follows from Equations 4-22 to 4-24 that, all other conditions remaining the same, the mutual electrostatic energy W_2 due to the two equivalent point charges and hence the total electrostatic energy of the charge configuration shown in Figure 4-42a decreases with increasing the CID channel length. Thus, the values of total CID energy given above for the lower bound on channel length of 100 m should be viewed as the upper bound. For a CID current pulse with a peak of 50 kA described in Section 4.2.3, assumed $\rho_v = 20$ nC/m³, and channel lengths of 350, 500, and 1000 m, the total electrostatic energy values will be 1.47×10^7 , 1.42×10^7 , and 1.35×10^7 J, respectively, versus 1.6×10^7 J for $\Delta h = 100$ m.

In our calculations of electrostatic energy, we have neglected the effect of ground. This simplifying assumption should not introduce a significant error because (1) CIDs occur at relatively large altitudes, typically greater than 10 km [Smith *et al.*, 2004; Section 4.1] and (2) W_2 is inversely proportional to the distance between equivalent point charges. Indeed, the mutual electrostatic energy between a charge and its image separated by more than 20 km is at least an order of magnitude smaller than that between the two actual charges separated by less than 1.4 km (the limiting case in Table 4-14; $\Delta h = 100$ m). This is true even for CID channel lengths of 1000 m in which case the two equivalent point charges representing the actual charges are separated by less than 2.3 km.

The total electrostatic energy of the charge configuration shown in Figure 4-42a can be alternatively estimated as the sum of energies stored inside the two spheres and energy stored between them. The internal energy can be computed as the volume integral of energy density, $\frac{\epsilon_0 E^2}{2}$, which is different from the self energy W_I in that E within each sphere should additionally include the contribution from the other sphere. As a zero approximation, we neglect this difference and assume that the internal energy is not much different from self energy W_I (the larger the separation between the spheres the smaller the difference). We will roughly estimate the external energy as the product of charge transfer Q and potential difference ΔV between the surfaces of the two spheres, with ΔV being found as the average electric field intensity E_{av} between the spheres times the distance Δh between their surfaces. Values of E_{av} , ΔV , and the total energy, $W = 2W_I + Q\Delta V$, are given in Table 4-14.

The total electrostatic energy values estimated using the two different approaches are fairly similar, particularly for lower (2 and 20 nC/m³) values of ρ_v . As expected, the GM electromagnetic energy of 31 kJ radiated during the first 5 μ s (see Figure 4-41) is much lower than the total CID energy estimates based on electrostatic considerations (see Table 4-14).

4.3.6 Discussion

Smith et al. [1999], using distant (essentially radiation) electric field signatures of 15 CIDs from thunderstorms in New Mexico and west Texas, estimated the mean CID dipole moment change to be 0.38 C km. The minimum and maximum values were 0.26 and 0.80 C km. The mean dipole moment change duration (10-90%) for the 15 CIDs was 13.7 μ s. They also inferred that CID channel lengths should be in the range of 300 to 1000 m. Using the mean dipole moment change (0.38 C km) and the limiting channel lengths we estimate the range of charge transfers for their CIDs to be 0.38 C to 1.27 C. Our estimated charge transfers for the first 5 μ s

are of the order of tens to hundreds of millicoulombs (see Tables 4-11, 4-12 and 4-13, and Figure 10) and are apparently consistent with *Smith et al.*'s values which correspond to the mean charge transfer time of 13.7 μ s.

Eack [2004], using simultaneous measurements of electric fields at near and far distances for seven CIDs, estimated that, on average, a CID transferred 0.3 C over a distance of 3.2 km. These results are based on a value of speed derived from the misinterpreted dipole approximation equation (see Section 4.2.9) and, therefore, are invalid. For one event produced by a New Mexico thunderstorm, *Eack* also estimated the peak current of 29 kA from the measured predominantly induction electric field peak (assuming a uniform current over the entire channel length). For the same event, *Watson and Marshall* [2007], using the transmission line model, inferred a considerably larger peak current of 74 kA, which is about the same as our estimates based on both the bouncing-wave model and Hertzian dipole approximation (see Section 4.2.8).

For downward negative lightning, *Berger et al.* [1975] reported a median total charge transfers of 5.2 C and 1.4 C for first strokes and subsequent strokes, respectively. *Schoene et al.* [2009] reported the geometric mean charge transfer within 1 ms after the beginning of the return stroke for 151 negative rocket-triggered lightning strokes (which are similar to subsequent strokes in natural lightning) to be 1.0 C. Using in-situ measured electric field profiles, *Maggio et al.* [2009] estimated the average (probably arithmetic mean) charge transferred by 29 IC flashes to be 17.6 C. Thus, charges transferred by individual CG strokes and by regular ICs are considerably larger than those transferred within the first 5 μ s by CIDs.

Rakov et al. [1998], from two-station measurements of electric and magnetic fields of a dart-stepped leader in triggered-lightning, estimated that the formation of each leader step is associated with a charge of a few millicoulombs and a current of a few kiloamperes. From

measurements of electric field pulses radiated by leader steps of first strokes in natural lightning, *Krider et al.* [1997] inferred that the minimum charge involved in the formation of a step is 1-4 mC and the peak step current is at least 2-8 kA. The charge transfers for cloud-to-ground lightning leader steps are one to two orders of magnitude smaller than those transferred during the first 5 μ s by CIDs. Our estimated CID peak currents of tens to hundreds of kiloamperes are at least an order of magnitude greater than those expected for leader steps. Note that the step-formation process is thought to occur on a time scale of the order of 1 μ s, and typical step lengths are 10 and 50 m for dart-stepped and stepped negative leaders, respectively [*Rakov and Uman*, 2003].

Krider et al. [1968] estimated the peak input power per unit channel length for a natural lightning first stroke to be 7.8×10^8 W/m. *Jayakumar et al.* [2006] estimated the mean value of peak input power per unit length for triggered-lightning strokes to be 9.6×10^8 W/m. *Krider and Guo* [1983] and *Krider* [1992] estimated the wideband radio-frequency electromagnetic power radiated by a subsequent return stroke at the time of the electric field peak to be 3 to 5 GW. The average zero-to-peak risetime of the subsequent-stroke field waveforms was 2.8 μ s, so that the radiating channel length at the time of field peak was probably some hundreds of meters, which is comparable to the channel length for CIDs. Our arithmetic mean peak radiated power (wideband) of 37 GW found for 48 CIDs is about an order of magnitude higher than the above estimates for subsequent return strokes. For first strokes, *Krider and Guo* [1983] estimated an arithmetic mean peak electromagnetic power of 20 GW, which is still lower than our estimate for CIDs.

Rison et al. [1999] and *Thomas et al.* [2001] each reported the peak radiated power in the narrowband VHF (60-66 MHz) frequency range of the Lightning Mapping Array (LMA) for one

New Mexico CID to be greater than 100 kW and greater than 300 kW, respectively. Source peak powers radiated at 60-66 MHz by "normal" lightning processes ranged from 1 W (minimum locatable value) up to 10-30 kW [Thomas et al. 2001]. Rison et al. [1999] stated that the peak VHF radiation from CIDs was typically 30 dB (a factor of 1000) stronger than that from other lightning processes.

Assuming a potential difference of 10^8 - 10^9 V between the earth and a cloud charge source, Uman [1987] estimated from electrostatic considerations the input energy for lightning leader-return stroke sequences lowering 5 C of charge from a height of 5 km to ground to range from 1 to 10×10^5 J/m. Hence the total energy for a 5 km long channel would be in the range of 5 to 50×10^8 J. For the same assumed channel length and charge transfer and using the concepts of self and mutual electrostatic energy, Cooray [1997] estimated that the energy dissipated by a typical first leader-return stroke sequence is 5.5×10^8 J. For cloud discharges occurring between two vertically separated spherical charge regions and neutralizing charges ranging from 1 to 8 C, Cooray [1997] found the dissipated energy to range from about 2.5×10^8 to 18×10^8 J. We estimated the energy dissipated by CIDs having a channel length of 100 m and neutralizing total charges in the range of 0.44 to 2.3 C, to be in the range of 7.7×10^6 to 5.3×10^8 J. For a 1-C charge transfer, the CID energy is 5.3×10^7 J, which is about a factor of 5 smaller than 2.5×10^8 J estimated by Cooray for regular cloud discharges. As stated in Section 4.3.5, all other conditions remaining the same, for channel lengths greater than 100 m the total electrostatic energy of the configuration shown in Figure 4-42a and hence the energy dissipated by CIDs will be lower.

Our estimates of CID energy per unit channel length (based on values in the next to last column of Table 4-14 and $\Delta h = 100$ m) range from 7.7×10^4 to 5.3×10^6 J/m. Interestingly, the

input energy per unit length for a natural lightning first stroke of 2.3×10^5 J/m reported by *Krider et al.* [1968] is within this range. For triggered lightning strokes, *Jayakumar et al.* [2006] estimated the mean value of input energy per unit length for 36 triggered-lightning strokes to be 3.6×10^3 J/m, which is more than an order of magnitude smaller than the lower bound estimated here for CIDs.

Cooray [1997] estimated the energy dissipated by a typical first leader return stroke sequence to be 5.5×10^8 J for a 5-km long channel, which corresponds to 1.1×10^5 J/m. Assuming that the first stroke channel length ranges from 5 to 8 km [e.g., *Rakov and Uman*, 2003] and *Cooray's* value of energy per unit length, we estimated the total energy range to be from 5.5 to 8.8×10^8 J. As noted above, *Cooray* [1997] estimated the dissipated energy for regular cloud discharges to be about 18×10^8 J for a charge transfer of 8 C. The corresponding channel length was 2.5 km. Taking the charge transfer of 8 C as typical for cloud discharges we estimate the energy per unit channel length to be 7.2×10^5 J/m. Using this latter value and the range of IC channel lengths of 2 to 5 km [e.g., *Shao and Krehbiel*, 1996], we estimate the IC energy range of 1.4 to 3.6×10^9 J. Using median charge transfers and average in-cloud potentials, *Maggio et al.* [2009] estimated the energy dissipated by 16 IC flashes to be 1.5×10^9 J per flash, which is near the lower bound of our range. Channel lengths for CIDs are within the range of 100 m to 1000 m (see Section 4.2). As seen in Table 4-14, the energy dissipated by a CID with $\Delta h = 100$ m and $\rho_v = 20$ C/m, dissipating 1.3 C of charge, is about 10^8 J, or 10^6 J/m. Using this energy per unit length and the range of channel lengths, we estimate the range of total energy dissipated by CIDs to be 10^8 to 10^9 J. Figure 4-43 summarizes the ranges of total energy dissipated by first strokes in cloud-to-ground discharges, regular intracloud discharges, and CIDs along with corresponding ranges for channel length. It appears that CIDs do not tend to surpass

either cloud-to-ground first strokes or regular cloud discharges in terms of energy. Hence, the labels like "energetic intracloud discharges" [e.g., *Eack, 2004; Smith et al., 2004*] and "high-energy discharges" [*Watson and Marshall, 2007*] that are sometimes used to refer to CIDs are probably not justified. As seen in Figure 4-43, the most distinctive feature of CIDs (besides their very intense HF-VHF radiation) is their small spatial extent.

Figure 4-44 shows the NLDN-reported peak current versus peak current estimated using the Hertzian dipole (HD) approximation for 48 CIDs. For 9 events, channel lengths were inferred using channel traversal times measured in dE/dt waveforms and assumed propagation speed of 2.5×10^8 m/s. For the other 39 events, an assumed channel length of 350 m (which implies that $v \geq 2 \times 10^8$ m/s) was used. The majority of NLDN-reported peak currents are considerably smaller than those predicted by the Hertzian dipole approximation. Some discrepancy is expected because NLDN-reported peak currents are assumed to be proportional to peak fields, which is a reasonable approximation for return strokes, while for the Hertzian dipole approximation, which applies to electrically short radiators, the peak of radiation electric field component is proportional to the peak of current time derivative (di/dt) (see Equation 4-13). It follows that the CID current peak is proportional to the peak of the integral of radiation electric field, which occurs at the time of field zero-crossing. In order to examine this discrepancy further, we computed CID peak currents using measured electric field peaks and the transmission line model [*Uman and McLain, 1969*] with $v = 1.8 \times 10^8$ m/s. The assumed value of speed provides a good match between NLDN-reported peak currents and those estimated using the TL model for negative first and subsequent return strokes (see Chapter 7, Figure 7-33). Thus, the TL-model based calculations presented here simulate, to some extent, NLDN peak current estimates. The results are shown in Figure 4-45. Clearly, the discrepancy between the TL-model predictions and

NLDN-reported values is appreciably smaller than in Figure 4-44, but there seem to be additional factors that make NLDN-reported currents underestimates. One of these factors is field attenuation due to its propagation over lossy ground. It is seen in Figure 4-45 that the discrepancy tends to increase with increasing the peak current. Events with larger peak currents are reported by a larger number of NLDN stations and, hence, their NLDN-reported current is more influenced by more strongly attenuated contributions from distant stations. The NLDN current estimation procedure does include compensation for far field propagation effects. However, if this compensation is not sufficient, the NLDN-reported peak current will be an underestimate. The 48 CIDs were reported by 4 to 22 (11 on average) NLDN stations, so that contributions from distances up to 625 km were included, while the distances for our TL model estimates were considerably smaller, ranging from 12 to 89 km. Another factor is the significant elevation of CIDs above ground. CIDs typically occur at heights greater than 10 km and hence radiation field peaks at relatively close distances can be significantly reduced relative to the case of sources near ground level, which is assumed in the NLDN field-to-current conversion equation. This can additionally contribute to underestimation of CID peak currents by the NLDN.

4.4 Summary

Compact Intracloud Discharges (CIDs) are cloud lightning discharges that produce single bipolar electric field pulses (so-called Narrow Bipolar Pulses or NBPs) having typical full widths of 10 to 30 μ s and intense HF-VHF radiation bursts (much more intense than those from any other cloud-to-ground or “normal” cloud discharge process). We examined wideband electric fields, electric and magnetic field derivatives, and narrowband VHF (36 MHz) radiation bursts produced by 157 CIDs. These lightning events appear to be the strongest natural producers of HF-VHF radiation. The initial polarity of distant wideband electric field pulses produced by

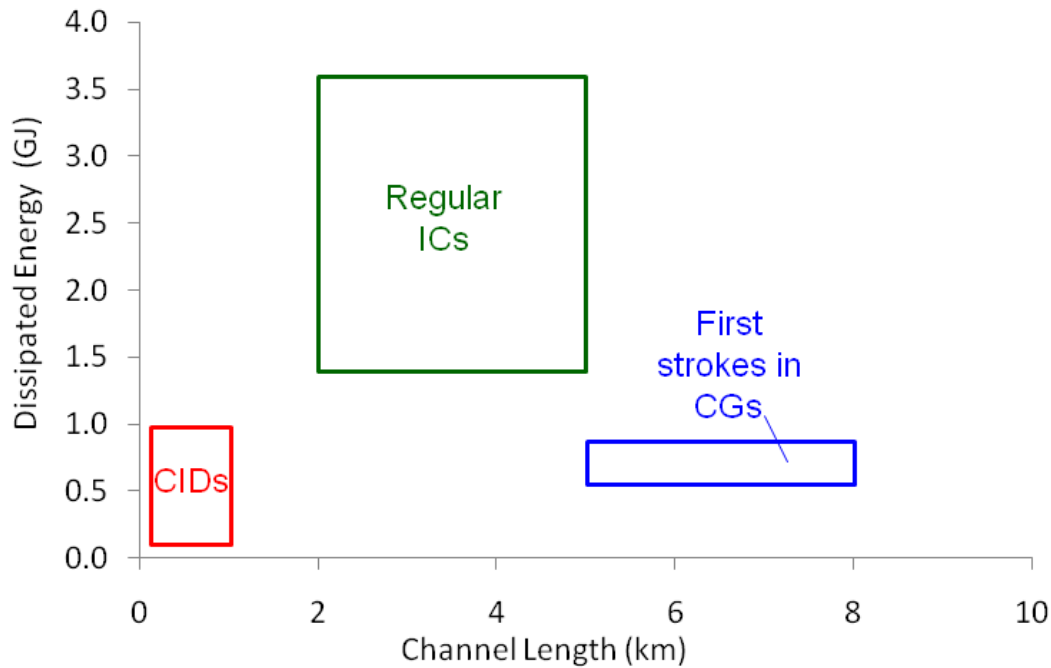


Figure 4-43. Ranges of dissipated energy and channel length for typical first strokes in cloud-to-ground flashes, regular intracloud flashes, and CIDs. Charge transfers were assumed to be 5 C, 8 C, and 1.3 C for these three types of discharges, respectively.

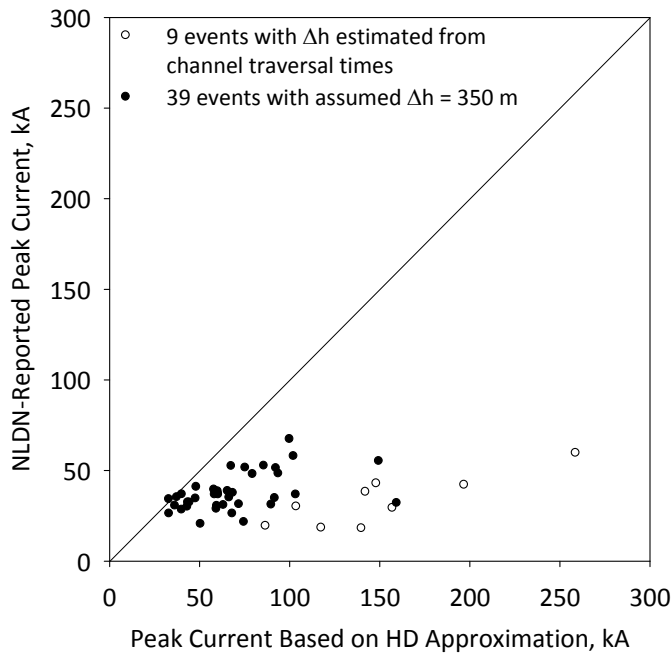


Figure 4-44. NLDN-reported peak current versus peak current estimated using the transmission line model with $v = 1.8 \times 10^8$ m/s for 48 CIDs. Hollow and solid circles represent the two subsets of events identified in Figure 15.

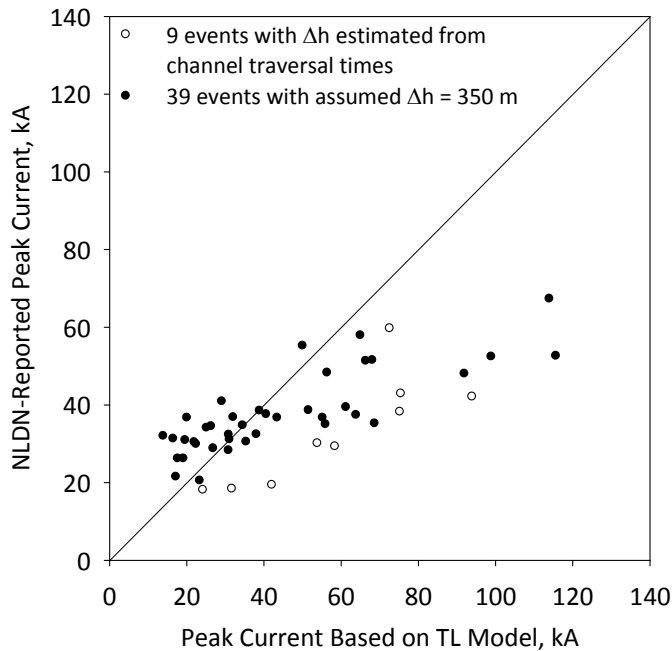


Figure 4-45. NLDN-reported peak current versus peak current estimated using the Hertzian dipole (HD) approximation for 48 CIDs. For 9 events (hollow circles), channel lengths were inferred using channel traversal times measured in dE/dt waveforms and assumed propagation speed of 2.5×10^8 m/s. For the other 39 events (solid circles) an assumed channel length of 350 m (with implied $v \geq 2 \times 10^8$ m/s) was used.

these CIDs was negative (opposite to that of negative return strokes). NLDN located 150 of the 157 CIDs at distances ranging from 5 to 132 km from the measurement station and correctly identified 149 (95%) of them as cloud discharges. Different types of electric field waveforms are presented and discussed. The majority (about 72%) of CIDs appeared to occur in isolation from any other lightning process, while about 24% were found to occur prior to, during, or following CG or “normal” IC lightning. About 18% were associated with cloud flashes and 6% with ground ones. In three cases two CIDs occurred within 43, 66, and 181 ms of each other (the first documented “multiple” CIDs), with a total of 4% of CIDs occurring in pairs. For 48 CIDs, the geometric means of source height and electric field peak normalized to 100 km and zero elevation angle were estimated to be 16 km and 20 V/m, respectively. The geometric means of

total pulse duration, width of initial half-cycle, and ratio of initial electric field peak to opposite polarity overshoot were 23 μs , 5.6 μs , and 5.7, respectively.

We examined the electric field derivative (dE/dt) signatures of 212 CIDs in Florida and found multiple secondary peaks (oscillations), which are indicative of reflections, in 15% of them. It is likely that the waveforms showing pronounced reflections correspond to shortest CID channels. The shortest radiating channel length appears to be about 100 m. Based on the experimental evidence of multiple reflections and modeling, we infer that the CID is essentially a bouncing-wave phenomenon. Some tens of reflections may occur at both radiating-channel ends. It is possible that the bouncing waves serve to maintain channel conductivity. Only higher-order reflections (in the later portion of the waveform) are detectable (if at all) in either electric field or dE/dt waveforms, while the undetectable lower-order reflections do influence the magnitude of the primary signature. In about 85% dE/dt signatures no reflections were observed. Factors that can make reflections undetectable include a relatively small magnitude of the incident wave, relatively long radiating channel, relatively large losses along the channel, and a relatively small (in absolute value) current reflection coefficients at channel ends. Reflections at channel extremities may result in corona-like electrical breakdown there, because a reduction of current is accompanied by an increase of line charge density and associated voltage (voltage doubles at an open circuit end and increases by a factor of 1.5 if the current reflection coefficient $\rho = -0.5$). This breakdown at channel ends is likely to produce intense bursts of HF-VHF radiation and increase "noisiness" of dE/dt signatures, which are characteristic features of CIDs. Thus, reflections are responsible for the fine structure of wideband electric field and dE/dt waveforms and, by inference, for "noisiness" of dE/dt waveforms and for accompanying HF-VHF radiation bursts.

We modeled the CID as a wave traveling on an elevated vertical transmission line. In order to account for multiple reflections that take place at the channel ends we specified two equivalent current sources, connected at the bottom and at the top of the channel. By comparing model-predicted electric fields with measurements we estimated that effective current reflection coefficients at channel ends should be in the range of 0 to -0.5, that the wave propagation speed ranges from 0.3 to 3×10^8 m/s, and channel length is less than 1000 m. In these calculations, we assumed that the current wave had a risetime of 6 μ s and a total duration of 30 μ s. Influence of current risetime on field waveforms was also examined, and it was found to be typically in the range from about 2 to 8.5 μ s. The current distribution along the CID channel is often not much different from uniform, as expected for a Hertzian (electrically short) dipole, because of relatively short channel length, relatively long current waveform, and relatively high propagation speed. Both the bouncing-wave model and the Hertzian-dipole approximations are capable of reproducing two-station CID electric field measurements of *Eack* [2004].

We estimated electrical parameters of 48 located CIDs using their measured electric fields and vertical Hertzian dipole approximation. This approximation is consistent with the bouncing-wave model for a reasonably large subset of allowed combinations of propagation speed and channel length. For example, for current zero-to-peak risetime $RT = 6 \mu$ s and propagation speed $v = 2 \times 10^8$ m/s the allowed range of channel length, Δh , is from 100 to 700 m, with the Hertzian dipole approximation being valid for Δh up to 375 m. For nine events, we estimated CID channel lengths from channel traversal times measured in dE/dt waveforms and assumed propagation speeds of 2×10^8 m/s and 3×10^8 m/s, which cover the entire range of allowed values. For $v = 2.5 \times 10^8$ m/s, the channel lengths for these nine events ranged from 108 to 142 m. The corresponding geometric mean values of peak current, zero-to-peak current risetime, 10-to-90%

current risetime, and charge transfer for the first 5 μs are 143 kA, 5.4 μs , 2.6 μs , and 303 mC, respectively. The geometric mean peak radiated power, and energy radiated for the first 5 μs are 29 GW and 24 kJ, respectively. For the remaining 39 events, there were no reflection signatures observed, and Δh was assumed to be 350 m, for which the Hertzian dipole approximation is valid for speeds in the range of 2 to 3 $\times 10^8$ m/s. In this case, geometric mean values of peak current, zero-to-peak current risetime, 10-to-90% current risetime, and charge transfer for the first 5 μs are 64 kA, 2.5 μs , and 142 mC, respectively. The geometric mean peak radiated power, and energy radiated for the first 5 μs are 28 GW and 32 kJ, respectively. Radiated power and energy are independent of Δh , while peak current and charge transfer can be scaled to other channel lengths, provided that they are consistent with the Hertzian dipole approximation. For the 39 events, we additionally considered $\Delta h = 170$ m, which is consistent with $v \geq 10^8$ m/s, and $\Delta h = 500$ m, which is consistent with $v = 3 \times 10^8$ m/s. For all 48 events, GM values of peak current, zero-to-peak current risetime, 10-to-90% current risetime, and charge transfer for the first 5 μs are 74 kA, 5 μs , 2.5 μs , and 164 mC, respectively. The geometric mean peak radiated power, and energy radiated for the first 5 μs are 29 GW and 31 kJ, respectively. Overall, the estimated CID current waveform parameters are comparable to their counterparts for first strokes in cloud-to-ground lightning, while their peak radiated electromagnetic power appears to be considerably higher.

CHAPTER 5 PRELIMINARY BREAKDOWN PULSE TRAINS IN NEGATIVE CLOUD-TO-GROUND LIGHTNING AND IN ATTEMPTED LEADERS

In this chapter preliminary breakdown (PB) pulse trains are characterized in detail. Additionally, lightning events exhibiting pulse trains that are characteristic of preliminary breakdown in negative cloud-to-ground discharges, but are not followed by return stroke waveforms are analyzed. Further, relationship between the lower positive charge region (LPCR) in thunderclouds (see Chapter 2) and the occurrence of PB pulse trains is examined. Assuming that the preliminary breakdown pulse train is a manifestation of interaction of a downward-extending negative leader channel with the lower positive charge region, the inferred dependence of lightning type on the magnitude of this charge region is qualitatively examined. Finally a set of conceptual scenarios for the occurrence of PB pulse trains are proposed that can be tested by future observations.

5.1 Characterization of Microsecond- and Submicrosecond-Scale Electric Field Pulses Prior to First Return-Stroke Waveforms

Microsecond- and submicrosecond-scale pulses in electric field records of cloud-to-ground lightning discharges acquired in summer 2006, in Gainesville, Florida were examined. A total of 12 ground flashes were analyzed in detail, with the electric field record length being 96 or 200 ms and sampling interval being 4 or 10 ns. Only pulses prior to the first return stroke in each flash were examined. 93% (655 out of 706) of these pulses were associated with the preliminary breakdown pulse train. The majority of them were relatively small in amplitude and duration. The peak-to-peak amplitude of each bipolar pulse and zero-to-peak amplitude of each unipolar pulse in a particular cloud-to-ground discharge was normalized with respect to that of the largest preliminary breakdown pulse (which was also the largest pulse prior to the first return stroke) in that flash. Pulses were classified into four different categories depending upon the value of their

normalized amplitude as shown in Table 5-1. The time at which the first return stroke occurred was relabeled as the zero of the time scale ($t=0$) and positions of all other pulses on the time axis were determined with respect to it. Only pulses with peak-to-peak amplitudes equal to or exceeding twice that of the local average noise level were considered.

The electric field record of each preliminary breakdown pulse train was examined using different time windows (mostly tens of microseconds). Overall preliminary breakdown pulse train duration is defined as the time interval between the peaks of the first and last pulses in the train. Pulses were considered as not belonging to the pulse train if they were separated from the last pulse of the train by at least 2 ms. Pulse duration is defined as the full width of the pulse, and interpulse interval is defined as the time interval between the peaks of two consecutive pulses. Further, in order to examine the occurrence of pulses in different parts of preliminary breakdown pulse trains, each pulse train was divided into four quarters, and the number of pulses within each quarter was counted.

Table 5-1. Categorization of pulses according to normalized amplitude.

Normalized Pulse Amplitude	Category
≤ 0.25	Very Small
> 0.25 and ≤ 0.5	Small
> 0.5 and ≤ 0.75	Medium
> 0.75 and ≤ 1.0	Large

For each of the 12 cloud-to-ground discharges the following characteristics were examined:

- Occurrence of pulses of different amplitude versus time prior to the first return stroke.
- Occurrence of pulses of different total duration versus time.
- Statistical distribution of pulse amplitude.
- Statistical distribution of total pulse duration.

Figure 5-1 shows an example of the measured electric field waveform of a cloud-to-ground discharge (flash 05/24/06_1078). In addition to “classical” preliminary breakdown pulses (see Figure 5-2a) having durations of the order of tens of microseconds, previously not reported

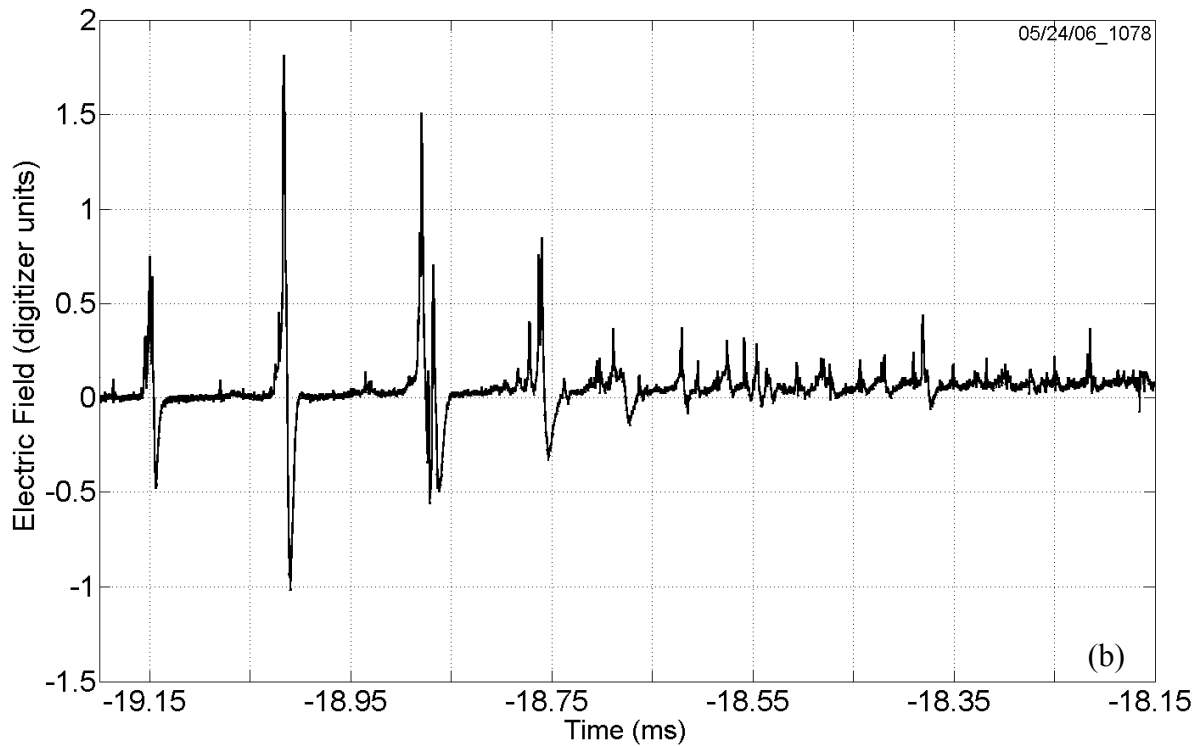
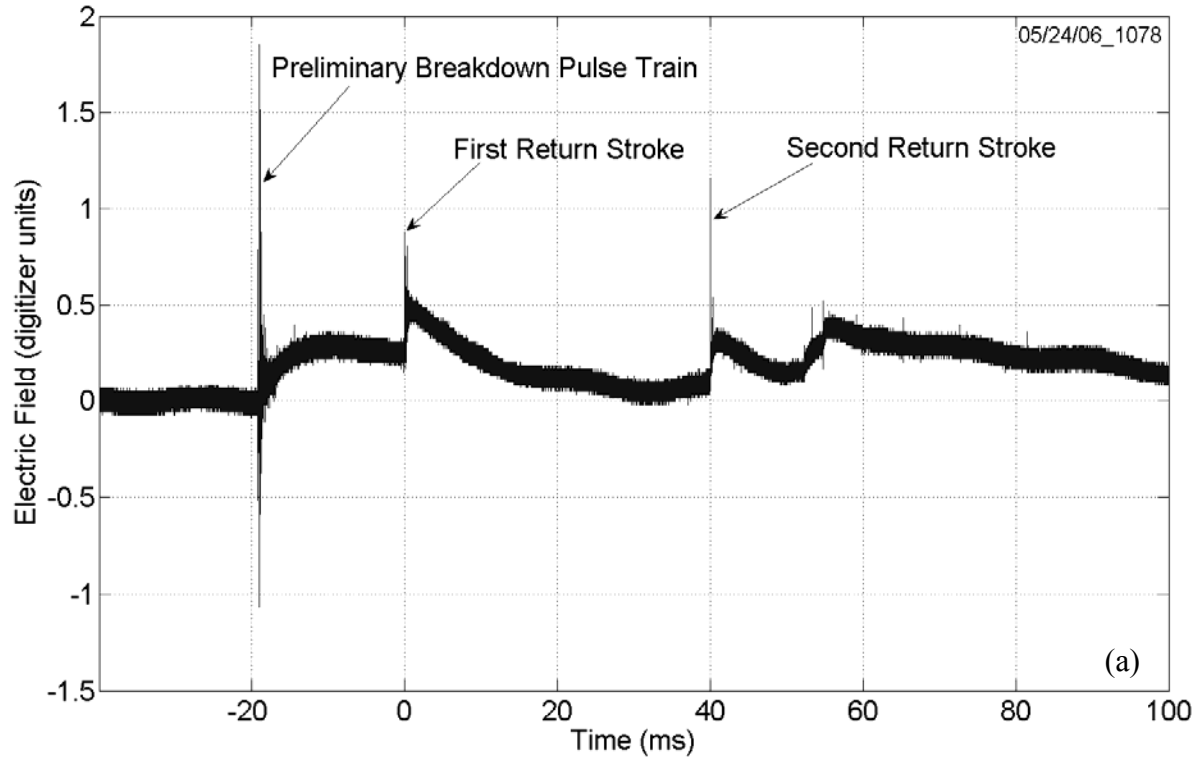


Figure 5-1. (a) Electric field record of cloud-to-ground flash 05/24/06_1078 showing preliminary breakdown pulse train followed by two return strokes. Note that the return-stroke peaks are smaller than those of some preliminary-breakdown pulses. (b) The preliminary breakdown pulse train shown on a 1.05 ms time scale.

“narrow” pulses with durations less than or equal to 4 μs (see Figure 5-2b) were also observed. Figures 5-3 to 5-6 show results of the analysis for the flash presented in Figure 5-1. The overwhelming majority (about 93%) of the 706 pulses in the 12 cloud-to-ground discharges examined in this study were associated with the preliminary breakdown pulse trains typically occurring tens of milliseconds before the first return-strokes of the flashes and lasting for a few milliseconds, as seen in Figures 5-3 and 5-4. Typically, the majority of pulses in a flash were found to be small or very small in amplitude and to have durations less than or equal to 4 μs . Also, pulses with durations less than or equal to 4 μs (including submicrosecond-scale pulses) were found to occur both before and after the largest pulse in the preliminary breakdown pulse train.

Table 5-2 summarizes the occurrence of smaller and narrower pulses in the 12 selected cloud-to-ground discharges. It was found that, for individual flashes, 57 to 98% of the pulses belonged to the small and very small amplitude categories. Further, 22 to 89% of the pulses had durations less than or equal to 4 μs . Figure 5-7 shows the distribution of total durations of pulses in all the 12 cloud-to-ground flashes. It can be seen from this Figure that 78% (553 out of 706) of the pulses had durations less than or equal to 4 μs , of which 87% (479 out of 553) were bipolar, and that 22% (157 out of 706) of the pulses had durations less than 1 μs . The arithmetic mean pulse duration was 4.7 μs , which is outside the 20–40 μs range of typical durations usually given for “classical” preliminary breakdown pulses in ground discharges [e.g., *Rakov and Uman, 2003*]. A moderate linear correlation was found between the amplitude and duration of pulses.

Figure 5-8 shows the occurrence of 655 pulses in four quarters of the preliminary breakdown pulse train for all the 12 cloud-to-ground flashes. The majority (532 of 655 or 81%) of the preliminary breakdown pulses occur during the first half of the pulse train. Also, 87% (129

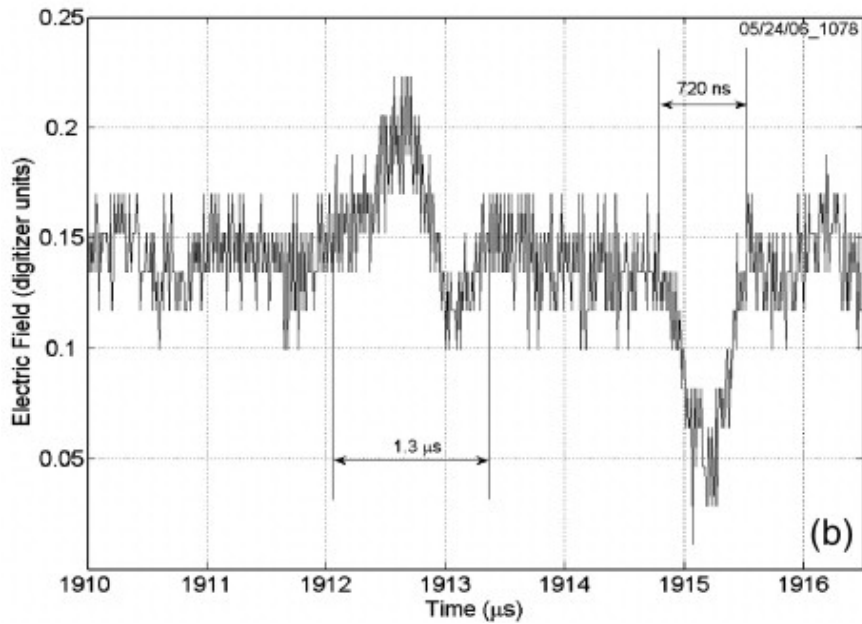
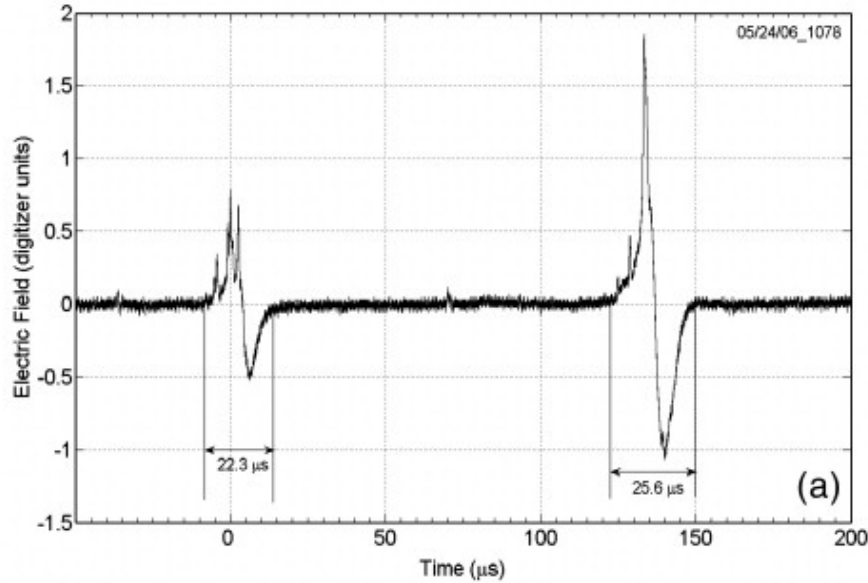


Figure 5-2. Examples of (a) “classical” and (b) “narrow” preliminary breakdown pulses in cloud-to-ground discharges analyzed in this study.

of 148) of the pulses with total durations greater than $4 \mu\text{s}$ occur during the first half of the pulse train. Figure 5-9 shows the histogram of the total duration of 655 preliminary breakdown pulse trains in 12 cloud-to-ground flashes. The range of variation and arithmetic mean of total pulse train durations are 1.1–5.0 ms and 3.4 ms, respectively. Figures 5-10 and 5-11 show ranges of variation (vertical bars) of pulse duration and interpulse interval in individual pulse trains,

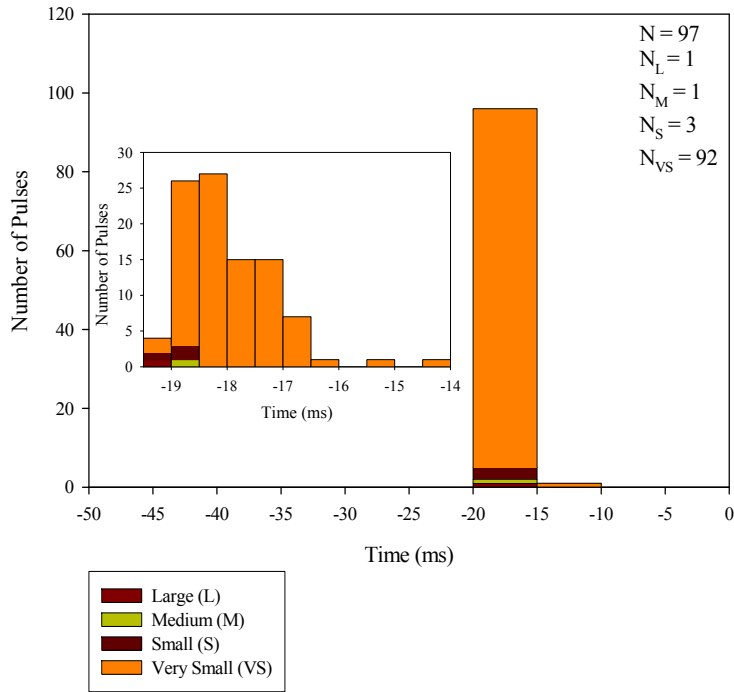


Figure 5-3. Occurrence of pulses of different amplitude prior to the first stroke of cloud-to-ground flash whose electric field record is shown in Figure 5-1. Inset shows the occurrence of pulses of different amplitude between -19.5 ms and -14 ms using bin size of 500 μ s.

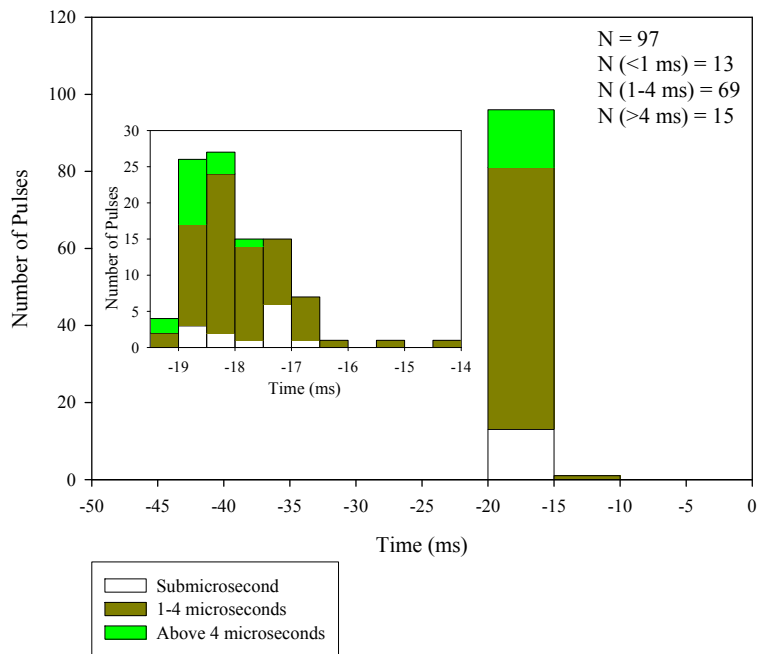


Figure 5-4. Occurrence of pulses of different total duration prior to the first stroke of cloud-to-ground flash whose electric field record is shown in Figure 5-1. Inset shows the occurrence of pulses of different total duration between -19.5 ms and -14 ms using bin size of 500 μ s.

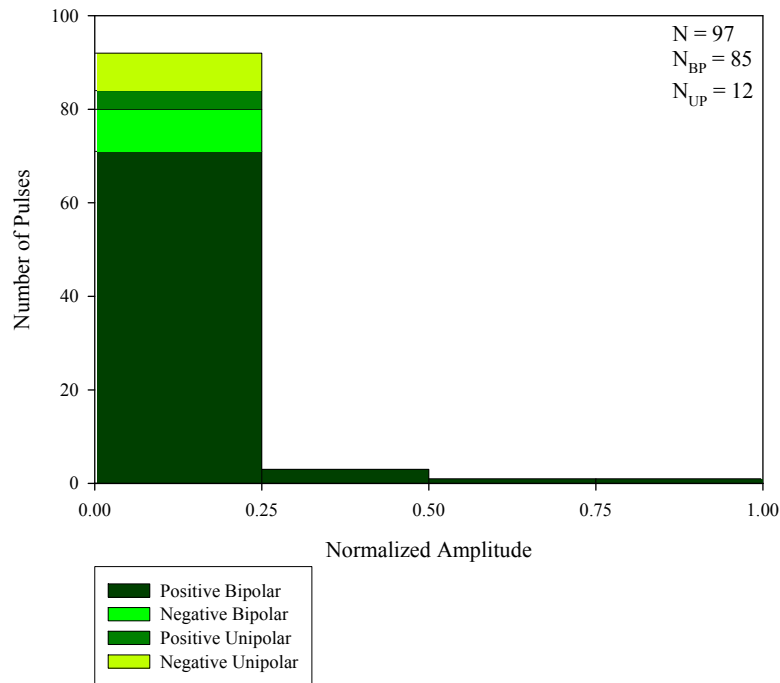


Figure 5-5. Histogram of pulse amplitude for four different types of pulses in cloud-to-ground flash whose electric field record is shown in Figure 5-1.

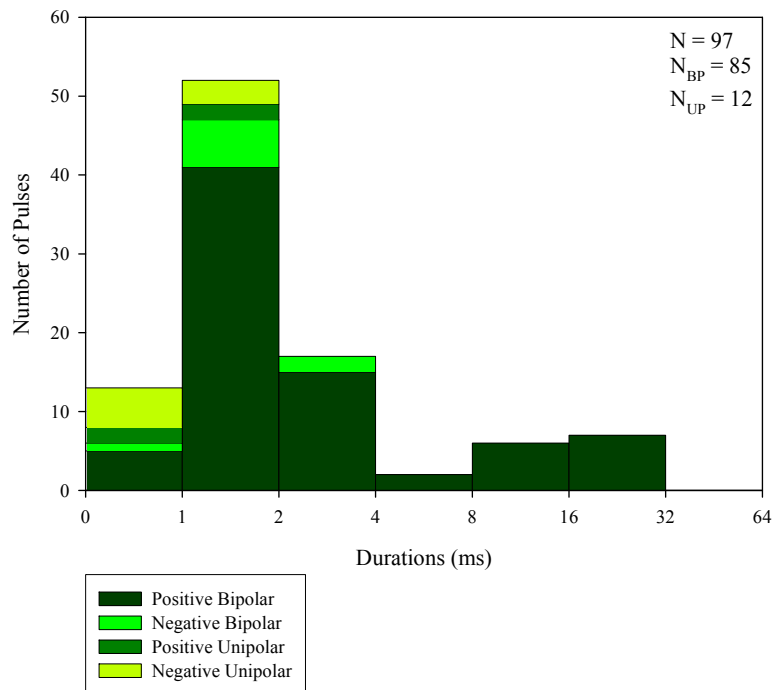


Figure 5-6. Histogram of total pulse duration for four different types of pulses in cloud-to-ground flash whose electric field record is shown in Figure 5-1.

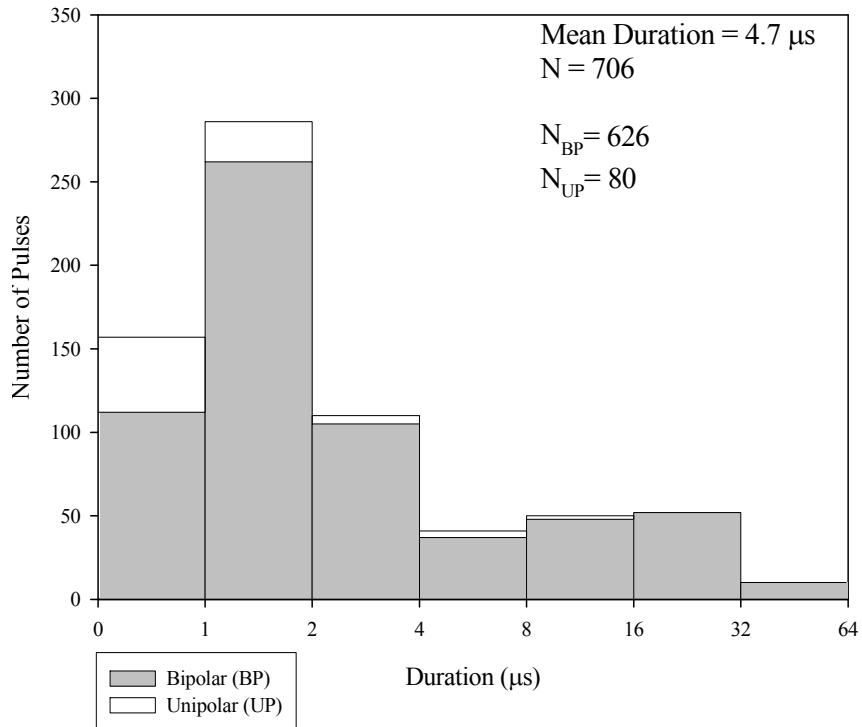


Figure 5-7. Histogram of total duration of unipolar and bipolar pulses in 12 cloud-to-ground discharges.

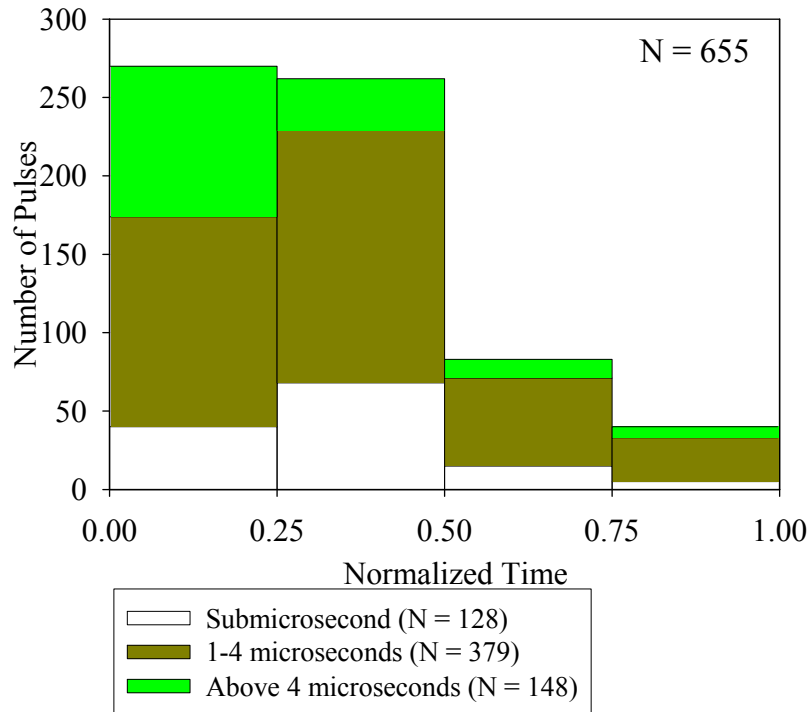


Figure 5-8. Occurrence of pulses of different total duration in different parts (four quarters) of the preliminary breakdown pulse train for all 12 cloud-to-ground flashes combined.

Table 5-2. Summary of occurrence of smaller and narrower pulses observed in the 12 cloud-to-ground discharges.

Flash ID	Total Number of Pulses	Number of pulses in the Small and Very Small categories (%)			Number of pulses having durations less than or equal to 4 μ s (%)		
		Bipolar	Unipolar	Total	Bipolar	Unipolar	Total
05/24/06_224	169	141 (83)	23 (14)	164 (97)	127 (75)	22 (13)	149 (88)
05/24/06_228	27	19 (70)	6 (22)	25 (93)	7 (26)	4 (15)	11 (41)
05/24/06_1078	97	83 (86)	12 (12)	95 (98)	70 (72)	12 (12)	82 (85)
05/28/06_1152	23	13 (57)	0 (0)	13 (57)	5 (22)	0	5 (22)
05/28/06_1360	41	35 (85)	1 (2.4)	36 (88)	33 (80)	1 (2.4)	34 (83)
06/01/06_21	44	38 (86)	2 (4.6)	40 (91)	29 (66)	2 (4.6)	31 (71)
06/02/06_120	25	19 (76)	2 (8.0)	21 (84)	8 (32)	1 (4.0)	9 (36)
06/02/06_139	72	58 (81)	6 (8)	64 (89)	58 (81)	6 (8.3)	64 (89)
06/02/06_207	48	36 (75)	6 (13)	42 (88)	34 (71)	6 (13)	40 (83)
06/02/06_212	65	48 (74)	9 (14)	57 (88)	43 (66)	9 (14)	52 (80)
07/15/06_23	73	58 (79)	11 (15)	69 (95)	52 (71)	9 (12)	61 (84)
07/17/06_54	22	14 (64)	2 (9.1)	16 (73)	13 (59)	2 (9.1)	15 (68)
Total	706	562 (80)	80 (11)	642 (91)	479 (68)	74 (10)	553 (78)

respectively. All the pulse trains were found to have minimum pulse durations less than 1.5 μ s (see Figure 5-10). The range of variation and the arithmetic mean of pulse durations for all 12 pulse trains were found to be 0.5–49 μ s and 4.8 μ s, respectively. The mean duration is significantly less than the lower bound of the 20–40 μ s range of typical durations previously reported for “classical” preliminary breakdown pulses [Rakov and Uman, 2003]. In the study of Weidman and Krider [1979], the minimum duration of such “classical” pulses was between 10

and 15 μs . Interestingly, if all pulses with durations equal to or less than 4 μs in our dataset were excluded, the mean duration of the remaining 108 (out of a total of 655) pulses would be 16 μs , which is closer to, but still outside of the 20–40 μs range for “classical” pulses. For interpulse intervals (see Figure 5-11), the range of variation and arithmetic mean are 0.6–1585 μs and 65 μs , respectively. The previously reported typical values of interpulse interval, presumably for larger pulses, are in the range of 70–130 μs [Rakov and Uman, 2003]. It appears that in previous studies of preliminary breakdown pulse trains, smaller (and narrower) pulses were arbitrarily disregarded, which led to biases toward larger average pulse durations and longer average interpulse intervals.

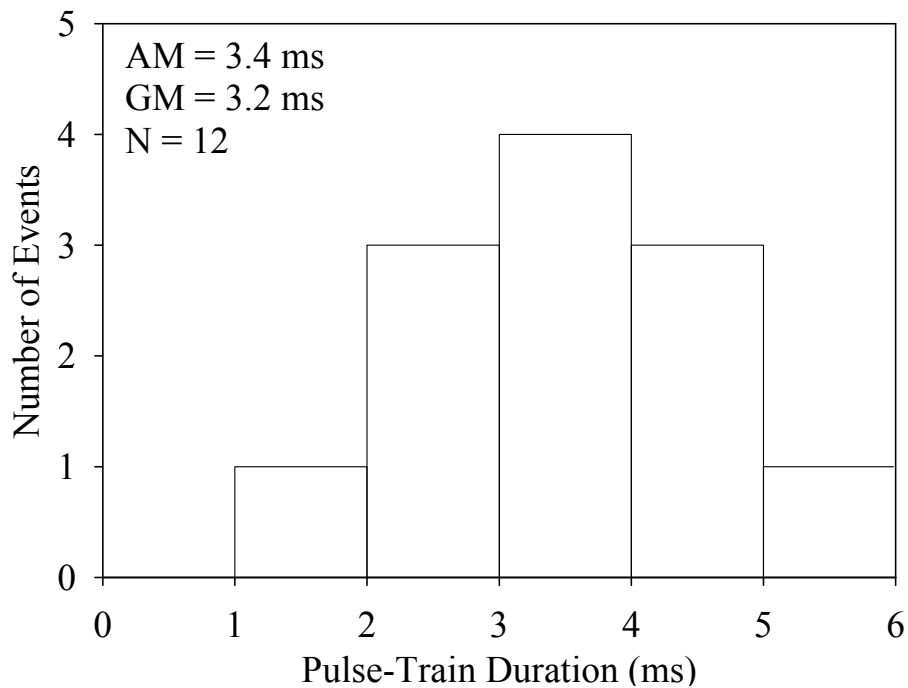


Figure 5-9. Histogram of the total duration of preliminary breakdown pulse trains for 12 cloud-to-ground flashes.

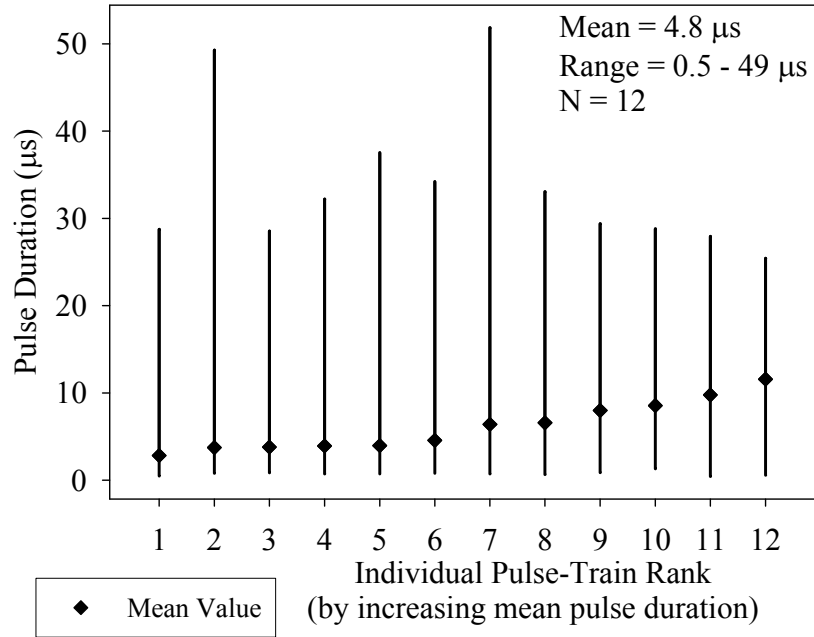


Figure 5-10. Ranges of variation (vertical bars) and mean values (diamonds) of pulse duration in individual preliminary breakdown pulse trains.

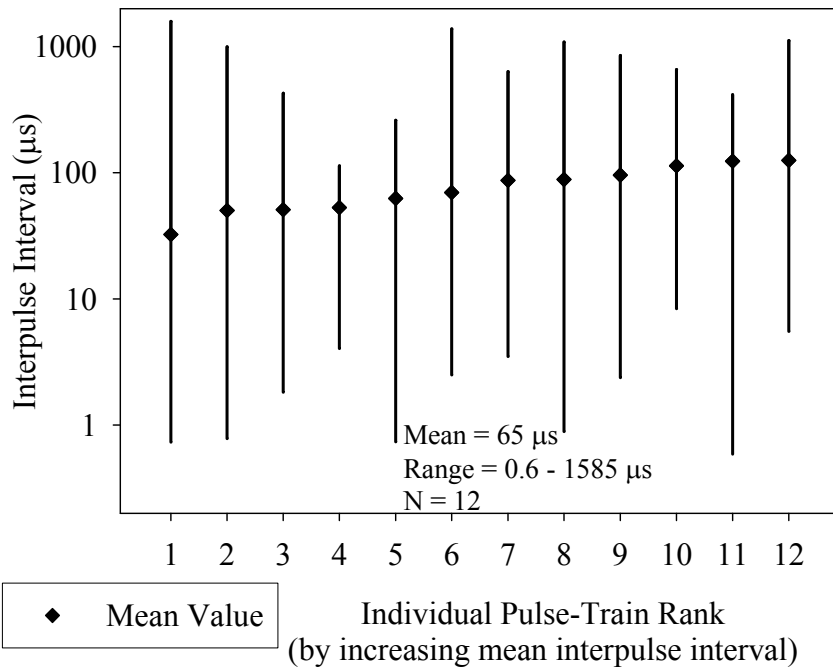


Figure 5-11. Ranges of variation (vertical bars) and mean values (diamonds) of interpulse interval in individual preliminary breakdown pulse trains.

5.2 Attempted Leaders

In this Section lightning events exhibiting pulse trains that are characteristic of preliminary breakdown in negative cloud-to-ground discharges, but are not followed by return stroke waveforms were identified and examined. It was assumed that these lightning events are manifestations of the initiation of downward negative stepped leaders that fail to propagate all the way to the ground. We refer to these events as “attempted first cloud-to-ground leaders”. In a total of 2475 electric field records of lightning events acquired (using a sampling interval of 4 or 10 ns) in Gainesville, Florida, in 2006, we found 35 waveforms in 33 of these records that satisfied the criteria (which are the characteristic features of preliminary breakdown pulse trains in negative cloud-to-ground flashes) set for attempted cloud-to-ground leaders. The electric field record of an attempted leader is shown in Figure 5-12.

Preliminary breakdown pulse trains of attempted cloud-to-ground leaders typically contained two types of pulses, larger “classical” pulses (see for example, Figure 5-13a) with durations of the order of tens of microseconds and “narrow” pulses (see for example, Figure 5-13b) whose durations were a few microseconds, with many being in the 1 to 2 μs range. Almost half (46%) of the pulse trains were found to have minimum pulse durations in the range of 1–2 μs . Smaller and narrower pulses tended to occur at the onset and toward the end of each pulse train. In addition to bipolar pulses with positive (atmospheric electricity sign convention) initial half-cycle, negative unipolar and negative (initial half-cycle) bipolar pulses were sometimes seen toward the end of the train.

Characteristics of preliminary breakdown pulse trains in attempted leaders can be summarized as follows: (1) The range of variation and arithmetic mean of total durations of pulse trains are 0.8–7.9 ms and 2.7 ms, respectively, with 74% of the pulse trains having total durations less than or equal to 3 ms (see Figure 5-14). (2) The range of variation and the

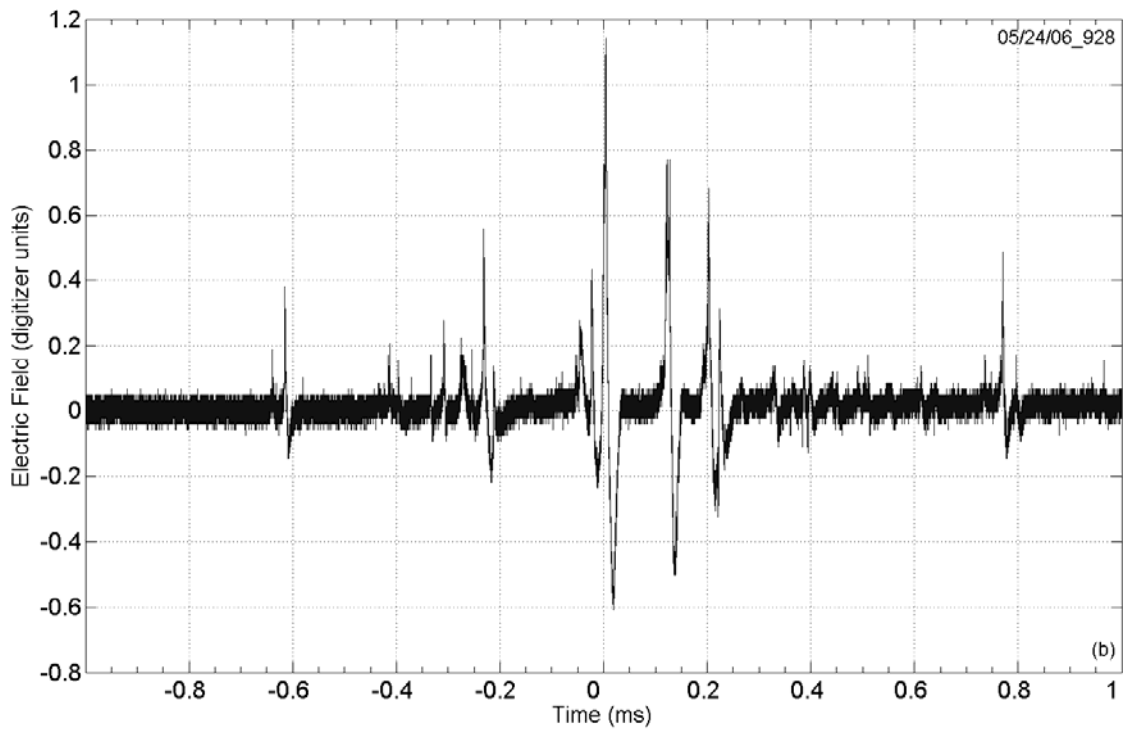
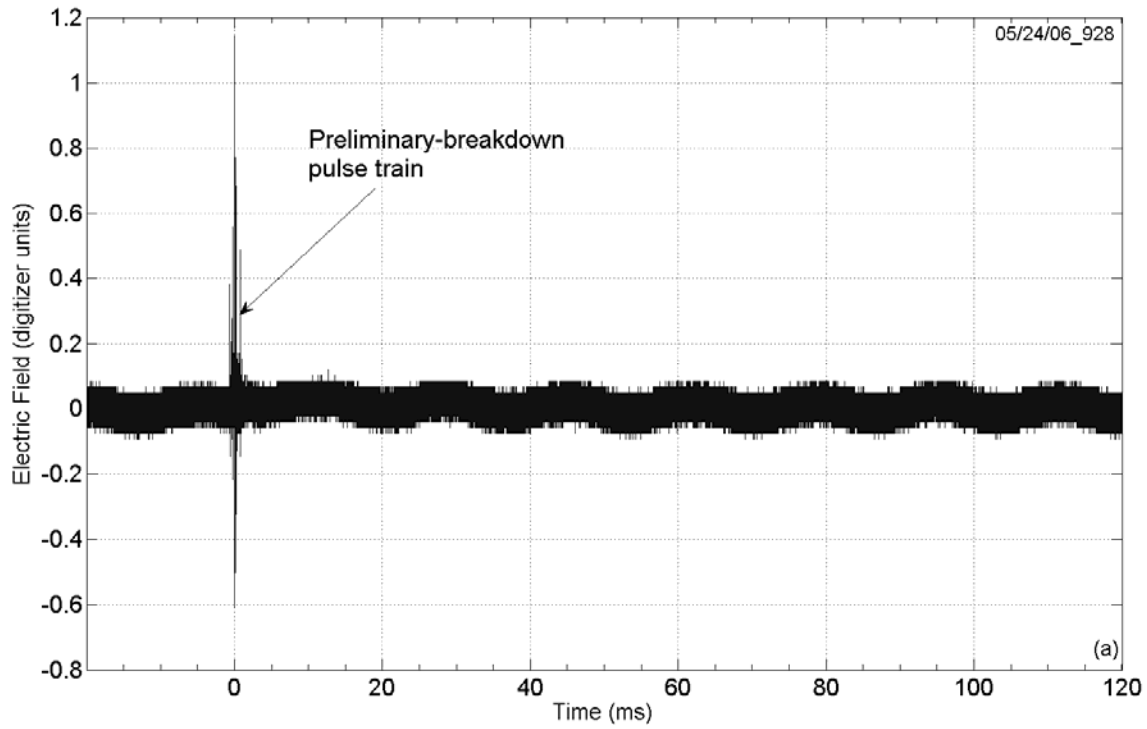


Figure 5-12. (a) Electric field record of an attempted leader with no pulse activity following the preliminary breakdown pulse train. (b) Preliminary breakdown-like pulses of the attempted leader shown in (a).

weighted arithmetic mean of individual pulse durations are 1–91 μs and 17 μs , respectively (see Figure 5-15). (3) The range of variation and the weighted arithmetic mean of interpulse intervals are 1– 530 μs and 73 μs , respectively (see Figure 5-16).

In Section 5.1.1, the arithmetic mean pulse duration and interpulse interval for preliminary breakdown pulse trains in cloud-to-ground discharges were found to be 4.8 and 65 μs , respectively, versus 17 and 73 μs for attempted cloud-to-ground leaders. This implies that preliminary breakdown pulse trains in ground discharges contain a larger fraction of “narrow” ($\leq 4 \mu\text{s}$) pulses than the pulse trains in attempted cloud-to-ground leaders. Both “classical” (having durations of tens of microseconds) and “narrow” pulses were found in both types of pulse trains. However, submicrosecond-scale pulses were only observed in preliminary breakdown pulse trains of ground discharges. Some of the isolated short-duration discharges which have been observed by *Maier et al.* [1996] and *Krehbiel et al.* [2003] who used VHF time-of-arrival lightning mapping systems and by *Defer et al.* [2001] who used a VHF interferometric lightning mapper, might be attempted cloud-to-ground leaders, similar to those considered in this study.

It is possible that some of the attempted leaders could also be classified as “inverted intracloud flashes,” occurring between the main negative and lower positive charge regions. In this latter case, the lower positive charge can be viewed as “blocking” the progression of descending negative leader from reaching ground and thus “converting” the potential cloud-to-ground flash to an intracloud one. Whatever the scenario, characteristics of preliminary breakdown–type pulses that were attributed to attempted leaders were indicative of a cloud-to-ground flash. Another possible interpretation of the observed pulse trains is a unique discharge

process in the cloud that may or may not be followed by formation of a stepped-leader channel terminating (or not terminating) on ground.

Since the preliminary breakdown-type pulses considered here have the same polarity as return stroke pulses in negative cloud-to-ground flashes and durations of the initial half cycle of these two types of pulses may be comparable (a few tens of microseconds), some of the attempted cloud-to-ground leaders can be misclassified by the NLDN as low-intensity negative cloud-to-ground discharges. If it is assumed that about 25% of the 2475 records examined here were due to negative cloud-to-ground flashes, and that 25% of these cloud-to-ground flashes had peak currents equal to or less than 10 kA, the expected number of low-intensity (≤ 10 kA) negative cloud-to-ground events would be 155. If the NLDN recorded all these 155 negative cloud-to-ground events plus all 35 attempted leaders (all assumed to have NLDN intensities ≤ 10 kA), about 18% of reported low-intensity cloud-to-ground flashes would be misclassified events.

5.3 Some Inferences on the Role of Lower Positive Charge Region in Facilitating Different Types of Lightning

5.3.1 Introduction

The gross charge structure of a “normal” thundercloud can be viewed as a vertical tripole consisting of three charge centers (regions), main positive at the top, main negative in the middle, and an additional positive below the main negative [Williams, 1989]. The magnitudes of the main positive and negative charges are typically some tens of coulombs, while the lower positive charge is probably 10 C or less. The negative charge region is apparently related to the -10 to -25°C (0 to -15°C in earlier studies) temperature range, while the lower positive charge is typically found just below the freezing level. Four different hypotheses regarding the origin of the lower positive charge region (LPCR) are reviewed by *Rakov and Uman* [2003, p. 88]. The LPCR can be associated with (a) graupel, which, according to the graupel-ice cloud

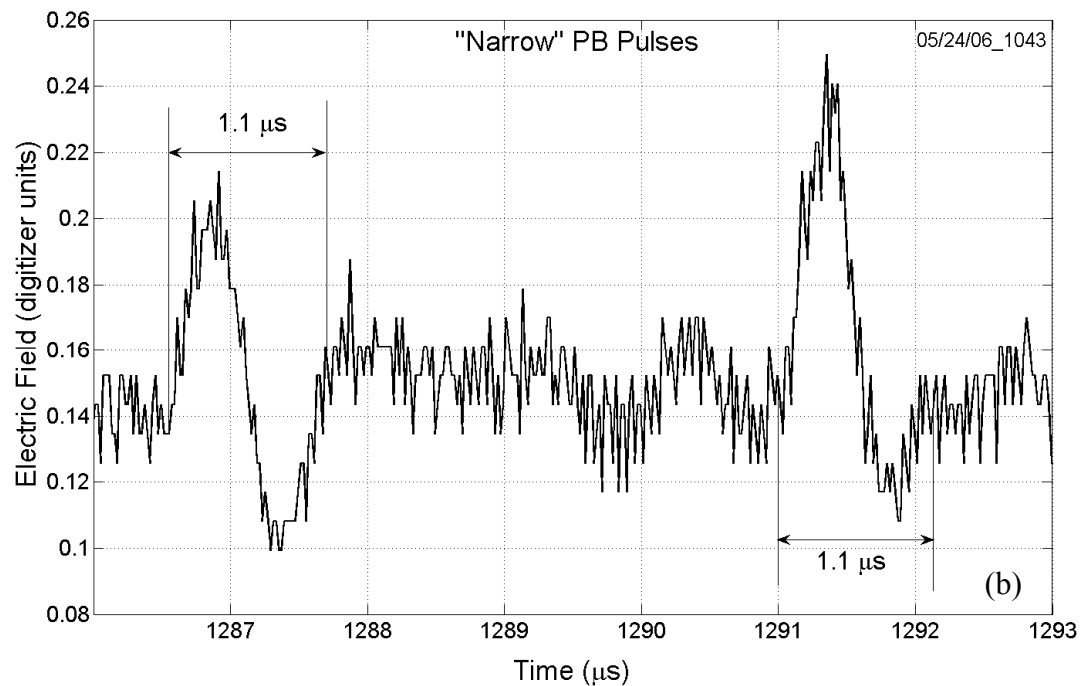
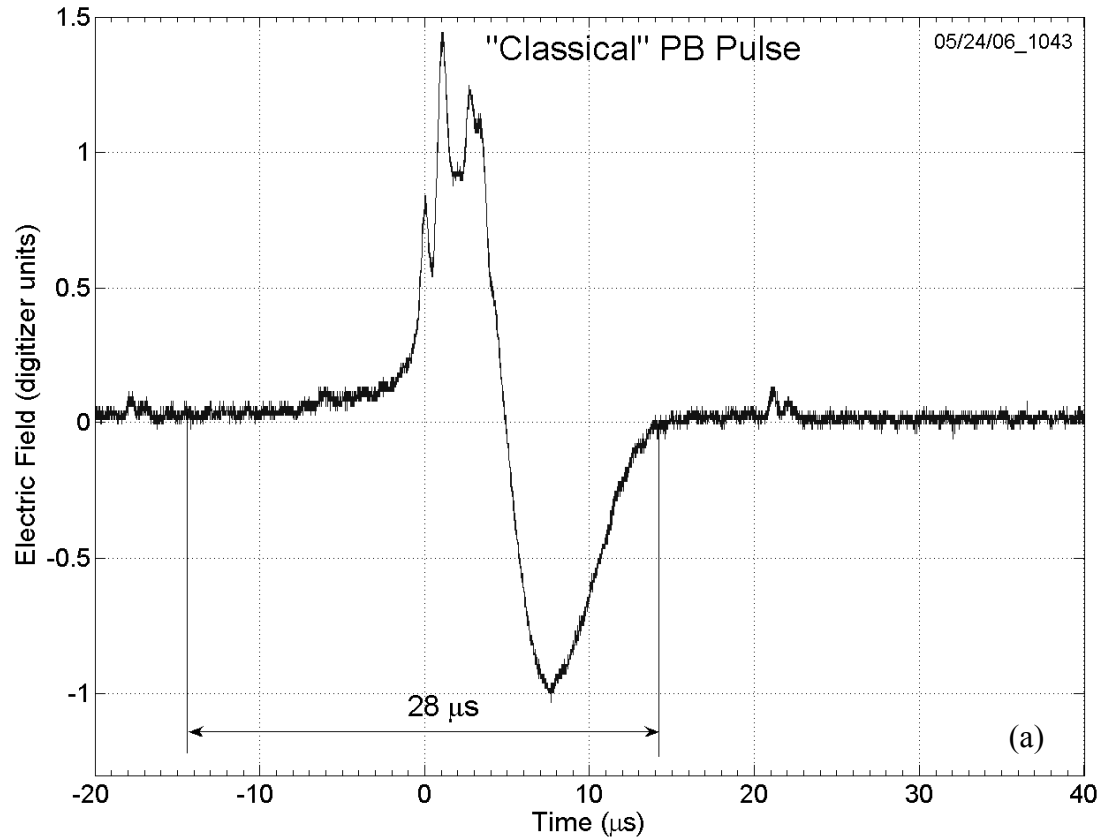


Figure 5-13. Typical (a) “classical” and (b) “narrow” pulses of a preliminary breakdown (PB) pulse train of an attempted leader.

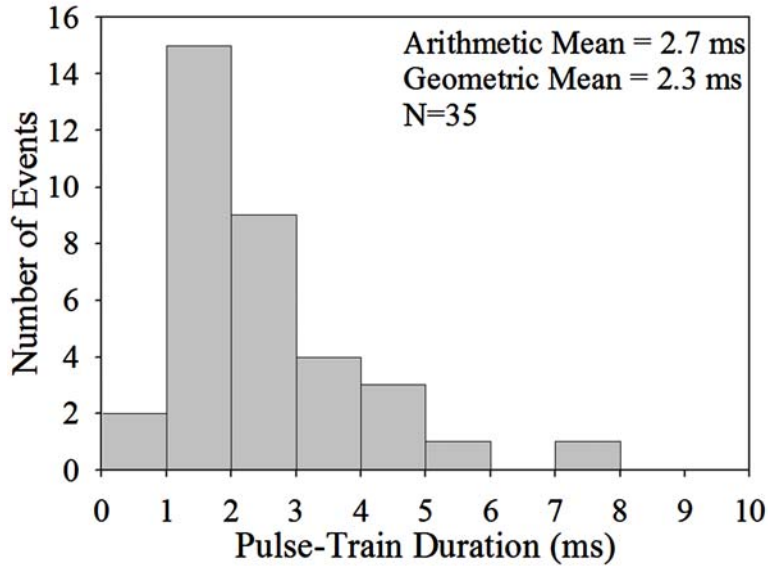


Figure 5-14. Histogram of preliminary breakdown pulse train duration for attempted leaders. Note that a total of 35 preliminary breakdown pulse trains were found in 33 electric field records.

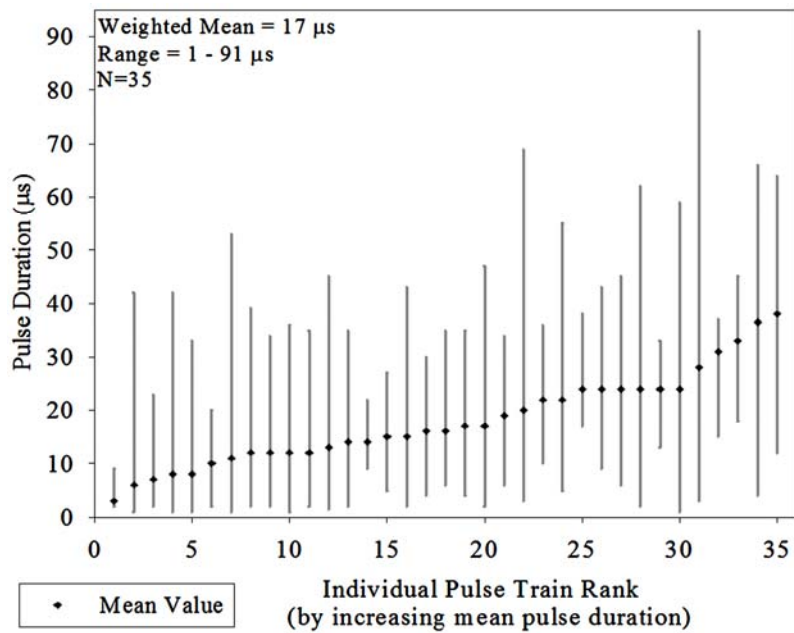


Figure 5-15. Ranges of variation (vertical bars) and mean values (diamonds) of pulse duration in individual preliminary breakdown pulse trains of attempted leaders.

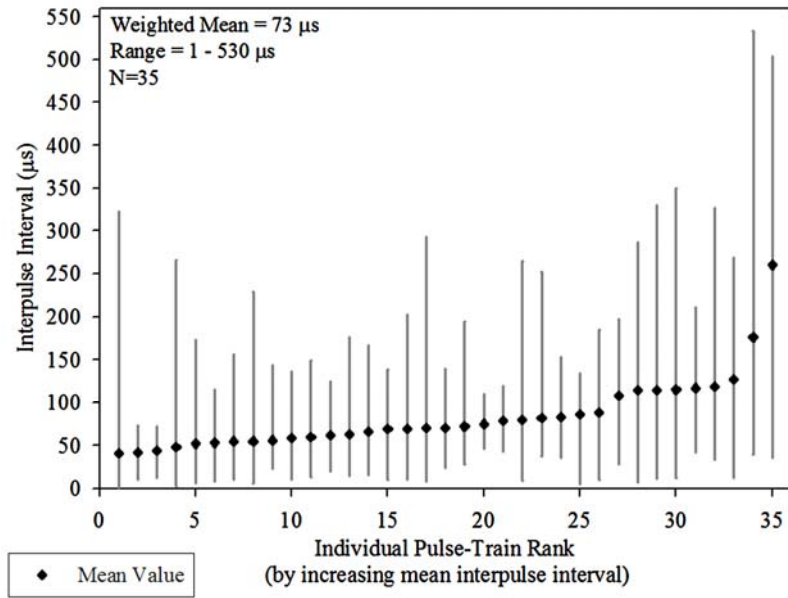


Figure 5-16. Ranges of variation (vertical bars) and mean values (diamonds) of interpulse interval in individual preliminary breakdown pulse trains of attempted leaders.

electrification mechanism, charges positively at temperatures warmer than the reversal temperature, (b) positive charge deposited in the cloud by lightning, (c) corona at ground surface, and (d) positive screening layer at the lower cloud boundary. In this paper, we assume that the charge that is produced by corona at ground under thunderclouds and subsequently carried by updraft into the cloud is a significant contributor to the LPCR. *Chauzy and Soula* [1999] have provided a quantitative evidence (the other three hypothetical scenarios remain largely qualitative) for the corona origin. They estimated, from measurements and modeling, that a significant portion (some tens to few hundred coulombs) of positive charge produced by corona at ground level could be transferred to an altitude of 1000 m (the upper limit of their computational domain) over an area of 10 x 10 km² for the entire thunderstorm lifetime. Chauzy and Soula noted that some positive charge will be carried by updrafts from 1000 m to higher altitudes. They concluded that the corona-produced charge can account for the formation of the LPCR, as earlier suggested by *Malan* [1952].

Whatever the source of the LPCR, it is generally thought that the LPCR serves to enhance the electric field at the bottom of the negative charge region and thereby facilitate the launching of a negatively-charged leader toward ground [e.g., *Clarence and Malan, 1957; Ogawa, 1993; Tessendorf et al., 2007*]. On the other hand, the presence of “excessive” lower positive charge in thunderclouds over the Tibetan Plateau has been reported to prevent the occurrence of negative cloud-to-ground discharges and facilitate intracloud discharges between the main negative and lower positive charge regions [*Qie et al., 2005*]. Thus, electric breakdown between the main negative and lower positive charge regions may result in either a cloud-to-ground (CG) or an intracloud (IC) flash.

Bipolar pulse trains in wideband electric field records typically occurring a few tens of milliseconds (sometimes considerably less) prior to the first return-stroke pulse and having overall duration of a few milliseconds are often attributed to preliminary breakdown (PB) process [e.g., *Brook, 1992; Heavner et al., 2002*]. The amplitude of largest pulses in PB pulse trains can be comparable to or even exceed that of the first return-stroke pulse [*Gomes et al., 1998; Schulz and Diendorfer, 2006; Nag and Rakov, 2009*]. These pulse trains are examined in Section 5.1. However, in many cases (at least in some locations, as discussed below) the first return-stroke pulse is not preceded by a detectable PB pulse train.

Electric field pulse trains that are characteristic of preliminary breakdown in negative CG discharges but are not followed by return-stroke waveforms have been identified and examined in Section 5.2. These trains were attributed to attempted cloud-to-ground leaders. Some of the attempted leaders examined in Section 5.2 could also be classified as “inverted intracloud flashes”, occurring between the main negative and lower positive charge regions. In that case, the lower positive charge can be viewed as “blocking” the progression of descending negative

leader from reaching ground and thus “converting” the potential CG flash to an intracloud (or cloud-to-air) one. The relationship between type of lightning discharge and cloud charge structure, with emphasis on blue and gigantic jets, was recently studied by *Krehbiel et al.* [2008] (see also commentary by E.R. Williams, on pp. 216-217).

PB pulse trains were observed to occur at the beginning of electrostatic field changes produced by stepped leaders [e.g., *Beasley et al.*, 1982], which implies that, when they do occur, they have something to do with initiation of appreciable charge transfer. *Beasley et al.* [1982, Fig. 26] reported that PB pulses in Florida were radiated between altitudes of 4 to 6 km and their VHF sources appeared to propagate downward, apparently from the lower boundary of main negative charge region toward and into the LPCR. Similar downward progression was also reported by *Heavner et al.* [2002]. Further, *Schonland* [1956], working in South Africa, attributed the initial (faster, brighter, and heavily branched) stage of the β leader, this initial stage being the same as the PB discussed here, to accumulations of positive space charge near the cloud base. Thus, it is likely that the PB pulse train is a manifestation of interaction of a downward-extending negative leader channel with the LPCR.

An attempt was made to obtain estimates of source heights of individual PB pulses using simultaneous measurements of electric and magnetic radiation fields of PB pulse train. This method is described in Chapter 4 (Section 4.1.4). Unfortunately, for the PB pulse trains analyzed in Sections 5.1 and 5.2 of this Chapter, magnetic field measurements were not available. So, a negative cloud-to-ground discharge (that occurred in August, 2008 in Gainesville, Florida) in which a PB pulse train preceded the first return stroke was selected for the purpose. The first pulse of the PB pulse train occurred 7.31 ms prior to the first stroke. The NLDN located the first stroke at a distance of 27.8 km from the measuring station. The PB pulse train (electric field

record of which is shown in Figure 5-17) consisted of five detectable pulses. The second pulse of the train, which occurred 7.14 ms prior to the first stroke, was detected by the NLDN as a cloud discharge at a distance of 28.5 km from the measuring station. The other four pulses in the train were not detected by the NLDN. The electric field waveforms of the second, third, and fifth pulses in the train had better signal-to-noise ratio relative to the other two pulses (as seen in Figure 5-17) and hence were selected for analysis to estimate their source heights. It was assumed that all pulses occurred at the same horizontal distance of 28.5 km as the second pulse for which NLDN-estimated distance was available. The source heights for the second, third, and fifth pulses were inferred to be 6.5 km, 7.1 km, and 5.8 km, respectively. The inferred source height of the third pulse is 600 m higher than that of the second pulse. The inferred source height for the fifth pulse is 700 m lower than that of the second pulse in the train and 1300 m lower than that of the third, which probably indicates a downward progressing channel. However, the sample of three pulses in one PB train is too small to make any conclusions. There are two primary sources of error in our estimated source heights: elevation angle error and distance error as discussed in Chapter 4 (Section 4.1.4). The median height error for the three PB pulses was estimated to be $\pm 19\%$. Further, an unknown error was introduced due to the assumption that all PB pulses in the train occurred at the same horizontal distance from the measuring station, as distances for individual pulses were not available. The differences in source heights of the three PB pulses (ranging from 600 m to 1300 m) are less than the height estimation error of $\pm 19\%$ (ranging from 1100 m to 1350 m). In order to use this method of height estimation effectively for determining source heights of PB pulses and examining direction of channel progression, height estimation errors have to be of the order of hundreds of meters or less so that locations of individual PB pulse sources (which probably occur within a few hundred meters of each other)

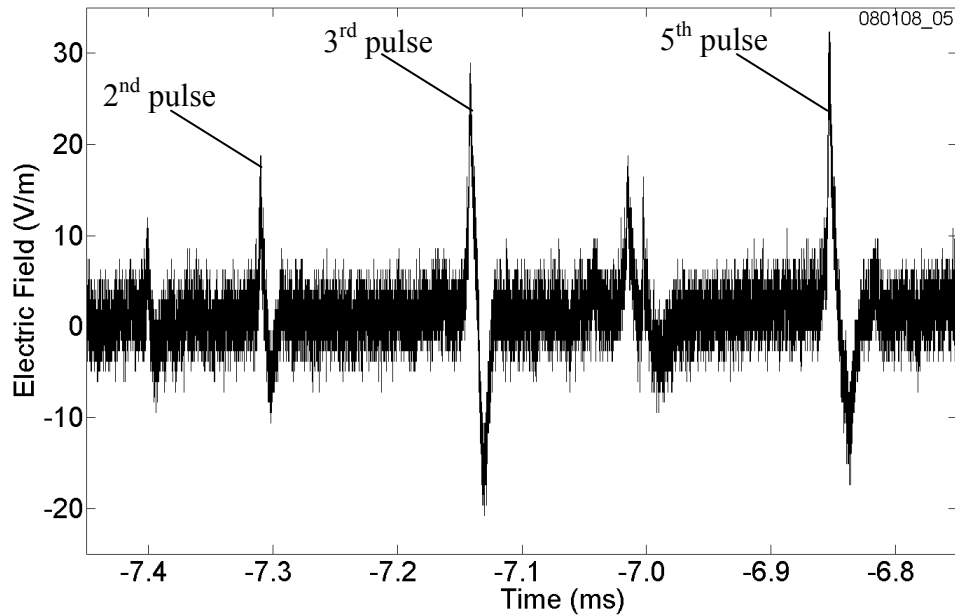


Figure 5-17. The electric field record of the PB pulse train of a negative cloud-to-ground discharge that occurred on August 1, 2008 in Gainesville, Florida at a distance of 28 km from the measuring station. The PB pulse train consisted of five detectable pulses with the signal-to-noise ratio for the second, third, and fifth pulses being better than the first and fourth pulses in the train.

can be accurately estimated. Distant electric and magnetic field measurements (in which the field change is essentially radiation) of PB pulses with high signal-to-noise ratio with each pulse preferably occurring at a known horizontal distance is required to obtain reliable results using this method.

In this study, we examine variations in occurrence of PB pulse trains in CG flashes. Assuming that the PB pulse train is a manifestation of interaction of a downward-extending negative leader channel with the LPCR, we qualitatively examine the inferred dependence of lightning type on the magnitude of this charge region. The result is a set of conceptual scenarios that can be tested by future observations.

5.3.2 Analysis and Discussion

5.3.2.1 Generation of preliminary breakdown pulse train

Figure 5-18 (left panel) shows the vertical components of electric field vectors, E_N and E_{LP} , due to the main negative and lower positive cloud charge regions, respectively. Between the negative and positive charge regions, E_N and E_{LP} are in the same direction and hence electric field is enhanced due to the presence of the LPCR. On the other hand, in the region below the LPCR E_N and E_{LP} are in opposite directions and hence the field is reduced. It follows that a descending leader originating at the lower boundary of main negative charge region would be initially accelerated and then (after traversing the LPCR) decelerated due to the presence of the LPCR. This scenario appears to be consistent with description of β -type leader [Schonland, 1956], which exhibits a higher speed near the cloud base and a lower speed at lower altitudes (although it does accelerate near ground). The initial part of the β -type leader is associated with pronounced electric field pulses, which are the same as the PB pulses considered here.

In the following, we assume that the PB pulse train occurs when a descending negative leader encounters a significant LPCR and continues to propagate through it in a primarily downward direction. The negative leader is stepped, and the presence of positive space charge along its path is expected to intensify the steps, compared to the case of stepping in the absence of ambient space charge. When the LPCR is small or absent, the initiation of negative leader is essentially not assisted by the LPCR (such initiation would generally require a stronger negative-charge source) and no appreciable pulse train is produced. In this view, the occurrence of pronounced PB pulse train can be used as a proxy of existence of significant LPCR.

The initial polarity of PB pulses in negative ground discharges is the same as that of the following return-stroke pulse. In effect, both types of pulses (negative return-stroke pulse and PB

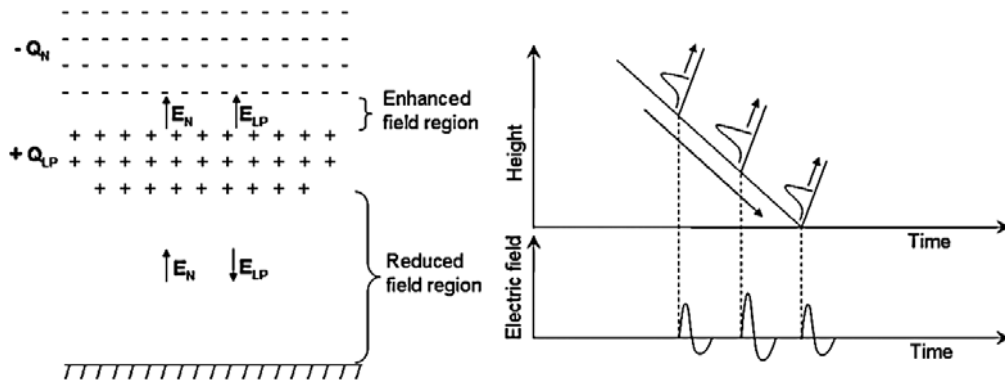


Figure 5-18. (left) A schematic illustration (not to scale) of electric field enhancement and reduction effects of the lower positive charge region (+ Q_{LP}) below the main negative charge region (- Q_N). The main positive charge region is not shown. Arrows indicate the direction of vertical components of electric field vectors. The total electric field is enhanced, ($E_N + E_{LP}$), between the negative and positive charge regions and reduced, ($E_N - E_{LP}$), below the positive charge region. (right, top) Schematic representation of preliminary breakdown stepping process in negative ground flashes. Negatively sloped arrow indicates the overall downward extension of negatively charged channel through the LPCR. Three steps giving rise to current (and light) pulses are shown. Each current pulse originates at the tip of downward-extending channel and propagates upward (positively-sloped arrows). (right, bottom) A sketch of expected electric field record of resultant wideband PB pulse train.

pulses) are due to a “recoil” process occurring when the negative leader channel comes in contact with ground (return-stroke pulse) or with progressively lower layers of the LPCR (PB pulses). Conceptually, the “recoil” process in the case of PB should be similar to the step-formation process optically observed in rocket-triggered lightning by *Wang et al.* [1999]. Based on this analogy, we schematically show in Figure 5-18 (right panel) the PB stepping process in the cloud and resultant electric field pulse train.

5.3.2.2 Variations in occurrence of preliminary breakdown pulse train

As noted in *Nag and Rakov* [2008], PB pulse trains are detected prior to the first return-stroke pulse in only about 18% of CG flashes in Florida. On the other hand, *Schulz and Diendorfer* [2006], who used a 12-bit measuring system set up at an electromagnetically quiet site in Austria, reported considerably larger percentage of ground flashes showing PB pulse trains. In their data set, 89% of 92 negative multiple-stroke flashes and 71% of 94 negative

single-stroke flashes (that is, 80% of 186 negative CG flashes) had detectable PB pulse trains. Further, *Gomes et al.* [1998] reported that essentially all electric field records of 41 negative CG flashes acquired in Sweden, contained detectable PB pulse trains, while the corresponding percentage for Sri Lanka was only 19%. It is important to note that the same instrumentation and methodology were used in both Sweden and Sri Lanka. *Ogawa* [1993] reported that 32 out of 89 (36%) CG flashes in Kyoto, Japan had electric field signatures indicative of PB pulse trains. *Clarence and Malan* [1957] found that out of their total 407 first-stroke electric field waveforms recorded at Johannesburg, South Africa, 16% were preceded by so-called “fast β -type leaders” (exhibiting pronounced PB pulses). They also observed “slow β -type leaders” that were characterized by small PB pulses and constituted 21% of their data set. If we combine both fast and slow β -type leaders, the percentage of flashes with detectable PB pulses in South Africa will be 37%. Recently, *Makela et al.* [2008] reported that at least 90% of CG flashes in southwest Finland exhibited PB pulse trains.

Percentage of flashes with detectable PB pulse trains as a function of latitude is shown in Figure 5-19a and discussed next. If the PB pulse train were indeed an indication of the presence of a significant LPCR in the thundercloud, the detection of PB pulse trains in the majority of negative ground discharges in Sweden, Finland, and Austria compared to just about 20% of negative ground discharges in Florida and Sri Lanka, 16 to 37% in South Africa, and 36% in Japan could be interpreted as being due to the more frequent presence of a significant LPCR at higher latitudes than at relatively low ones. This could be due to more intense corona at ground (which we assume to be a significant, if not dominant, source of the LPCR) at higher latitudes. This hypothesis is consistent with the work of *Chauzy and Soula* [1999] who used measured electric fields and numerical modeling to estimate the amount of charge produced by corona

during thunderstorms in Florida (lower latitude) and in southwestern France (higher latitude). The corona-produced positive charge at ground level over a 10 x 10 km² area varied from 63 to 124 C (94 C on average) in Florida and from 106 to 362 C (214 C on average) in southwestern France; that is, the average positive charge at the higher-latitude location was found to be more than twice larger than at the lower-latitude one (although the higher terrain in France could have also been a factor). Further, it is known that the height of the main negative charge region, shown to be between the 0°C and -15°C isotherms in Figure 5-19b, above ground tends to be smaller at higher latitudes [e.g., *Rakov and Dulzon, 1984*], as seen in Figure 5-19b. This can increase electric field at ground and make positive corona production at ground more efficient (due to the cubic dependence of corona current on surface electric field) at higher latitudes.

5.3.2.3 Type of discharge versus magnitude of lower positive charge region

We now discuss four conceptual scenarios (shown in Figure 5-20, left panel) that may arise depending upon the magnitude of the LPCR when a negative leader channel extends downward from the negative charge region. Examples of expected electric field signatures for these scenarios are shown in the right panel of Figure 5-20. The field signatures were recorded in Gainesville, Florida, and interpreted as resulting from proposed scenarios, although no information on cloud charge structure was available.

When the magnitude of LPCR is abnormally large, say, comparable in magnitude to that of main negative charge, as shown in Figure 5-20A (left panel), inverted IC discharges are expected to occur. This type of discharge bridging the main negative and abnormally large lower positive charge regions have been reported by *Qie et al. [2005]*. In this scenario, a descending negative leader would likely change its direction of propagation to predominantly horizontal [*Coleman et al., 2008*], interact with the LPCR, and be unable to forge its way to ground. The result is an inverted IC flash. VHF imaging presented by *Tessendorf et al. [2007]* indicates that the LPCR

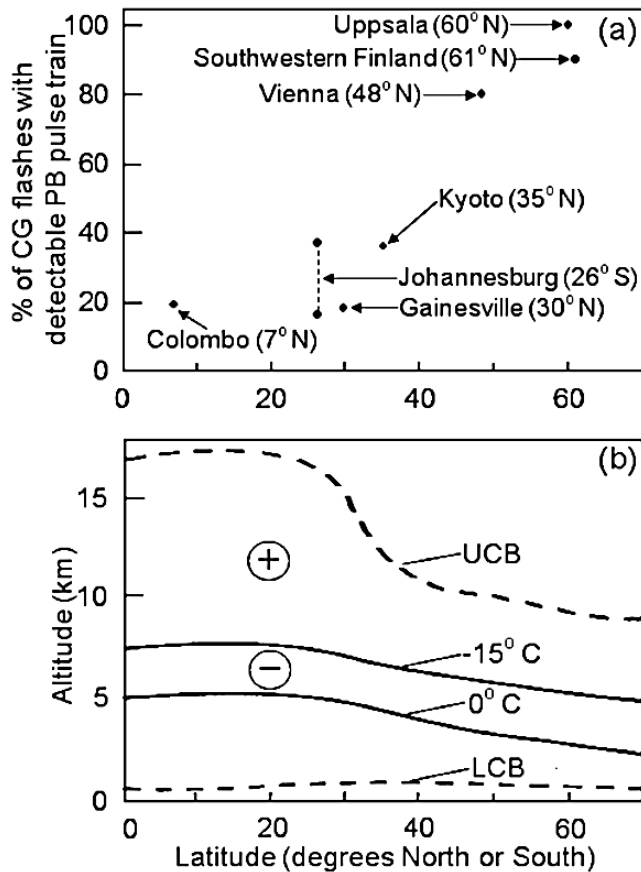


Figure 5-19. (a) Percentage of flashes with detectable PB pulse train and (b) altitudes of the upper cloud boundary (UCB), the main negative charge region (assumed to be between the 0°C and -15°C isotherms), and the lower cloud boundary (LCB) [Rakov and Dulzon, 1984], each as a function of latitude. The altitudes are averages for the Northern Hemisphere in July, but assumed to be applicable, as a first approximation, to the Southern Hemisphere as well. Note that the lower percentage of flashes with detectable PB pulse train appears to be associated with higher altitude of main negative charge region above ground and vice versa.

appears to be vertically deeper and to have a larger horizontal extent when such IC flashes occur.

An example of expected electric field signature of such a discharge is shown in Figure 5-20A

(right panel), which exhibits a PB pulse train followed by static field change some tens of milliseconds in duration, indicative of an inverted IC flash (attempted cloud-to-ground leader;

Section 5.2). If the lightning channel emerges from the cloud, it can be viewed as an "air

discharge" or even as a "spider" lightning, if it develops over a large distance near the cloud

base.

Figure 5-20B (left panel) shows the scenario where the magnitude of the LPCR is somewhat smaller than in scenario A. Similar to scenario A, a negatively-charged leader channel extending vertically from the main negative charge region would become predominantly horizontal, but would eventually make termination on ground. In this case, the discharge can be viewed as a hybrid flash (an IC followed by a CG). Such flashes (with IC durations ranging from a few tens to over 100 ms) were examined by *Coleman et al.* [2008]. The electric field signature expected for this type of discharge is shown in Figure 5-20B (right panel), which shows a PB pulse train followed by a field change characteristic of a cloud discharge lasting for about 50 ms, followed by the first return stroke waveform of a CG flash.

If the magnitude of the lower positive charge relative to the main negative charge is even smaller, as shown in Figure 5-20C (left panel), the descending negative leader would traverse the positive charge region and continue to propagate in a predominantly vertical direction to ground. The electric field signature expected to be produced in this case is shown in Figure 5-20C (right panel). It exhibits a PB pulse train and stepped-leader waveform followed by the first return stroke (RS) waveform. Leader duration, found as the time interval between PB and RS, is about 20 ms. Negative stepped leaders that are characterized by very short (a few milliseconds) durations and, by inference, very high speeds ($\sim 10^6$ m/s versus typical $\sim 10^5$ m/s) also belong to this category. In this latter case, the lower positive charge is either entirely consumed by the negative leader or whatever remains of it is incapable of decelerating this leader. Very fast stepped leaders, which are probably associated with very strong negative-charge sources, were observed in different geographical locations, in different seasons, and both over water and over land [e.g., *Clarence and Malan*, 1957; *Heavner et al.*, 2002; *Frey et al.*, 2005]. In Florida, only

about 5% of stepped leaders are shorter than 5 ms, suggesting that such very fast stepped leaders are relatively rare.

Figure 5-20D (left panel) shows the scenario when the LPCR is insignificant. This scenario is similar to scenario C, except for the LPCR playing essentially no role in negative leader initiation. The electric field signature produced in this case is expected to be that of a stepped leader/return stroke sequence not preceded by a detectable PB pulse train, as shown in Figure 5-20D (right panel).

5.4 Summary

Lightning events exhibiting pulse trains that are characteristic of preliminary breakdown in negative cloud-to-ground discharges, but are not followed by return stroke waveforms, are assumed to be manifestations of attempted cloud-to-ground leaders. Preliminary breakdown pulse trains in negative cloud-to-ground discharges and in attempted leaders were examined. Both “classical” (having durations of tens of microseconds) and “narrow” (having durations of a few microseconds) pulses were found in both types of pulse trains. However, submicrosecond-scale pulses were only observed in preliminary breakdown pulse trains of ground discharges. The arithmetic mean pulse duration and interpulse interval for preliminary breakdown pulse trains in cloud-to-ground discharges were found to be 4.8 and 65 μs , respectively, versus 17 and 73 μs for attempted cloud-to-ground leaders. This implies that preliminary breakdown pulse trains in ground discharges contain a larger fraction of “narrow” ($\leq 4 \mu\text{s}$) pulses than the pulse trains in attempted cloud-to-ground leaders.

The majority of pulses occurring in PB pulse trains prior to the first return stroke in cloud-to-ground discharges are typically small in both amplitude and duration. Amplitudes of these most common pulses are 50% or less than that of the largest pulse, and their durations are less than or equal to 4 μs . A significant fraction (22%) of examined pulses had total durations less

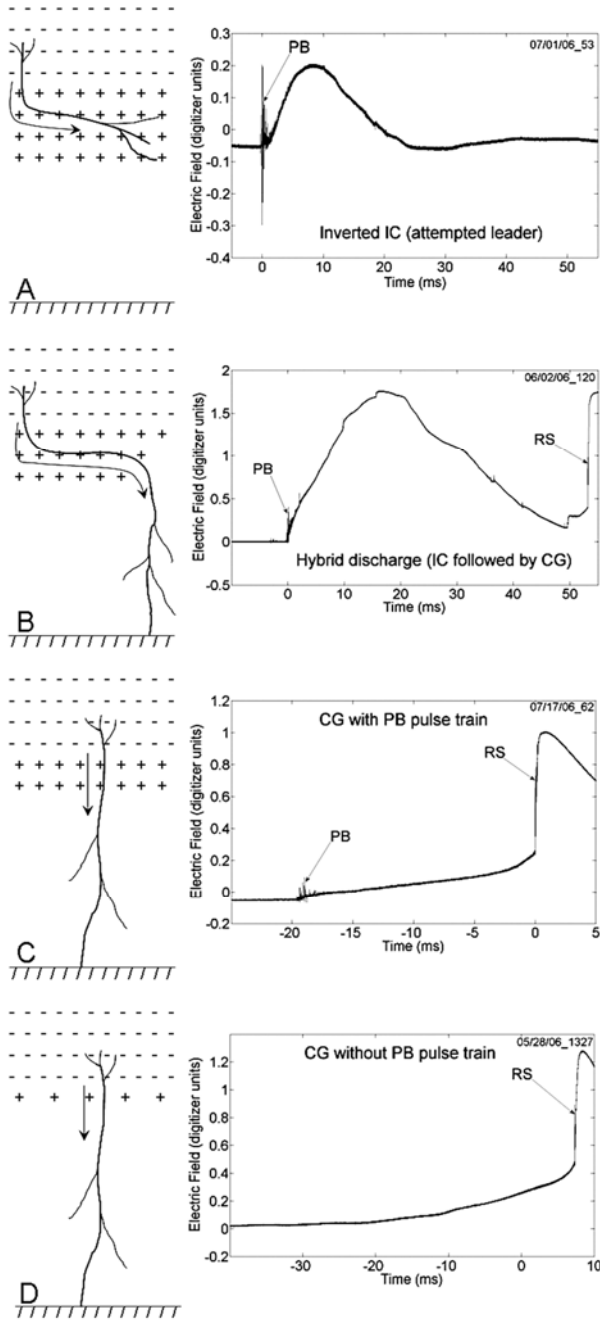


Figure 5-20. (left) Schematic representation of four types of lightning, A–D, that may arise depending upon the magnitude of the LPCR. The charge configuration in each of the scenarios represents only its vertical profile (no lateral boundaries are shown). Arrows indicate the direction of propagation of negative leader. (right) The corresponding examples of expected electric field signatures. The field waveforms are from four different thunderstorms recorded at some tens of kilometers in Gainesville, Florida, using the same instrumentation with a decay time constant of 10 ms. PB = preliminary breakdown pulse train; RS = return-stroke waveform.

than 1 μs . The largest pulses in the preliminary breakdown pulse train can exceed in magnitude the following first return-stroke pulse. Pulses with larger durations ($>4 \mu\text{s}$) tend to occur earlier in the train.

Almost half (46%) of the PB pulse trains in attempted leaders were found to have minimum pulse durations in the range of 1–2 μs . Smaller and narrower pulses tended to occur at the onset and toward the end of each pulse train. In addition to bipolar pulses with positive (atmospheric electricity sign convention) initial half-cycle, negative unipolar and negative (initial half-cycle) bipolar pulses were sometimes seen toward the end of the train. It is possible that some of the attempted leaders could also be classified as “inverted intracloud flashes,” occurring between the main negative and lower positive charge regions. In this latter case, the lower positive charge can be viewed as “blocking” the progression of descending negative leader from reaching ground and thus “converting” the potential cloud-to-ground flash to an intracloud one.

The PB pulse train appears to be generated when a negatively-charged channel extends downward from the main negative charge region and encounters an appreciable LPCR. When the LPCR is small no PB pulse train may be produced. In this view, the fact that in some negative CG flashes no PB pulse train is detectable could be due to insignificant LPCR. It appears that at higher latitudes a larger percentage of CG discharges exhibit detectable PB pulse trains than at lower latitudes. This implies that a significant LPCR (or its portion originating from corona at ground) is present in thunderclouds more often at higher latitudes than at relatively low latitudes. While the LPCR may serve to enhance the electric field at the bottom of the negative charge region and thereby facilitate the launching of a negatively-charged leader toward ground, presence of excessive LPCR may prevent the occurrence of negative CG flashes by “blocking”

the progression of descending negative leader from reaching ground. Four conceptual lightning scenarios are inferred that may arise depending upon the magnitude of the LPCR.

CHAPTER 6
TWO-STATION MEASUREMENTS OF CLOUD-TO-GROUND LIGHTNING ELECTRIC
FIELDS

6.1 Introduction

In this chapter, the fine structure of electric field waveforms produced by first return strokes in negative cloud-to-ground lightning is examined. As discussed in Chapter 2, the initial rising part of return stroke electric field waveforms can be separated into two phases. The first one is the so-called “initial slow front” or simply “slow front”, described by *Weidman and Krider* [1978] as an initial portion or front, which for first strokes rises slowly for 2–8 μs to about half the field peak. The second part which follows the slow front is an abrupt transition to peak, typically referred to as the “fast transition”. The latter, according to *Weidman and Krider* [1978], has a 10-to-90% risetime of 0.2 μs or less for first strokes, when the field propagation was over seawater. [*Weidman and Krider*, 1980 give a 10-to-90% risetime of 0.1 μs for propagation over seawater]. The shape of the slow front is typically concave, although *Weidman and Krider* [1978] do report some convex slow fronts.

Return-stroke models [e.g., *Rakov and Uman*, 1998] are used to relate the channel base current to the current distribution along the channel, which, in turn, can be used to calculate return-stroke electric and magnetic fields. Specifically, the transmission line (TL) model [*Uman and McLain*, 1969] has been demonstrated to work reasonably well in reproducing both close [e.g., *Schoene et al.*, 2003] and relatively distant [e.g., *Willett et al.*, 1988] fields for the first few microseconds of strokes in rocket-triggered lightning (which are thought to be similar to natural negative lightning subsequent strokes).

The slow-front current in first strokes has often been attributed to the presence of an upward connecting leader [e.g., *Rakov and Uman*, 2003, p. 144]. *Weidman and Krider* [1978] noted that “the shapes and relative amplitudes of the fronts and fast transitions in the current

waveforms are surprisingly similar to those in the radiated fields'' (currents and fields being measured in different studies), perhaps indicating that the TL model, with the equivalent current waveforms starting at ground level and propagating upward, might be applicable to computing both the slow front and fast transition of natural-lightning first-stroke fields. On the other hand, there are experimental data [Willett *et al.*, 1989a, p. 13,283], although for triggered-lightning strokes, which suggest that radiation field waveforms can exhibit pronounced slow fronts without similar features in corresponding current waveforms. Weidman and Krider [1978] considered the possibility that the slow front in radiation field waveforms of return strokes is due to an upward connecting discharge. They estimated that such a discharge would appear to have a length in excess of 100 m and a peak current of the order of 10 kA or more. According to Thottappillil and Uman [1993], who examined measured current and electric field waveforms of negative return strokes from rocket-triggered lightning, the slow front at the beginning of the return stroke current waveform could be due to an upward propagating positive streamer or streamers, and not due to the return stroke. Using the modified Diendorfer-Uman model, they showed that a better agreement between initial peaks of calculated and measured radiation fields of a rocket-triggered lightning return stroke with a current waveform containing a slow front could be obtained if the return stroke velocity was assumed to increase exponentially with height. Cooray *et al.* [2004] used the travelling current source type model and associated the slow front in the incident channel base current waveform with the upward connecting leader.

Jerauld et al. [2007], showed, using an unusual triggered-lightning stroke, that both close and distant fields can be predicted by a version of the TL model in which both the slow-front and fast-transition currents are generated at the junction point of the upward and downward leaders and propagate away from that point, a model that is more physically reasonable than the model

assuming that the current is generated at ground level. According to *Jerauld et al.* [2007] the source of the slow fronts observed in the currents and in the distant radiation fields of natural first strokes is likely to be the slow fronts in a pair of microsecond-scale current waves propagating in opposite directions from the junction of the descending and upward connecting leaders at a speed on the order of 10^8 m/s. The current waves have magnitudes of up to some tens of kiloamperes. However, *Jerauld et al.* assumed that the initial downward wave exhibits no reflection at ground which is unrealistic [e.g., *Rakov et al.*, 1998].

In this chapter we examine the shapes and relative magnitudes of slow fronts and fast transitions in electric field waveforms of first return strokes in negative cloud-to-ground lightning measured simultaneously at two stations, one at about 45 km (far station), and the other at hundreds of meters to a few kilometers (near station) from the lightning channel. We examine, via modeling, whether electric field waveforms can exhibit pronounced slow fronts without similar features in corresponding current waveforms. Further, model predicted return stroke electric field waveforms produced at close and far distances due to two current waves moving in opposite directions (up and down) from a junction point tens of meters above ground are presented. The effect of reflection of the downward moving wave from ground is also examined.

6.2 Measured Electric Field Waveforms

In 2007 and 2008, five natural negative cloud-to-ground lightning discharges were simultaneously measured at Camp Blanding and in Gainesville, Florida, which are 45 km apart. Table 6-1 summarizes the data available at both stations. The Camp Blanding data was acquired and provided by Joseph Howard, Dustin Hill, and Christopher Biagi. Flash identification (ID) numbers for both Camp Blanding and Gainesville stations are given. In this chapter, flashes are referred to by their Gainesville flash ID. Note that the electric field waveform of the first return

stroke in flash 100507_470 was saturated at the far (Gainesville) station due to its relative large magnitude and is not examined here any further.

The return stroke electric field at the near station is expected to be dominated by its electrostatic component, while that at the far station is expected to be essentially radiation. Figures 6-1 to 6-4 show the overall electric field records of the four flashes obtained at the two stations. Note that for flash 070608_020, which contained six return strokes, only the first and the third strokes were recorded at Gainesville. The electric field waveforms of the first leader-return stroke sequence of each flash measured at the near and far stations are shown in Figures 6-5 to 6-8. Figures 6-9 to 6-12 show initial rising portions of the first strokes at the two stations overlaid for direct comparison. The electric field waveforms were amplitude normalized by setting the radiation field peaks of corresponding return strokes at the two stations to be approximately equal to unity. It can be seen from Figures 6-9 to 6-12 that the initial rising portions of the near and far field return stroke waveforms for all four first strokes are generally in good agreement with each other up to the initial (predominantly radiation) field peaks.

Characteristics of the first return stroke electric field waveforms at the two stations are summarized in Table 6-2. The AM and GM zero-to-peak risetimes for the four first strokes were 7.2 μs and 6.6 μs , respectively, at the near station, and 7.0 μs and 6.5 μs , respectively, at the far station. The AM and GM 10-to-90% risetimes for the four first strokes were 4.9 μs and 4.6 μs , respectively, at the near station, and 4.0 μs and 3.6 μs , respectively, at the far station. Out of the four first strokes, three strokes displayed the two distinct phases of the slow front and fast transition while for the first stroke of flash 070608_020, a distinct slow front phase is not seen probably due to overlap with the final leader step, as seen in Figure 6-16. Figures 6-12 to 6-16 show the magnitudes of the radiation field peak, slow front, and fast transition for each return

Table 6-1. Summary of natural lightning fields simultaneously measured at Camp Blanding and in Gainesville, Florida.

Flash ID	Camp Blanding					Gainesville			
	Measuring station	Distance (for first stroke), km		E	dE/dt	Flash ID	Distance (for first stroke), km	E	dE/dt
		TOA ^a	NLDN ^b						
MSE 07-05	E4	508	263 (400)	Y	Y	073107_1252	46	Y	Y
MSE 07-06	E4	979	704 (400)	Y	Y	100407_360	46	Y	Y
MSE 07-07	E4	834	-	Y	Y	100507_470	45	Y ^c	Y
MSE 08-01	E11 and E18	81 and 667	3604 and 2962 (400)	Y	Y	070508_008	48	Y	Y
MSE 08-02	E18	-	1520 (500)	Y	Y	070608_020	46	Y	Y

^a Determined using the time of arrival (TOA) technique accurate to about 100 m. [Howard, 2009 and Hill, 2009, personal communication]. ^b Determined using NLDN-estimated locations. The values in the parentheses indicate the semi-major axis length of the NLDN 50% location error ellipse (the median location error). ^c Saturated.

stroke in the dataset presented here. For two first return strokes (in flashes 073107_1252 and 070508_008, shown in Figures 6-13 and 6-15, respectively) the slow front appears to be concave at both the near and far stations, while for one first strokes (in flash 100407_360, shown in Figures 6-14), the slow front appears to be convex at both stations. Note that for flash 100407_360, the small change in slope from the relatively slow convex portion of the return stroke waveform to the fast rising portion was used to determine the duration and magnitude of the slow front. The AM and GM slow front durations for the three first strokes were 4.6 μ s and 4.3 μ s, respectively, at the near station, and 4.3 and 4.0 μ s, respectively, at the far station. The amplitude of the slow front was, on average, 47% of the peak at the near station and 35% of the peak at the far station. The AM and GM 10-to-90% risetimes for the fast transition were both 0.6 μ s at the near station versus 0.9 μ s at the far station. From the above discussion it is evident that the overall field waveform characteristics of first return strokes up to the radiation field peak are

similar for near (where the electric field is dominated by its electrostatic component) and far (where the electric field change is essentially radiation) distances.

Similar field waveform characteristics have been reported from single-station measurements at distances ranging from 1 to 200 km for negative first return strokes by other researchers. *Master et al.* [1984] reported the AM zero-to-peak and 10-to-90% risetimes for 105 first strokes in negative cloud-to-ground discharges in Florida to be 4.4 μs and 2.6 μs , respectively. Their AM slow front duration was 2.9 μs . *Weidman and Krider* [1978] reported the AM slow front duration for 62 negative first return strokes in Florida to be 4 μs . *Cooray and Lundquist* [1982] found the AM duration of the slow front for negative first strokes in Sweden to be 5 μs . The AM 10-to-90% risetime of the fast transition for negative first strokes in Florida was reported to be 0.97 μs and 0.2 μs by *Master et. al* [1984] and *Weidman and Krider* [1978], respectively. The AM slow front magnitude relative to peak for negative first strokes was reported to be 28%, 41%, and 50% by *Master et al.* [1984], *Cooray and Lundquist* [1982], and *Weidman and Krider* [1978], respectively. These values are comparable to the AM value of 47% (near station) and 35% (far station) found for return strokes in our dataset.

Jerauld et al. [2009], who examined electric and magnetic fields from an unusual cloud-to-ground lightning flash containing two positive strokes followed by four negative strokes, compared the magnetic field of their first positive stroke measured at 288 m (see Figure 6-17) to the electric field measured a distance of 45 km by the Los Alamos Sferic Array (LASA) (see Figure 6-18). They found the close and distant waveforms to be remarkably similar during the slow front and the fast transition, up to the time of the return stroke peak as seen in Figure 6-19.

For each stroke in the four flashes recorded at both near and far stations, Table 6-3 gives the measured initial (radiation) field peaks along with the NLDN-estimated peak currents. The

Table 6-2. Characteristics of electric field waveforms produced by negative first return strokes measured at near (Camp Blanding) and far (Gainesville) stations.

Flash ID	Zero-to-peak risetime, μs		10-90% risetime, μs		Slow front duration, μs		Slow front magnitude relative to peak, %		Fast-transition 10-90% risetime, μs	
	Near	Far	Near	Far	Near	Far	Near	Far	Near	Far
073107_1252 (Figure 6-1)	6.6	6.4	3.7	2.4	6.0	5.3	43	18	0.4	1.1
100407_360 (Figure 6-2)	3.9	3.7	2.8	2.6	2.7	2.3	49	44	0.9	0.7
070508_008 (Figure 6-3)	6.1	6.5	5.2	4.0	5.0	5.3	49	44	0.5	0.9
070608_020 (Figure 6-4)	12.3	11.4	8.0	7.0	-	-	-	-	-	-
Sample Size	4	4	4	4	3	3	3	3	3	3
AM	7.2	7.0	4.9	4.0	4.6	4.3	47	35	0.6	0.9
GM	6.6	6.5	4.6	3.6	4.3	4.0	47	33	0.6	0.9

far field distance is approximately 45 km. The near field distance for the first strokes of flashes 073107_1252 and 100407_360 were determined using the Camp Blanding multiple-station network and the time of arrival (TOA) technique by *Howard* [2009, personal communication] and are accurate to about 100 m. The second and third strokes of flash 073107_1252 were most likely along the same channel as the first stroke (NLDN-estimated locations for the three strokes are within 900 m of each other) and hence were at the same distance from the near field measuring station. For flash 070508_008, the distance was estimated using the TOA technique by *Hill* [2009, personal communication], while for flash 070608_020, this technique did not yield accurate results. Flashes 070508_008 and 070608_020 were probably either at the edge of the Camp Blanding field measuring network or outside its perimeter. Note that TOA and NLDN-estimated distances are in reasonable agreement for flashes 073107_1252 and 100407_360, while for flash 070508_008, they are different. The reason for this discrepancy in presently

unknown. In this chapter, NLDN-estimated locations, which are probably accurate to about 200 m [Nag *et al.*, 2008], are used for flashes 070508_008 and 070608_020.

The radiation field component of vertical electric field is approximately inversely proportional to distance. As a result, the ratio of near and far initial (radiation) field peaks is expected to be close to the inverse ratio of near and far field distances. However, one can see from Table 6-3 that out of the 8 negative return strokes recorded at the two stations, the two ratios are equal for only one event (stroke 3 of flash 073107_1252). Figure 6-20 shows the scatter plot for ratio of near and far initial (radiation) field peaks versus inverse ratio of near and far field distances. This deviation from the expected inverse proportionality dependence of the radiation field peak on distance may be attributed to contributions from electrostatic and induction field components to the measured initial field peak at the near station and to propagation effects. Also, the initial field peak at the near station is often not well defined (see, for example, Figures 6-14 and 6-16).

The scatter plot for NLDN-estimated peak current versus initial (radiation) field peak normalized to 100 km for 8 negative return strokes recorded at Camp Blanding (near station) and Gainesville (far station) is shown in Figure 6-21. Note, that for the third stroke in flash 073107_1252, whose NLDN-estimated peak current is 19 kA, the initial field peak normalized to 100 km obtained from both near and far field measurements is equal to 5.2 V/m and hence the corresponding points in the plot overlap. One can see from Figure 6-21 that the scatter for the normalized initial field peaks at the near station is larger than that at the far station. This further points to the fact that the measured initial field peak at the near station is affected by uncertainties in identifying those peaks in electric field waveforms and contributions to the peaks from electrostatic and induction field components.

Table 6-3. Initial (radiation) electric field peaks for each stroke in four flashes recorded at near (Camp Blanding) and far (Gainesville) stations. Also given are the NLDN-estimated peak currents, ratios of near and far field peaks, and inverse ratios of near and far field distances.

Flash ID	Stroke order	NLDN-estimated peak currents (absolute values), kA	Near field distance, m	NLDN-estimated far field distance, km	Initial (radiation) field peak at near station, kV/m	Initial (radiation) field peak at far station, V/m	Ratio of near and far field peaks	Inverse ratio of near and far field distances
073107_1252	1	41.3		46	3.65	25.18	145	91
	2	12.9	508 ^a	46	1.13	7.36	154	91
	3	19.4		46	1.02	11.30	91	91
100407_360	1	92.3	979 ^a	46	5.28	42.47	124	47
070508_008	1	30.6	3604 ^b (400)	48	0.08	16.74	5	13
	2	11.5	611 ^b (1000)	45	1.18	9.29	127	74
070608_020	1	133.1	1520 ^b (500)	46	3.17	69.83	45	30
	3	22	3225 ^b (400)	48	0.52	11.72	45	15

^a Determined using the time of arrival technique [Howard, 2009], accurate to about 100 m.

^b Determined using NLDN-estimated locations. The values in the parentheses indicate the semi major axis length of the NLDN 50% location error ellipse (the median location error).

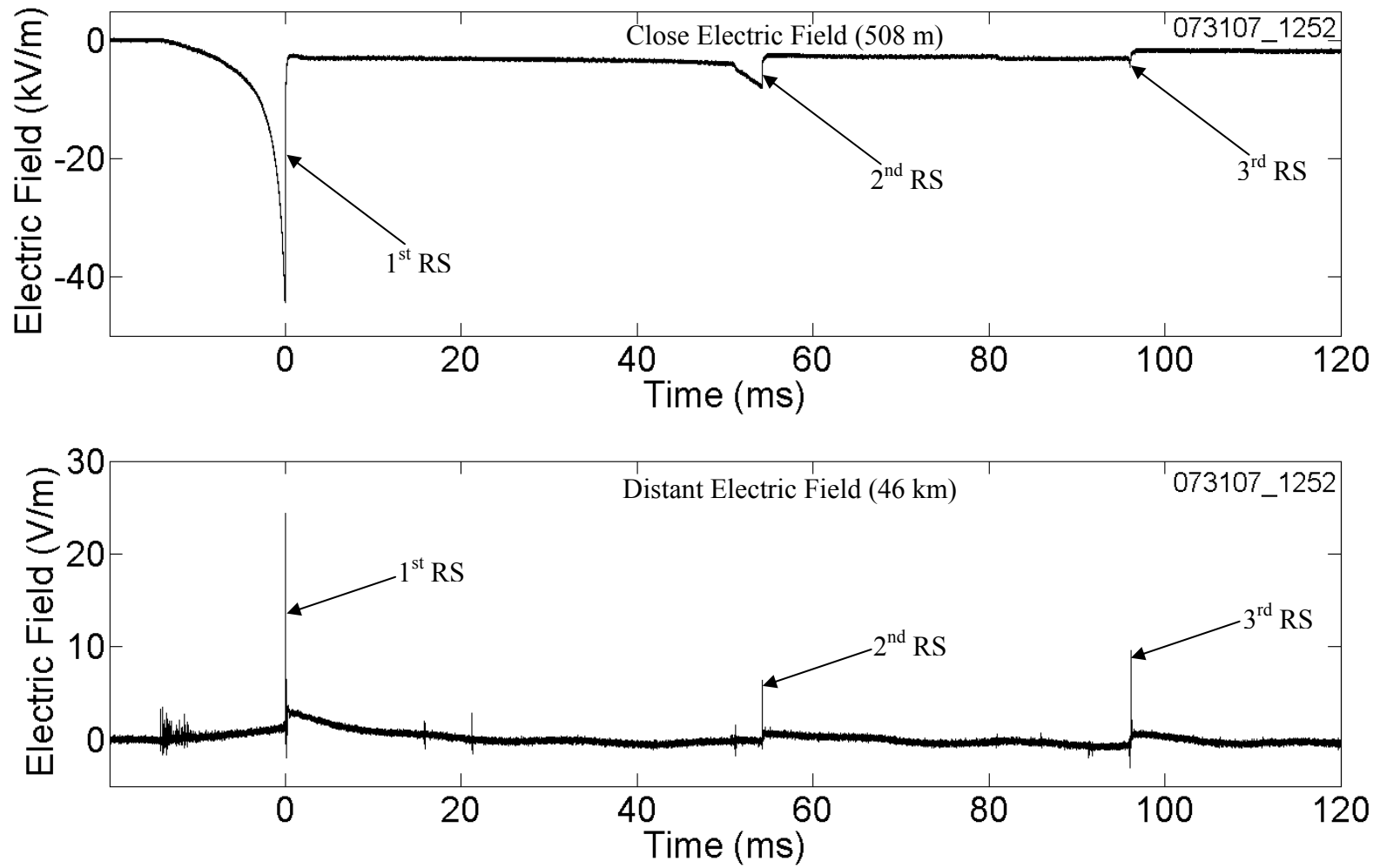


Figure 6-1. The electric field waveforms of three-stroke flash 073107_1252, measured at the near (top panel) and far (bottom panel) stations both shown on a 140 ms time scale.

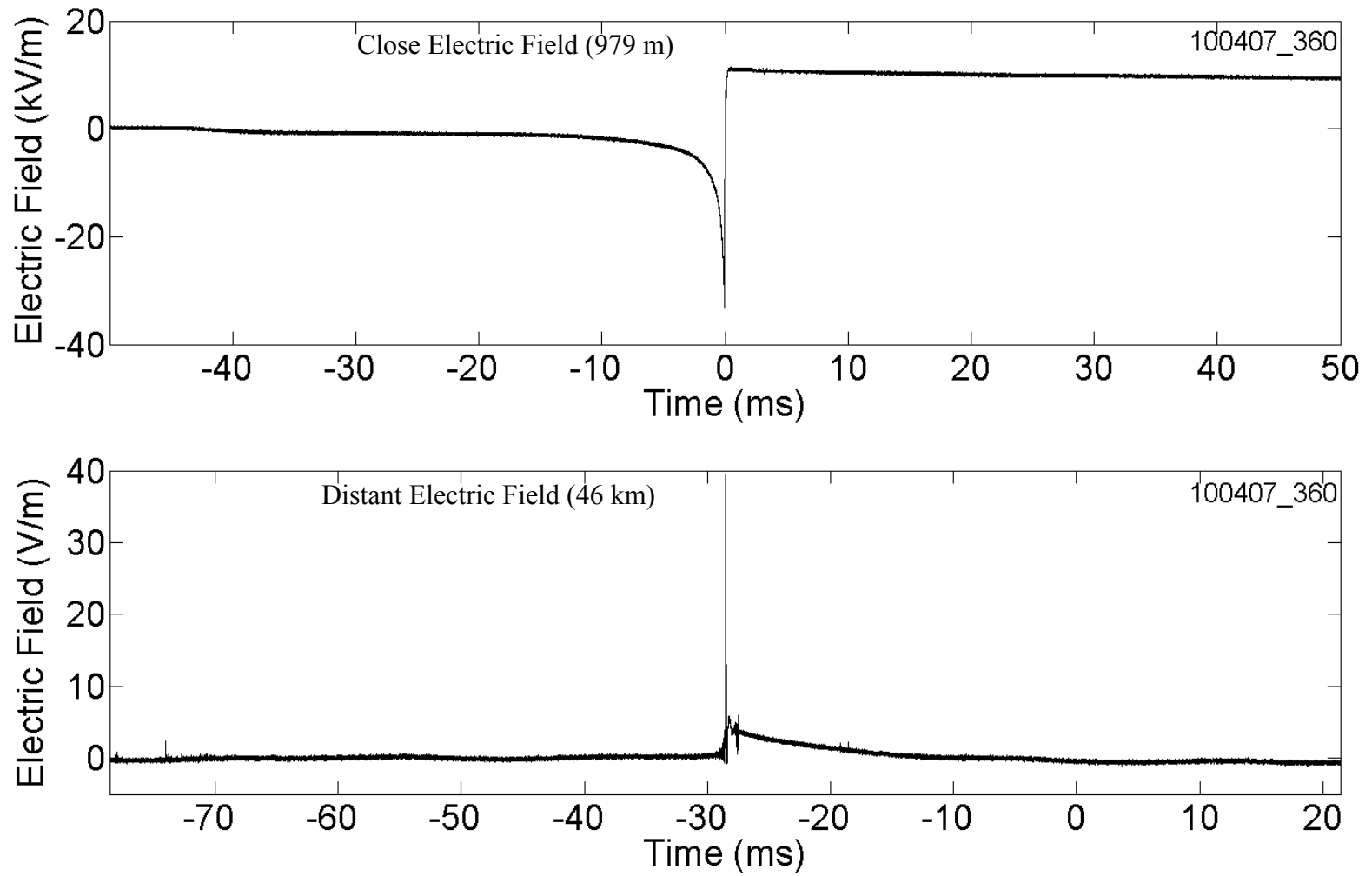


Figure 6-2. The electric field waveforms of single-stroke flash 100407_360, measured at the near (top panel) and far (bottom panel) stations both shown on a 100 ms time scale.

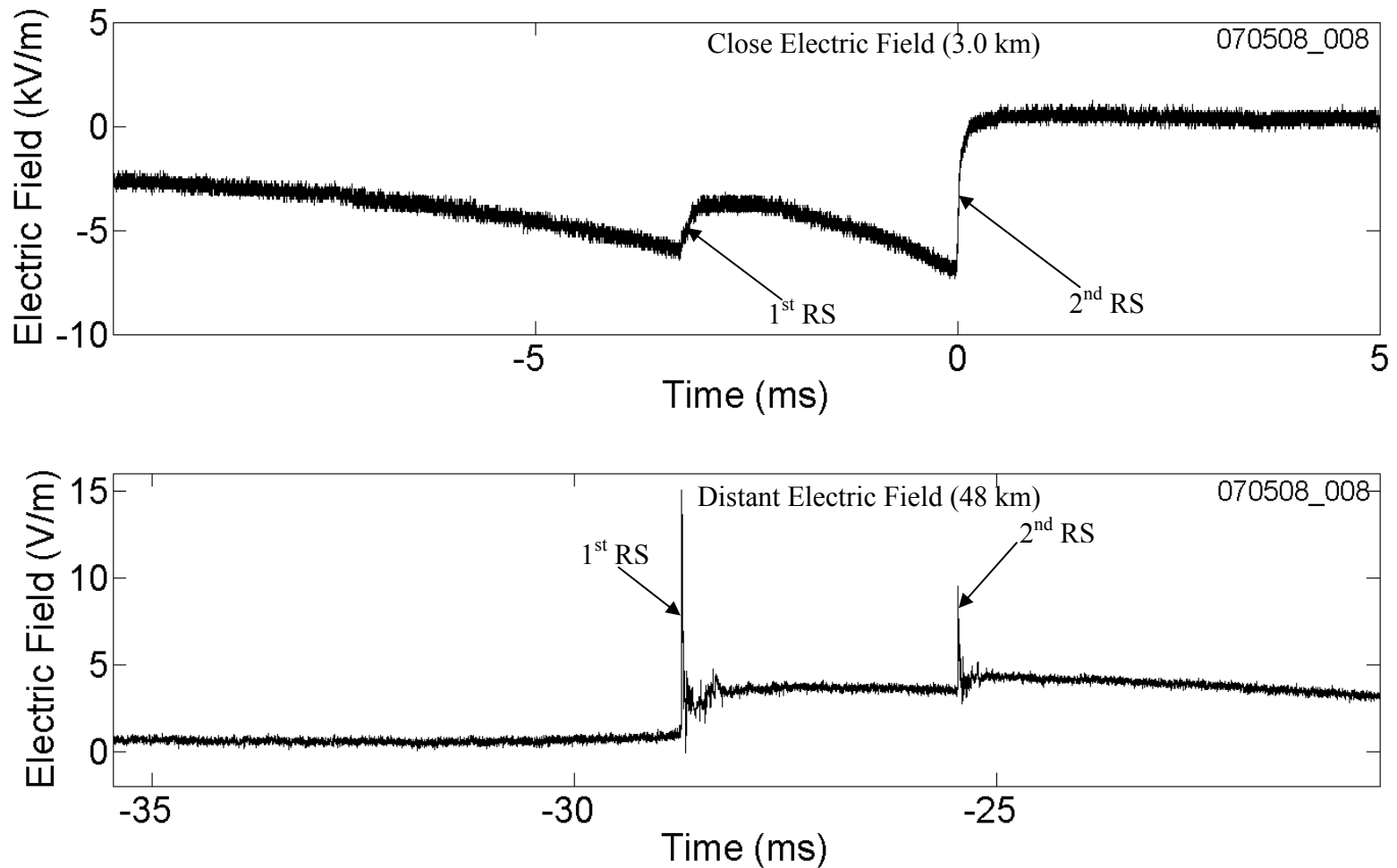


Figure 6-3. The electric field waveforms of a two-stroke flash 070508_008, measured at the near (top panel) and far (bottom panel) stations shown on a 15 ms time scale. Distance indicated is for the first stroke only.

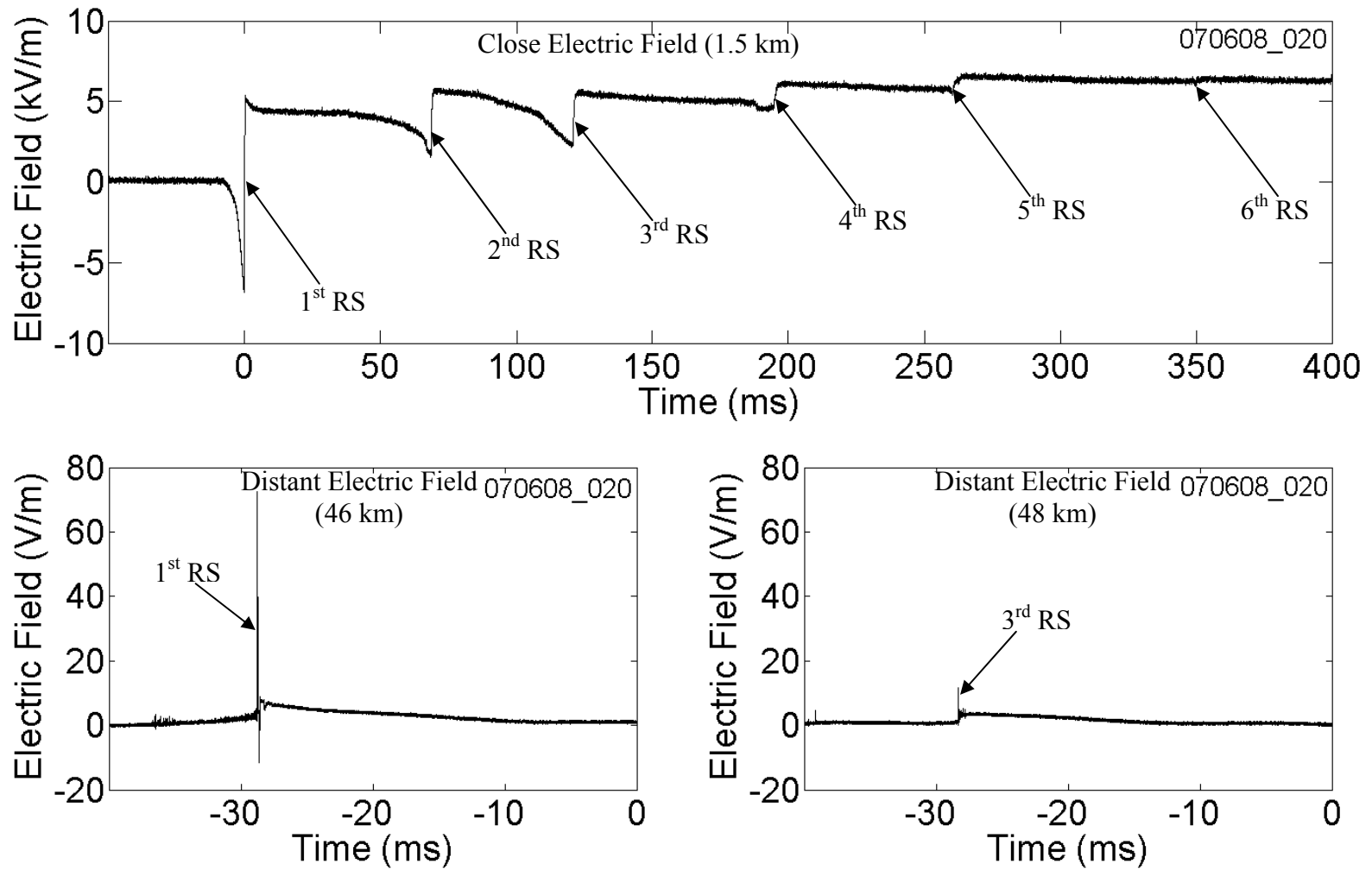


Figure 6-4. The electric field waveform of six-stroke flash 070608_020, measured at the near (top panel) station shown on a 450 ms time scale. Only the first and third return strokes were recorded at the far station, the electric field waveforms of which are shown in the bottom panels each on a 40 ms time scale.

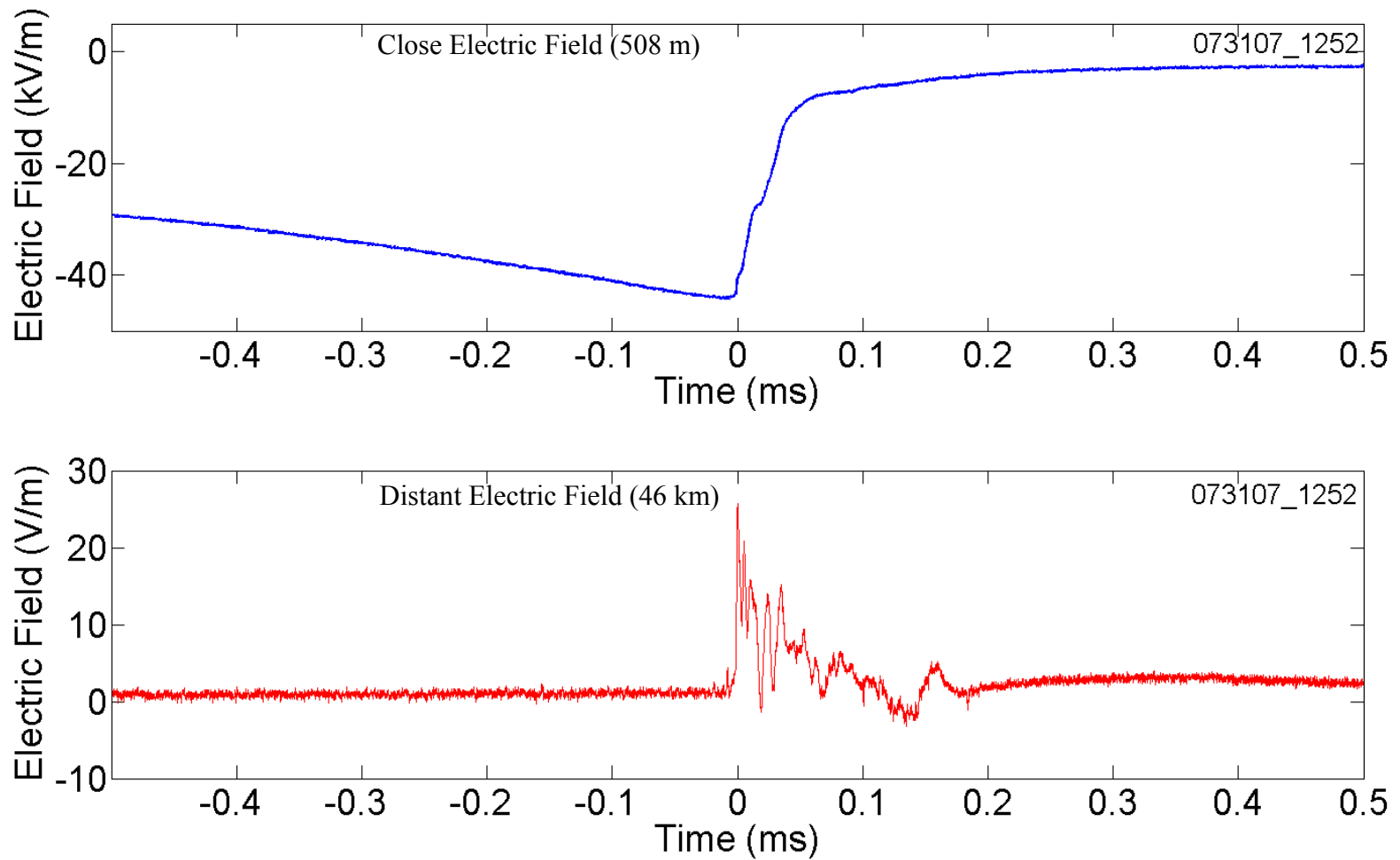


Figure 6-5. The electric field waveforms of the first return stroke of flash 073107_1252, measured at the near (top panel) and far (bottom panel) stations shown on a 1 ms time scale.

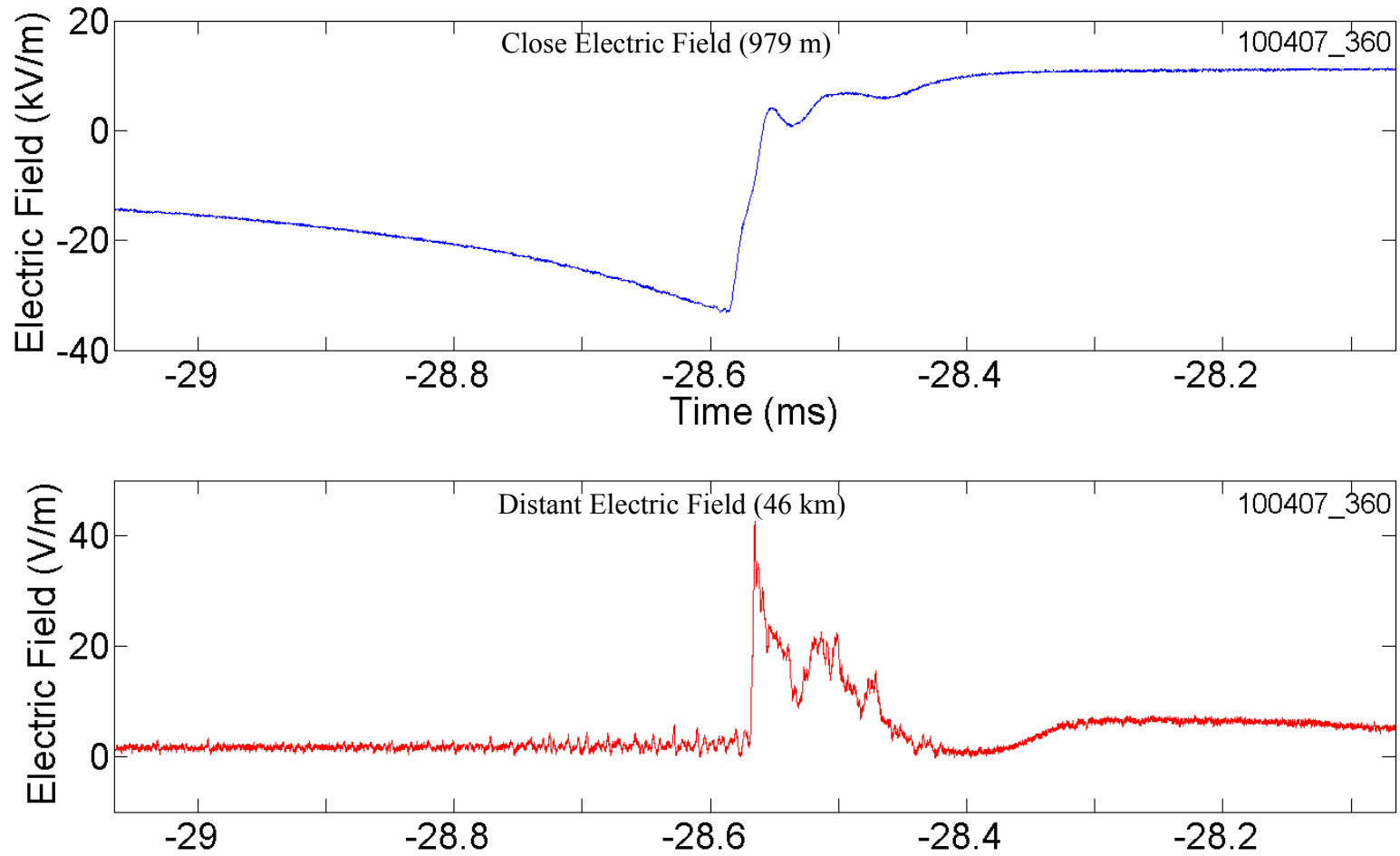


Figure 6-6. The electric field waveforms of the first return stroke of flash 100407_360, measured at the near (top panel) and far (bottom panel) stations shown on a 1 ms time scale.

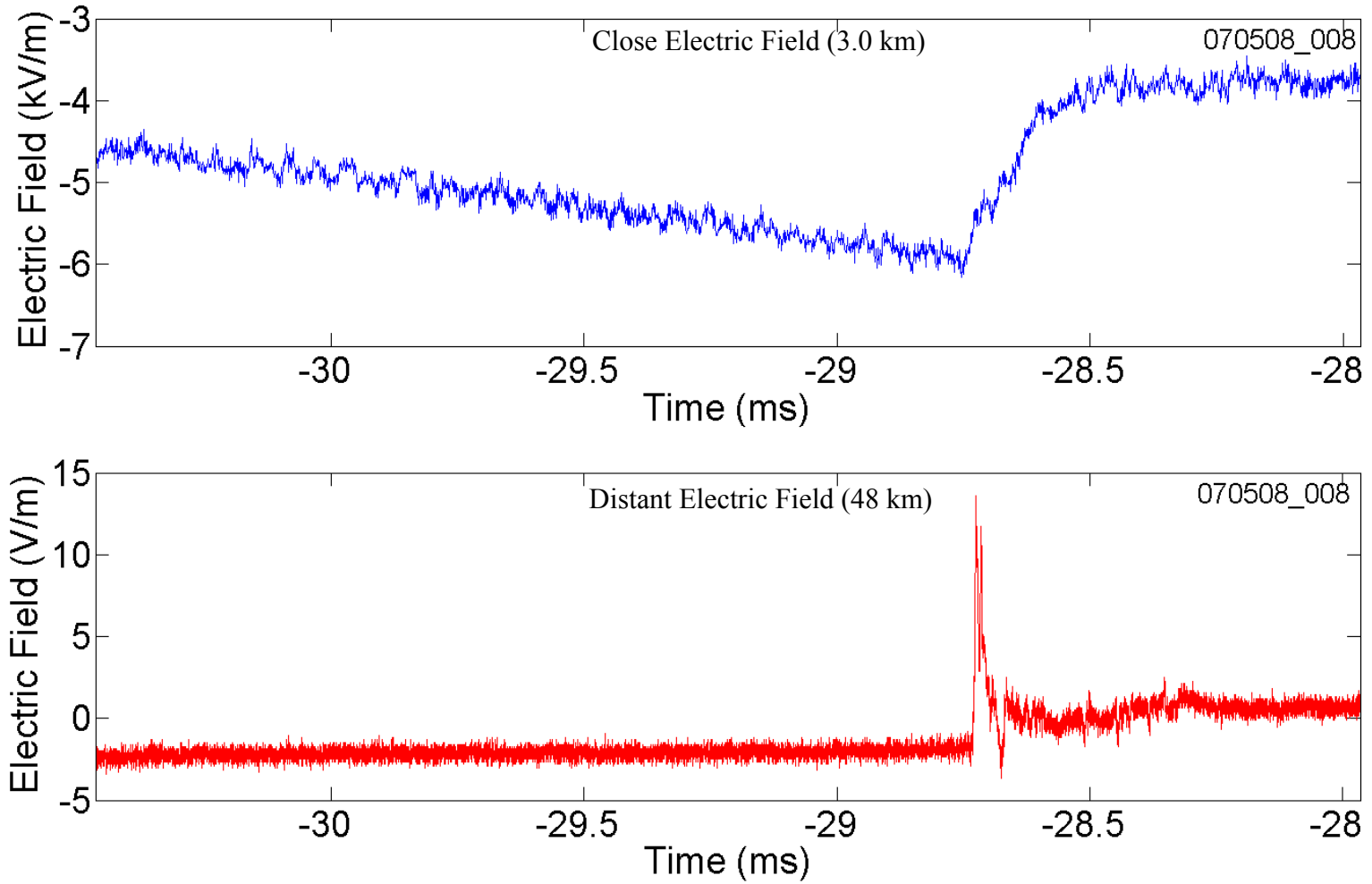


Figure 6-7. The electric field waveforms of the first return stroke of flash 070508_008, measured at the near (top panel) and far (bottom panel) stations shown on a 2.5 ms time scale.

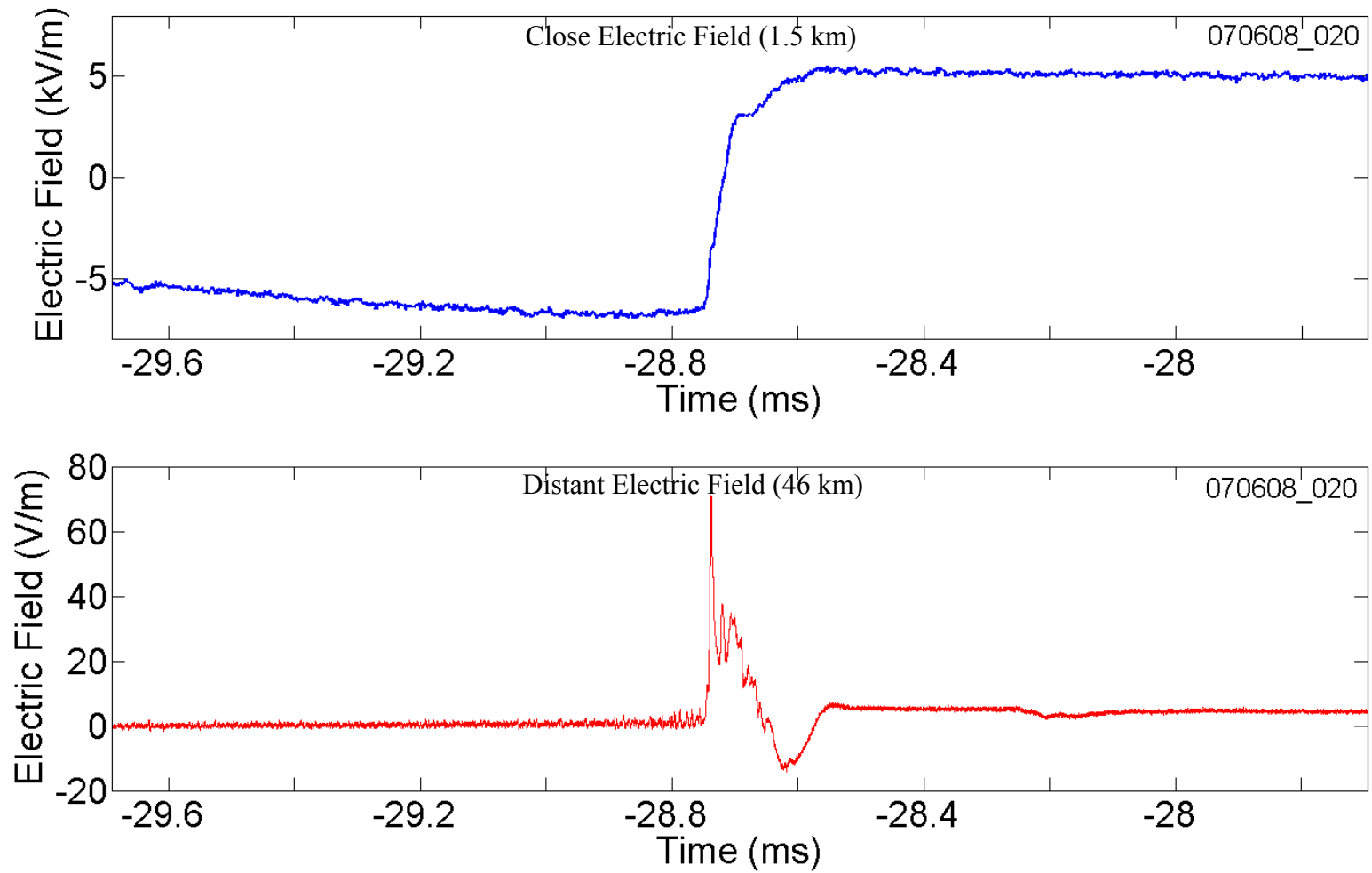


Figure 6-8. The electric field waveforms of the first return stroke of flash 070608_020, measured at the near (top panel) and far (bottom panel) stations shown on a 2 ms time scale.

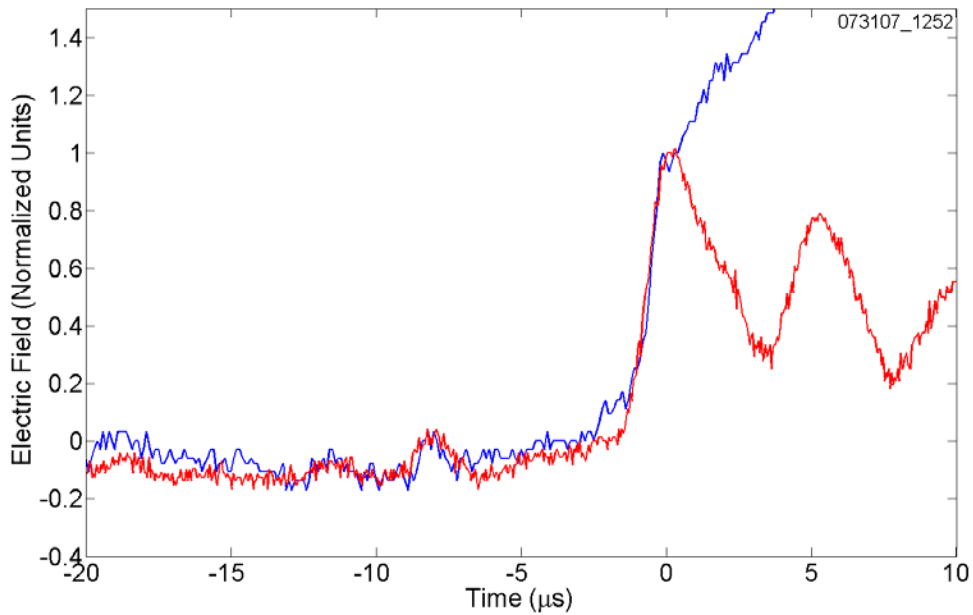


Figure 6-9. The initial rising portion of the first strokes of flash 073107_1252 at the near (blue line) and far (red line) stations overlaid for direct comparison, shown on a 30 μs time scale.

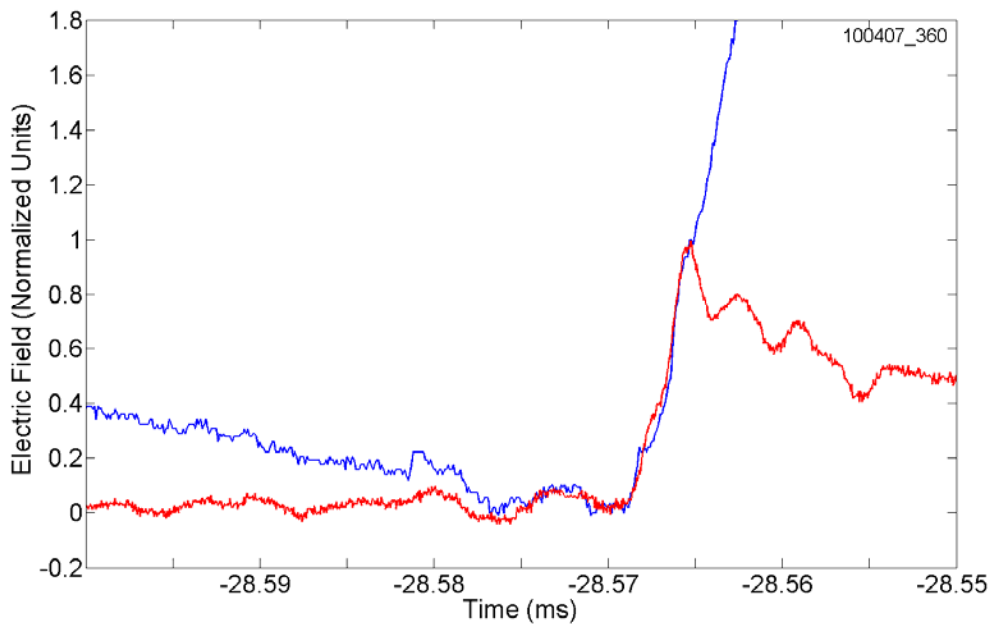


Figure 6-10. The initial rising portion of the first strokes of flash 100407_360 at the near (blue line) and far (red line) stations overlaid for direct comparison, shown on a 50 μs time scale.

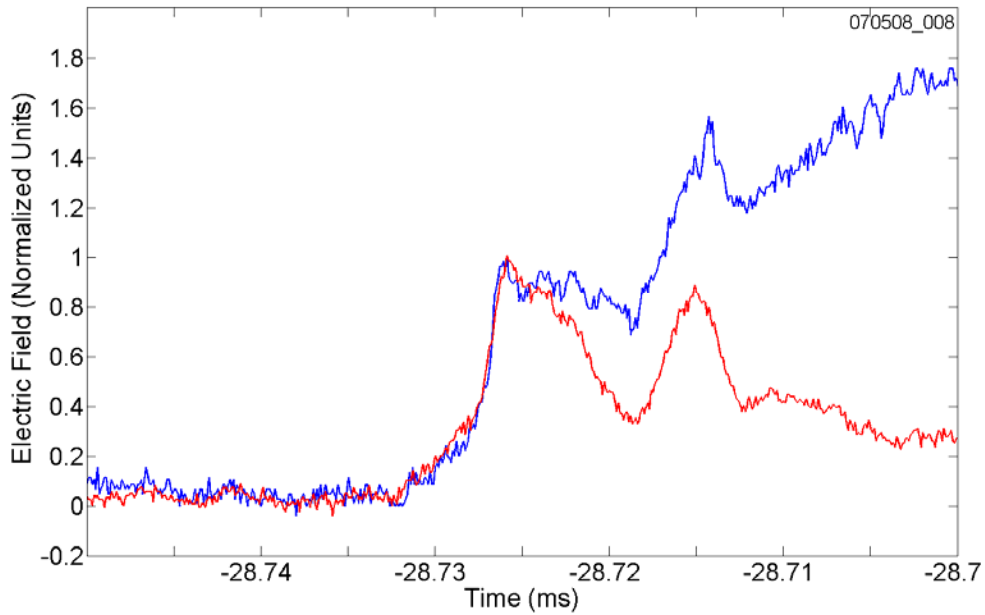


Figure 6-11. The initial rising portion of the first strokes of flash 070508_008 at the near (blue line) and far (red line) stations overlaid for direct comparison, shown on a 50 μ s time scale.

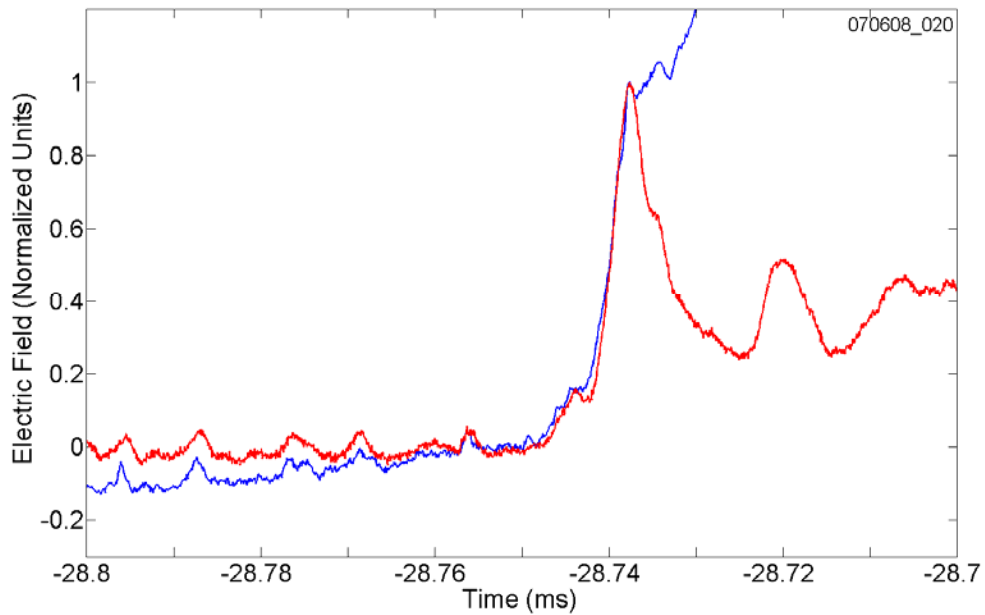


Figure 6-12. The initial rising portion of the first strokes of flash 070608_020 at the near (blue line) and far (red line) stations overlaid for direct comparison, shown on a 100 μ s time scale.

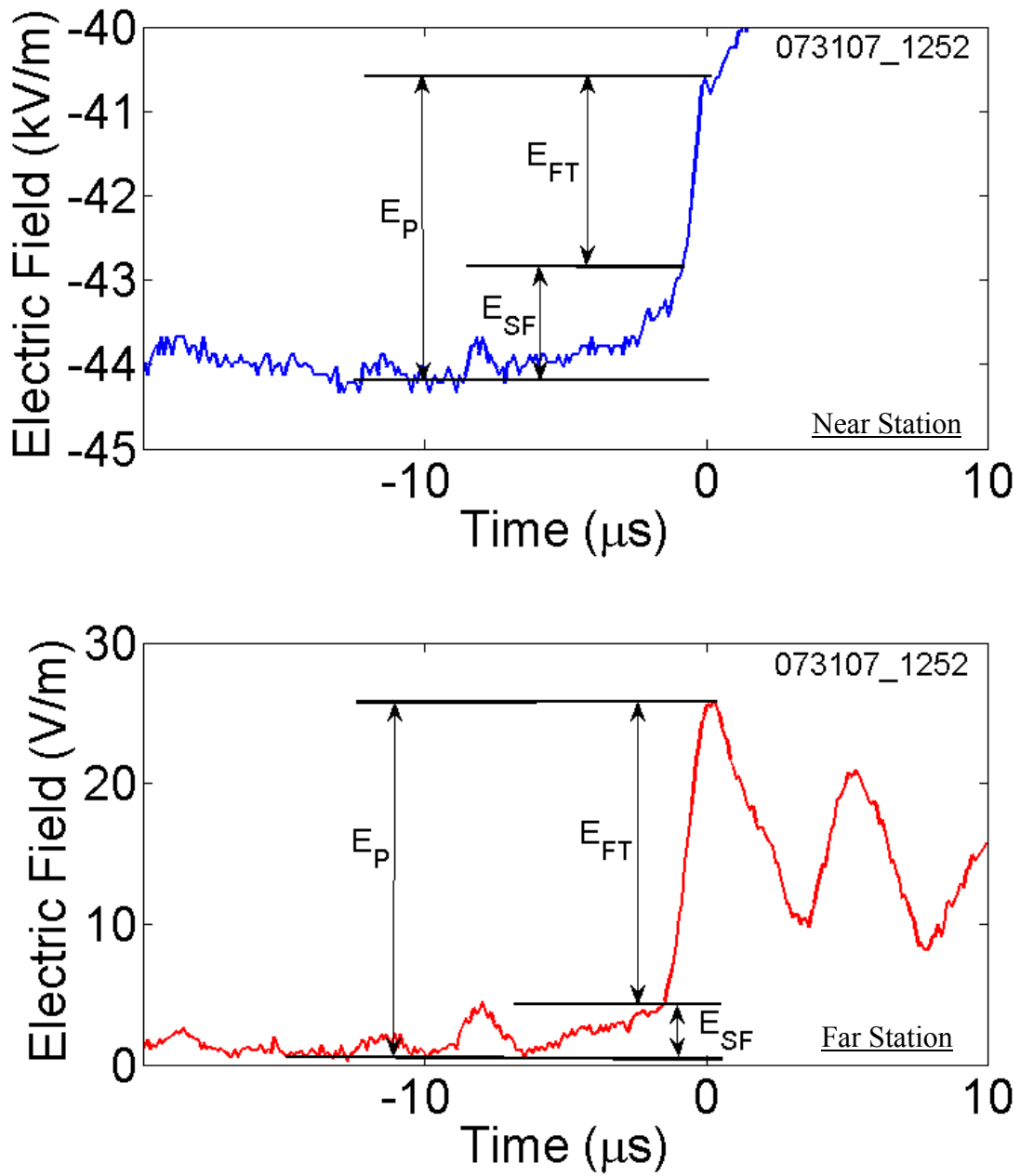


Figure 6-13. The initial rising portion of the first stroke of flash 073107_1252 at the near (blue line, top panel) and far (red line, bottom) stations each shown on a 30 μ s time scale. E_P , E_{SF} , and E_{FT} are the magnitudes of the radiation field peak, slow front and fast transition, respectively.

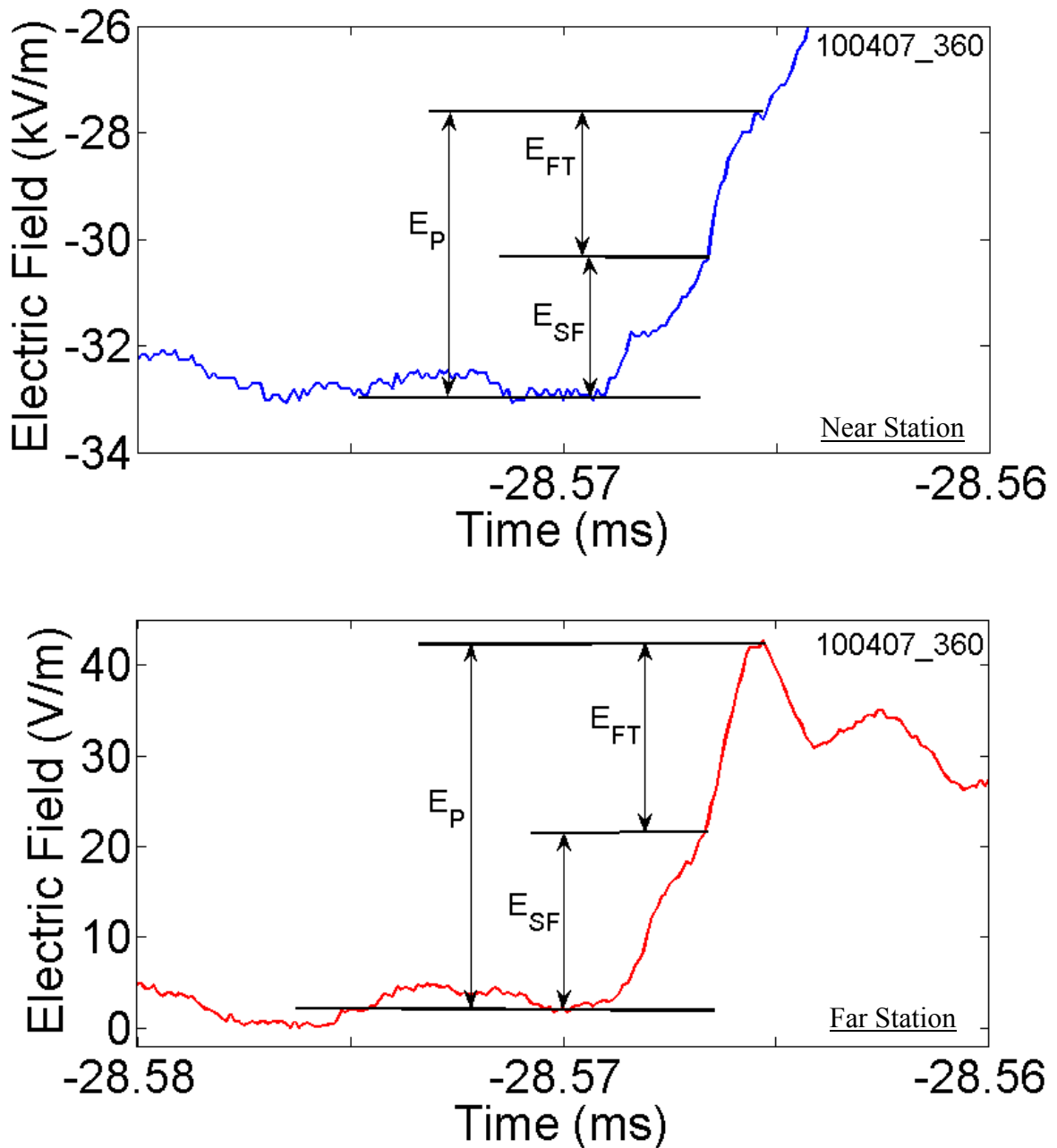


Figure 6-14. The initial rising portion of the first stroke of flash 100407_360 at the near (blue line, top panel) and far (red line, bottom) stations each shown on a 20 μ s time scale. E_P , E_{SF} , and E_{FT} are the magnitudes of the radiation field peak, slow front and fast transition, respectively. The change in slope from the relatively slow convex portion (partly concave at the near station) of the return stroke waveform to the fast rising portion was used to determine the duration and magnitude of the slow front.

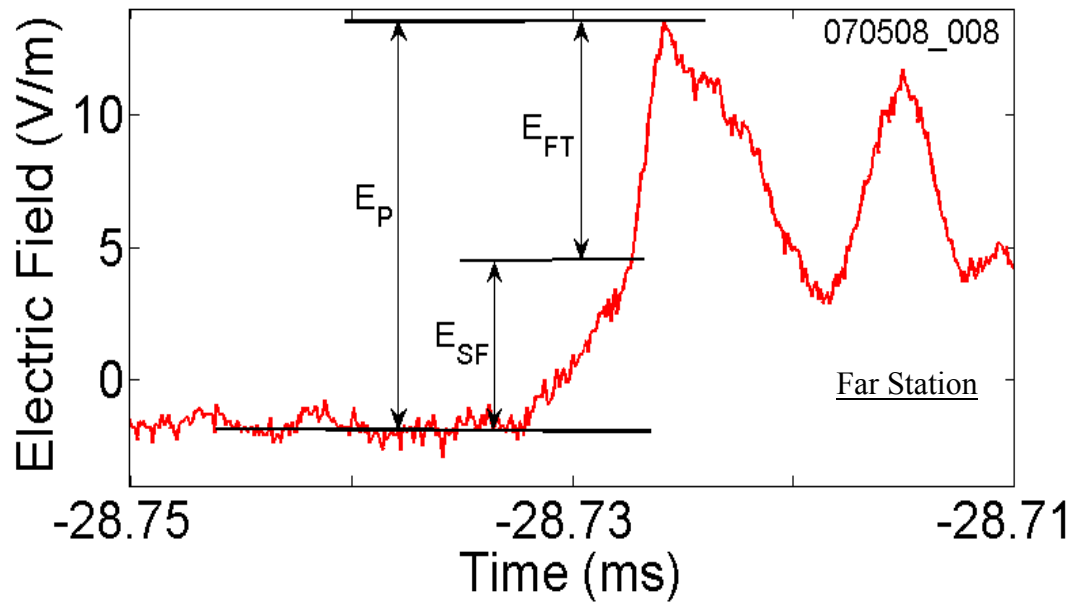
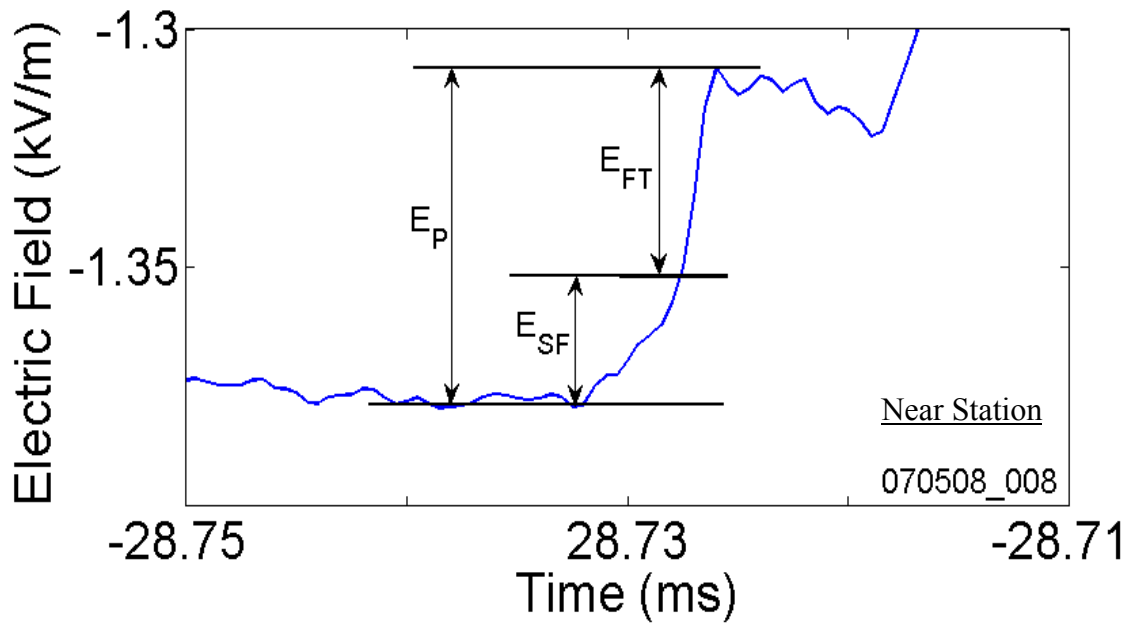


Figure 6-15. The initial rising portion of the first stroke of flash 070508_008 at the near (blue line, top panel) and far (red line, bottom) stations each shown on a $40 \mu\text{s}$ time scale. E_P , E_{SF} , and E_{FT} are the magnitudes of the radiation field peak, slow front and fast transition, respectively.

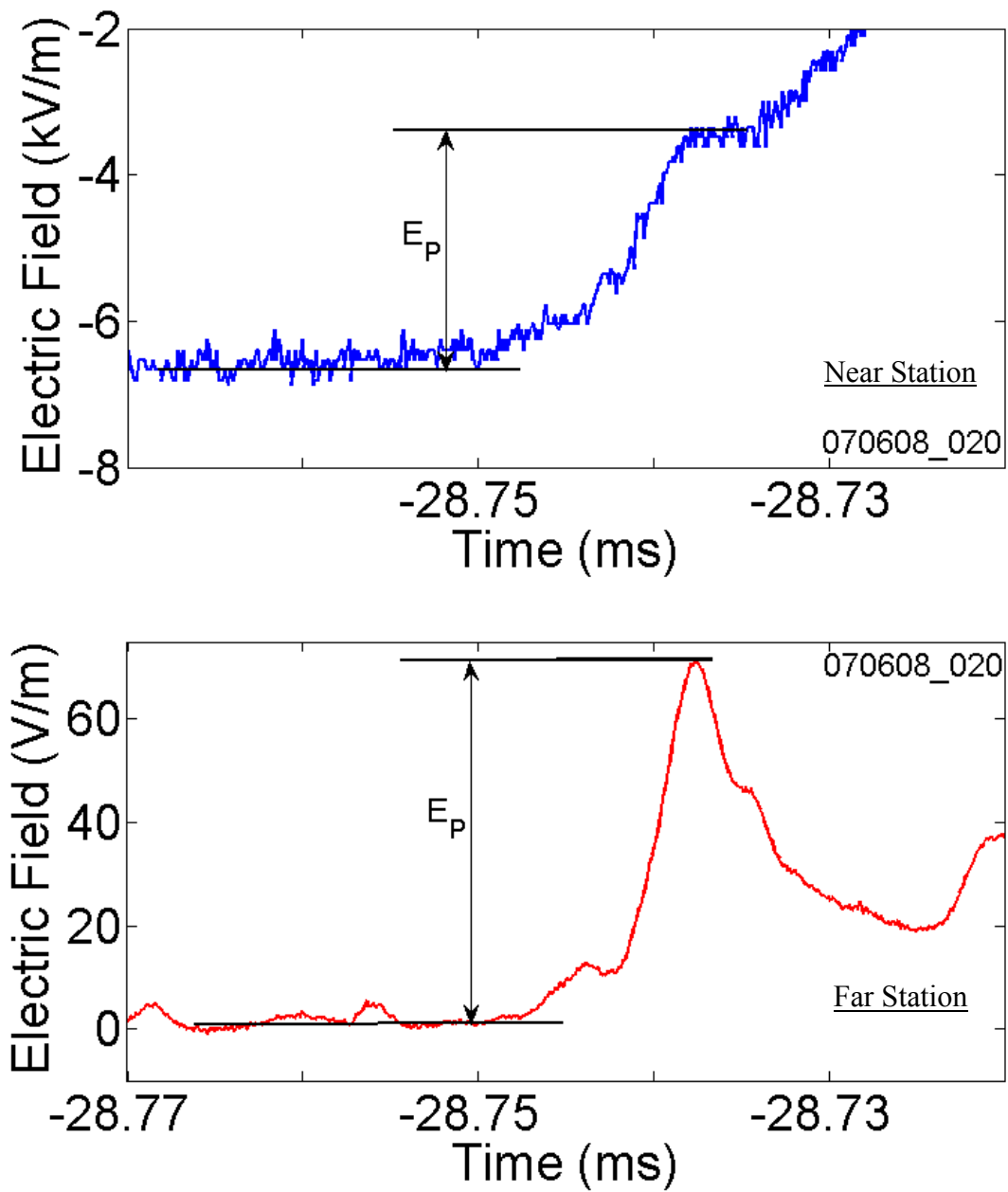


Figure 6-16. The initial rising portion of the first stroke of flash 070608_020 at the near (blue line, top panel) and far (red line, bottom) stations each shown on a 50 μ s time scale. E_p is the magnitudes of the radiation field peak. A distinct slow front phase is not seen probably due to overlap with the final leader step, as seen in the distant electric field waveform.

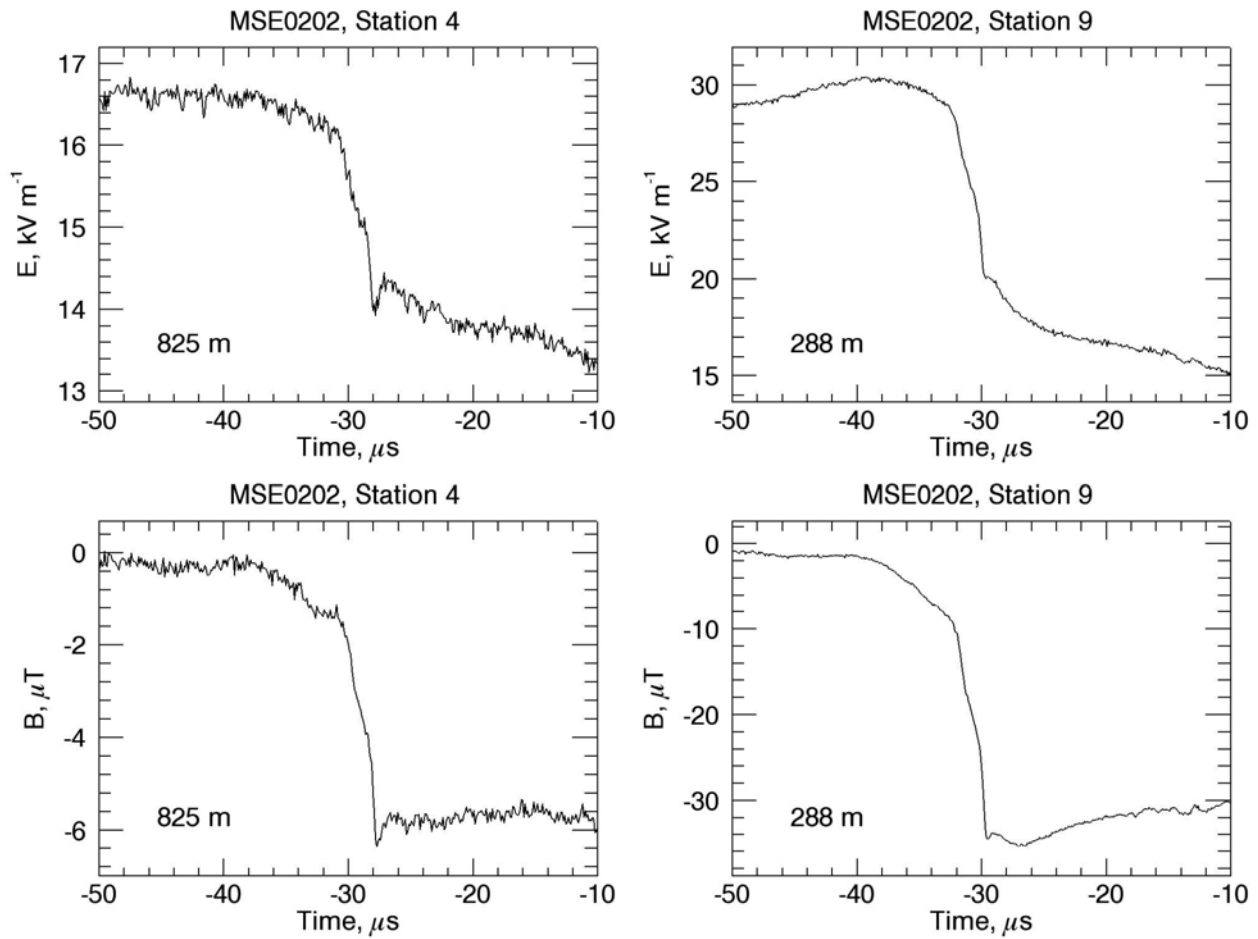


Figure 6-17. First positive stroke electric and magnetic field waveforms measured at 825 and 288 m at Camp Blanding, Florida, by *Jerauld et al.* [2009] on a 40-ns timescale. Only the east-west component of the magnetic fields was measured. Taken from *Jerauld et al.* [2009].

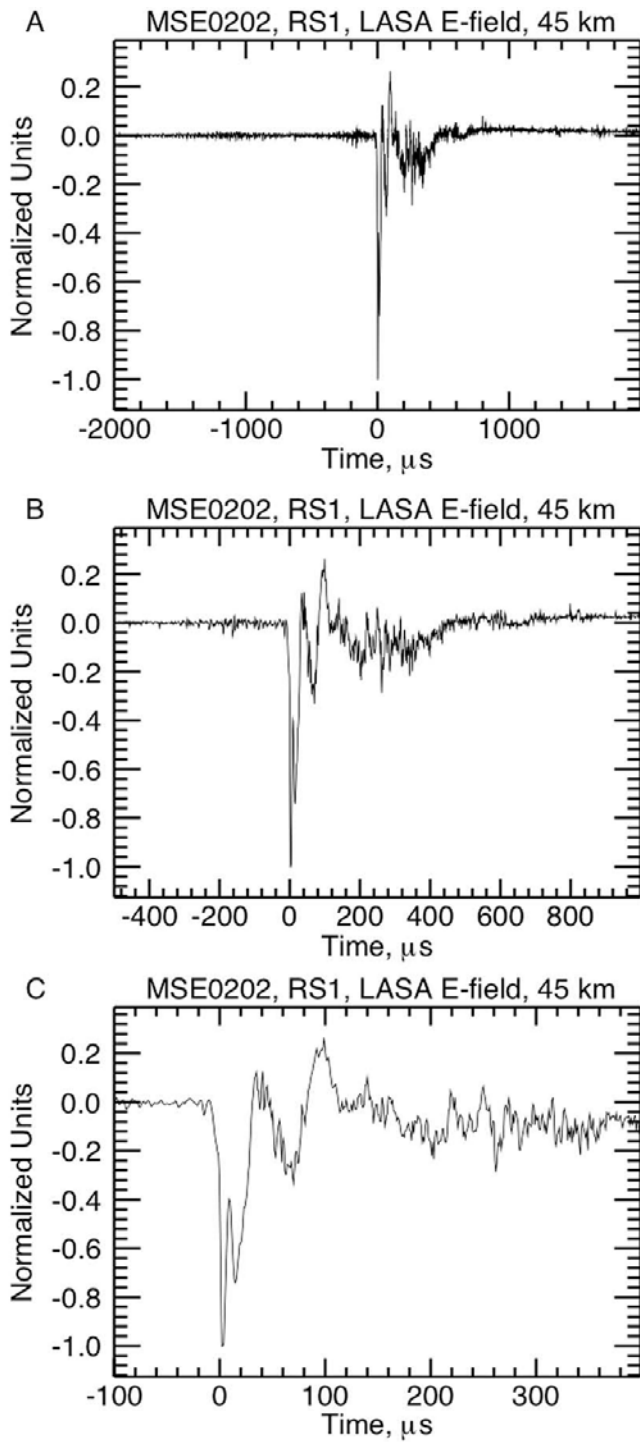


Figure 6-18. Electric field of the first positive stroke measured in Gainesville, at a distance of 45 km by the Los Alamos Sferic Array (LASA). The waveform is displayed on (a) 2-ms, (b) 1.5-ms, and (c) 500- μs timescales. The amplitude of the waveform has been normalized to its initial peak. Time zero corresponds to the beginning of the fast transition. Data provided courtesy of Los Alamos National Laboratories (LANL). Taken from *Jerauld et al.* [2009].

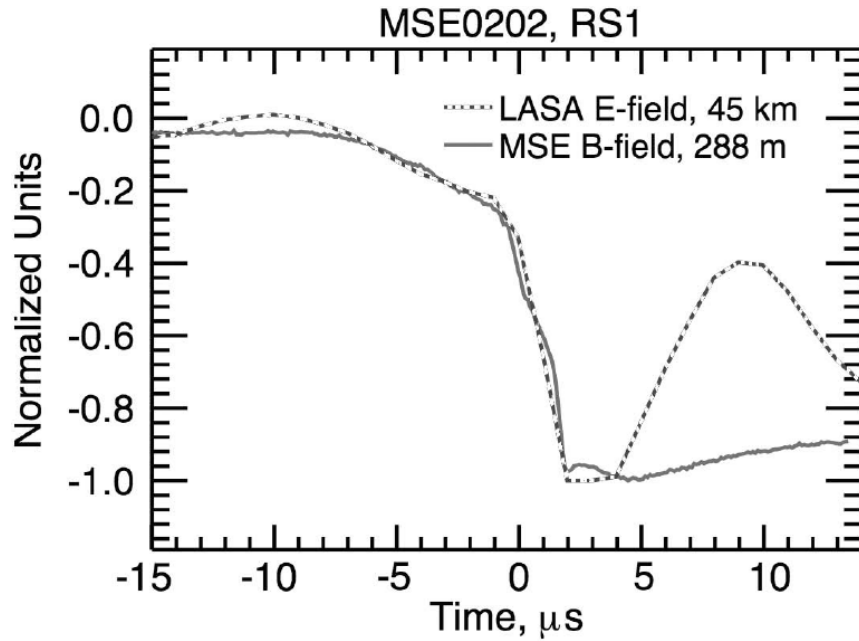


Figure 6-19. Magnetic field measured at 288 m by *Jerauld et al.* [2009], overlaid with the electric field measured a distance of 45 km from the first positive stroke. Time zero corresponds to the beginning of the fast transition. The distant field was measured by the Los Alamos Sferics Array (LASA) and is provided courtesy of Los Alamos National Laboratories (LANL). Taken from *Jerauld et al.* [2009].

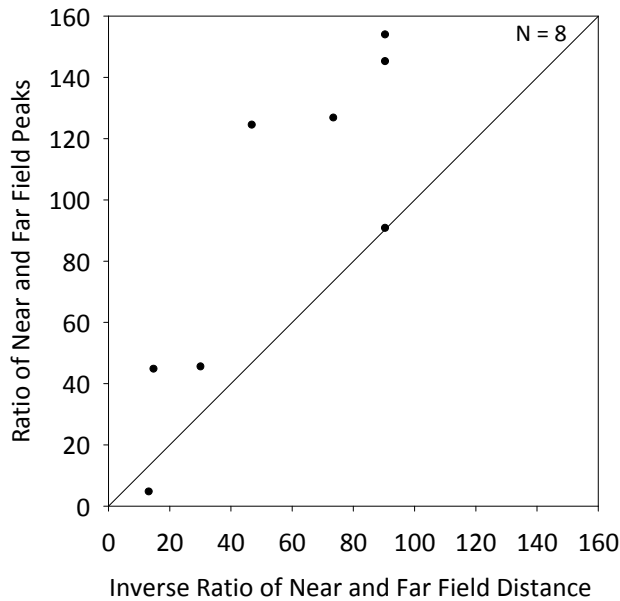


Figure 6-20. Ratio of near and far initial (radiation) field peaks versus inverse ratio of near and far field distances for 8 negative return strokes recorded at Camp Blanding and in Gainesville.

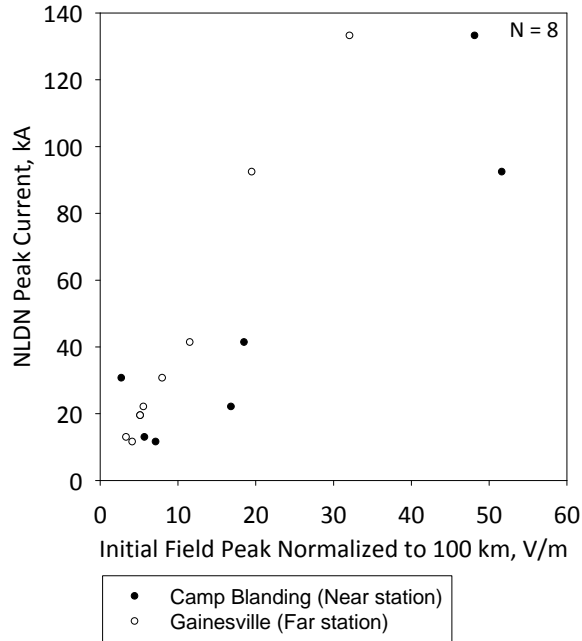


Figure 6-21. NLDN-estimated peak current versus initial (radiation) field peak normalized to 100 km for 8 negative return strokes recorded at Camp Blanding (near station) and in Gainesville (far station). Note that for the third stroke in flash 073107_1252, whose NLDN-estimated peak current is 19 kA, the initial field peak normalized to 100 km obtained from both near and far field measurements is equal to 5.2 V/m and hence the corresponding points in the plot overlap.

6.3 Transmission Line Model

The transmission line (TL) model [*Uman and McLain, 1969*] for return strokes involves a current wave injected at the bottom of the lightning channel travelling upward at constant velocity v without attenuation or distortion. For the TL model the longitudinal current $i(z,t)$ at any height z and any time t is related to the current at the channel origin (which in this case is at ground level) is given by Equation 6-1 and illustrated in Figure 6-22.

$$i(z,t) = i\left(0, t - \frac{z}{v}\right) \quad (6-1)$$

Modifications to the TL model include a linear [MTLL, *Rakov and Dulzon, 1987*] and exponential [MTLE, *Nucci et al., 1988*] current decay with height, represented by equations 6-2 (MTLL) and 6-3 (MTLE), respectively.

$$i(z,t) = (1 - \frac{z}{H})i(0, t - \frac{z}{v}) \quad (6-2)$$

$$i(z,t) = e^{-\frac{z}{\lambda}}i(0, t - \frac{z}{v}) \quad (6-3)$$

H in Equation 6-2 is the assumed channel height and λ in Equation 6-3 is the assumed decay height constant. The overall electric field waveforms at close distances are best reproduced by the MTL model. However, for the initial few microseconds all three models predict essentially the same fields.

In this chapter, we use the original TL model to compute near and far electric field waveforms of return strokes with focus on their initial rising portion for the purpose of trying to understand better the slow-front and fast transition processes. In addition, we extend the original, one-wave TL model to include two and three current waves. The two-wave model [e.g., *Jerauld et al., 2007*] involves two initial current waves assumed to originate from a lumped current source at some height above ground (assumed here to be the junction point of the downward and upward leaders) and propagate in both directions (up and down), at constant speeds v_u and v_d , respectively, away from the junction point without attenuation or distortion. It is usually assumed that the amplitude of the upward wave is equal to that of the downward wave, and that the downward-moving wave is absorbed at ground. The three-wave model introduced here, additionally accounts for the reflection at ground of the downward wave, with this reflected wave travelling up the channel (toward the junction point and beyond) at constant speed v_r . The amplitude of the reflected current wave, i_r , is related to that of the downward (incident) current wave, i_d by Equation 6-4.

$$i_r = \rho i_d \quad (6-4)$$

where ρ is the current reflection coefficient at ground, assumed to be constant. If the lightning channel below the junction point is modeled as a transmission line, having characteristic impedance Z_d and is terminated at ground in a grounding impedance Z_g , then ρ is given by Equation 6-5.

$$\rho = \frac{Z_d - Z_g}{Z_d + Z_g} \quad (6-5)$$

Note that ρ is positive for the case of $Z_d > Z_g$ and negative for the case of $Z_d < Z_g$. Here, ρ is assumed to be positive, because the characteristic impedance of a lightning channel is thought to be on the order of 1 k Ω [Rakov and Uman, 2003], while Z_g is likely to be on the order of tens to hundreds of ohms (depending on grounding conditions at the strike point).

We assume here that v_d , v_u , and v_r are all equal to each other. If the speed of i_r is assumed to be higher than the speed at which the current i_u moves upward from the junction point, the ground reflected wave will "catch up" with i_u and get reflected off the impedance discontinuity at the front, with the resultant second reflection moving downward. This scenario introduces additional complications in the model and is not further considered here.

The general time-domain equation for computing the vertical electric field dE_z due to a vertical differential current element idz (channel segment of length dz carrying a uniform current $i(t)$) at a height z above a perfectly conducting ground plane for the case of an observation point P on the plane at a horizontal distance r from the dipole is given by [e.g., Uman, 1987]:

$$dE_z(r, t) = \frac{1}{2\pi\epsilon_0} \left[\frac{(2z^2 - r^2)}{R^5(z)} dz \int_0^t i(z, \tau - \frac{R(z)}{c}) d\tau + \frac{(2z^2 - r^2)}{cR^4(z)} i(z, t - \frac{R(z)}{c}) dz - \frac{r^2}{c^2 R^3(z)} \frac{di(z, t - \frac{R(z)}{c})}{dt} dz \right] \quad (6-6)$$

where ϵ_0 is the electric permittivity of free space, R is the inclined distance from the dipole to the observation point, which is given by $R = \sqrt{z^2 + r^2}$.

From Equation 6-6 for the geometry shown in Figure 6-22, the total electric field at the observation point for a finite-length channel whose lower and upper ends are at altitudes of $z = 0$ and $z = H$, respectively, is given by:

$$E_z(r, t) = \frac{1}{2\pi\epsilon_0} \int_0^H \left[dz \frac{(2z^2 - r^2)}{R^5(z)} \int_0^t i(z, \tau - \frac{R(z)}{c}) d\tau + \frac{(2z^2 - r^2)}{cR^4(z)} i(z, t - \frac{R(z)}{c}) dz - \frac{r^2}{c^2 R^3(z)} \frac{di(z, t - \frac{R(z)}{c})}{dt} dz \right] \quad (6-7)$$

6.3.1 Channel-Base Current without Pronounced Slow Front

The Heidler function [Heidler, 1985] is used to represent the channel-base current waveform not containing a pronounced slow front in this Chapter, and is given by:

$$i(0, t) = \frac{I_0}{\eta} \frac{\left(\frac{t}{\tau_1}\right)^n}{\left(\frac{t}{\tau_1}\right)^n + 1} e^{-\frac{t}{\tau_2}} \quad (6-8)$$

where $I_0 = 26$ kA, $\eta = 0.5$, $n = 3$, $\tau_1 = 4$ μ s, and $\tau_2 = 6$ μ s. The current waveform is shown in Figure 6-23 and has a peak of about 15 kA and a zero-to-peak risetime of 5.4 μ s.

6.3.2 Electric Fields Computed Using the Original Transmission Line Model

Figures 6-24a and b show the electrostatic, induction, and radiation components of electric field and the total electric field up to 10 μ s at 500 m and 100 km, respectively, from the lightning channel computed using the original TL model and the current shown in Figure 6-23. For the purpose of comparison of electric field and current waveshapes, the total electric field and current waveforms are overlaid (with the current scaled so that its peak is equal to the electric field peak) in Figures 6-24c and d for distances of 500 m and 100 km, respectively. Note that the

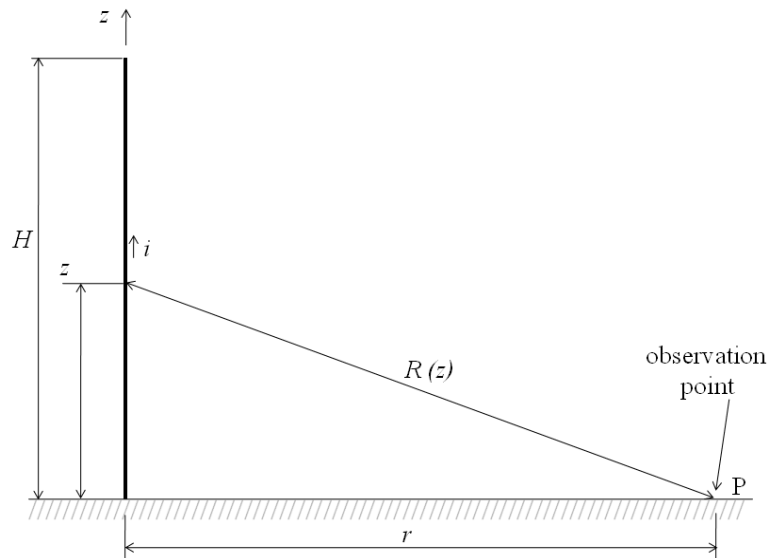


Figure 6-22. Geometrical parameters used in calculating the electric field at observation point P on perfectly conducting ground at horizontal distance r from the vertical return-stroke channel extending between ground and height H .

electric field peak at 500 m, predicted by the TL model, is not consistent with the experimental data. The current wave is assumed to travel upward along the 4 km long channel at an assumed speed of 0.5×10^8 m/s. The electric field at 500 m from the channel is dominated by its electrostatic component, while that at 100 km from the channel is essentially radiation. Figures 6-25 and 6-26 show the model predicted electric fields at 500 m and 100 km for current-wave speeds of 1×10^8 m/s and 2×10^8 m/s, respectively.

6.3.3 Electric Fields Computed Using the Two-Wave Transmission Line Model

Figures 6-27a and b show the electrostatic, induction, and radiation components of electric field and the total electric field up to $10 \mu\text{s}$ at 500 m and 100 km computed using the two-wave TL model which considers two current waves moving in opposite directions from the junction point at height $h = 20$ m above ground. The channel length is 4 km. The speed of both the upward and downward moving current waves is assumed to be 0.5×10^8 m/s. For the purpose of comparison of waveshapes, the total electric field and current waveforms are overlaid (with the

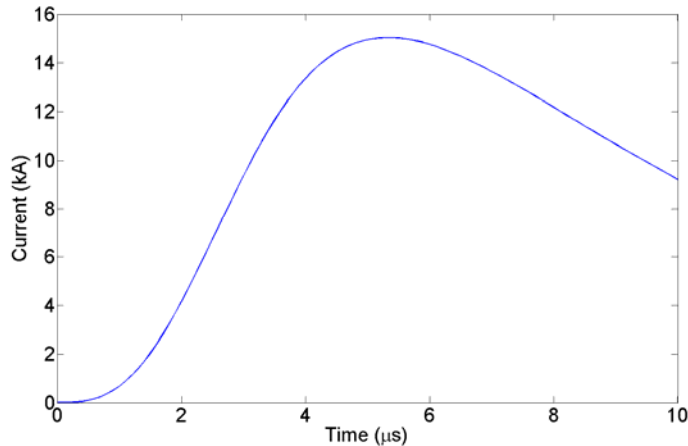


Figure 6-23. The channel-base current waveform given by Equation 6-8 used to calculate return stroke electric fields for the one-wave, two-wave and three-wave models. The parameters chosen are $I_0 = 26$ kA, $\eta = 0.5$, $n = 3$, $\tau_1 = 4$ μ s, and $\tau_2 = 6$ μ s. The current has a peak of about 15 kA and a zero-to-peak risetime of 5.4 μ s.

current scaled so that its peak is equal to the electric field peak) in Figures 6-27c and d for distances of 500 m and 100 km, respectively. Figures 6-28 and 6-29 show the model-predicted electric fields at 500 m and 100 km when the speed of both current waves is 1×10^8 m/s and 2×10^8 m/s, respectively. The individual field contributions due to the upward and downward moving current waves along with the total electric field at 500 m for current propagation speeds of 0.5×10^8 , 1×10^8 , and 2×10^8 , are shown in Figure 6-30a, b, and c, respectively.

6.3.4 Electric Fields Computed Using the Three-Wave Transmission Line Model

Figures 6-31a and b show the electrostatic, induction, and radiation components of electric field and the total electric field up to 10 μ s at 500 m and 100 km computed using the three-wave TL model which considers two currents moving in opposite directions from the junction point at a height h of 20 m above ground and the ground reflected wave moving upward from ground. The channel length is 4 km. The speed of all three current waves is assumed to be 0.5×10^8 m/s. For the purpose of comparison of waveshapes, the total electric field and current waveforms are overlaid (with the current scaled so that its peak is equal to the electric field peak) in the Figures

6-31c and d for distances of 500 m and 100 km, respectively. Figures 6-32 and 6-33 show the model-predicted electric fields at 500 m and 100 km when the speed of both current waves is 1×10^8 m/s and 2×10^8 m/s, respectively. The individual field contributions due to the two incident current waves (upward and downward moving), and the ground reflected current wave along with the total electric field at 500 m for current propagation speeds of 0.5×10^8 , 1×10^8 , and 2×10^8 , are shown in Figure 6-34a, b, and c, respectively.

6.3.5 Channel-Base Current with Pronounced Slow Front and Computed Electric Fields

An expression for first return stroke current proposed by *De Conti and Visacro* [2007] is used to represent the channel-base current waveform containing a pronounced slow front in this Chapter, and is given by:

$$i(0, t) = \sum_{k=1}^m \frac{I_{0k}}{\eta_k} \frac{\left(\frac{t}{\tau_{1k}}\right)^{n_k}}{\left(\frac{t}{\tau_{1k}}\right)^{n_k} + 1} e^{-\frac{t}{\tau_{2k}}} \quad (6-9)$$

where $\eta_k = e^{\left[-\frac{\tau_{1k}}{\tau_{2k}} \left(n_k \frac{\tau_{2k}}{\tau_{1k}}\right)^{\frac{1}{n_k}}\right]}$. The values of the parameters m , I_0 , η , n , τ_1 , and τ_2 for different values of k are taken from Table II of *De Conti and Visacro* [2007] and given here in Table 6-4. This current waveform has a pronounced slow front and is shown in Figure 6-35.

The electric field waveforms at 500 m computed using the one-wave, two-wave and three-wave models are shown in Figures 6-36a, 6-37a, and 6-38a, respectively. Current-wave speed is assumed to be 10^8 m/s and the channel length is 4 km. For the two-wave and three-wave models, the height of the junction point is assumed to 20 m. The electric field waveforms at 100 km computed using the one-wave, two-wave and three-wave models are shown in Figures 6-36b, 6-37b, and 6-38b, respectively.

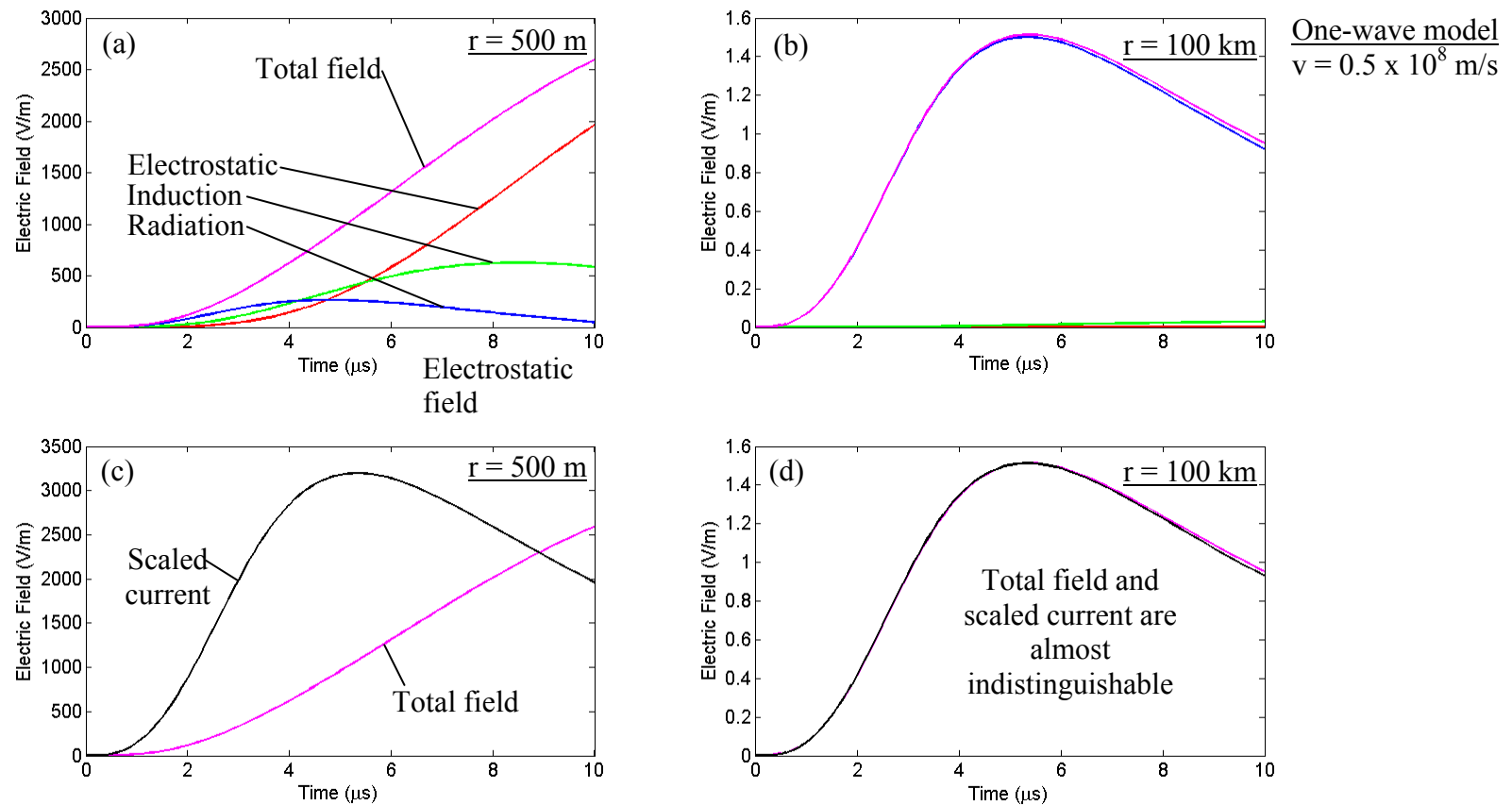


Figure 6-24. Electrostatic (red), induction (green), and radiation (blue) components of electric field and the total electric field (magenta) up to $10 \mu\text{s}$ at (a) 500 m and (b) 100 km from the lightning channel computed using the original, one-wave TL model for an assumed current-wave propagation speed of $0.5 \times 10^8 \text{ m/s}$ and channel length of 4 km. The total electric fields are overlaid with current waveforms scaled so that its peak is equal to the electric field peak (though at $r = 500 \text{ m}$, the electric field peak occurs after $10 \mu\text{s}$ and is not consistent with experimental data), for direct comparison of the initial rising portions for distances of (c) 500 m and (d) 100 km. Channel-base current waveform is given by Equation 6-8.

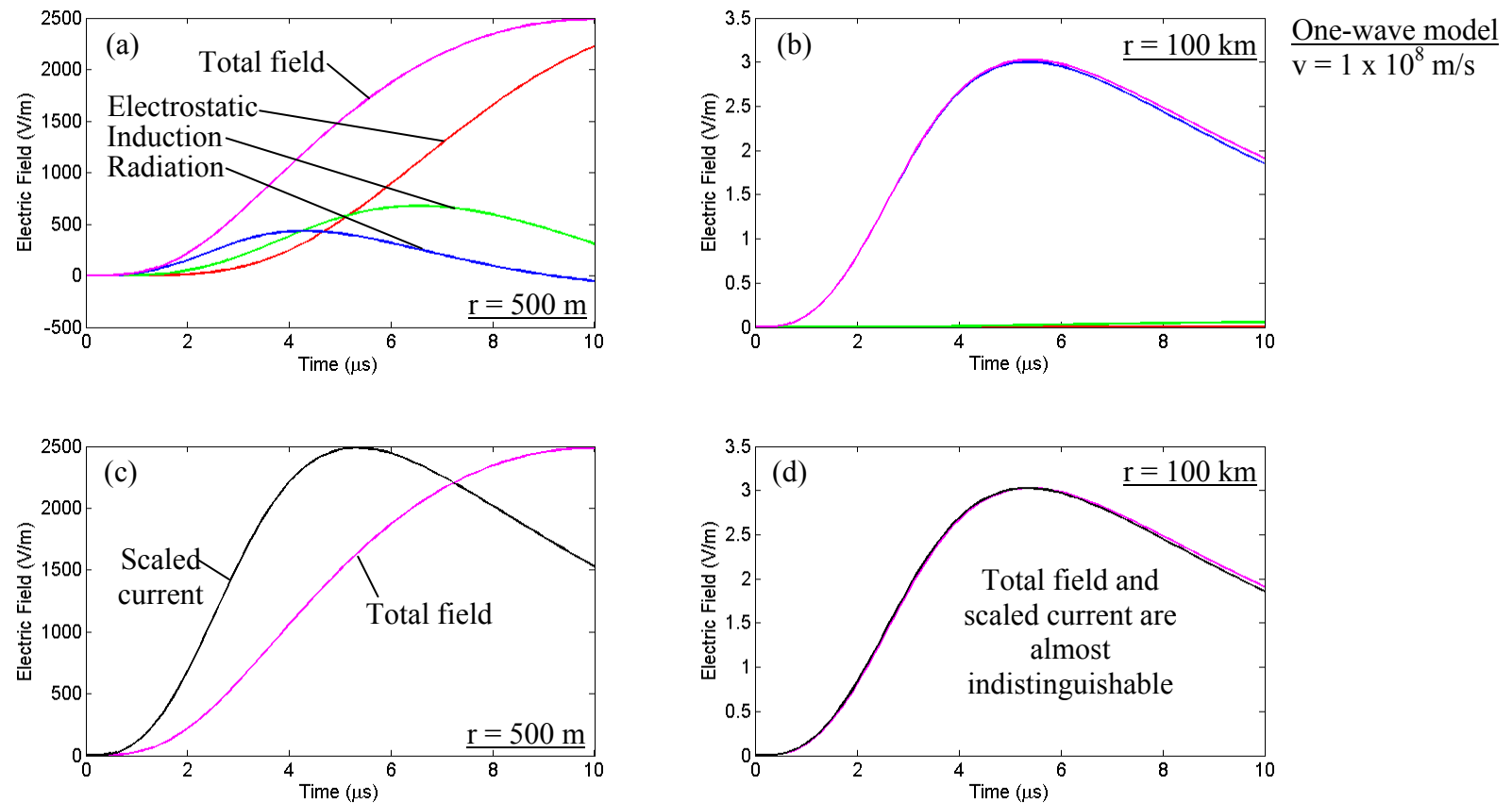


Figure 6-25. Electrostatic (red), induction (green), and radiation (blue) components of electric field and the total electric field (magenta) up to $10 \mu\text{s}$ at (a) 500 m and (b) 100 km from the lightning channel computed using the original, one-wave TL model for an assumed current-wave propagation speed of 1×10^8 m/s and channel length of 4 km. The total electric fields are overlaid with current waveforms scaled so that its peak is equal to the electric field peak, for direct comparison of the initial rising portions for distances of (c) 500 m and (d) 100 km. Channel-base current waveform is given by Equation 6-8.

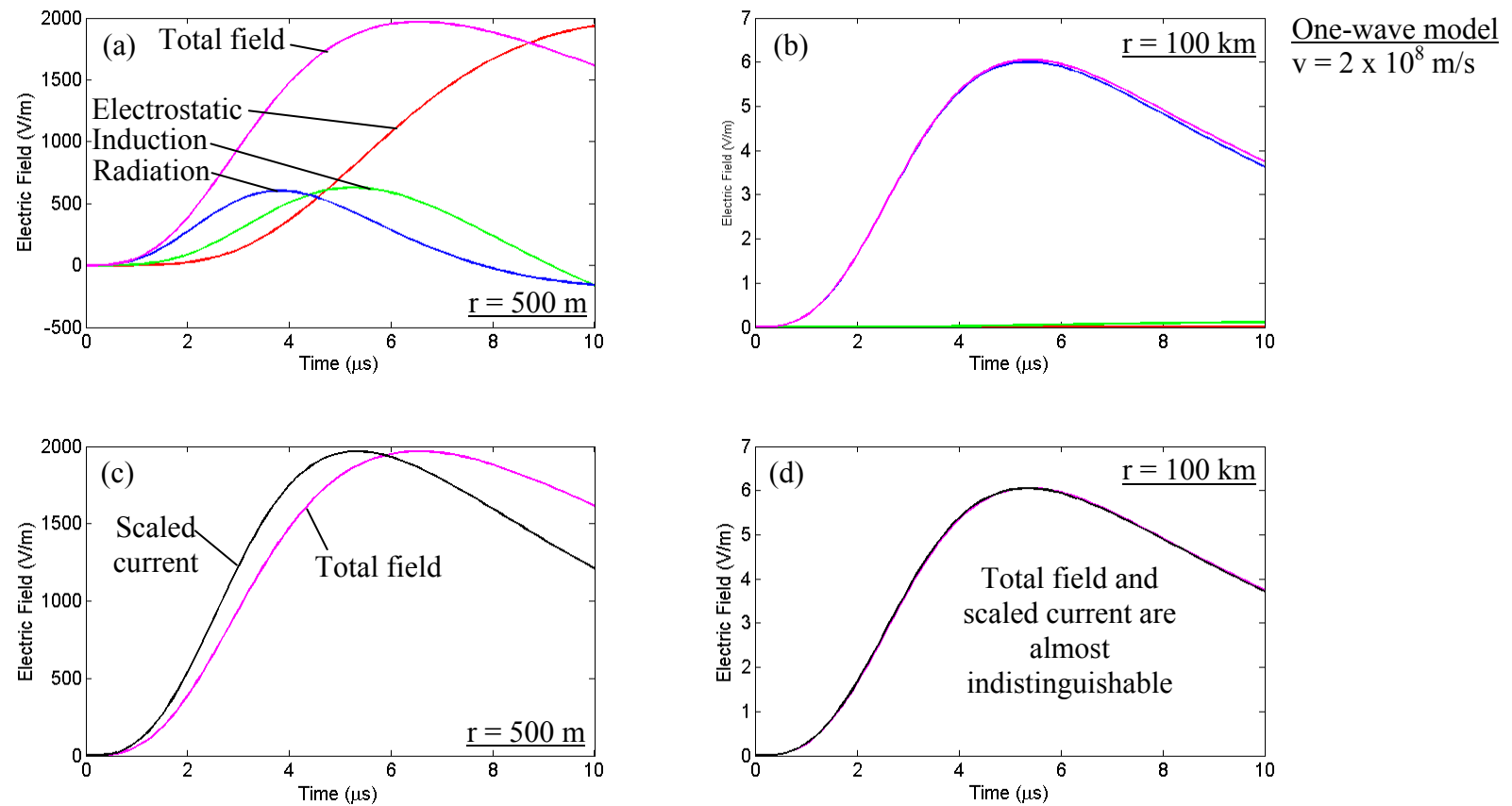


Figure 6-26. Electrostatic (red), induction (green), and radiation (blue) components of electric field and the total electric field (magenta) up to $10 \mu\text{s}$ at (a) 500 m and (b) 100 km from the lightning channel computed using the original, one-wave TL model for an assumed current-wave propagation speed of $2 \times 10^8 \text{ m/s}$ and channel length of 4 km . The total electric fields are overlaid with current waveforms scaled so that its peak is equal to the electric field peak, for direct comparison of the initial rising portions for distances of (c) 500 m and (d) 100 km . Note that the portion of the predicted electric field waveform after the peak in (a) and (c) at 500 m is inconsistent with experimental data. However, for the initial few microseconds (probably up to the peak) the predicted close fields are expected to be correct. Channel-base current waveform is given by Equation 6-8.

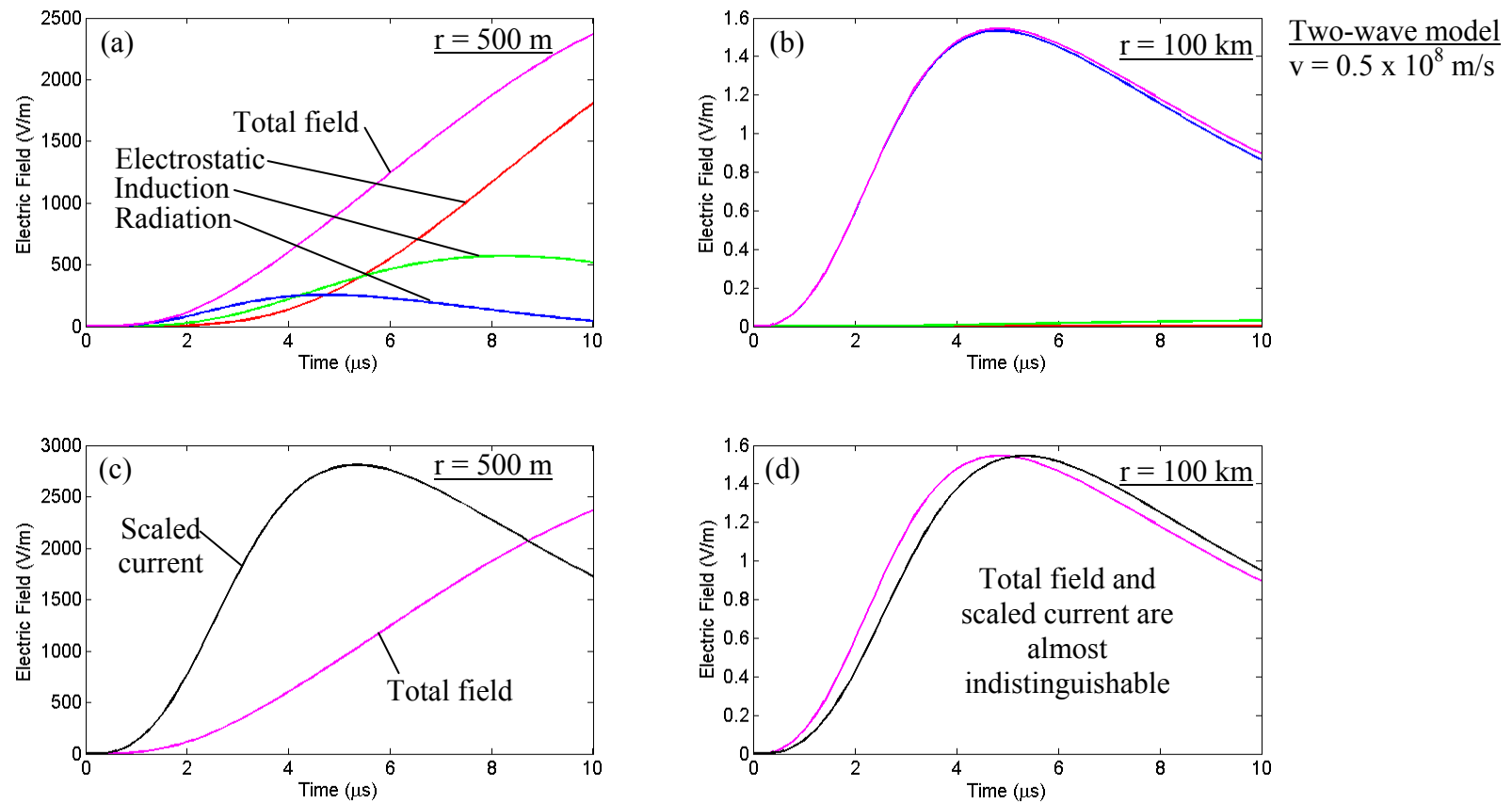


Figure 6-27. Electrostatic (red), induction (green), and radiation (blue) components of electric field and the total electric field (magenta) up to $10 \mu\text{s}$ at (a) 500 m and (b) 100 km from the lightning channel computed using the two-wave model for an assumed current-wave propagation speed of $0.5 \times 10^8 \text{ m/s}$ and channel length of 4 km . The total electric fields are overlaid with current waveforms scaled so that its peak is equal to the electric field peak (though at $r = 500 \text{ m}$, the electric field peak occurs after $10 \mu\text{s}$), for direct comparison of the initial rising portions for distances of (c) 500 m and (d) 100 km . The junction point is assumed to be at a height h of 20 m above ground. Channel-base current waveform is given by Equation 6-8.

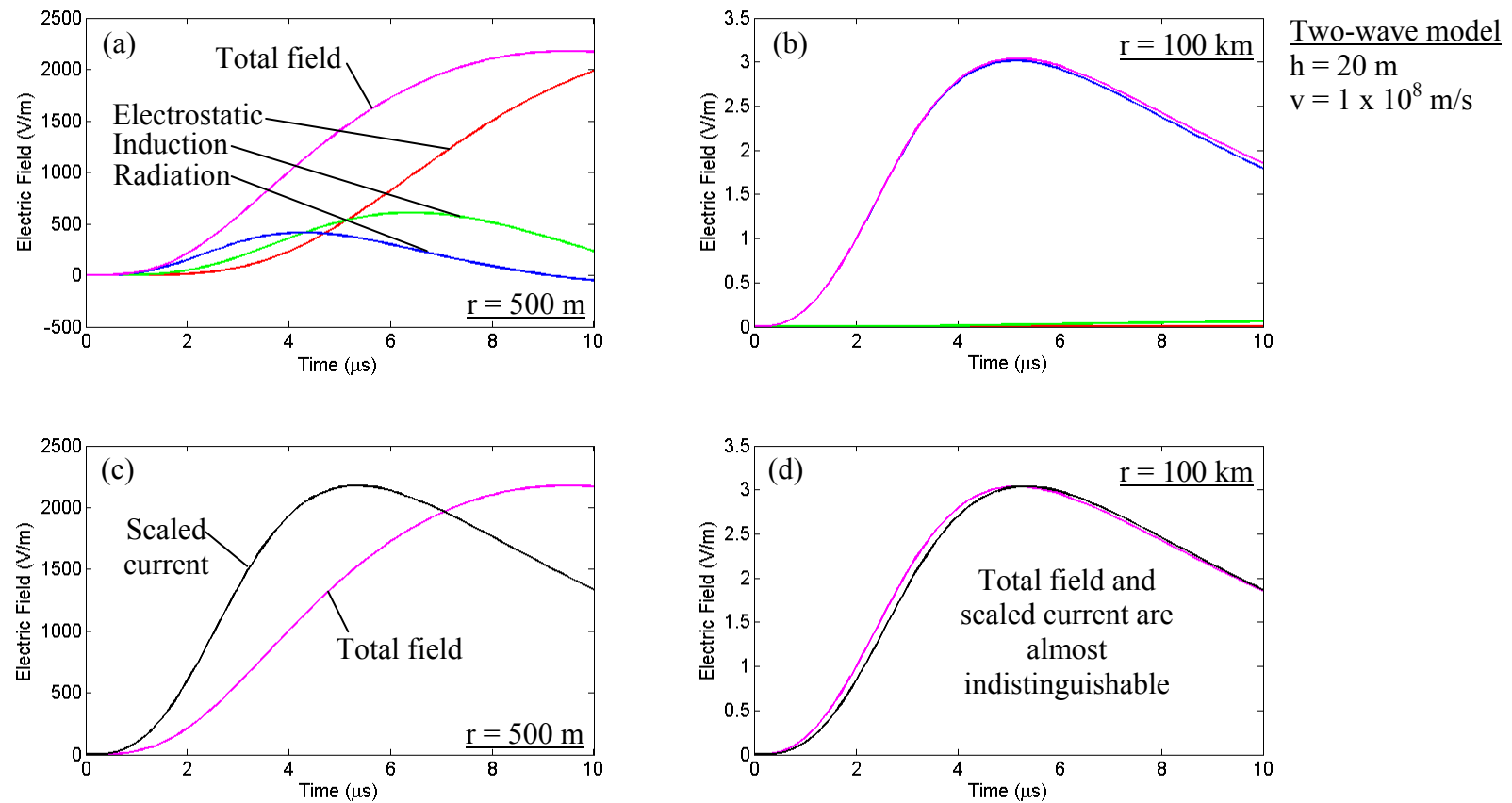


Figure 6-28. Electrostatic (red), induction (green), and radiation (blue) components of electric field and the total electric field (magenta) up to $10 \mu\text{s}$ at (a) 500 m and (b) 100 km from the lightning channel computed using the two-wave model for an assumed current-wave propagation speed of 1×10^8 m/s and channel length of 4 km. The total electric fields are overlaid with current waveforms scaled so that its peak is equal to the electric field peak, for direct comparison of the initial rising portions for distances of (c) 500 m and (d) 100 km. The junction point is assumed to be at a height h of 20 m above ground. Channel-base current waveform is given by Equation 6-8.

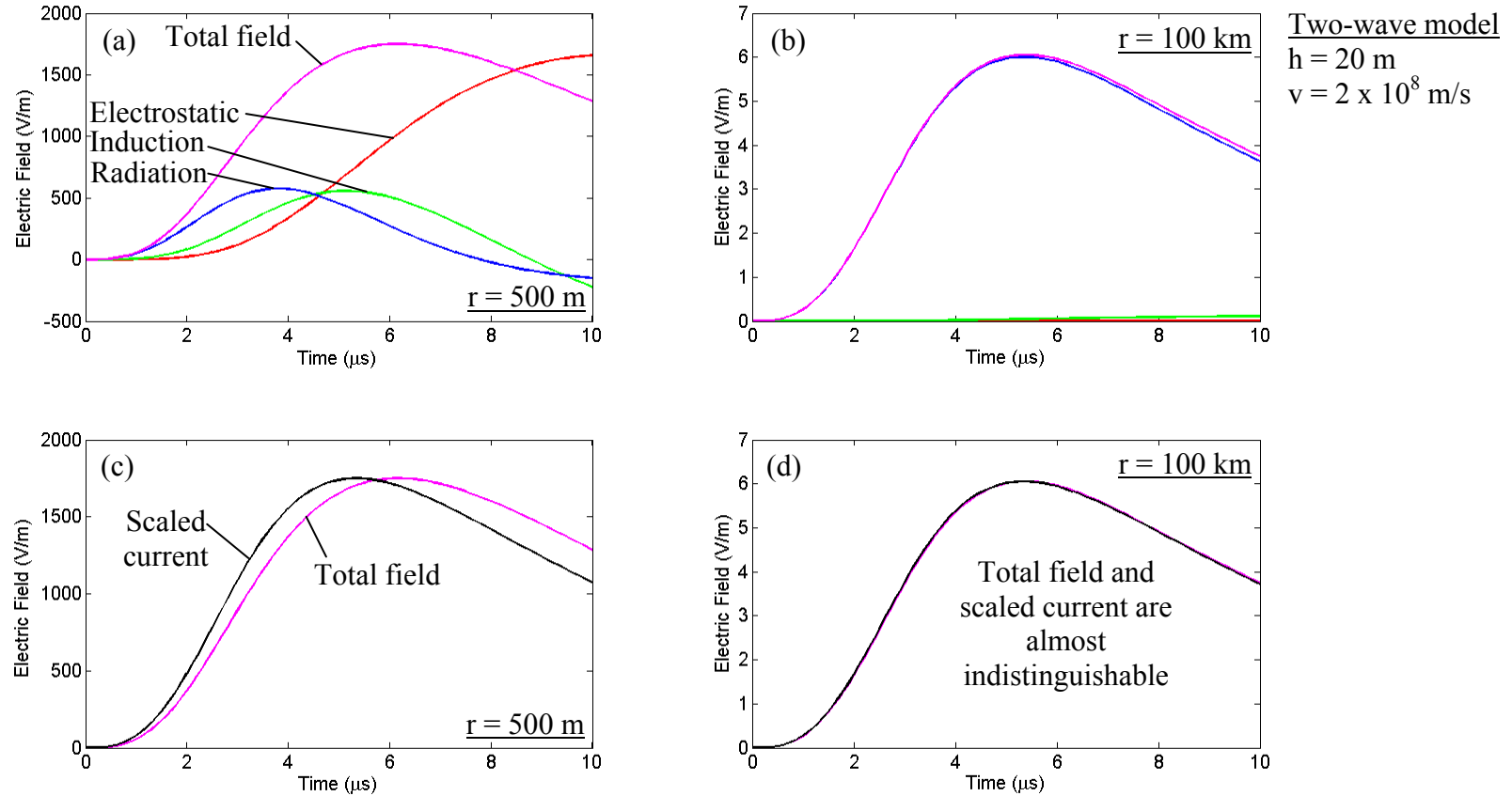
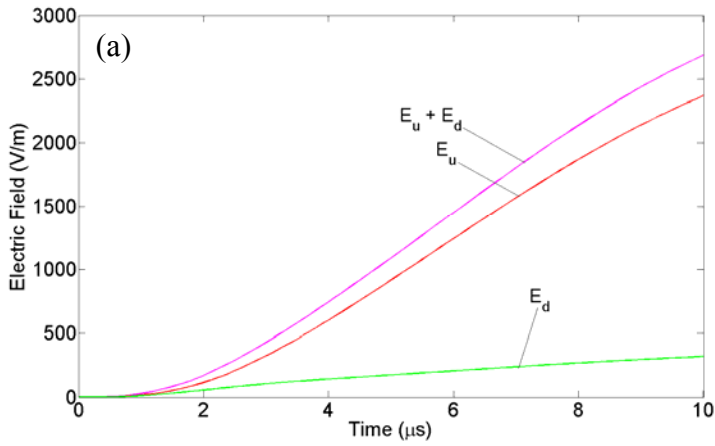
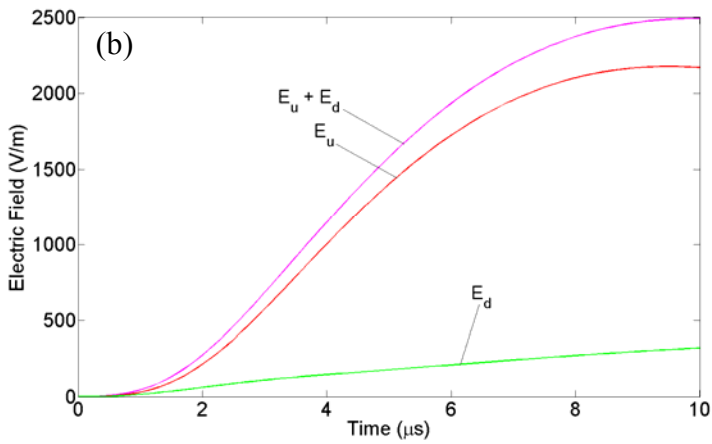


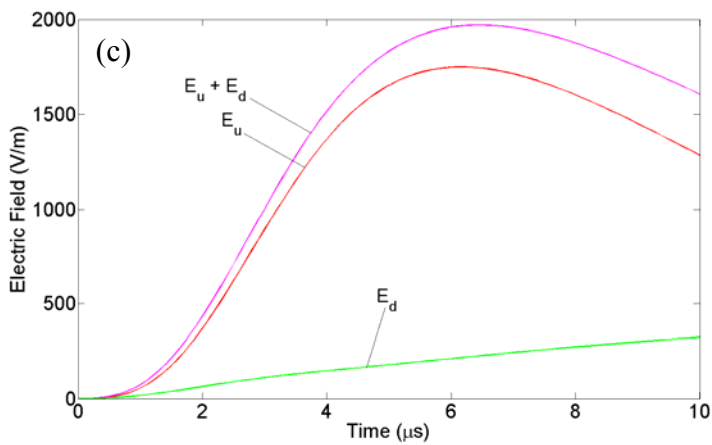
Figure 6-29. Electrostatic (red), induction (green), and radiation (blue) components of electric field and the total electric field (magenta) up to 10 μs at (a) 500 m and (b) 100 km from the lightning channel computed using the two-wave model for an assumed current-wave propagation speed of $2 \times 10^8 \text{ m/s}$ and channel length of 4 km. The total electric fields are overlaid with current waveforms scaled so that its peak is equal to the electric field peak, for direct comparison of the initial rising portions for distances of (c) 500 m and (d) 100 km. The junction point is assumed to be at a height h of 20 m above ground. Note that the portion of the predicted electric field waveform after the peak in (a) and (c) at 500 m is inconsistent with experimental data. However, for the initial few microseconds (probably up to the peak) the predicted close fields are expected to be correct. Channel-base current waveform is given by Equation 6-8.



Two-wave model
 $h = 20 \text{ m}$
 $v = 0.5 \times 10^8 \text{ m/s}$
 $r = 500 \text{ m}$



Two-wave model
 $h = 20 \text{ m}$
 $v = 1 \times 10^8 \text{ m/s}$
 $r = 500 \text{ m}$



Two-wave model
 $h = 20 \text{ m}$
 $v = 2 \times 10^8 \text{ m/s}$
 $r = 500 \text{ m}$

Figure 6-30. Electric field components E_u and E_d due to the upward and downward moving current waves, respectively, along with the total electric field ($E_u + E_d$) at 500 m for current propagation speeds of (a) 0.5×10^8 , (b) 1×10^8 , and (c) 2×10^8 for the two-wave model.

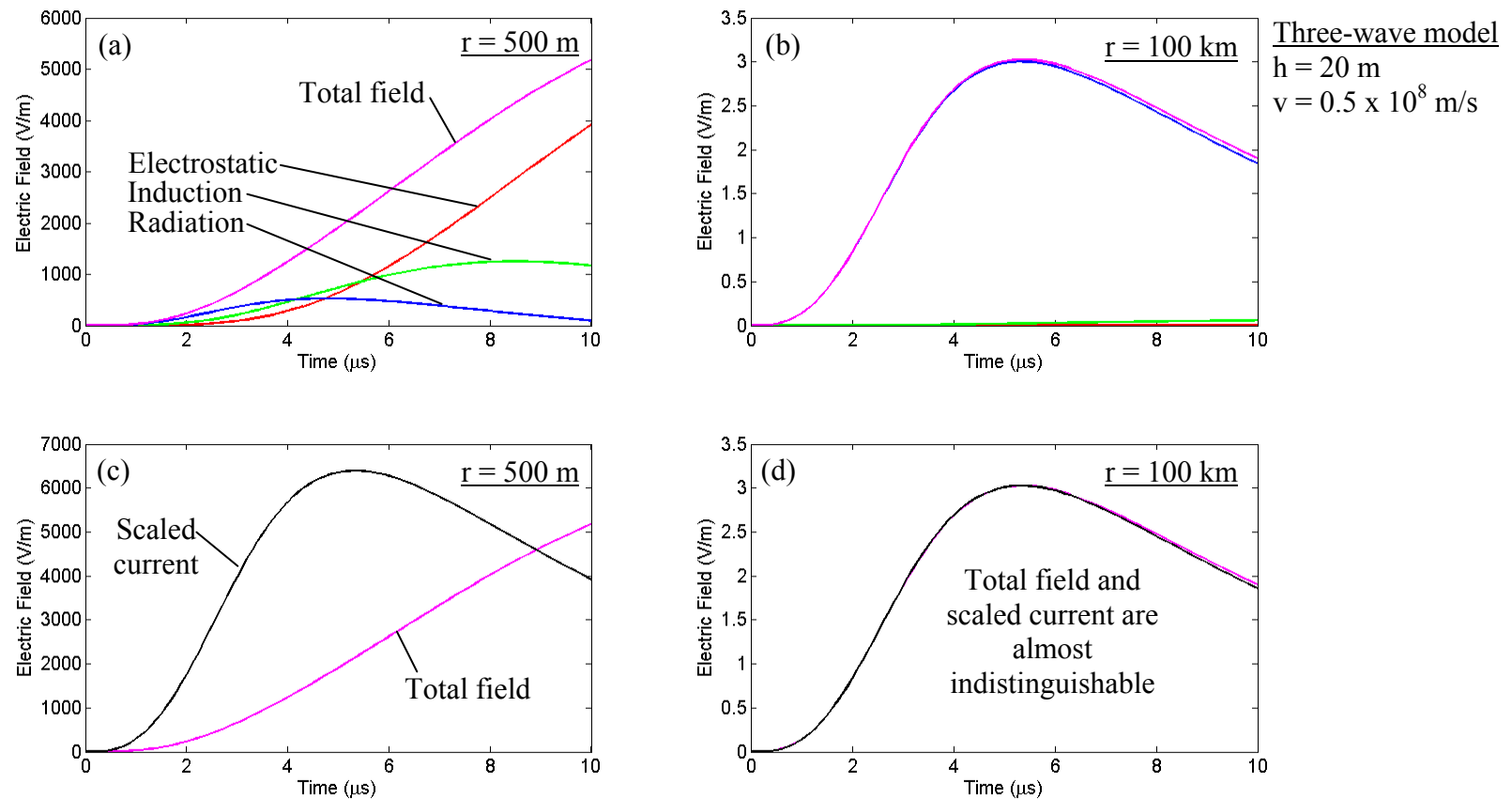


Figure 6-31. Electrostatic (red), induction (green), and radiation (blue) components of electric field and the total electric field (magenta) up to $10 \mu\text{s}$ at (a) 500 m and (b) 100 km from the lightning channel computed using the three-wave model for an assumed current-wave propagation speed of $0.5 \times 10^8 \text{ m/s}$ and channel length of 4 km . The total electric fields are overlaid with current waveforms scaled so that its peak is equal to the electric field peak (though at $r = 500 \text{ m}$, the electric field peak occurs after $10 \mu\text{s}$), for direct comparison of the initial rising portions for distances of (c) 500 m and (d) 100 km . The junction point is assumed to be at a height h of 20 m above ground. Channel-base current waveform is given by Equation 6-8.

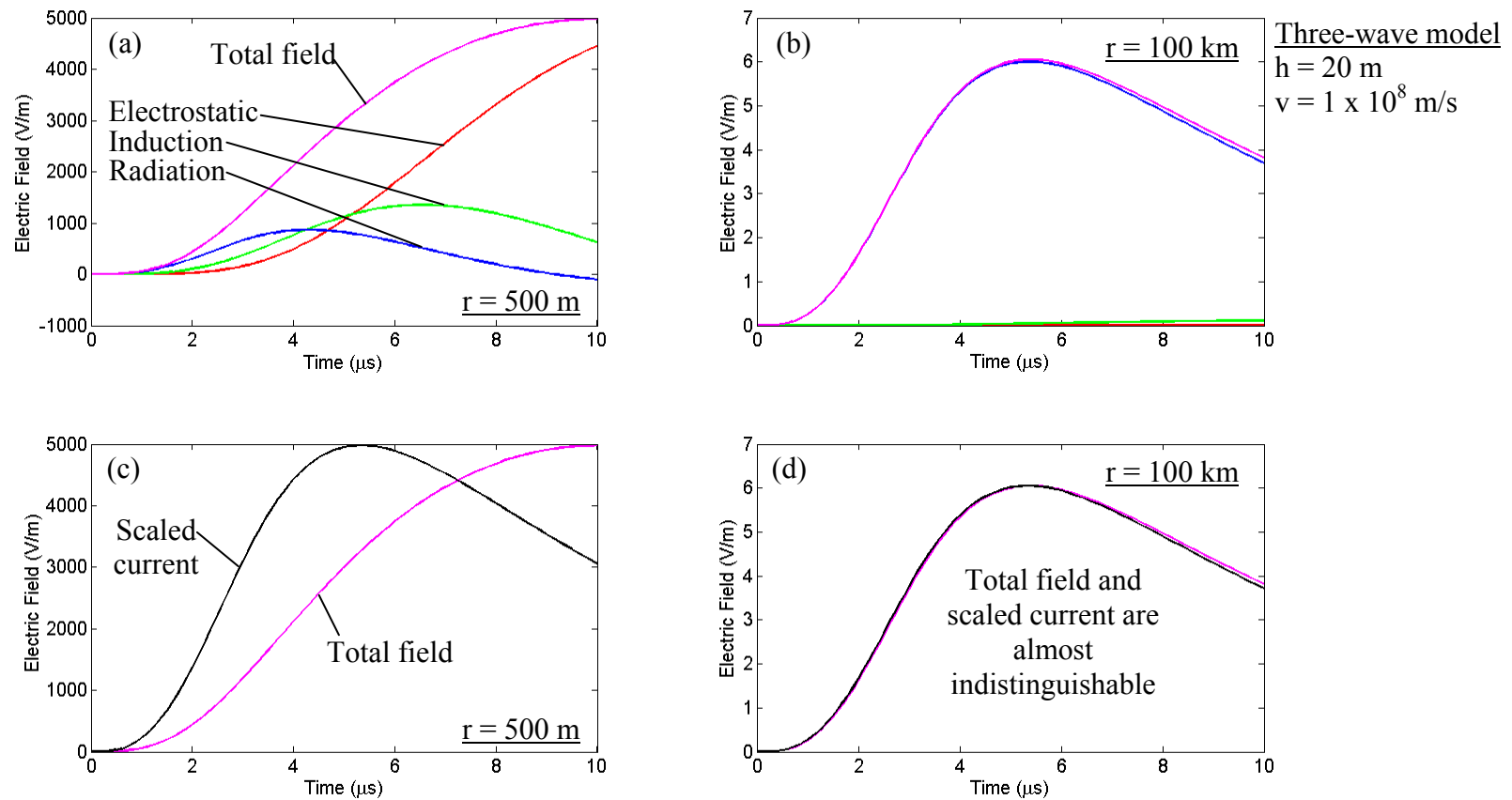


Figure 6-32. Electrostatic (red), induction (green), and radiation (blue) components of electric field and the total electric field (magenta) up to 10 μs at (a) 500 m and (b) 100 km from the lightning channel computed using the three-wave model for an assumed current-wave propagation speed of $1 \times 10^8 \text{ m/s}$ and channel length of 4 km. The total electric fields are overlaid with current waveforms scaled so that its peak is equal to the electric field peak, for direct comparison of the initial rising portions for distances of (c) 500 m and (d) 100 km. The junction point is assumed to be at a height h of 20 m above ground. Channel-base current waveform is given by Equation 6-8.

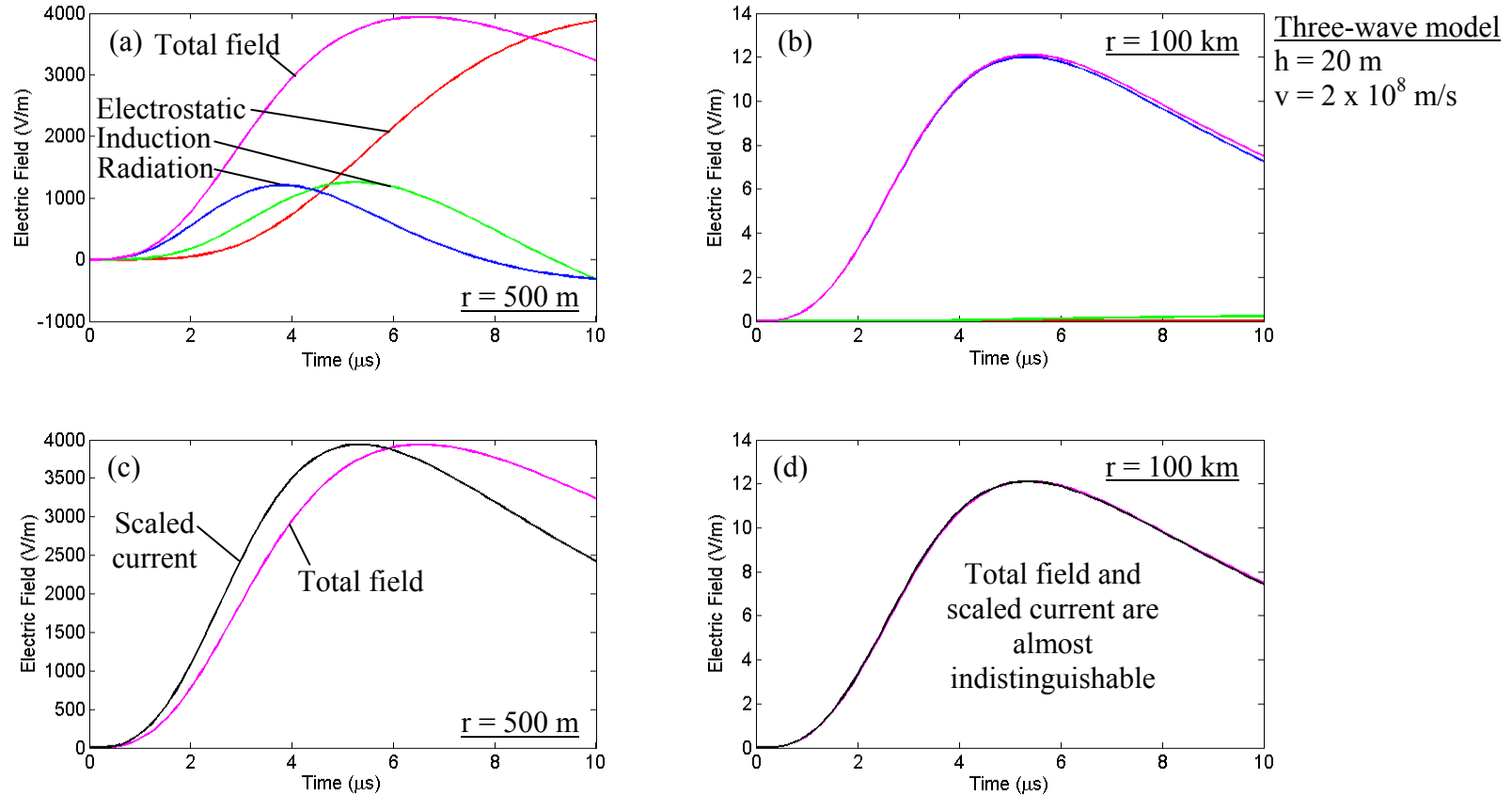
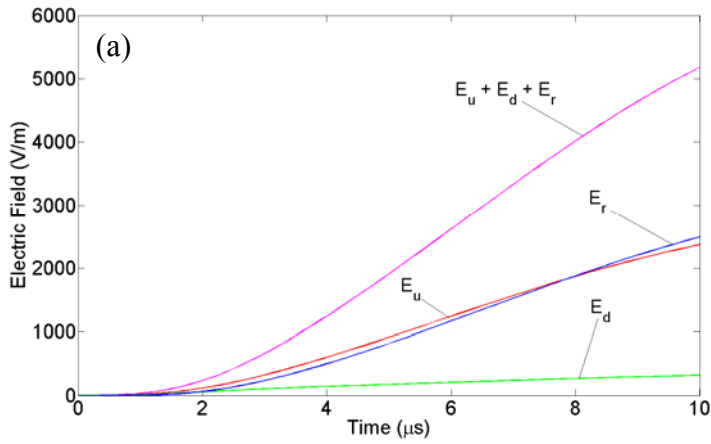


Figure 6-33. Electrostatic (red), induction (green), and radiation (blue) components of electric field and the total electric field (magenta) up to 10 μs at (a) 500 m and (b) 100 km from the lightning channel computed using the three-wave model for an assumed current-wave propagation speed of $2 \times 10^8 \text{ m/s}$ and channel length of 4 km. The total electric fields are overlaid with current waveforms scaled so that its peak is equal to the electric field peak, for direct comparison of the initial rising portions for distances of (c) 500 m and (d) 100 km. The junction point is assumed to be at a height h of 20 m above ground. Note that the portion of the predicted electric field waveform after the peak in (a) and (c) at 500 m is inconsistent with experimental data. However, for the initial few microseconds (probably up to the peak) the predicted close fields are expected to be correct. Channel-base current waveform is given by Equation 6-8.

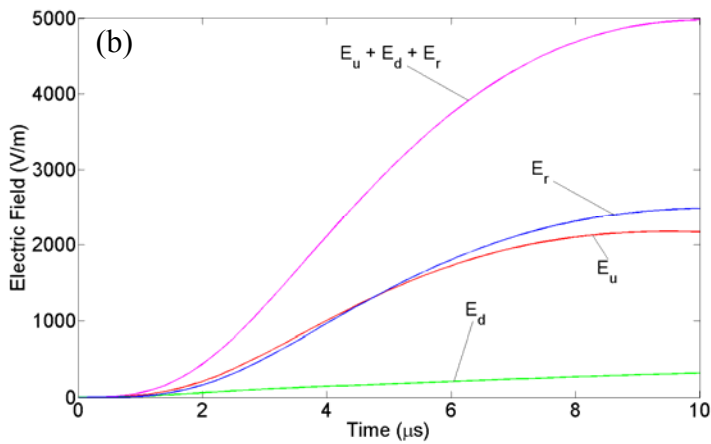


Three-wave model

$h = 20 \text{ m}$

$v = 0.5 \times 10^8 \text{ m/s}$

$r = 500 \text{ m}$

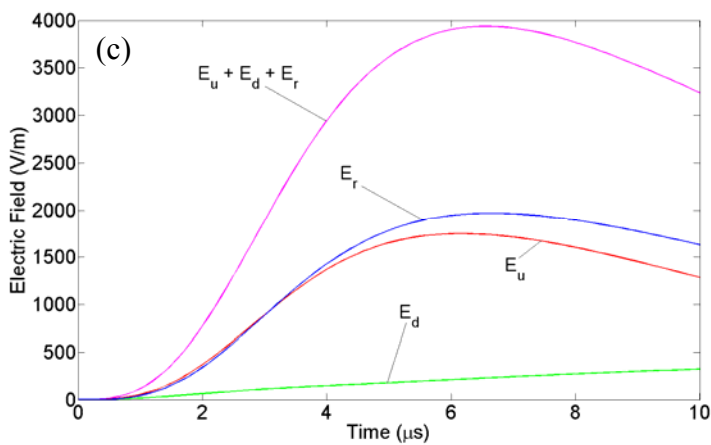


Three-wave model

$h = 20 \text{ m}$

$v = 1 \times 10^8 \text{ m/s}$

$r = 500 \text{ m}$



Three-wave model

$h = 20 \text{ m}$

$v = 2 \times 10^8 \text{ m/s}$

$r = 500 \text{ m}$

Figure 6-34. Electric field components E_u , E_d , and E_r due to the two incident current waves (upward and downward moving), and the ground reflected current wave, respectively, along with the total electric field ($E_u + E_d + E_r$) at 500 m for current propagation speeds of (a) 0.5×10^8 , (b) 1×10^8 , and (c) 2×10^8 for the three-wave model.

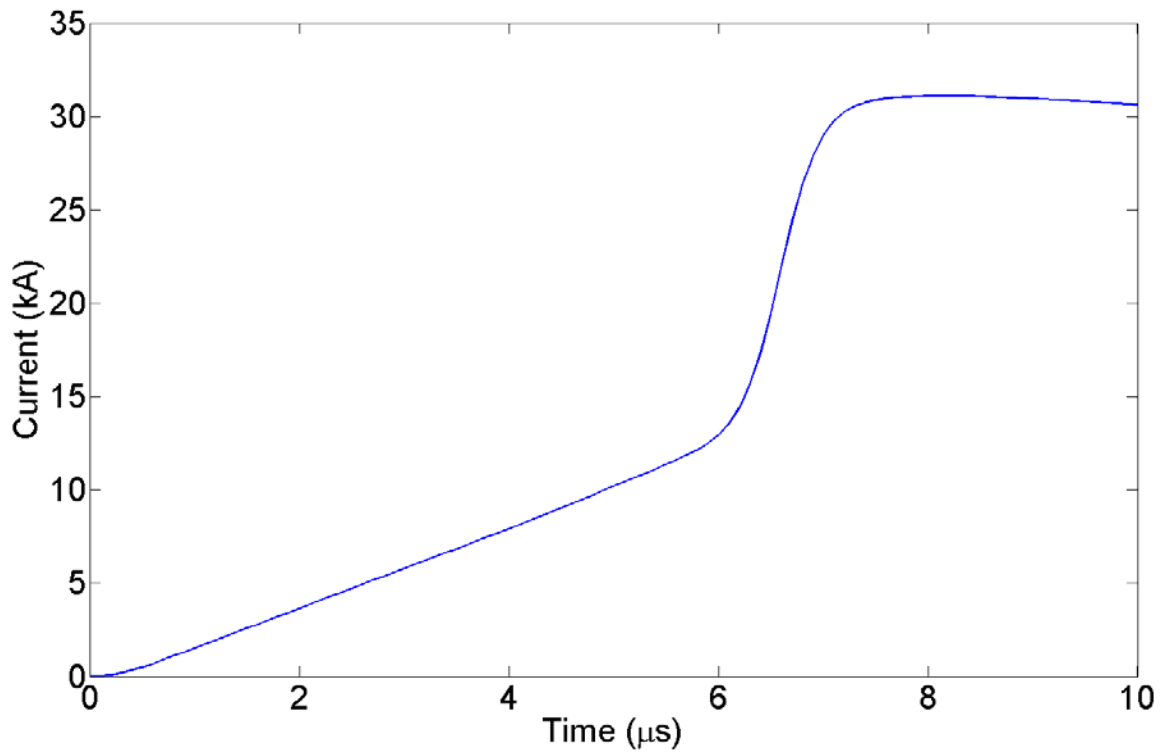


Figure 6-35. Current waveform represented by Equation 6-9 with parameters given in Table 6-4.

Table 6-4. The values of the parameters m , I_0 , η , n , τ_1 , and τ_2 for different values of k , reproduced from Table II of *De Conti and Visacro* [2007], used in Equation 6-9 to produce current waveform shown in Figure 6-35.

k	I_{0k} (kA)	n_k	τ_{1k} (μ s)	τ_{2k} (μ s)
1	2.8	2	1.2	100
2	4.8	3	3	100
3	2.9	5	4.8	25
4	4.1	7	6	60
5	16.7	36	6.6	44
6	11	2	100	600

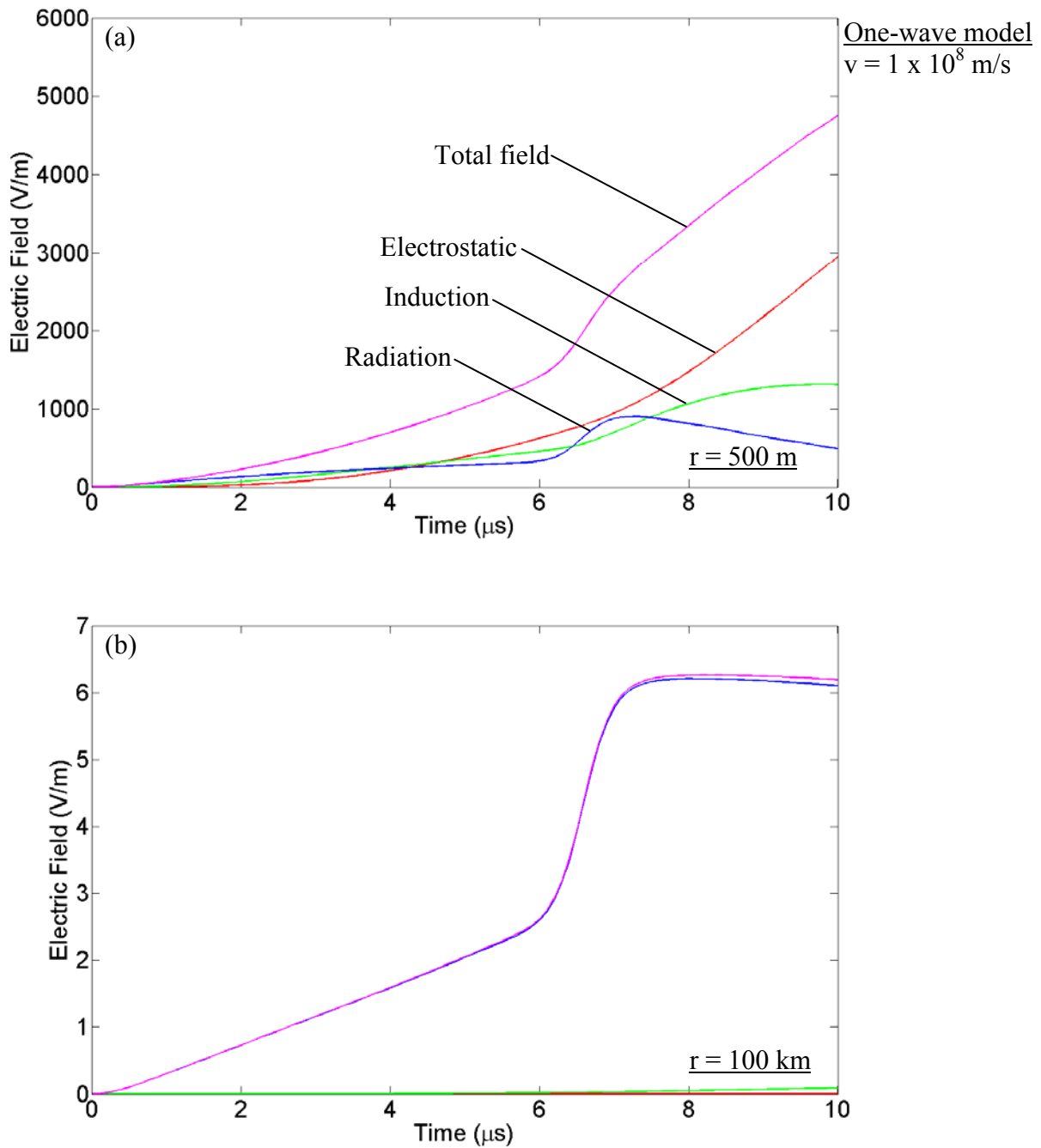


Figure 6-36. Electrostatic (red), induction (green), and radiation (blue) components of electric field and the total electric field (magenta) up to 10 μ s at (a) 500 m and (b) 100 km computed using the one-wave model. Current-wave speed is assumed to be 10^8 m/s and the channel length is 4 km. Channel-base current waveform is given by Equation 6-9.

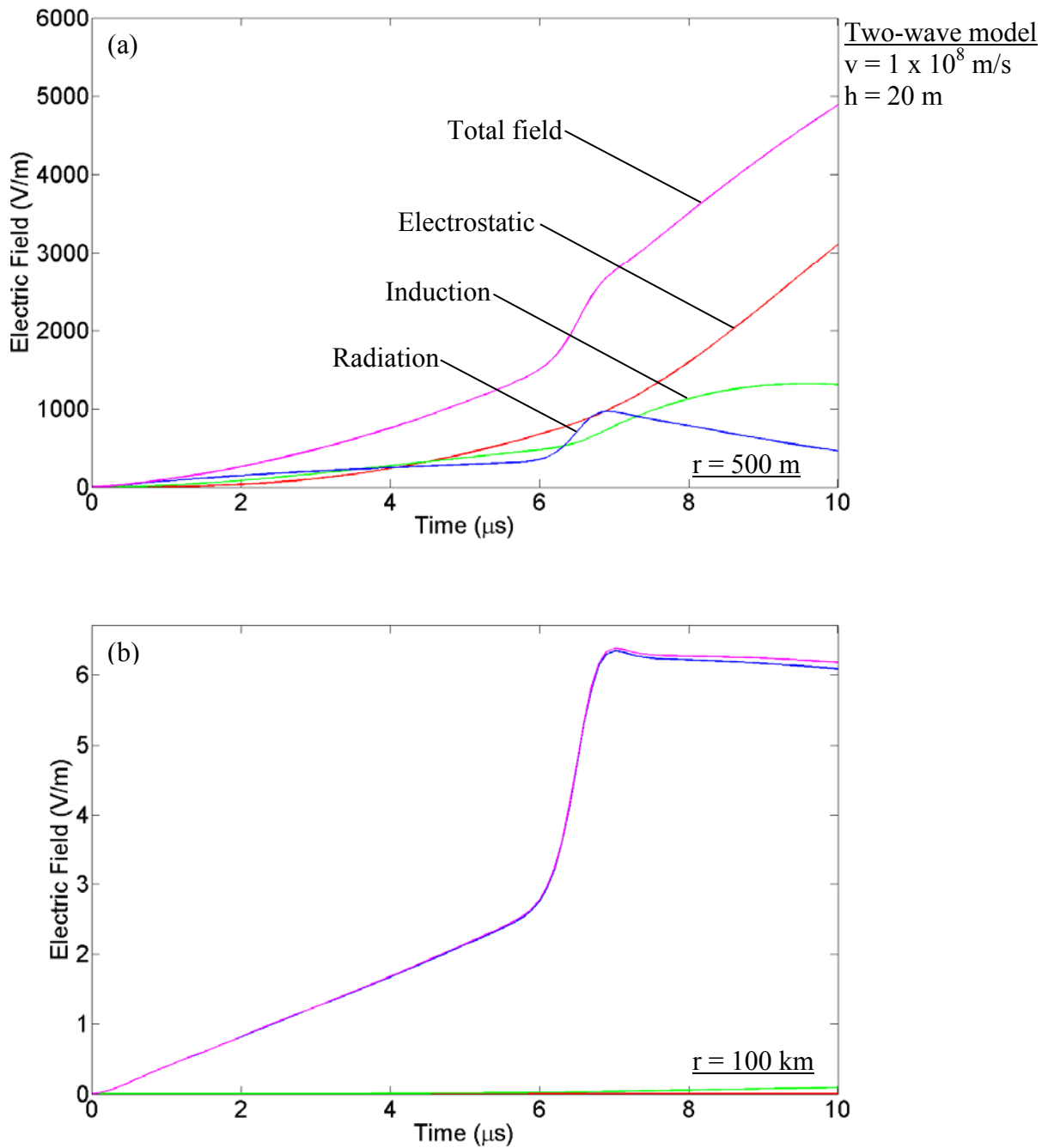


Figure 6-37. Electrostatic (red), induction (green), and radiation (blue) components of electric field and the total electric field (magenta) up to 10 μs at (a) 500 m and (b) 100 km computed using the two-wave model. Current-wave speed is assumed to be 10^8 m/s and the channel length is 4 km. The junction point is at a height of 20 m. Channel-base current waveform is given by Equation 6-9.

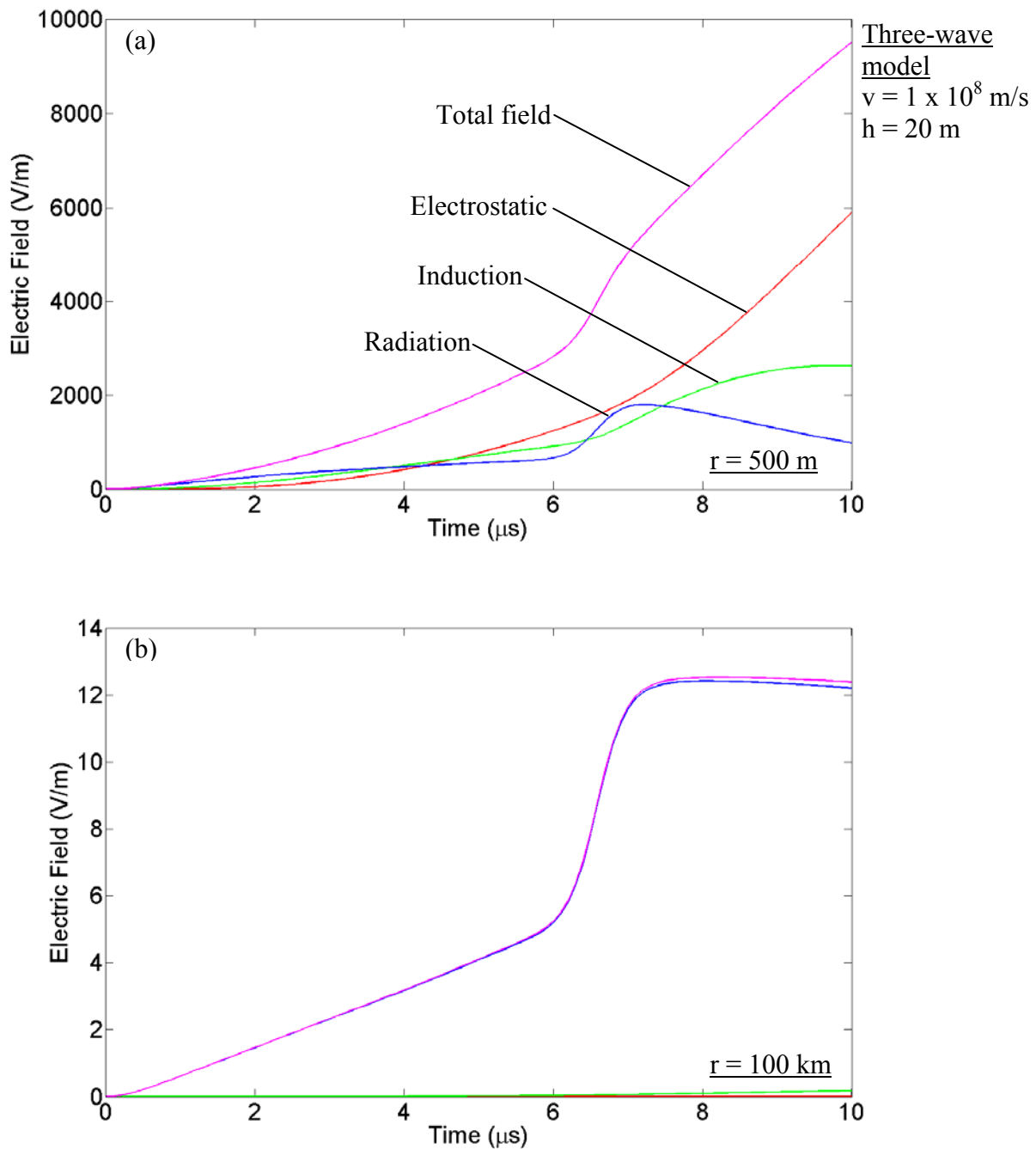


Figure 6-38. Electrostatic (red), induction (green), and radiation (blue) components of electric field and the total electric field (magenta) up to 10 μ s at (a) 500 m and (b) 100 km computed using the three-wave model. Current-wave speed is assumed to be 10^8 m/s and the channel length is 4 km. The junction point is at a height of 20 m. Channel-base current waveform is given by Equation 6-9.

6.4 Discussion

From Figures 6-24 to 6-26 (original, one-wave TL model), 6-27 to 6-29 (two-wave model), and 6-31 to 6-33 (three-wave model) we can see that as expected, the return stroke electric field at 500 m for all three models is dominated by its electrostatic component, while that at 100 km is essentially radiation. The electric field peak at far distance (100 km) increases with increasing current propagation speed for all three models. Also, at far distance current and total electric field waveshapes are almost identical for all three models and for all values of speed. Figures 6-39a and b show the total electric fields at 500 m and 100 km, respectively, for the one-wave, two-wave, and three-wave models for $v = 10^8$ m/s overlaid for direct comparison. At 100 km, the return stroke electric field peak for the one-wave and two-wave models are approximately half of that for the three-wave model. This is due to the inclusion of the reflected wave from ground (see Figure 6-34) that is not part of the one-wave model and is neglected in the two-wave model. In order to avoid this discrepancy, the incident waves for the one-wave and two-wave models have to be adjusted to effectively account for the reflected wave at ground such that the model-predicted electric fields can be directly compared. Note that for all three models, for $v = 2 \times 10^8$ m/s, the falling portion of the electric field waveform at 500 m after the peak is not consistent with experimental data. However, for the initial few microseconds (probably up to the peak) the predicted close fields are expected to be correct. As stated in Section 6.3, the overall electric field waveforms at close distances are best reproduced by the MTLL model. However, for the initial few microseconds the MTLL and TL models predict essentially the same fields. In all three models, no distinct slow front is seen in the initial rising portion of the of return stroke electric field waveform for any considered value of speed.

Next, we examine the effect of the variation in the height of the junction point from ground for the two-wave and three-wave models on the initial rising portion of the return stroke electric

field waveform. Figure 6-40a shows the return stroke electric fields at 100 km for the two-wave model, when the height of the junction point is 20 m (red line) and 100 m (blue line) above ground. The current propagation speed is 10^8 m/s. The electric field risetime appears to decrease from 5.1 to 4.2 μ s and the peak electric field increases from 3.04 to 3.49 V/m, due to the increase in the length of the channel below the junction point. Figure 6-40b shows the return stroke electric fields at 100 km for the three-wave model, when the height of the junction point is 20 m (red line) and 100 m (blue line) above ground. The current propagation speed is 10^8 m/s. The electric field waveforms are almost indistinguishable from each other, and neither exhibits a distinct slow front in the electric field waveform.

Jerauld et al. [2007], showed, using an unusual triggered-lightning stroke, that both close and distant fields can be predicted by the two-wave model in which both the slow-front and fast-transition currents are generated at the junction point of the upward and downward leaders and propagate away from that point. They used the measured current waveform which consisted of a slow front fast transition sequence to produce dE/dt (at 30 m, see Figure 6-41) and electric field (at 100 km, see Figure 6-42) displaying the same features. In the present study, we also used a two wave model to compute fields at the near and far distances and a current wave (given by Equation 6-8, see Figure 6-23) that did not contain a pronounced slow front. The resultant electric fields at near and far distances (see Figure 6-39) do not contain a slow front. Similar results are seen for the three-wave model, which is more realistic [e.g., *Rakov et al.*, 1998] as it additionally accounts for the reflection at ground of the downward current wave, with this reflected wave travelling up the channel (toward the junction point and beyond) at constant speed. *Weidman and Krider* [1978] noted that “the shapes and relative amplitudes of the fronts and fast transitions in the current waveforms are surprisingly similar to those in the radiated

fields'' (currents and fields being measured in different studies). On the other hand, there are experimental data [Willett *et al.*, 1989a], although for triggered-lightning strokes, which suggest that radiation field waveforms can exhibit pronounced slow fronts without similar features in corresponding current waveforms. It is possible that the physics of attachment process and the mechanism of the slow front/fast transition sequence generation is more complex than the simple models examined in this Chapter.

It appears that a current containing a pronounced slow front is needed to produce slow fronts in electric field at both near and far distances. In order to demonstrate this, we used an expression for first return stroke current proposed by *De Conti and Visacro* [2007] which is given by Equation 6-9. From the electric field waveforms shown in Figures 6-36, 6-37, and 6-38 computed using the one-wave, two-wave, and three-wave models, respectively, for this channel-base current and for a current propagation speed of 10^8 m/s, it can be seen that for all three models the slow front in electric field is observed in both the near and far field waveforms. The total electric fields at 500 m and 100 km computed using the three models for $v = 10^8$ m/s are overlaid in Figures 6-43a and 6-43b, respectively, for direct comparison. Apart from the difference in the return stroke electric field peak between the one-wave and two-wave models on one hand and the three-wave model on the other hand (due to reasons discussed above), the characteristics of the slow front/fast transition sequences (duration of the slow front and its magnitude relative to peak) are also approximately the same in all three models. However, one can see from Figures 6-36b, 6-37b, and 6-38b, that the slow front at 100 km is primarily due to the radiation field component, the contributions due to electrostatic and induction components being negligible, while at 500 m (see Figures 6-36a, 6-37a, and 6-38a), the slow front is composed of more or less equal (or comparable) contributions from all three components of

electric field. The electric field waveform at 500 m and 100 km computed using the three-wave model for $v = 2 \times 10^8$ m/s are shown in Figures 6-44a and 6-44b, respectively. For $v = 2 \times 10^8$ m/s the initial radiation field peak at 500 m is more pronounced than that for $v = 10^8$ m/s. The slow front duration at both 500 m and 100 km is 6.1 μ s. The amplitude of the slow front is 52% of the peak at 500 m and 44% of the peak at 100 km. For electric field waveforms of first return strokes measured at two-stations discussed in Section 6.2, the AM slow front duration for the three first return strokes at the near and far stations, were 4.6 and 4.3 μ s, respectively. The amplitude of the slow front was, on average, 47% of the peak at the near station and 35% of the peak at the far station. The amplitude of the slow front relative to the peak was found to be similar in close and distant waveforms for two out of three first return strokes having a pronounced slow front. Note that there is some uncertainty involved in identifying the initial field peak at close distances to which the small differences may probably be attributed.

The mechanism of formation of slow front in the current is probably related to the break-through phase of the attachment process by which the extending plasma channels of the upward and downward leaders make contact. This process begins when the relatively low-conductivity streamer zones ahead of the two propagating leader tips meet to form a common streamer zone. The subsequent accelerated extension of the two relatively high-conductivity plasma channels toward each other takes place inside the common streamer zone. The break-through phase can be viewed as a switch-closing operation that serves to launch two return-stroke waves from the point of junction between two plasma channels [Rakov and Uman, 2003]. The transition from a low conductivity streamer zone to a highly conducting channel is likely to produce a slow front followed by a fast transition when current quickly rises to its peak value.

6.5 Summary

In this chapter we examine the shapes and relative magnitudes of slow fronts and fast transitions in electric field waveforms of first return strokes in negative cloud-to-ground lightning measured simultaneously at two stations, one at about 45 km (far station), and the other at hundreds of meters to a few kilometers (near station) from the lightning channel. It was found that the overall field waveform characteristics of first return strokes up to the radiation field peak are similar for near (where the electric field is dominated by its electrostatic component) and far (where the electric field is essentially radiation) distances. The radiation field component of electric field is expected to be inversely proportional to distance. However, the data examined here deviated from this expectation due to the measured initial field peaks at the near station being not so well defined and contributions from electrostatic and induction components. The return stroke slow front duration in close electric field waveforms, though not identical, is similar to that in distant electric field waveforms for experimental data. The amplitude of the slow front relative to the peak was found to be similar in close and distant waveforms for two out of three first return strokes having a pronounced slow front.

We examined, via modeling, whether electric field waveforms can exhibit pronounced slow fronts without similar features in corresponding current waveforms. Three different models, the one-wave, two-wave and three-wave, were used and close and distant return stroke electric fields computed and examined. For all three models, the computed electric field waveforms do not exhibit distinct slow fronts. There are experimental data [Willett *et al.*, 1989a], although for triggered-lightning strokes, which suggest that radiation field waveforms can exhibit pronounced slow fronts without similar features in corresponding current waveforms. It is possible that the physics of attachment process and the mechanism of the slow front/fast transition sequence generation is more complex than the simple models examined in this Chapter. For an incident

current wave containing a pronounced slow front, the duration of the slow front in model-predicted electric fields and its magnitude relative to peak are approximately the same at near and far distances. The slow front at 100 km is primarily due to the radiation field component, the contributions due to electrostatic and induction components being negligible. At 500 m the slow front is composed of more or less equal (or comparable) contributions from all three components of electric field. It is likely that a slow front in return stroke current is responsible for a slow front in return stroke electric field. The mechanism of formation of slow front in the current is probably related to the break-through phase of the attachment process by which the extending plasma channels of the upward and downward leaders make contact.

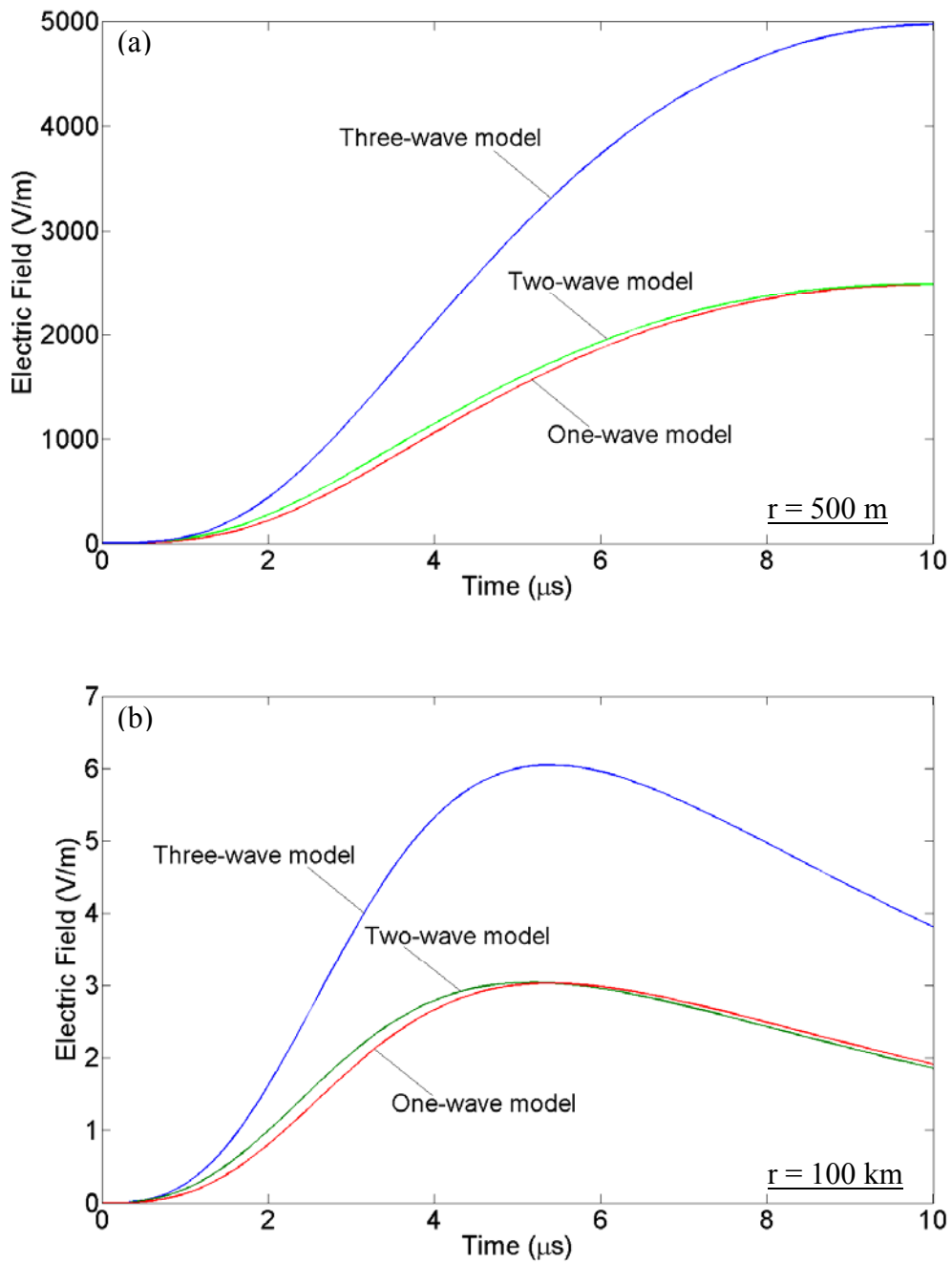


Figure 6-39. Total electric fields at (a) 500 m and (b) 100 km for the one-wave (red line), two-wave (green line), and three-wave (blue line) models for $v = 10^8$ m/s overlaid for direct comparison. Channel-base current waveform is given by Equation 6-8.

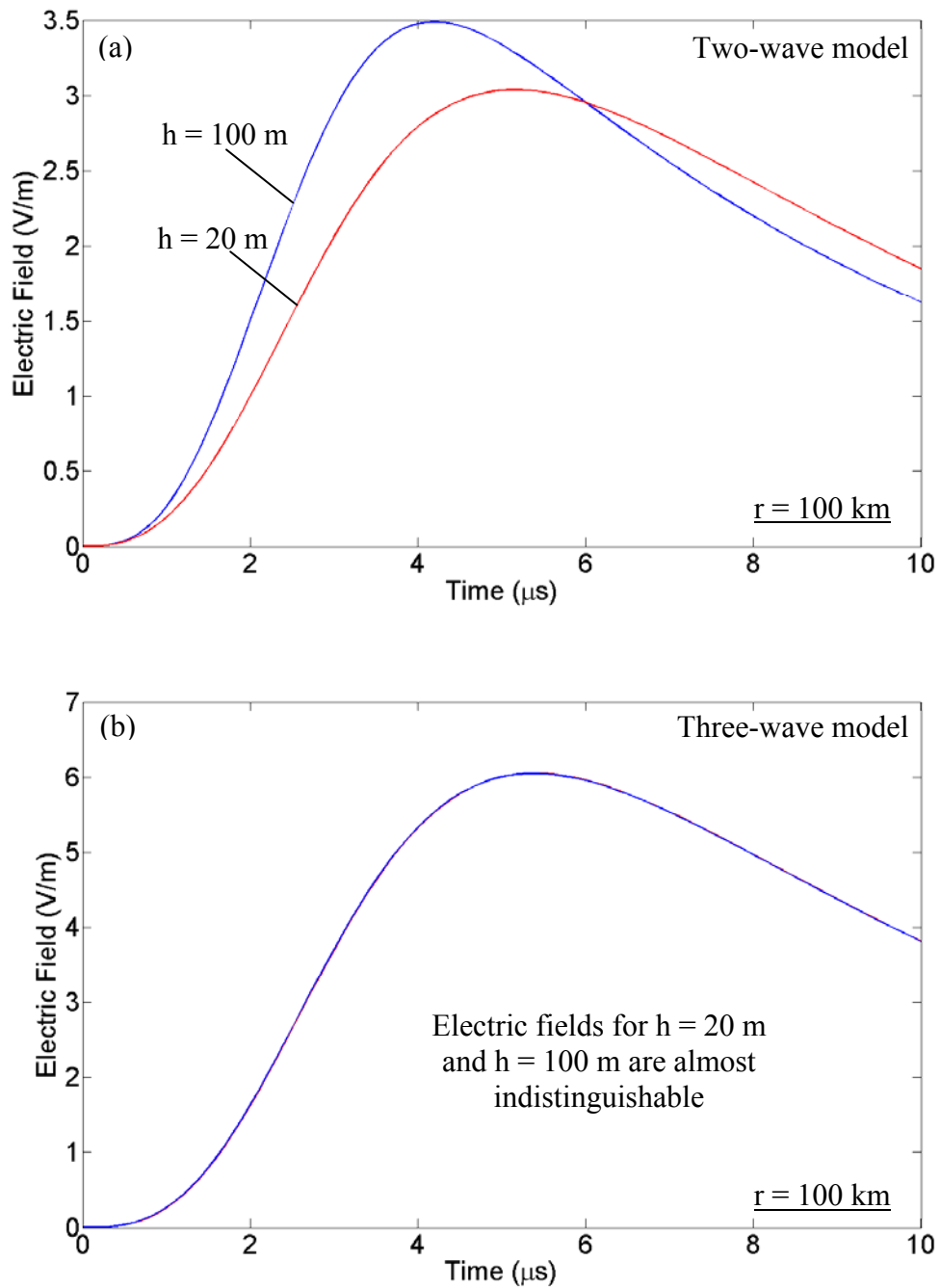


Figure 6-40. The return stroke electric fields at 100 km for the (a) two-wave and (b) three-wave models when the height of the junction point is 20 m (red line) and 100 m (blue line) above ground. The current propagation speed is 10^8 m/s. Channel-base current waveform is given by Equation 6-8.

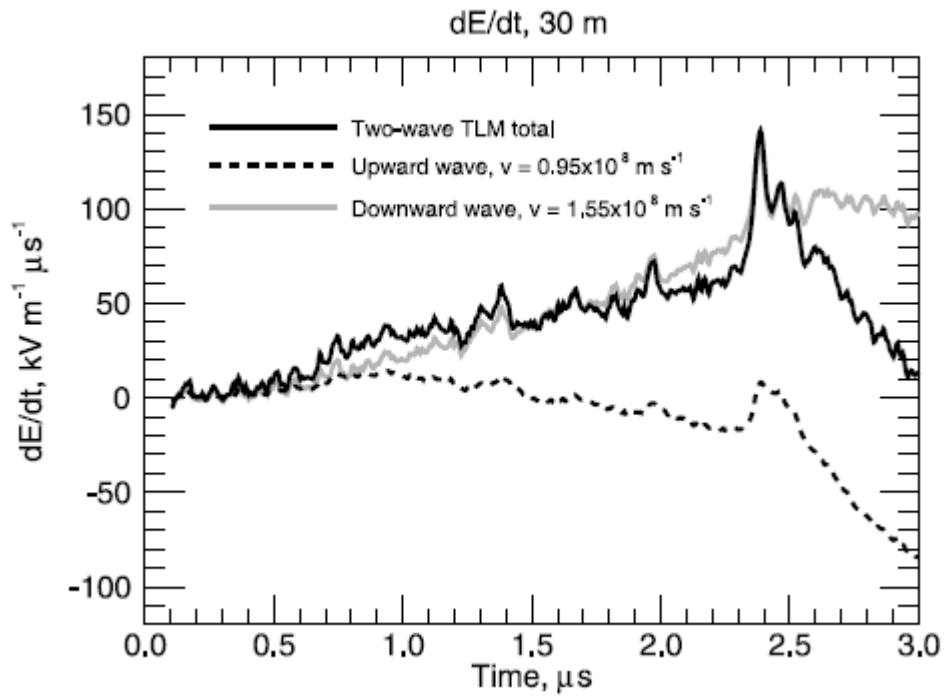


Figure 6-41. Contributions from upward (dotted curve) and downward (solid gray curve) waves to the model-predicted dE/dt waveform at 30 m calculated by *Jerauld et al.* [2007] using the two-wave model with dI/dt as input and current originating at a height of 6.5 m. The total field (sum of the two components) is also shown (solid black curve). Taken from *Jerauld et al.* [2007].

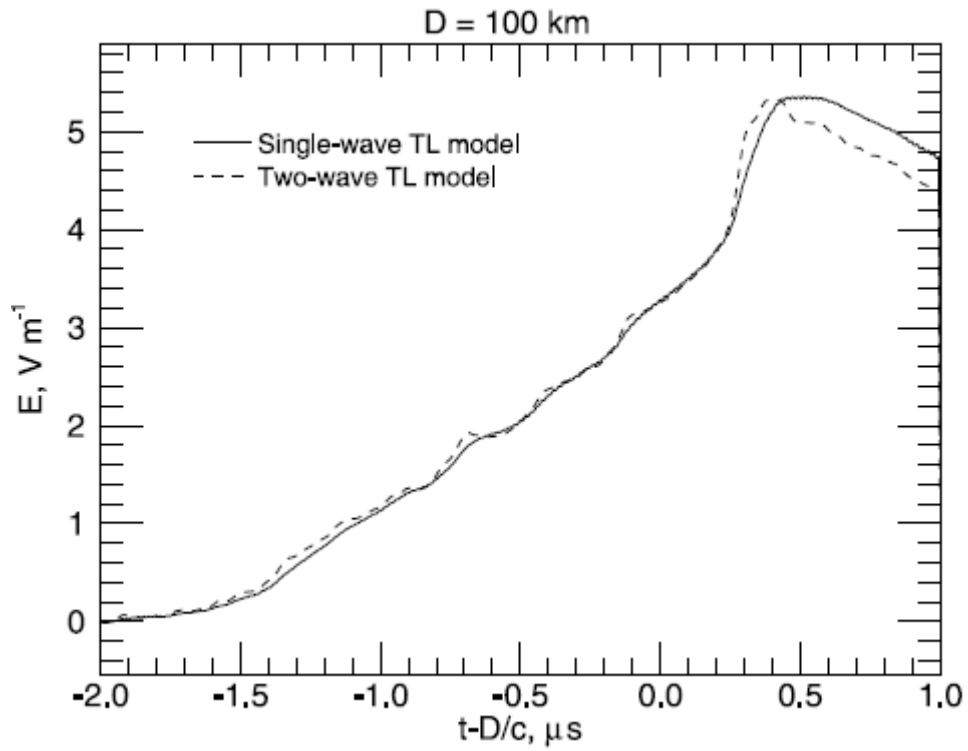


Figure 6-42. Electric fields at 100 km calculated by *Jerauld et al.* [2007] using the single- and two-wave models, assuming propagation over a perfectly conducting ground. Integrated dI/dt was used as input to both models. Taken from *Jerauld et al.* [2007].

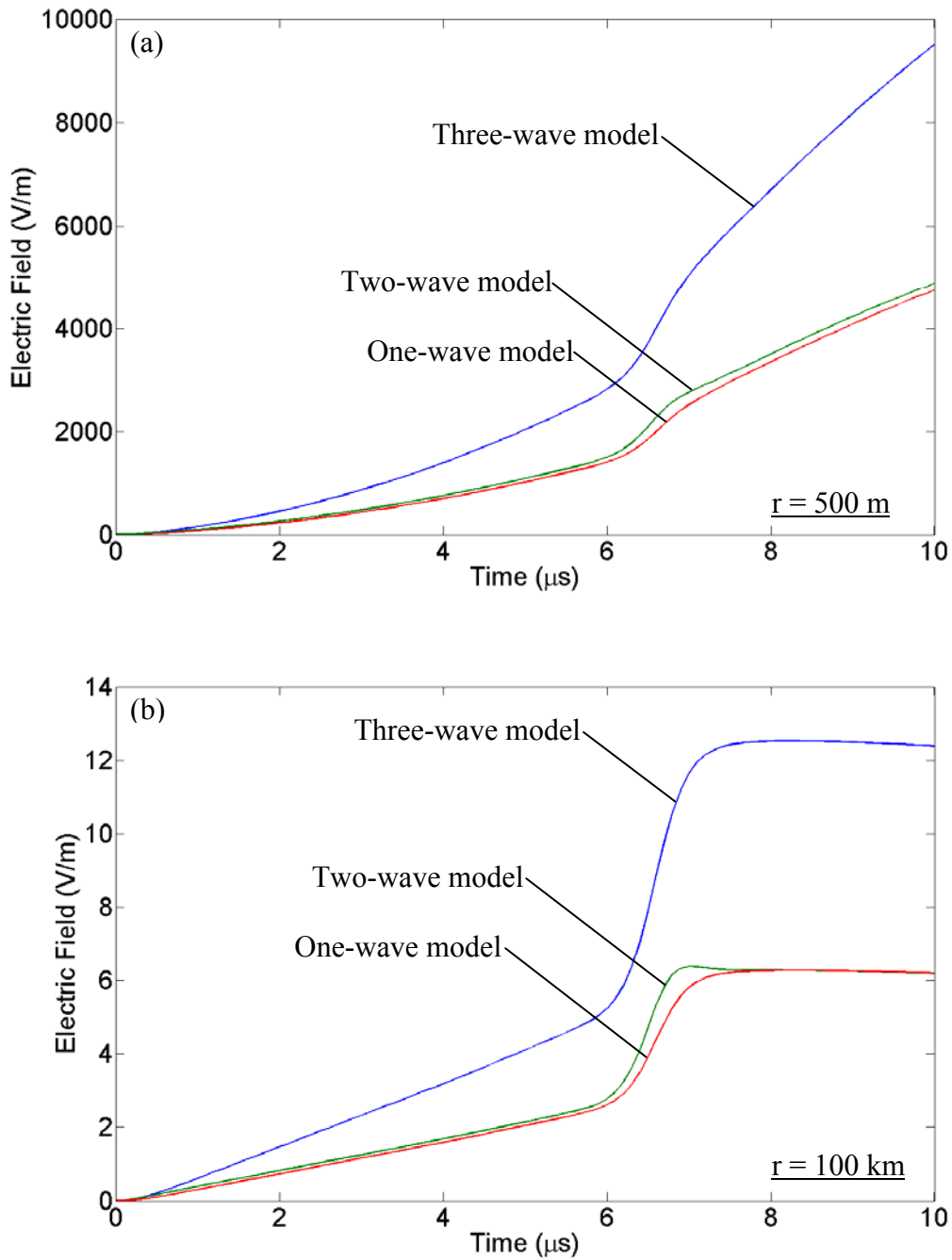


Figure 6-43. Total electric fields at (a) 500 m and (b) 100 km for the one-wave (red line), two-wave (green line), and three-wave (blue line) models for $v = 10^8$ m/s overlaid for direct comparison. Channel-base current waveform is given by Equation 6-9.

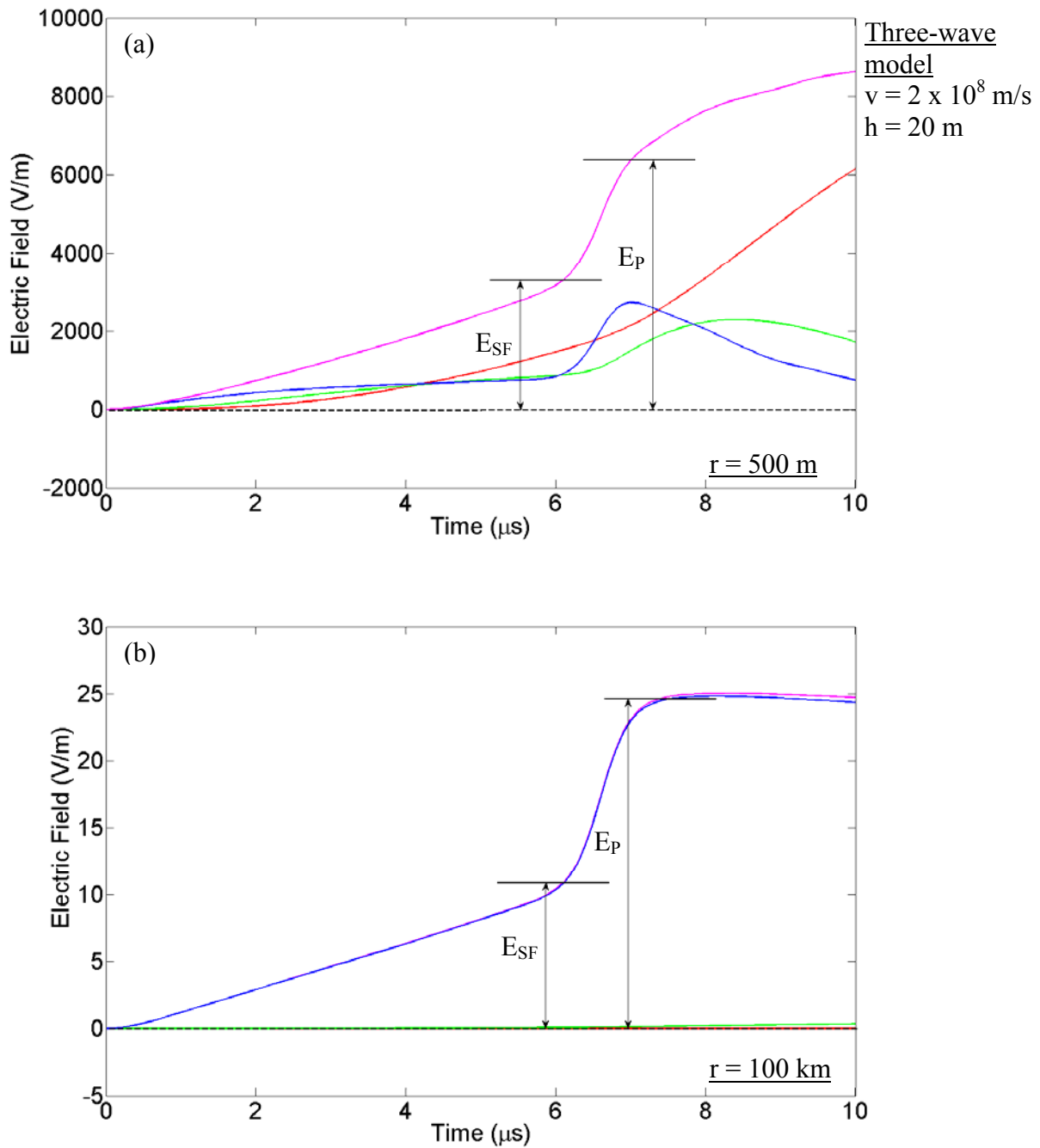


Figure 6-44. Electrostatic (red), induction (green), and radiation (blue) components of electric field and the total electric field (magenta) up to 10 μ s at (a) 500 m and (b) 100 km computed using the three-wave model. Current-wave speed is assumed to be 2×10^8 m/s and the channel length is 4 km. The junction point is at a height of 20 m. Channel-base current waveform is given by Equation 6-9.

CHAPTER 7 CHARACTERIZATION OF POSITIVE CLOUD-TO-GROUND LIGHTNING

Positive lightning discharges are considerably less understood than their negative counterparts (see Chapter 2). In this chapter, various features of positive cloud-to-ground lightning discharge, including multiplicity, parameters of return-stroke electric field waveforms, peak currents inferred from radiation electric field peaks, charge transferred by return stroke, leader stepping, preliminary breakdown pulse trains, and occurrence within otherwise negative cloud-to-ground flashes (which constitutes a bipolar flash) are examined. Presented here are 52 positive and 2 bipolar cloud-to-ground flashes recorded in 2007-2008 in Gainesville, Florida. Table 7-1 summarizes the positive and bipolar cloud-to-ground lightning data recorded at the LOG. Of these 54 discharges, 41 occurred during the warmer (April-October) season and 13 during the colder (November-February) season. We had GPS timing information for 45 positive flashes (containing 53 strokes) and 1 bipolar flash (1 positive return stroke). The National Lightning Detection Network (NLDN) located 52 (96%) out of 54 positive return strokes, of which 48 were correctly identified and 4 positive return strokes were misidentified as cloud discharges. NLDN-reported distances from the field measuring station (LOG) for the 48 correctly identified strokes ranged from 7.8 to 157 km and for 4 misidentified strokes from 1.8 to 5 km.

7.1 Multiplicity

The term multiplicity is often used to denote number of strokes per flash, not necessarily along the same channel to ground. Positive flashes are usually composed of a single stroke, whereas about 80% of negative flashes contain two or more strokes [e.g., *Rakov et al.* 1994]. Multiple-stroke positive flashes do occur but they are relatively rare. *Heidler et al.* [1998], from electric field measurements in 1995–97 in Germany, found that out of a total of 36 positive

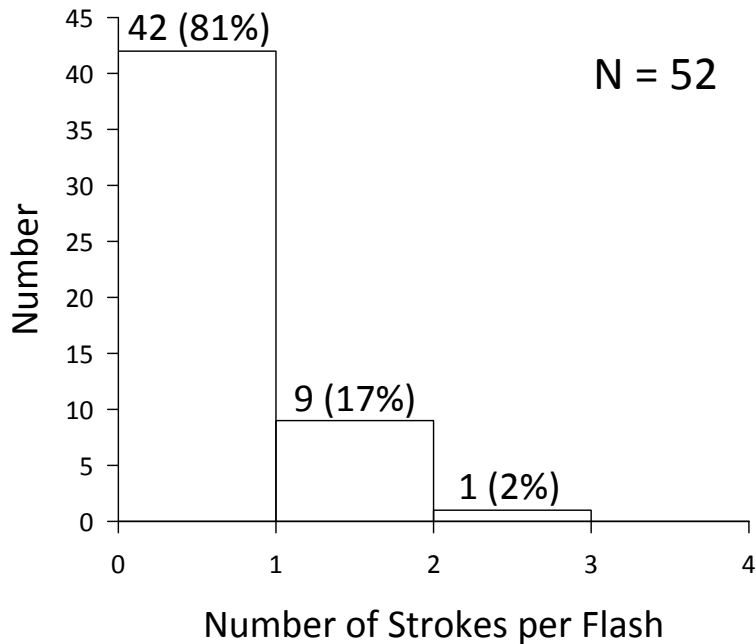


Figure 7-1. Histogram of the number of strokes per flash for 52 positive cloud-to-ground flashes in Florida.

flashes, 32 (89%) contained one stroke and 4 (10%) contained two strokes. Out of the 52 positive cloud-to-ground flashes presented here 42 (81%) were single-stroke, 9 (17%) two-stroke, and 1 (2.0%) three-stroke flashes, as shown in Figure 7-1. The electric field of the three-stroke flash is shown in Figure 7-2 (GPS timing information for this flash was not available and hence no NLDN data could be obtained). There were a total of 63 return strokes in 52 flashes with an average number of strokes per flash (multiplicity) of 1.2. For comparison, *Rakov and Uman* [1990b] reported an average multiplicity of 4.6 for 76 negative cloud-to-ground flashes in Florida.

Note that for the dataset presented here, the record length was either 240 ms with a pre-trigger of 80 ms, or 500 ms with a pre-trigger of 100 ms. There is a small possibility that a subsequent stroke of a multiple-stroke positive flash triggered our field measuring system and, due to insufficient pre-trigger, the first stroke of the flash was missed. In order for this to happen,

the field peak of the "missed" first stroke would have to be smaller than that of the subsequent stroke and it would have to occur at least 80 ms (the minimum pre-trigger time of our electric field records) prior to the subsequent stroke. Thus, some first return strokes in our dataset may actually be subsequent strokes, and some single stroke flashes may actually be multiple-stroke flashes. If that were the case, the calculated multiplicity of 1.2 would be an underestimate.

We found that 13 out of 52 (25%) positive flashes in our dataset were associated with (either preceded or followed by) intracloud discharges. However, this might be an underestimate due to the limited pre-trigger time and record length, as discussed above.

For 8 out of the 9 two-stroke flashes NLDN estimated locations for all strokes were available. These flashes occurred at distances ranging from 10 to 157 km from the field measuring station. Of these 8 flashes, the distance between the first and second strokes was less than 1 km for 1 flash, within 1 to 4 km for 3 flashes, and within 10 to 15 km for 3 flashes. In one flash, the two strokes were separated by 29 km. The interstroke interval, distance between first and second strokes for each flash, and the semi-major axis (SMA) length of NLDN 50% location error ellipse, which is defined as NLDN median location error, for each stroke are given in Table 7-2.

Figures 7-44 to 7-51 (at the end of this chapter) show electric field records of the first and second return strokes for all eight located two-stroke positive flashes. A second stroke that exhibits a wave shape similar to that of the corresponding first stroke probably follows the same channel as the first one. Distance between strokes being smaller than the largest NLDN median location error (SMA length) is also an indication of the two strokes sharing the same channel. Out of 8 two-stroke flashes, 3 contained strokes characterized by both similar electric field waveshapes and spatial separations that are smaller than stroke location uncertainties. For

example, in flash 06/02/08_431 (shown in Figure 7-37) for which the two strokes occurred within 83 ms and 222 m of each other (NLDN median location errors of 800 m and 500 m for the first and second stroke, respectively) the second stroke likely followed the same channel as the first stroke. In one flash (05/16/08_49), field waveshapes were similar but separation (14 km) was much larger than median location errors (0.4 km). For 5 two-stroke flashes, different field waveshapes were accompanied by distances larger than location errors. Thus, only in one case out of eight the two criteria were inconsistent with each other.

The issue of the number of channels to ground formed within a flash can, however, be only addressed conclusively when optical records (video or still images) of the flash are available. Optical evidence of negative strokes following the channel of preceding positive stroke in a bipolar flash in Florida has been reported by *Jerauld et al.* [2009]. *Fleenor et al.* [2009] observed four bipolar flashes (about 1% of the flashes in their dataset) in the Great Plains each of which had a positive first stroke that was followed by 1 (in 3 flashes) or 2 (in 1 flash) negative strokes. The intervals between the first and second strokes ranged from 43 ms to 348 ms. Two of their four negative second strokes followed the same channel to ground as the preceding positive first stroke. Examples of a positive subsequent stroke following the same channel as the preceding negative stroke have been previously reported for tower lightning and rocket-triggered lightning. *Janischewskyj et al.* [1999] in Canada reported a flash that was initiated by an upward leader from the 553-m high Canadian National (CN) tower in Toronto. The flash contained three strokes, the second of which was positive, following the same channel within at least 535 m above the tower top. The three consecutive return stroke peak currents, in stroke order, were -10.6 kA, +6.5 kA, and -8.9 kA. *Jerauld et al.* [2004] reported a triggered lightning flash containing both negative and positive strokes. The first stroke lowered negative charge to ground

and the second stroke lowered positive charge via the same channel. The measured negative return stroke peak current was -11 kA and the positive +5 kA. The two return strokes were separated by about 58 ms.

Table 7-1. Summary of the positive and bipolar cloud-to-ground lightning data (a total of 54 flashes) recorded at the LOG. Data recorded is indicated by "Y" and not recorded by "N".

Flash ID	Electric Field	dE/dt	dB/dt	HF (5 MHz)	VHF (36 MHz)
062007_00	Y	N	N	N	N
082407_286	Y	Y	N	Y	Y
082407_452	Y	Y	N	Y	Y
100507_186	Y	Y	N	Y	Y
100507_376	Y	Y	N	Y	Y
121607_49	Y	Y	N	N	N
121607_61	Y	Y	N	Y	Y
121607_63	Y	Y	N	Y	Y
011908_441	Y	Y	N	N	N
011908_481	Y	Y	N	N	N
012208_05	Y	Y	N	Y	Y
012208_06	Y	Y	N	Y	Y
012208_08	Y	Y	N	Y	Y
012208_10	Y	Y	N	Y	Y
012208_13	Y	Y	N	Y	Y
012208_14	Y	Y	N	Y	Y
012208_23	Y	Y	N	Y	Y
042608_00	Y	Y	N	N	Y
042608_01	Y	Y	N	N	Y
051608_27	Y	Y	N	N	Y
051608_29	Y	Y	N	N	Y
051608_31	Y	Y	N	N	Y
051608_47	Y	Y	N	N	Y
051608_49	Y	Y	N	N	Y
051808_86	Y	Y	N	N	Y
051808_88	Y	Y	N	N	Y
051808_106	Y	Y	N	N	Y
061008_05	Y	Y	N	N	Y
060108_131	Y	Y	N	N	Y
060108_208	Y	Y	N	N	Y
060108_215	Y	Y	N	N	Y
060208_431	Y	Y	N	N	Y
060908_700	Y	Y	N	N	Y

Table 7-1. Continued

Flash ID	Electric Field	dE/dt	dB/dt	HF (5 MHz)	VHF (36 MHz)
080808_01	Y	Y	N	N	N
081308_31	Y	Y	N	N	Y
081308_40	Y	Y	N	N	Y
081308_41	Y	Y	N	N	Y
081308_57	Y	Y	N	N	Y
081308_58	Y	Y	N	N	Y
081408_84	Y	Y	Y	N	N
081408_85	Y	Y	Y	N	N
081408_87	Y	Y	Y	N	N
081408_90	Y	Y	Y	N	N
082308_173	Y	N	Y	N	Y
082308_338	Y	N	Y	N	Y
082308_339	Y	N	Y	N	Y
082308_343	Y	N	Y	N	Y
082308_344	Y	N	Y	N	Y
082308_345	Y	N	Y	N	Y
082308_346	Y	N	Y	N	Y
082308_348	Y	Y	Y	N	Y
082308_350	Y	Y	Y	N	Y
082408_783	Y	Y	Y	N	Y
113008_01	Y	Y	Y	N	N

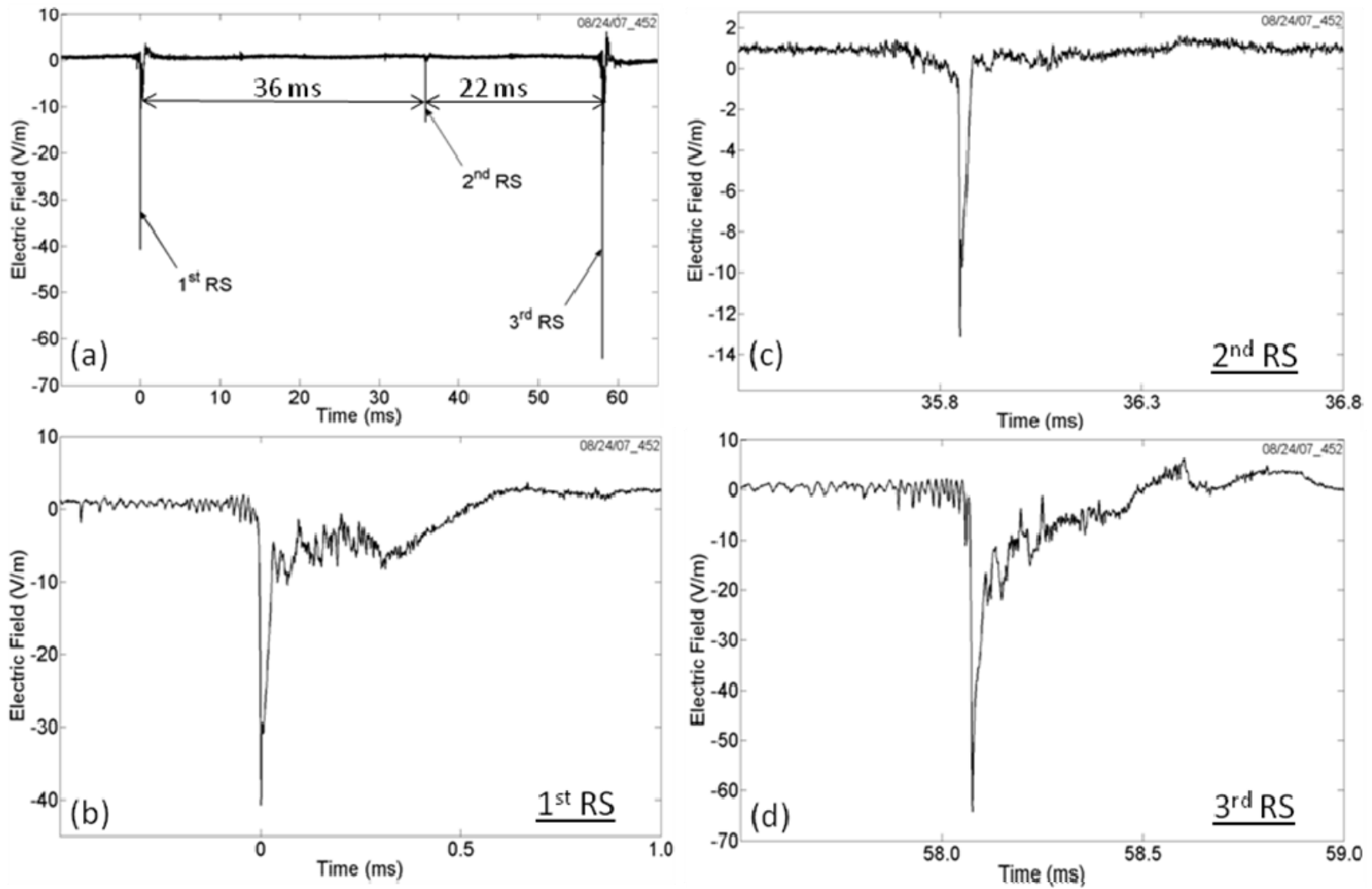


Figure 7-2. (a) Electric field record of a multiple-stroke positive cloud-to-ground flash in Florida with three return strokes (RS) shown on a 75-ms time scale. (b), (c), and (d). Electric fields of the first, second, and third return strokes, on a 1.5-ms time scale, respectively. GPS timestamps and NLDN information were not available for this flash.

Table 7-2. Interstroke interval, distance between first and second strokes, and semi-major axis (SMA) length of NLDN 50% location error ellipse for each stroke of 8 two-stroke positive flashes.

Flash ID	Figure showing electric field waveforms	Interstroke interval, ms	Distance between first and second strokes, km	SMA length for first stroke, km	SMA length for second stroke, km	Distance between strokes is smaller than largest SMA length	Similarity of first and second stroke electric field waveforms
06/20/07_00	7-44	19	1.7	4.0	0.5	Y	Y
01/22/08_05	7-45	79	12	0.7	0.4	N	N
01/22/08_06	7-46	8.5	2.0	2.4	0.5	Y	Y
05/16/08_49	7-47	116	14	0.4	0.4	N	Y
06/02/08_431	7-48	83	0.22	0.8	0.5	Y	Y
08/14/08_85	7-49	70	10	0.6	0.8	N	N
08/23/08_350	7-50	201	29	0.5	0.4	N	N
11/30/08_01	7-51	41	3.7	0.4	0.4	N	N
AM	-	77	9.1	1.2	0.5	-	-
GM	-	54	4.4	0.8	0.5	-	-
Min	-	8.5	0.22	0.4	0.4	-	-
Max	-	201	29	4	0.8	-	-

7.2 Parameters of Return Stroke Electric Field and Field Derivative Waveforms

The electric field and field derivative (dE/dt) waveforms of positive return strokes were examined in detail. The various field waveform parameters of positive return strokes are discussed in the following Sections and summarized in Table 7-3. Since not all the parameters could be measured in each waveform, sample sizes in Table 7-3 are not the same.

7.2.1 Distance-Normalized Electric Field Peaks

The measured initial electric field peak normalized to 100 km for 48 positive return strokes located at distances of 7.8 to 157 km ranged from 4.34 to 66.3 V/m. The AM and GM fields were 21.7 V/m and 18.1 V/m, respectively. Note that the electric field change due to a positive return stroke is negative according to the atmospheric electricity sign convention. Only the magnitude of the electric field change is considered here. The histogram of the initial electric

field peak normalized to 100 km for the 48 return strokes is shown in Figure 7-3. *Cooray and Lundquist* [1982] and *Cooray et al.* [1998] reported the AM electric field peak normalized to 100 km to be 11.5 V/m and 13.9 V/m in Sweden and Denmark, respectively. These values are roughly 0.5 to 0.7 times of their counterpart found in this study. Figure 7-4 shows the scatter plot for the distance-normalized electric field peak versus distance from the measuring station for the 48 positive return strokes in this dataset. Ideally, there should be no dependence. It can be seen in Figure 7-4 that even though the minimum normalized electric field peak tends to increase with distance, the dependence is rather weak (determination coefficient = 0.20). The dependence of the minimum value on distance suggests a bias toward larger field peaks, which increases with increasing distance. Indeed, the GM normalized electric field peaks for distance ranges of 7.8-50 km and 64-157 km in this dataset are 14.8 V/m (N = 31) and 26.3 V/m (N = 17), respectively. Table 7-4 shows the number of positive return strokes in different distance ranges along with the GM electric field peak normalized to 100 km for each distance range.

For negative lightning, *Rakov and Uman* [1990b] and *Pavlick et al.* [2002] found the GM electric field peak normalized to 100 km to be 5.9 V/m and 7.6 V/m for 76 and 178 first strokes, respectively, in Florida versus 19.8 V/m for 40 positive first strokes in this study. For 270 negative subsequent strokes, the GM electric field peak normalized to 100 km was 2.9 V/m in Florida [*Rakov and Uman*, 1990a, b], while for the 8 positive subsequent strokes in the dataset presented here the value was 11.7 V/m. Note that even for distances less than 20 km (see Table 7-4) the GM electric field peak normalized to 100 km for positive strokes examined here is higher than for negative return strokes.

7.2.2 Risetime

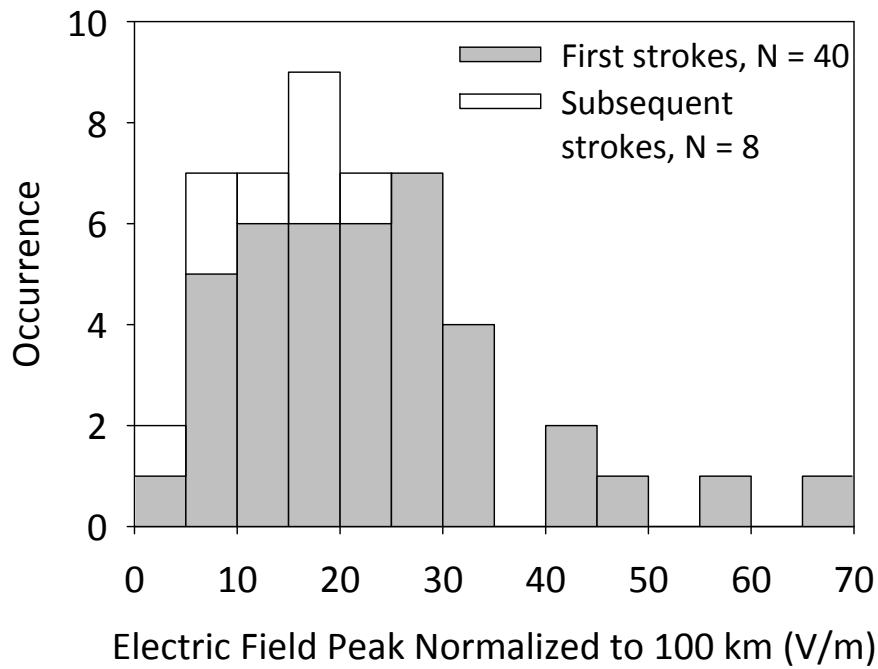
Histogram of the zero-to-peak risetime and 10-90% risetime for 62 (out of the total of 63) return strokes recorded, the electric field waveform for one return stroke was saturated due to its

Table 7-3. Parameters of electric field waveforms produced by first and subsequent return strokes in positive lightning.

Parameter	Sample size	AM	SD	GM	Median	SD (logx)	Range
Initial electric field peak normalized to 100 km, V/m	48	21.7	13.2	18.1	19.5	0.275	4.34-66.3
Zero-to-peak risetime, μ s	62	7.77	3.76	6.92	7.19	0.213	2.26-21.1
10-to-90 percent risetime, μ s	62	4.02	2.12	3.40	3.71	0.279	0.36-10.4
Slow front duration, μ s	62	5.94	3.63	4.95	5.15	0.276	0.77-18.6
Slow front amplitude relative to peak, percent	62	39.4	15.0	36.7	36.7	0.167	14.1-79.4
Fast-transition 10-to-90 percent risetime, μ s	62	1.21	0.774	1.02	1.05	0.258	0.28-4.58
Zero-crossing time, μ s	41	53.6	42.9	42.1	42.7	0.299	11.3-197
Opposite polarity overshoot relative to peak, percent	31	15.6	9.49	13.0	14.3	0.273	4.13-43.6
Width of dE/dt pulse at half peak value, μ s	37	1.53	1.09	1.27	1.30	0.265	0.33-6.20
Peak electric field derivative normalized to 100 km, V/m/ μ s	27	10.0	5.08	9.02	8.58	0.201	3.23-25.8
NLDN estimated peak current, kA	48	87.8	50.3	74.6	79.5	0.256	19.8-234

Table 7-4. Number of positive return strokes in different distance ranges and corresponding GM electric field peaks normalized to 100 km.

Distance range, km	5-20	20-40	40-60	60-80	80-100	100-160	0-160
Number of events	6	14	11	4	5	8	48
GM NLDN-estimated peak current, kA	10.8	17.3	14.4	23.8	23.0	30.1	18.1



	First return stroke	Subsequent return stroke	All
AM, V/m	23.4	13.2	21.7
GM, V/m	19.8	11.7	18.1
Min, V/m	5.0	4.34	4.34
Max, V/m	66.3	20.3	66.3
N	40	8	48

Figure 7-3. Histogram of the initial electric field peak normalized to 100 km for 48 positive return strokes. Statistics given are arithmetic mean (AM), geometric mean (GM), minimum (min), and maximum (max) values for first and subsequent strokes, as well as for all data combined.

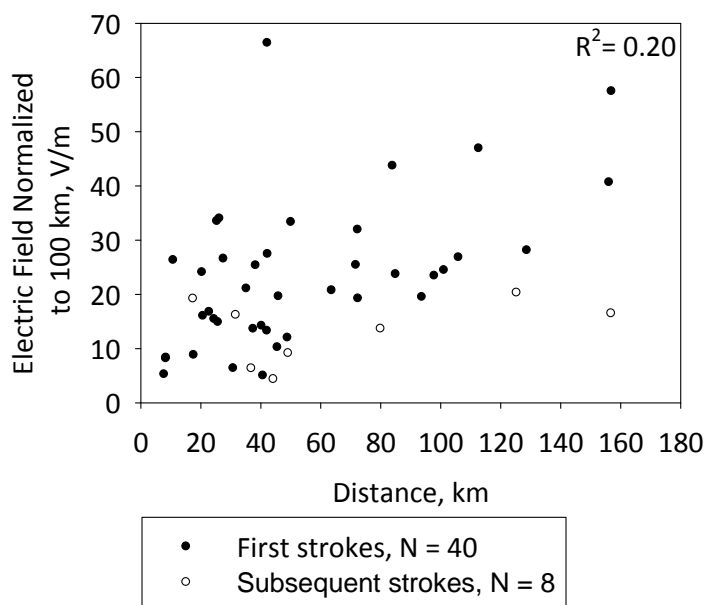


Figure 7-4. Distance-normalized electric field peak versus distance from the measuring station for 48 positive return strokes. Note that the electric field change due to a positive return stroke is negative according to the atmospheric electricity sign convention. Only the magnitude of the electric field change is shown in this plot.

proximity to the measuring station) return stroke electric fields are shown in Figures 7-5 and 7-6, respectively. The zero-to-peak risetimes range from 2.26 to 21.1 μs , with the arithmetic mean (AM) and geometric mean (GM) being 7.77 and 6.92 μs , respectively. *Rust et al.* [1981] found the AM zero-to-peak risetime to be 6.9 μs (which is similar to that found in this study) with a range of 4-10 μs for 15 positive return strokes in the Great Plains, USA. *Cooray and Lundquist* [1982] found the AM zero to peak risetimes for 64 and 52 positive return strokes (from two different storms) in Sweden to be 13 and 12 μs , respectively, each with a range of 5-25 μs . For winter positive lightning in Japan, *Ishii and Hojo* [1989] found the zero to peak risetime for 123 return strokes to be in the range of 8-44 μs with the AM being 21.2 μs . For 32 strokes in summer, they reported the AM to be 13.2 μs , which is shorter than that for winter positive lightning. Similarly, in the data presented here, for 45 return strokes in the warm (March to October) season, the AM and GM zero-to-peak risetimes were 7.5 μs and 6.8 μs , respectively,

which are shorter than the AM and GM zero-to-peak risetimes of 8.5 μs and 7.4 μs , respectively, for 17 return strokes that occurred during the cold (November-February) season.

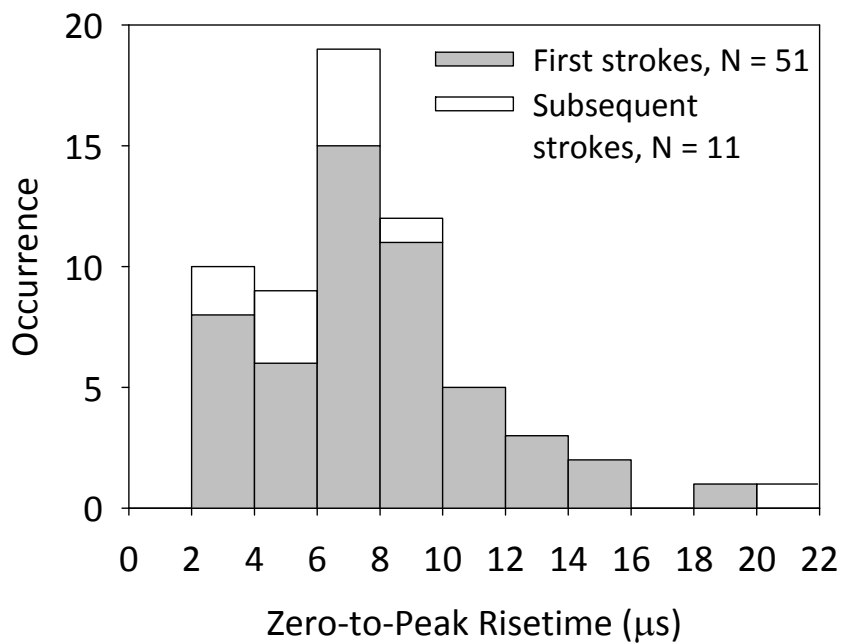
In the data presented here, the AM and GM 10-90% risetimes were 4.02 μs and 3.40 μs , respectively with a range of 0.36 to 10.4 μs . *Beasley et al.* [1983] found the AM 10-90% risetime for 6 positive return strokes in Florida to be 2.7 μs . The AM 10-90% risetimes in Sweden and for winter lightning in Japan were reported to be 6.2 μs [*Cooray, 1986a,b*] and 8.7 μs [*Hojo et al. 1985*], respectively. For return strokes in summer in Japan, *Hojo et al.* [1985] reported the AM risetime to be 6.7 μs , which is shorter than that in winter. In the data presented here, for 17 return strokes that occurred during the cold season the AM and GM 10-90% risetimes were 3.8 μs and 3.1 μs . For 45 return strokes in the warm season, the AM and GM 10-to-90% risetimes were 4.1 μs and 3.5 μs which are longer than those in winter.

From the above discussion it appears that the zero-to-peak and 10-to-90% risetimes for positive return strokes in Sweden and Japan are, in general, longer than those reported in this study for Florida and those reported by *Rust et al.* [1981] for the Great Plains. Table 7-5 compares the risetimes of positive return strokes in summer and winter in Florida with those in other regions.

The scatter plot of the zero-to-peak and 10-to-90% risetimes versus distance for 48 positive return strokes (out of 62) located at distances ranging from 7.8 to 157 km from the measuring station are shown in Figures 7-7 and 7-8. No correlation between risetimes and distance is found (determination coefficients of 0.02 and 0.05, respectively).

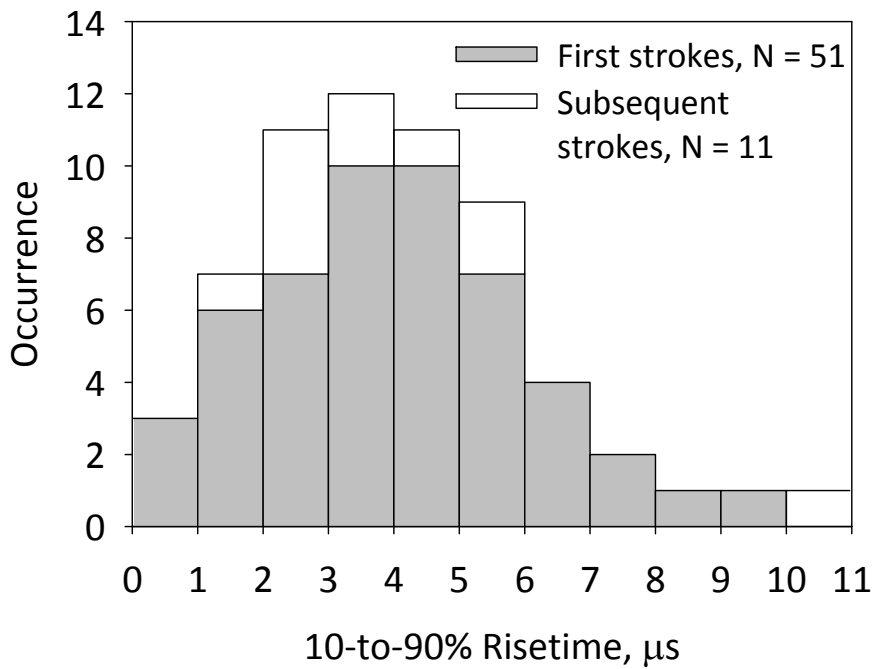
The AM zero-to-peak and 10-to-90% risetimes for 105 first strokes in negative cloud-to-ground discharges in Florida were reported by *Master et al.* [1984] to be 4.4 μs and 2.6 μs , respectively, which are shorter than the corresponding values of 7.88 μs and 4.03 μs for 51

positive first strokes for the dataset analyzed here. For 220 negative subsequent strokes in Florida, [Master *et al.*, 1984] reported, the AM zero-to-peak and 10-to-90% risetimes to be 2.8 μs and 1.5 μs , respectively, versus 7.28 μs and 3.95 μs for 11 positive subsequent strokes analyzed here. In summary, it appears that electric field risetimes for positive subsequent return strokes are appreciably longer than for negative return strokes.



	First return stroke	Subsequent return stroke	All
AM, μs	7.88	7.28	7.77
GM, μs	7.06	6.39	6.94
Min, μs	2.26	3.58	2.26
Max, μs	19.4	21.1	21.1
N	51	11	62

Figure 7-5. Histogram of the zero-to-peak risetime for 62 positive return strokes. Statistics given are arithmetic mean (AM), geometric mean (GM), minimum (min), and maximum (max) values for first and subsequent strokes, as well as for all data combined.



	First return stroke	Subsequent return stroke	All
AM, μs	4.03	3.95	4.01
GM, μs	3.40	3.41	3.40
Min, μs	0.36	1.55	0.36
Max, μs	9.41	10.40	10.4
N	51	11	62

Figure 7-6. Histogram of the 10-90% risetime for 62 positive return strokes. Geometric mean (GM) value is given for all data combined (N = 62). Statistics given are arithmetic mean (AM), geometric mean (GM), minimum (min), and maximum (max) values for first and subsequent strokes, as well as for all data combined.

Table 7-5. Risetimes of return stroke electric field waveforms in different regions and in different seasons.

Parameter	Reference and Location	Season	Sample size	AM, μ s	Remarks
Zero-to-peak risetime	Present study, Florida	Summer	45	7.5	(a) The zero-to-peak risetime for positive return strokes in Sweden and Japan are, in general, longer than those reported in this study for Florida and those reported by <i>Rust et al.</i> [1981] for the Great Plains. (b) Zero-to-peak risetime for positive return strokes in summer is shorter than that for winter positive lightning.
		Winter	17	8.5	
	<i>Cooray and Lundquist</i> [1982], Sweden	Summer	64 and 52	12 and 13	
		<i>Ishii and Hojo</i> [1989], Japan	Summer	32	
	Winter		123	21.2	
10-to-90% risetime	Present study, Florida	Summer	45	4.1	(a) The 10-to-90% risetime for positive return strokes in Sweden and Japan are, in general, longer than those reported in this study for Florida and those reported by <i>Rust et al.</i> [1981] for the Great Plains. (b) The 10-to-90% risetimes in summer are (i) longer than those in winter for positive return strokes in Florida, and (ii) shorter than those in winter for positive return strokes in Japan.
		Winter	17	3.8	
	<i>Beasley et al.</i> [1983], Florida	Summer	6	2.7	
	<i>Cooray</i> [1986a,b], Sweden	Summer	15	6.2	
		<i>Hojo et al.</i> [1985], Japan	Summer	44	
	Winter		32	8.7	

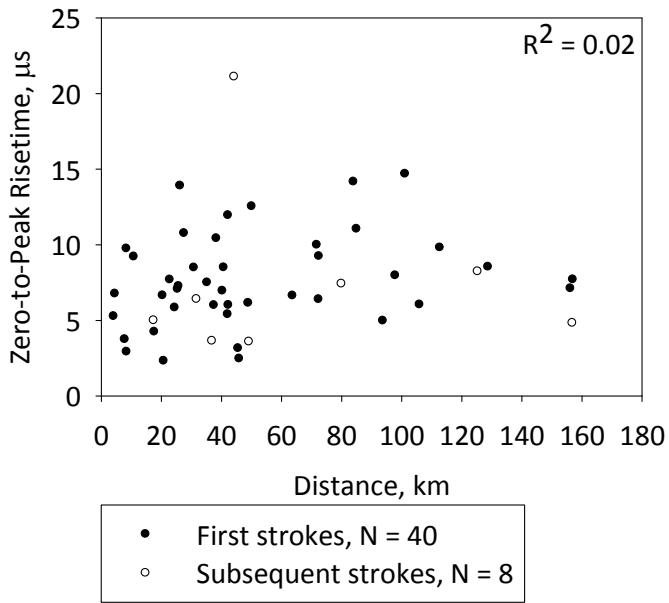


Figure 7-7. Zero-to-peak risetime time versus the distance from the measuring station for 48 positive return strokes.

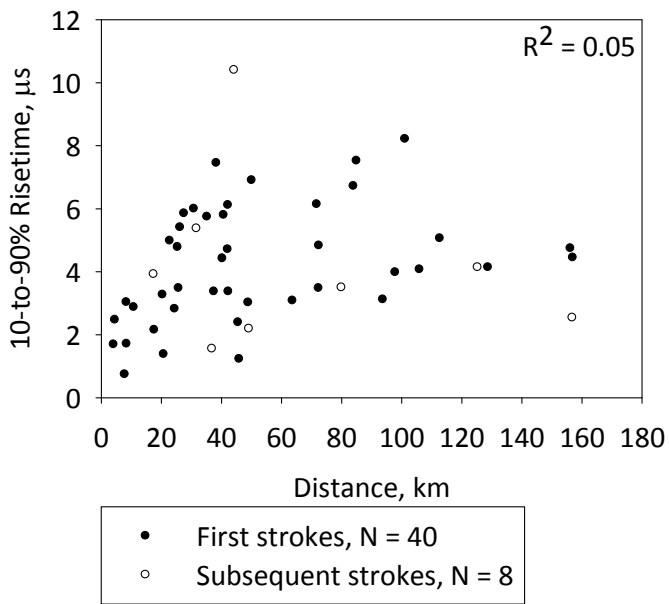


Figure 7-8. 10-to-90% risetime time versus the distance from the measuring station for 48 positive return strokes.

7.2.3 Slow Front and Fast Transition

The initial rising portion of electric field waveform of positive return stroke (and negative return stroke as discussed in Chapter 2) is often viewed as being composed of initial relatively slow rising portion, called the slow front, and a portion showing a fast rise to peak, called the fast transition. A typical slow front-fast transition sequence in a positive return stroke electric field waveform is shown in Figure 7-9. The break-point between the slow front and fast transition was determined subjectively by examination of waveforms. The duration of the slow front for 62 positive return strokes in this dataset ranged from 0.77 μs to 18.6 μs . The AM and GM were 5.94 μs and 4.95 μs , respectively. Figure 7-10 and 7-11 show the histograms of the slow front duration and slow front amplitude relative to peak. The amplitude of the slow front in our dataset of 62 positive return strokes was on average 39.4% (with a range of 14.1 to 79.4% and a GM of 36.7%) of the return stroke peak. The 10-90% risetime of the fast transition ranged from 0.28 to 4.58 μs with AM and GM of 1.21 μs and 1.02 μs , respectively. The distribution of the fast transition 10-to-90% risetime is shown in Figure 7-12. Figures 7-13 and 7-14 show the scatter plots of the slow front duration and slow front amplitude relative to peak, respectively, versus distance for 48 positive return strokes (out of 62) located at distances ranging from 7.8 to 157 km from the measuring station. No correlation was found between these parameters and distance (determination coefficients of 0.003 and 0.02, for slow front duration and slow front amplitude relative to peak, respectively). Figure 7-15 shows the scatter plots of the fast transition 10-to-90% risetime versus distance. It can be seen that even though the minimum fast transition 10-to-90% risetime tends to increase with distance, its dependence on distance for the sample of 48 positive return strokes is rather weak (determination coefficient = 0.26).

Cooray and Lundquist [1982] reported the AM duration of the slow front (whose amplitude relative to the peak was on average 38% and within a range of 10-70%) to be 10 μs .

Cooray [1986a, b] found the 10-to-90% risetime of the fast transition to be in the range of 0.40-0.80 μs (AM of 0.56 μs). In Japan, *Hojo et al.* [1985] reported the AM duration of the slow front to be 19.3 μs and *Ishii and Hojo* [1989] reported the AM 10-90% risetime of the fast transition to be 0.11 μs . From the above discussion it can be seen that while the slow front duration for positive return strokes in Florida is, on average, shorter than that in Sweden and Japan, the 10-to-90% risetime of the fast transition for positive return strokes in Florida is at least a factor of two longer than that in the other two geographical locations.

For negative lightning, *Master et al.* [1984] reported the AM slow front duration for 105 first strokes in Florida to be 2.9 μs , which is about half of that found for positive return strokes presented here. Similarly, *Cooray and Lundquist* [1982] found the AM duration of the slow front for negative first strokes in Sweden to be 5 μs , which is a factor of 2 smaller than the AM value for positive return strokes reported by them. *Weidman and Krider* [1978] reported the AM slow front duration for 62 negative first return strokes in Florida to be 4 μs . The AM 10-to-90% risetime of the fast transition for negative first strokes in Florida was reported to be 0.97 μs and 0.2 μs by *Master et. al* [1984] and *Weidman and Krider* [1978], respectively, both values being less than that found for positive discharges examined here. The AM slow front amplitude relative to peak for negative first strokes was reported to be 28%, 41% and 50% by *Master et al.* [1984], *Cooray and Lundquist* [1982], and *Weidman and Krider* [1978], respectively. These values are comparable to the AM value of 39.4% found for positive return strokes in our dataset. Table 7-6 summarizes the slow front-fast transition characteristics in positive and negative return strokes in different regions.

7.2.4 Zero Crossing Time

The histogram of the zero-crossing time (defined in Figure 7-16) for 41 positive return strokes (out of 62 examined, 21 return stroke waveforms did not exhibit zero crossing due to

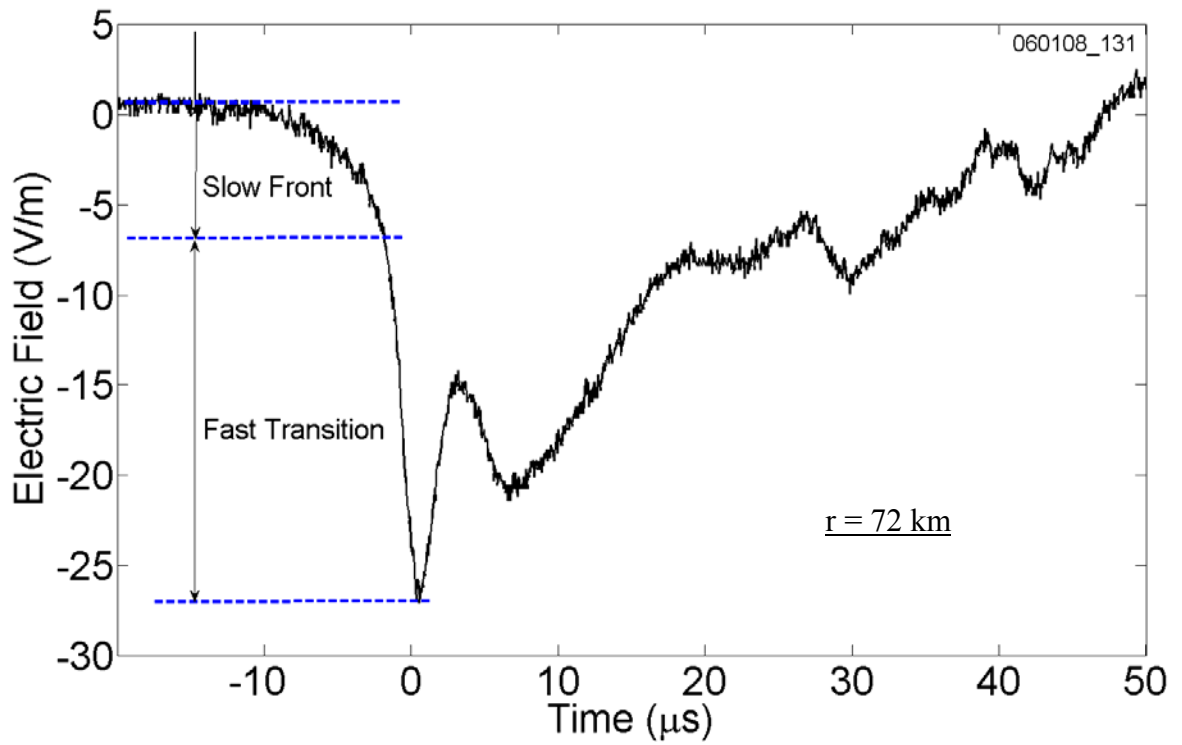
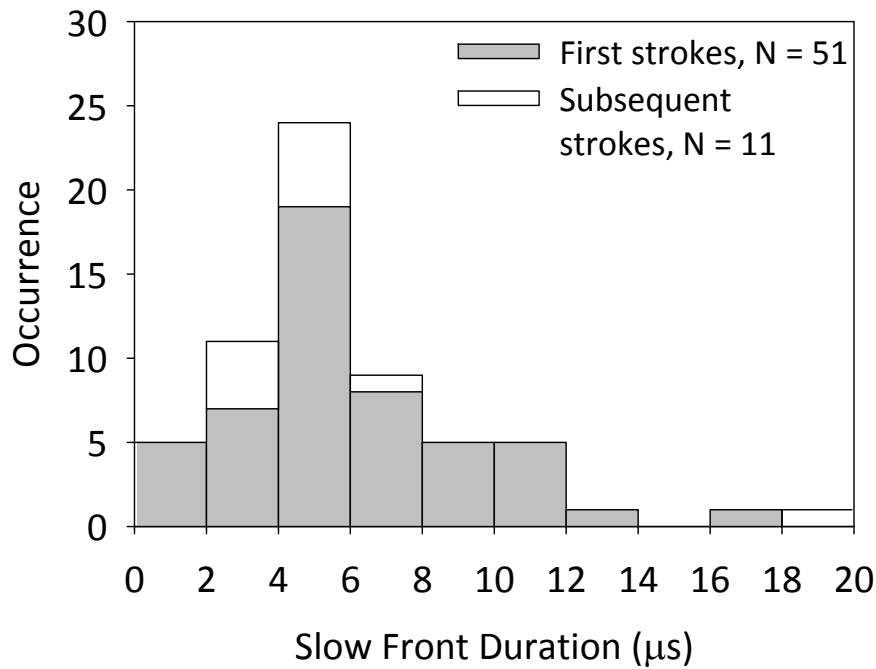
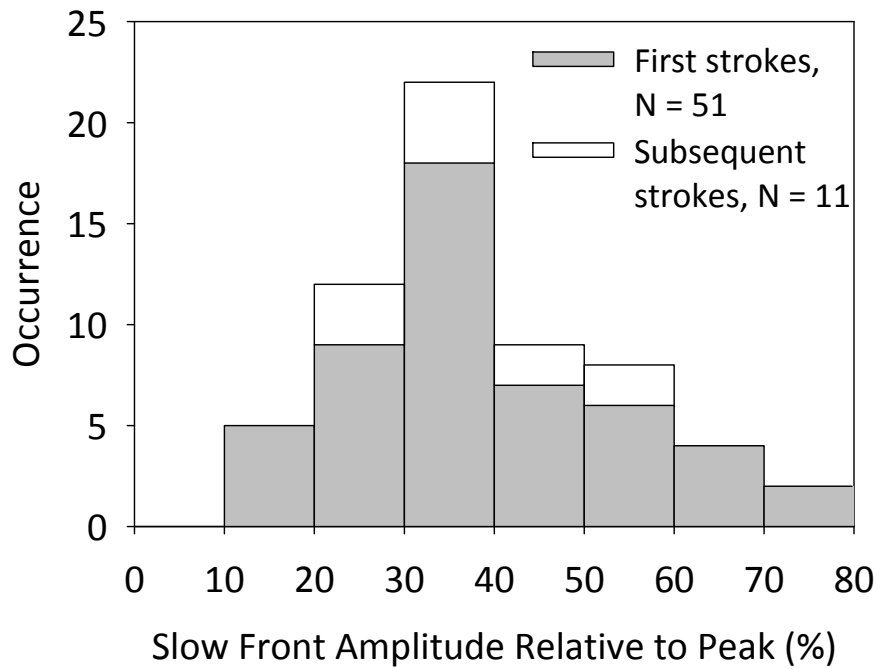


Figure 7-9. A typical slow front-fast transition sequence in a positive return stroke electric field waveform recorded on June 1, 2008 in Gainesville, Florida, shown on a 70 μs time scale. The discharge occurred at a distance of 72 km, so that the field waveform is dominated by its radiation component.



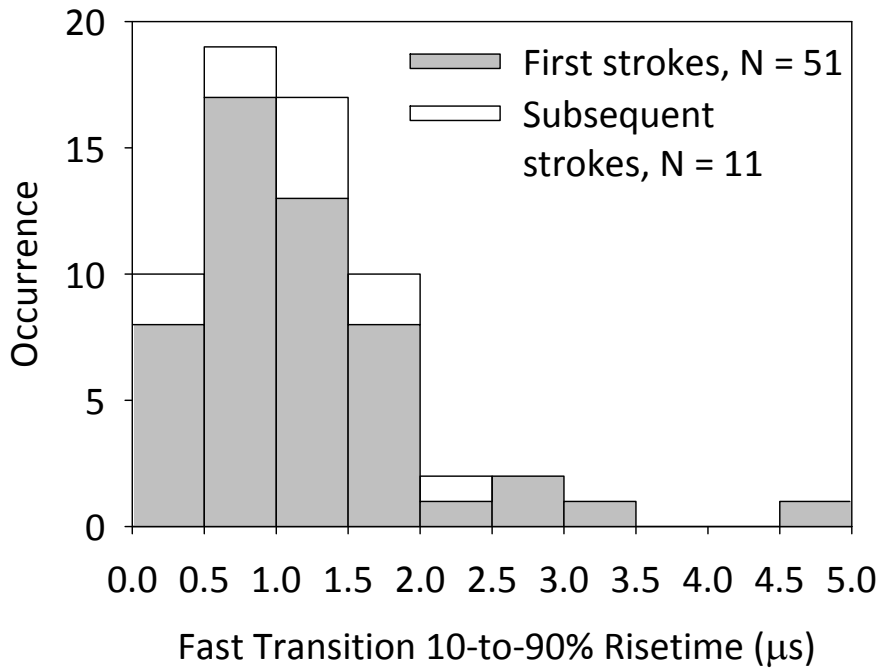
	First return stroke	Subsequent return stroke	All
AM, μs	6.06	5.36	5.94
GM, μs	5.09	4.35	4.95
Min, μs	0.77	2.02	0.77
Max, μs	17.4	18.6	18.6
N	51	11	62

Figure 7-10. Histogram of the slow front duration for 62 positive return strokes. Statistics given are arithmetic mean (AM), geometric mean (GM), minimum (min), and maximum (max) values for first and subsequent strokes, as well as for all data combined.



	First return stroke	Subsequent return stroke	All
AM, %	39.64	38.5	39.4
GM, %	36.67	37.1	36.7
Min, %	14.12	25.1	14.1
Max, %	79.43	56.9	79.4
N	51	11	62

Figure 7-11. Histogram of the slow front amplitude relative to peak for 62 positive return strokes. Statistics given are arithmetic mean (AM), geometric mean (GM), minimum (min), and maximum (max) values for first and subsequent strokes, as well as for all data combined.



	First return stroke	Subsequent return stroke	All
AM, μs	1.21	1.20	1.21
GM, μs	1.01	1.08	1.02
Min, μs	0.28	0.42	0.28
Max, μs	4.58	2.06	4.58
N	51	11	62

Figure 7-12. Histogram of the fast transition 10-to-90% risetime for 62 positive return strokes. Statistics given are arithmetic mean (AM), geometric mean (GM), minimum (min), and maximum (max) values for first and subsequent strokes, as well as for all data combined.

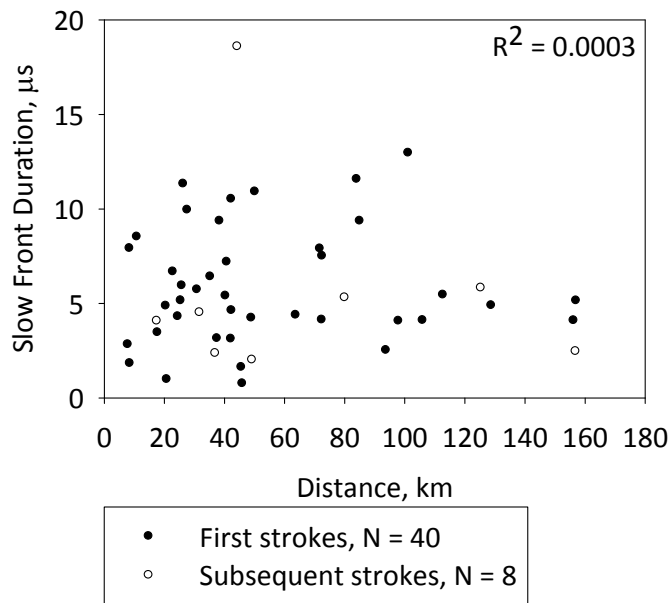


Figure 7-13. Slow front duration versus the distance from the measuring station for 48 positive return strokes.

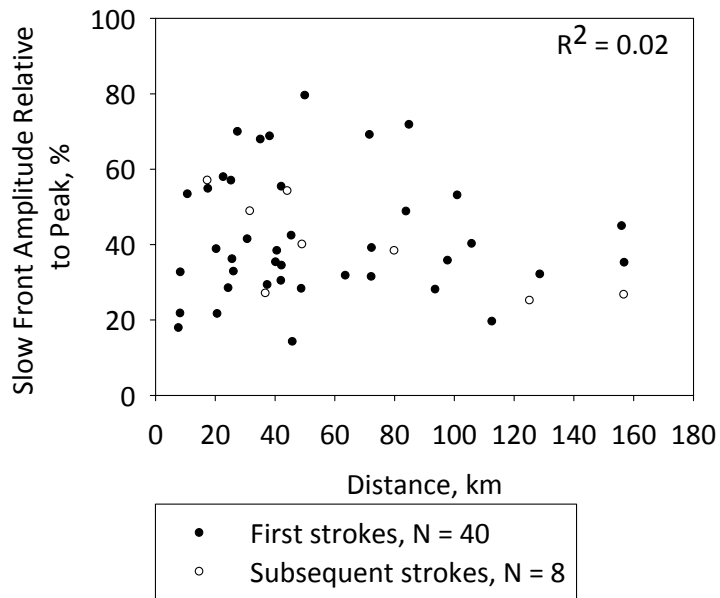


Figure 7-14. Slow front amplitude relative to peak versus the distance from the measuring station for 48 positive return strokes.

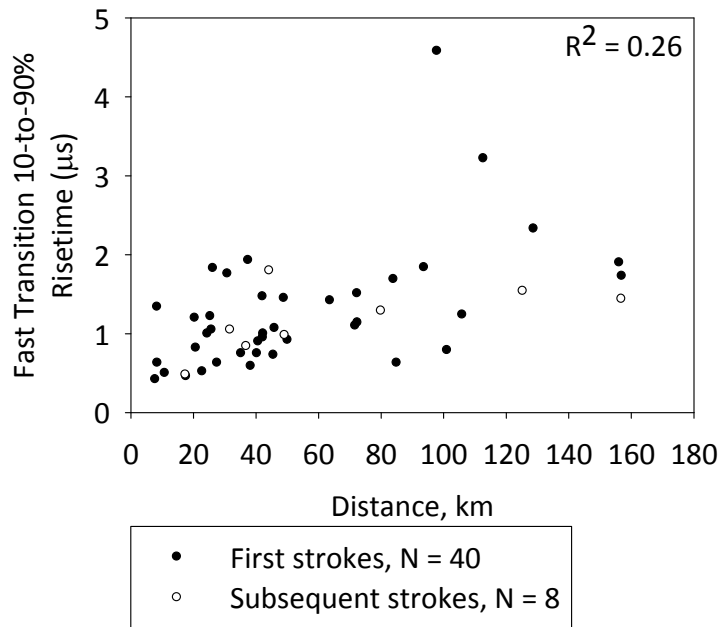


Figure 7-15. Fast transition 10-to-90% risetime time versus the distance from the measuring station for 48 positive return strokes.

Table 7-6. Characteristics of the slow front and fast transition in positive and negative returns strokes in different regions.

References and Location	Sample size	AM slow front duration, μs	AM slow front amplitude relative to peak, percent	AM fast-transition 10-to-90 percent risetime, μs	Remarks
Positive return strokes					
Present study, Florida	62	5.94	39.4	1.21	(a) The slow front duration for positive return strokes in Florida is, on average, shorter than that in Sweden and Japan. (b) The 10-to-90% risetime of the fast transition in Florida is at least a factor of two longer than that in Sweden and Japan.
<i>Cooray and Lundquist</i> [1982], Sweden	63	10	38	-	
<i>Cooray</i> [1986a,b], Sweden	20	8.2	45	0.56	
<i>Hojo et al.</i> [1985], Japan	-	19.3	-	-	
<i>Ishii and Hojo</i> [1989], Japan	24	-	-	0.11	
Negative return strokes					
<i>Master et al.</i> [1984]	105	2.9	28	0.97 (N = 102)	The slow front duration for positive return strokes in Florida and Sweden is, on average, longer for positive return strokes than for negative return strokes.
<i>Cooray and Lundquist</i> [1982], Sweden	83	5 (N= 82)	41	-	
<i>Weidman and Krider</i> [1978], Florida	62	4.0	50	0.2 (N = 38)	

them being relatively close to the measuring station) in this dataset is shown in Figure 7-17. The values ranged from 11.3 to 197 μs with the AM and GM being 53.6 μs and 42.1 μs , respectively. Figure 7-18 shows the scatter plot of the zero crossing time for 34 positive return strokes (out of 41) located at distances ranging from 18 to 157 km versus distance from the measuring station. No correlation between zero crossing time and distance is found (determination coefficient = 0.02). *Ishii and Hojo* [1989] found the AM zero-crossing time for 34 positive return strokes in

summer and 89 positive return strokes in winter at distances in the range of 100-300 km in Japan to be 151 μs and 93 μs , respectively. For 10 positive strokes that occurred during the cold season in our dataset and displayed zero-crossing, the AM and GM zero-crossing times were 52.7 μs and 41.4 μs , respectively, which are not much different from those for the overall sample.

Figure 7-19 shows the histogram of the opposite polarity overshoot relative to peak for 31 positive return strokes (out of 41 exhibiting zero crossing, for 10 return stroke waveforms the opposite polarity overshoot was not measurable due to poor signal-to-noise ratio) in the dataset presented here. The overshoots were found to be from 4.13 to 43.6% of the return stroke peak with the AM and GM being 15.6% and 13.0%, respectively. The scatter plot of the opposite polarity overshoot for 27 positive return strokes (out of 31) located at distances ranging from 21 to 157 km versus distance from the measuring station is shown in Figure 7-20. No correlation between opposite polarity overshoot and distance is found (determination coefficient = 0.001). *Ishii and Hojo* [1989] found the opposite polarity overshoot to be, on average, 24% of the peak for 34 positive return strokes (in summer), and 40% of the peak for 89 positive return strokes (in winter), occurring at distances in the range of 100-300 km in Japan.

For 178 negative return strokes in summer in Florida occurring at distances ranging from 50 to 250 km, *Pavlick et al.* [2002] reported the AM zero-crossing time to be 49.5 μs and the opposite polarity overshoot to be, on average, 18.5% of the peak. These values are similar to those of 53.6 μs and 15.6% for positive return strokes examined in this study. Table 7-7 summarizes the zero crossing time and opposite polarity overshoot relative to peak of the return stroke electric field waveform for different seasons in Florida and Japan.

7.2.5 dE/dt Waveform Characteristics

The peak electric field derivative (see Figure 7-21) normalized to 100 km for 27 positive return strokes in our dataset was in the range of 3.23 to 25.8 V/m/ μs with the AM and GM values

being 10.0 V/m/μs and 9.02 V/m/μs, respectively. Figure 7-22 shows the histogram of the peak electric field derivative normalized to 100 km. The electric field derivative waveforms of the 27 positive return strokes located at distances ranging from 7.8 to 157 km are shown in Appendix B. The AM peak electric field derivative normalized to 100 km for 22 positive return strokes in Denmark for propagation over salt water was reported by *Cooray et al.* [1998] to be 22 V/m/μs, about a factor of 2 greater than our value. Figure 7-23 shows the scatter plot of the distance-normalized peak electric field derivative for 27 positive return strokes versus distance from the measuring station. No correlation is found (determination coefficient = 0.01).

The width of the dE/dt pulse at half peak value (defined in Figure 7-21) for 37 positive return strokes ranged from 0.33 to 6.2 μs. The AM and GM were 1.53 μs and 1.27 μs, respectively. The histogram of the width of the dE/dt pulse at half peak value is shown in Figure 7-24. The AM width of the dE/dt pulse at half peak value for 21 positive return strokes in Denmark (for propagation over salt water) was reported by *Cooray et al.* [1998] to be 0.15 μs, which is an order of magnitude shorter than that in our dataset. Figure 7-25 shows the scatter plot of the dE/dt half-peak width for 27 positive return strokes (out of 37) versus distance from the measuring station. It can be seen that even though the dE/dt half-peak width generally tends to increase with distance, its dependence on distance for the sample of 27 positive return strokes is rather weak (determination coefficient = 0.30).

For negative lightning, *Krider et al.* [1996] reported the average peak electric field derivative normalized to 100 km for 63 negative return strokes in Florida to be 39 V/m/μs, about four times larger than the average value for the positive return strokes examined here. The average width of the dE/dt pulse at half peak value for 61 return strokes in Florida (for propagation over salt water) was 0.1 μs [*Krider et al.*, 1996], which is about an order of

magnitude shorter than that for positive lightning in the dataset presented here. From the above discussion it appears that the peak electric field derivative for positive return strokes in our dataset are smaller and the dE/dt half-peak width longer than those for both positive and negative return strokes reported in the literature. This could be due to field propagation effects over finitely conducting soil in our experiment.

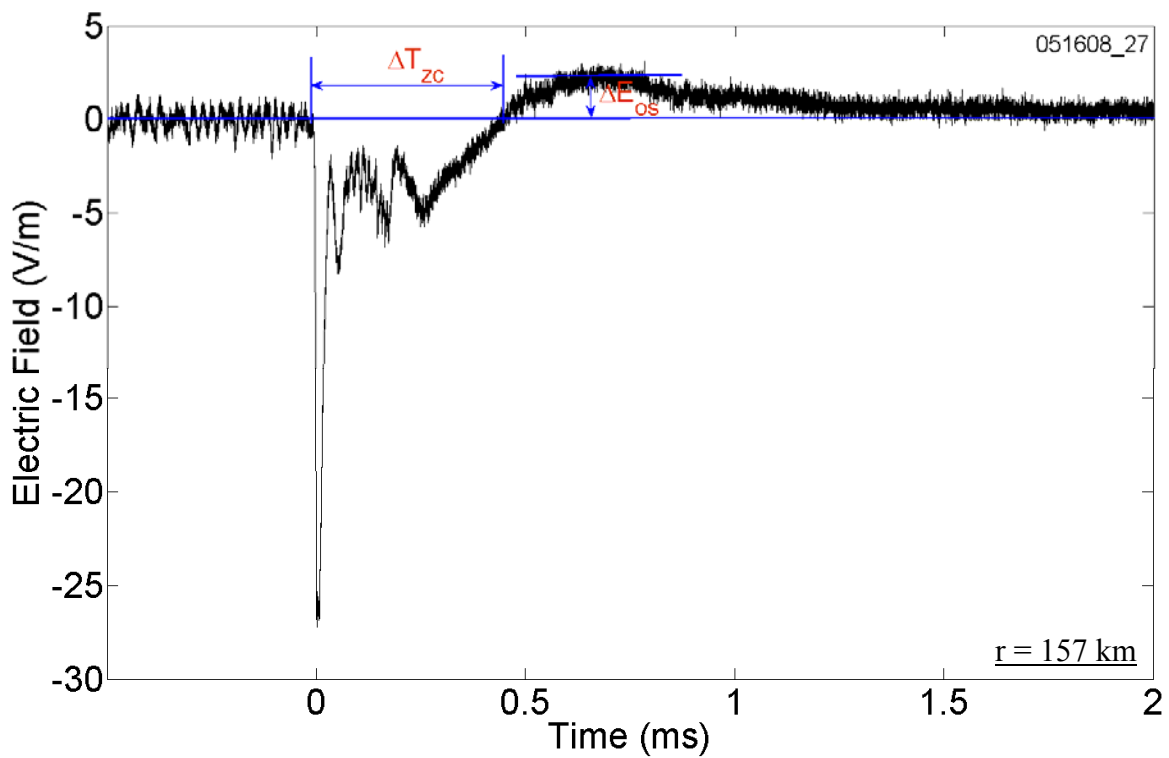
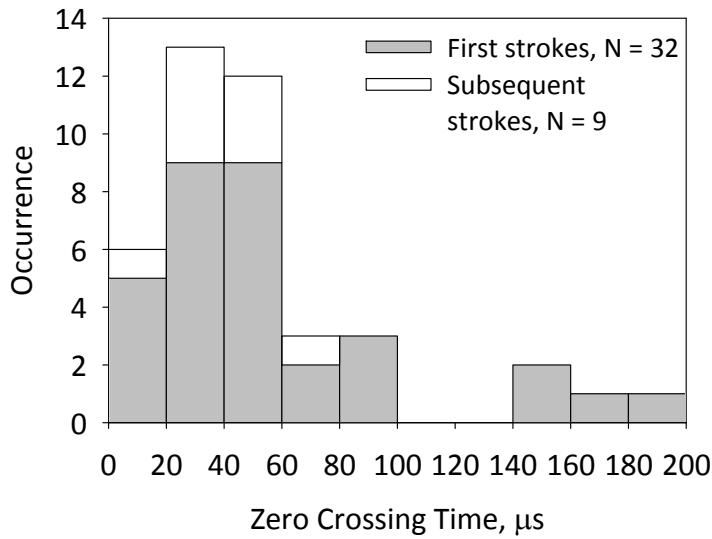


Figure 7-16. The electric field waveform of a positive return stroke that occurred at a distance of 157 km on May 5, 2008 in Gainesville, Florida, shown on a 2.5 ms time scale. The electric field waveform is dominated by its radiation component. Shown are the zero-crossing time (ΔT_{zc}), defined as the crossing of the preceding background field level, and the opposite polarity overshoot (ΔE_{os}).



	First return stroke	Subsequent return stroke	All
AM, μs	57.8	38.8	53.6
GM, μs	44.4	34.7	42.1
Min, μs	13.7	11.3	11.3
Max, μs	197	64.7	197
N	32	9	41

Figure 7-17. Histogram of the zero crossing time for 41 positive return strokes. Statistics given are arithmetic mean (AM), geometric mean (GM), minimum (min), and maximum (max) values for first and subsequent strokes, as well as for all data combined.

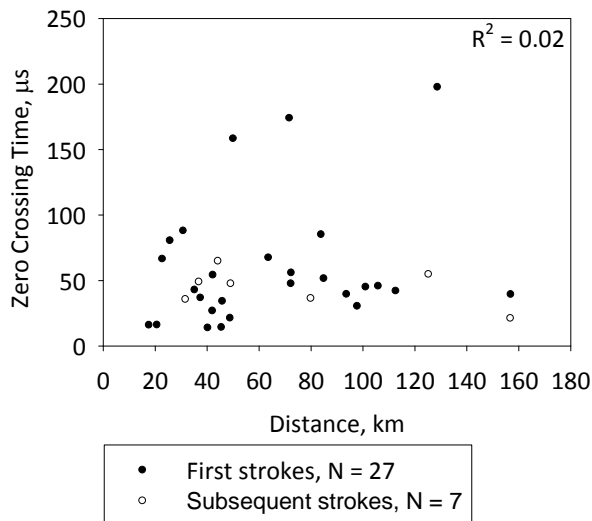
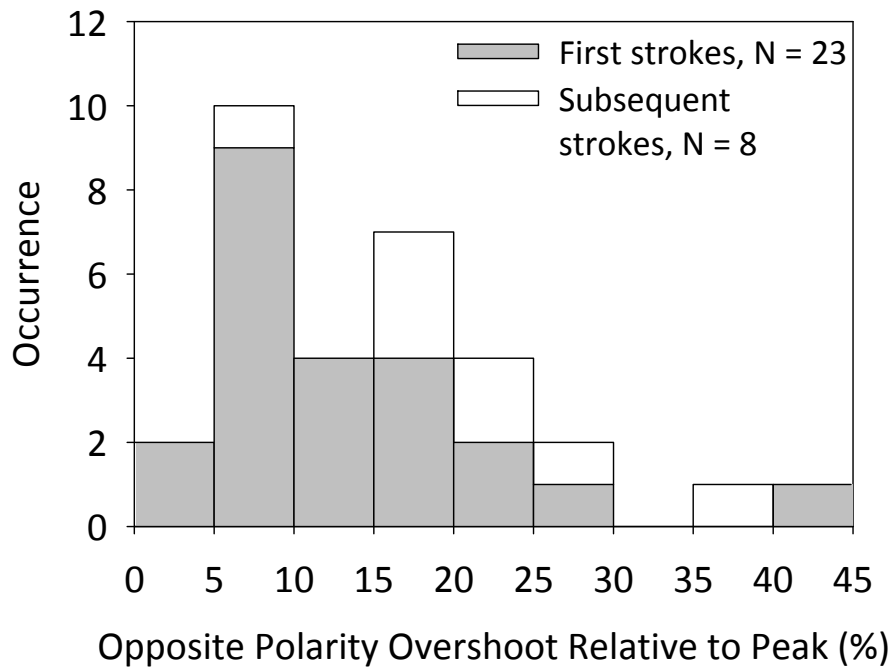


Figure 7-18. Zero crossing time versus distance from the measuring station for 34 positive return strokes.



	First return stroke	Subsequent return stroke	All
AM, %	13.6	21.5	15.6
GM, %	11.3	19.9	13.0
Min, %	4.13	8.03	4.13
Max, %	43.6	36.9	43.6
N	23	8	31

Figure 7-19. Histogram of the opposite polarity overshoot relative to peak for 31 positive return strokes. Statistics given are arithmetic mean (AM), geometric mean (GM), minimum (min), and maximum (max) values for first and subsequent strokes, as well as for all data combined.

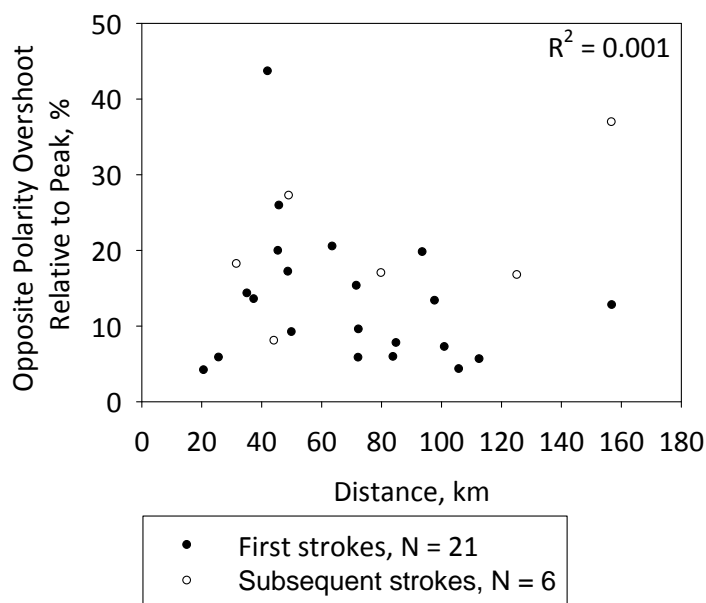


Figure 7-20. Opposite polarity overshoot relative to peak versus distance from the measuring station for 27 positive return strokes.

Table 7-7. Zero-crossing time and opposite polarity overshoot relative to peak of the return stroke electric field waveform for different seasons in Florida and Japan.

References and Location	Season	AM zero-crossing time, μ s	AM opposite polarity overshoot relative to peak, percent	Remarks
Positive return strokes				
Present study, Florida	Summer	53.9 (N = 31)	15.6 (N = 21)	Zero-crossing times for positive return strokes in summer and winter in Florida are, on average, shorter than those in Japan.
	Winter	52.7 (N = 10)	15.8 (N = 10)	
<i>Ishii and Hojo</i> [1989], Japan	Summer	151 (N = 34)	24 (N = 34)	
	Winter	93 (N = 89)	40 (N = 89)	
Negative return strokes				
<i>Pavlick et al.</i> [2002], Florida	Summer	49.5 (N = 178)	18.5 (N = 178)	Zero-crossing times for positive and negative return strokes in Florida are similar.

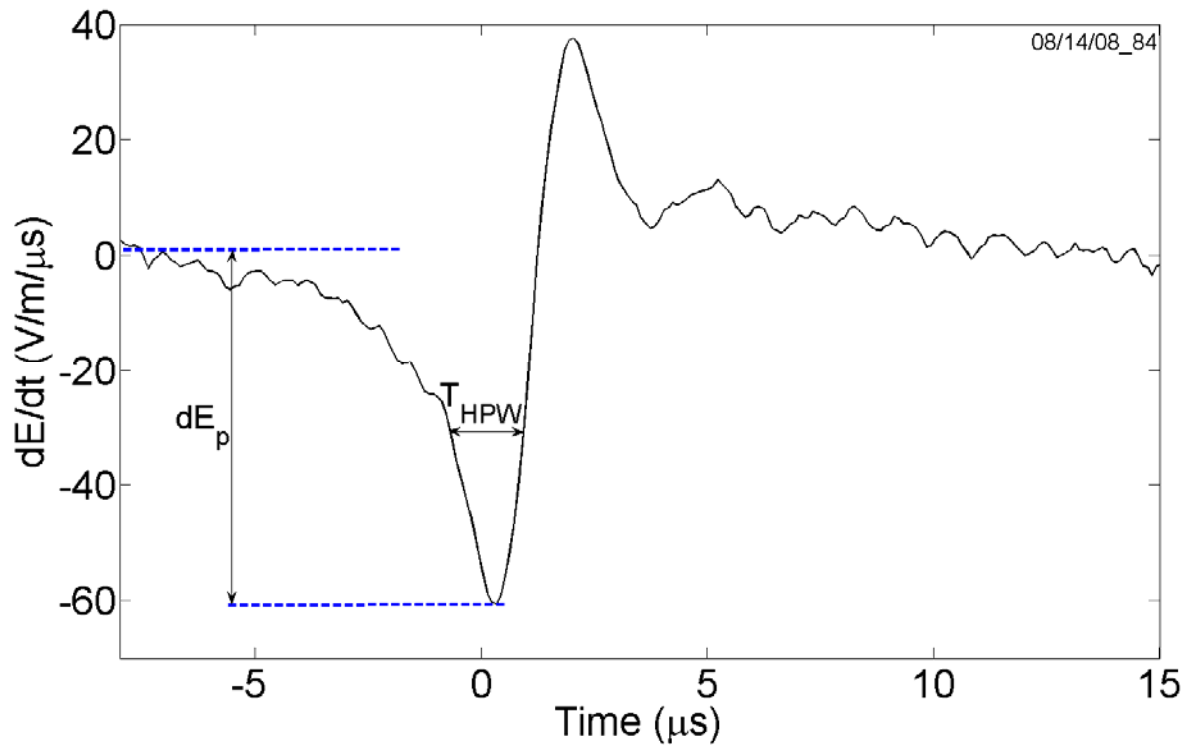
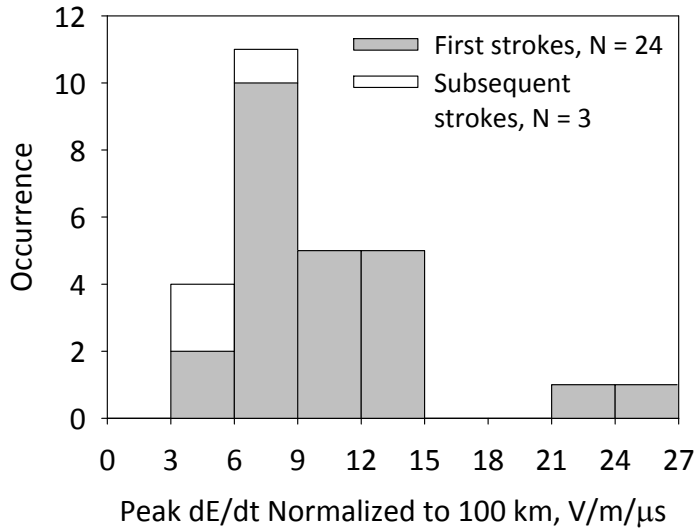


Figure 7-21. A typical electric field derivative (dE/dt) waveform of a positive return stroke in the dataset presented here shown on a 23 μ s time scale. Also shown are the peak electric field derivative (dE_p) and the width of the pulse at half peak value (T_{HPW}).



	First return stroke	Subsequent return stroke	All
AM, V/m/μs	10.6	5.55	10.0
GM, V/m/μs	9.61	5.42	9.02
Min, V/m/μs	3.23	4.15	3.23
Max, V/m/μs	25.8	7.12	25.8
N	24	3	27

Figure 7-22. Histogram of the peak electric field derivative normalized to 100 km for 27 positive return strokes. Statistics given are arithmetic mean (AM), geometric mean (GM), minimum (min), and maximum (max) values for first and subsequent strokes, as well as for all data combined.

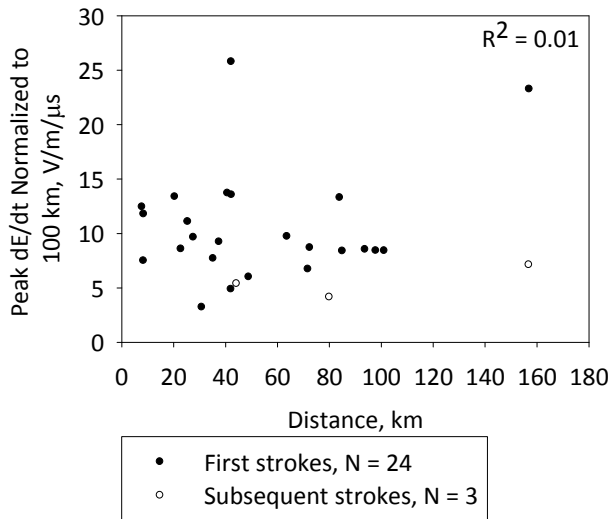
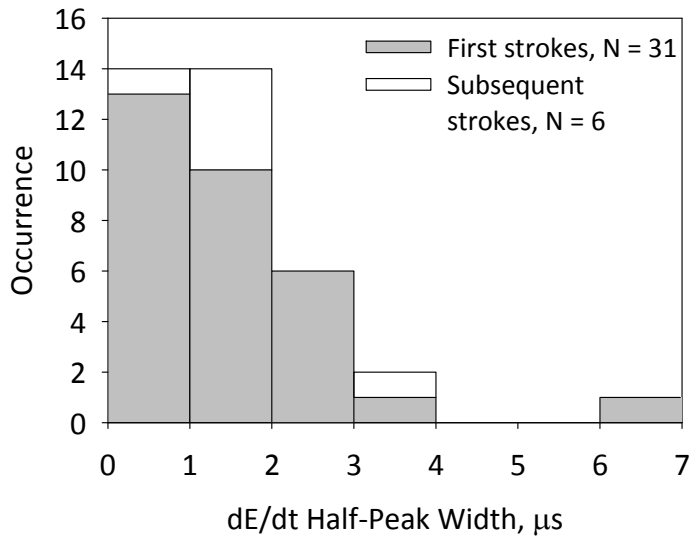


Figure 7-23. Peak dE/dt normalized to 100 km versus distance from the measuring station for 27 positive return strokes.



	First return stroke	Subsequent return stroke	All
AM, μs	1.52	1.59	1.53
GM, μs	1.24	1.43	1.27
Min, μs	0.33	0.67	0.33
Max, μs	6.20	3.04	6.20
N	31	6	37

Figure 7-24. Histogram of the width of the dE/dt pulse at half peak value for 37 positive return strokes. Statistics given are arithmetic mean (AM), geometric mean (GM), minimum (min), and maximum (max) values for first and subsequent strokes, as well as for all data combined.

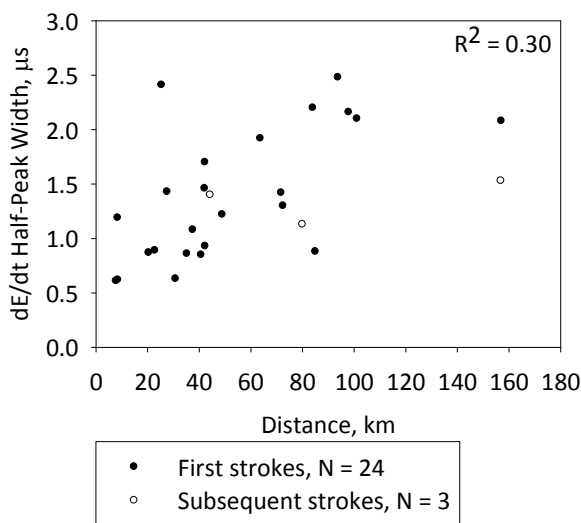


Figure 7-25. dE/dt half-peak width versus the distance from measuring station for 27 (out of 37) located positive return strokes.

7.3 Peak Current

7.3.1 Peak Current Estimated by the National Lightning Detection Network (NLDN)

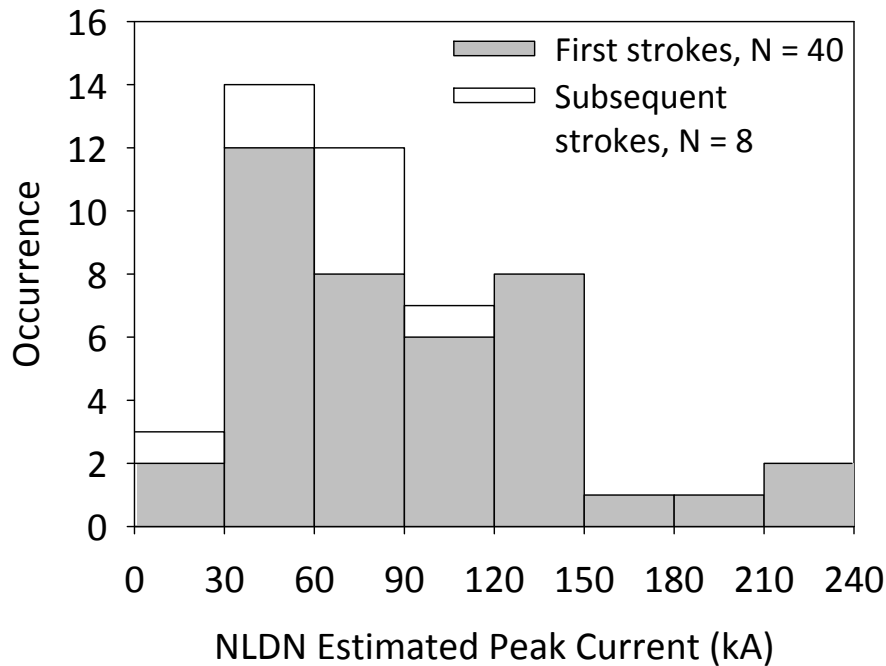
The distribution of the NLDN-estimated peak currents for 48 positive return strokes (in 40 flashes) occurring at distances ranging from 7.8 to 157 km is shown in Figure 7-26. The peak currents range from 19.8 to 238 kA with the AM and GM being 87.8 kA and 74.6 kA, respectively. For 40 first strokes, the AM and GM peak currents were 93.4 kA and 78.9 kA, respectively, and for 8 subsequent strokes the AM and GM values were 59.5 kA and 56.4 kA, respectively. Figure 7-27 shows the scatter plot for NLDN-estimated peak current versus distance from the measuring station for the 48 positive return strokes presented here. It can be seen that even though the minimum NLDN-estimated peak current tends to increase with distance, the dependence of the NLDN-estimated peak current on distance for the sample of 48 positive return strokes is rather weak (determination coefficient = 0.27). Table 7-8 gives the number of recorded strokes in different distance ranges along with the GM NLDN-estimated peak current for each distance range. The GM peak current generally increases with increasing distance which suggests a bias toward higher-intensity events, recorded from larger distances. Note that even for distances less than 20 km the GM peak current is higher than for negative return strokes [*Rakov and Uman, 2003*].

7.3.2 Linear Regression Equations Relating NLDN Currents and Distance-Normalized Fields

According to the atmospheric electricity sign convention, for positive return strokes the electric field change is negative. The corresponding current is assumed here to be positive. The scatter plot of the NLDN-estimated peak current I_{NLDN} versus electric field peak normalized to 100 km E is shown in Figure 7-28. The two parameters appear to be linearly correlated (determination coefficient = 0.85), with the linear regression equation being given by

Table 7-8. Number of positive return strokes in different distance ranges and corresponding GM current peaks.

Distance range, km	5-20	20-40	40-60	60-80	80-100	100-160	0-160
Number of events	6	14	11	4	5	8	48
GM NLDN-estimated peak current, kA	44.7	61.1	66.4	119	95.5	124	74.6



	First return stroke	Subsequent return stroke	All
AM, A	93.4	59.5	87.8
GM, A	78.9	56.4	74.6
Min, A	19.8	28.2	19.8
Max, A	234	91.6	234
N	40	8	48

Figure 7-26. Histogram of the NLDN-estimated peak currents for 48 positive return strokes. Statistics given are arithmetic mean (AM), geometric mean (GM), minimum (min), and maximum (max) values for first and subsequent strokes, as well as for all data combined.

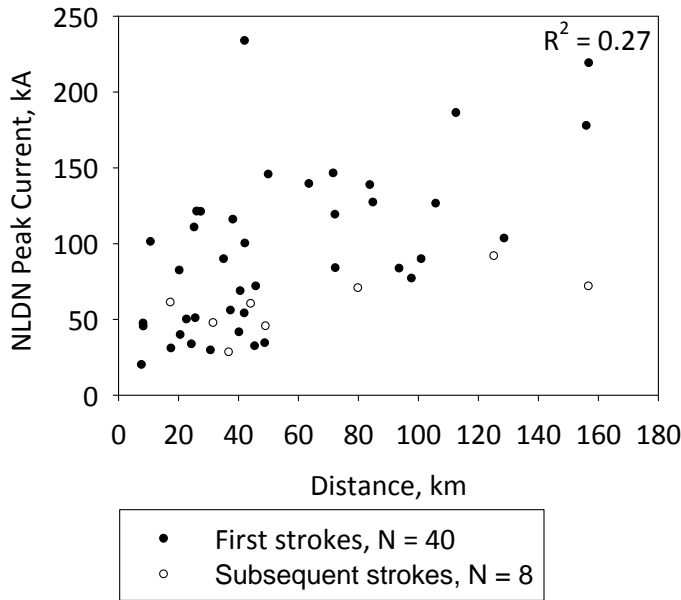


Figure 7-27. NLDN-estimated peak current versus distance from the measuring station for 48 positive return strokes.

$$I_{NLDN} = 11.3 - 3.5E \quad (7-1)$$

where E is negative and in V/m and I_{NLDN} is positive in kA.

Rakov et al. [1992b] used the electric fields measured at 5 km and directly measured currents for 28 negative triggered-lightning strokes published by *Willett et al.* [1989a] to derive a regression equation that relates the negative subsequent return-stroke peak current I to the corresponding peak electric field E at distance D .

$$I = 1.5 - 0.037ED \quad (7-2)$$

where E is positive and in V/m, d is in kilometers, and I is negative and in kA. For $D = 100$ km, Equation 7-2 reduces to $I = 1.5 - 3.7E$. *Pavlick et al.* [2002] used Equation 7-2 to estimate the peak currents from measured electric fields for 178 negative first return strokes occurring at distances ranging from 50 to 250 km. They found the NLDN-reported peak currents to be, on average, 10% lower than those estimated using Equation 7-2.

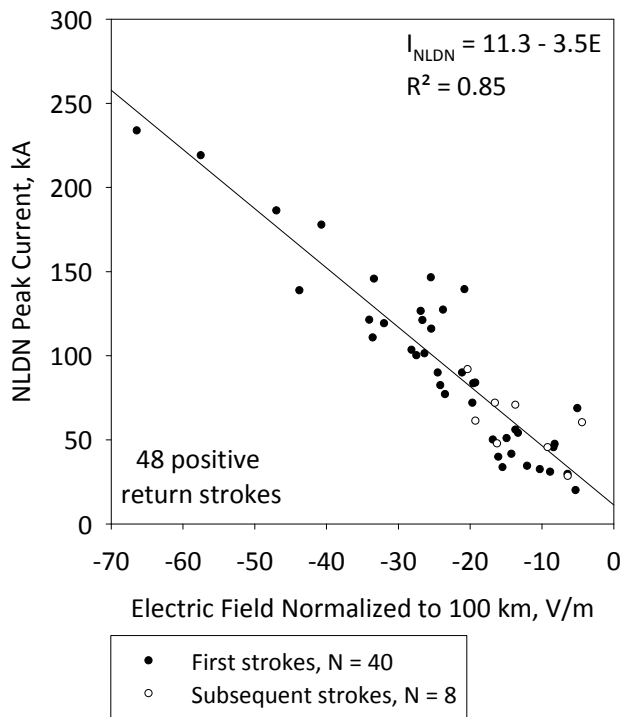


Figure 7-28. NLDN-estimated peak current versus normalized electric field peak for 48 positive return strokes. Also shown is the regression equation line.

Equation 7-2 (with E being negative) was formally applied here to estimate peak currents for 48 (40 first and 8 subsequent) positive return strokes from their measured electric field peaks. The scatter plot of the peak current estimated from Equation 7-2 versus NLDN-estimated peak current is shown in Figure 7-29. The slanted (diagonal) solid line (slope = 1) is the locus of points for which the regression-equation-estimated peak current and the NLDN-estimated peak current are equal. For the sample of 48 positive return strokes, the points are approximately evenly scattered around this line. Also shown is the linear regression line (dashed) having a slope of 0.95 and determination coefficient of 0.85. The NLDN-reported peak currents were found to be, on average, 16% greater than those estimated using Equation 7-2.

For comparison, we examined 116 negative return strokes that were recorded in August, 2008, during two thunderstorms in Gainesville, Florida, using the same instrumentation as that

employed for recording the positive return strokes discussed above. The negative return strokes (41 first strokes and 75 subsequent) occurred at distances ranging from 4 to 35 km (versus 7.8 to 157 km for the 48 positive strokes) from the field measuring station and had NLDN estimated peak currents ranging from 4.7 to 154 kA (versus 19.8 to 238 kA for the 48 positive strokes). Figure 7-30 shows the scatter plot for NLDN-estimated peak current versus distance from the measuring station for the 116 negative return strokes presented here. Note that while the peak currents for negative return strokes are assumed to be negative in Equation 7-2, only their magnitudes are shown in Figure 7-30. The dependence of the NLDN-estimated peak current on distance for this sample of negative return strokes is rather weak (determination coefficient = 0.32). However, there is a bias toward larger peak currents, which increases with increasing distance. Table 7-9 gives the number of recorded strokes in different distance ranges along with the GM NLDN-estimated peak current for each distance range.

The scatter plot of the NLDN-estimated peak current I_{NLDN} versus electric field peak normalized to 100 km E for 116 negative return strokes is shown in Figure 7-31a. The two parameters are linearly correlated (determination coefficient = 0.95), the relationship being given by the following regression equation.

$$I_{NLDN} = 2.29 - 3.06E \quad (7-3)$$

where E is positive and in V/m and I_{NLDN} is negative and in kA. The intercept (2.29) and slope (-3.06) in Equation 7-3 can be compared to the those of Equation 7-1 (regression equation for 48 positive return strokes examined in this Chapter) and to those of Equation 7-2 for $D = 100$ (regression equation of *Rakov et al.* [1992b] for negative rocket-triggered lightning strokes). The values of corresponding regression equation parameters are similar. The variation in the parameters may be due to physical differences between natural negative return strokes (Equation

7-3), negative rocket-triggered lightning strokes (Equation 7-2), and natural positive return strokes (Equation 7-1) or due to smaller sample sizes for Equations 7-1 and 7-2. Figure 7-32 shows the scatter plot of the NLDN-estimated peak current versus measured electric field for all strokes combined (a total of 164 return strokes, of which 48 are positive and 116 are negative).

The combined regression equation is given by:

$$I_{NLDN} = 7.81 - 3.58E \quad (7-4)$$

where E is positive for negative strokes and negative for positive ones and in V/m, and I_{NLDN} is negative for negative strokes and positive for positive ones and in kA.

It is important to note that the NLDN field-to-current conversion algorithm has been calibrated only for subsequent strokes [GM peak current estimation error is about 20%, *Jerauld et al.*, 2005, *Nag et al.*, 2008]. Interestingly, there appears to be not much difference between first and subsequent strokes in Figures 7-29 and 7-31b. In fact, the slopes in regression equations for negative first strokes and negative subsequent strokes given in Figure 7-31b are almost the same. This observation suggests that the NLDN procedure to compensate for field propagation effects and find the average range-normalized signal strength (RNSS) works equally for both subsequent and first return strokes.

7.3.3 Peak Currents Inferred from Measured Electric Field Peaks Using the Transmission Line Model

In this Section, we use the transmission line model [*Uman et al.*, 1975] to infer peak currents from measured electric field peaks, NLDN reported distances, and assumed return-stroke speed. The relationship between the magnitudes of return-stroke peak current, I , and electric field peak, E , measured at distance D , based on the transmission line model, is given by [*Rakov and Uman*, 2003, Chapter 4].

Table 7-9. Number of negative return strokes in different distance ranges and corresponding GM current peaks.

Distance range, km	5-10	10-20	20-30	30-40	0-40
Number of events	26	80	3	7	116
GM NLDN-estimated peak current, kA	14.3	19.3	14.7	57.1	19.1

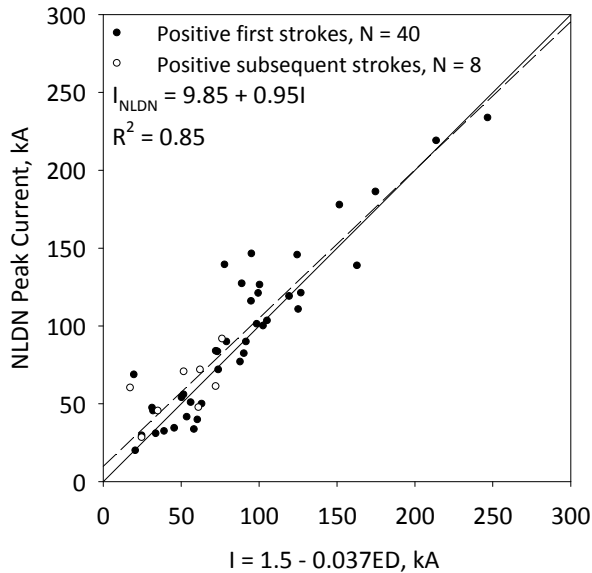


Figure 7-29. NLDN-estimated peak current versus peak current estimated using Equation 7-2 (with E being negative). The solid line is the diagonal with slope = 1 and the dashed line is the linear regression line.

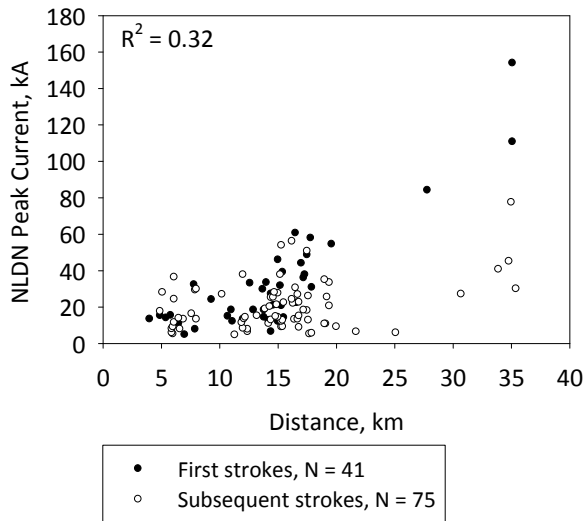


Figure 7-30. Normalized electric field peak versus distance from the measuring station for 116 negative return strokes.

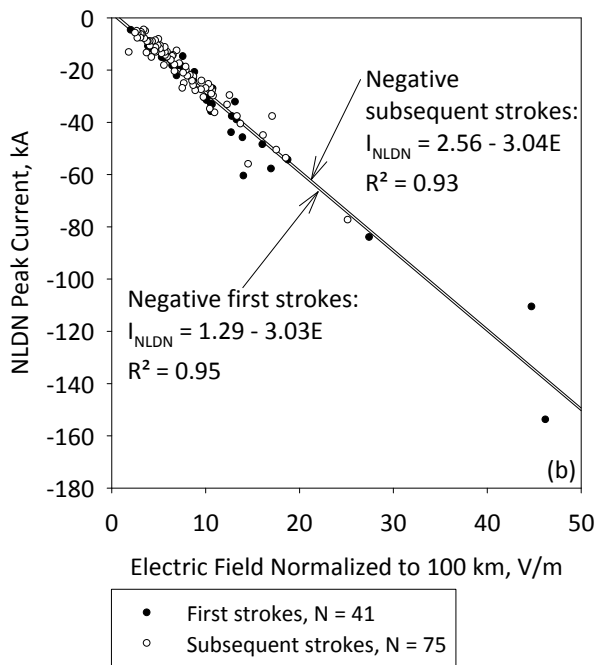
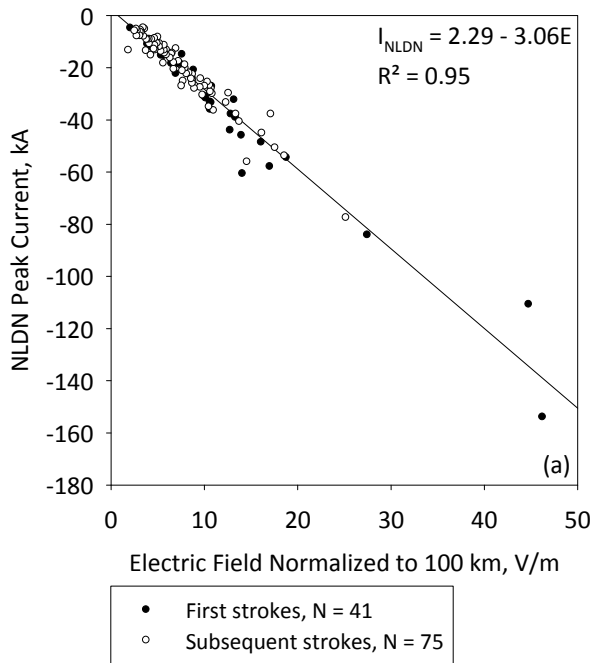


Figure 7-31. (a) NLDN-estimated peak current versus distance-normalized electric field peak for 116 first and subsequent negative return strokes. Also shown is the regression line. (b) Same as in (a) but with individual regression lines for 41 first and 75 subsequent strokes.

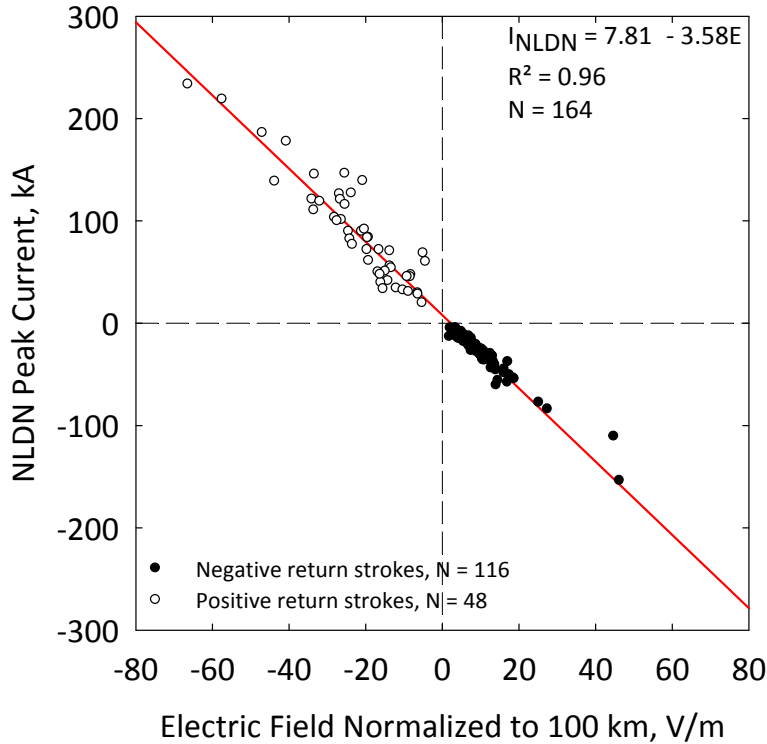


Figure 7-32. NLDN-estimated peak current versus measured electric field peak for 48 positive and 116 negative return strokes.

$$E = \frac{v}{2\pi\epsilon_0 c^2 D} I \tag{7-5}$$

where ϵ_0 is the permittivity of free space, c is the speed of light, and v is the return stroke speed.

Figure 7-33 shows scatter plots for the NLDN estimated peak current magnitudes versus magnitudes of peak currents estimated (for different values of v) using Equation 7-5 for 75 negative subsequent return strokes (discussed in Section 7.3.2). Return-stroke speeds were assumed to be 10^8 m/s (Figure 7-33a), 1.5×10^8 m/s (Figure 7-33b), 1.8×10^8 m/s (Figure 7-33c), and 3×10^8 m/s (Figure 7-33d). The slanted line (slope = 1) is the locus of points for which the transmission line model estimated peak current and the NLDN-reported peak current are equal. It can be seen that the overwhelming majority of the points are above this line for $v = 10^8$ m/s and $v = 1.5 \times 10^8$ m/s, and below it for $v = 3 \times 10^8$ m/s. For $v = 1.8 \times 10^8$ m/s the points are found to be

scattered more or less evenly around the line. Thus, it appears that the NLDN-reported peak currents are equal to the transmission line model predicted peak currents (for the 75 negative subsequent return strokes) for an assumed return stroke speed of 1.8×10^8 m/s. This suggests that the implied return-stroke speed in the NLDN field-to-current conversion equation is 1.8×10^8 m/s, provided that the NLDN measured field peak is consistent with ours.

The NLDN uses the same field-to-current conversion procedure (and hence the same implied return-stroke speed) for negative first strokes and positive return strokes as it does for negative subsequent strokes. Therefore, for $v = 1.8 \times 10^8$ m/s one should expect a good match between NLDN-reported currents and transmission line model predicted currents for negative first strokes and positive return strokes as well. Figures 7-34a and b show scatter plots of the NLDN-reported peak current versus the corresponding peak current estimated using Equation 7-5 for a return stroke speed of 1.8×10^8 m/s, for 41 negative first return strokes discussed in Section 7.3.2 and the 48 positive return strokes presented in Section 7.3.1, respectively. The solid slanted line (slope = 1) in both plots is the locus of points for which the transmission line model estimated peak current and the NLDN-reported peak current are equal. One can see from Figure 7-34a that for the 41 negative first return strokes the NLDN-reported peak currents tend to be equal to the transmission line model predicted peak currents for the assumed return stroke speed of 1.8×10^8 m/s. However, for positive return strokes (Figure 7-34b) most data points are above the diagonal (slope = 1 line). The relationship between the NLDN-reported peak current and the transmission line model estimated peak current for positive return strokes is given by the following regression equation:

$$|I_{NLDN}| = 11.3 + 1.27 |I_{TL}| \quad (7-6)$$

where I_{NLDN} and I_{TL} are in kA. For comparison, a similar regression equation for negative first and subsequent strokes for an assumed return stroke speed of 1.8×10^8 m/s is:

$$|I_{NLDN}| = -2.29 + 1.10 |I_{TL}| \quad (7-7)$$

where I_{NLDN} and I_{TL} are in kA. Note that Equations 7-6 can be derived from Equations 7-1 by using $E = 0.36 I_{TL}$ (I_{TL} being positive and in kA and E being negative and in V/m), which is the relationship between electric field and current for the transmission line model for $v = 1.8 \times 10^8$ m/s. Similarly, Equation 7-7 can be derived from Equations 7-3 using the same relation between E and I_{TL} (I_{TL} being negative and in kA and E being positive and in V/m). The discrepancy between negative first and subsequent strokes on the one hand and positive return strokes on the other hand suggests that the NLDN procedure to compensate for field propagation effects and find the average range-normalized signal strength (RNSS) works differently for these two groups of strokes.

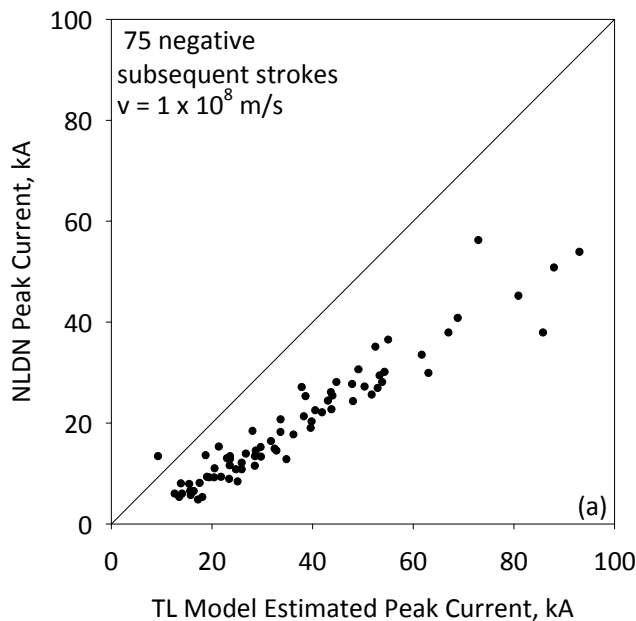


Figure 7-33. The NLDN-estimated peak currents versus peak currents estimated using the transmission line model for assumed return-stroke speeds of (a) 10^8 m/s, (b) 1.5×10^8 m/s, (c) 1.8×10^8 m/s, and (d) 3×10^8 m/s for 75 negative subsequent return strokes. Only the magnitudes of peak currents are considered.

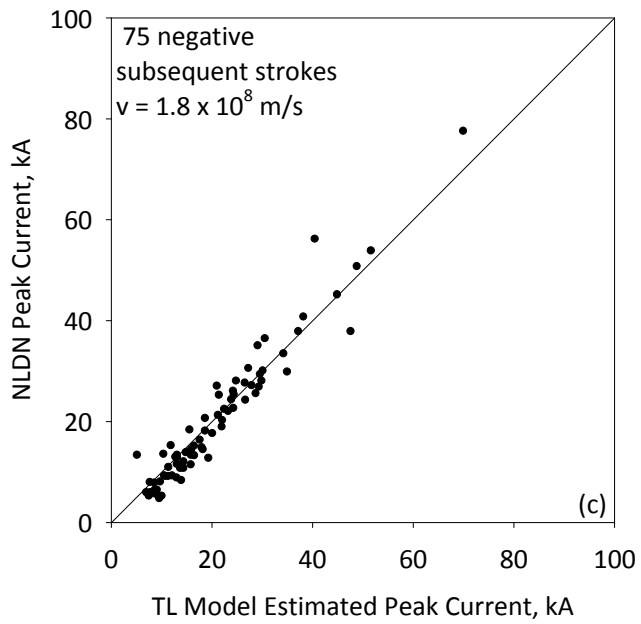
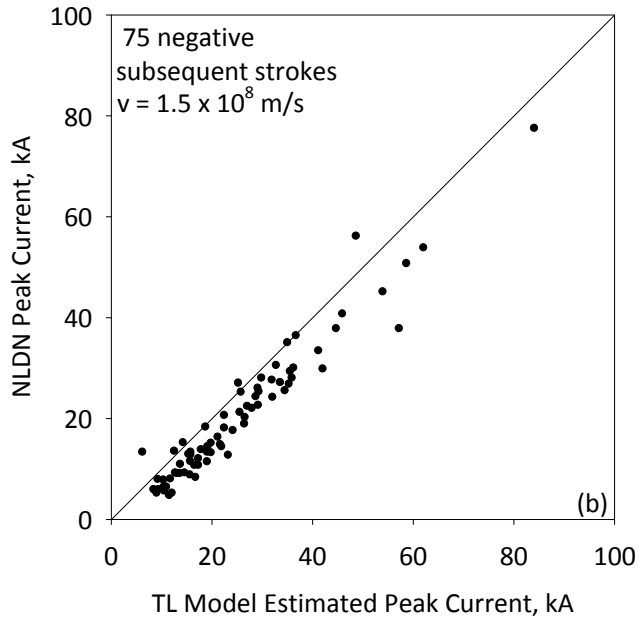


Figure 7-33. Continued

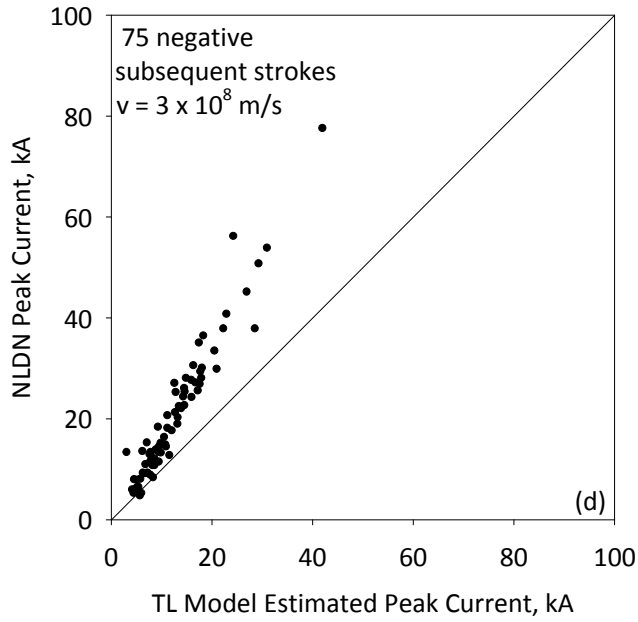


Figure 7-33. Continued

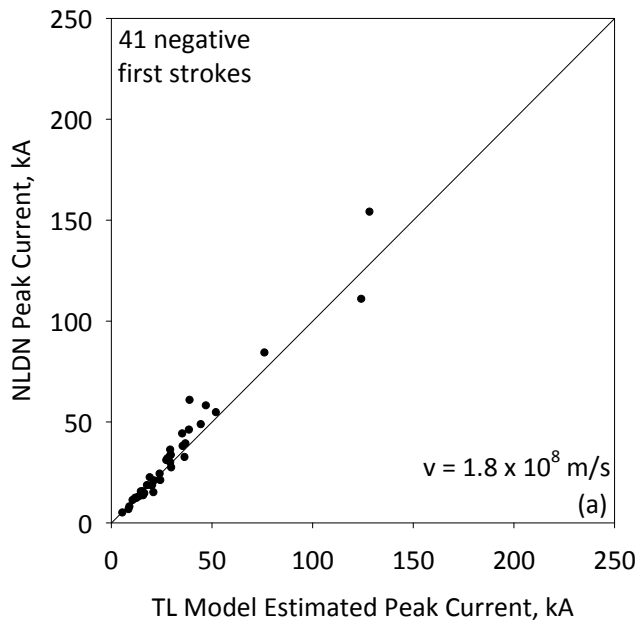


Figure 7-34. The NLDN-estimated peak currents versus peak currents estimated using the transmission line model for assumed return-stroke speed of 1.8×10^8 m/s for (a) 41 negative first return strokes and (b) 48 positive return strokes. Only the magnitudes of peak currents are considered.

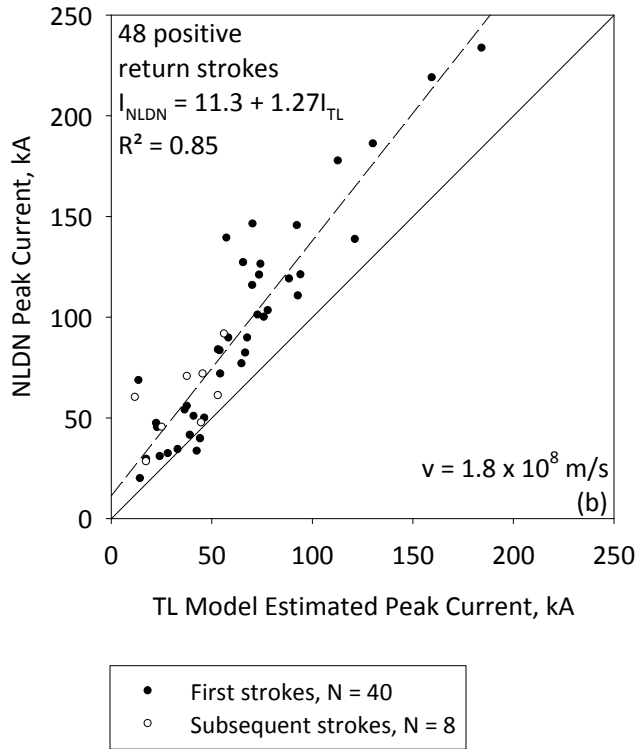


Figure 7-34. Continued

7.4 Charge Transferred by Return Strokes

The electric field change, ΔE , at a horizontal distance r on perfectly conducting ground due to removal of a point charge, ΔQ , from height H is given by [Rakov and Uman, 2003].

$$\Delta E = \frac{\Delta Q H}{2\pi\epsilon_0 (H^2 + r^2)^{\frac{3}{2}}} \quad (7-8)$$

We will apply this point-charge model to positive return strokes to estimate the charge transfer, ΔQ , from measured ΔE , NLDN-reported r , and assumed H . As discussed in Chapter 2, the charge structure of a cumulonimbus can be approximated as a vertical tripole consisting of three charge centers, main positive at the top, main negative in the middle, and an additional smaller positive at the bottom. In Florida, the main positive and negative charges are located at heights of about 12 and 7 km [Krehbiel, 1986], respectively. We will assume that positive cloud to ground

discharges originate in the main positive charge region and hence $H = 12$ km. Solving Equation 7-8 for ΔQ we get:

$$\Delta Q = \frac{2\pi\epsilon_0(H^2 + r^2)^{\frac{3}{2}}}{H} \Delta E \quad (7-9)$$

Charge transfer was estimated for 19 (17 first and 2 subsequent) positive return strokes (occurring at distances ranging from 11 to 46 km) within 0.5, 1, and 1.5 ms of the beginning of return stroke electric field change. Measurements of electric field changes (assumed to be essentially electrostatic) at these times are illustrated in Figure 7-35. The decay time constant of the field measuring system used to acquire the data was 10 ms, so that electrostatic field changes after 1.5 ms or so could be significantly influenced by the instrumental decay. This is why we did not attempt to estimate charge transfers over longer periods.

Table 7-10 summarizes the values of charge transfer at different times. Histograms of charge transfers at different times are shown in Figure 7-36a-c. The charge transfer in 0.5, 1, and 1.5 ms ranged from 1.67 to 26.5 C, 3.16 to 33.7 C, and 4.35 to 34.6 C, respectively, and the median charge transfer was 6.98 C, 12.2 C, and 13.2 C, respectively. These values are comparable to the median impulse charge (excluding continuing current) of 16 C for a sample of 26 positive return strokes reported by *Berger et al.* [1975] but considerably smaller than the median total charge transfer of 80 C. Total charge transfers of hundreds of coulombs or more have been reported for positive discharges in Japanese winter thunderstorms [*Goto and Narita, 1995*]. As noted earlier, our electric field records were not suitable for estimating total charge transfers due to relatively short decay time constant of the measuring system. The average currents (ratio of charge transfer and time) at 0.5 ms, 1 ms, and 1.5 ms vary from 3.34 to 53 kA, 3.16 to 33.7 kA, and 2.9 to 23.1 kA, respectively.

Scatter plot for charge transfer at 1.5 ms versus the distance from the measuring station for 19 positive return strokes occurring at distances ranging from 11 to 46 km is shown in Figure 7-37. A weak dependence of charge transfer on distance is found (determination coefficient = 0.29), with larger charge transfers occurring in strokes at greater distances. However, the sample size of 19 strokes is rather small to draw any conclusions.

Schoene et al. [2009] reported the charge transfer within 1 ms after the beginning of the return stroke for 151 negative rocket triggered lightning strokes at Camp Blanding, Florida. As stated in Chapter 2, rocket triggered lightning strokes are similar to subsequent strokes in natural downward lightning. The minimum and maximum charge transfers within 1 ms after the beginning of the return stroke were 0.3 C and 8.3 C, respectively, with the AM and GM values being 1.4 C and 1.0 C, respectively. The mean values are about an order of magnitude smaller than the AM and GM values of 13.2 C and 10.7 C, respectively, for charge transfer within 1 ms for 19 positive return strokes in this study.

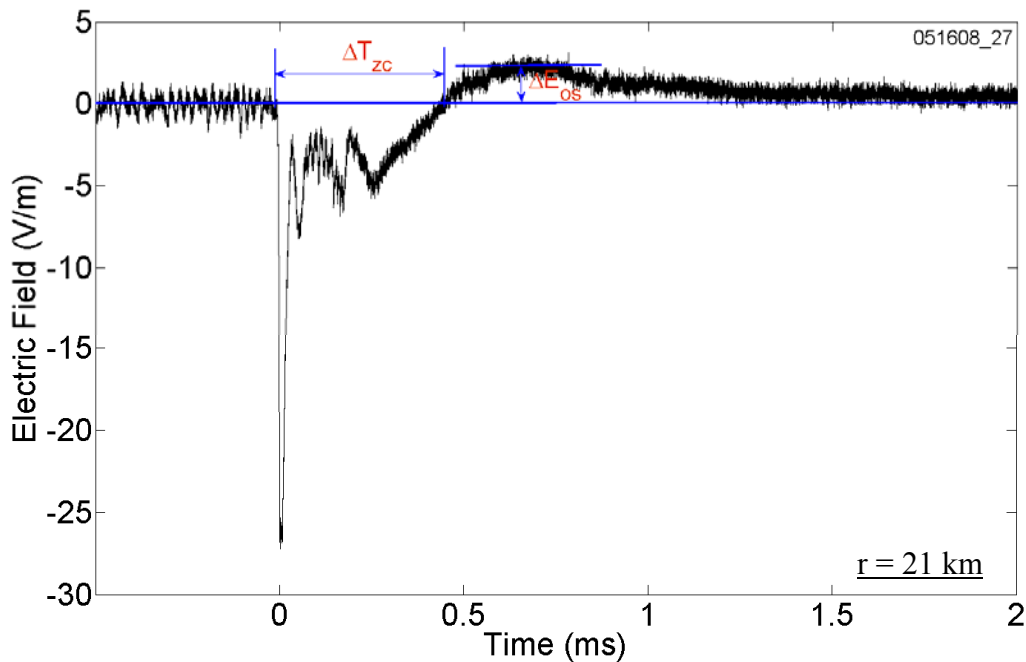


Figure 7-35. Measurements of electric field changes (ΔE) at times $\Delta t = 0.5$ ms, 1.0 ms, and 1.5 ms after the beginning of the return stroke.

Table 7-10. Summary of electric field change (ΔE), charge transfer (ΔQ), and average current ($\Delta Q/\Delta t$) at different times (Δt) after the beginning of the return stroke field change for 17 first and 2 subsequent positive return strokes.

Flash ID	r , km	$\Delta t = 0.5$ ms			$\Delta t = 1.0$ ms			$\Delta t = 1.5$ ms		
		ΔE ,	ΔQ ,	$\Delta Q/\Delta t$,	ΔE ,	ΔQ ,	$\Delta Q/\Delta t$,	ΔE ,	ΔQ ,	$\Delta Q/\Delta$
		V/m	C	kA	V/m	C	kA	V/m	C	t , kA
First Strokes										
12/16/07_49	38	18.0	5.10	10.2	25.7	7.28	7.28	26.9	7.64	5.09
08/13/08_31	20	257	15.9	31.8	253	15.6	15.6	244	15.1	10.1
08/13/08_57	23	82.9	6.61	13.2	154	12.2	12.2	181	14.4	9.62
08/13/08_58	28	129	16.2	32.5	164	20.7	20.7	169	21.3	14.2
08/14/08_85	11	286	5.61	11.2	288	5.65	5.65	276	5.40	3.60
08/14/08_87	18	37.3	1.69	3.38	99.3	4.50	4.50	132	5.98	3.99
08/14/08_90	25	157	16.2	32.4	154	15.8	15.8	152	15.6	10.4
08/23/08_173	24	82.3	7.75	15.5	104	9.82	9.82	112	10.5	7.00
08/23/08_338	40	19.9	6.9	13.7	37.9	13.1	13.1	56	19.3	12.8
08/23/08_339	21	32.5	2.08	4.17	49.3	3.16	3.16	68.0	4.35	2.90
08/23/08_343	26	107	11.9	23.8	118	13.2	13.2	119	13.2	8.81
08/23/08_344	46	3.44	1.67	3.34	7.79	3.78	3.78	15.7	7.62	5.08
08/23/08_345	46	20.0	9.92	19.8	44.5	22.1	22.1	51.7	25.7	17.1
08/23/08_346	26	44.9	4.79	9.59	75.4	8.05	8.05	89.2	9.52	6.35
08/23/08_348	42	23.4	9.12	18.2	39.9	15.6	15.6	52.0	20.3	13.5
08/23/08_350	42	67.1	26.5	53.0	85.4	33.7	33.7	87.7	34.6	23.1
08/24/08_783	35	86.4	20.7	41.4	137	32.7	32.7	144	34.5	23.0
AM	30	85.5	9.92	19.8	108	13.9	13.9	116	15.6	10.4
SD	11	82.2	7.07	14.1	77.9	9.16	9.16	72.9	9.38	6.25
GM	28	52.9	7.47	14.9	79.5	11.2	11.2	92.5	13.1	8.71
Median	26	67.1	7.75	15.5	99.3	13.1	13.1	112	14.4	9.62
Minimum	11	3.44	1.67	3.34	7.79	3.16	3.16	15.7	4.35	2.90
Maximum	46	286	26.5	53.0	288	33.7	33.7	276	34.6	23.1
Subsequent Strokes										
08/14/08_85	17	158	6.98	14.0	203	8.97	8.97	241	10.6	7.09
08/23/08_350	32	16.3	2.94	5.88	31.3	5.67	5.67	44.9	8.14	5.42

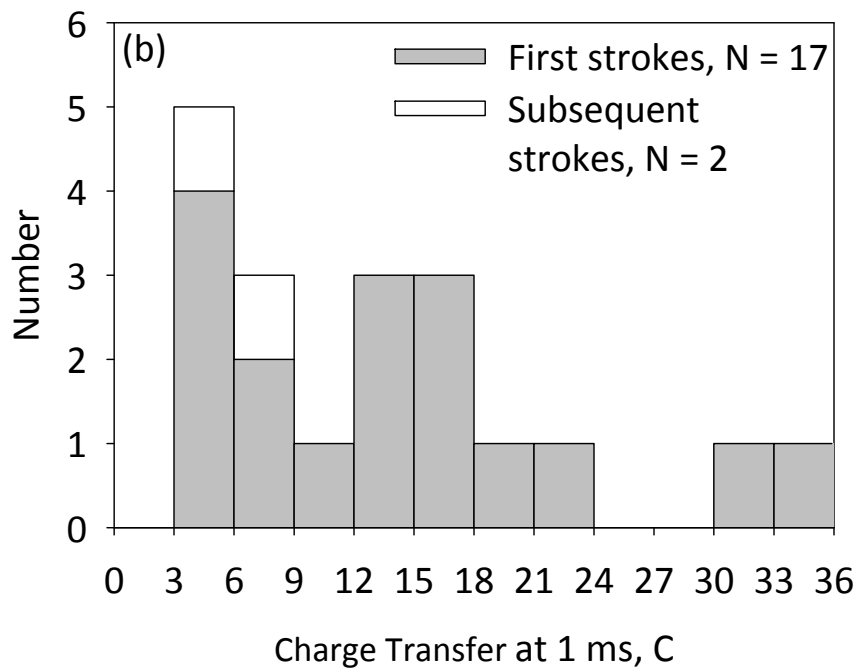
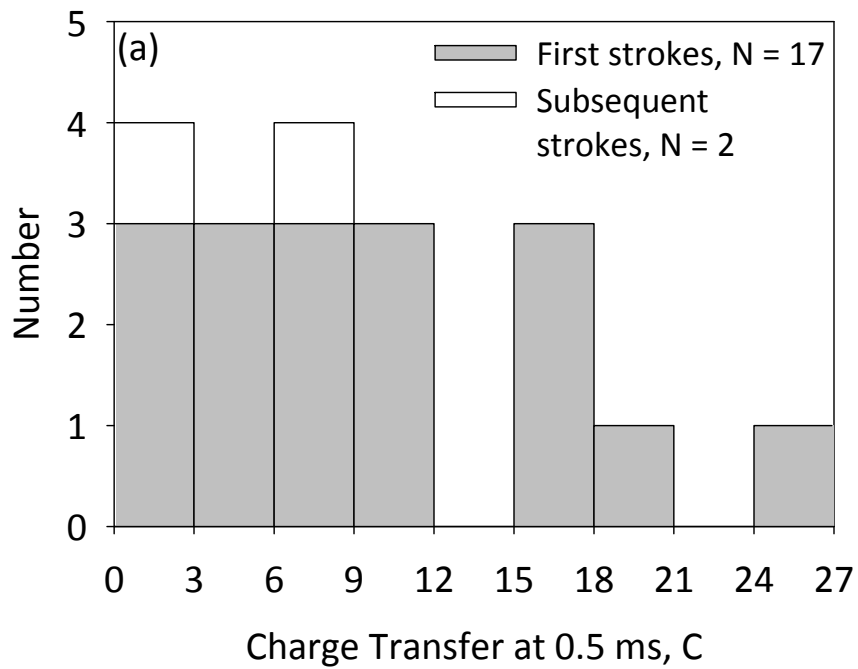


Figure 7-36. Histograms of charge transfer within (a) 0.5 ms, (b) 1 ms, and (c) 1.5 ms of the beginning of the return stroke field change.

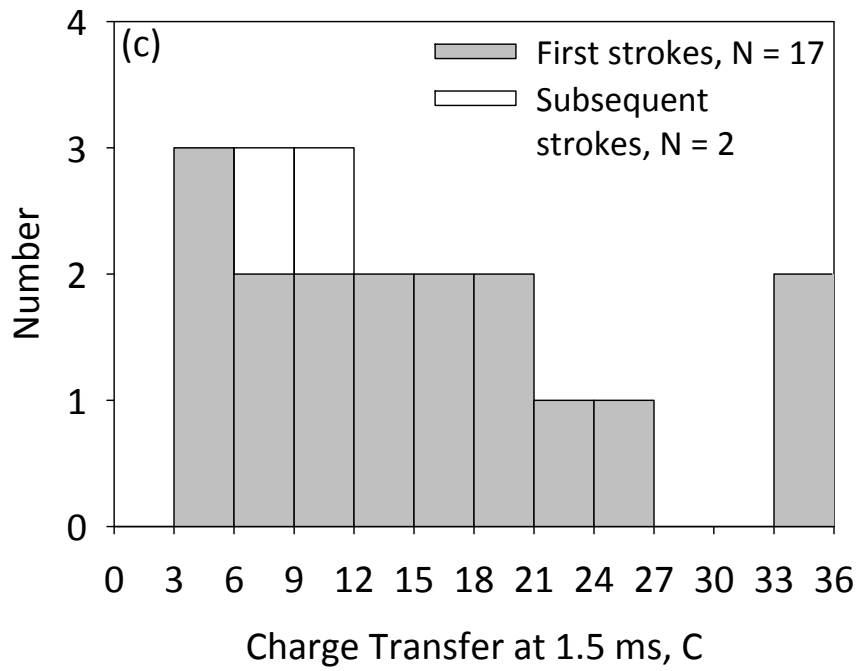


Figure 7-36. Continued

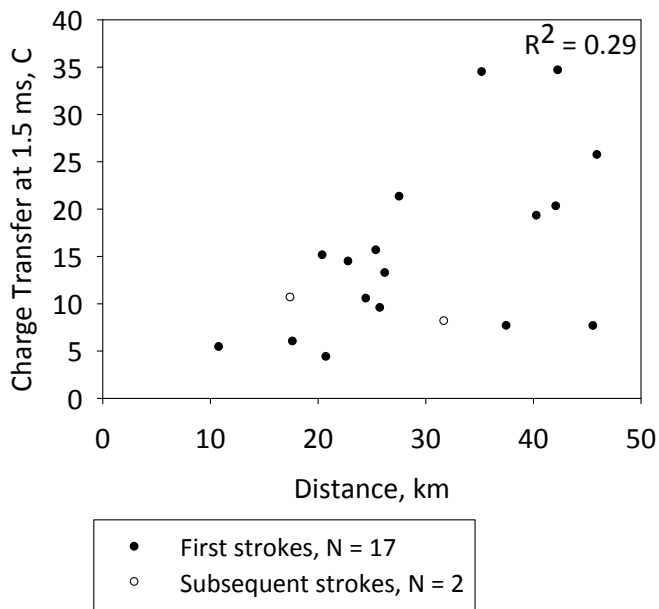


Figure 7-37. Charge transfer at 1.5 ms versus the distance from the measuring station for 19 positive return strokes.

7.5 Ratio of Electric and Magnetic Field Peaks

The ratio of electric and magnetic field peaks can be used to estimate the source heights when the horizontal distance is known. This method is described in Chapter 4. The ratio was computed for seven positive return strokes in the dataset examined here. The return-stroke initial field peaks for these seven strokes were primarily radiation. They occurred at distances ranging from 26 to 46 km. The ratios were within $\pm 9\%$ of the speed of light with the AM and GM both being $1.01c$. This is comparable to the ratio of the electric to magnetic field peaks for 43 first return strokes in negative lightning computed in Chapter 3. The ratios were within $\pm 16\%$ of the speed of light with the AM being $0.99c$. This suggests that the positive return-stroke initial field peaks are produced by sources near ground, so that the elevation angle, $\alpha \approx 0$, and the expected ratio of electric to magnetic field peak is near the speed of light. Table 7-11 summarizes the ratio for the seven positive return strokes.

Table 7-11. Ratio of electric and magnetic field peaks for the seven positive return strokes.

Flash ID	Distance, km	Electric field peak, V/m	Magnetic field peak, μT	Ratio of electric and magnetic field peaks, m/s	The ratio as a percentage of the speed of light
081408_84	42	159	0.553	2.87×10^8	0.96
082308_345	46	52.1	0.175	2.98×10^8	0.99
082308_346	26	62.2	0.190	3.27×10^8	1.09
082308_350	42	64.7	0.217	2.98×10^8	0.99
082408_783	35	59.7	0.208	2.87×10^8	0.96
113008_01	41	12.2	0.039	3.17×10^8	1.06
113008_01	44	9.80	0.031	3.16×10^8	1.05

7.6 Leader Stepping

It appears that positive leaders can move through virgin air either continuously or intermittently (in a stepped fashion), as determined from time-resolved optical images [Rakov and Uman, 2003, Chapter 5]. This is in contrast with negative leaders, which are always

optically stepped when they propagate in virgin air. Further, distant (radiation) electric and magnetic field waveforms due to positive discharges are less likely to exhibit step pulses immediately prior to the return-stroke waveform than are first strokes in negative lightning. Out of 63 positive return strokes (52 first strokes, 10 second strokes, and 1 third stroke) in the dataset presented here, 14 (27%) first strokes (see for example, Figure 7-2b) and 1 third stroke (see Figure 7-2d) were preceded by pronounced step pulses. *Hojo et al.* [1985] found that 26-30% of return stroke waveforms in Japanese thunderstorms in both summer and winter exhibited pulses indicative of a leader stepping process.

The step pulses in the dataset presented here were observed to start 74 to 626 μs before the positive return-stroke pulse with the AM interval between pulse peaks being 20 μs (ranging from 5.8 to 37 μs). This is comparable to the average time interval of 17 μs (ranging from 3 to 31 μs) between leader pulses that occurred during the last 500 μs prior to a positive return stroke examined by *Kong et al.* [2008]. Figure 7-38 shows an example of electric field (integrated dE/dt) signature of one of the positive first strokes in the dataset presented here that apparently involved a stepped leader. For stepped leader electric field pulses prior to negative return-stroke pulse, *Krider et al.* [1977] reported the AM interpulse interval of 16 μs and 25 μs for Florida and Arizona, respectively. *Cooray and Lundquist* [1982] reported that the mean time interval between the electric field pulses just preceding return strokes in Sweden was 26 μs for positive lightning versus 14 μs in negative lightning.

The reason for the occurrence of pulses indicative of stepping prior to the return-stroke pulse in some positive cloud-to-ground discharges is not known. It could be associated with an upward connecting negative leader which may be launched in response to the non-stepped positive downward leader.

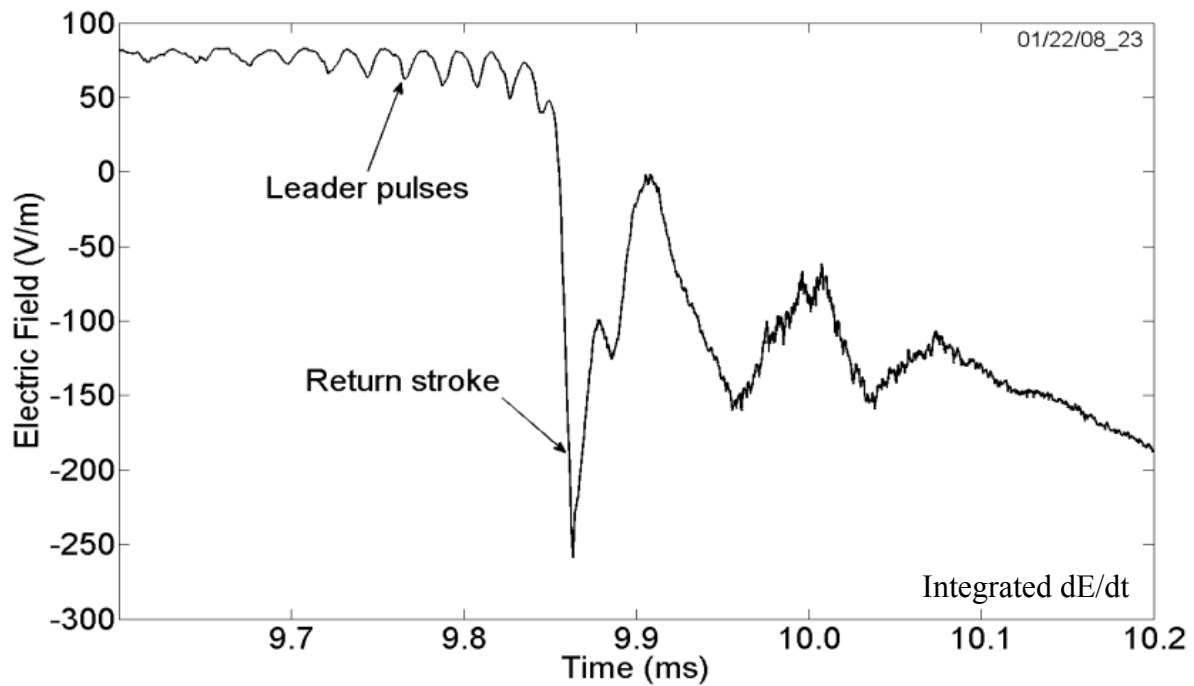


Figure 7-38. Electric field (integrated dE/dt) signature of the return stroke of a single-stroke positive flash that apparently involved a stepped leader shown on a $600\text{-}\mu\text{s}$ time scale. The electric field record of this flash was saturated. This flash was not detected by the NLDN.

7.7 Preliminary Breakdown Pulse Trains

The first return stroke in a negative cloud-to-ground lightning discharge is thought to be preceded by the initial or preliminary breakdown, which is defined as an in-cloud process that initiates or leads to the initiation of the downward-moving stepped leader [Rakov and Uman, 2003]. The preliminary breakdown process in negative ground flashes sometimes (in 18% of cases in Florida; see Chapter 5) produces a train of relatively large microsecond-scale electric field pulses whose initial polarity is the same as that of the following return-stroke pulse. The preliminary breakdown pulse train in negative cloud-to-ground discharges may be viewed as a manifestation of interaction of a downward-extending negative leader channel with the lower positive charge region, as discussed in Chapter 5. The typical total pulse duration of individual

pulses in the train is 20 to 40 μs with typical interpulse interval in the range of 70 to 130 μs [Rakov *et al.* 1996].

In the dataset presented here, only 5 (10%) out of 52 positive cloud-to-ground discharges had detectable preliminary breakdown pulse trains, an example of which is shown in Figure 7-39. The mean total pulse duration of individual pulses in the trains is 22 μs with mean interpulse interval of 155 μs . For preliminary breakdown pulse trains in positive cloud-to-ground discharges in Japanese winter storms, *Ushio et al.* [1998] reported a mean total pulse duration of 18 μs and a mean interpulse interval of 54 μs . In contrast with negative discharges, the initial polarity of preliminary breakdown pulses in positive discharges can be either the same as or opposite to that of the following return-stroke pulse [see, for example, *Ushio et al.*, 1998 and *Gomes and Cooray*, 1998]. Out of the 5 preliminary breakdown pulse trains in the dataset presented here, pulses in four trains had the same initial polarity as that of the following return-stroke pulse, while pulses in one train had opposite polarity (see Figure 7-40). There were no significant differences in the characteristics of the two types of pulse trains apart from their polarity. The preliminary breakdown pulse train with the same initial polarity as that of the following positive return stroke may be viewed as a manifestation of the interaction of a positive leader (moving downward from the upper positive charge region) with the main negative charge region. On the other hand, according to *Cooray and Scuka* [1996], the opposite polarity preliminary breakdown in positive lightning takes place between the main negative and the lower positive cloud charge regions, similar to the preliminary-breakdown in negative lightning, but the negative charge is largely expended in neutralizing the lower positive charge. As a result, the vertical channel created by the preliminary breakdown process is "re-polarized" in the field of the main positive charge region and serves to launch a positive leader toward ground.

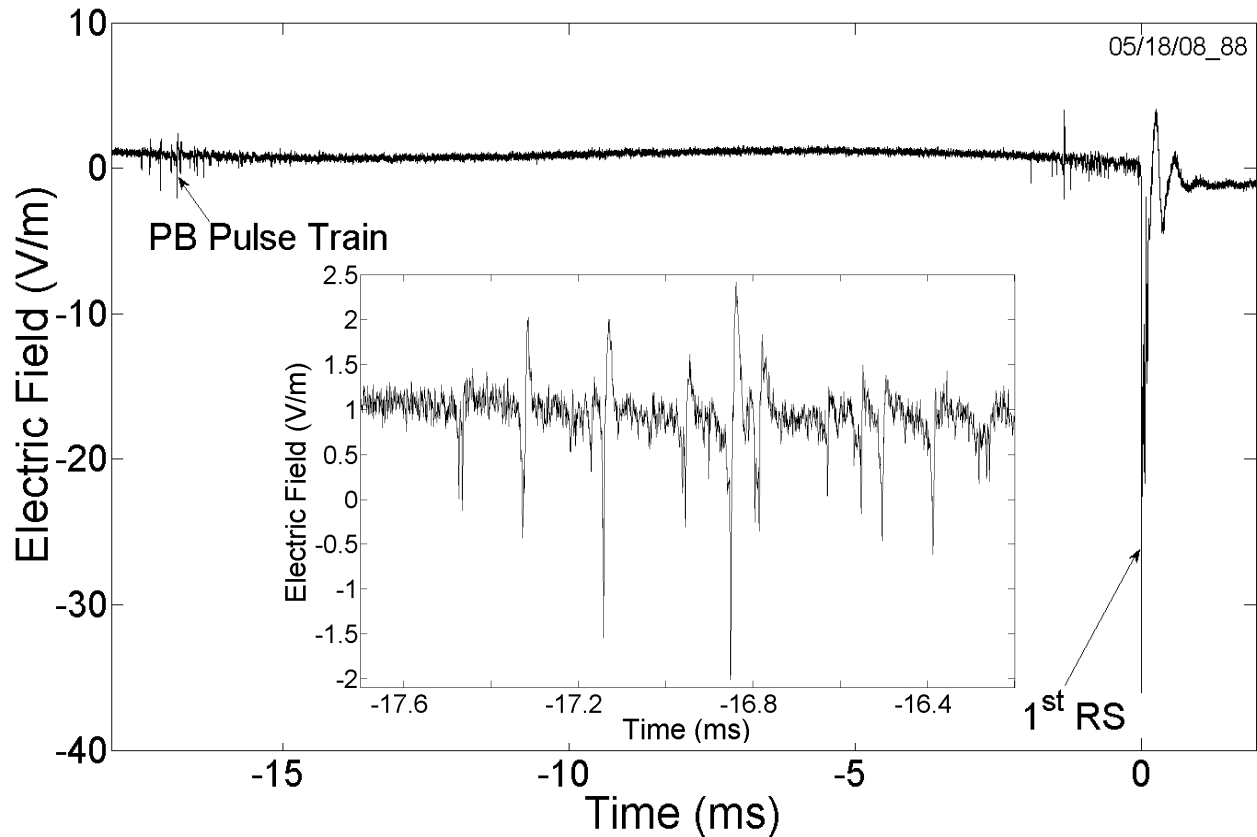


Figure 7-39. Electric field signature of preliminary breakdown (PB) pulse train having the same initial polarity as the following return stroke (RS) of a positive flash on a 20-ms time scale. This flash occurred at a distance of 72 km from the measuring station and had an NLDN-estimated peak current of 146 kA. Inset shows initial part of the preliminary breakdown pulse train on a 1.5-ms time scale.

7.8 Bipolar Lightning Discharges

Bipolar lightning discharge, as described in Chapter 2, is cloud-to-ground lightning that sequentially lowers both positive and negative charge to ground. All bipolar lightning flashes can be divided into three categories, based on the characteristics of the current polarity reversal [Rakov and Uman, 2003; Rakov, 2003, 2005]. A bipolar flash of Type 1 involves a current and charge polarity reversal during the initial stage of a natural upward or a rocket-triggered (triggered using a small rocket trailing a grounded wire) lightning discharge. This initial stage is characterized by a steady current flow of the order of 100 A for a time of the order of tenths of a second during and following the propagation of an upward-going leader toward and into the

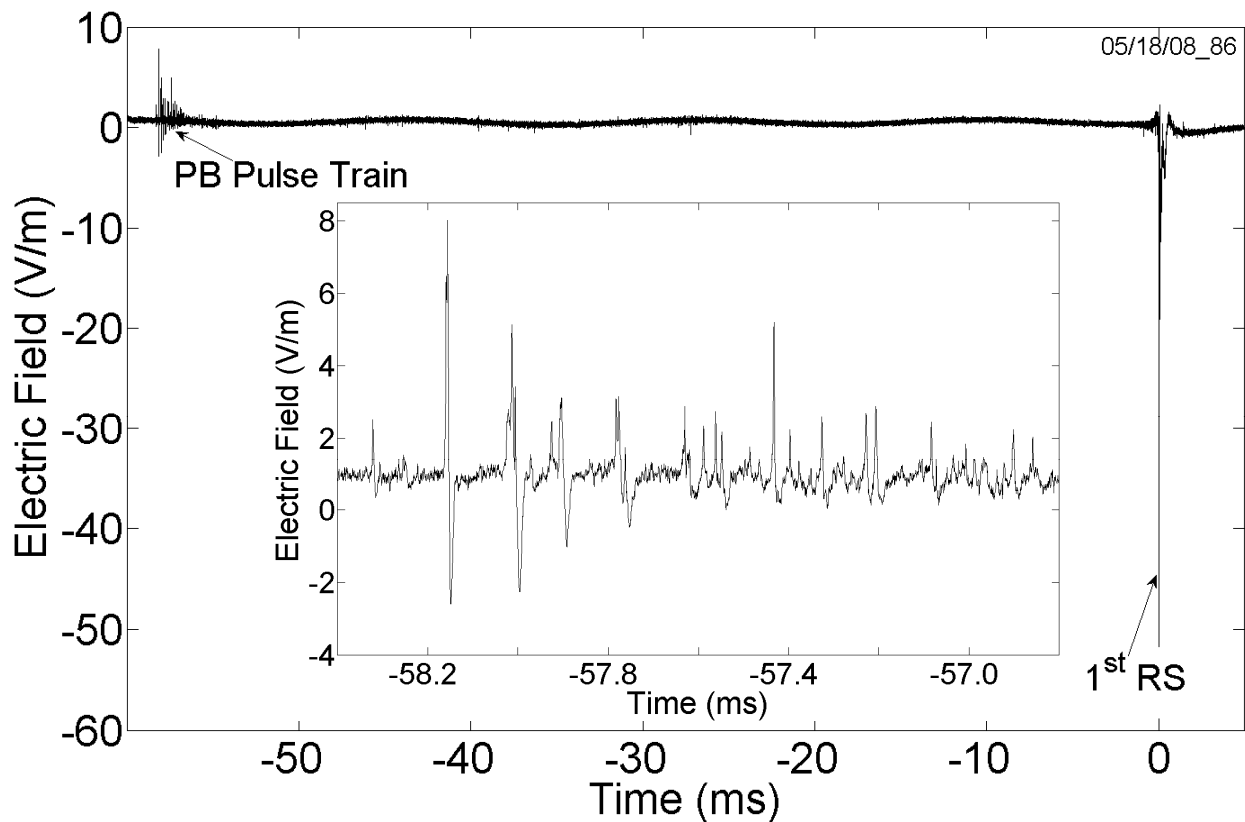


Figure 7-40. Electric field signature of preliminary breakdown pulse train having initial polarity opposite to that of the following return stroke of a positive flash on a 65-ms time scale. This flash occurred at a distance of 84 km from the measurement station and had an NLDN-estimated peak current of 139 kA. Inset shows initial part of the preliminary breakdown pulse train on a 1.6-ms time scale.

cloud charge. Bipolar flashes of Type 2 is characterized by different polarities of the initial-stage current and of the following return stroke or strokes. A Type 3 bipolar flash involves return strokes of opposite polarity. Type 3 flashes can be grouped into two sub-categories, with Type 3a events being natural upward or rocket-triggered lightning discharges, while Type 3b events are natural downward cloud-to-ground flashes. Thus, types 1, 2, and 3a are all associated with natural upward or rocket-triggered lightning discharges, while Type 3b is the only natural downward cloud-to-ground bipolar lightning and is the type of bipolar lightning discussed in this Section.

As noted in Section 2, there are two bipolar cloud-to-ground flashes in the dataset presented here. Figure 7-41 shows the electric field signature of a bipolar flash composed of three negative strokes followed by a positive stroke and then by a negative one. The interstroke interval between the third stroke (negative) and the fourth stroke (positive) was 69 ms and that between the fourth and the fifth (negative) strokes was 20 ms. Figure 7-42 shows electric field waveforms of individual return strokes of this flash. No GPS timestamps (and hence no NLDN information) were available for this flash. It is not clear if the fourth (positive) stroke shared a channel with any of the negative strokes of the flash.

The other bipolar flash (whose electric field record is shown in Figure 7-43a) was composed of three strokes, the first and the third being negative and the second being positive. The interstroke interval between the first (negative, shown in Figure 7-43b) and second (positive, shown in Figure 7-43c) strokes was 130 ms and that between the second and third (negative, shown in Figure 7-43d) strokes was 249 ms. The two negative strokes (the first and the third ones) were, therefore, separated by 379 ms. The first stroke was preceded by a cloud discharge lasting for about 660 ms. Both the first and third strokes occurred at a distance of 46 km from the field measuring station (semi-major axis length of NLDN 50% location error ellipse being 400 m for both strokes) and NLDN-estimated peak currents of 52 kA and 25 kA, respectively. The NLDN reported the third (positive) stroke as an intracloud discharge at a distance of 39 km (semi-major axis length of 1.2 km). It appears that the second (positive) stroke formed a channel to ground different from that of the first and third (negative) strokes.

Jerauld et al. [2009] examined one natural bipolar lightning flash, producing two channel terminations on ground and containing two strokes (strokes 1 and 2) that lowered positive charge to ground followed by four strokes that lowered negative charge. All strokes occurred within 1

km of a multiple-station electric field measuring network at Camp Blanding, Florida. Strokes 1 and 2 (both positive) were in separate channels, while strokes 3 to 6 (all negative) followed the same channel as stroke 2. The two positive leader/return-stroke sequences were separated in time by approximately 53 ms, followed by a negative leader/return-stroke sequence approximately 526 ms later. The interstroke intervals for strokes 3 to 6 were 280 ms, 260 ms, and 300 ms. The NLDN-estimated peak currents for the first five strokes of the flash were +50.7, +49.9, -14.2, -13.5, and -10 kA. The sixth stroke (negative) was not detected by the NLDN.

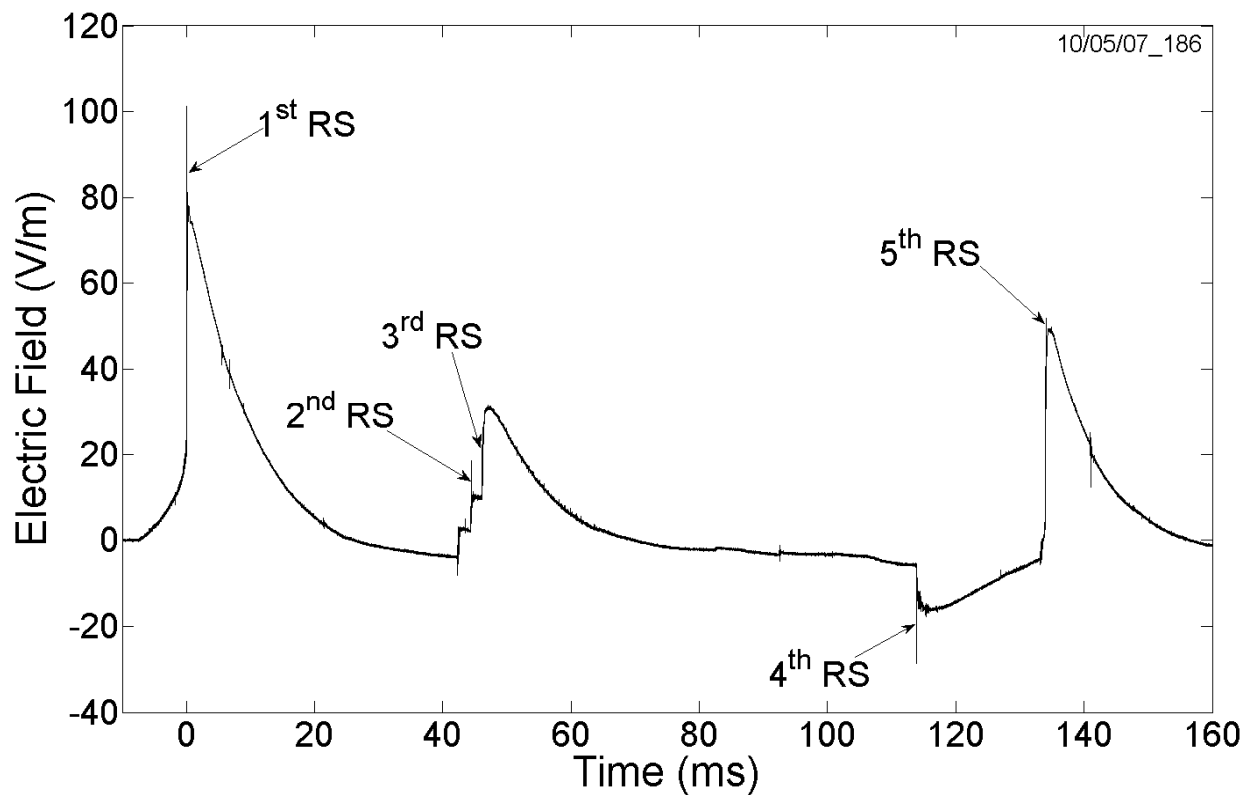


Figure 7-41. Electric field record of bipolar flash composed of three negative strokes followed by a positive stroke and then by a negative one, recorded in Gainesville, Florida, on October 5, 2007. GPS timestamps and NLDN information were not available for this flash.

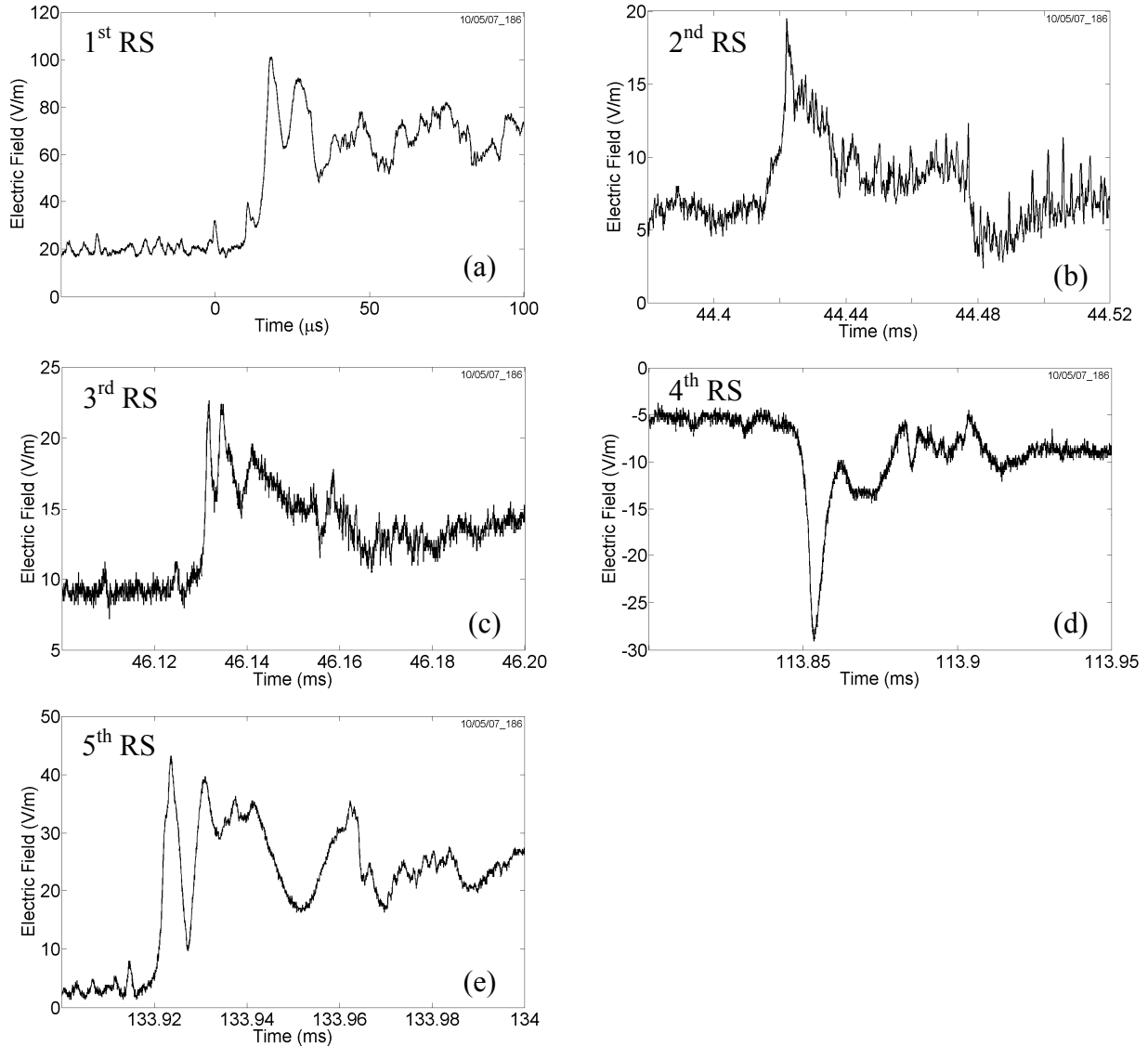


Figure 7-42. Electric field waveforms of individual return strokes of the five-stroke bipolar flash shown in Figure 7-41. Strokes 1 and 4 are shown on a 150- μ s time scale, strokes 3 and 5 on a 100- μ s time scale, and stroke 2 on a 140- μ s time scale.

7.9 Summary

Experimental data on positive and bipolar lightning acquired in Gainesville, Florida, in 2007-2008 are presented. Various features of positive discharge, including multiplicity, parameters of return stroke electric field waveforms, inferred currents, charge transferred by return stroke, leader stepping, and preliminary breakdown pulse trains were examined. There were a total of 63 return-strokes in 52 positive flashes with an average multiplicity of 1.2.

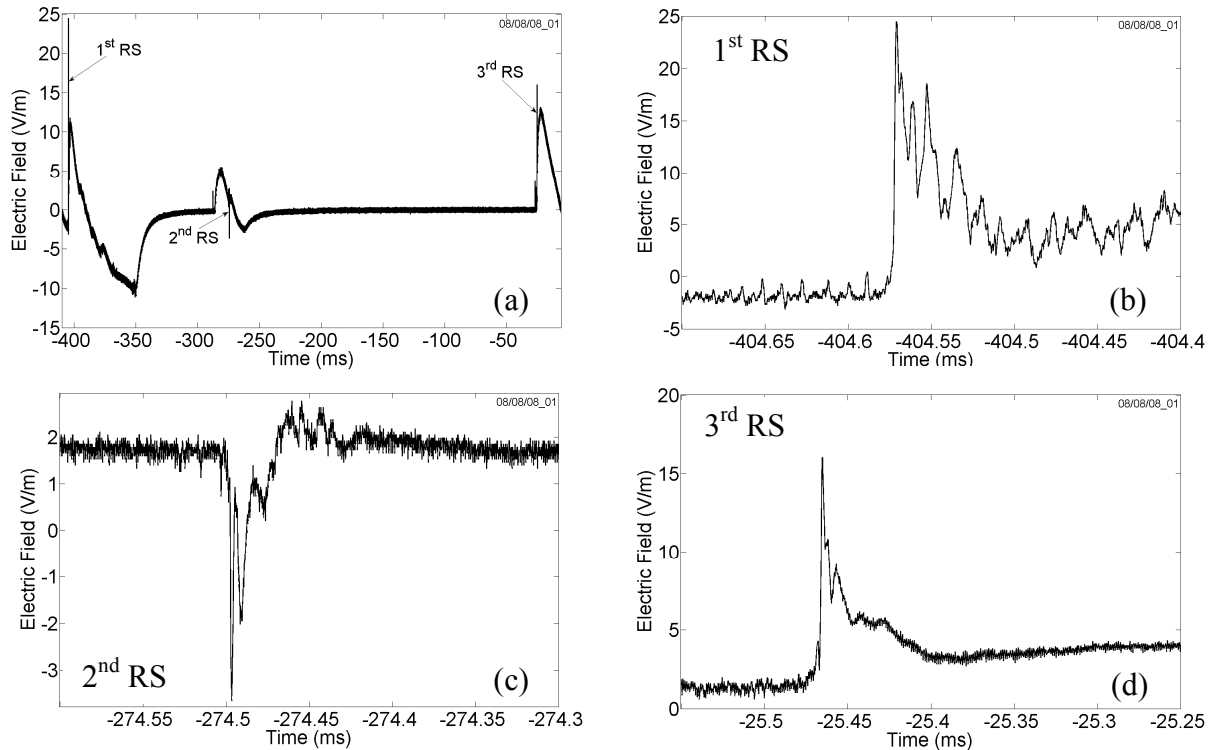


Figure 7-43. (a) Electric field record of a three-stroke bipolar cloud-to-ground flash with two negative and one positive return strokes (RS), shown on a 404-ms time scale. (b), (c), and (d) Electric field waveforms of the first, second, and third return strokes, respectively, each shown on a 300- μ s time scale. NLDN reported the positive stroke as an IC discharge at a distance of 39 km. The first and third strokes both occurred at a distance of 46 km and had NLDN-estimated peak currents of 52 kA and 25 kA, respectively.

Out of the 52 positive cloud-to-ground flashes presented here 42 (81%) were single-stroke, 9 (17%) two-stroke, and 1 (2.0%) three-stroke flashes. 89% of the positive return strokes were correctly identified by the NLDN. A second stroke that exhibits a waveshape similar to that of the corresponding first stroke probably follows the same channel as the first one. Distance between strokes being smaller than the largest NLDN median location error (SMA length) is also an indication of the two strokes sharing the same channel. Out of 8 NLDN-located two-stroke flashes, 3 contained strokes characterized by both similar electric field waveshapes and spatial separations that are smaller than stroke location uncertainties.

The GM electric field peak and electric field derivative peak, both normalized to 100 km, for 48 positive return strokes occurring at distances ranging from 7.8 to 157 km were 18.1 V/m and 9.02 V/m/ μ s, respectively. The GM normalized electric field peak for distance ranges of 7.8-50 km and 64-157 km in this dataset are 14.8 V/m (N = 31) and 26.3 V/m (N = 17), respectively.

The GM zero-to-peak risetime and 10-90% risetime for positive return strokes were 6.92 μ s and 3.40 μ s, respectively. Similar values were reported by *Rust et al.* [1981] in USA and by *Beasley et al.* [1983] in Florida. The zero to peak and 10-90% risetimes for positive return strokes in Sweden and Japan were found to be, in general, longer than those reported for Florida and by *Rust et al.* [1981].

The GM slow front duration, slow front amplitude relative to peak, and fast-transition 10-90% risetime were 4.95 μ s, 36.7%, and 1.02 μ s, respectively. It was found that while the slow front duration for positive return strokes in Florida is, on average, shorter than that in Sweden and Japan, the 10-90% risetime of the fast transition in Florida is at least a factor of two longer than that in the other two geographical locations. The duration of the slow front for positive return strokes in Florida was found to be, on average, longer than that for negative first return strokes in Florida reported by *Weidman and Krider* [1978] and *Master et al.* [1984].

For positive return strokes examined here, the AM zero-crossing time was 53.6 μ s and the opposite polarity overshoot was, on average, 15.6% of the peak. These values are similar to those of 49.5 μ s and 18.5% reported by *Pavlick et al.* [2002] for negative return strokes in Florida.

The NLDN field-to-current conversion algorithm has been calibrated only for negative subsequent strokes [GM peak current estimation error is about 20%, *Jerauld et al.*, 2005, *Nag et al.*, 2008]. Interestingly, for negative cloud-to-ground lightning, regression equations relating NLDN-estimated peak currents and measured electric field peaks are not much different for first

and subsequent strokes. This observation suggests that the NLDN procedure to compensate for field propagation effects and find the average range-normalized signal strength (RNSS) works equally for both subsequent and first return strokes. The discrepancy between regression equations for negative first and subsequent strokes on the one hand and positive return strokes on the other hand suggests that the NLDN procedure to compensate for field propagation effects and find the average RNSS works differently for these two groups of strokes.

Charge transfer was estimated for 19 positive return strokes (occurring at distances ranging from 11 to 46 km) within 0.5 ms, 1 ms, and 1.5 ms after the beginning of return stroke electric field change. The median charge transfer within 0.5 ms, 1 ms, and 1.5 ms were estimated to be 6.98 C, 12.2 C, and 13.2 C, respectively. These values are comparable to the median impulse charge (excluding continuing current) of 16 C for a sample of 26 positive return strokes reported by *Berger et al.* [1975]. *Schoene et al.* [2009] reported the GM charge transfer within 1 ms after the beginning of the return stroke for 151 negative rocket triggered lightning strokes (considered similar to subsequent strokes in natural downward lightning) at Camp Blanding, Florida to be 1.0 C which is about an order of magnitude smaller than the GM charge transfer within 1 ms of 10.7 C, found for positive lightning in our dataset.

Positive leaders can move through virgin air either continuously or intermittently (in a stepped fashion), as determined from time-resolved optical images which is in contrast with negative leaders, which are always optically stepped when they propagate in virgin air. Out of 63 positive return strokes (52 first strokes, 10 second strokes, and 1 third stroke) in the dataset presented here, 14 (27%) first strokes and 1 third stroke were preceded by pronounced step-like pulses. The AM interval between pulse peaks was found to be 20 μ s, which is similar to the

average time interval of 17 μs between leader pulses prior to a positive return stroke examined by *Kong et al.* [2008].

Preliminary breakdown pulses were identified and examined. In the dataset presented here, only 5 (10%) out of 52 positive cloud-to-ground discharges had detectable preliminary breakdown pulse trains. The mean total pulse duration of individual pulses in the trains was 22 μs with mean interpulse interval of 155 μs . In contrast with negative discharges, the initial polarity of preliminary breakdown pulses in positive discharges can be either the same as or opposite to that of the following return-stroke pulse. Out of the 5 preliminary breakdown pulse trains in the dataset presented here, pulses in four trains had the same initial polarity as that of the following return-stroke pulse, while pulses in one train had opposite polarity. There were no significant differences in the characteristics of the two types of pulse trains apart from their polarity.

Two bipolar lightning discharges, which sequentially lower both positive and negative charge to ground are examined. One of them was composed of three negative strokes followed by a positive stroke and then by a negative one. It is not clear if the fourth (positive) stroke shared a channel with any of the negative strokes of the flash. The other bipolar flash was composed of three strokes, the first and the third being negative and the second being positive. NLDN reported the positive stroke in this flash as an intracloud discharge. It appears that the second (positive) stroke formed a channel to ground different from that of the first and third (negative) strokes.

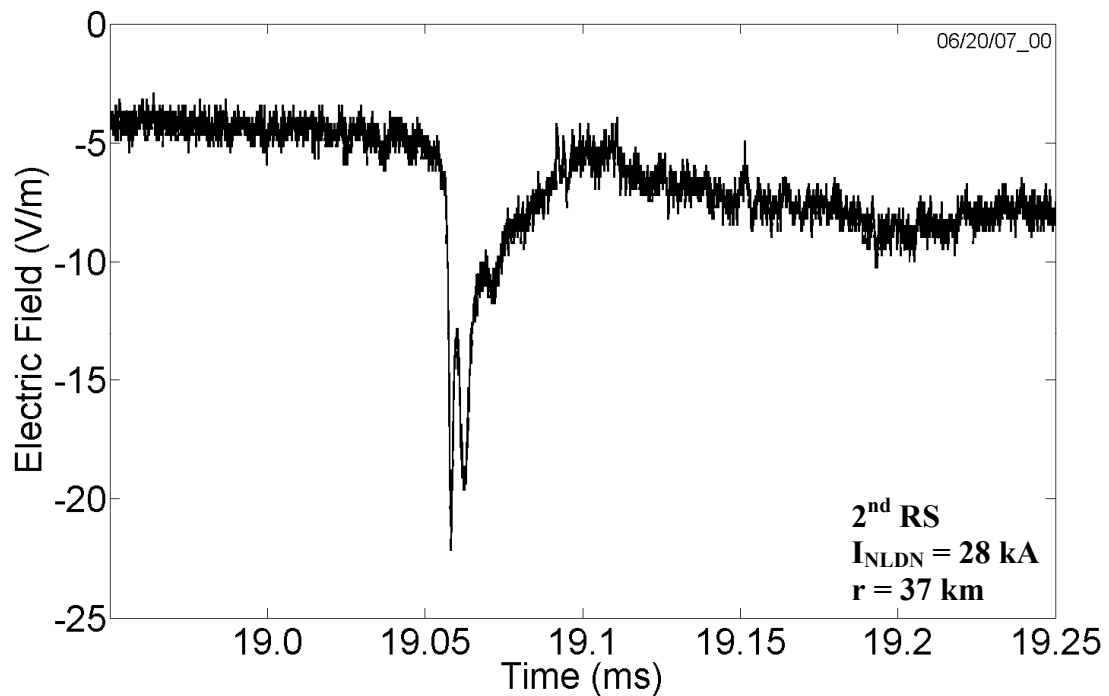
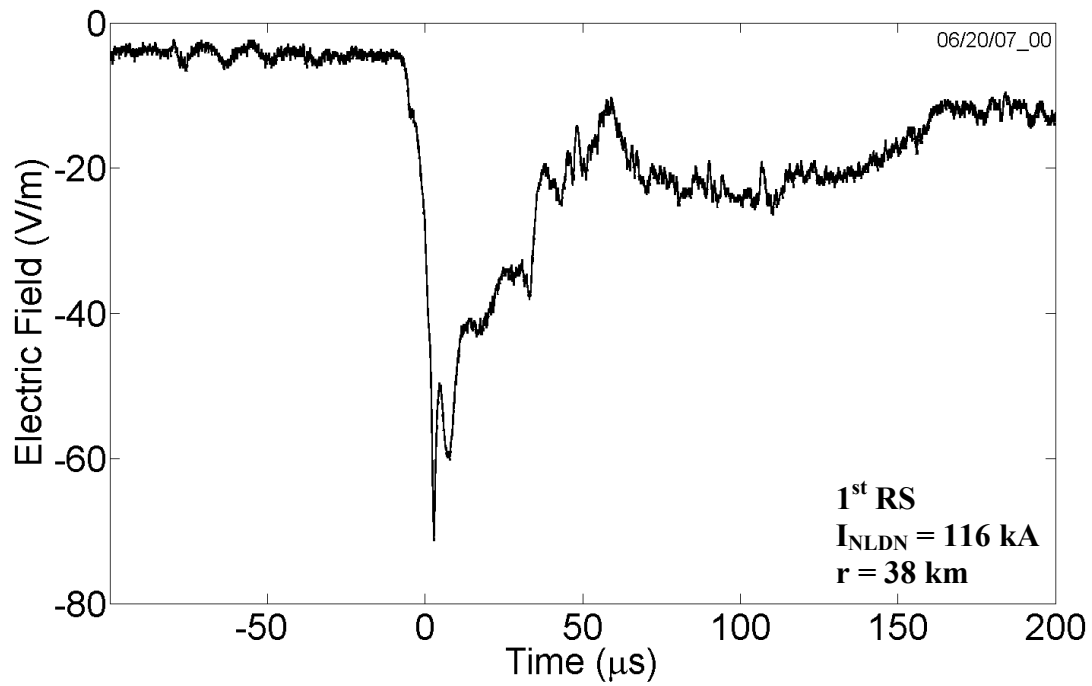


Figure 7-44. Electric field waveforms of the first (top panel) and second (bottom panel) return strokes of a two-stroke flash, each shown on a 300 μs time scale. The interstroke interval was 19 ms. The NLDN-estimated distance between strokes was 1.7 km, and NLDN median location errors were 4.0 and 0.5 km for the first and second strokes, respectively.

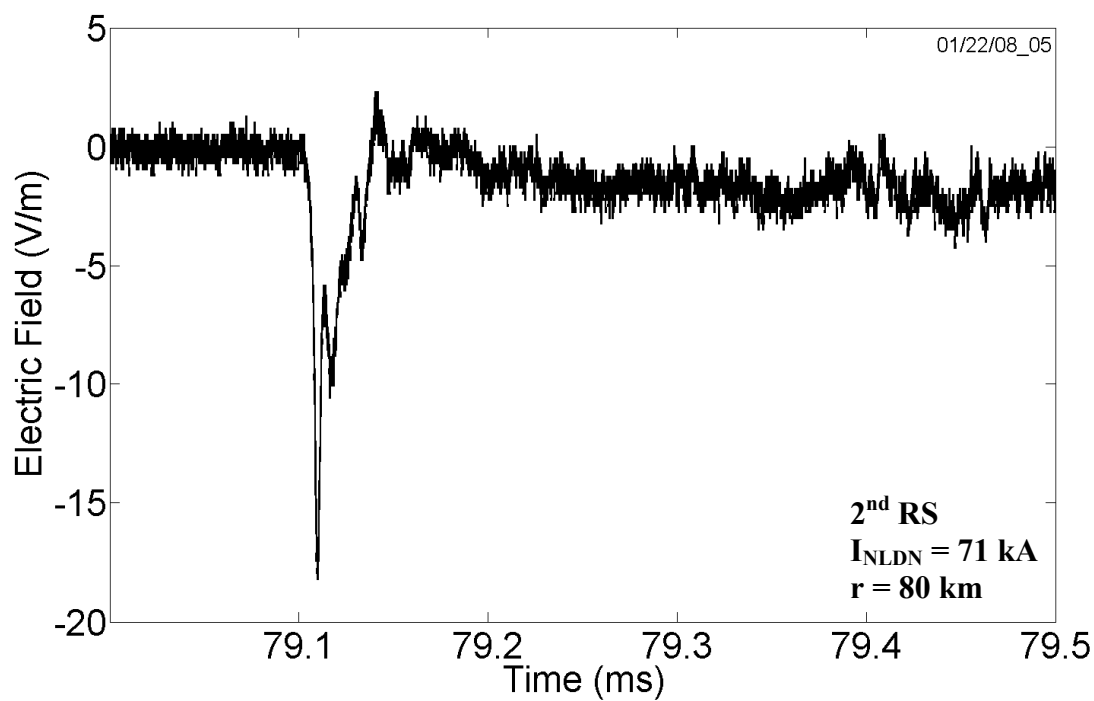
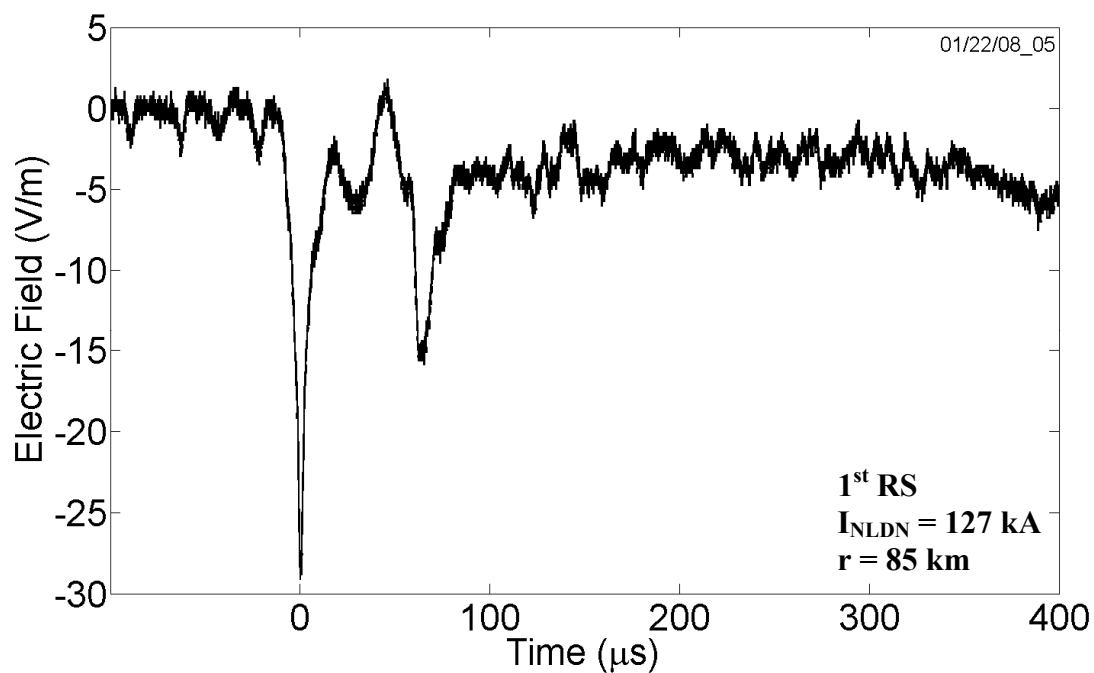


Figure 7-45. Electric field waveforms of the first (top panel) and second (bottom panel) return strokes of a two-stroke flash, each shown on a 500 μs time scale. The interstroke interval was 79 ms. The NLDN-estimated distance between strokes was 12 km, and NLDN median location errors were 0.7 and 0.4 km for the first and second strokes, respectively.

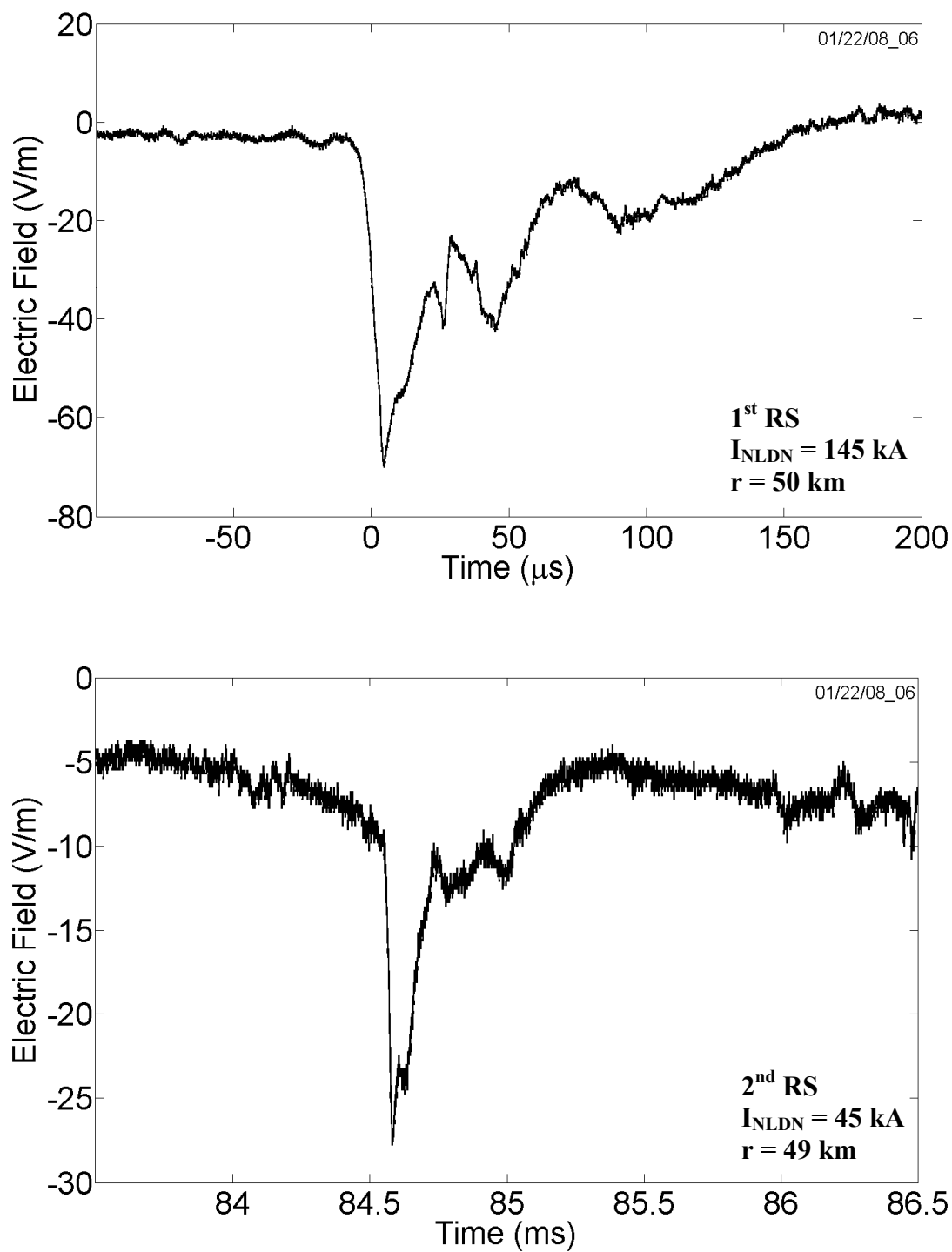


Figure 7-46. Electric field waveforms of the first (top panel) and second (bottom panel) return strokes of a two-stroke flash, each shown on a 300 μs time scale. The interstroke interval was 8.5 ms. The NLDN-estimated distance between strokes was 2 km, and NLDN median location errors were 2.4 and 0.5 km for the first and second strokes, respectively.

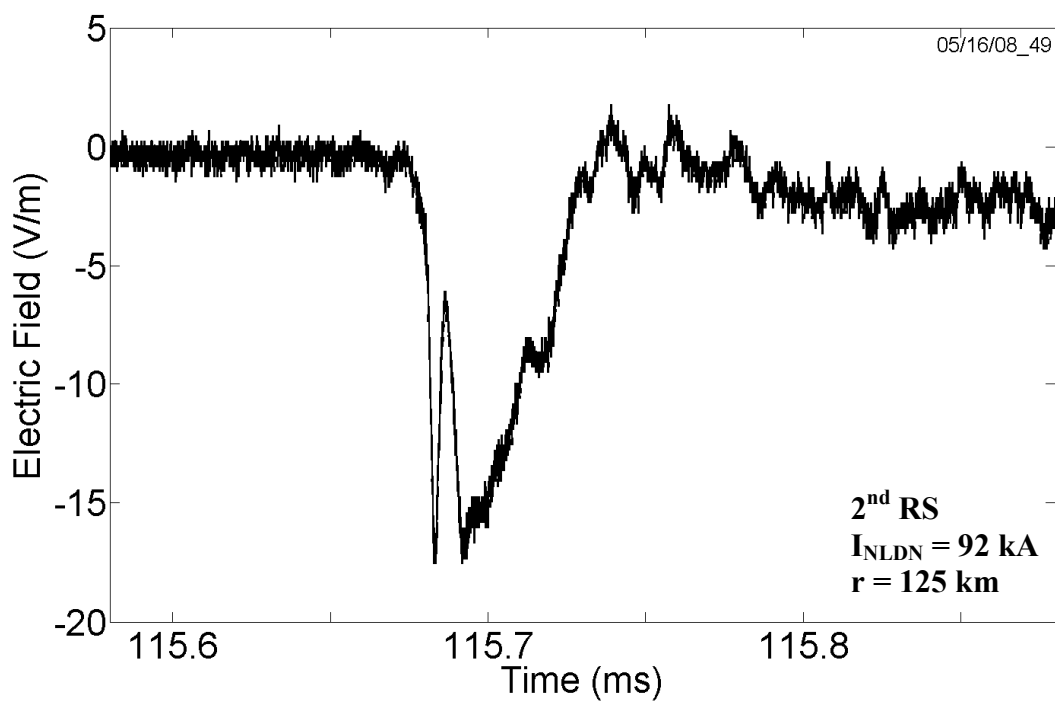
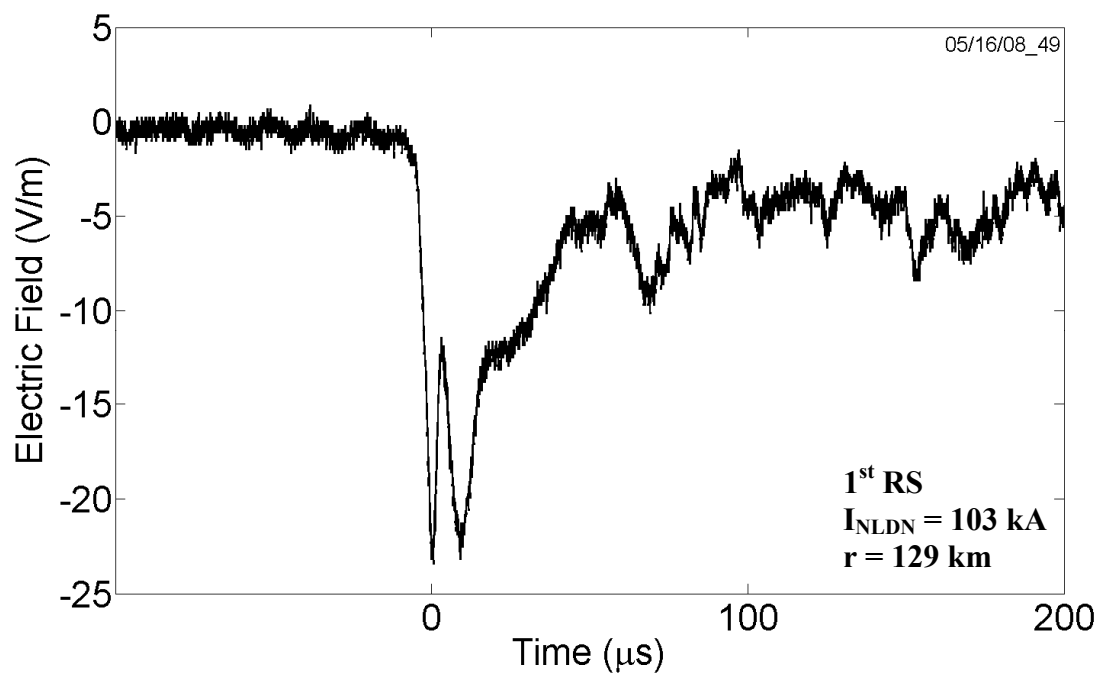


Figure 7-47. Electric field waveforms of the first (top panel) and second (bottom panel) return strokes of a two-stroke flash, each shown on a 300 μs time scale. The interstroke interval was 116 ms. The NLDN-estimated distance between strokes was 14 km, and NLDN median location error for both the first and second strokes was 0.4 km.

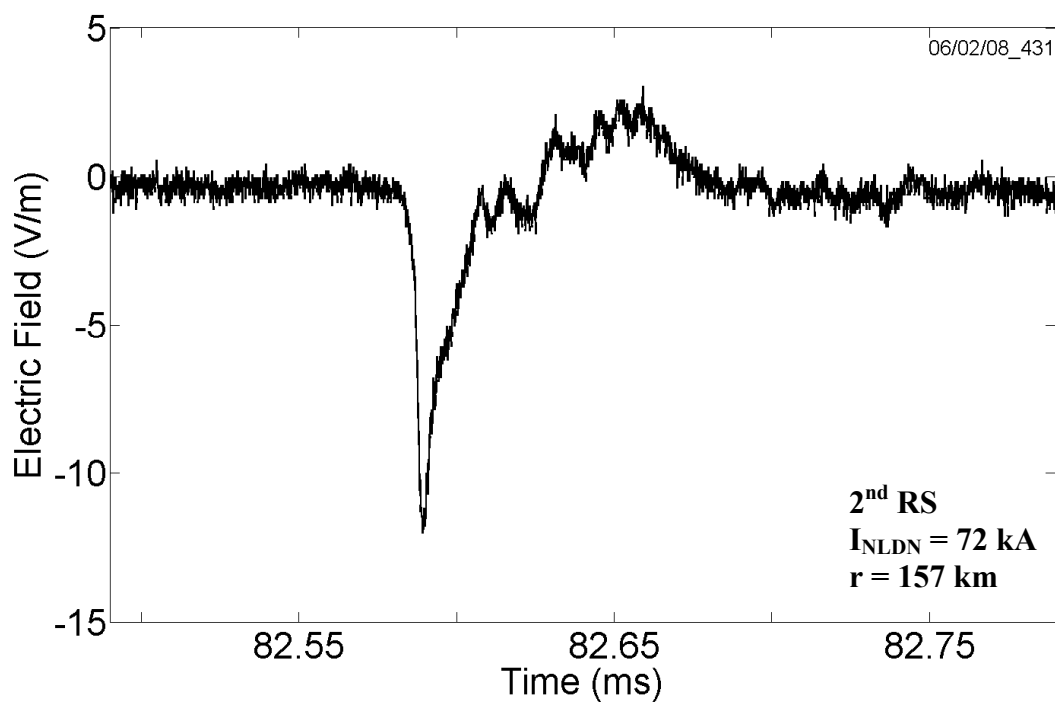
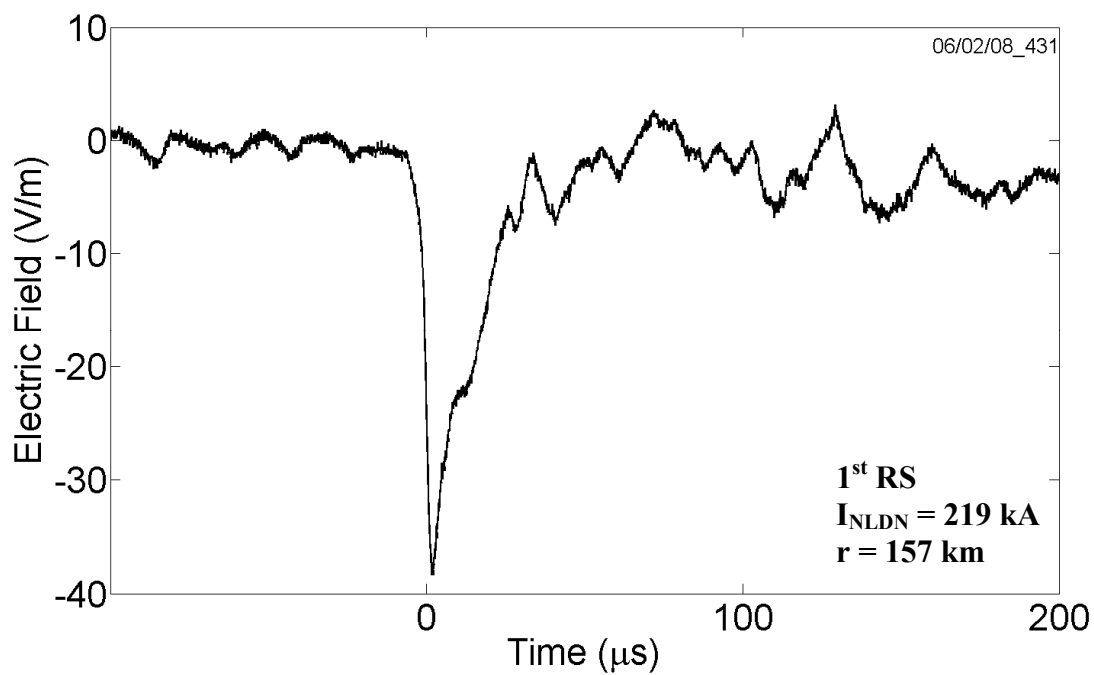


Figure 7-48. Electric field waveforms of the first (top panel) and second (bottom panel) return strokes of a two-stroke flash, each shown on a 300 μs time scale. The interstroke interval was 83 ms. The NLDN-estimated distance between strokes was 222 m, and NLDN median location errors were 0.8 and 0.5 km for the first and second strokes, respectively.

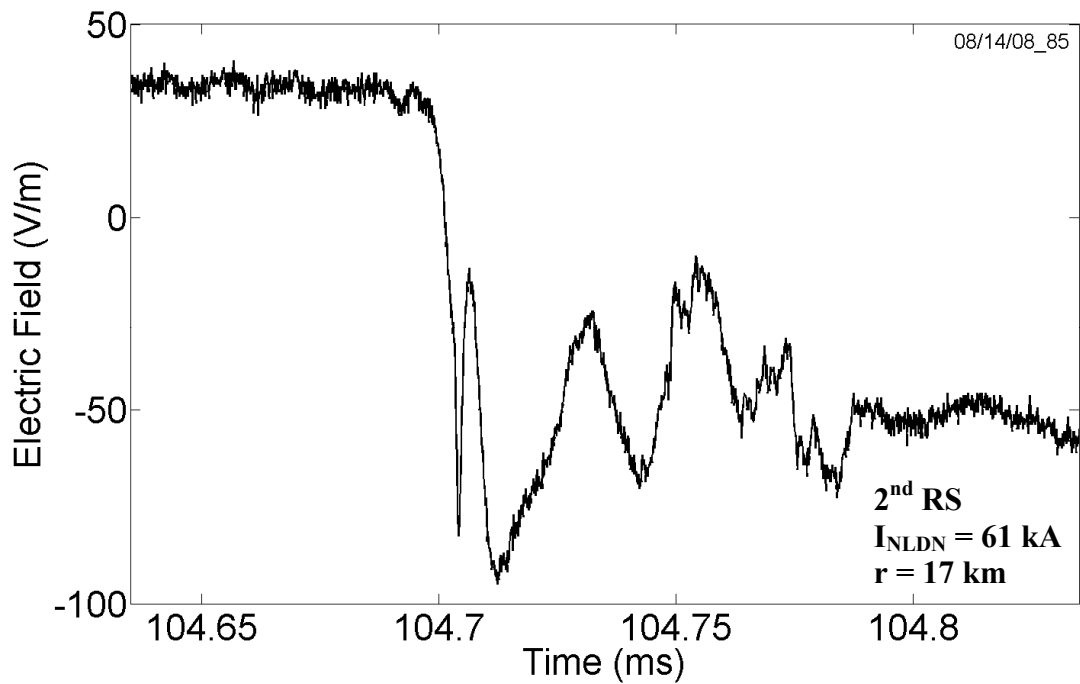
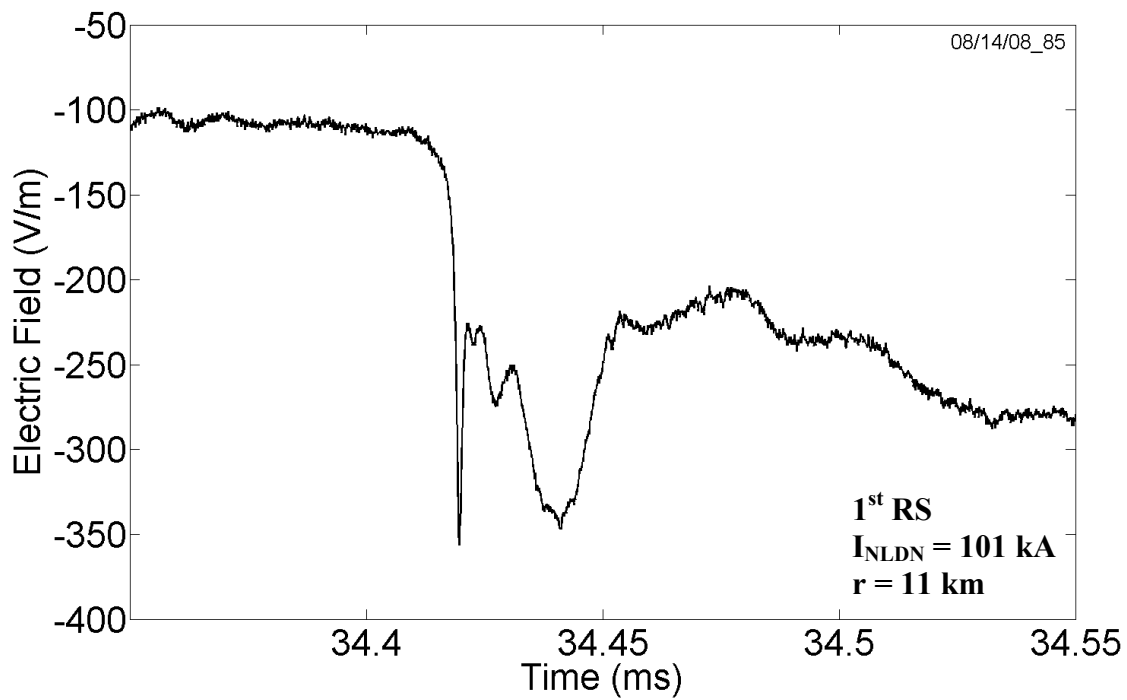


Figure 7-49. Electric field waveforms of the first (top panel) and second (bottom panel) return strokes of a two-stroke flash, each shown on a 200 μ s time scale. The interstroke interval was 70 ms. The NLDN-estimated distance between strokes was 10 km, and NLDN median location errors were 0.6 and 0.8 km for the first and second strokes, respectively.

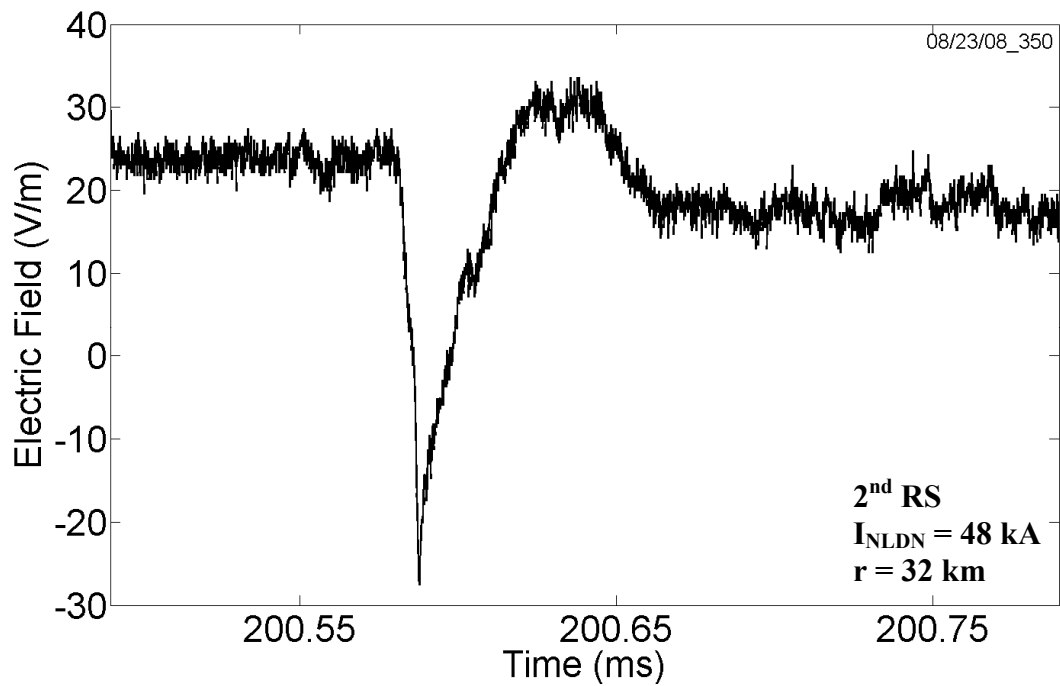
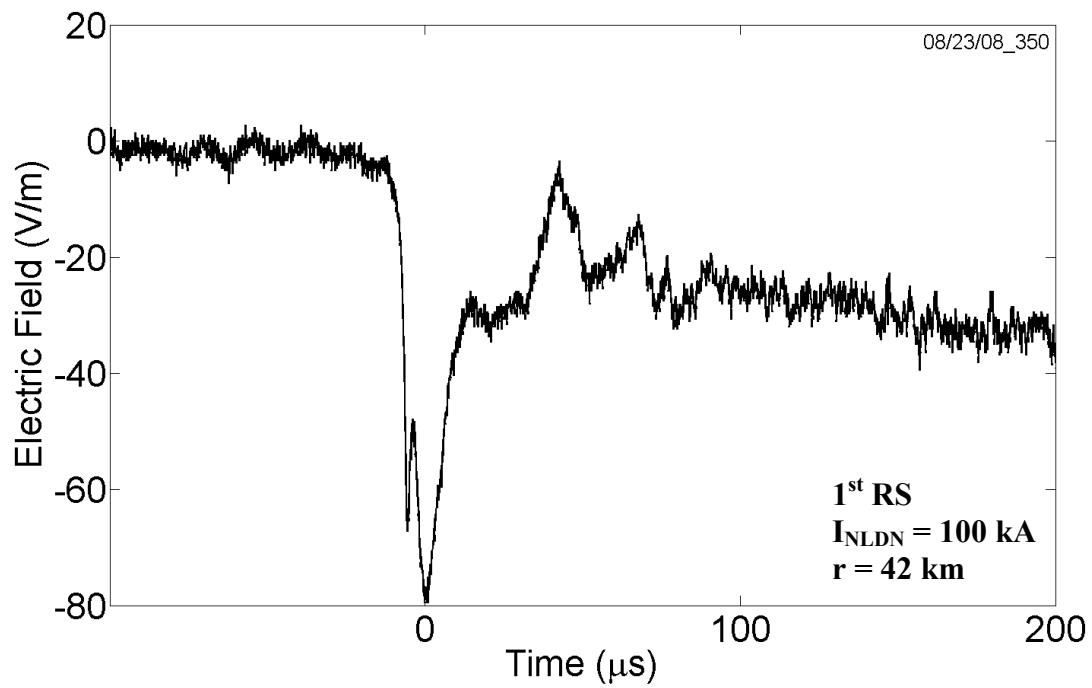


Figure 7-50. Electric field waveforms of the first (top panel) and second (bottom panel) return strokes of a two-stroke flash, each shown on a 300 μs time scale. The interstroke interval was 201 ms. The NLDN-estimated distance between strokes was 29 km, and NLDN median location errors were 0.5 and 0.4 km for the first and second strokes, respectively.

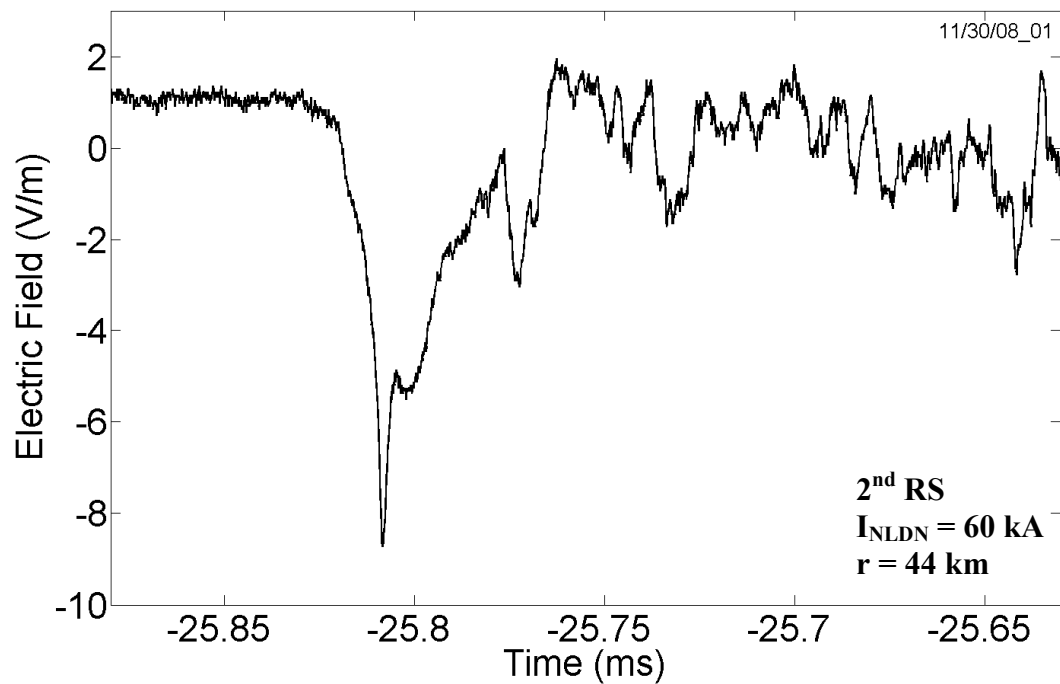
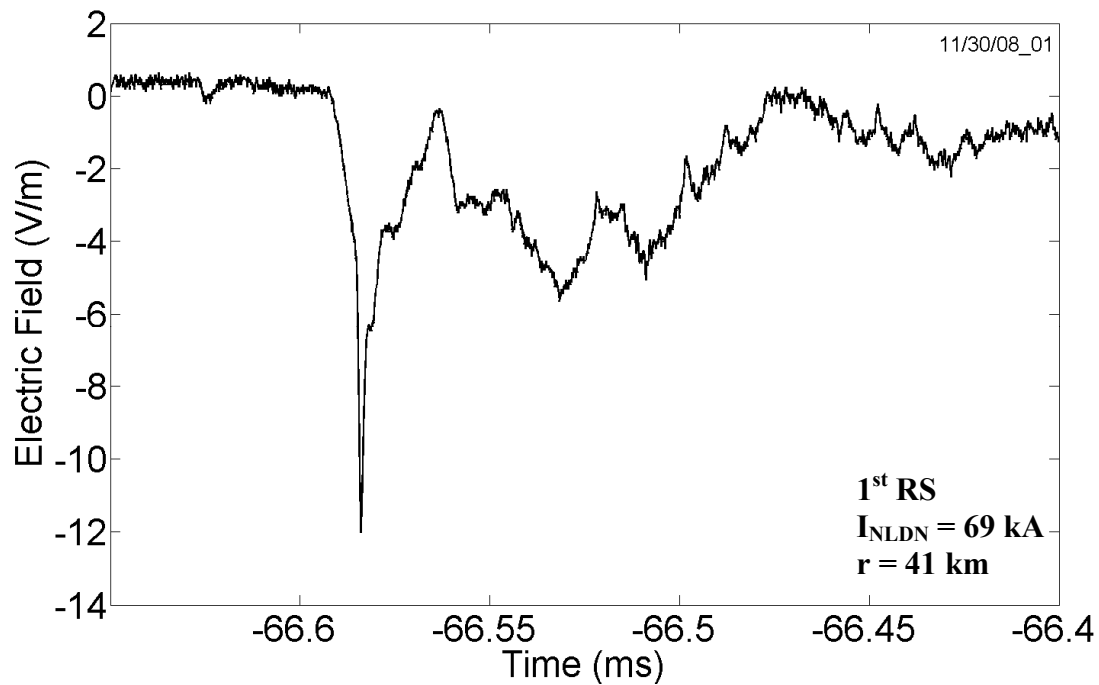


Figure 7-51. Electric field waveforms of the first (top panel) and second (bottom panel) return strokes of a two-stroke flash, each shown on a 250 μs time scale. The interstroke interval was 41 ms. The NLDN-estimated distance between strokes was 3.7 km, and NLDN median location error for both the first and second strokes was 0.4 km.

CHAPTER 8
FIRST VERSUS SUBSEQUENT RETURN-STROKE CURRENT AND FIELD PEAKS IN
NEGATIVE CLOUD-TO-GROUND LIGHTNING DISCHARGES

8.1 Introduction

Return-stroke peak currents and electric and magnetic peak fields are often used to measure relative intensity of first and subsequent strokes. It is generally thought that for negative cloud-to-ground lightning discharges first strokes are typically a factor of 2 to 3 larger than subsequent strokes [e.g., *Berger et al.*, 1975; *Rakov et al.*, 1994; *Cooray and Perez*, 1994; *Cooray and Jayaratne*, 1994; *Visacro et al.*, 2004]. In contrast, peak currents inferred from measured fields by lightning locating systems (LLSs) for first and subsequent strokes are often not much different from each other [e.g., *Diendorfer et al.*, 1998; *Rakov and Uman*, 2003, Ch. 17]. In this Chapter, we examine relative intensities of first and subsequent strokes using electric field data acquired in Gainesville, Florida in 2006 (see *Nag* [2007] and Chapter 3), and compare the results with those of other lightning electric field measuring studies in Austria, [*Schulz and Diendorfer*, 2006], Brazil [*Oliveira et al.*, 2007], and Sweden [*Schulz et al.*, 2008]. Additionally, we will consider results of recent LLS studies conducted in conjunction with video observations in USA [*Biagi et al.*, 2007; *Krider et al.*, 2007] and Brazil [*Saba et al.*, 2006a]. In this Chapter, there are two Florida data sets, one acquired as a part of the present study in 2006 in Gainesville, Florida, and the other [*Rakov and Uman*, 1990b] near Tampa, Florida, in 1979. Unless otherwise mentioned, the data set acquired in this study in 2006 is referred to as the Florida data set throughout this Chapter.

8.2 Methodology

There are different approaches to estimating relative intensity of first and subsequent strokes. One approach is to form the ratio of geometric mean (GM), arithmetic mean (AM), or median intensities of first strokes and all subsequent strokes combined. This approach was used,

for example, by *Rakov and Uman* [1990a, b] and *Diendorfer et al.* [1998]. Usually, intensities of strokes in single-stroke flashes are included, which results in a somewhat lower first-to-subsequent-stroke ratio than in the absence of single-stroke flashes, since strokes in single-stroke flashes are on average smaller than first strokes in multiple-stroke flashes. Another approach is to form the ratios for individual subsequent strokes and then find the AM, GM, or median of the resultant statistical distribution. This approach was employed, for example, by *Thottappillil et al.* [1992], *Cooray and Perez* [1994], and *Cooray and Jayaratne* [1994]. Clearly, the latter approach applies only to multiple-stroke flashes. For either of the two approaches, the use of GM (or median) values, as opposed to AM values, should probably be preferred, because distributions of current or field peaks or distributions of the ratios are close to log-normal. It is worth noting that subsequent strokes creating new terminations on ground are on average larger than subsequent strokes following previously formed channels [*Rakov et al.*, 1994], so that the occurrence of new channel terminations can potentially influence the field ratios examined here.

In this Chapter, using our own measurements and data found in the literature we compiled statistical distributions of the ratio of first to corresponding subsequent return stroke electric field peaks and the ratio of subsequent to corresponding first return stroke field peaks for Florida, Austria, Brazil, and Sweden (additional information about data acquired in Austria, Brazil, and Sweden were provided by *Schulz*, *Saba*, and *Thottappillil*, respectively, via personal communication). Then the AM and GM for each of the two distributions were calculated. Ratios of AM (GM, median) first to AM (GM, median) subsequent stroke peaks were also computed, when possible. Further, we examined relative magnitudes of strokes of different order for Florida [*Rakov and Uman*, 1990; present study], Austria [*Diendorfer et al.*, 1998; *Schulz and Diendorfer*, 2006], Brazil [*Oliveira et al.*, 2007], and Sweden [*Schulz et al.*, 2008]. For the present study in

Florida, we normalized the electric field peak of each subsequent stroke in a particular flash with respect to the field peak of the first return-stroke in that flash. Then, for each stroke order (sequential number of a stroke in a flash), the geometric mean of the normalized field peaks was calculated. For all the other studies, the GM field peaks for subsequent strokes were normalized to the GM field peak for first strokes (including those in single-stroke flashes for data of *Rakov and Uman* [1990b] and *Diendorfer et al.* [1998]).

Note that while computing the ratios for Florida, Austria, Sweden, and Brazil, it has been assumed that for flashes having multiple ground terminations the distances from the antenna to all terminations are approximately the same. This assumption is justified when distances between different channel terminations of the same flash are small compared to the distance between them and the antenna. For the overwhelming majority of flashes examined here the distances were larger than 20 km, which is much greater than the geometric mean separation of 1.7 km between multiple channel terminations within a flash estimated in Florida by *Thotappillil et al.* [1992].

8.3 Instrumentation and Data

A brief description of the electric field measuring systems used in Gainesville, Florida (present study) and in Austria, Brazil, and Sweden and the data analyzed in this study is given below, followed by an overview of pertinent output of lightning locating systems. Descriptions of instrumentation and data of other studies are available in the literature, in appropriate references provided in this Chapter.

8.3.1 Electric Field Measurements in Gainesville, Florida

The electric field measuring system used to acquire the data analyzed in this study has been described in *Nag* [2007] and Chapter 3. Electric field signals from a flat-plate antenna and associated electronics were relayed to a digitizing oscilloscope via a fiber-optic link. The

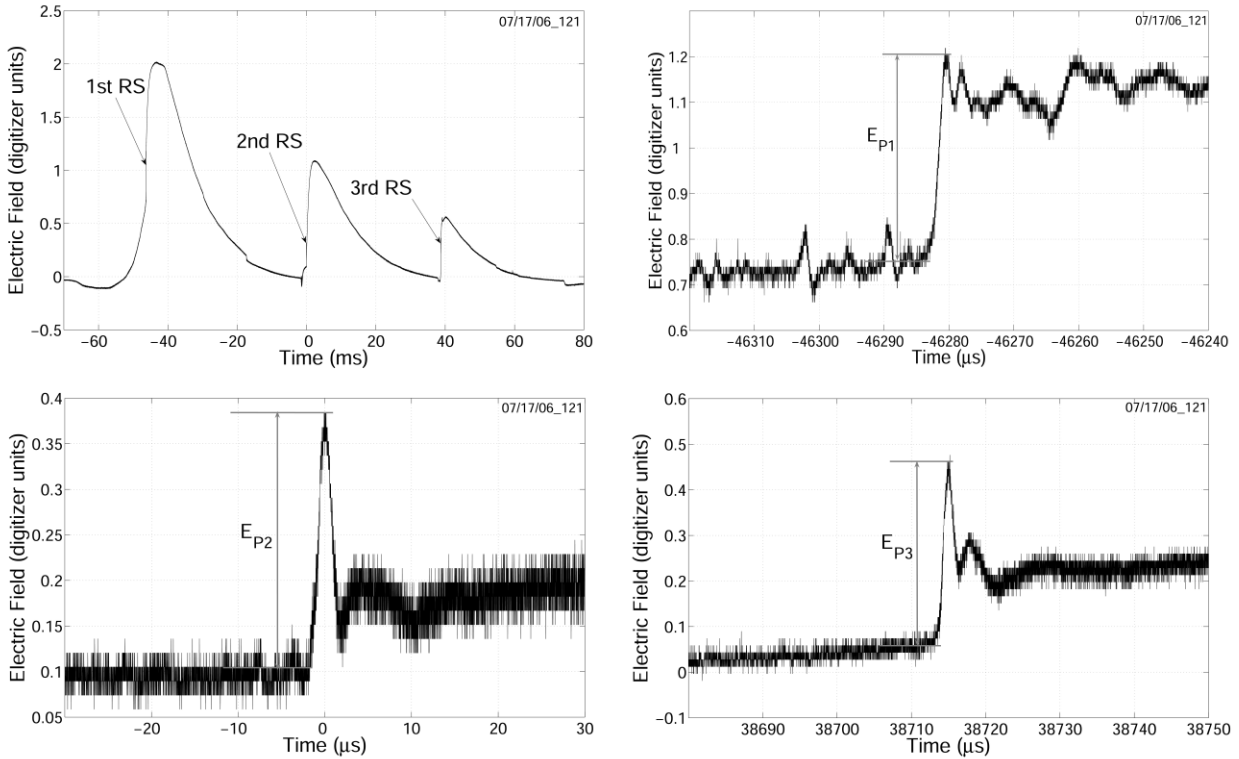


Figure 8-1. (a) Typical electric field record of a multiple-stroke negative cloud-to-ground flash in Florida with three return strokes (RS) shown on a 150-ms timescale. (b) Electric field of the first return stroke, on an 80-ms timescale, of flash shown in Figure 8-1a. (c) Electric field of the second return stroke, on a 60-ms timescale. (d) Electric field of the third return stroke, on a 70-ms timescale. Initial (radiation) electric field peaks of return strokes of order 1, 2, and 3 are labeled as E_{P1} , E_{P2} , and E_{P3} , respectively. Note that radiation field peaks seen in Figures 8-1b – 8-1d are not resolved in Figure 8-1a.

sampling interval was 10 ns. The measurement system had a useful frequency bandwidth of 16 Hz to 10 MHz. The record length was 200 ms. Using thunder ranging and the characteristic features of return-stroke electric field waveforms at known distances in the 50 to 250 km range [Pavlick *et. al*, 2002; Figure 5] we estimated that the majority of our records were due to lightning discharges occurring at distances ranging from a few to about a hundred kilometers from the field measuring station. An example of electric field record of multiple-stroke negative cloud-to-ground discharge in this dataset is shown in Figure 8-1. The data set consists of 176 multiple-stroke negative cloud-to-ground flashes recorded on July 15 and 17, 2006 in

Gainesville, Florida. Each of the 176 records was examined to measure the amplitude of the initial (radiation) electric field peak (in digitizer units) of individual return stroke waveform. Electric field peaks of subsequent strokes were normalized with respect to the electric field peak of the corresponding first stroke.

It should be noted that the maximum number of strokes per flash in the Florida data set is four, although some higher-order strokes were likely missed due to limited record length of 200 ms. Since higher order return strokes are expected to have somewhat smaller peak fields [*Rakov and Uman*, 1990b], the ratio of the first to subsequent return stroke field peaks based on this Florida data set should be viewed as a lower bound (the actual value can be somewhat higher).

8.3.2 Electric Field Measurements in Austria

The electric field measuring system used to acquire the data analyzed in this study has been described by *Schulz and Diendorfer* [2006]. The system could record fields continuously during the entire thunderstorm. A fiber-optic link was used to relay signals from a flat-plate antenna to a digitizing oscilloscope. The sampling interval was 200 ns. The measurement system had a useful frequency bandwidth of 350 Hz to 1.5 MHz. Electric field records of lightning discharges occurring at distances of 50 to 100 km from the field measuring station were included in the data set analyzed in this study. This data set consists of 81 multiple-stroke negative cloud-to-ground flashes recorded during about one hour on July 11, 2005 in Bad Voeslau, Austria. Lightning locating system (ALDIS) data were used to normalize electric field peaks to 100 km.

8.3.3 Electric Field Measurements in Brazil

The electric field measuring system used in Brazil was the same as that used in Austria and described above, but a double-shielded coaxial cable instead of the fiber optic link was used to transmit signals from the antenna to the digitizer. The data set analyzed in this study consists of 259 multiple-stroke negative cloud-to-ground flashes occurring within 200 km of the field

measuring station that were recorded during about one hour each on each February 11 and March 11, 2007 in São José dos Campos, Brazil. Electric field peaks were normalized to 100 km using lightning locating system (BrasilDat) data. Additional information can be found in *Oliveira et al.* [2007].

8.3.4 Electric Field Measurements in Sweden

The electric field measuring system was the same as that used in Brazil, although the antenna was installed on the top of a building, while in Brazil (and in Austria) it was installed at ground level. A total of 93 multiple-stroke negative cloud-to-ground flashes occurring at distances ranging from 20 to 60 km on July 24, 2006 in Uppsala, Sweden, are analyzed in this study. Electric field peaks were normalized to 100 km using lightning locating system data. Additional information can be found in *Schulz et al.* [2008].

8.3.5 Currents Estimated by Lightning Locating Systems

Modern multiple-station lightning locating systems (LLSs) output a peak current estimate for each stroke using the measured magnetic radiation field peaks and distances to the ground strike point reported by individual sensors. The field and current peaks are usually assumed to be proportional to each other. For data examined in this study, the magnetic-field-to-current conversion factor was 0.185 for the U.S. and Brazilian systems and 0.23 for the Austrian system, where the magnetic field was expressed in so-called LLP units. In the U.S. and Brazilian systems, a model was employed to increase the measured field peak (normalized to 100 km) in order to compensate for its attenuation due to propagation over finitely-conducting ground, while no such model was implemented in the Austrian system. In this study, we used only those LLS-reported events confirmed by video records as having cloud-to-ground channels, except for the Austrian LLS data for which no video records were available.

8.4 Analysis and Discussion

Figure 8-2 shows the distributions of the ratio of the first return stroke field peak to the corresponding subsequent return stroke field peak for Florida, Austria, Brazil, and Sweden. The arithmetic and geometric means of the ratio were, respectively, 2.1 and 1.7 for Florida, 2.3 and 1.6 for Austria, and 2.4 and 1.9 for either Brazil or Sweden. Thus, on average, the electric field peak of the first stroke is roughly 2 times larger than the field peak of the subsequent stroke.

Distributions of the ratio of the subsequent to the corresponding first return stroke field peaks, shown in Figure 8-3 are characterized by arithmetic and geometric means, respectively, of 0.75

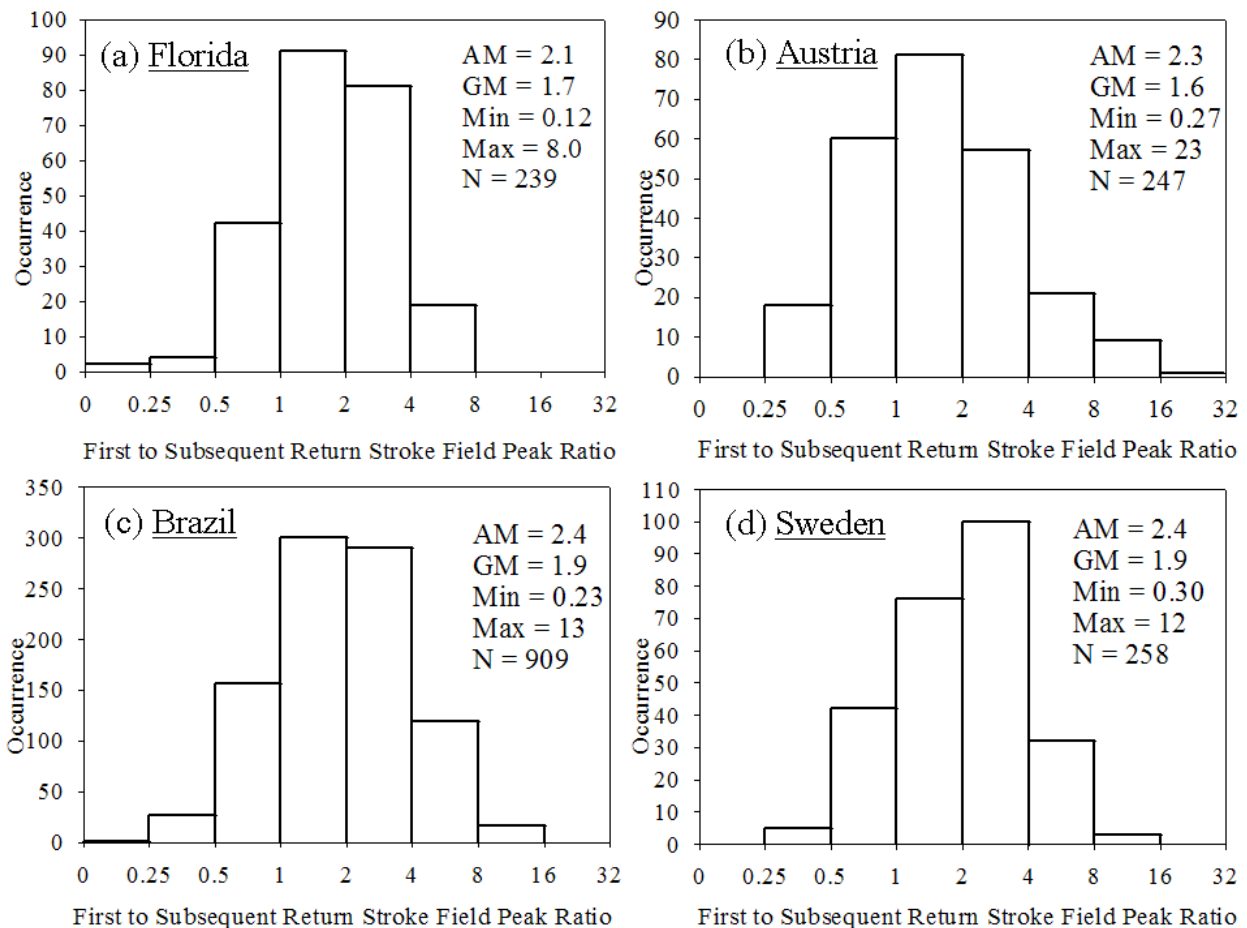


Figure 8-2. Histogram of the ratio of the first-to-subsequent-return-stroke electric field peak for multiple stroke negative cloud-to-ground lightning flashes in (a) Florida, (b) Austria, (c) Brazil, and (d) Sweden.

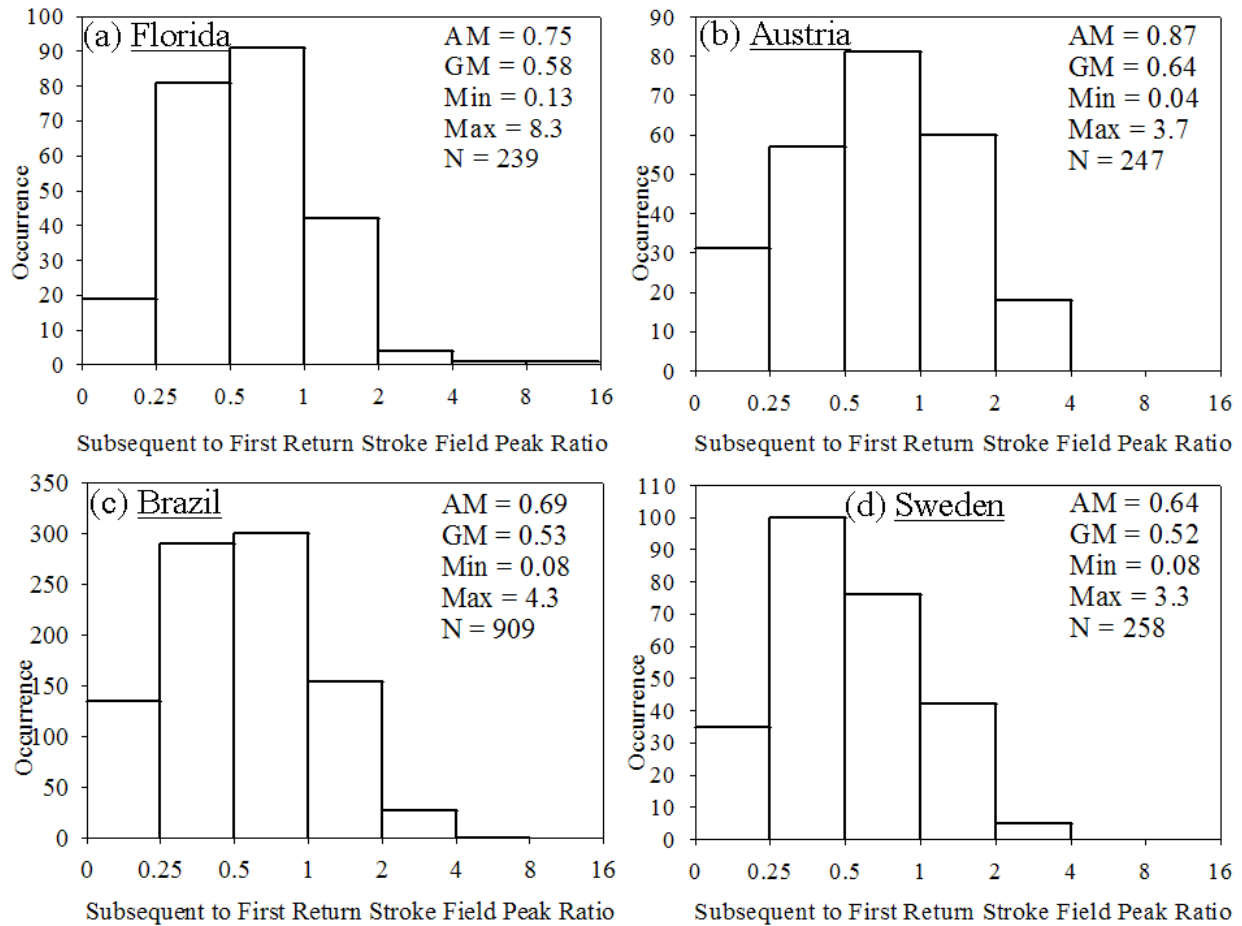


Figure 8-3. Histogram of the ratio of the subsequent-to-first-return-stroke electric field peak for multiple stroke negative cloud-to-ground lightning flashes in (a) Florida, (b) Austria, (c) Brazil, and (d) Sweden.

and 0.58 for Florida, 0.87 and 0.64 for Austria, 0.69 and 0.53 for Brazil, and 0.64 and 0.52 for Sweden. The geometric mean electric field peaks for strokes of different order normalized (as described in Section 2 and in the caption of Figure 8-4) to the corresponding first stroke field peak from different studies in Florida, Austria, Brazil, and Sweden are shown in Figure 8-4.

Data of *Rakov and Uman* [1990b] were acquired using simultaneous single-station electric field and multiple-station TV records near Tampa, Florida, in 1979. The normalized field peaks for subsequent strokes in the 1979 and 2006 Florida data (see columns labeled A and B, respectively, in Figure 8-4) are found to be in good agreement, confirming the notion that the

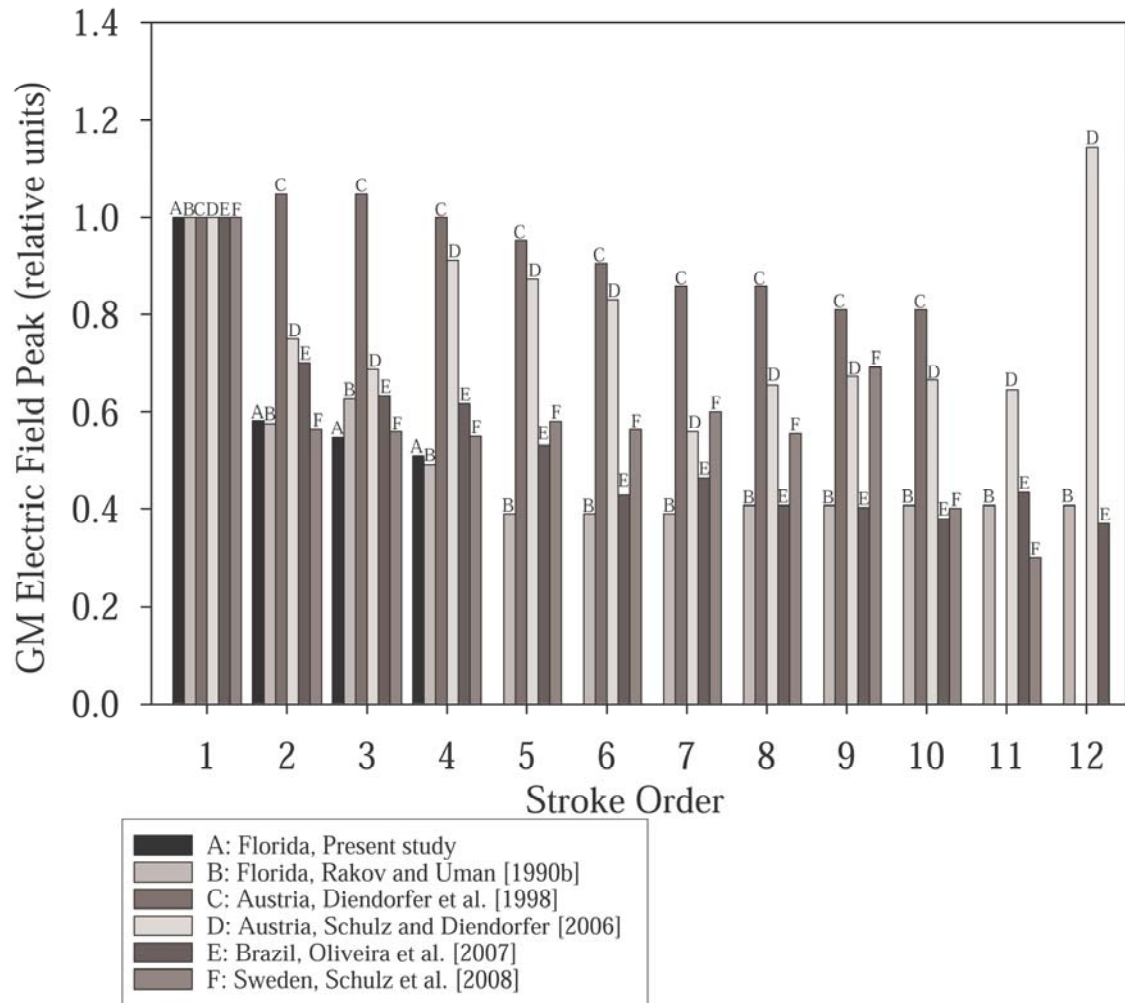


Figure 8-4. Geometric mean (GM) electric field peaks for strokes of different order estimated from different studies, labeled A, B, C, D, E, and F. For A, field peaks of subsequent strokes of different order are normalized to the electric field peak of the corresponding first return stroke and for B, C, D, E, and F the GM field peaks of subsequent strokes of different order are normalized to the GM field peak for first strokes (including those in single-stroke flashes for B and C). Sample size for strokes of order 12 in study D was as low as three (there were six in study E, and for study B the value is the average for 53 strokes of order 8 through 18).

electric field (or current peak) of the first return stroke is appreciably larger than that of the subsequent stroke. In contrast, *Diendorfer et al.* [1998], who examined return strokes recorded by the Austrian lightning locating system (ALDIS), found the values of the field peaks (and ALDIS-reported peak currents, assumed to be proportional to measured field peaks) of the first and subsequent strokes to be approximately equal (see columns labeled C in Figure 8-4). Further,

Rakov and Uman [2003, Ch. 17] noted that similar first and subsequent stroke intensities were reported by the U.S. National Lightning Detection Network (NLDN) prior to its 2002 upgrade [*Cummins et al.*, 2006]. Geometric mean values of the electric field peak for subsequent strokes of different order found from electric field measurements in Austria (see columns labeled D in Figure 8-4) are generally larger than the corresponding values in other studies, except for those based on ALDIS data, particularly for stroke order 12. However, the later value may be unreliable due to the small sample size (there were only 3 strokes of order 12 in study D).

We discuss next recent LLS studies conducted in conjunction with video observations. *Saba et al.* [2006a], using data from the Brazilian lightning locating system (BrasilDat), found the mean peak current of 55 first return strokes (28.3 kA) to be 2.1 times the mean peak current of 193 subsequent return strokes (13.5 kA). The corresponding ratio of geometric mean values is 1.7. Note that *Saba et al.*'s data are for strokes followed by continuing currents with durations ranging from 4 to 350 ms and are accompanied by high-speed (1000 frames per second) video records. The presence of continuing currents with durations down to a few milliseconds is unlikely to introduce any significant bias in LLS-inferred peak currents. Indeed, *Shindo and Uman* [1989] found that geometric mean electric field peak (normalized to 100 km) for return strokes followed by "questionable" continuing currents with durations ranging from 1 to 10 ms was equal to that for "regular" subsequent return strokes (not followed by any continuing current). *Biagi et al.* [2007] examined post-2002-upgrade NLDN data (for 2003 and 2004) that were confirmed by ordinary video camera records in Arizona, Texas, and Oklahoma and reported the ratio of GM first to GM subsequent current peaks to be 1.3 and 1.2 in Arizona and Texas-Oklahoma, respectively. From a similar study in the Great Plains of eastern Colorado,

western Kansas, and western Nebraska, the value of the ratio estimated from 2005 NLDN data is 1.3 [*Krider et al.*, 2007].

Table 8-1 summarizes the values of first to subsequent stroke electric field (or current) peak ratio estimated in different studies. The ratio varies from 1.0 to 2.5. The lowest value, 1.0, corresponds to the LLS study in Austria. The highest values, 2.3 to 2.5, correspond to direct current measurements on towers.

Assuming that the radiation field peak is roughly proportional to the product of the current and return-stroke speed, we infer that the smaller ratio for fields than for currents implies a lower average return-stroke speed for first strokes than for subsequent strokes. This is consistent with optical speed measurements [*Idone and Orville*, 1982], who reported mean speeds of 9.6×10^7 m/s and 1.2×10^8 m/s for 17 first and 46 subsequent strokes, respectively. The difference, though, is not very large.

Alternatively, the higher ratios for directly measured currents (relative to the ratios for fields) could be due to the lack of new channel terminations for currents, since subsequent strokes in newly-formed channels are on average larger than those in previously-formed ones [*Rakov et al.*, 1994]. However, the ratios do not change much if the strokes in the newly-formed channels are excluded (see Table 8-2): for Florida data of *Rakov and Uman* [1990a, b] the ratio of GM field peaks increases from 2.0 to 2.2 and for data of *Biagi et al.* [2007] and *Krider et al.* [2007] they remain unchanged at 1.3, 1.2 and 1.3 in Arizona, Texas-Oklahoma, and the Great Plains, respectively.

Note that, the ratios in Table 8-1 calculated from LLS studies (ALDIS, BrasilDat, and NLDN), are for both multiple- and single-stroke flashes combined. As noted in Section 2, this may result in some underestimation of the first-to-subsequent-stroke ratio, since strokes in

Table 8-1. Summary of first to subsequent stroke electric field or current peak ratios estimated from different studies.

Reference(s) and location	AM of first to subsequent stroke peak ratio	Ratio of AM first to AM subsequent stroke peak	GM of first to subsequent stroke peak ratio	Ratio of GM first to GM subsequent stroke peak	Ratio of median first to median subsequent stroke peak	Number of subsequent strokes	Number of first strokes	Number of single-stroke flashes	Stroke identification method
<i>Electric Field</i>									
<i>Rakov and Uman</i> [1990a, b], Florida	-	1.9	-	2.0 ^a	-	270	76	13	Electric field and TV records
<i>Diendorfer et al.</i> [1998], Austria	-	-	-	1.0	1.0	53443	43133	24120	LLS reports
<i>Schulz and Diendorfer</i> [2006], Austria	2.3	1.4	1.6	1.3	1.1	247	81	0	Electric field records
<i>Oliveira et al.</i> [2007], Brazil	2.4	1.7	1.9	1.7	1.8	909	259	0	
<i>Schulz et al.</i> [2008], Sweden	2.4	2.0	1.9	1.8	2.0	258	93	0	
Present study, Florida	2.1	-	1.7	-	1.7 ^b	239	176	0	
<i>Current</i>									
<i>Berger et al.</i> [1975], Switzerland	-	-	-	-	2.5	135	101	~50	Direct current measurements
<i>Anderson and Eriksson</i> [1980], Switzerland	-	-	-	2.3	2.3	114	75	-	
<i>Visacro et al.</i> [2004], Brazil	-	-	-	2.5	2.5	59	31	15	
<i>Saba et al.</i> [2006a], Brazil	-	2.1 ^c	-	1.7 ^c	1.6 ^c	193	55	16	LLS reports confirmed by video records
<i>Biagi et al.</i> [2007], Arizona	-	1.5	-	1.3	1.2	1602	953	388	
<i>Biagi et al.</i> [2007], Texas-Oklahoma	-	1.6	-	1.2	1.1	371	273	131	
<i>Krider et al.</i> [2007], Great Plains	-	1.3	-	1.3	1.2	150	90	40	

^a For all subsequent strokes combined. For subsequent strokes following a previously-formed channel, *Rakov et al.* [1994] reported the ratio to be 2.2.

^b The median of the ratio of first to corresponding subsequent stroke peak (in multiple stroke flashes), not the ratio of the medians of the first and subsequent stroke peaks, as for other studies in this column. ^c For strokes followed by continuing currents with durations ranging from 4 to 350 ms.

Table 8-2. Summary of first to subsequent stroke electric field or current peak ratios for subsequent strokes following a previously-formed channel.

Reference(s) and location	Ratio of GM first to GM subsequent stroke peak for all subsequent strokes combined ^a	Ratio of GM first to GM subsequent stroke peak for subsequent strokes following a previously-formed channel	Stroke identification method
<i>Rakov and Uman</i> [1990a, b], Florida	2.0	2.2	Electric field and TV records
<i>Biagi et al.</i> [2007], Arizona	1.3	1.3	LLS reports
<i>Biagi et al.</i> [2007], Texas-Oklahoma	1.2	1.2	confirmed by video
<i>Krider et al.</i> [2007], Great Plains	1.3	1.3	records

^a Taken from Table 8-1. Both subsequent strokes following a previously-formed channel and those creating new terminations on ground are included.

single-stroke flashes are on average smaller than first strokes in multiple-stroke flashes. The ratios of GM first to GM subsequent current peaks estimated from NLDN data in Texas-Oklahoma and the Great Plains are, respectively, 1.4 and 1.5, when only multiple-stroke flashes are considered (see Table 8-3), somewhat larger than 1.2 and 1.3, respectively, estimated for the case when both multiple- and single-stroke flashes were combined (see Table 8-1). On the other hand, when single-stroke flashes are excluded, the ratio of GMs for Arizona remains unchanged at 1.3. For the electric field measurements of *Rakov and Uman* [1990a, b] in Florida the ratio of GMs after excluding single-stroke flashes changed only slightly, from 2.0 to 2.1. Overall, the effect of excluding single-stroke flashes appears to be relatively small.

Table 8-4 summarizes the values of subsequent to first stroke electric field (or current) peak ratio estimated in different studies. All the geometric mean ratios and ratios of geometric means and medians are between 0.40 and 0.76, except for those based on LLS reports, which range from 0.60 to 0.93. The arithmetic mean ratios and ratios of arithmetic means in Table 8-4 range from 0.48 to 0.87.

Table 8-3. Summary of first to subsequent stroke electric field or current peak ratios for multiple-stroke flashes only.^a

Reference(s) and location	Ratio of AM first to subsequent stroke peak	Ratio of GM first to subsequent stroke peak	Ratio of median first to median subsequent stroke peak	Number of subsequent strokes	Number of first strokes	Stroke identification method
<i>Rakov and Uman</i> [1990a, b], Florida	2.0 (1.9)	2.1 (2.0)	-	270	63	Electric field and TV records
<i>Biagi et al.</i> [2007], Arizona	1.3 (1.5)	1.3 (1.3)	1.3 (1.2)	1602	565	
<i>Biagi et al.</i> [2007], Texas-Oklahoma	1.5 (1.6)	1.4 (1.2)	1.3 (1.1)	371	142	LLS reports confirmed by video records
<i>Krider et al.</i> [2007], Great Plains	1.5 (1.3)	1.5 (1.3)	1.5 (1.2)	150	50	

^aValues in the parentheses are taken from Table 8-1 and correspond to both multiple- and single-stroke flashes combined. It appears that the ratios are not much influenced by the exclusion of single-stroke flashes.

The question remains if the observed discrepancies are due to differences in lightning characteristics in different geographical locations or due to different instrumentation and methodologies involved. We will discuss each of these two possibilities below.

From the methodology point of view, the NLDN (prior to the 2002 upgrade) and ALDIS results could be due to poor detection of relatively small subsequent strokes, rejection of the first stroke by the waveform discrimination algorithm and acceptance of the second stroke as the first stroke, and misclassification of a preliminary-breakdown pulse (associated with an in-cloud process; see Chapter 5) as the first return stroke. More research is needed to quantify these effects. Also, the accuracy of first stroke peak current estimates derived from LLS data has not yet been confirmed by independent measurements [e.g., *Krider et al.*, 2007]. Additionally, time resolution of video records (17 ms in *Biagi et al.* [2007] versus 1 ms in *Saba et al.* [2006a]) can play a role in detecting smaller subsequent strokes. *Saba et al.* [2006b] estimated that 19% of the

total number of strokes in their study would be missed if an ordinary video camera with 17 ms time resolution (inter-field interval) were used.

On the other hand, the occurrence of larger than first subsequent strokes can vary for different types of storms or for different locations. Table 8-5 presents a summary of percentages of multiple-stroke flashes with at least one subsequent stroke field peak greater than the first and percentages of subsequent strokes with field peaks greater than the first estimated in different studies. In Florida, Austria, Brazil, and Sweden, respectively, 21, 32, 20, and 18 % of the subsequent strokes were found to have field peaks greater than that of the first stroke. Percentages of flashes containing at least one subsequent stroke with field peak greater than that of the first stroke in these studies were 24, 49, 38, and 32%, respectively. Also given in Table 8-5 are the percentages estimated from earlier electric field measurements in Sri Lanka and Sweden and from LLS reports in Austria. The highest percentages of flashes with at least one subsequent stroke field peak greater than the first were reported in Austria (49% for Schulz and *Diendorfer* [2006] and 51% for *Diendorfer et al.* [1998]). This possibly explains (at least in part) the smaller first-to-subsequent-stroke field peak ratio estimated from the Austrian studies compared to those for other regions in the world. It is presently not known if the larger subsequent strokes in Austria are associated with new channel terminations on ground or not.

8.5 Summary

Relative magnitudes of electric field peaks of first and subsequent return strokes in negative cloud-to-ground lightning flashes recorded in Florida, Austria, Brazil, and Sweden are analyzed in this study. On average, the electric field peak of the first stroke is appreciably, 1.7 to 2.4 times, larger than the field peak of the subsequent stroke (except for studies in Austria where the ratio varies from 1.0 to 2.3, depending on methodology and instrumentation). Similar results were previously reported from electric field studies in Florida, Sweden, and Sri Lanka by *Rakov*

Table 8-4. Summary of subsequent to first stroke electric field or current peak ratio estimated from different studies.

Reference(s) and location	AM of subsequent to first stroke peak ratio	Ratio of AM subsequent to AM first stroke peak	GM of subsequent to first stroke peak ratio	Ratio of GM subsequent to GM first stroke peak	Ratio of median subsequent to median first stroke peak	Number of subsequent strokes	Number of first strokes	Number of single-stroke flashes	Stroke identification method
<i>Electric Field</i>									
<i>Rakov and Uman</i> [1990a, b], Florida	-	0.52 0.49	-	0.49 ^a 0.47	-	270 270	76 63	13 0	Electric field and TV records
<i>Thottappillil et al.</i> [1992], Florida	-	-	0.42 ^b	-	-	199	46	0	
<i>Cooray and Perez</i> [1994], Sweden	0.63	-	0.51	-	-	314	-	0	Electric field records
<i>Cooray and Jayaratne</i> [1994], Sri Lanka	0.55	-	0.43	-	-	284	81	0	
<i>Diendorfer et al.</i> [1998], Austria	-	-	-	1.0	1.0	53443	43133	24120	LLS reports
<i>Schulz and Diendorfer</i> [2006], Austria	0.87	0.71	0.64	0.76	0.90	247	81	0	Electric field records
<i>Oliveira et al.</i> [2007], Brazil	0.69	0.59	0.53	0.58	0.55	909	259	0	
<i>Schulz et al.</i> [2008], Sweden	0.64	0.51	0.52	0.56	0.50	258	93	0	
Present study, Florida	0.75	-	0.58	-	0.57 ^c	239	176	0	
<i>Current</i>									
<i>Berger et al.</i> [1975], Switzerland	-	-	-	-	0.40	135	101	~50	Direct current measurements
<i>Anderson and Eriksson</i> [1980], Switzerland	-	-	-	0.43	0.43	114	75	-	
<i>Visacro et al.</i> [2004], Brazil	-	-	-	0.40	0.40	59	31	15	
<i>Saba et al.</i> [2006a], Brazil	-	0.48 ^d	-	0.60 ^d	0.64 ^d	193	55	16	LLS reports confirmed by video records
<i>Biagi et al.</i> [2007], Arizona	-	0.65 ^e	-	0.78	0.81	1602	953	388	
<i>Biagi et al.</i> [2007], Texas-Oklahoma	-	0.63 ^e	-	0.83	0.93	371	273	131	
<i>Krider et al.</i> [2007], Great Plains	-	0.78 ^f	-	0.78	0.81 ^f	150	90	40	

^a For all subsequent strokes combined. For subsequent strokes following a previously-formed channel, *Rakov et al.* [1994] reported the ratio to be 0.46. ^b For all subsequent strokes combined. For subsequent strokes following a previously-formed channel, *Thottappillil et al.* [1992] reported the GM ratio to be 0.39 (176 events). ^c The median of the ratio of subsequent to corresponding first stroke peaks (in multiple-stroke flashes), not the ratio of the medians of subsequent and first stroke peaks, as for other studies in this column. ^d For strokes followed by continuing currents with durations ranging from 4 to 350 ms. ^e For all subsequent strokes combined. For subsequent strokes following a previously-formed channel, *Biagi et al.* [2007] reported the ratio to be 0.61 and 0.59 for Arizona and Texas-Oklahoma, respectively. ^f For all subsequent strokes combined. For subsequent strokes following a previously-formed channel, *Krider et al.* [2007] reported the ratio of arithmetic means to be 0.75 and the ratio of medians to be 0.70.

Table 8-5. Summary of multiple-stroke flash characteristics reported in different studies.

Reference(s) and location	Total number of flashes	Percentage of flashes with at least one subsequent stroke field peak greater than the first	Percentage of subsequent strokes with field peaks greater than the first	Stroke identification method
<i>Thottappillil et al.</i> [1992], Florida	46	33	13	Electric field and TV records
<i>Cooray and Perez</i> [1994], Sweden	276	24	15	Electric field records
<i>Cooray and Jayaratne</i> [1994], Sri Lanka	81	35	12	
<i>Diendorfer et al.</i> [1998], Austria	15905	51	-	LLS reports
<i>Schulz and Diendorfer</i> [2006], Austria	81	49	32	Electric field records
<i>Oliveira et al.</i> [2007], Brazil	259	38	20	
<i>Schulz et al.</i> [2008], Sweden	93	32	18	
Present study, Florida	176	24	21	

et al. [1994], *Cooray and Perez* [1994], and *Cooray and Jayaratne* [1994], respectively. For comparison, directly measured peak currents for first strokes are, on average, a factor of 2.3 to 2.5 larger than those for subsequent strokes. [*Berger et al.*, 1975; *Anderson and Eriksson*, 1980; *Visacro et al.*, 2004]. The generally larger ratio for currents than for fields possibly implies a lower average return-stroke speed for first strokes than for subsequent strokes. There appear to be some differences between first versus subsequent stroke intensities reported from different studies based on data reported by lightning locating systems (LLSs). The ratio of LLS-reported peak currents for first and subsequent strokes confirmed by video records is 1.7 to 2.1 in Brazil (for strokes followed by continuing currents with durations ranging from 4 to 350 ms), while in the U.S. (Arizona, Texas, Oklahoma, and the Great Plains) it varies from 1.1 to 1.6, depending

on methodology used. Ratios involving arithmetic means are generally larger than those involving geometric means. The smaller ratios derived from the LLS studies are likely to be due to poor detection of relatively small subsequent strokes. The smaller values in Austria are possibly related (at least in part) to the higher percentage (about 50% versus 24 to 38% in other studies) of flashes with at least one subsequent stroke greater than the first. The effects on the ratio of excluding single-stroke flashes or subsequent strokes in newly-formed channels appear to be relatively small. Additional data are needed to further clarify the issue of relative intensity of first and subsequent strokes in different geographical locations, as well as possible instrumental and methodological biases involved.

CHAPTER 9
SUMMARY OF RESULTS AND RECOMMENDATIONS FOR FUTURE RESEARCH

9.1 Summary of Results

Measurements of electromagnetic signals from lightning discharges performed at the Lightning Observatory in Gainesville (LOG), on the University of Florida campus, in 2006, 2007, and 2008 are presented. In 2008, the experimental setup included wideband electric field, electric field derivative (dE/dt), magnetic field derivative (dB/dt), and narrowband very high frequency (VHF) measurements and was operated in either single-station or two-station mode. The single-station experiment was designed to obtain correlated wideband electric field, electric field derivative, magnetic field derivative, and narrowband VHF signatures of cloud and natural ground lightning discharges. The emphasis was on compact intracloud discharges, preliminary breakdown pulse trains, and positive cloud-to-ground lightning. The two-station experiment was designed to measure far field waveforms (primarily radiation) at the Gainesville station due to natural and rocket-triggered lightning at Camp Blanding, Florida, in conjunction with near field measurements there. The Gainesville and Camp Blanding measuring stations are 45 km apart. The data acquired were used to improve our understanding of the various lightning processes, infer parameters of these processes, and develop models that can be used to describe and predict their salient properties. The primary results presented in this dissertation are briefly summarized below.

9.1.1 Compact Intracloud Discharges

Compact Intracloud Discharges (CIDs) are cloud lightning discharges that produce single bipolar electric field pulses (so-called Narrow Bipolar Pulses or NBPs) having typical full widths of 10 to 30 μ s and intense HF-VHF radiation bursts (much more intense than those from any other cloud-to-ground or “normal” cloud discharge process). We examined wideband electric

fields, electric and magnetic field derivatives, and narrowband VHF (36 MHz) radiation bursts produced by 157 CIDs. The majority (about 72%) of CIDs appeared to occur in isolation from any other lightning process, while about 24% were found to occur prior to, during, or following CG or “normal” IC lightning. About 18% were associated with cloud flashes and 6% with ground ones. In three cases two CIDs occurred within 43, 66, and 181 ms of each other (the first documented "multiple" CIDs), with a total of 4% of CIDs occurring in pairs. For 48 CIDs, the geometric means of source height and electric field peak normalized to 100 km and zero elevation angle were estimated to be 16 km and 20 V/m, respectively. The geometric means of total pulse duration, width of initial half-cycle, and ratio of initial electric field peak to opposite polarity overshoot were 23 μ s, 5.6 μ s, and 5.7, respectively.

Based on the experimental evidence of multiple reflections and modeling, we infer that the CID is essentially a bouncing-wave phenomenon. Some tens of reflections may occur at both radiating-channel ends. It is possible that the bouncing waves serve to maintain channel conductivity. Only higher-order reflections (in the later portion of the waveform) are detectable (if at all) in either electric field or dE/dt waveforms, while the undetectable lower-order reflections do influence the magnitude of the primary signature. In about 85% dE/dt signatures no reflections were observed. Reflections at channel extremities may result in corona-like electrical breakdown there, which is likely to produce intense bursts of HF-VHF radiation and increase "noisiness" of dE/dt signatures, which are characteristic features of CIDs.

We modeled the CID as a wave traveling on an elevated vertical transmission line. In order to account for multiple reflections that take place at the channel ends we specified two equivalent current sources, connected at the bottom and at the top of the channel. By comparing electric fields predicted by this bouncing-wave model with measurements we estimated that effective

current reflection coefficients at channel ends should be in the range of 0 to -0.5, that the wave propagation speed ranges from 0.3 to 3×10^8 m/s, and channel length is less than 1000 m. The lower bound on CID channel length appears to be about 100 m. Influence of current risetime on field waveforms was also examined, and it was found to be typically in the range from about 2 to 8.5 μ s.

The current distribution along the CID channel is often not much different from uniform, as expected for a Hertzian (electrically short) dipole, because of relatively short channel length, relatively long current waveform, and relatively high propagation speed. We estimated electrical parameters of 48 located CIDs using their measured electric fields and vertical Hertzian dipole approximation. This approximation is consistent with the bouncing-wave CID model for a reasonably large subset of allowed combinations of propagation speed and channel length. For nine events, we estimated channel lengths from observed reflection signatures in measured dE/dt waveforms and assumed propagation speeds of 2×10^8 m/s and 3×10^8 m/s, which cover the entire range of allowed values. For $v = 2.5 \times 10^8$ m/s (average value), the channel lengths for these nine events ranged from 108 to 142 m. For the remaining 39 events, there were no reflection signatures observed, and Δh was assumed to be 350 m, for which the Hertzian dipole approximation is valid for speeds in the range of 2 to 3×10^8 m/s. For all 48 events, GM values of peak current, zero-to-peak current risetime, 10-to-90% current risetime, and charge transfer for the first 5 μ s are 74 kA, 5 μ s, 2.5 μ s, and 164 mC, respectively. The geometric mean peak radiated power, and energy radiated for the first 5 μ s are 29 GW and 31 kJ, respectively. Overall, the estimated CID current waveform parameters are comparable to their counterparts for first strokes in cloud-to-ground lightning, while their peak radiated electromagnetic power appears to

be considerably higher. Total energy dissipated by CIDs does not appear to be higher than that dissipated by first strokes in CG flashes or by regular IC flashes.

9.1.2 Preliminary Breakdown in Cloud-to-Ground Flashes and in Attempted Leaders

Lightning events exhibiting pulse trains that are characteristic of preliminary breakdown in negative cloud-to-ground discharges, but are not followed by return stroke waveforms, are assumed to be manifestations of attempted cloud-to-ground leaders. Preliminary breakdown (PB) pulse trains in 12 negative cloud-to-ground discharges and in 33 attempted leaders were examined. Both “classical” (having durations of tens of microseconds) and “narrow” (having durations of a few microseconds) pulses were found in both types of pulse trains. However, submicrosecond-scale pulses were only observed in preliminary breakdown pulse trains of ground discharges. In fact, for cloud-to-ground discharges, a significant fraction (22%) of examined pulses had total durations less than 1 μ s. The majority of pulses in PB pulse trains are typically small in both amplitude and duration. The largest pulses in the train can exceed in magnitude the following first return-stroke pulse. About 19% of the 59 preliminary breakdown pulse trains were found to contain pulses whose peaks were greater than those of the corresponding first return strokes [*Nag and Rakov, 2009*]. Pulses with larger durations ($>4 \mu$ s) tend to occur earlier in the train.

The PB pulse train appears to be generated when a negatively-charged channel extends downward from the main negative charge region and encounters an appreciable lower positive charge region (LPCR). When the LPCR is small no PB pulse train may be produced. In this view, the fact that in some negative CG flashes no PB pulse train is detectable could be due to insignificant LPCR. It was found that at higher latitudes a larger percentage of CG discharges exhibit detectable PB pulse trains than at lower latitudes. This implies that a significant LPCR is present in thunderclouds more often at higher latitudes than at relatively low latitudes. While the

LPCR may serve to enhance the electric field at the bottom of the negative charge region and thereby facilitate the launching of a negatively-charged leader toward ground, presence of excessive LPCR may prevent the occurrence of negative CG flashes by “blocking” the progression of descending negative leader from reaching ground. Four conceptual lightning scenarios are inferred that may arise depending upon the magnitude of the LPCR.

9.1.3 First Return Strokes in Negative Cloud-to-Ground Lightning

Simultaneous measurements at Camp Blanding and in Gainesville were used to compare slow fronts in near and far electric field waveforms. A total of four first strokes in natural lightning were examined. For three of them the slow-front duration was similar at both stations, while for one first stroke a pronounced slow front was not observed. The amplitude of the slow front relative to the peak was found to be similar in close and distant waveforms for two out of three first return strokes having a pronounced slow front.

The one-wave, two-wave, and three-wave transmission line models were used to compute close and distant return stroke electric fields. For all three models, the computed electric field waveforms do not exhibit distinct slow fronts, if there is no similar feature in the causative current. For an incident current wave containing a pronounced slow front, the duration of the slow front in model-predicted electric fields and its magnitude relative to peak are approximately the same at near and far distances. The slow front at far distances (100 km) is primarily due to the radiation field component, with the contributions due to electrostatic and induction components being negligible. At near distances (500 m), the slow front is composed of more or less equal (or comparable) contributions from all three components of electric field. It appears that a slow front in return stroke current is responsible for a slow front in return stroke electric field. The mechanism of formation of slow front in the current is probably related to the break-

through phase of the attachment process by which the extending plasma channels of the upward and downward leaders make contact.

9.1.4 Positive Cloud-to-Ground Lightning

Experimental data on 52 positive and 2 bipolar lightning flashes acquired in Gainesville, Florida, in 2007-2008 are presented. Various features of positive discharge, including multiplicity, parameters of return stroke electric field waveforms, inferred currents, charge transferred by return stroke, leader stepping, and preliminary breakdown pulse trains were examined. There were a total of 63 return-strokes in 52 positive flashes with an average multiplicity of 1.2. Out of the 52 positive cloud-to-ground flashes, 42 (81%) were single-stroke, 9 (17%) two-stroke, and 1 (2.0%) three-stroke flashes. 89% of the positive return strokes were correctly identified by the NLDN.

The GM electric field peak and electric field derivative peak, both normalized to 100 km, for 48 positive return strokes occurring at distances ranging from 7.8 to 157 km were 18.1 V/m and 9.02 V/m/ μ s, respectively. The GM zero-to-peak risetime and 10-90% risetime for positive return strokes were 6.92 μ s and 3.40 μ s, respectively. The GM slow front duration, slow front amplitude relative to peak, and fast-transition 10-90% risetime were 4.95 μ s, 36.7%, and 1.02 μ s, respectively. The duration of the slow front for positive return strokes in Florida was found to be, on average, longer than that for negative first return strokes in Florida reported by *Weidman and Krider* [1978] and *Master et al.* [1984]. The AM zero-crossing time for positive return strokes was 53.6 μ s and the opposite polarity overshoot was, on average, 15.6% of the peak. These values are similar to those, 49.5 μ s and 18.5%, reported by *Pavlick et al.* [2002] for negative return strokes in Florida.

The median charge transfer within 0.5 ms, 1 ms, and 1.5 ms for 19 positive return strokes were estimated to be 6.98 C, 12.2 C, and 13.2 C, respectively.

Out of 63 positive return strokes (52 first strokes, 10 second strokes, and 1 third stroke), 14 (27%) first strokes and 1 third stroke were preceded by pronounced step-like pulses. The AM interval between pulse peaks was found to be 20 μ s.

Only 5 (10%) out of 52 positive cloud-to-ground discharges had detectable preliminary breakdown pulse trains. The mean total pulse duration of individual pulses in the trains was 22 μ s with mean interpulse interval of 155 μ s. In contrast with negative discharges, the initial polarity of preliminary breakdown pulses in positive discharges can be either the same as or opposite to that of the following return-stroke pulse. Out of the 5 preliminary breakdown pulse trains in the dataset presented here, pulses in four trains had the same initial polarity as that of the following return-stroke pulse, while pulses in one train had opposite polarity.

Two bipolar lightning discharges, which sequentially lowered positive and negative charge to ground are examined. One of them was composed of three negative strokes followed by a positive stroke and then by a negative one. The other bipolar flash was composed of three strokes, the first and the third being negative and the second being positive. For this flash, both the first and third strokes occurred at a distance of 46 km from the field measuring station (semi-major axis length of NLDN 50% location error ellipse being 400 m for both strokes) and NLDN-reported peak currents were 52 kA and 25 kA, respectively. The NLDN reported the third (positive) stroke as an intracloud discharge at a distance of 39 km (semi-major axis length of 1.2 km). It appears that the second (positive) stroke formed a channel to ground different from that of the first and third (negative) strokes.

9.1.5 Ratio of First versus Subsequent Return Stroke Intensities in Negative Cloud-to-Ground Discharges

In collaboration with ALDIS (Austria), INPE (Brazil), and Uppsala University (Sweden), relative magnitudes of electric field peaks of first and subsequent return strokes in negative

cloud-to-ground lightning flashes recorded in Florida, Austria, Brazil, and Sweden were analyzed. On average, the electric field peak of the first stroke is appreciably, 1.7 to 2.4 times, larger than the field peak of the subsequent stroke (except for studies in Austria where the ratio varies from 1.0 to 2.3, depending on methodology and instrumentation). Similar results were previously reported from electric field studies in Florida, Sweden, and Sri Lanka by *Rakov et al.* [1994], *Cooray and Perez* [1994], and *Cooray and Jayaratne* [1994], respectively. For comparison, directly measured peak currents for first strokes are, on average, a factor of 2.3 to 2.5 larger than those for subsequent strokes. [*Berger et al.*, 1975; *Anderson and Eriksson*, 1980; *Visacro et al.*, 2004]. The generally larger ratio for currents than for fields possibly implies a lower average return-stroke speed for first strokes than for subsequent strokes.

9.2 Recommendations for Future Research

Various types of lightning discharges have been characterized and modeled in this dissertation using data primarily obtained at the Lightning Observatory in Gainesville (LOG). A few modifications and upgrades to the measuring station can be undertaken to further expand the scope of the experiments. Also, some of the models presented here can be improved. It is the author's opinion that the following topics all warrant additional investigation, and a detailed study of each could yield important insights into the lightning discharge process.

- High-speed video records: Optical records obtained using a high speed (≥ 1000 frames per second) video camera will help identify channels to ground in both negative and positive cloud-to-ground lightning both of which were examined in this study. Optical images of positive (and bipolar) lightning channels are very rare. Further, high-speed video records can help one gain further insight into the attachment process in cloud-to-ground lightning.
- Multiple-station measurement of CIDs: Simultaneous measurement of CID wideband electric fields at multiple stations can be used to determine source locations using the time of arrival technique. Further, simultaneous close and distant field measurements of CIDs [e.g., *Eack*, 2004] are very rare, and can be used to test theoretical models of this type of lightning discharge and gain further insight into its mechanism and parameters.

- Improvement of the bouncing-wave CID model: The bouncing-wave model presented in Chapter 4 considers both attenuation along the CID channel and absorption at the channel ends as lumped at the channel ends. In order to make the model more realistic, attenuation of the current wave along the channel should be separated from absorption at channel ends. In other words, the current attenuation and reflection coefficients should be considered as separate model parameters. Additionally, the CID incident current can be represented by functions other than the Gaussian function used in Chapter 4 (e.g., Heidler function [Heidler, 1985]).
- Examination of two-station data for rocket-triggered lightning acquired in 2008 and 2009: Only natural lightning flashes simultaneously recorded at Camp Blanding and in Gainesville are considered in this dissertation. Twelve rocket triggered lightning flashes acquired simultaneously at the two stations in 2008 and 2009 are to be examined.
- Introduction of reflections from upward-moving front in the return-stroke model: In Chapter 6, a three-wave model for return strokes, which considers two current waves moving in opposite directions (up and down) from an attachment point some tens of meters above ground and the reflection of the downward moving wave from ground, has been introduced. The speeds of all the three waves have been assumed to be equal. If the speed of the upward moving ground-reflected current wave is assumed to be higher than that at which the current front moves upward from the attachment point, the reflected wave will "catch up" with the original upward-moving current front and get reflected off the impedance discontinuity at the front, with the reflection moving downward. This scenario which is probably more realistic, is not considered in Chapter 6. Multiple reflections of the current wave in the return stroke channel along with current attenuation along the channel (such as that in the MTLL model) needs to be incorporated in the model.
- Evaluation of NLDN performance characteristics using 2008 and 2009 rocket-triggered lightning data: *Jerauld et al.* [2005] examined the performance characteristics of the NLDN for the 2001-2003 period using rocket triggered lightning data acquired at Camp Blanding, Florida. *Nag et al.* [2008] extended their study using Camp Blanding data from 2004, 2005, and 2007 (there was no lightning triggering in 2006). Twelve flashes containing a total of 28 leader/return stroke sequences were used for this purpose (see Appendix C). Rocket-triggered lightning data acquired at the ICLRT in 2008 and 2009 (98 strokes in 24 flashes) can be used for additional evaluation of the NLDN performance characteristics in Florida. Besides return strokes, NLDN detection efficiency, location accuracy, and current estimation errors should be evaluated for pulses occurring during the initial stage of rocket-triggered lightning.

APPENDIX A

INVENTORY TABLE AND CATALOG OF 48 COMPACT INTRACLOUD DISCHARGE WAVEFORMS

Table A-1. Summary of horizontal distance (r), measured electric (E_p) and magnetic (B_p) field peaks, height (h), elevation angle (α), inclined distance (R), and normalized electric field ($E_N = E(\frac{R}{100})\frac{\cos 0^\circ}{\cos \alpha}$) for 48 CIDs recorded at the LOG in 2008. Also given are the semi major axis (SMA) length of the NLDN 50% error ellipse, distance error ($r_E = \frac{SMA}{r}100\%$), electric field peak measurement error (M_E), and the total root mean square error ($RMS_E = \sqrt{r_E^2 + M_E^2}$).

Flash ID	r , km	SMA, km	E_p , V/m	B_p , μT	E_p/B_p , m/s	h , km	α , degrees	R , km	E_N , V/m	r_E , %	M_E , %	RMS_E , %
082308_163	68	0.7	35.99	0.1248	2.89E+08	19	15.9	71	27	1.0	19	19
082308_164	64	2.3	64.08	0.2202	2.91E+08	16	14.1	66	44	3.6	10	11
082308_165	63	0.4	37.87	0.1347	2.81E+08	24	20.4	67	27	0.6	14	14
082308_174	62	0.6	53.02	0.1950	2.72E+08	29	25.0	69	40	1.0	13	13
082308_180	24	0.4	35.24	0.1483	2.38E+08	18	37.6	30	13	1.7	19	19
082308_207	12	0.4	42.89	0.2700	1.59E+08	19	58.0	22	18	3.4	16	16
082308_326	40	0.4	88.32	0.3057	2.89E+08	11	15.6	42	38	1.0	5	5
082408_364	38	0.6	48.83	0.1869	2.61E+08	21	29.4	44	24	1.6	14	14
082408_368	24	4.9	38.36	0.1505	2.55E+08	15	31.8	28	13	21	10	23
082408_370	38	0.5	40.93	0.1531	2.67E+08	19	27.0	43	20	1.3	17	17
082408_374	27	0.4	35.78	0.1499	2.39E+08	20	37.3	33	15	1.5	19	19
082408_378	37	0.4	54.00	0.2174	2.48E+08	25	34.1	44	29	1.1	13	13
082408_382	27	0.4	41.42	0.1496	2.77E+08	11	22.6	29	13	1.5	14	14
082408_386	32	0.4	55.76	0.2242	2.49E+08	22	34.0	39	26	1.2	10	10
082408_387	34	0.4	36.74	0.1623	2.26E+08	29	41.0	45	22	1.2	15	15
082408_394	35	0.6	66.08	0.2473	2.67E+08	18	27.0	39	29	1.7	8	9
082408_422_1	32	0.4	34.97	0.1339	2.61E+08	18	29.4	37	15	1.3	19	19
082408_422_2	17	0.4	40.61	0.1804	2.25E+08	15	41.4	23	13	2.3	16	16

Table A-1. Continued

Flash ID	r, km	SMA, km	E_p , V/m	B_p , μ T	E_p/B_p , m/s	h, km	α , degrees	R, km	E_N , V/m	r_E , %	M_E , %	RMS_{E_s} , %
082408_427	19	0.4	45.45	0.1909	2.38E+08	15	37.5	24	14	2.1	15	15
082408_428	14	0.4	50.38	0.2363	2.13E+08	14	44.7	19	14	2.9	15	15
082408_429	13	0.4	45.73	0.2484	1.84E+08	17	52.2	21	16	3.1	12	12
082408_669	17	0.4	62.78	0.2502	2.51E+08	11	33.2	20	15	2.4	9	9
083008_09	89	0.6	38.11	0.1300	2.93E+08	19	12.2	91	35	0.7	18	18
083008_12	63	0.4	34.78	0.1248	2.79E+08	25	21.8	68	26	0.6	20	20
083008_16	49	0.6	41.42	0.1592	2.60E+08	28	29.9	57	27	1.2	17	17
083008_24	57	0.4	35.46	0.1201	2.95E+08	10	10.2	58	21	0.7	17	17
083008_31	52	0.6	49.96	0.1737	2.88E+08	16	16.5	55	28	1.1	13	13
083008_33	61	0.5	68.01	0.2324	2.93E+08	14	12.7	63	44	0.8	5	6
083008_45	50	0.4	54.15	0.1897	2.86E+08	16	17.9	53	30	0.8	10	10
083008_52	50	0.4	54.78	0.1926	2.84E+08	17	18.5	52	30	0.8	13	13
083008_61	12	0.4	54.47	0.2524	2.16E+08	11	44.0	16	12	3.4	13	13
083008_67	41	0.4	33.33	0.1157	2.88E+08	12	16.2	43	15	1.0	18	18
091008_120	21	0.4	71.31	0.2843	2.51E+08	13	33.3	25	21	2.0	9	9
091008_121	20	0.4	37.07	0.1525	2.43E+08	14	35.9	24	11	2.1	19	19
091008_123	19	0.4	73.64	0.3009	2.45E+08	13	35.4	23	21	2.1	11	11
091008_127	21	0.4	54.00	0.2139	2.52E+08	13	32.7	24	16	1.9	13	13
091008_128	17	0.5	45.99	0.2055	2.24E+08	15	41.8	23	14	2.9	12	12
091008_129	19	0.4	61.75	0.2385	2.59E+08	11	30.4	22	16	2.1	9	9
091008_132	19	0.4	50.90	0.1964	2.59E+08	11	30.3	22	13	2.1	14	14
091008_133	20	0.4	64.08	0.2391	2.68E+08	10	26.7	22	16	2.0	11	11
091008_135	18	0.4	34.27	0.1496	2.29E+08	15	40.2	24	11	2.2	20	20
091008_138	33	0.4	35.03	0.1293	2.71E+08	16	25.4	36	14	1.2	16	16
091008_140	36	0.4	53.99	0.1920	2.81E+08	13	20.4	38	22	1.1	13	13
091108_152	21	0.4	38.68	0.1512	2.56E+08	13	31.5	25	11	1.9	18	18
091108_161	30	0.4	70.79	0.2502	2.83E+08	10	19.4	31	24	1.3	8	8
091108_165	46	2.2	51.42	0.1911	2.69E+08	22	26.3	51	29	4.8	13	14

Table A-1. Continued

Flash ID	r, km	SMA, km	E_p , V/m	B_p , μ T	E_p/B_p , m/s	h, km	α , degrees	R, km	E_N , V/m	r_E , %	M_E , %	RMS_{E_s} , %
091108_175	37	0.4	67.37	0.2310	2.92E+08	8.9	13.6	38	26	1.1	10	10
091108_176	43	0.4	35.58	0.1211	2.94E+08	8.8	11.7	44	16	0.9	16	16

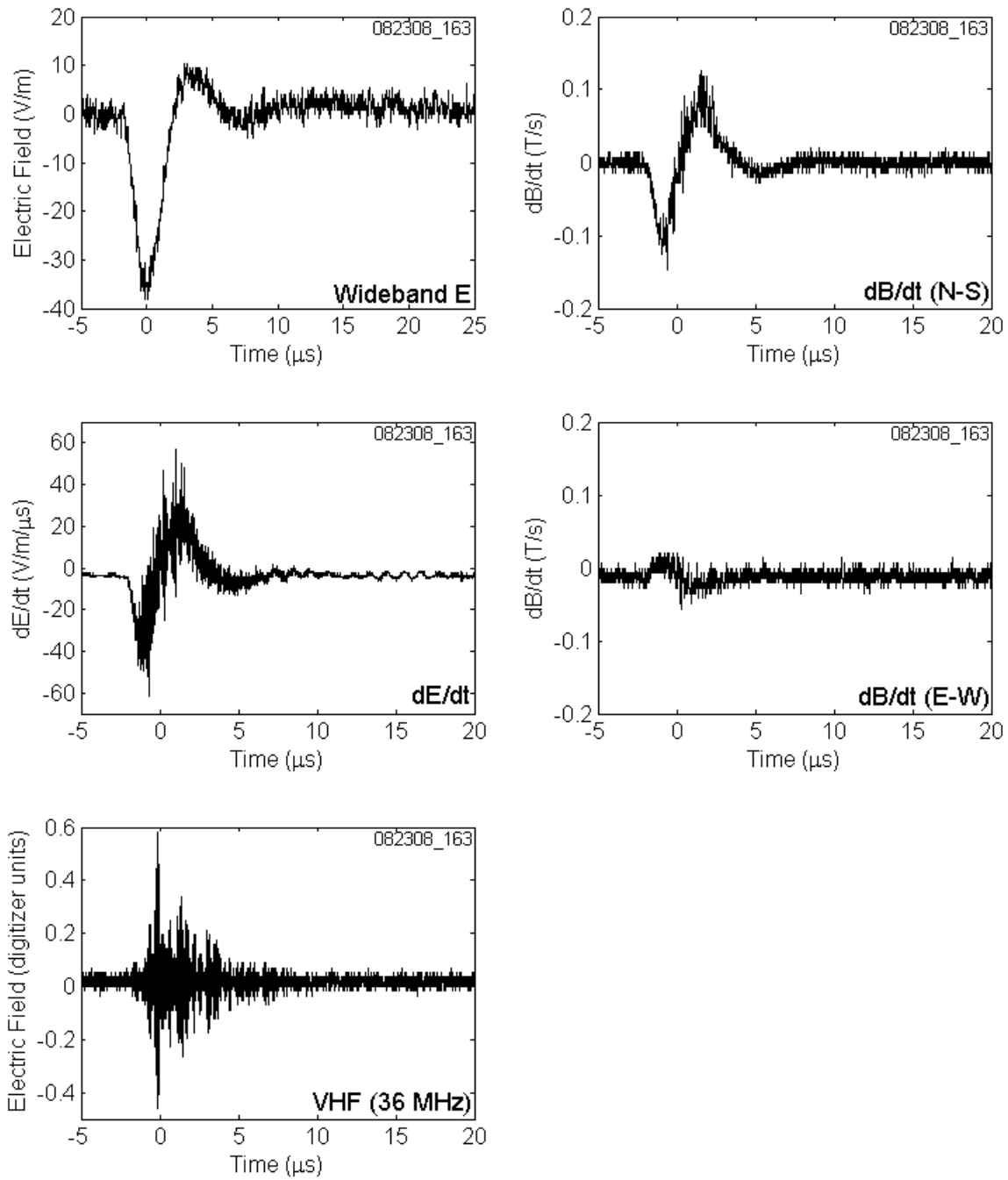


Figure A-1. CID 082308_163 shown on a 25 μs time scale.

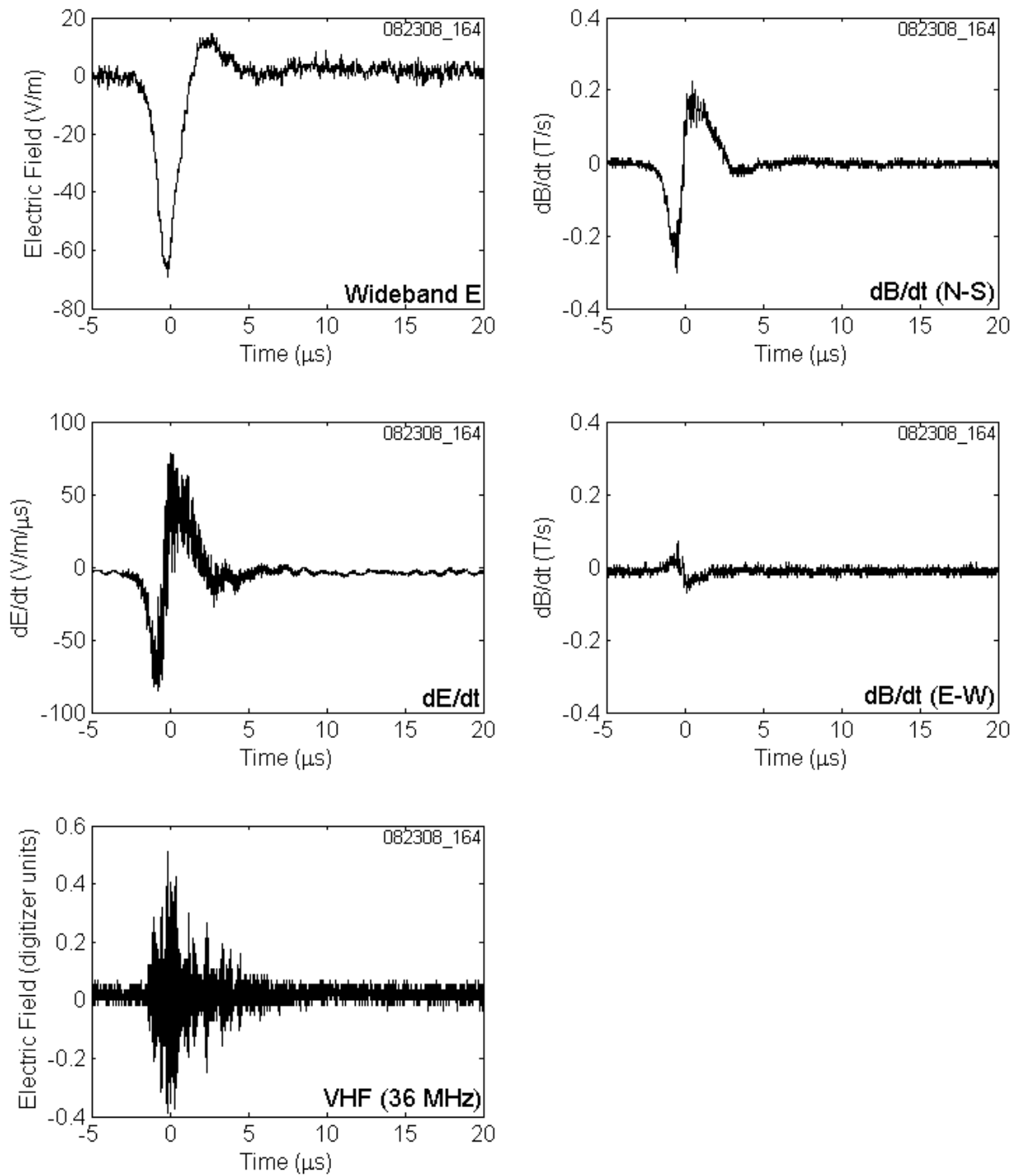


Figure A-2. CID 082308_164 shown on a 25 μs time scale.

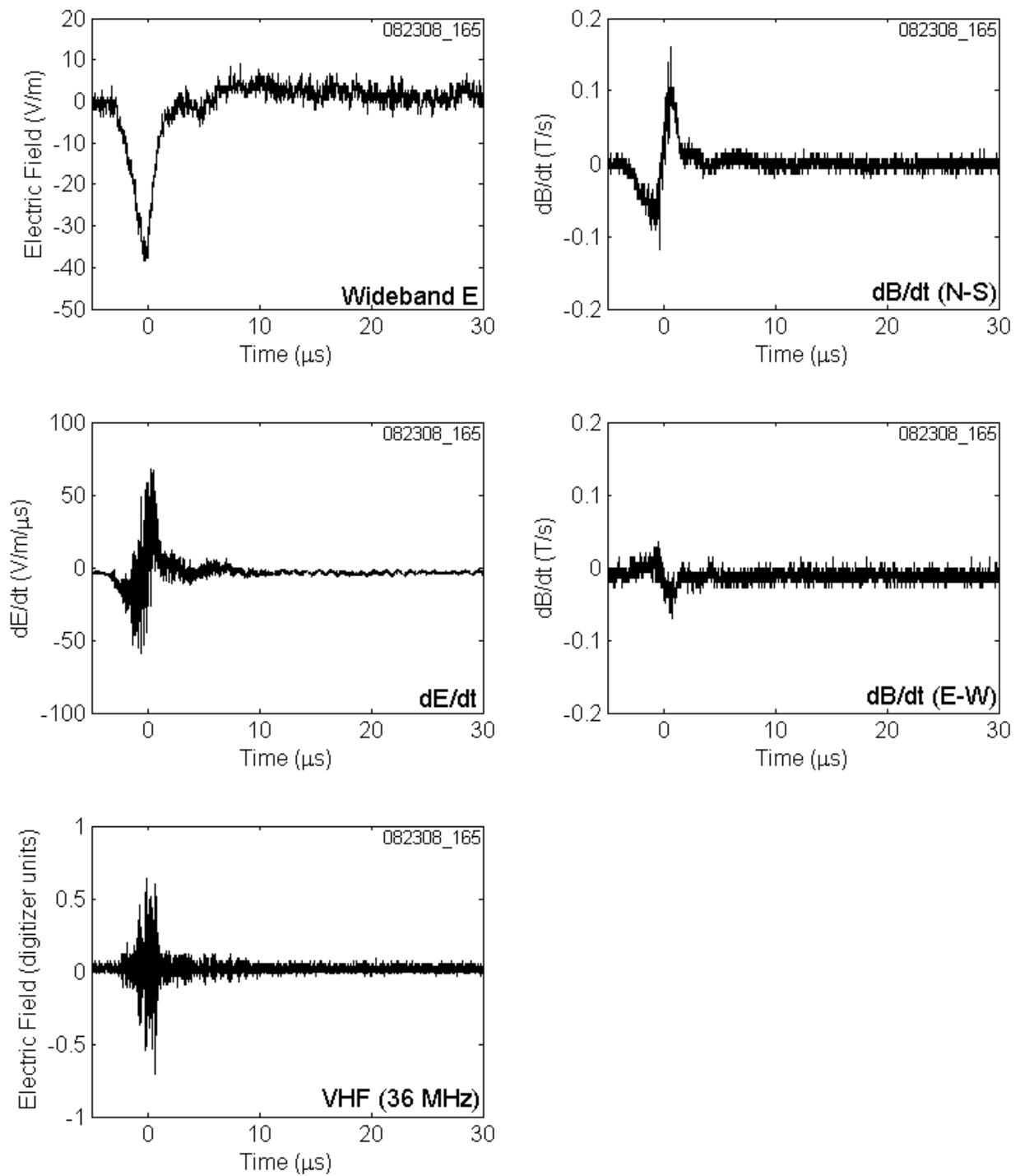


Figure A-3. CID 082308_165 shown on a 35 μs time scale.

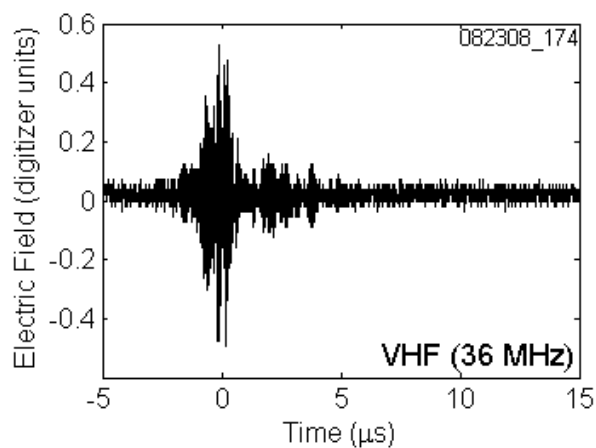
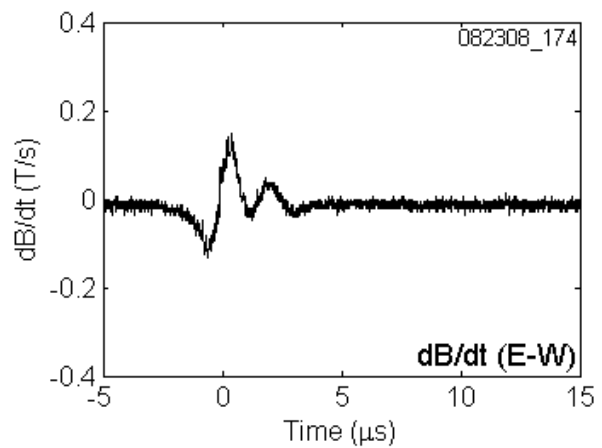
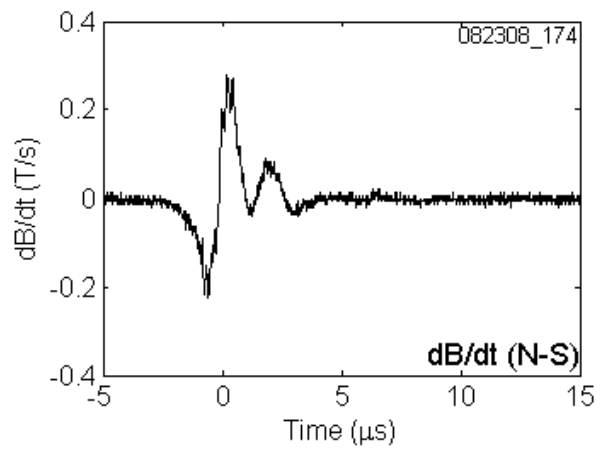
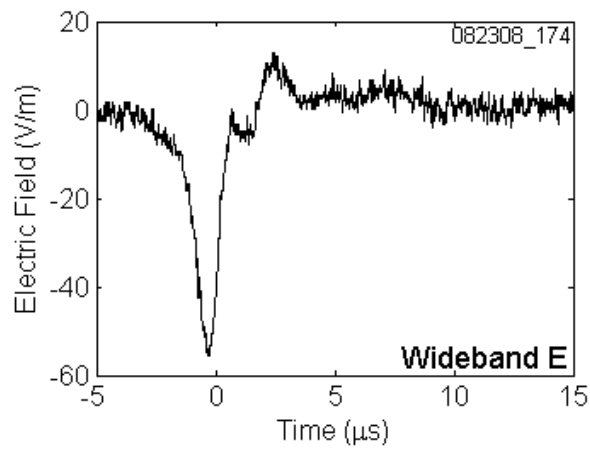


Figure A-4. CID 082308_174 shown on a 20 μs time scale. dE/dt is not available.

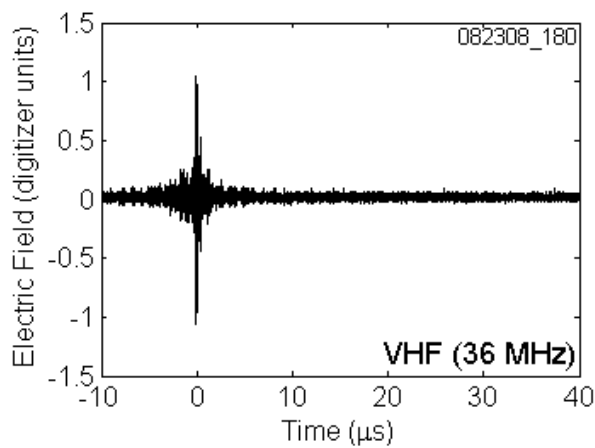
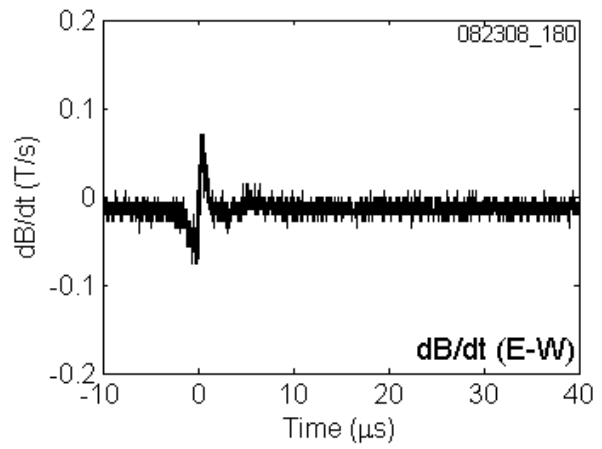
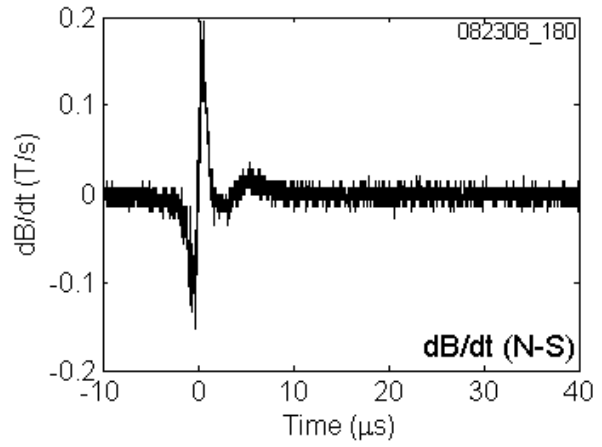
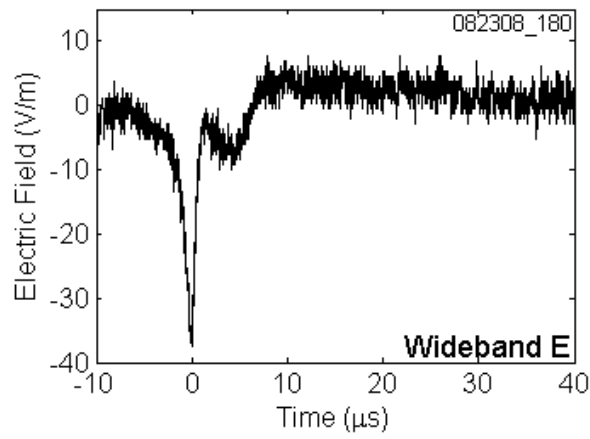


Figure A-5. CID 082308_180 shown on a 50 μs time scale. dE/dt is not available.

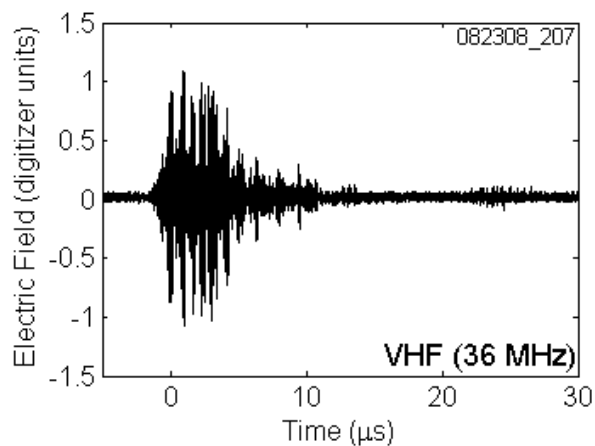
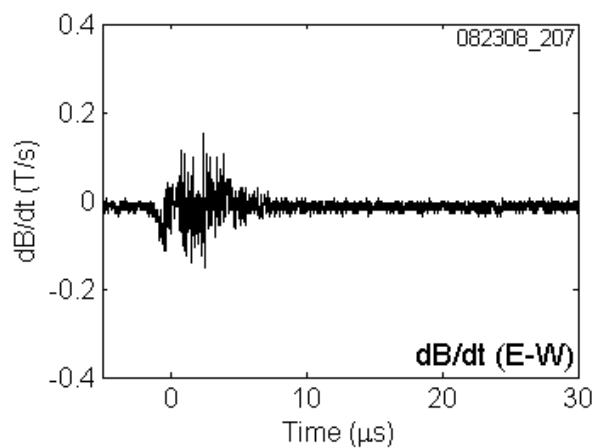
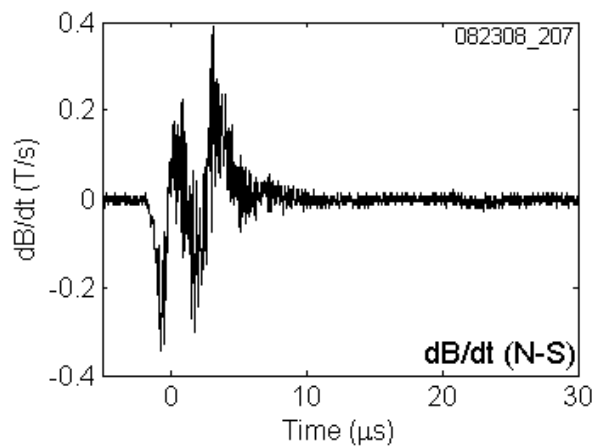
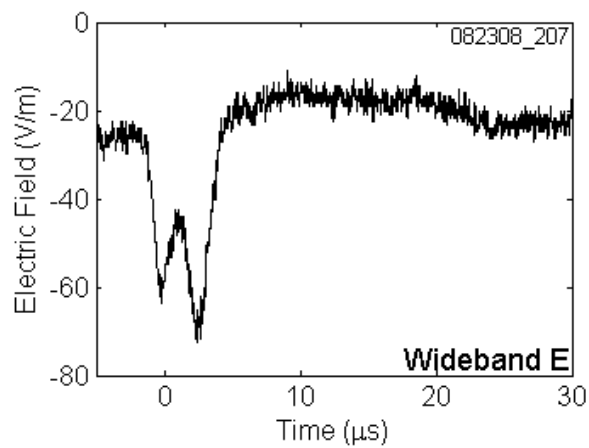


Figure A-6. CID 082308_207 shown on a 35 μs time scale. dE/dt is not available.

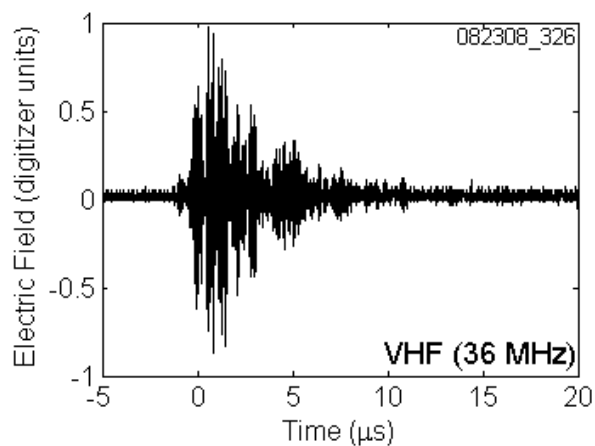
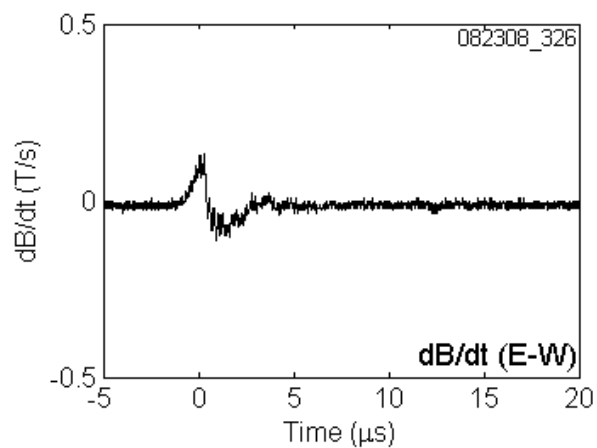
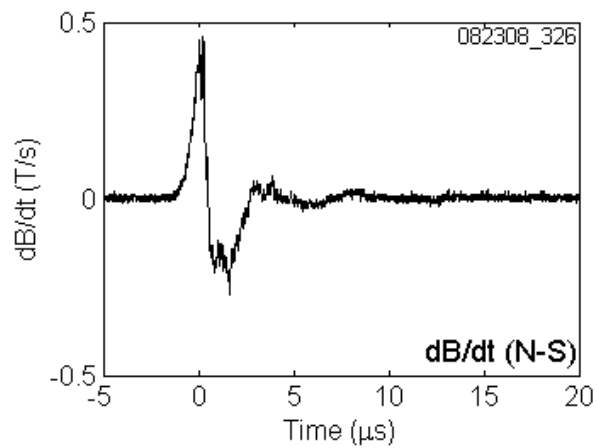
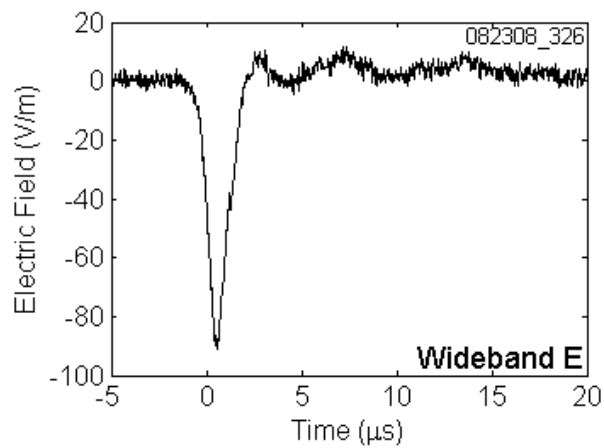


Figure A-7. CID 082308_326 shown on a 25 μs time scale. dE/dt is not available.

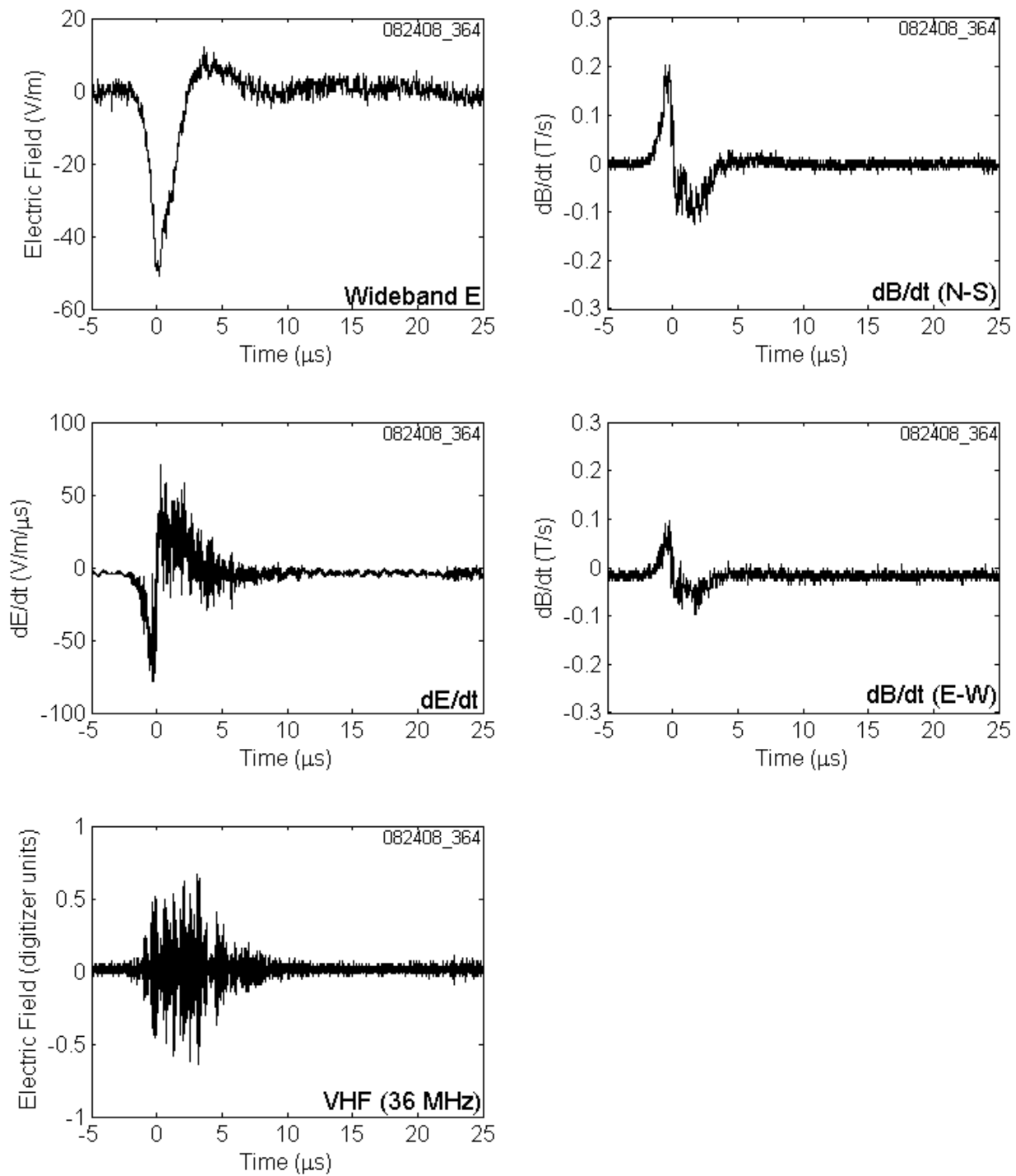


Figure A-8. CID 082408_364 shown on a 30 μs time scale.

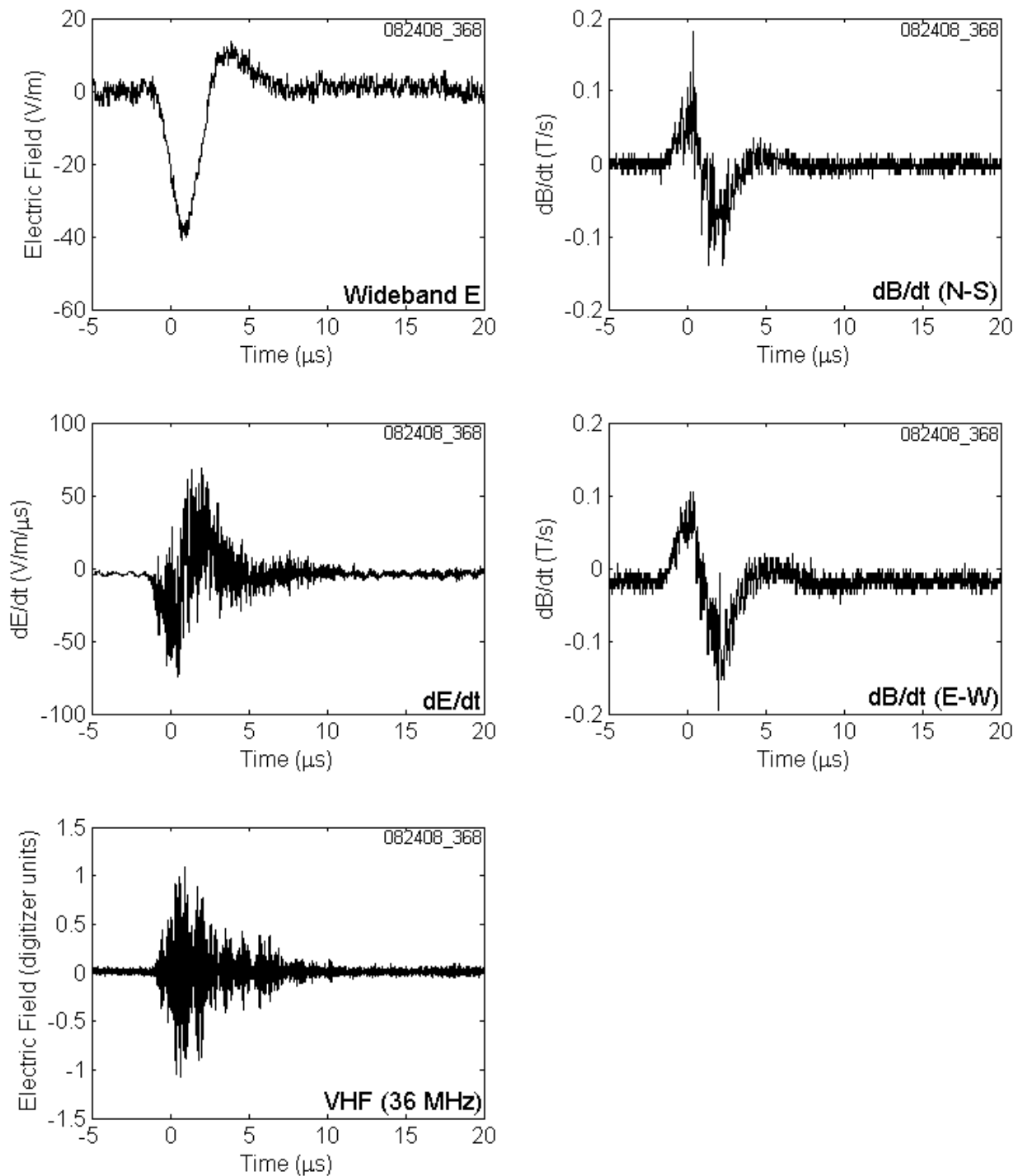


Figure A-9. CID 082408_368 shown on a 25 μs time scale.

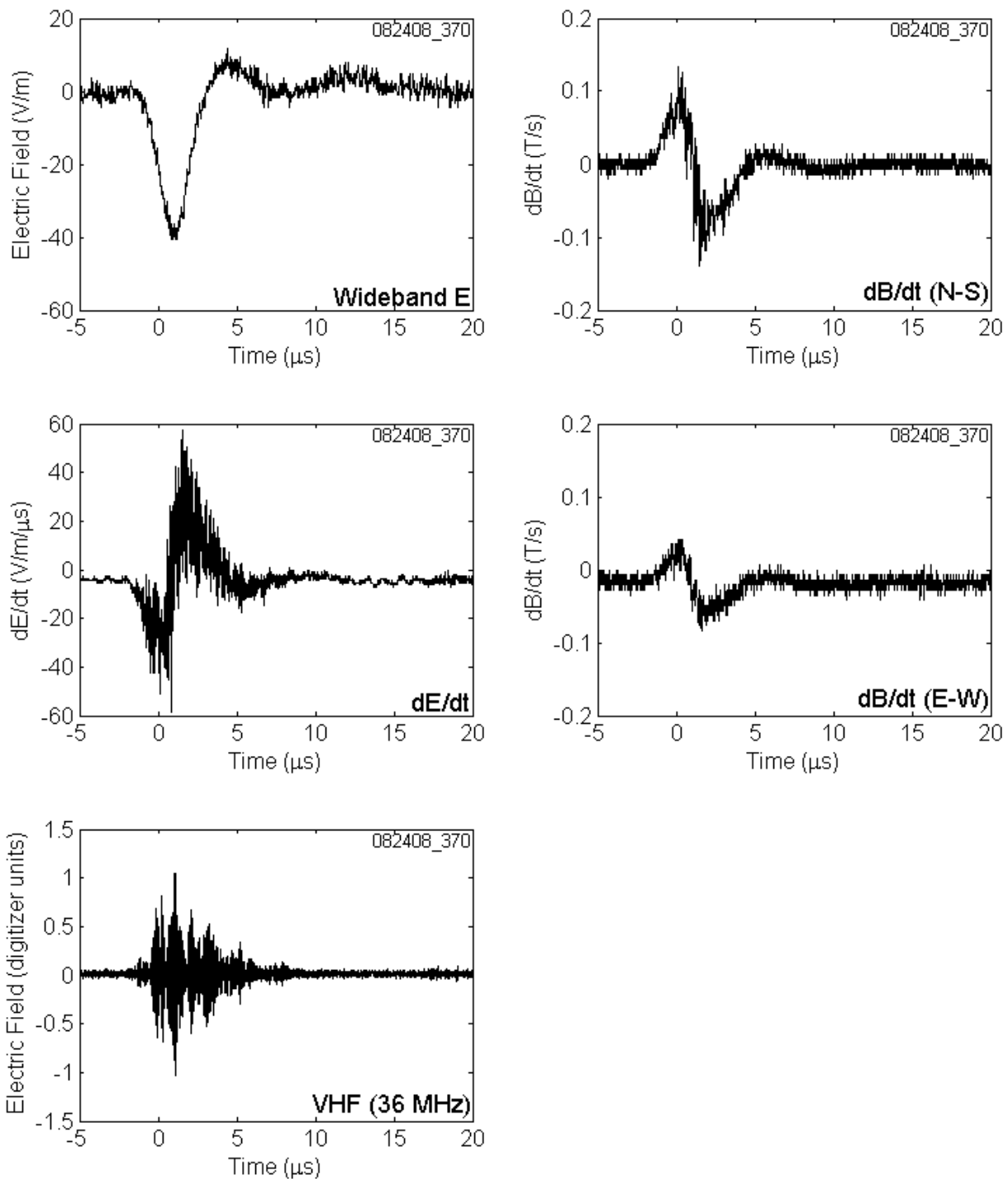


Figure A-10. CID 082408_370 shown on a 25 μs time scale.

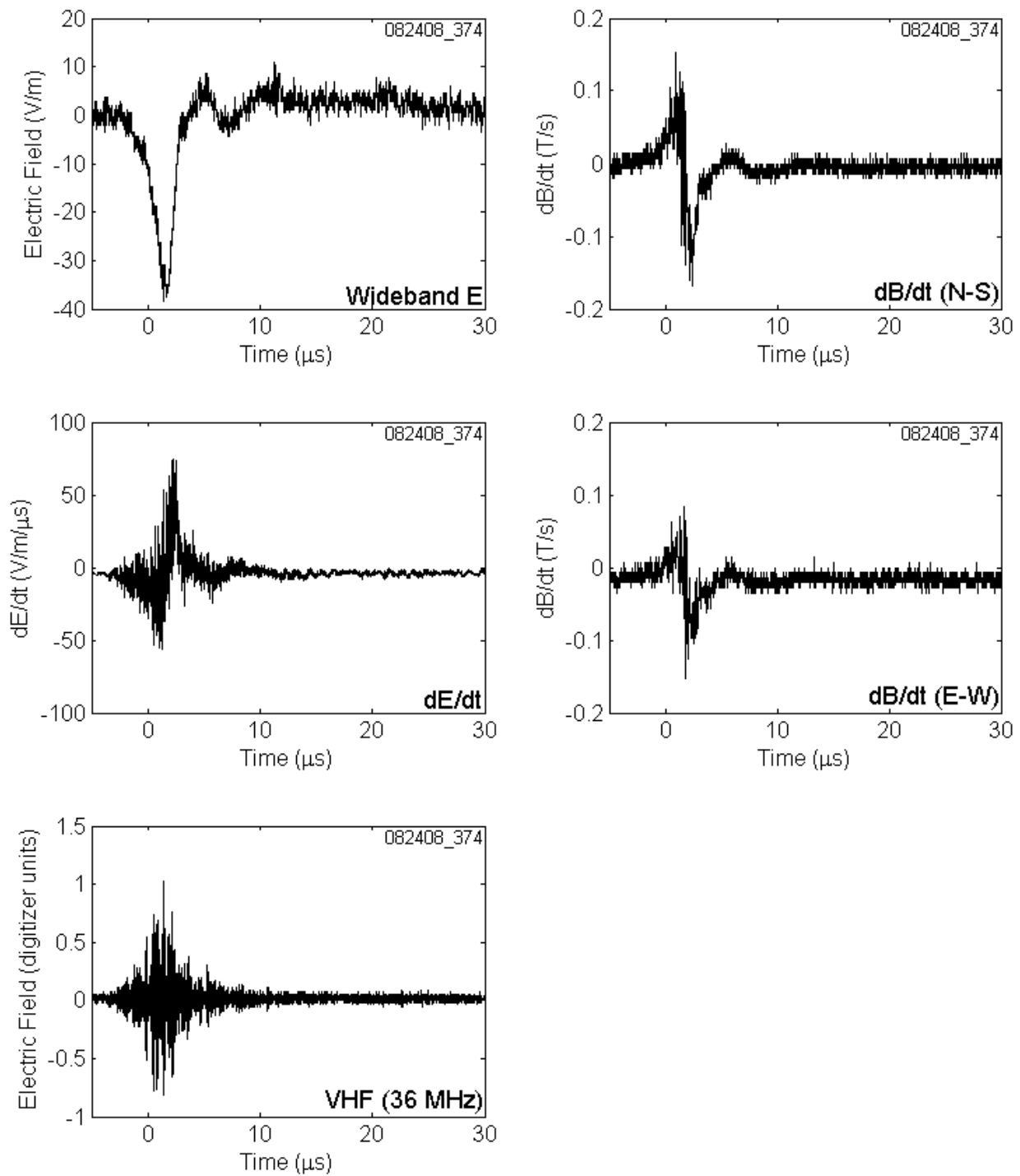


Figure A-11. CID 082408_374 shown on a 35 μs time scale.

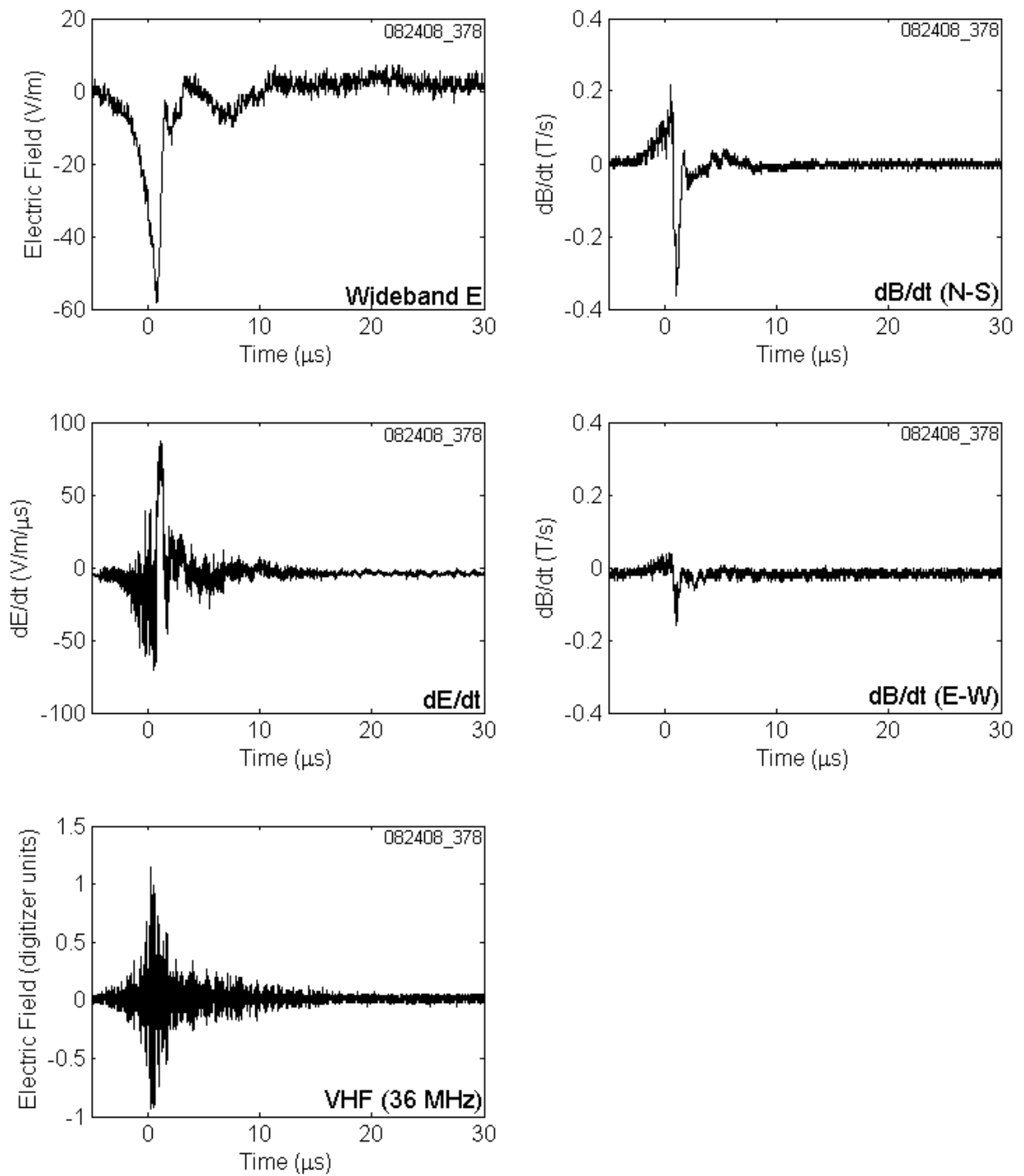


Figure A-12. CID 082408_378 shown on a 35 μs time scale.

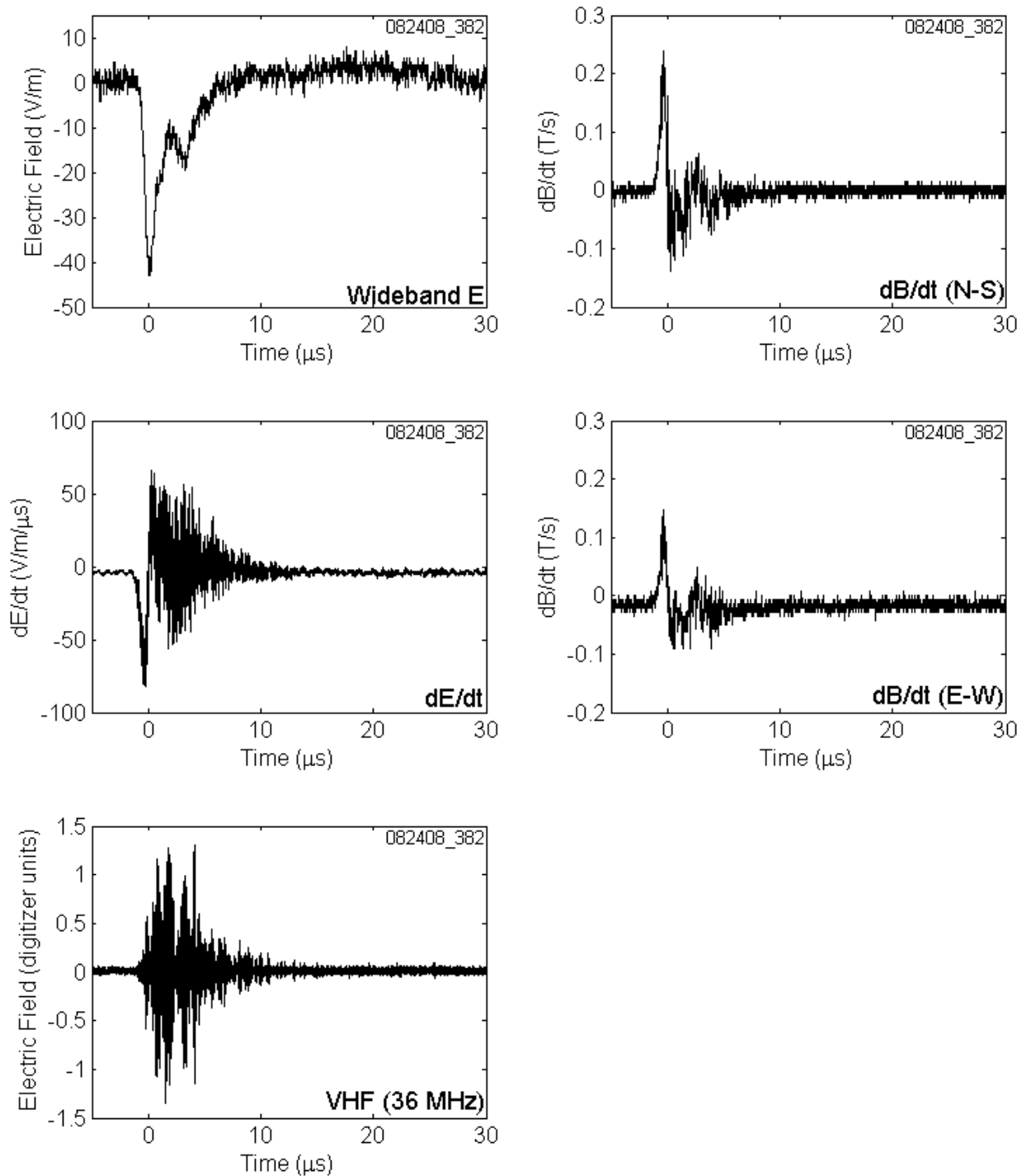


Figure A-13. CID 082408_382 shown on a 35 μs time scale.

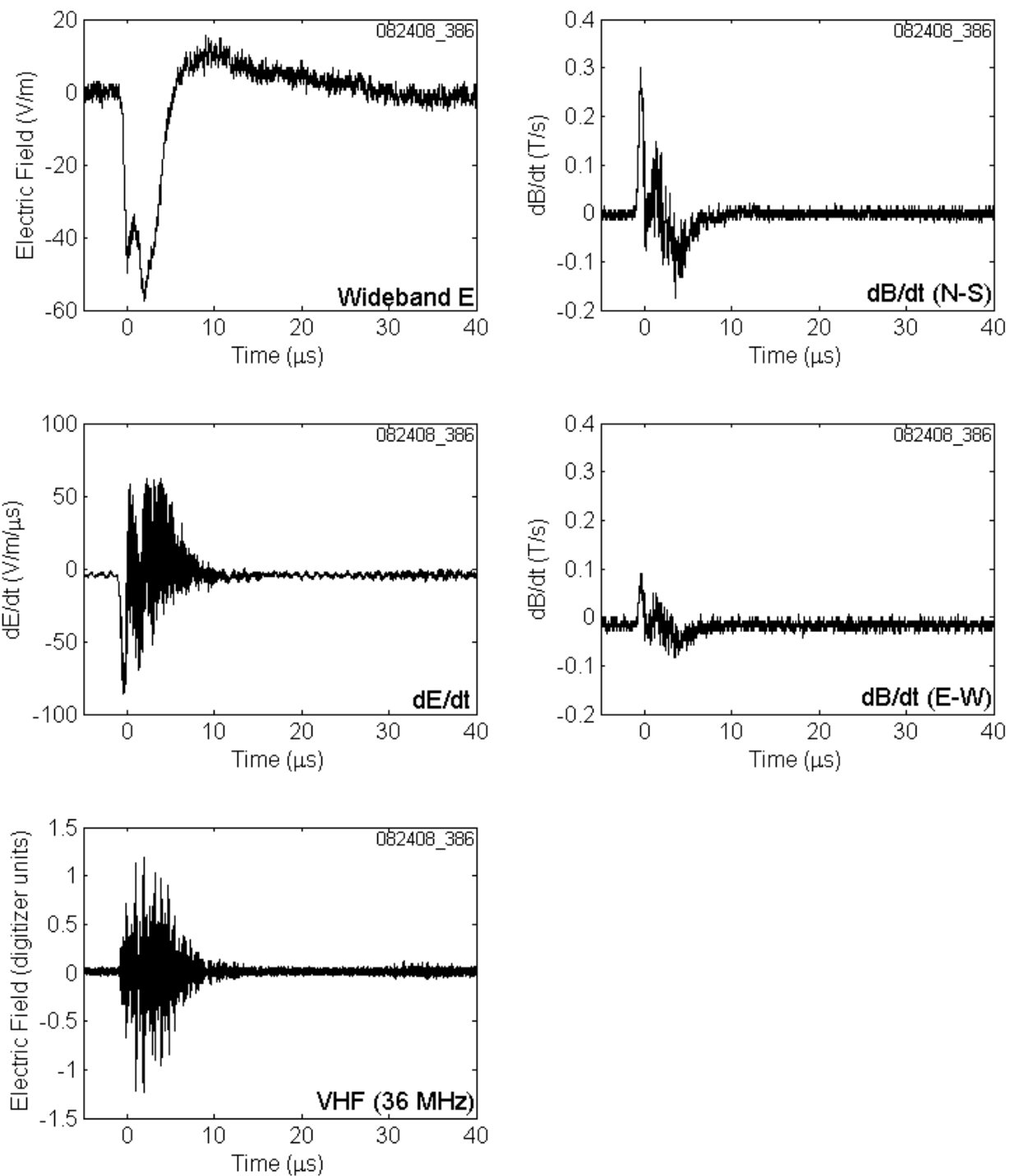


Figure A-14. CID 082408_386 shown on a 45 μs time scale.

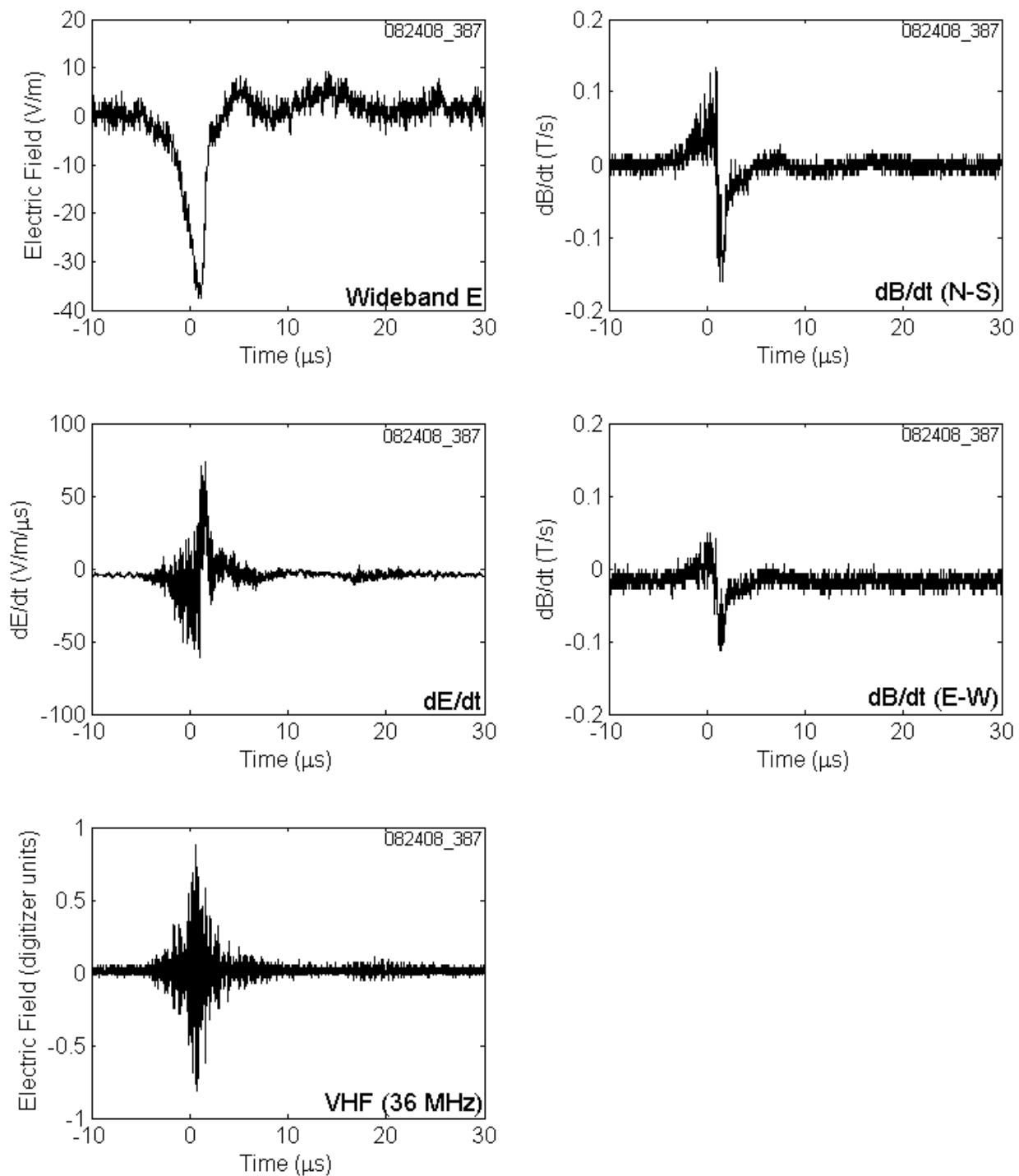


Figure A-15. CID 082408_387 shown on a 40 μs time scale.

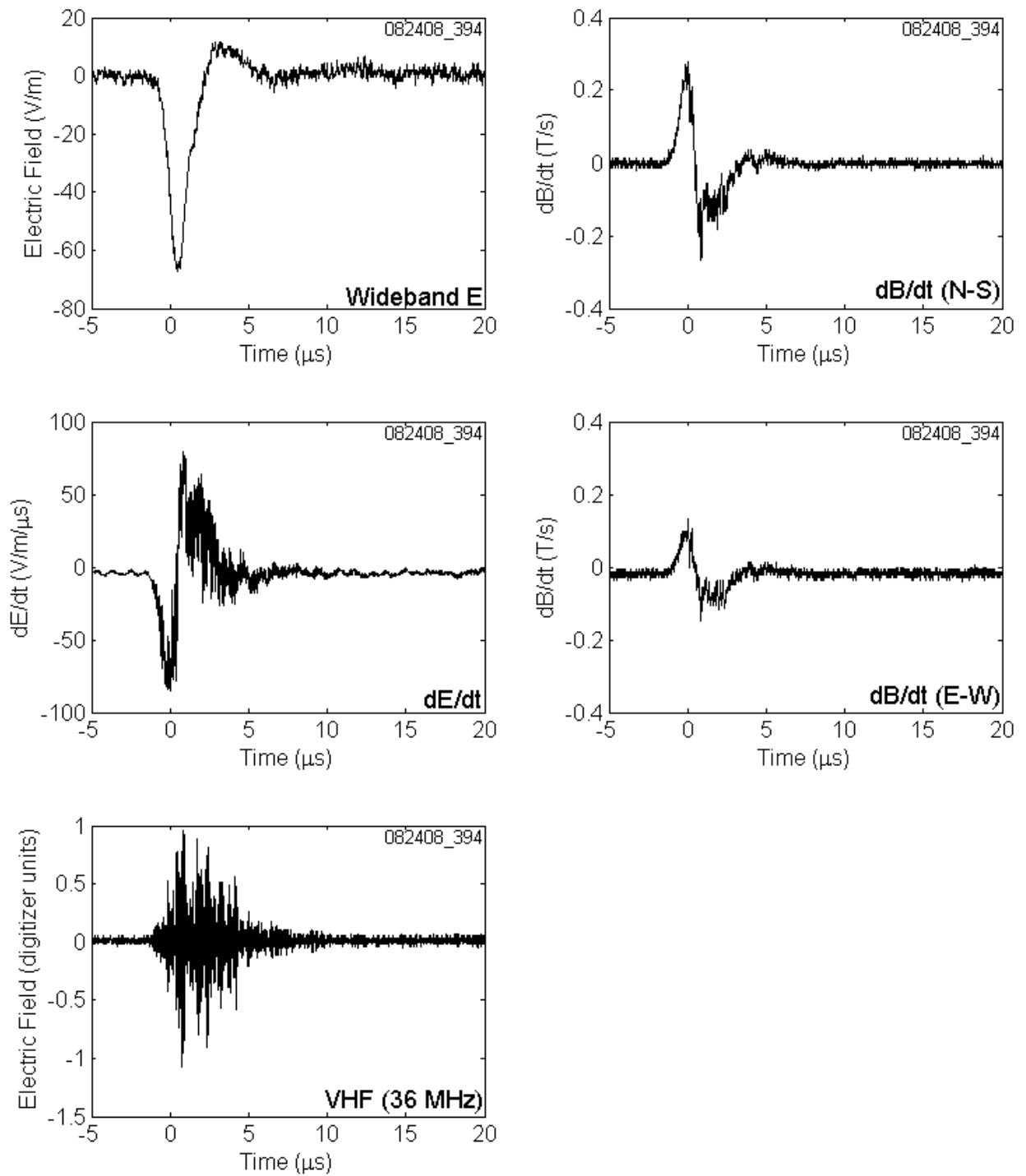


Figure A-16. CID 082408_394 shown on a 25 μs time scale.

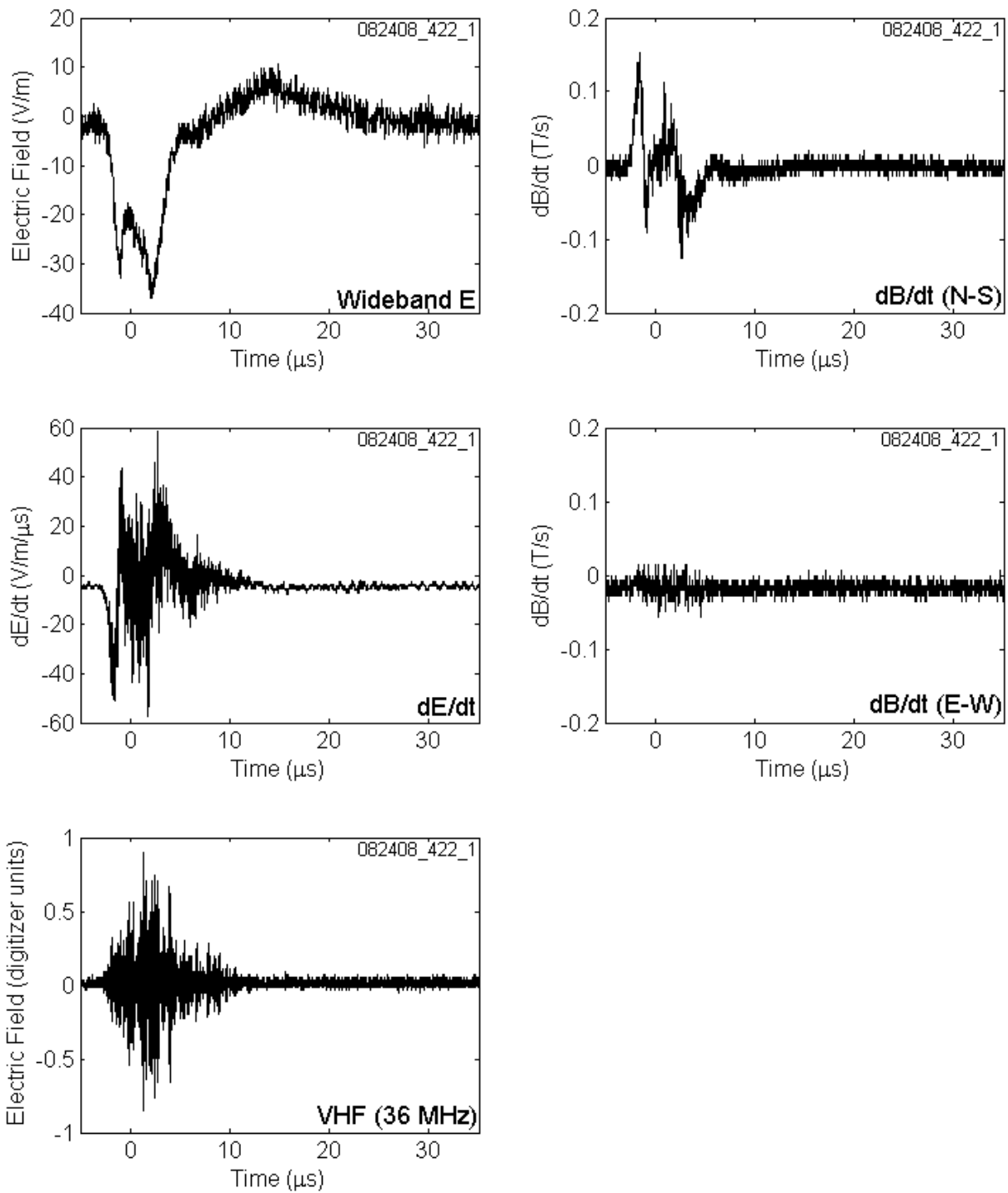


Figure A-17. CID 082408_422_1 shown on a 40 μs time scale.

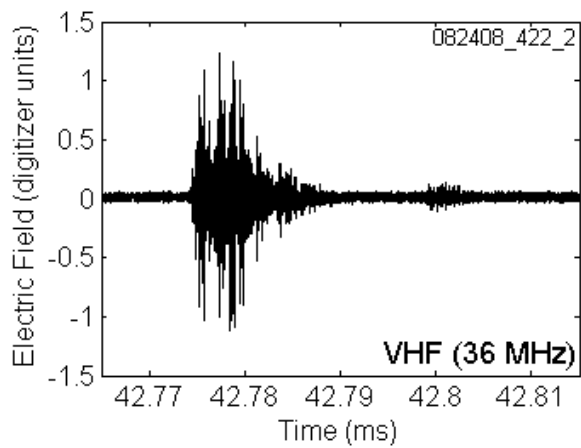
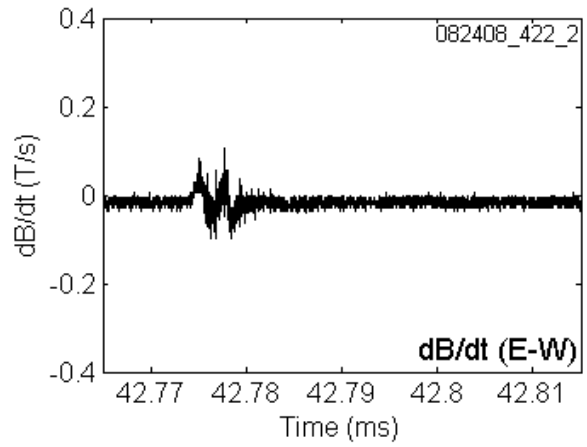
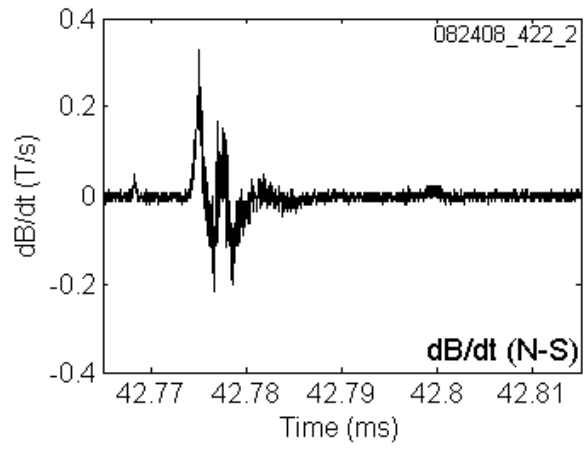
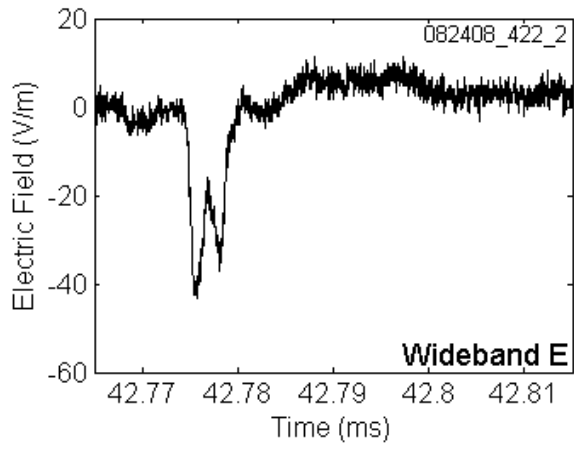


Figure A-18. CID 082408_422_2 shown on a 50 μ s time scale. dE/dt is not available.

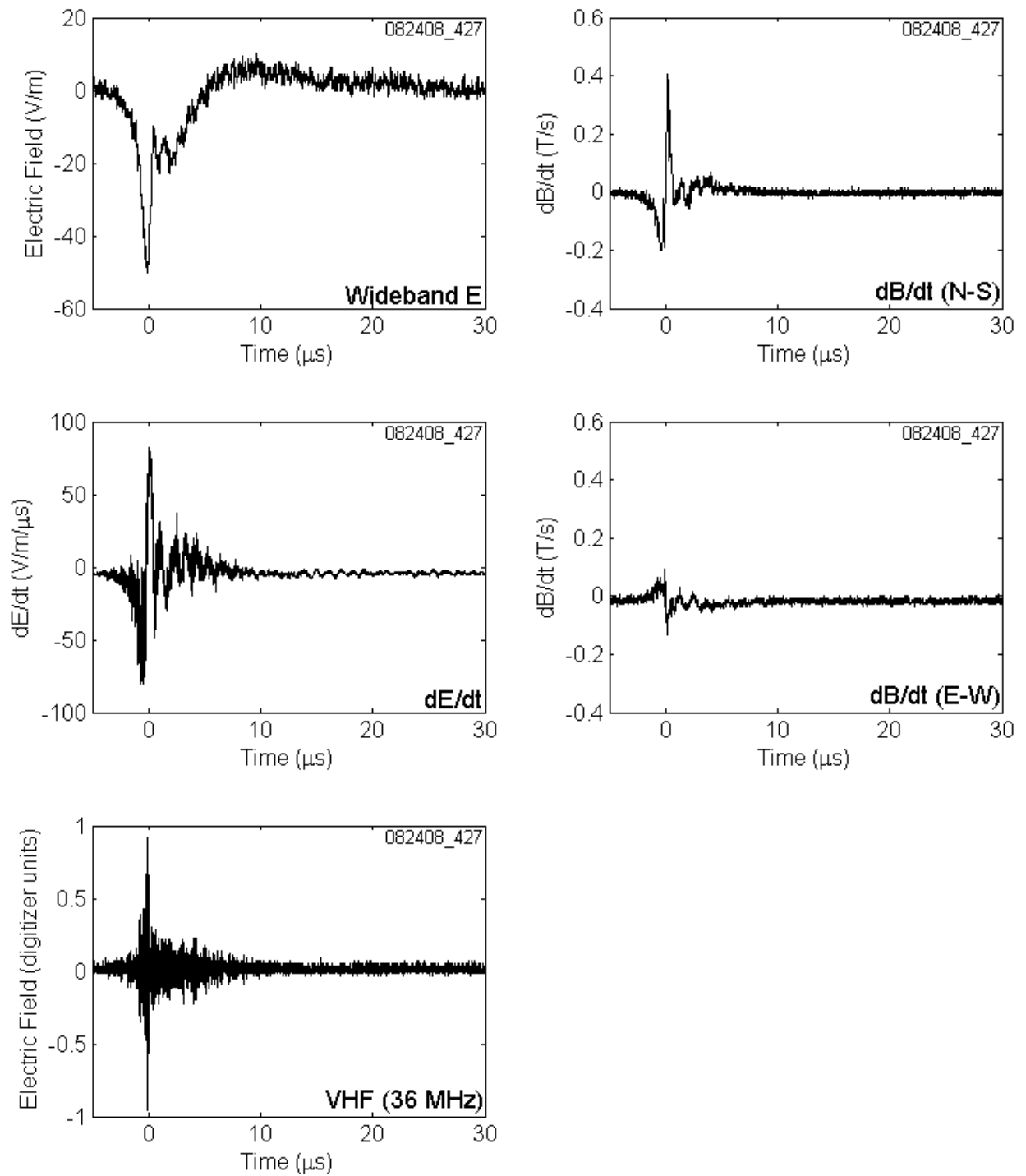


Figure A-19. CID 082408_427 shown on a 35 μs time scale.

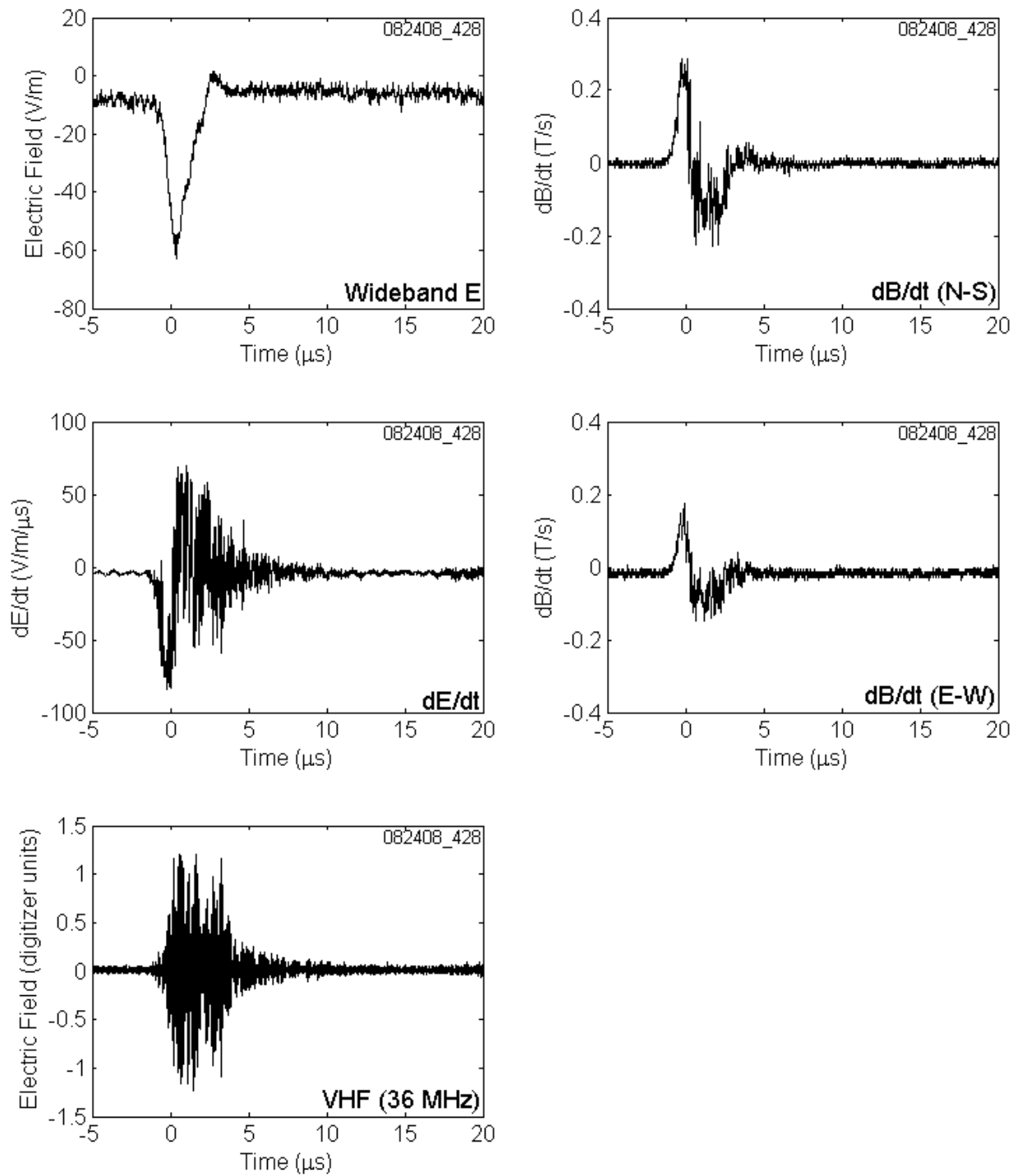


Figure A-20. CID 082408_428 shown on a 25 μs time scale.

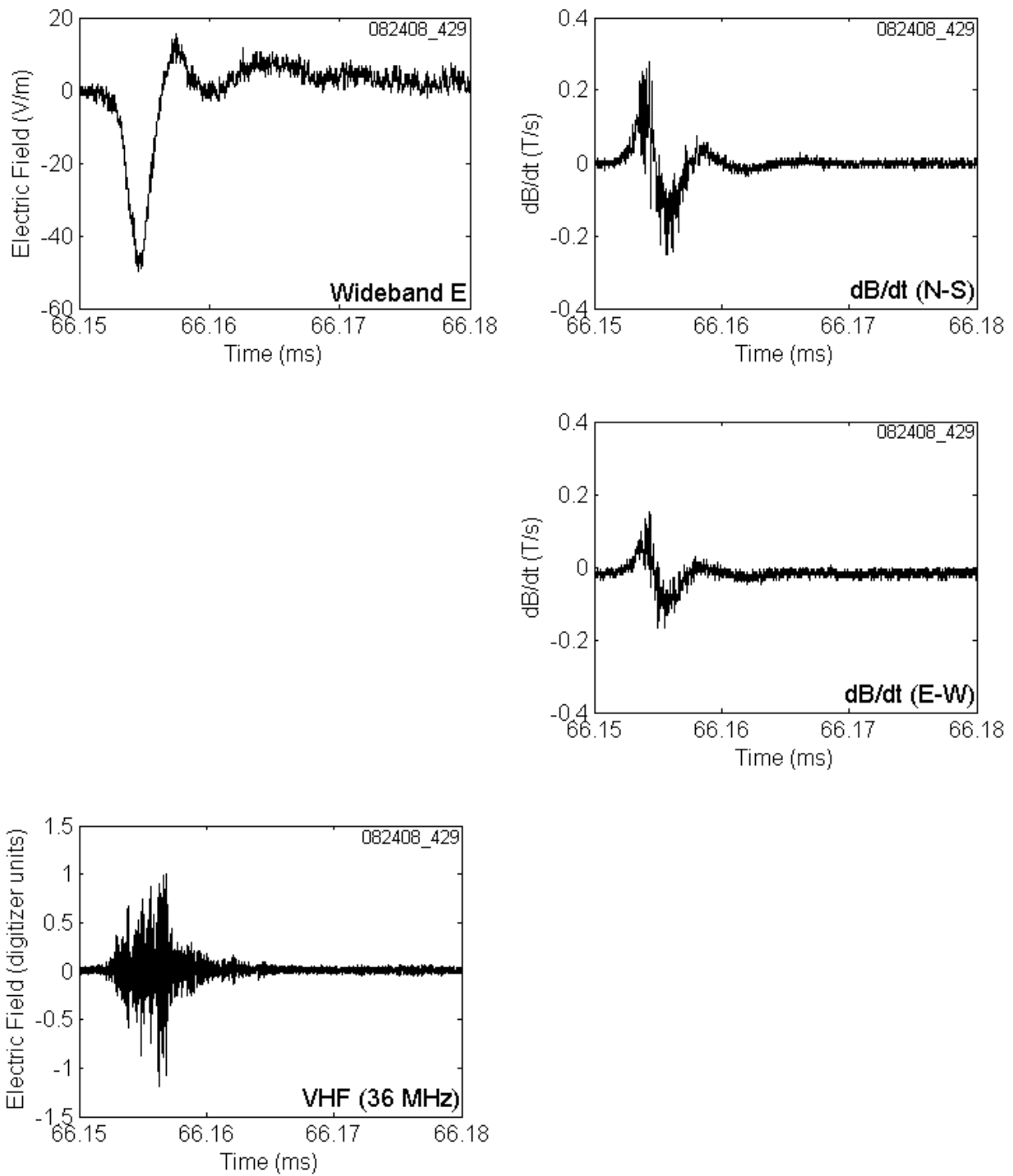


Figure A-21. CID 082408_429 shown on a 30 μ s time scale. dE/dt is not available.

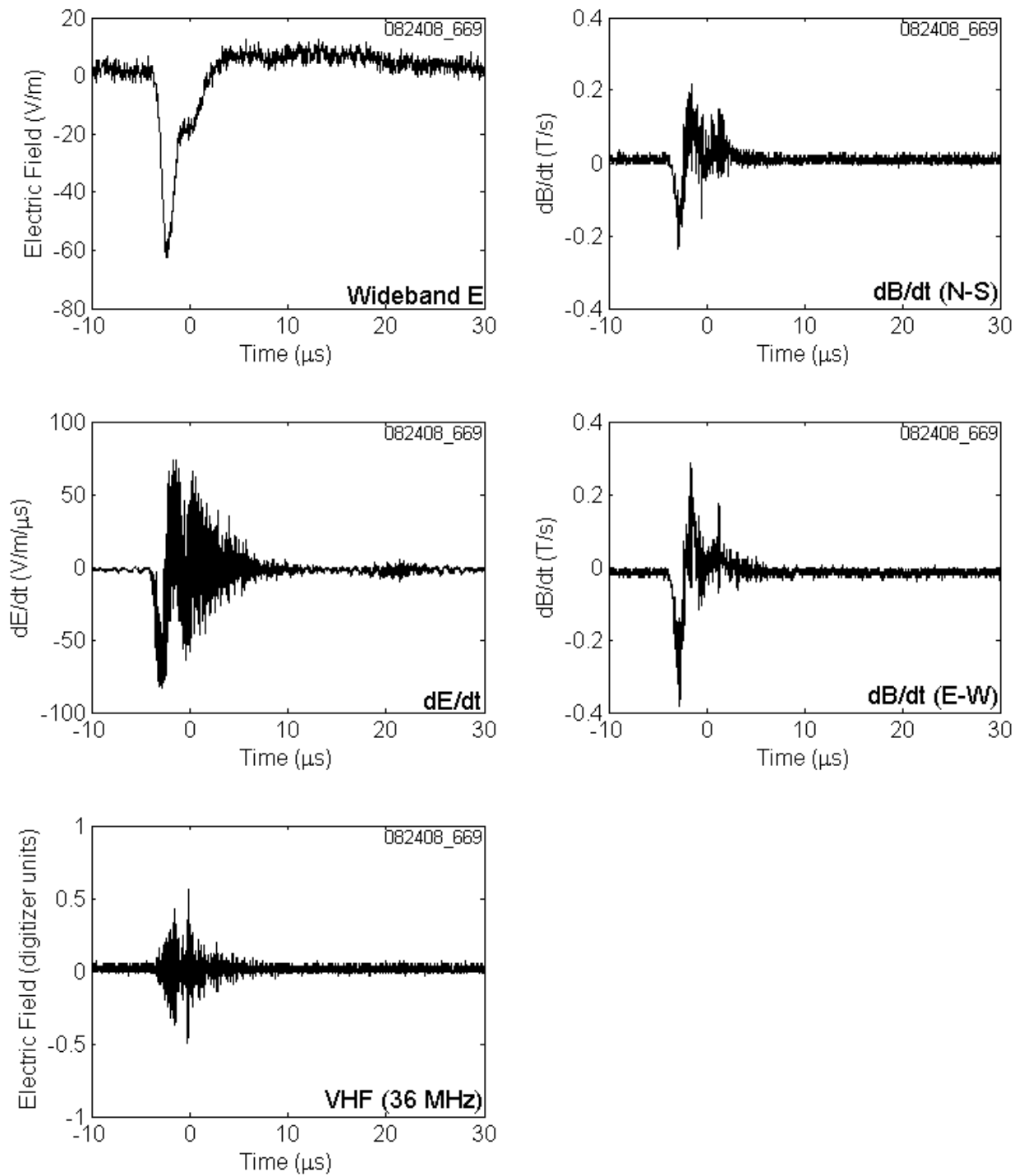


Figure A-22. CID 082408_669 shown on a 40 μs time scale.

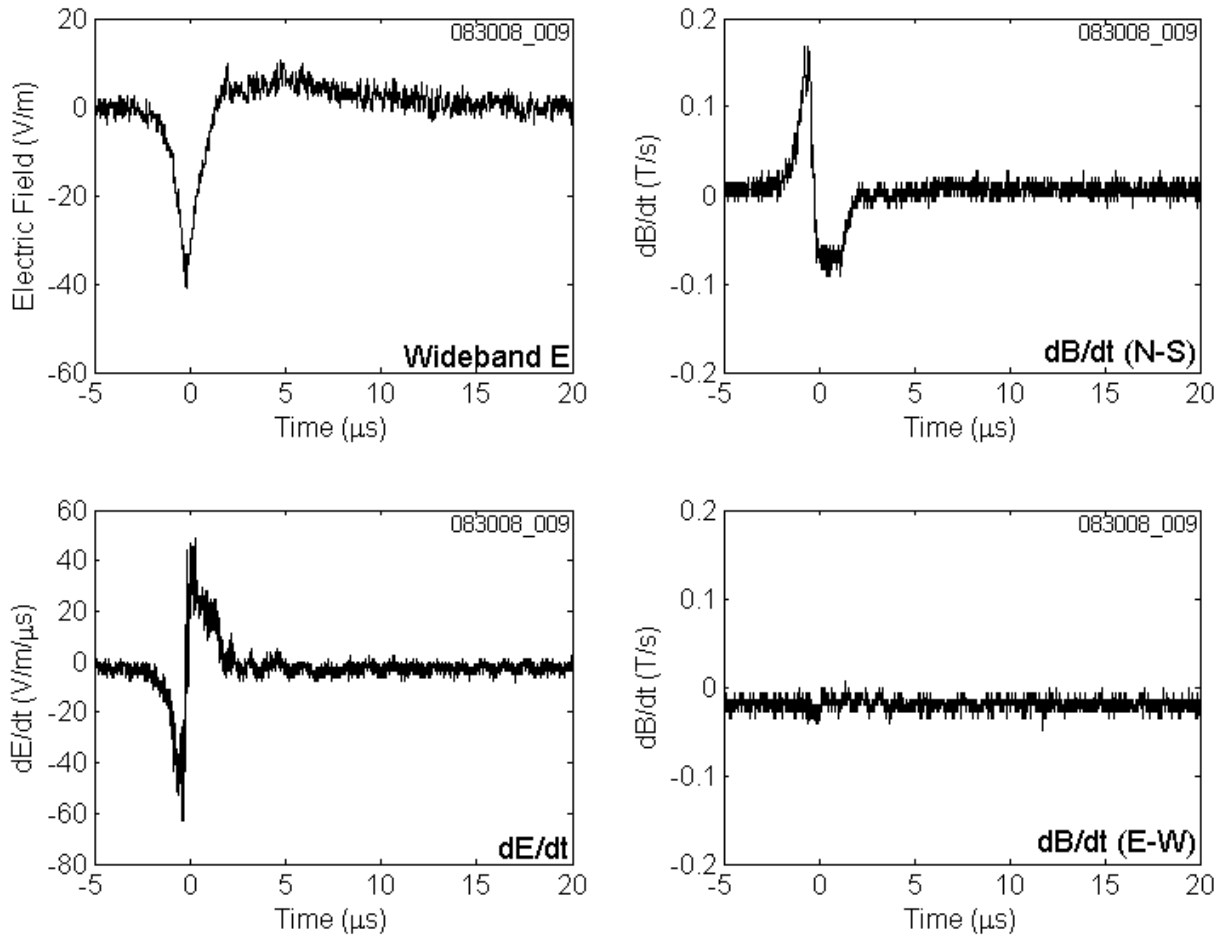


Figure A-23. CID 083008_009 shown on a 25 μs time scale. VHF is not available.

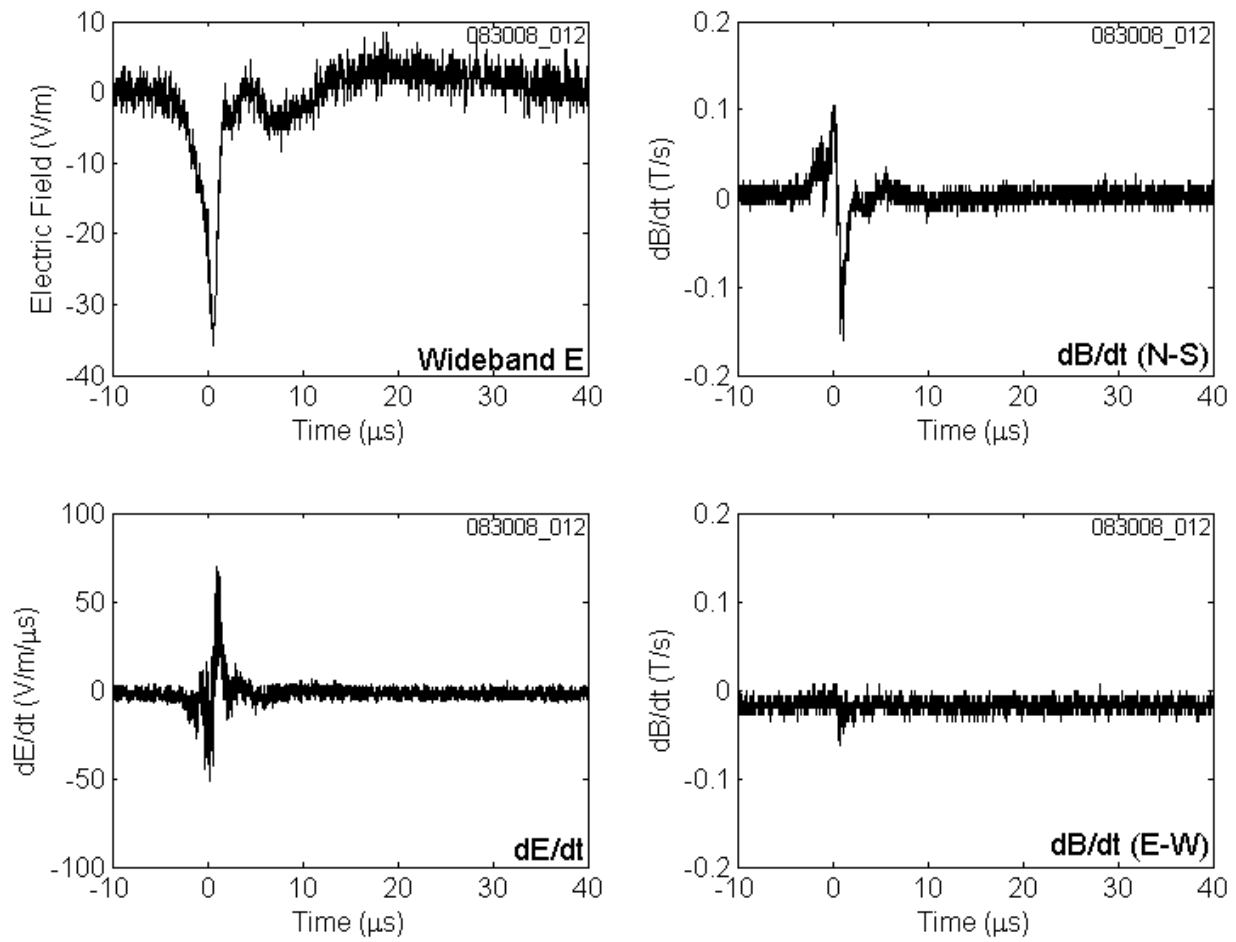


Figure A-24. CID 083008_012 shown on a 50 μs time scale. VHF is not available.

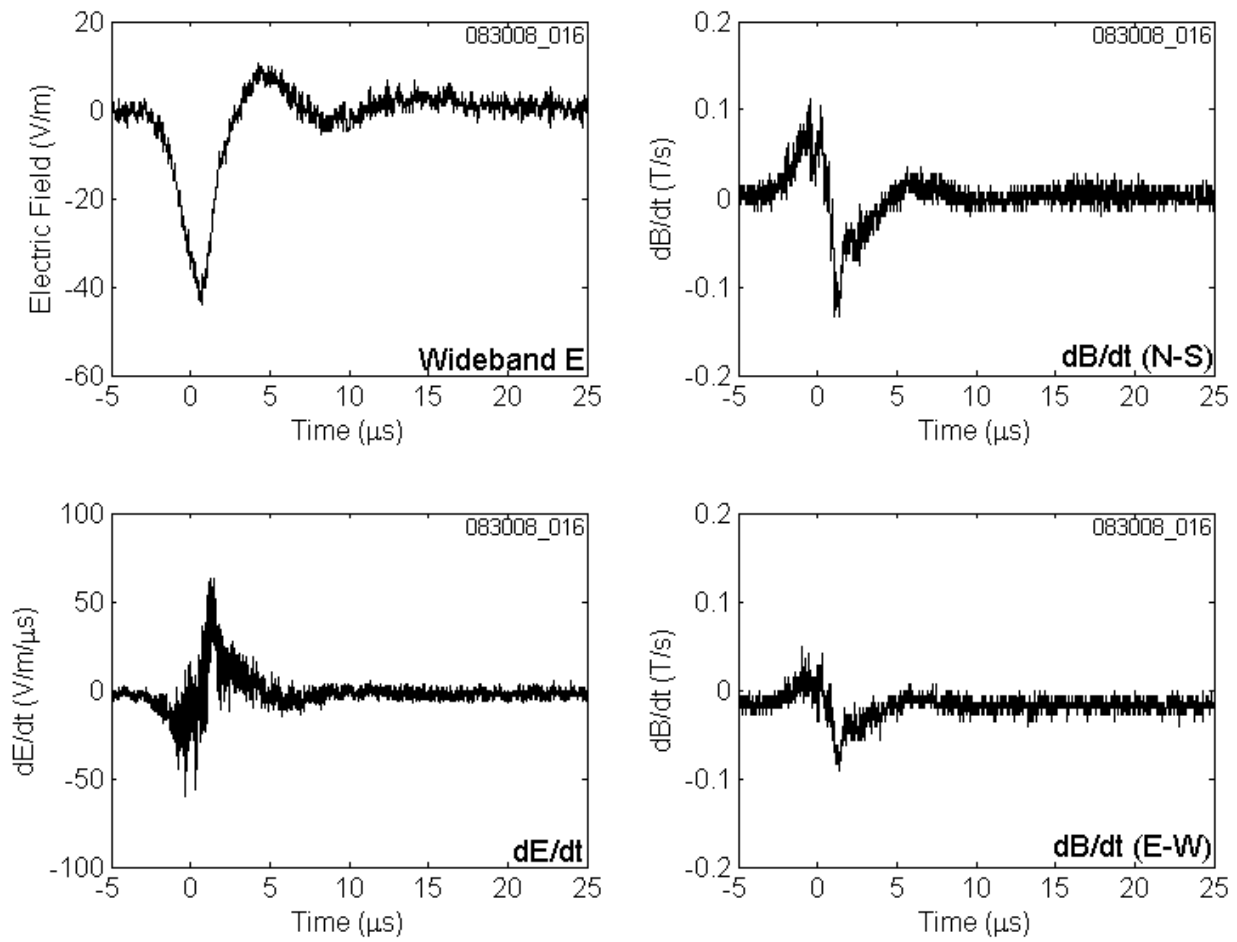


Figure A-25. CID 083008_016 shown on a 30 μs time scale. VHF is not available.

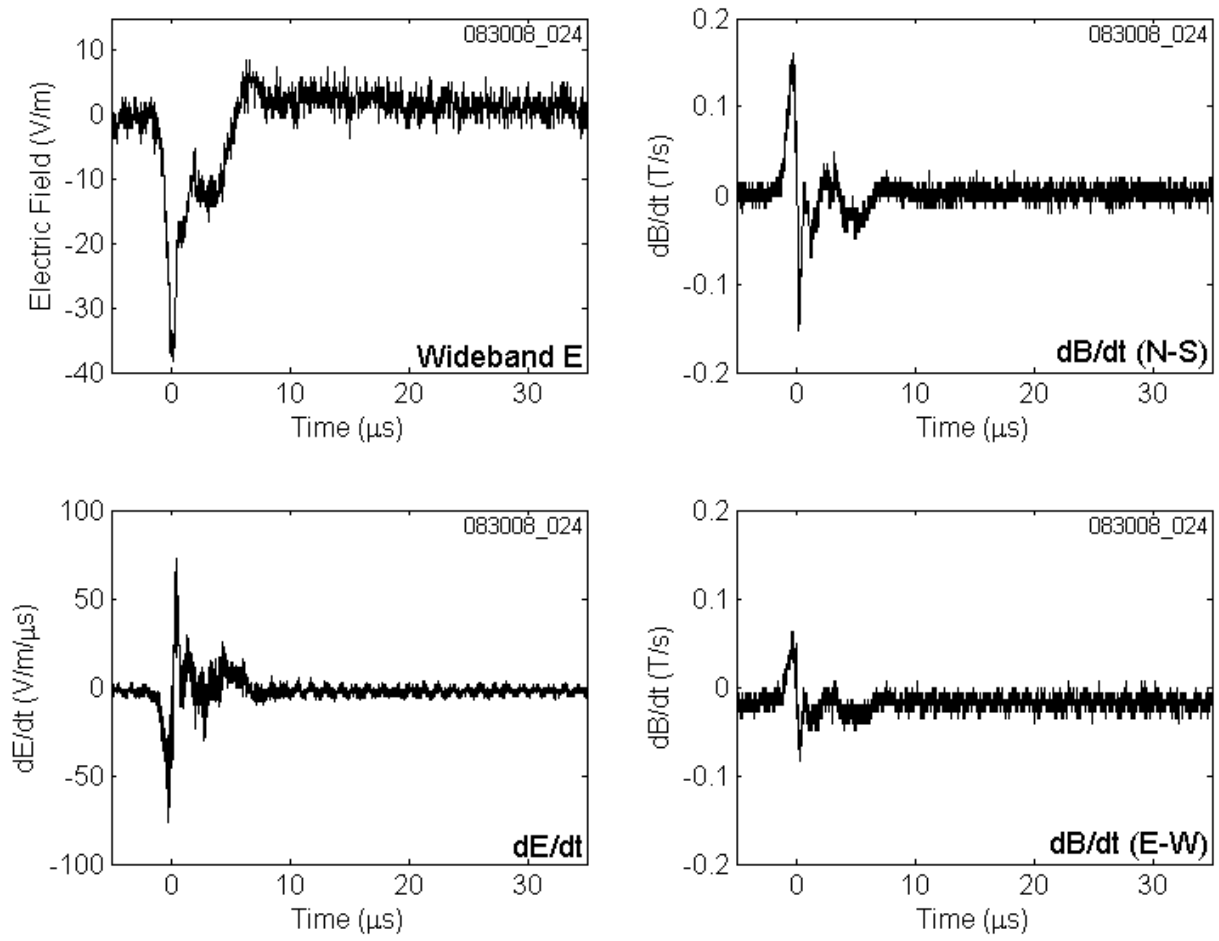


Figure A-26. CID 083008_024 shown on a 40 μs time scale. VHF is not available.

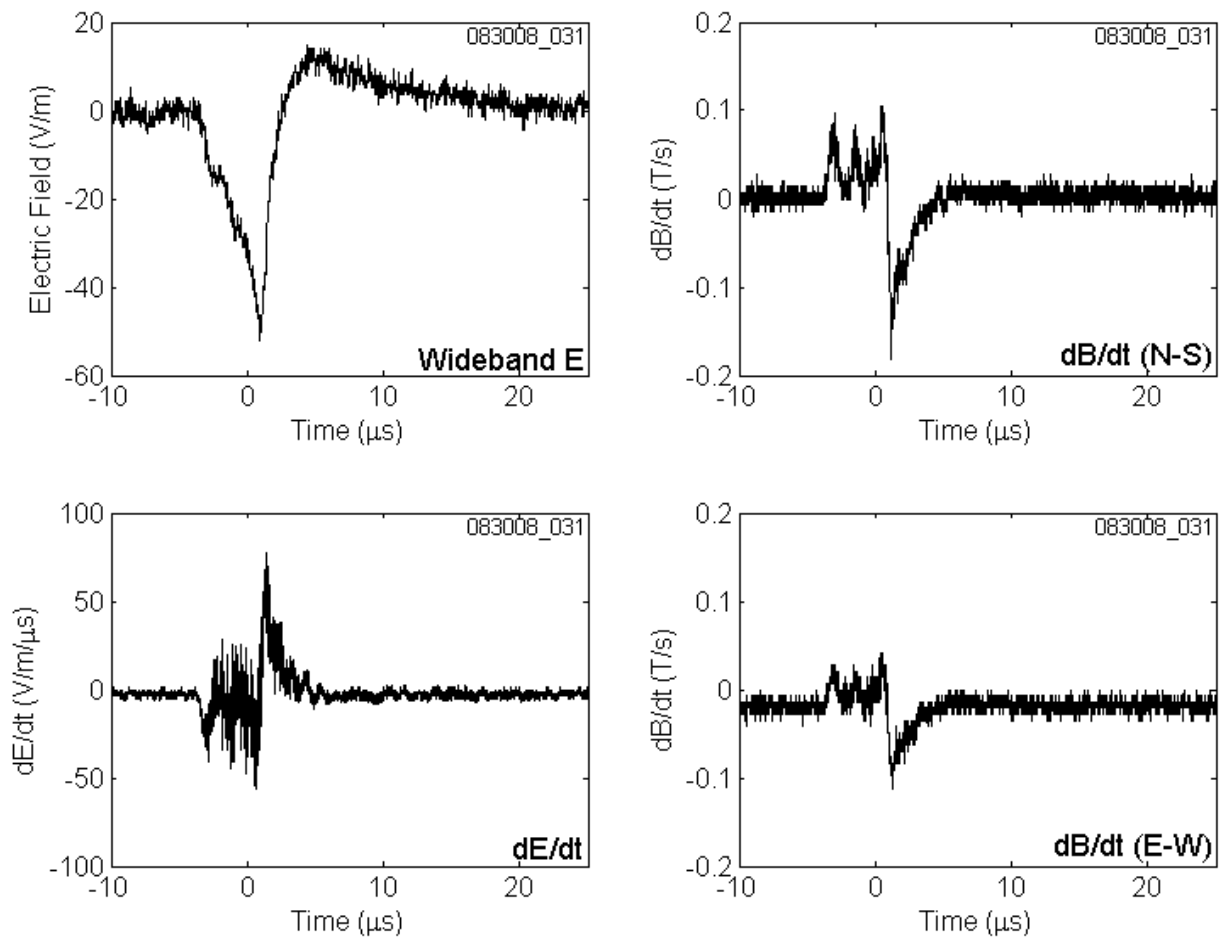


Figure A-27. CID 083008_031 shown on a 35 μs time scale. VHF is not available.

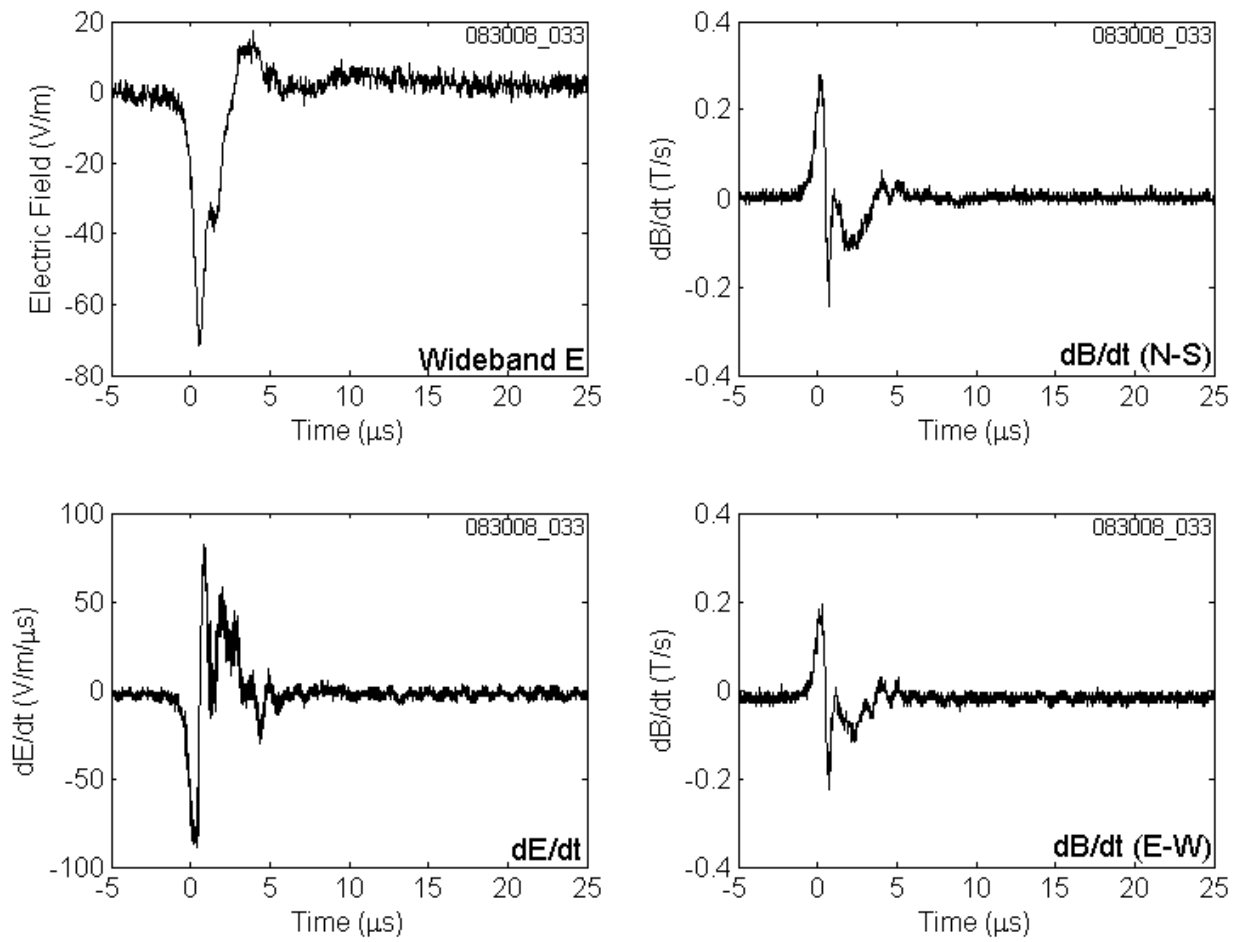


Figure A-28. CID 083008_033 shown on a 30 μs time scale. VHF is not available.

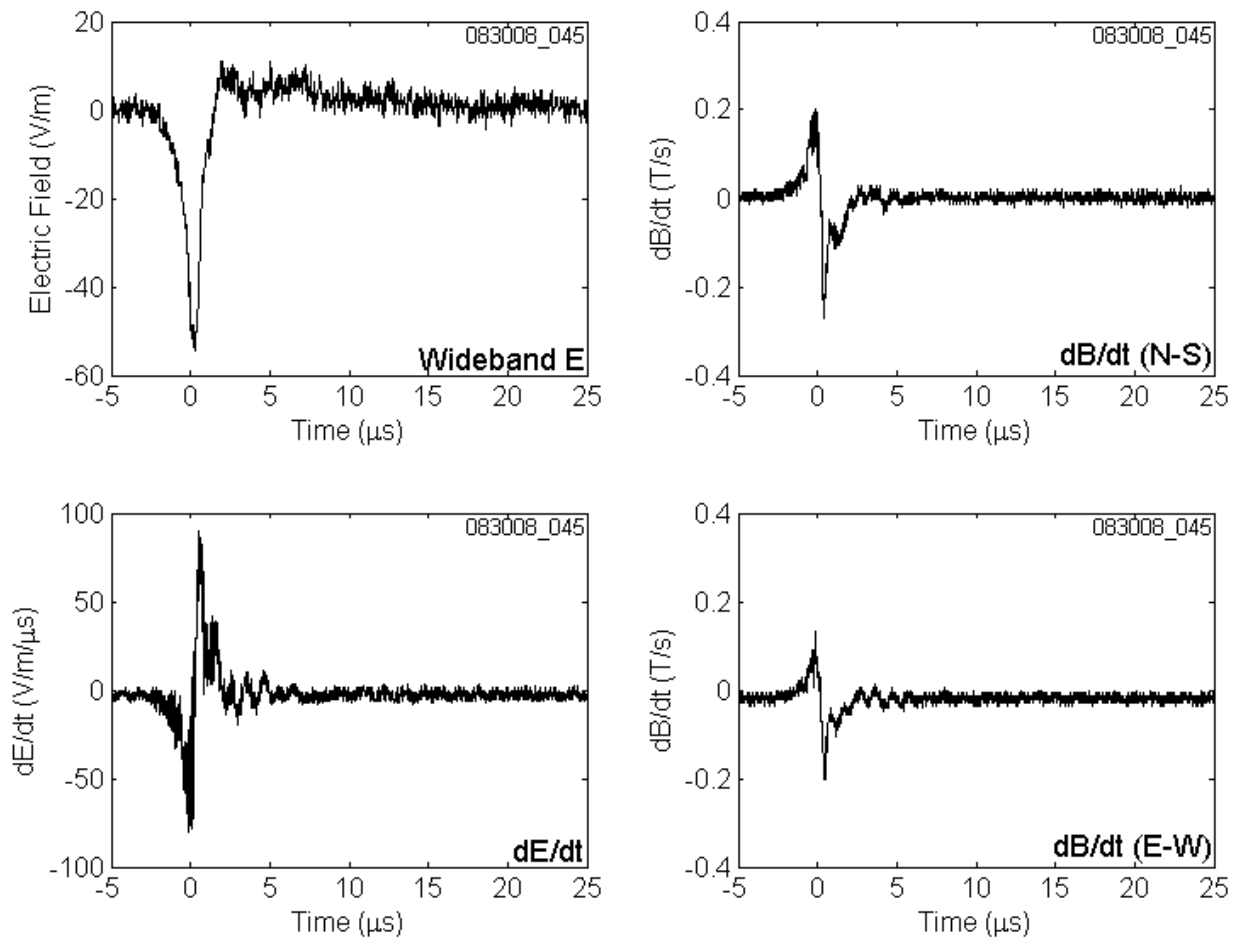


Figure A-29. CID 083008_045 shown on a 30 μs time scale. VHF is not available.

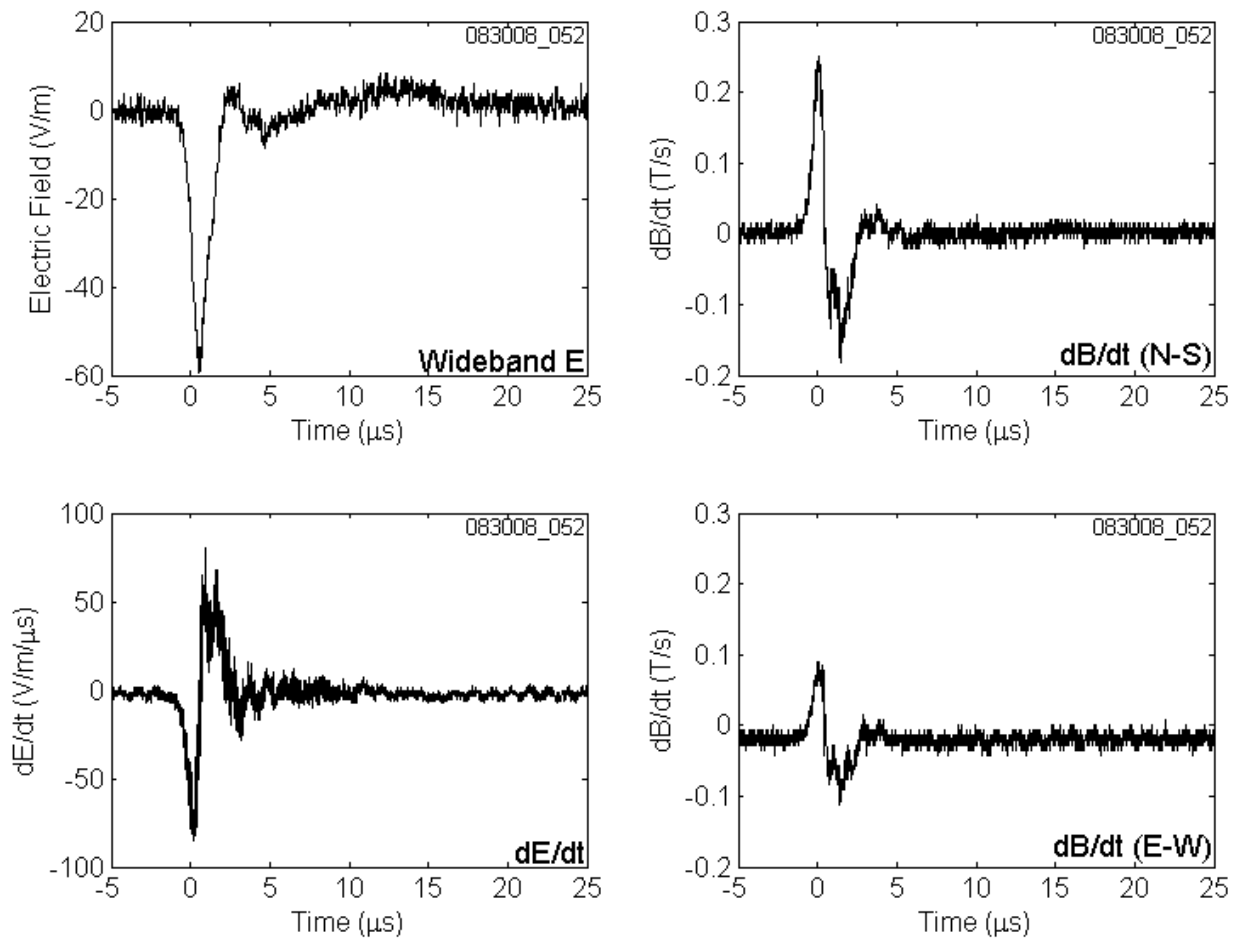


Figure A-30. CID 083008_052 shown on a 30 μs time scale. VHF is not available.

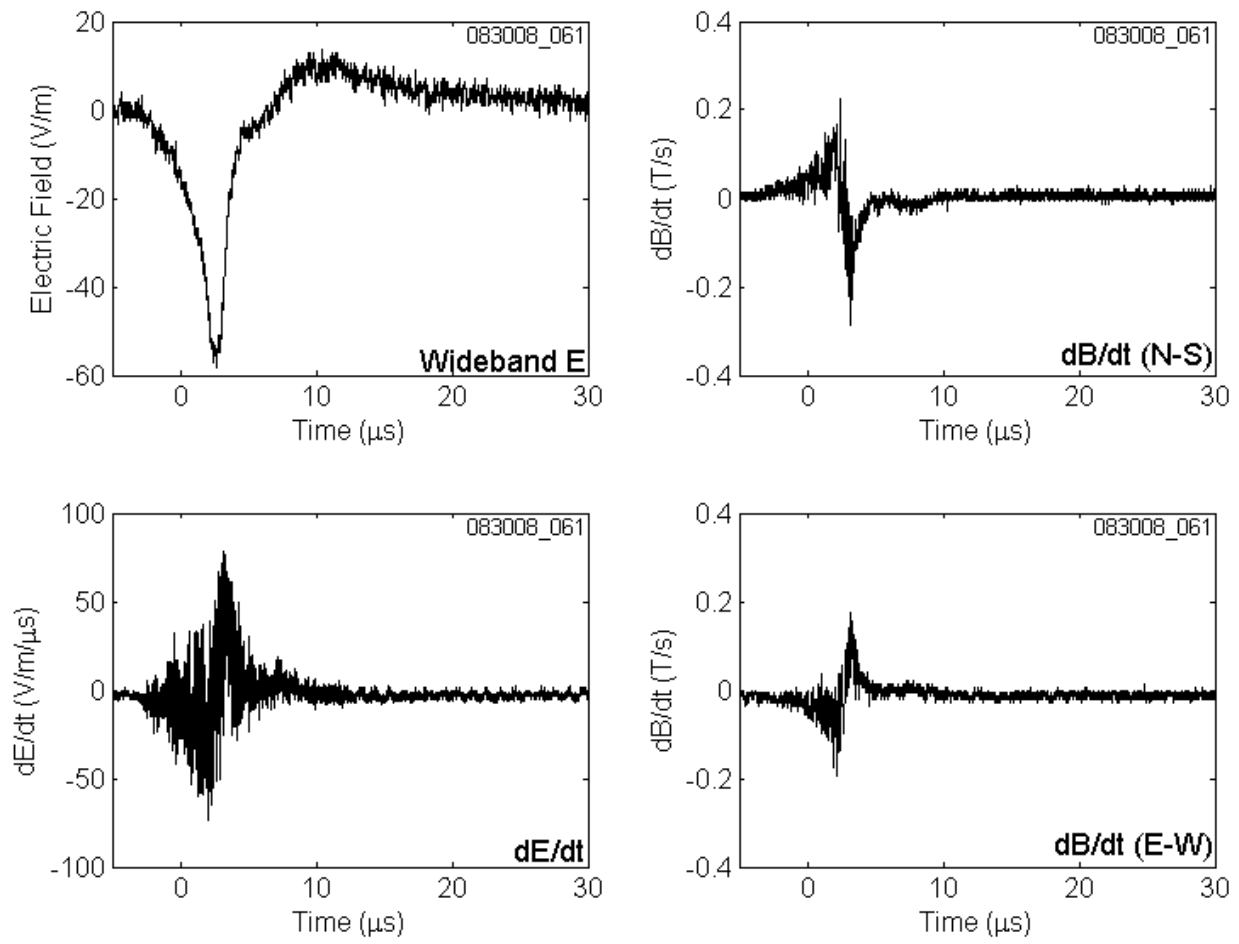


Figure A-31. CID 083008_061 shown on a 35 μs time scale. VHF is not available.

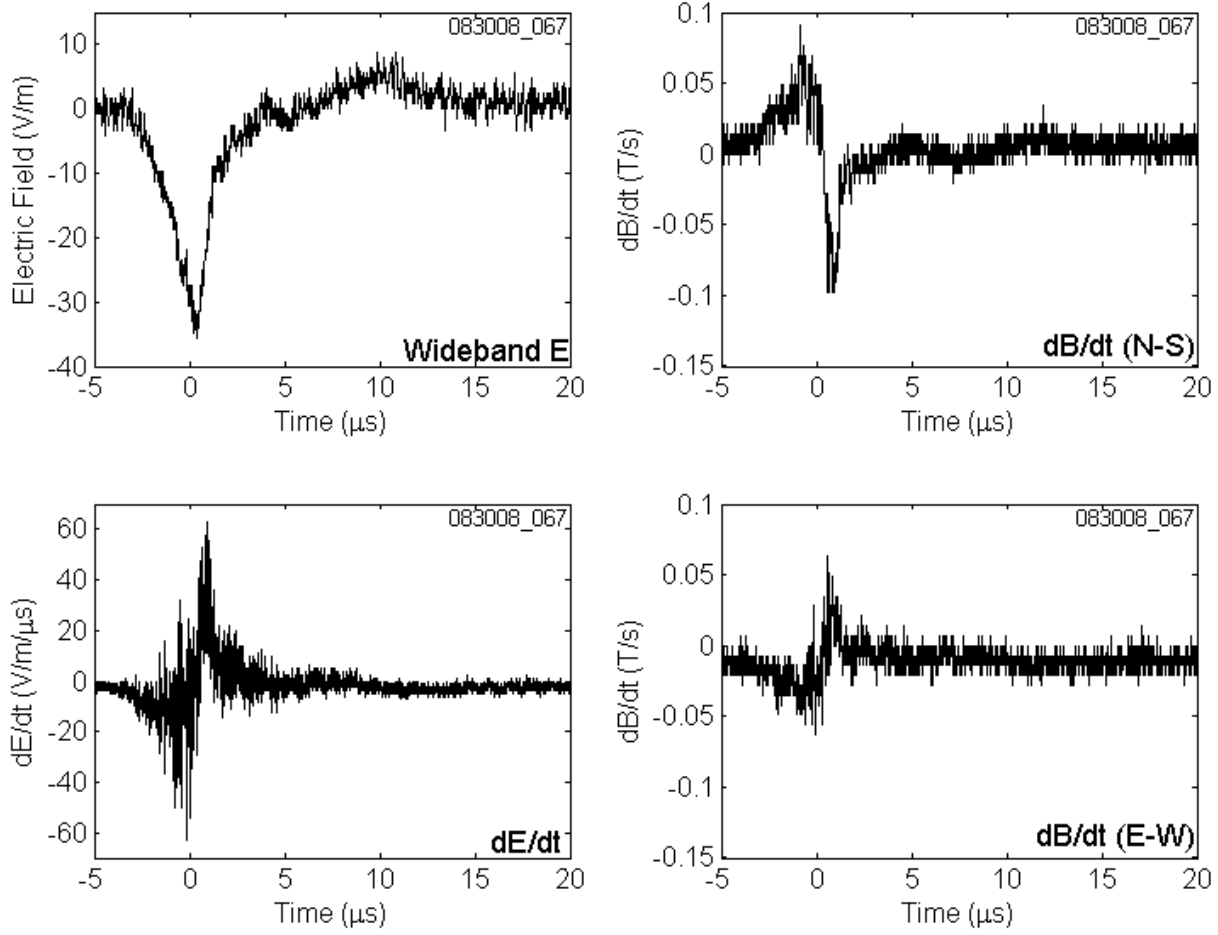


Figure A-32. CID 083008_067 shown on a 25 μs time scale. VHF is not available.

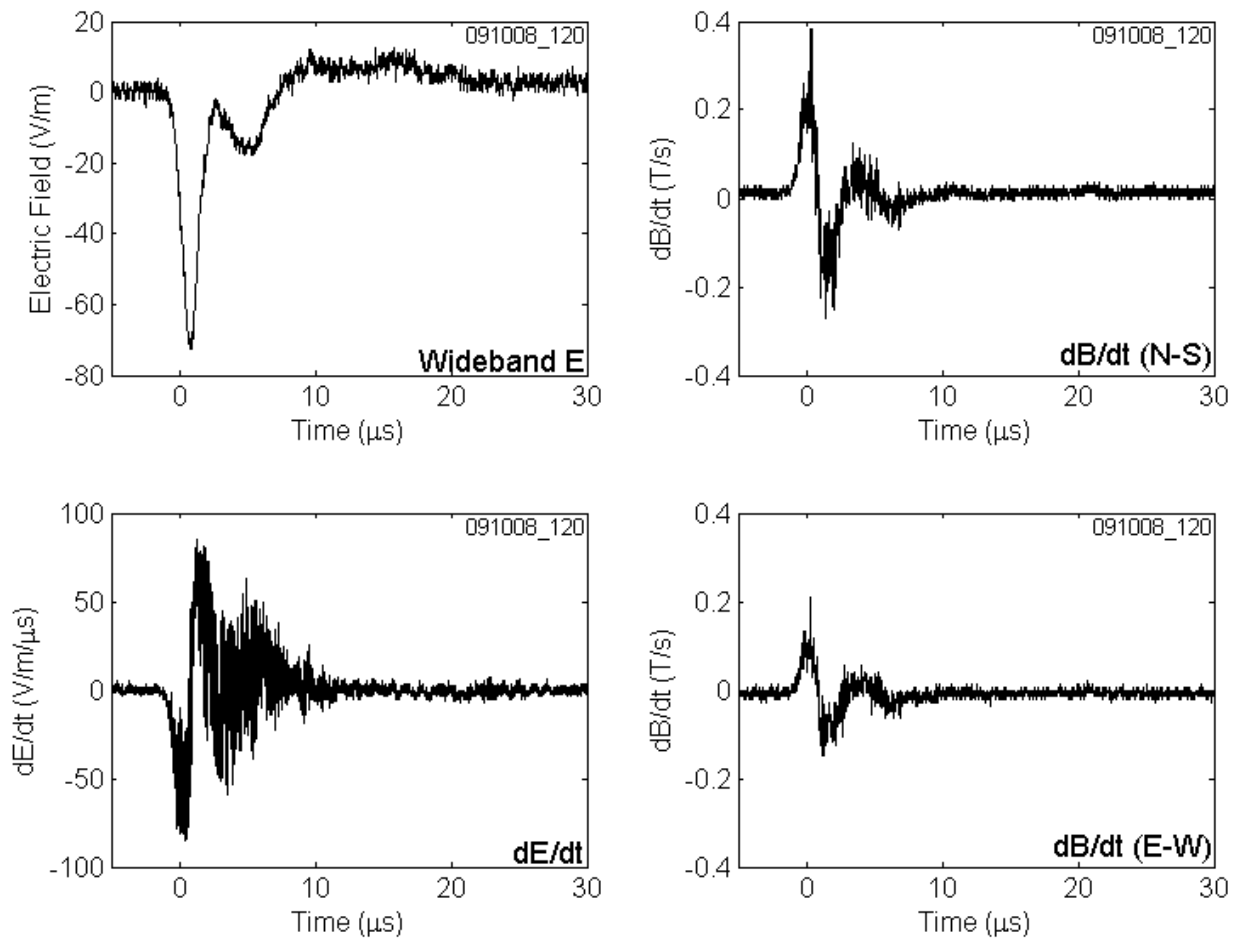


Figure A-33. CID 091008_120 shown on a 35 μs time scale. VHF is not available.

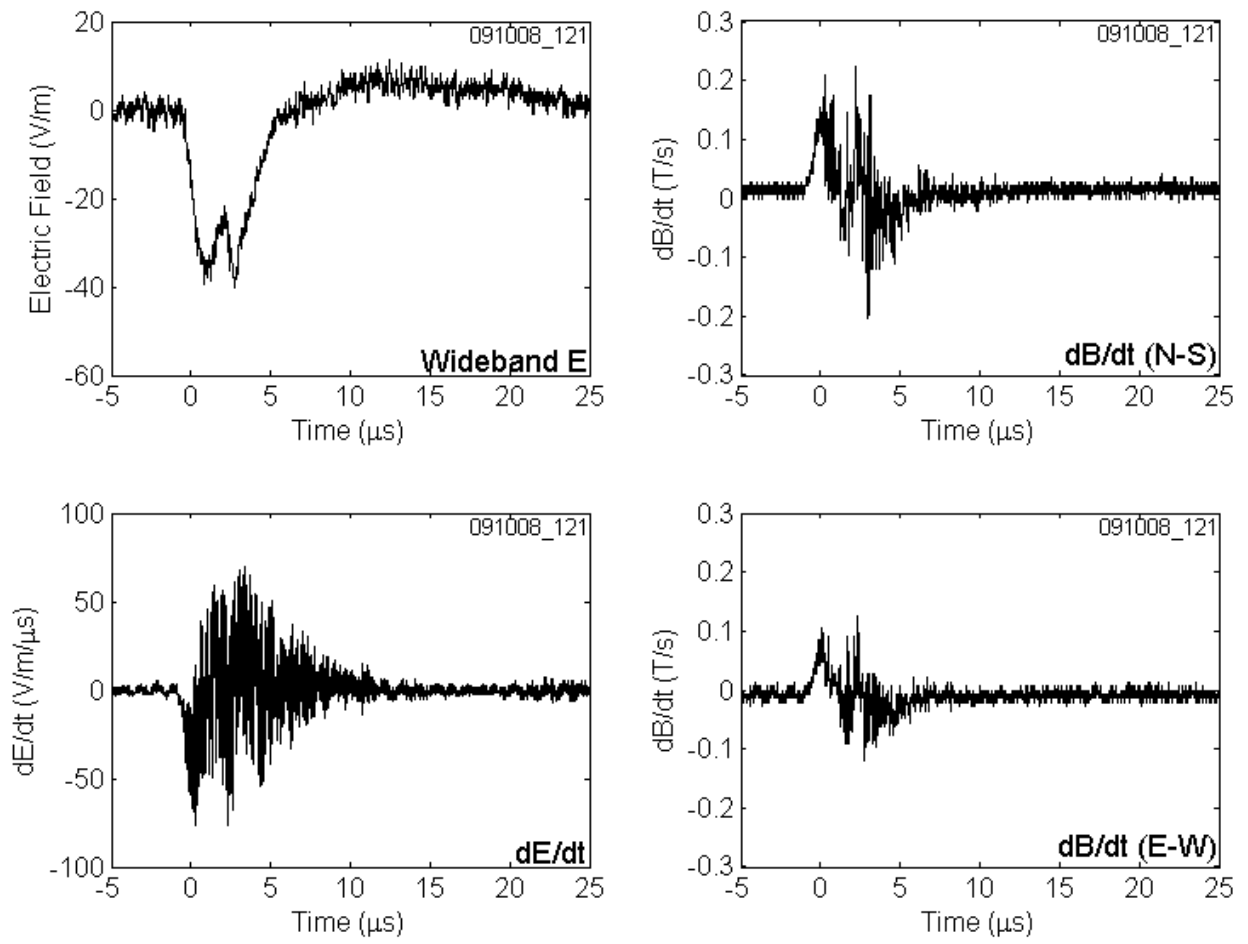


Figure A-34. CID 091008_121 shown on a 30 μs time scale. VHF is not available.

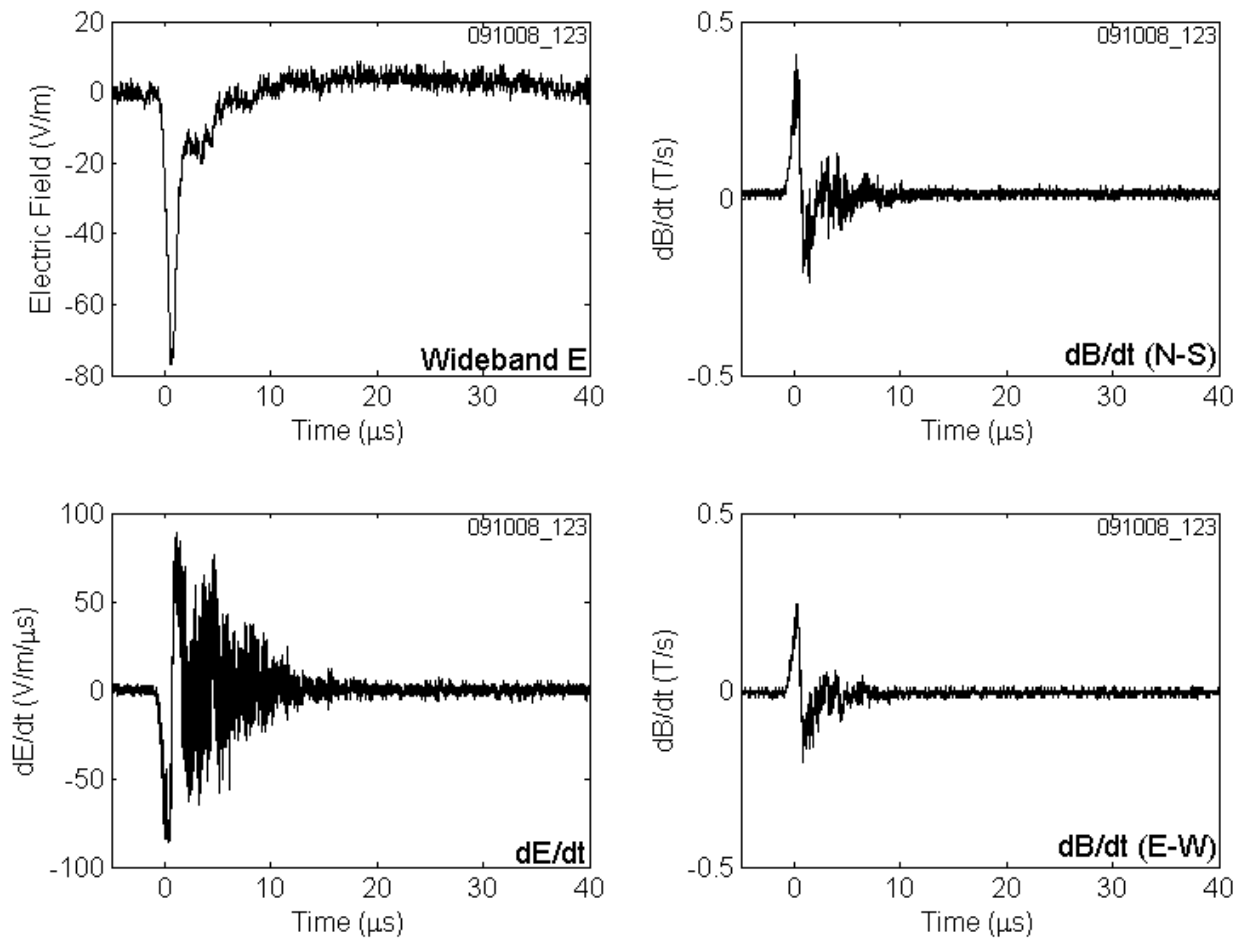


Figure A-35. CID 091008_123 shown on a 45 μs time scale. VHF is not available.

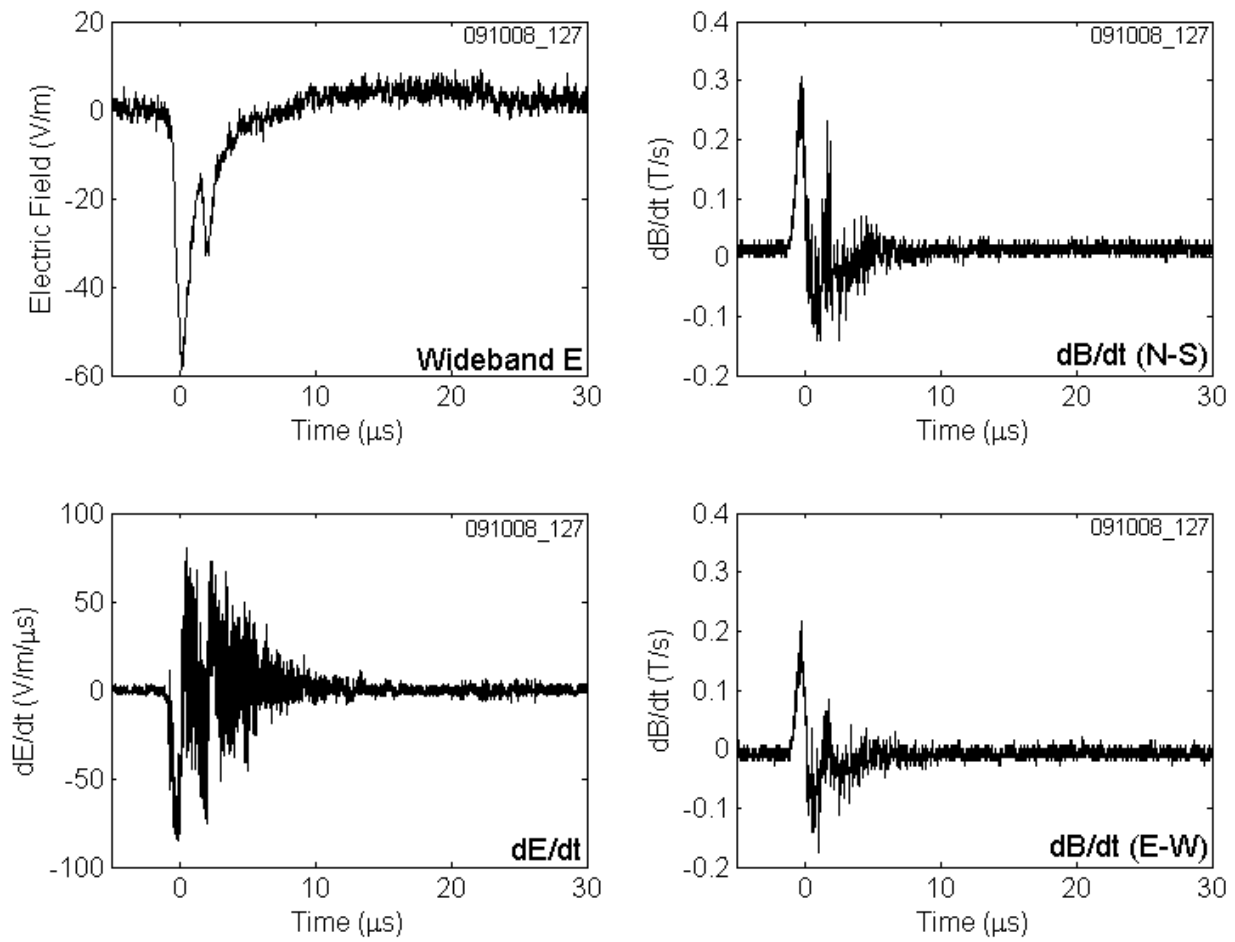


Figure A-36. CID 091008_127 shown on a 35 μs time scale. VHF is not available.

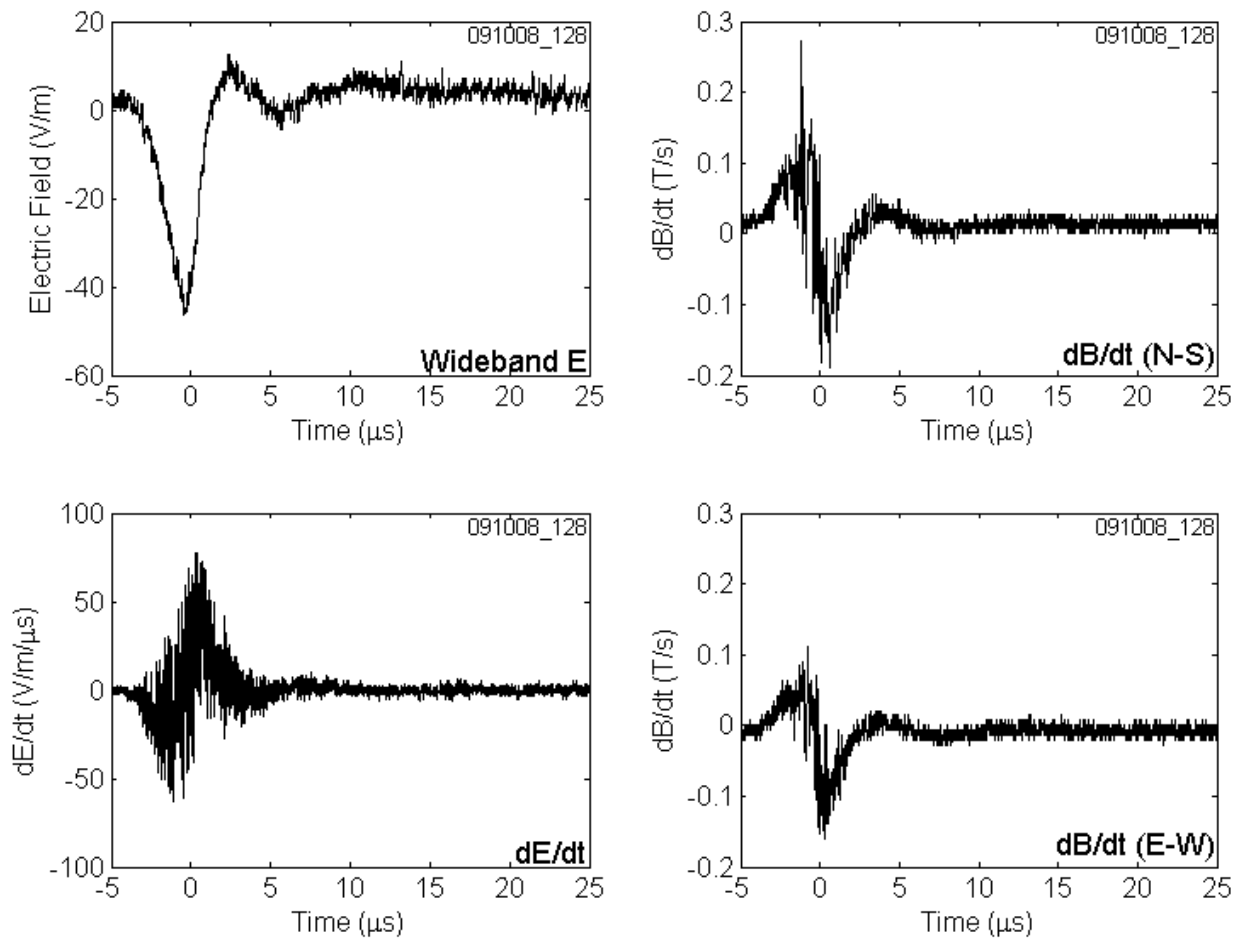


Figure A-37. CID 091008_128 shown on a 30 μs time scale. VHF is not available.

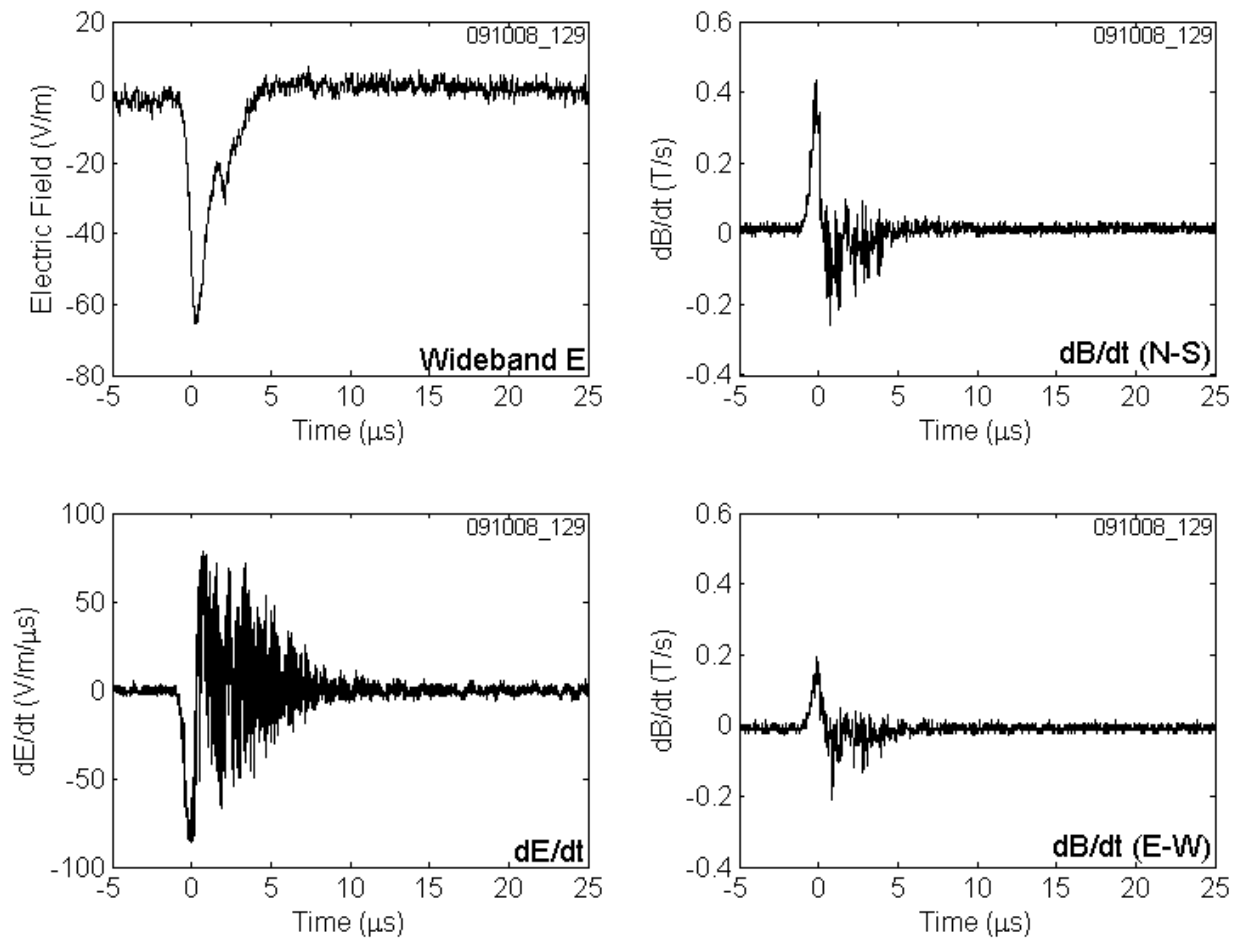


Figure A-38. CID 091008_129 shown on a 30 μs time scale. VHF is not available.

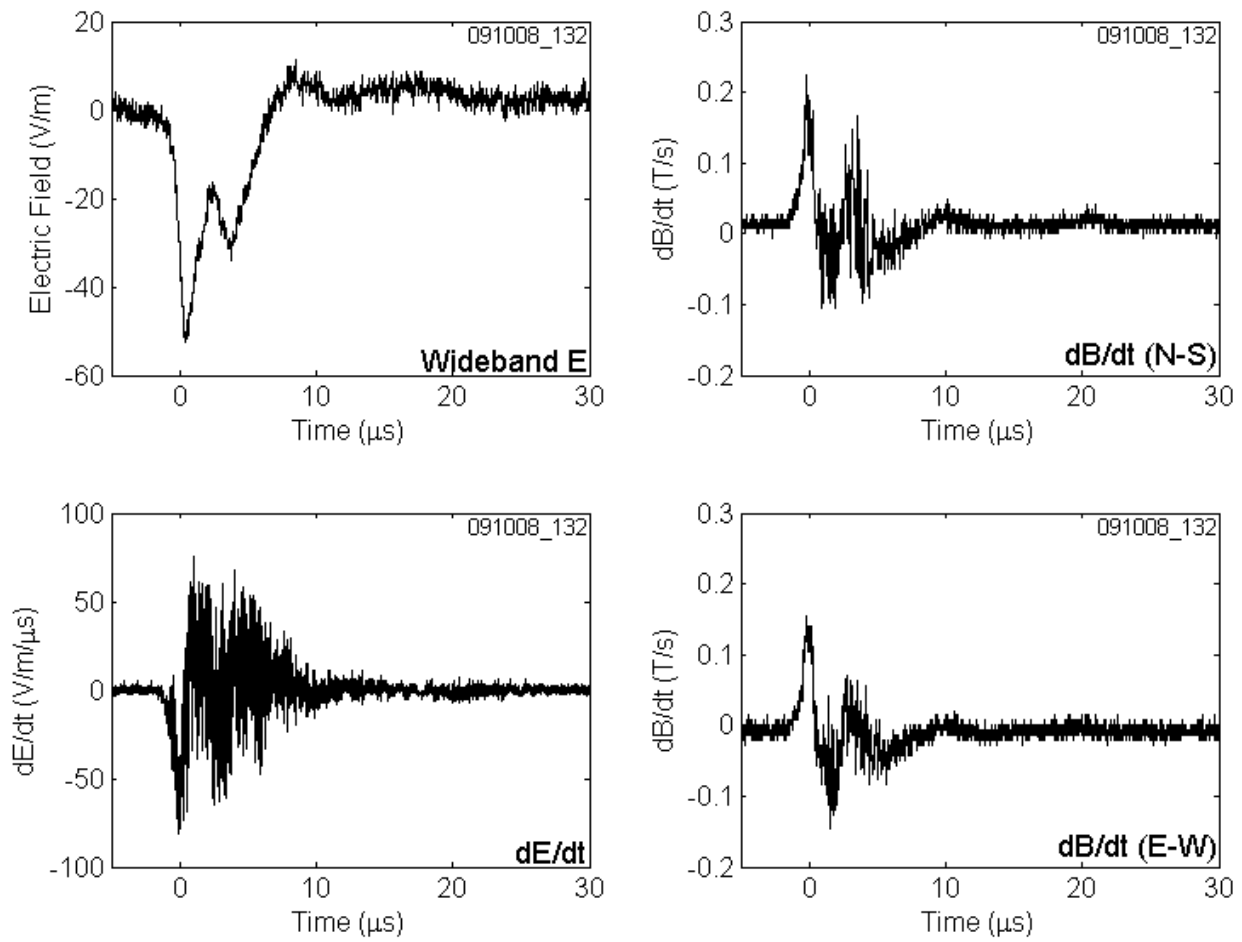


Figure A-39. CID 091008_132 shown on a 35 μs time scale. VHF is not available.

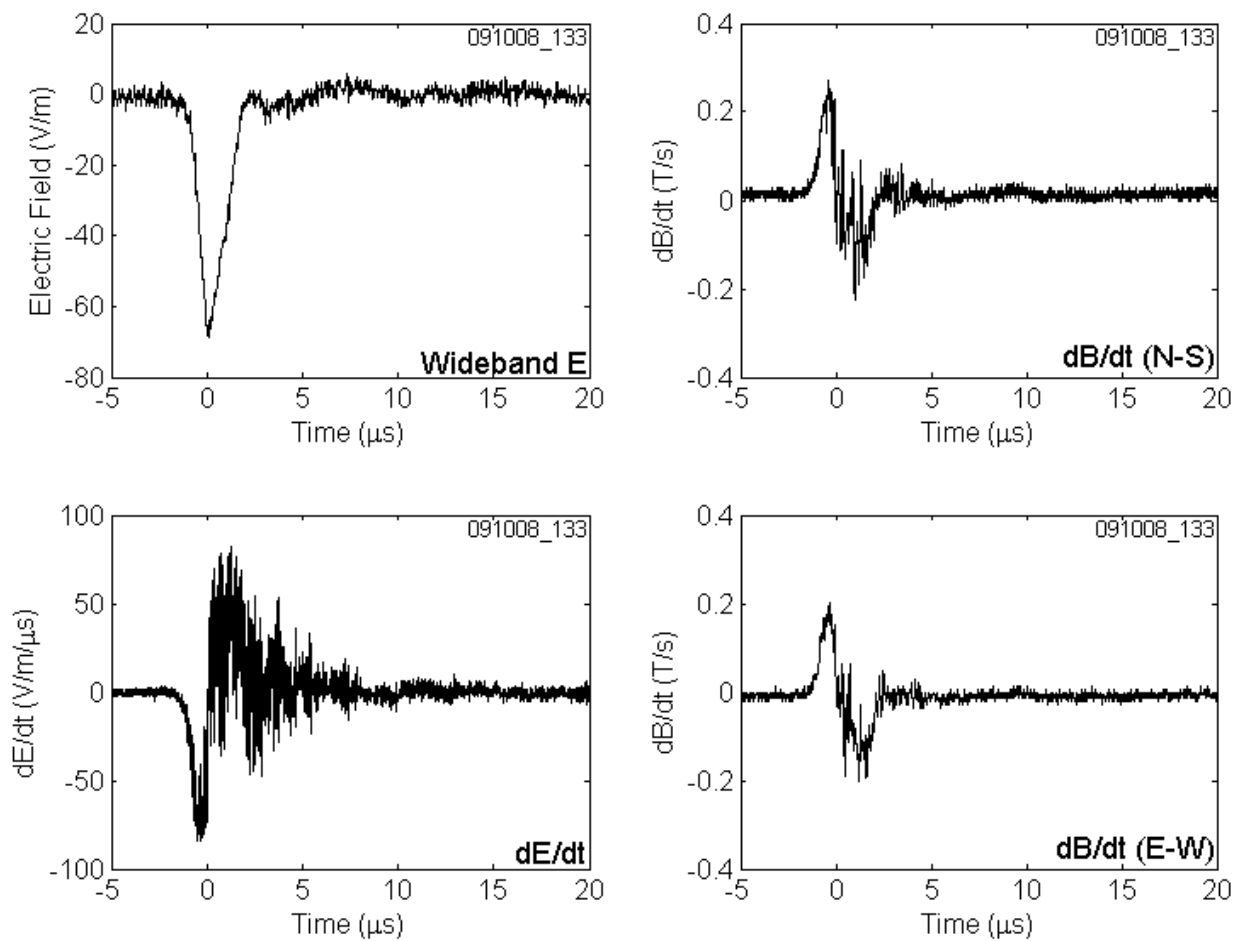


Figure A-40. CID 091008_133 shown on a 25 μs time scale. VHF is not available.

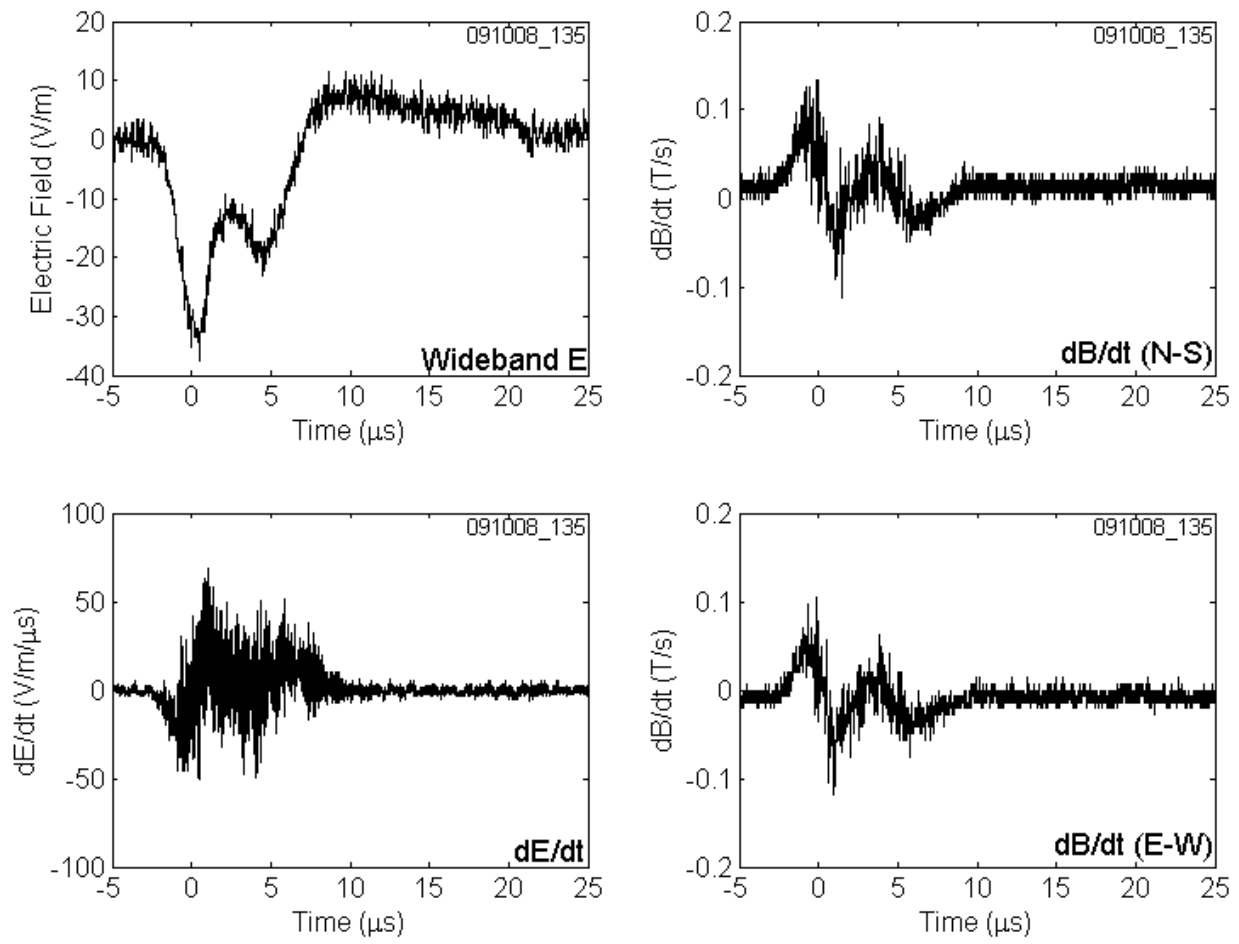


Figure A-41. CID 091008_135 shown on a 30 μs time scale. VHF is not available.

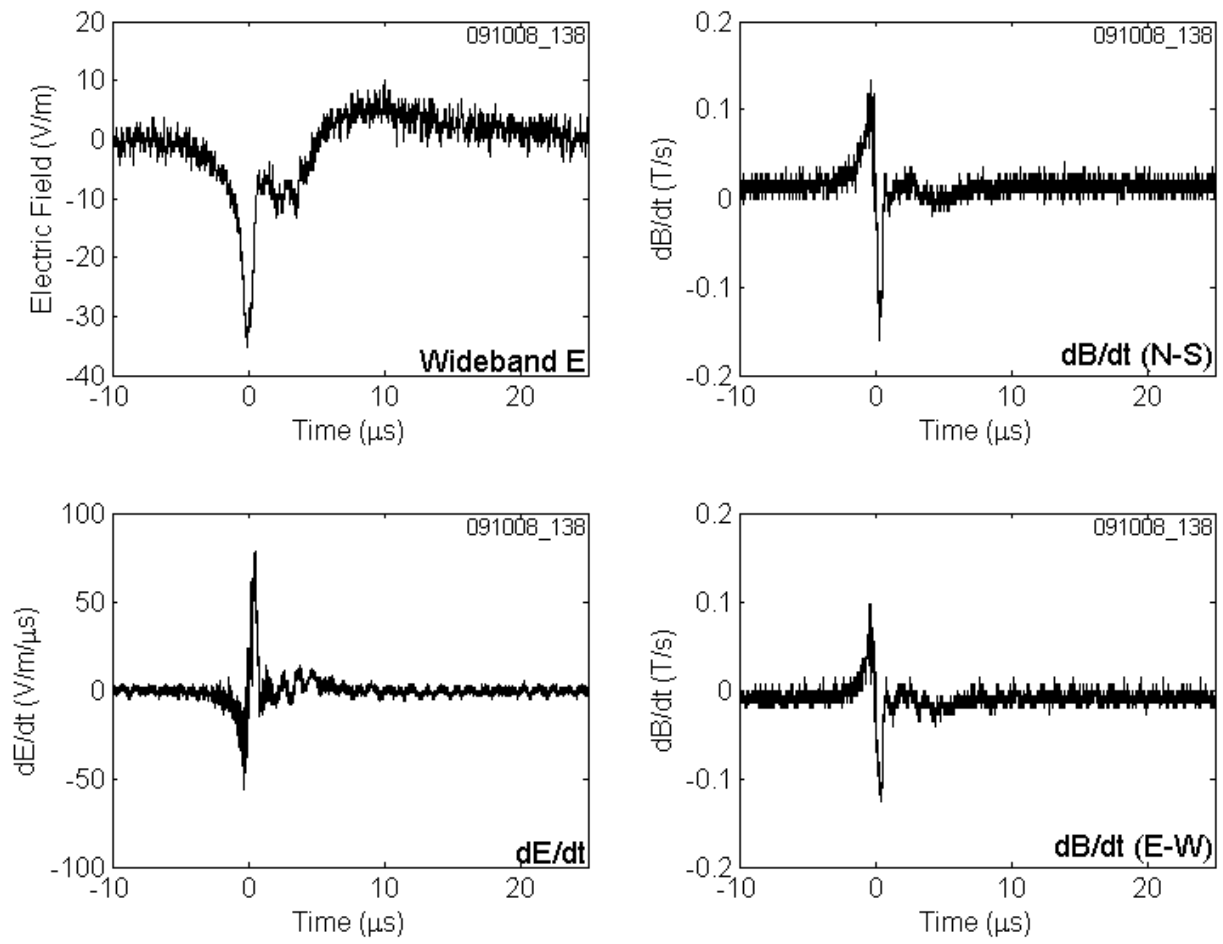


Figure A-42. CID 091008_138 shown on a 35 μs time scale. VHF is not available.

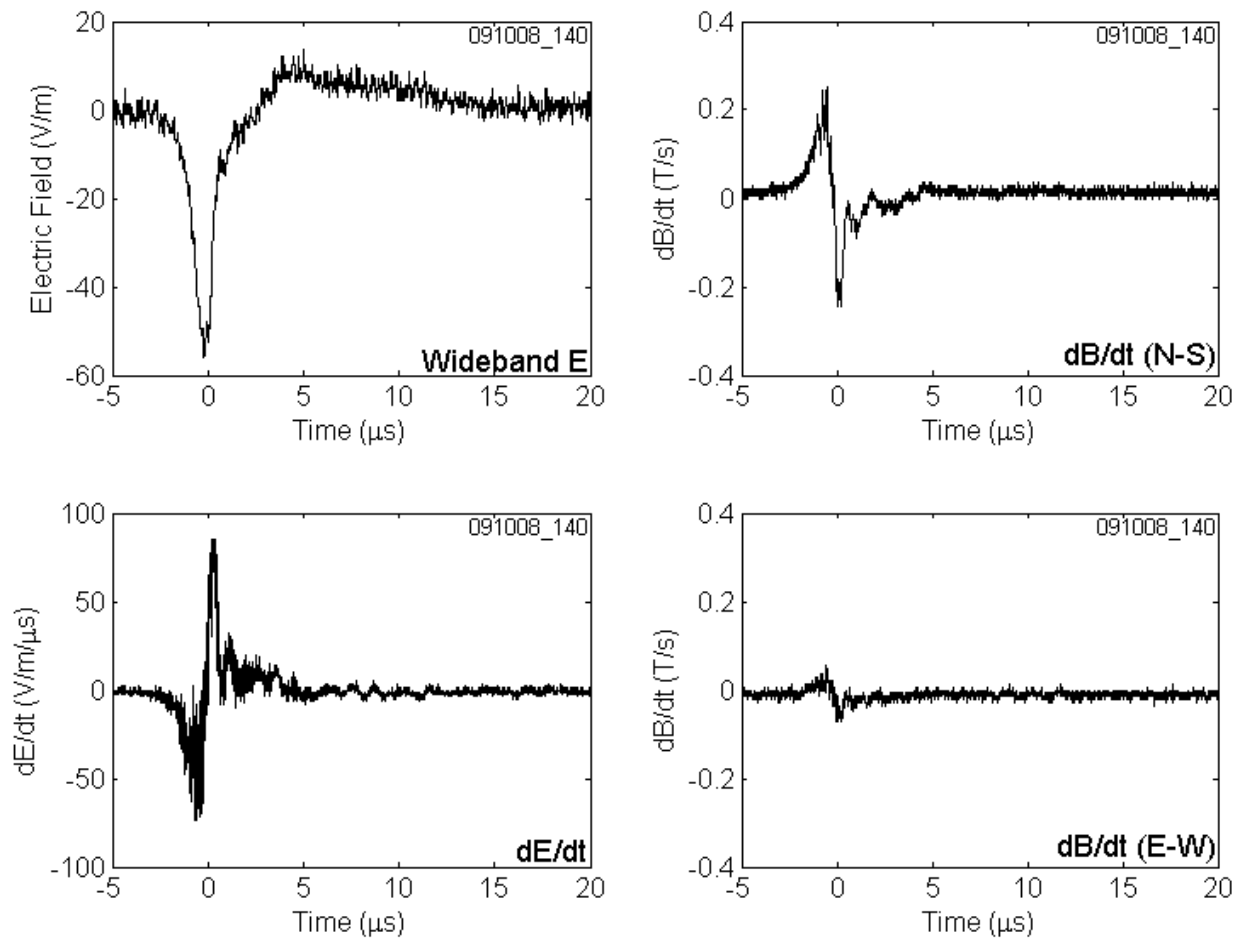


Figure A-43. CID 091008_140 shown on a 25 μs time scale. VHF is not available.

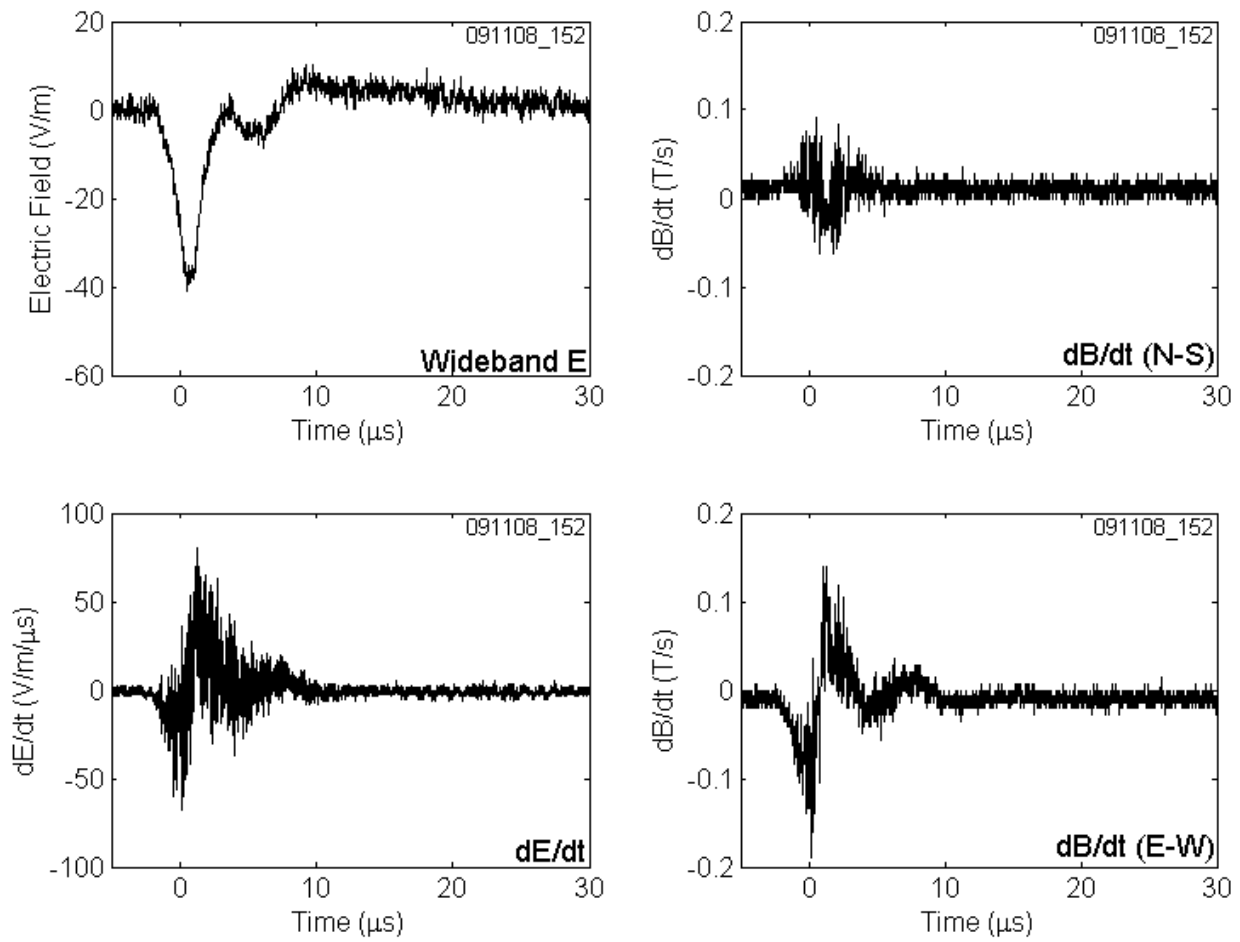


Figure A-44. CID 091108_152 shown on a 35 μs time scale. VHF is not available.

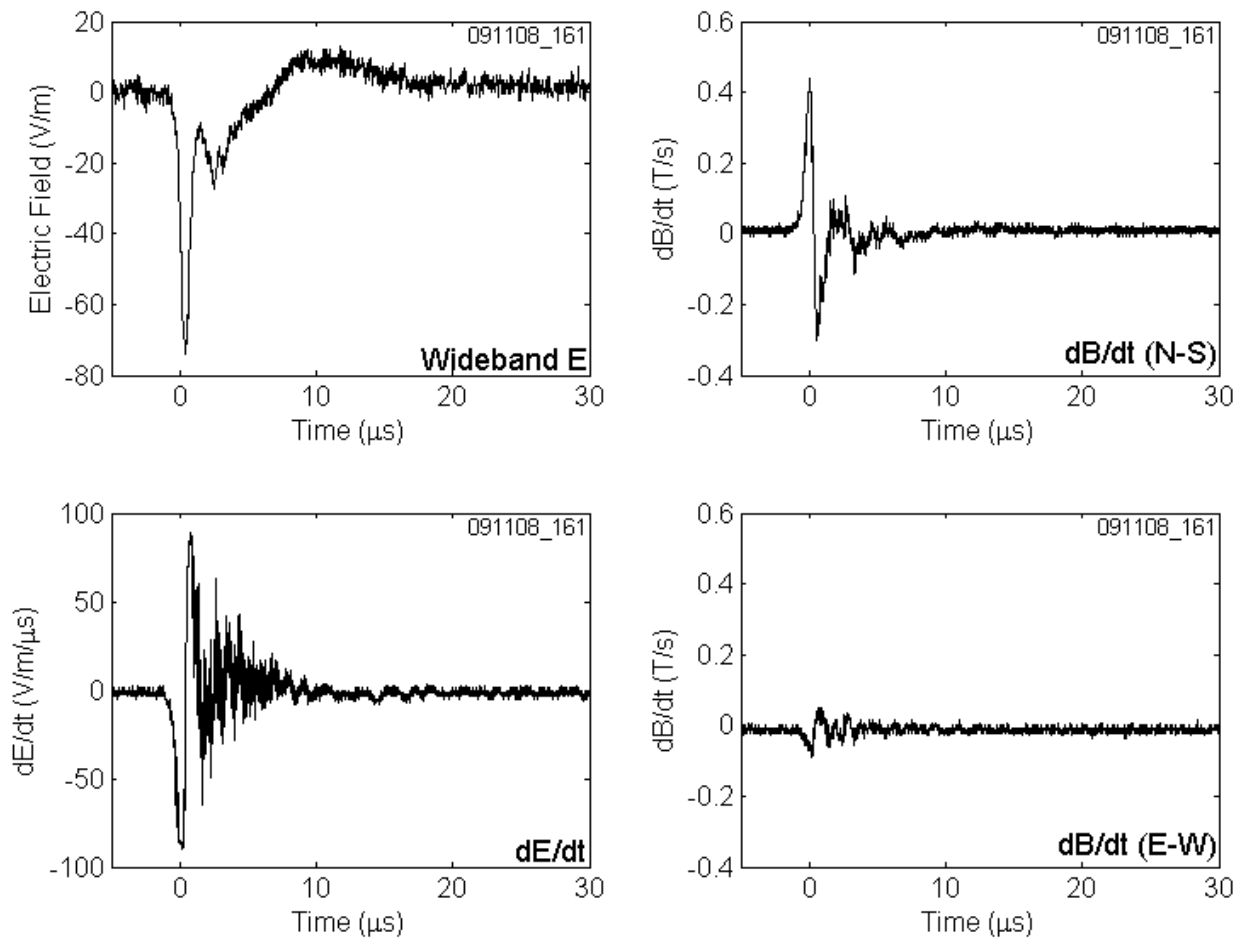


Figure A-45. CID 091108_161 shown on a 35 μs time scale. VHF is not available.

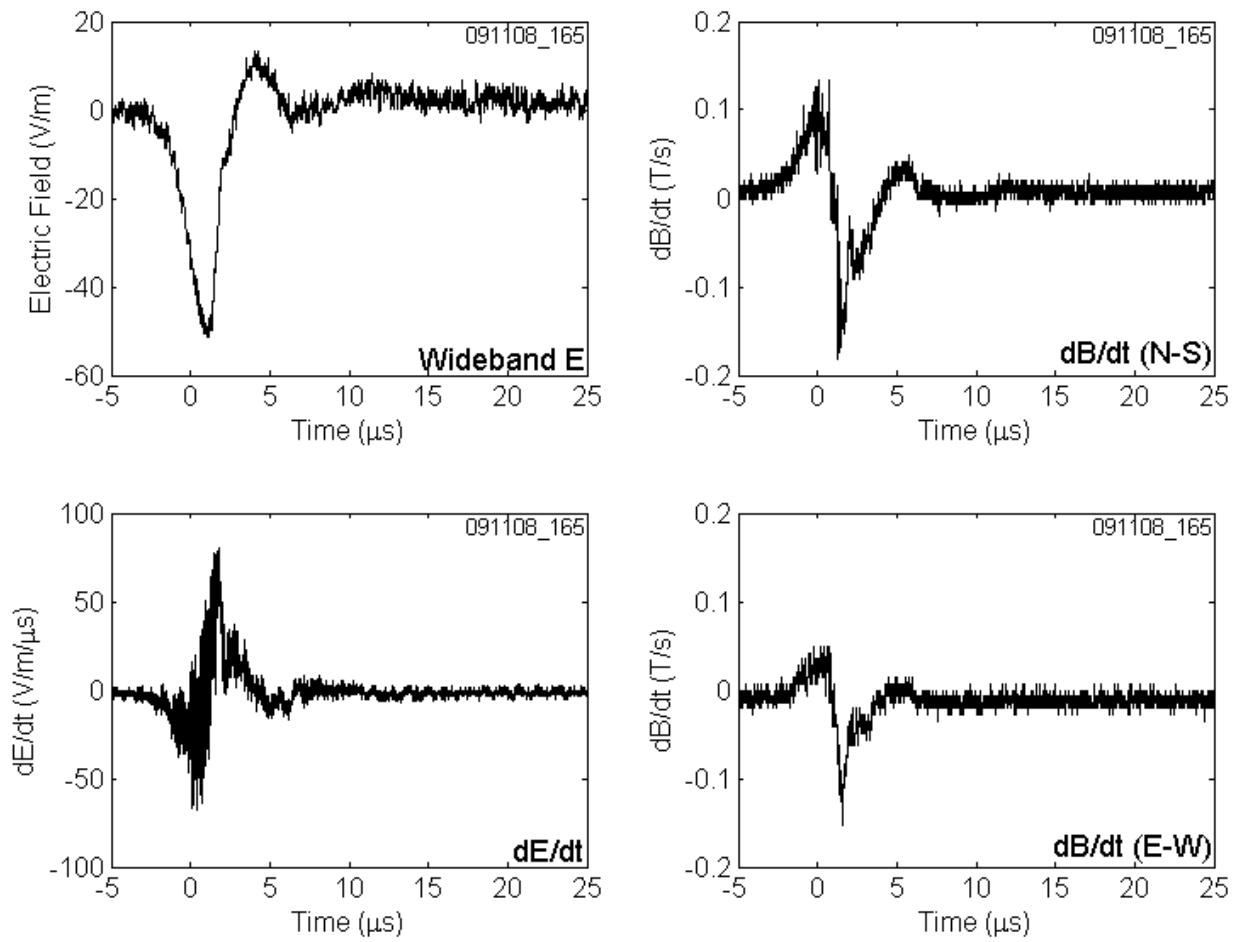


Figure A-46. CID 091108_165 shown on a 30 μs time scale. VHF is not available.

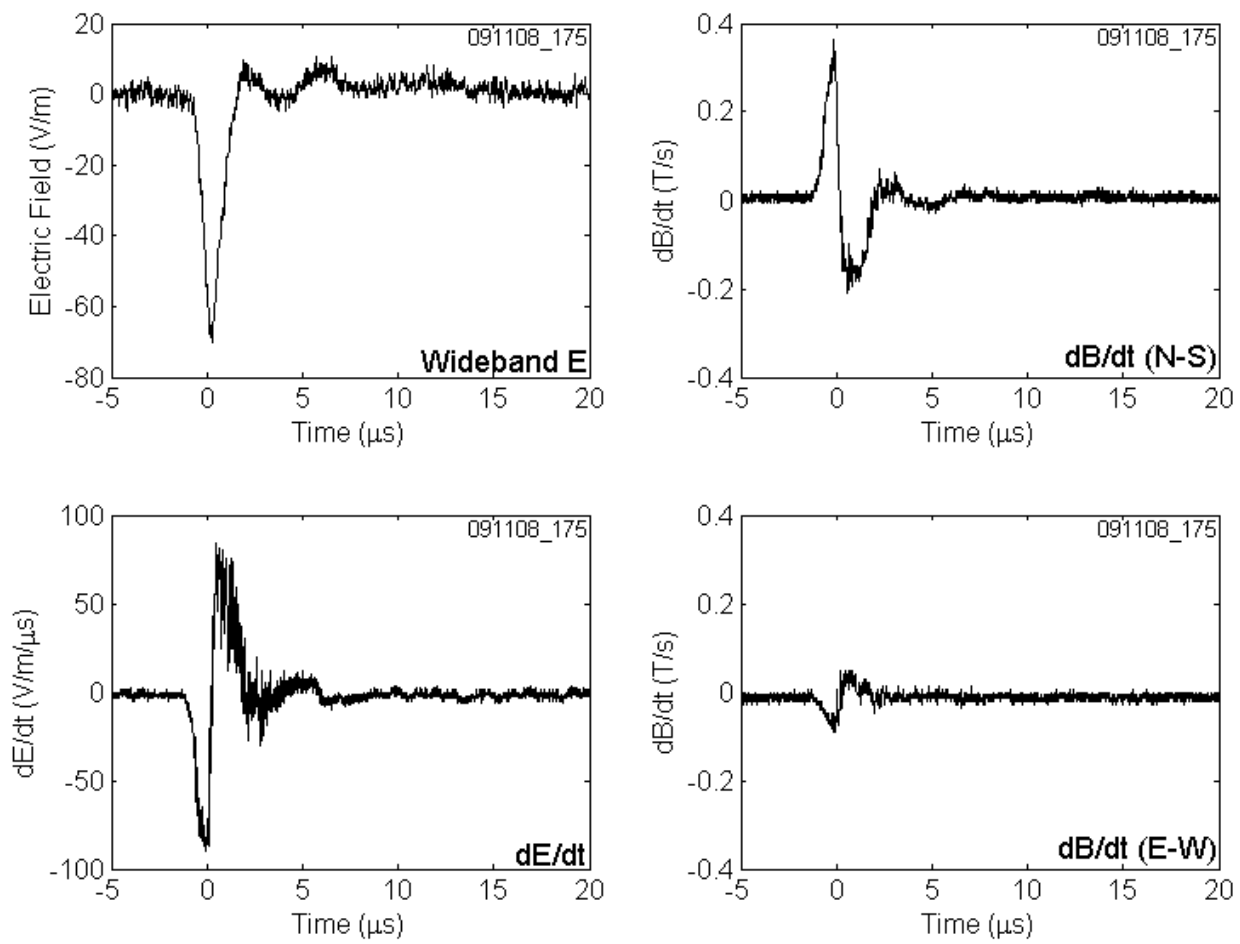


Figure A-47. CID 091108_175 shown on a 25 μs time scale. VHF is not available.

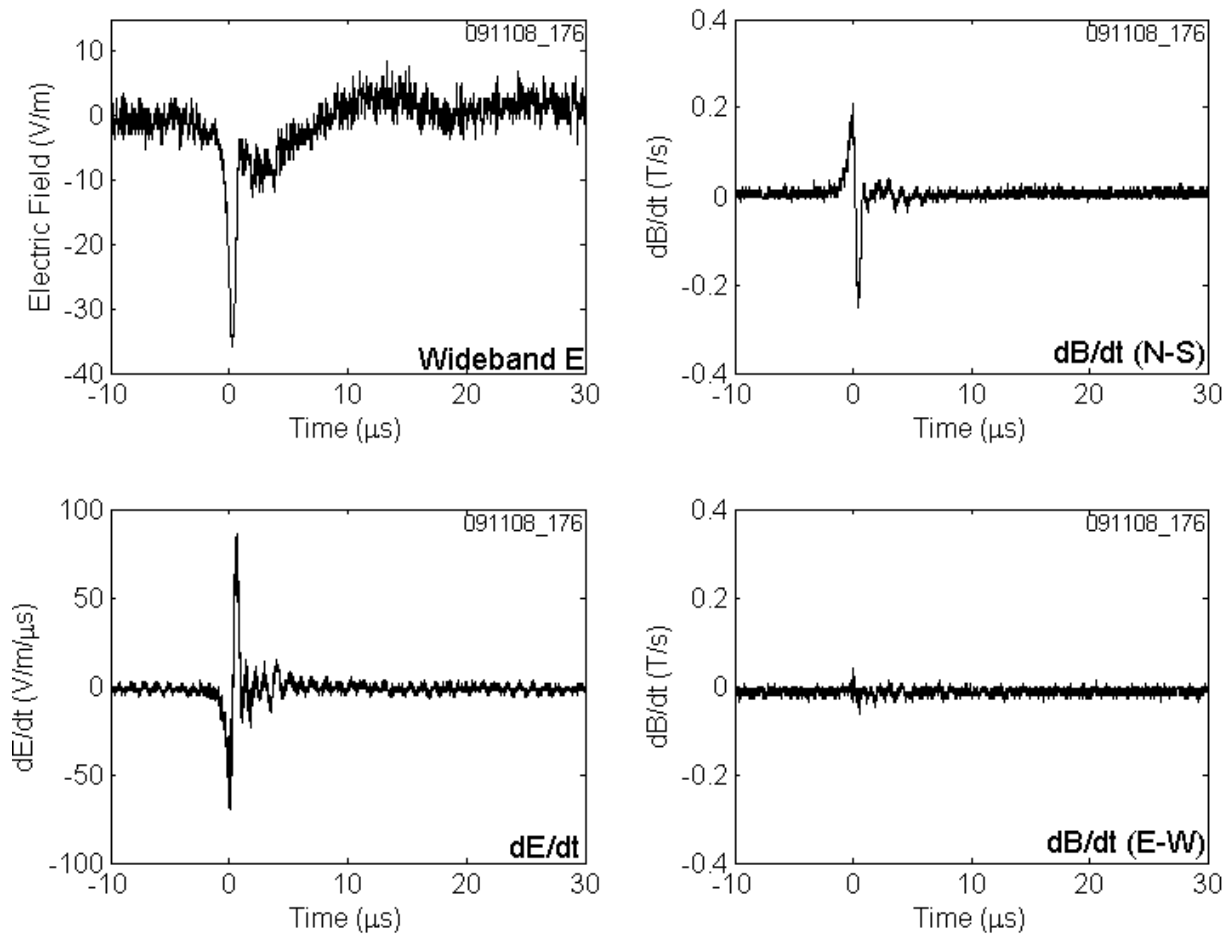


Figure A-48. CID 091108_176 shown on a 40 μs time scale. VHF is not available.

APPENDIX B
ELECTRIC FIELD DERIVATIVE WAVEFORMS OF 27 POSITIVE RETURN STROKES

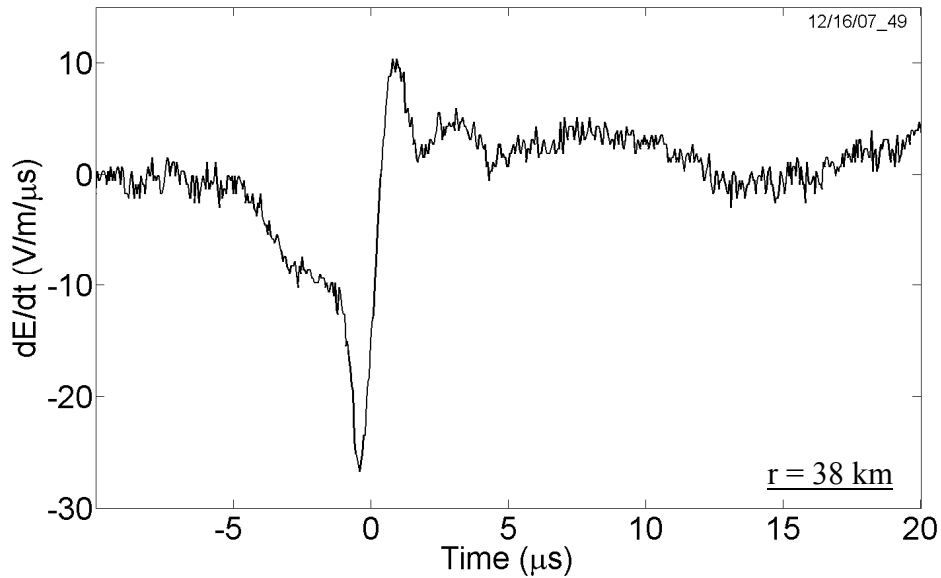


Figure B-1. Electric field derivative waveform of a positive return stroke that occurred on December 16, 2007, at 06:50:27 (UTC) at a distance of 38 km, shown on a 30- μ s time scale.

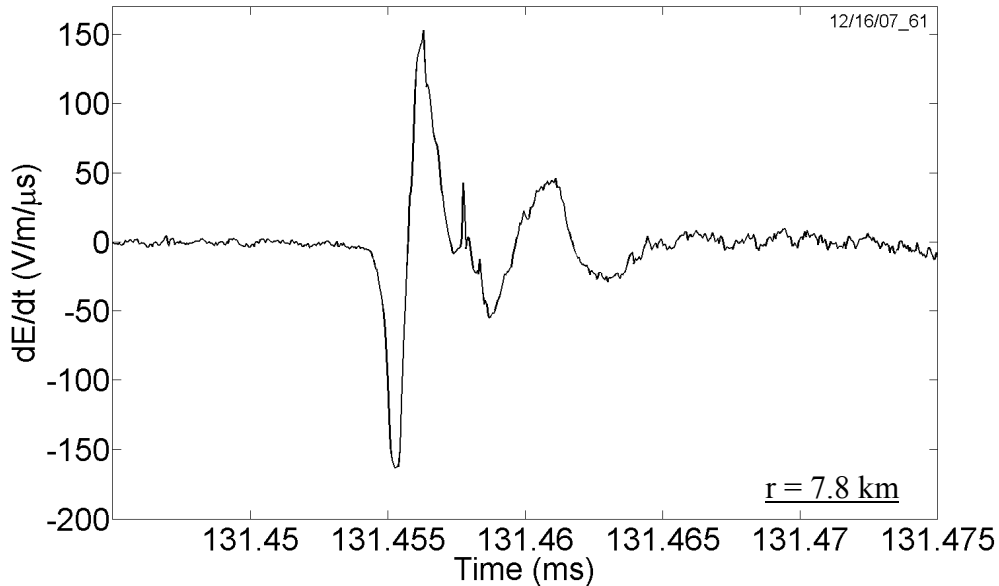


Figure B-2. Electric field derivative waveform of a positive return stroke that occurred on December 16, 2007, at 06:55:35 (UTC) at a distance of 7.8 km, shown on a 30- μ s time scale. Note that the initial (negative) peak may be slightly clipped (saturated), due to proximity of the flash to the measuring station.

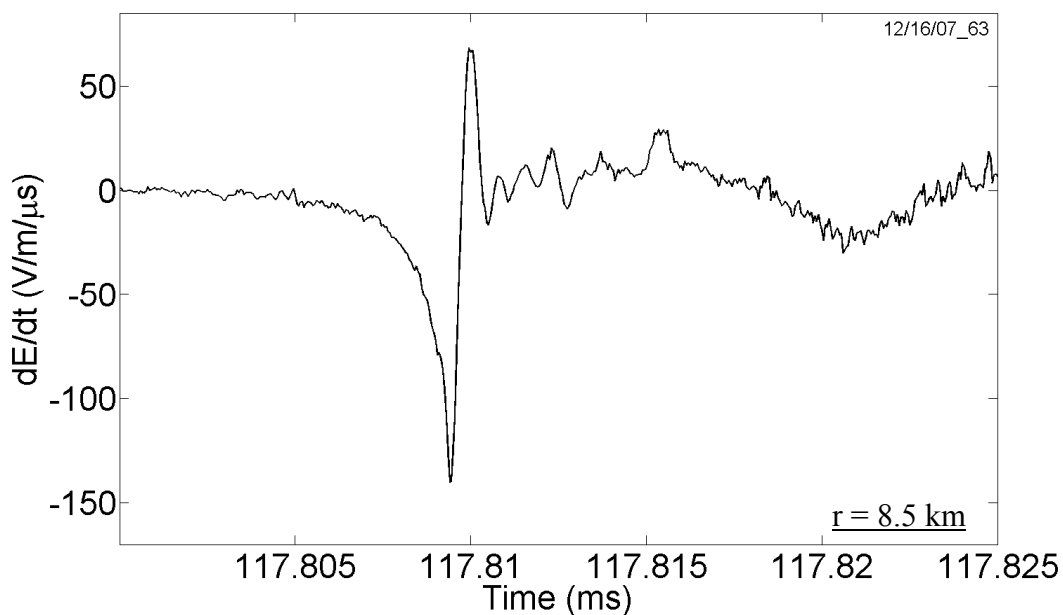


Figure B-3. Electric field derivative waveform of a positive return stroke that occurred on December 16, 2007, at 07:02:55 (UTC) at a distance of 8.5 km, shown on a 25- μ s time scale.

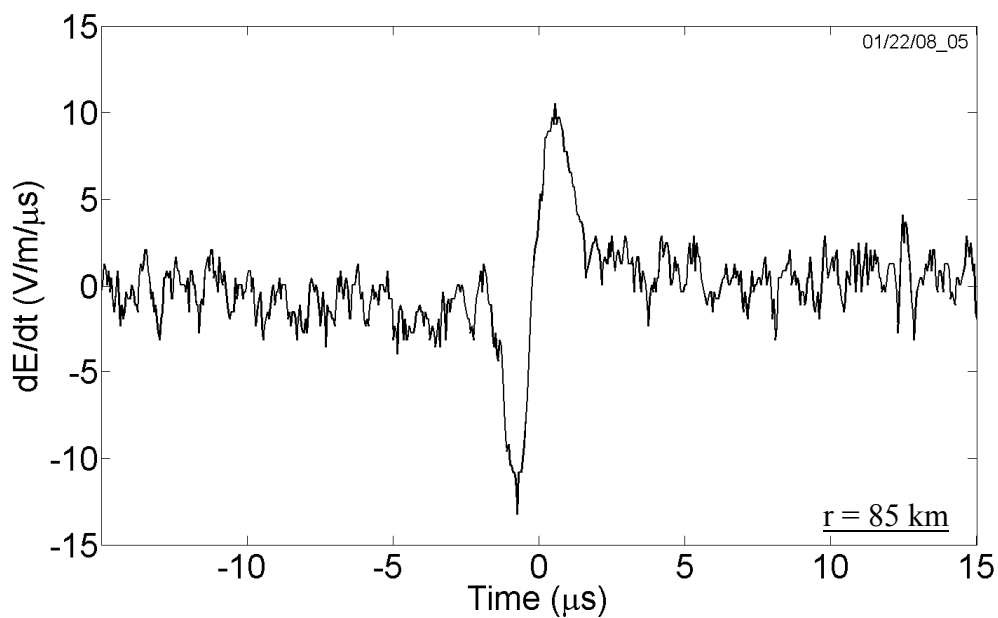


Figure B-4a. Electric field derivative waveform of the first return stroke (of a two-stroke positive flash) that occurred on January 22, 2008, at 23:55:10 (UTC) at a distance of 85 km, shown on a 30- μ s time scale.

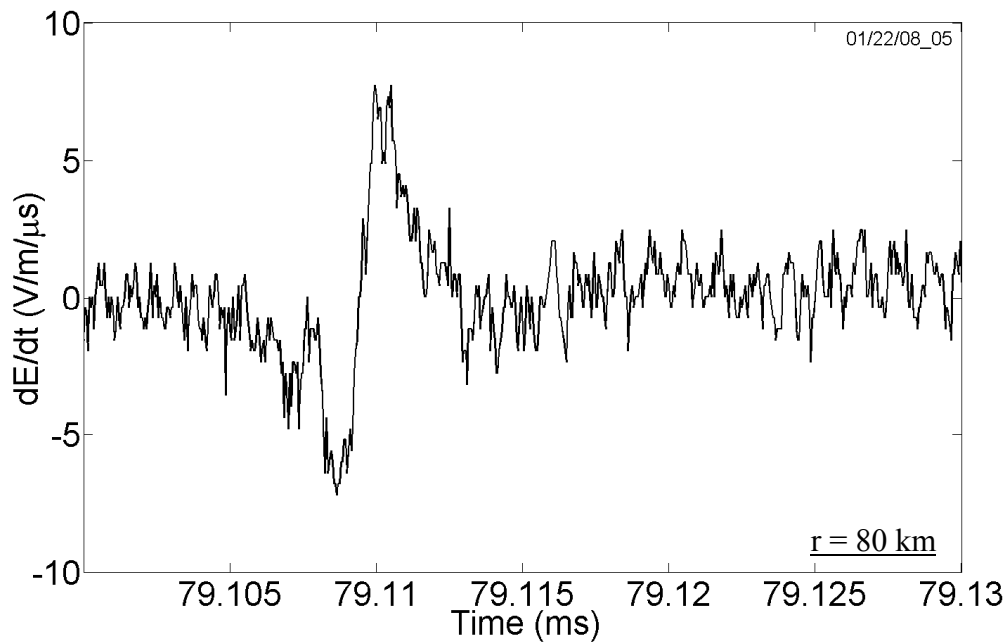


Figure B-4b. Electric field derivative waveform of the second return stroke (of a two-stroke positive flash) that occurred on January 22, 2008, at 23:55:10 (UTC) at a distance of 80 km, shown on a 30- μ s time scale.

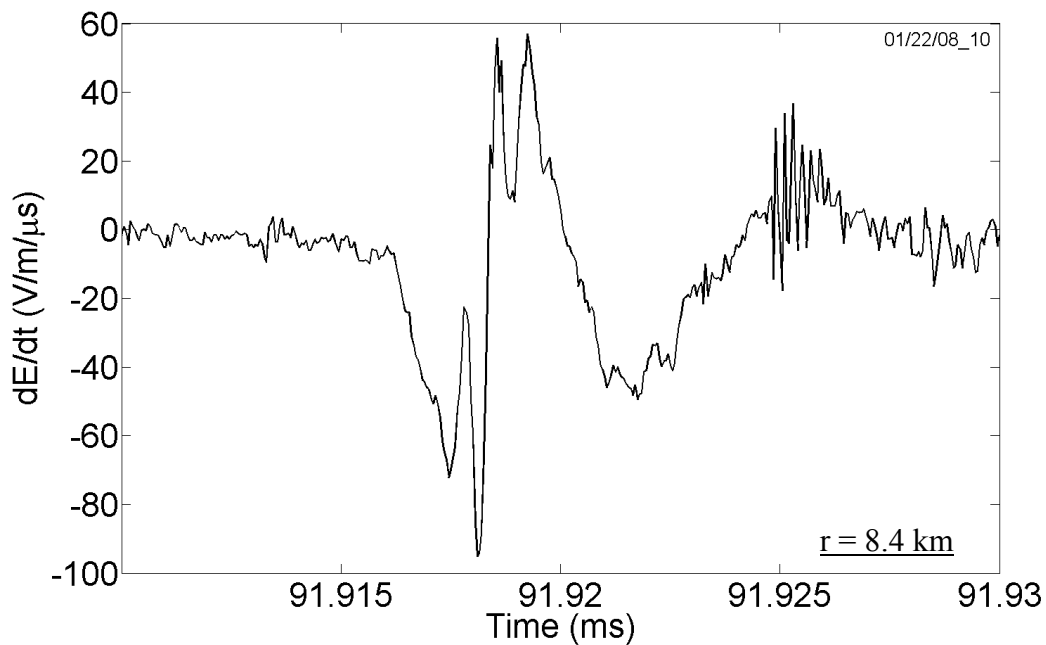


Figure B-5. Electric field derivative waveform of a positive return stroke that occurred on January 23, 2008, at 02:35:47 (UTC) at a distance of 8.4 km, shown on a 20- μ s time scale.

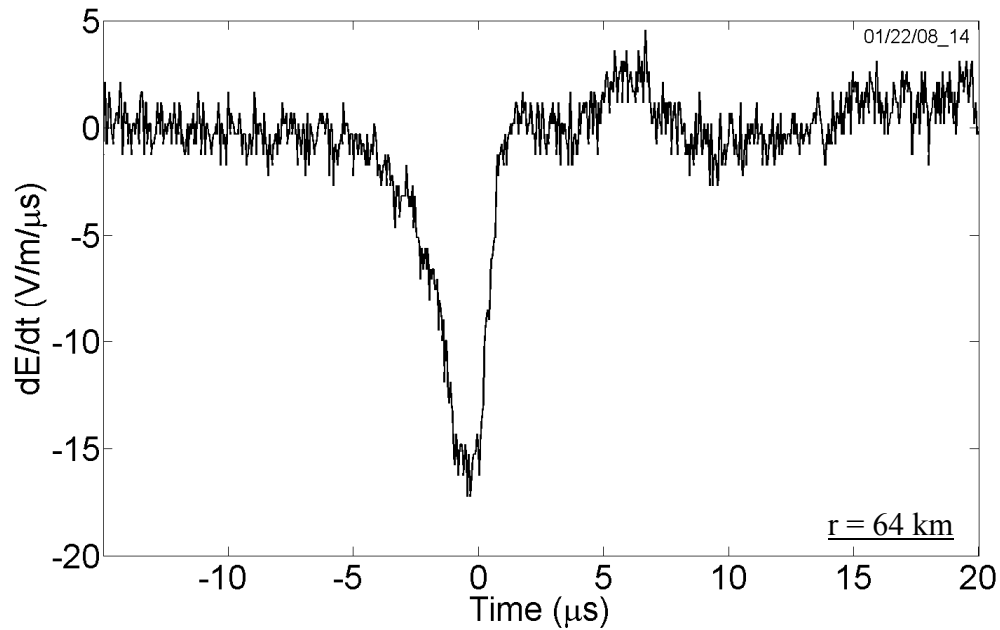


Figure B-6. Electric field derivative waveform of a positive return stroke that occurred on January 23, 2008, at 02:56:28 (UTC) at a distance of 64 km, shown on a 35- μ s time scale.

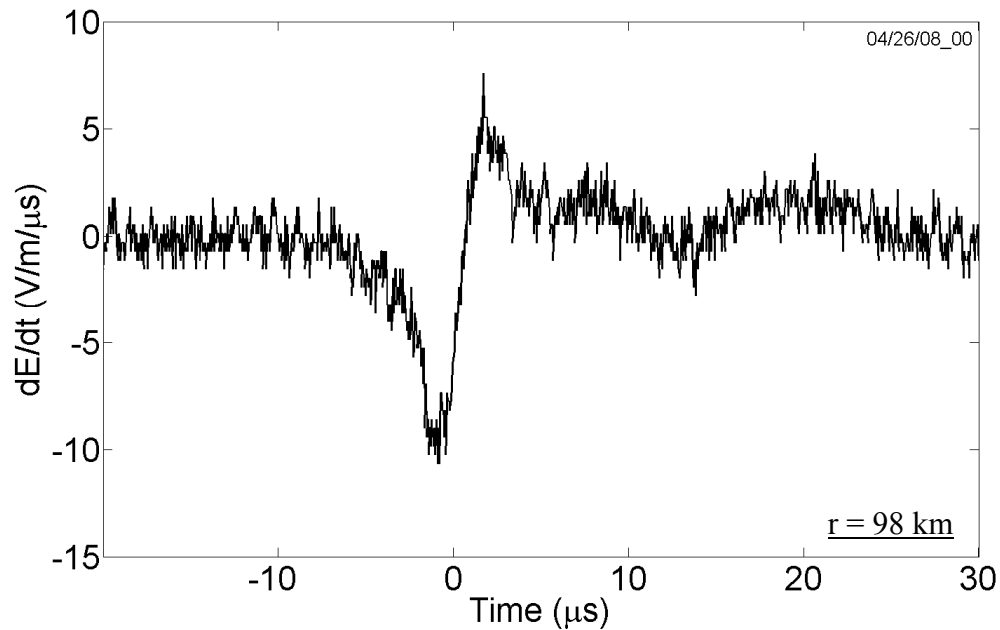


Figure B-7. Electric field derivative waveform of a positive return stroke that occurred on April 26, 2008, at 22.16.22 (UTC) at a distance of 98 km, shown on a 40- μ s time scale.

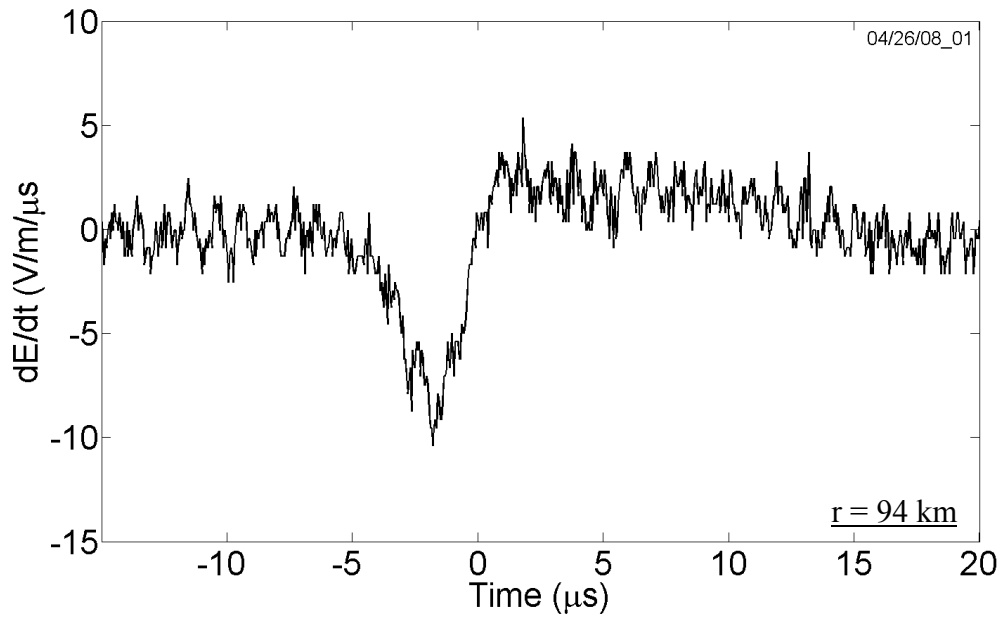


Figure B-8. Electric field derivative waveform of a positive return stroke that occurred on April 26, 2008, at 22:26:10 (UTC) at a distance of 94 km, shown on a 35- μ s time scale.

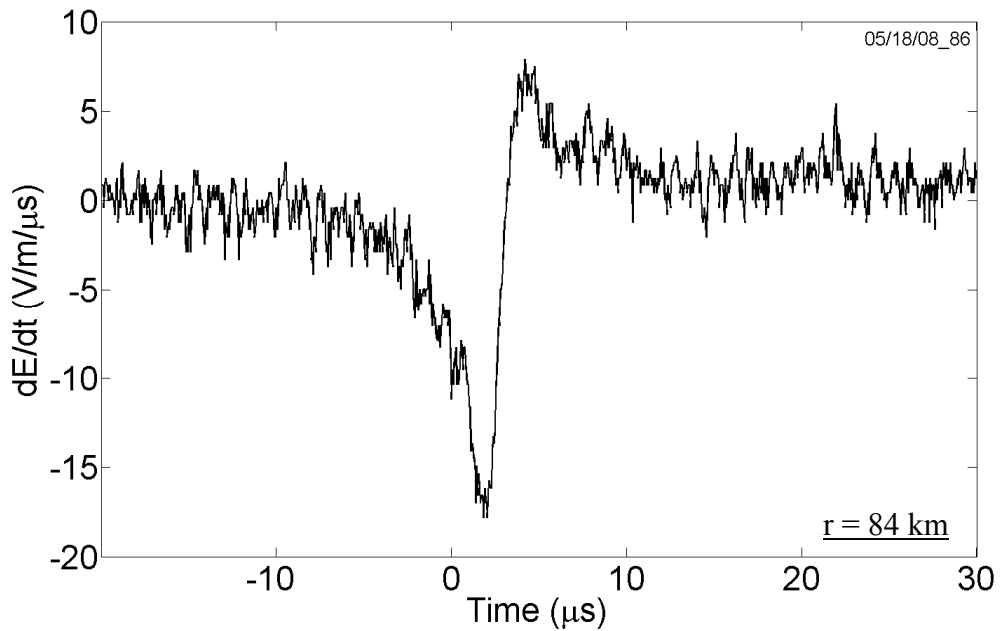


Figure B-9. Electric field derivative waveform of a positive return stroke that occurred on May 18, 2008, at 17:27:12 (UTC) at a distance of 84 km, shown on a 40- μ s time scale.

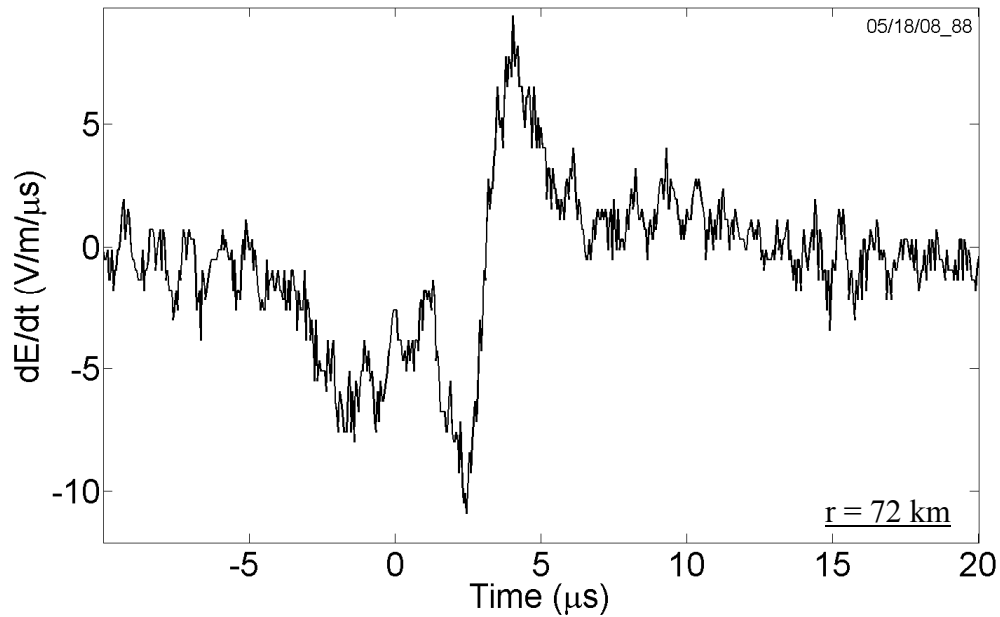


Figure B-10. Electric field derivative waveform of a positive return stroke that occurred on May 18, 2008, at 19:07:38 (UTC) at a distance of 72 km, shown on a 30- μ s time scale.

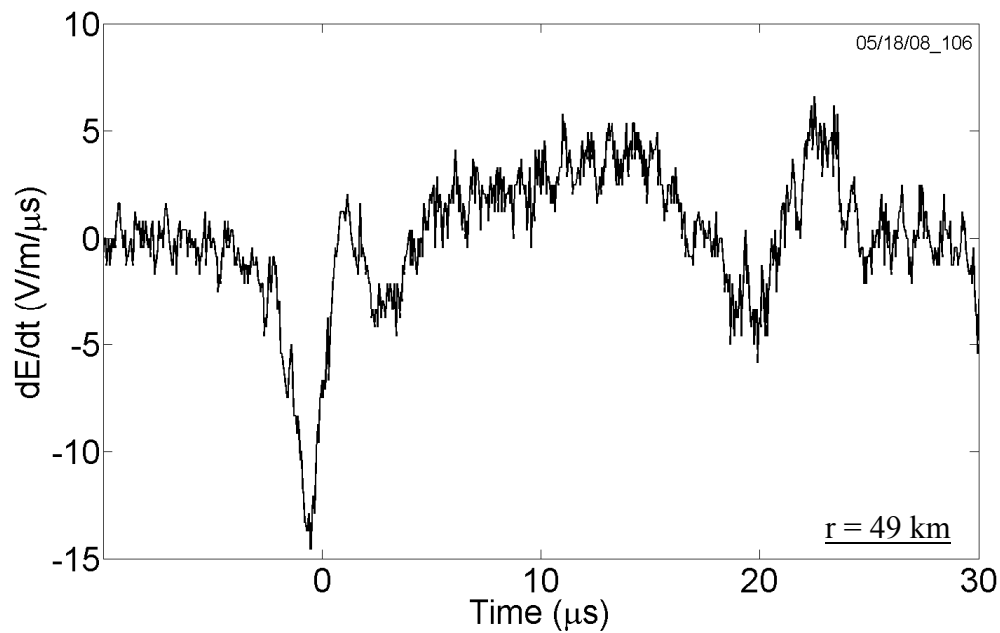


Figure B-11. Electric field derivative waveform of a positive return stroke that occurred on May 18, 2008, at 21:25:29 (UTC) at a distance of 49 km, shown on a 40- μ s time scale.

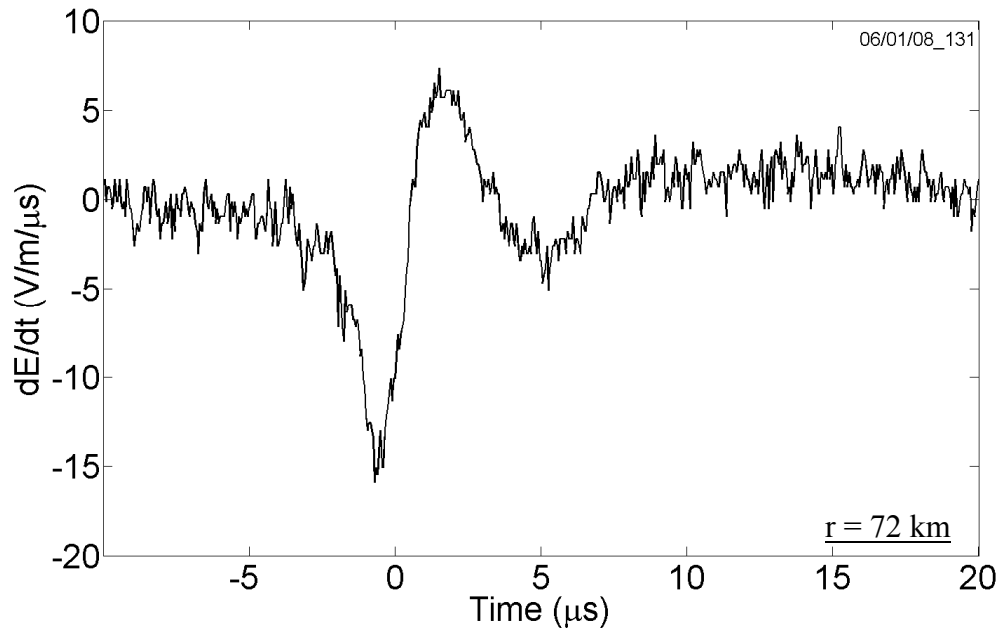


Figure B-12. Electric field derivative waveform of a positive return stroke that occurred on June 1, 2008, at 19:35:47 (UTC) at a distance of 72 km, shown on a 30- μ s time scale.

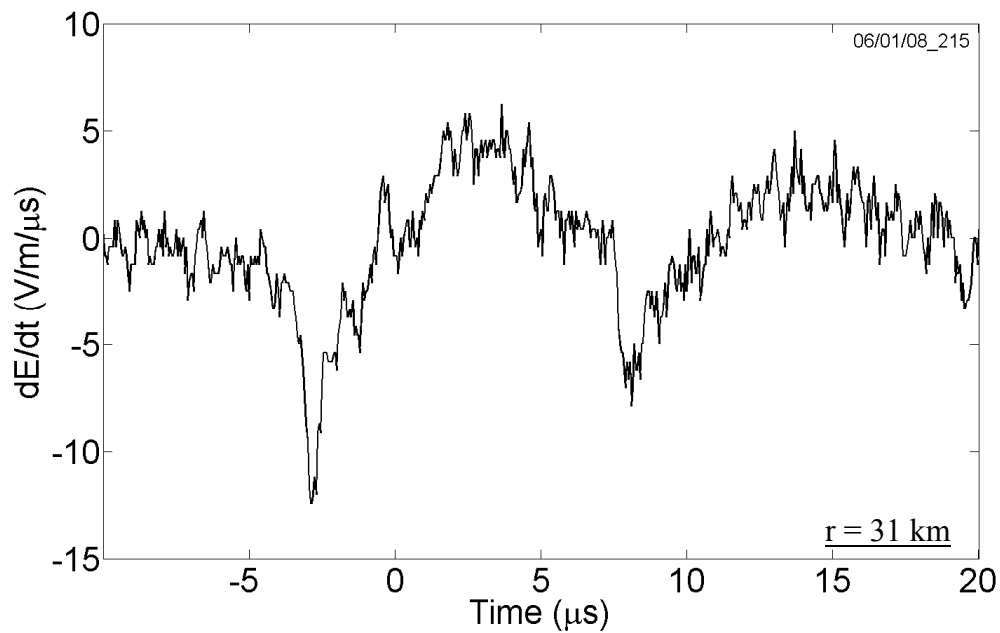


Figure B-13. Electric field derivative waveform of a positive return stroke that occurred on June 1, 2008, at 21:23:41 (UTC) at a distance of 31 km, shown on a 30- μ s time scale.

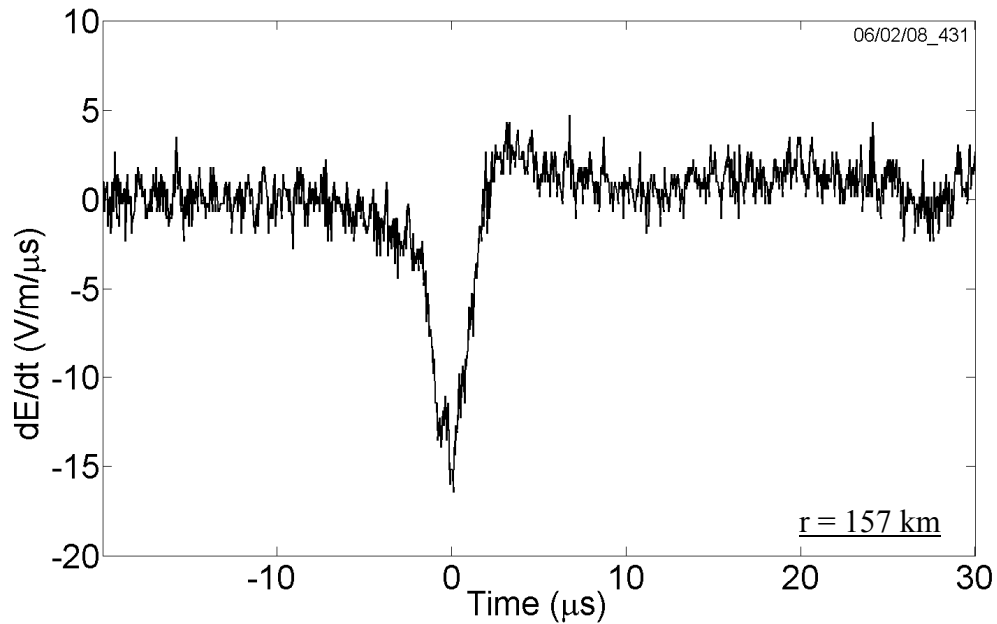


Figure B-14a. Electric field derivative waveform of the first return stroke (of a two-stroke positive flash), that occurred on June 2, 2008, at 23:06:25 (UTC) at a distance of 157 km, shown on a 50- μ s time scale.

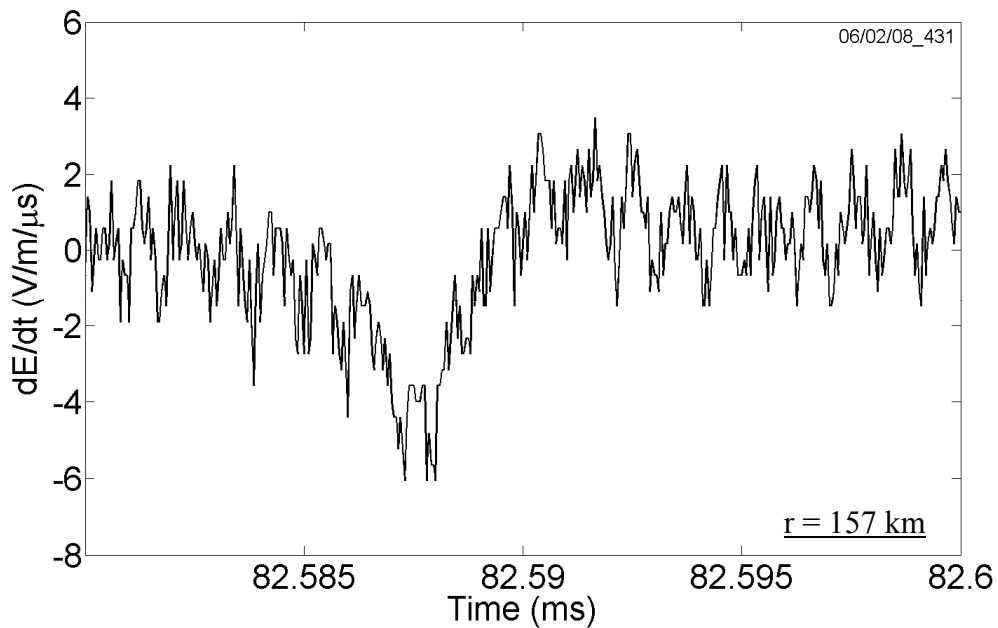


Figure B-14b. Electric field derivative waveform of the second return stroke (of a two-stroke positive flash), that occurred on June 2, 2008, at 23:06:25 (UTC) at a distance of 157 km, shown on a 20- μ s time scale.

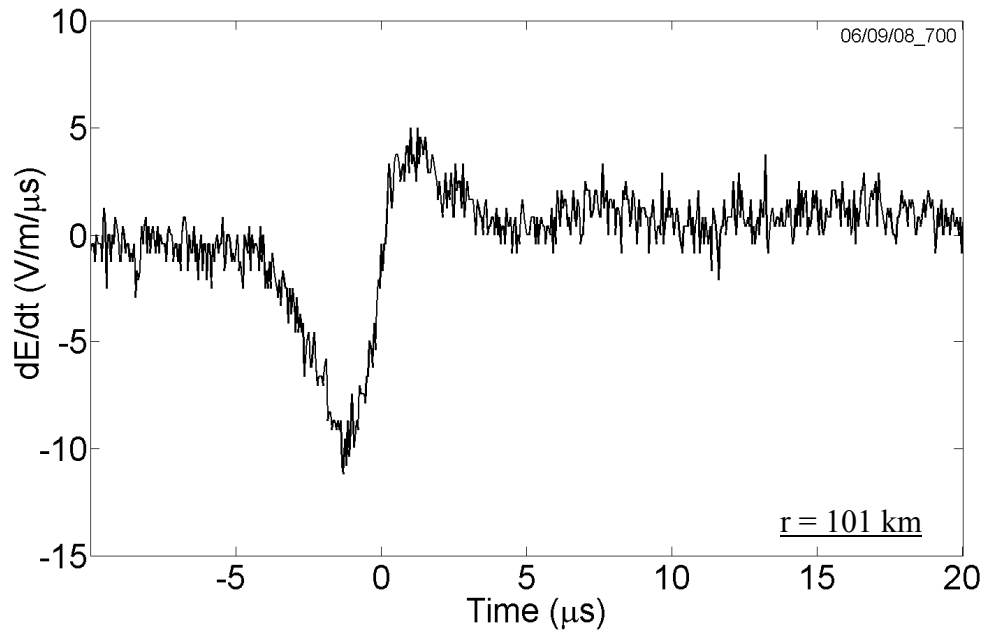


Figure B-15. Electric field derivative waveform of a positive return stroke that occurred on June 9, 2008, at 20:27:05 (UTC) at a distance of 101 km, shown on a 30- μ s time scale.

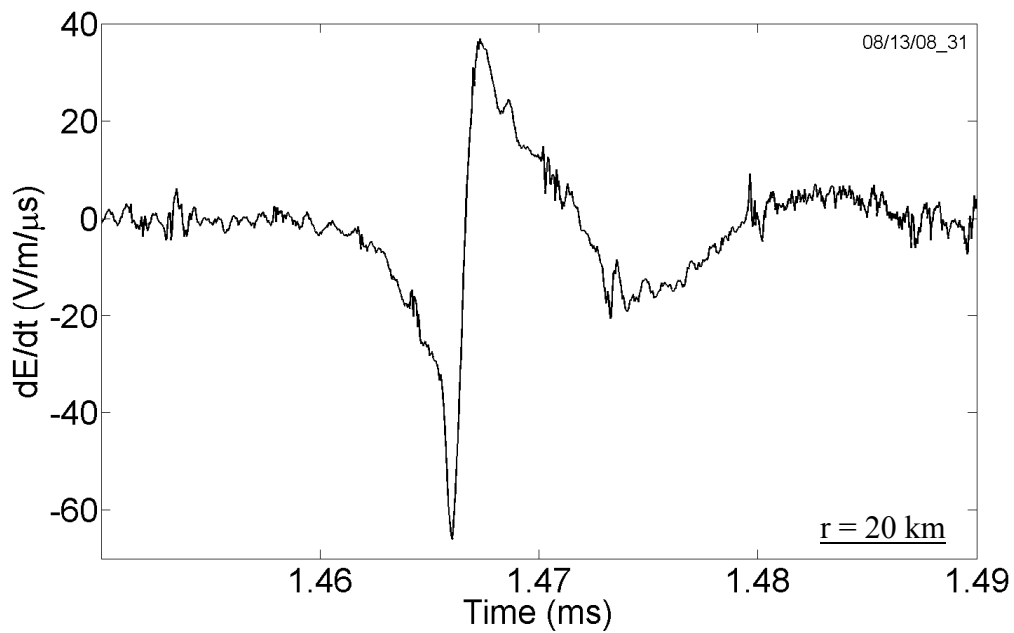


Figure B-16. Electric field derivative waveform of a positive return stroke that occurred on August 13, 2008, at 21:23:59 (UTC) at a distance of 20 km, shown on a 40- μ s time scale.

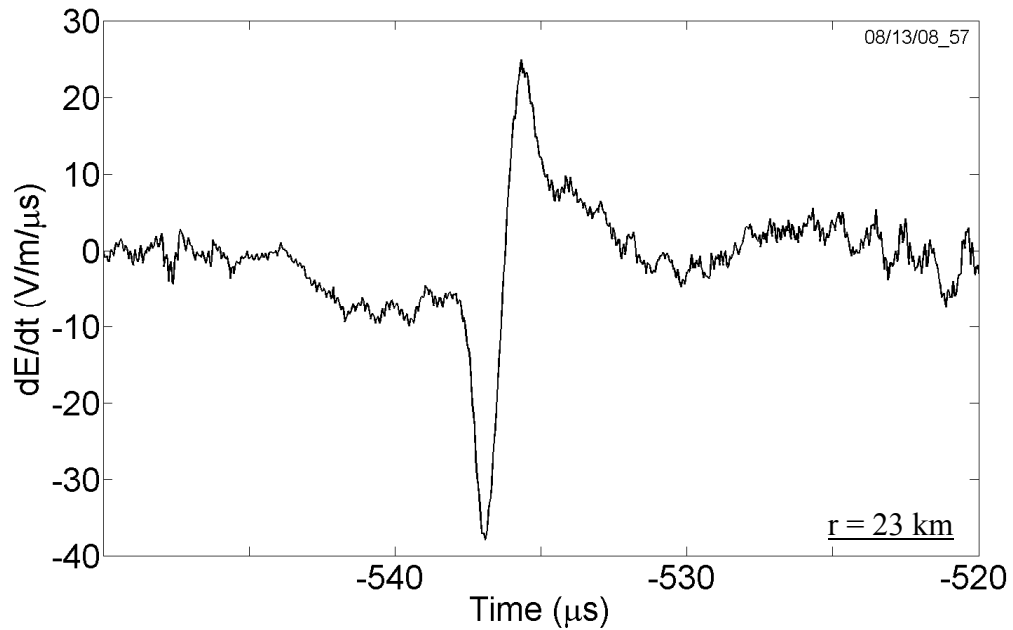


Figure B-17. Electric field derivative waveform of a positive return stroke that occurred on August 13, 2008, at 22:08:10 (UTC) at a distance of 23 km, shown on a 30- μ s time scale.

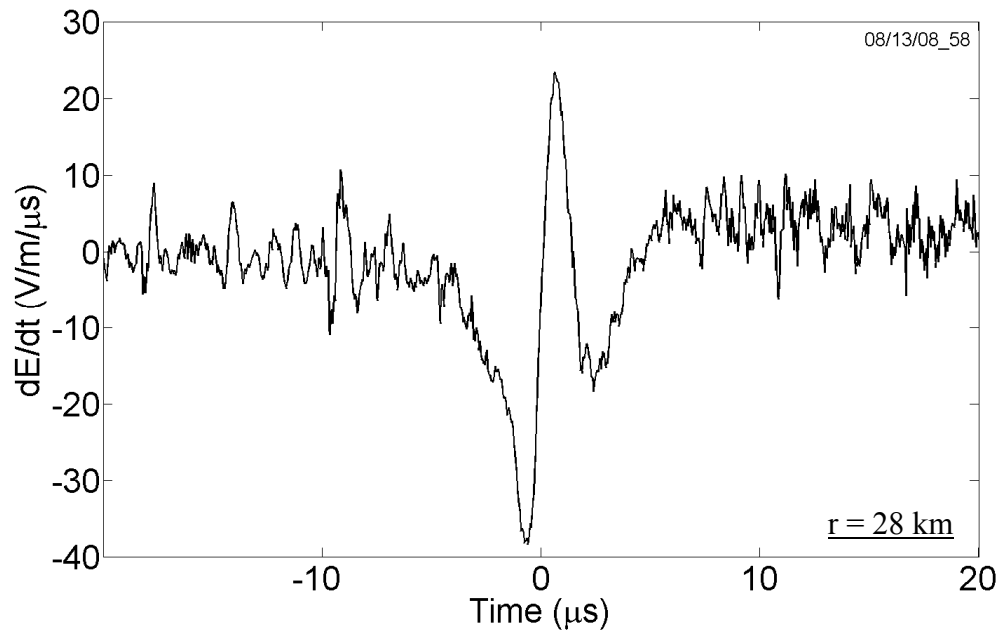


Figure B-18. Electric field derivative waveform of a positive return stroke that occurred on August 13, 2008, at 22:11:17 (UTC) at a distance of 28 km, shown on a 40- μ s time scale.

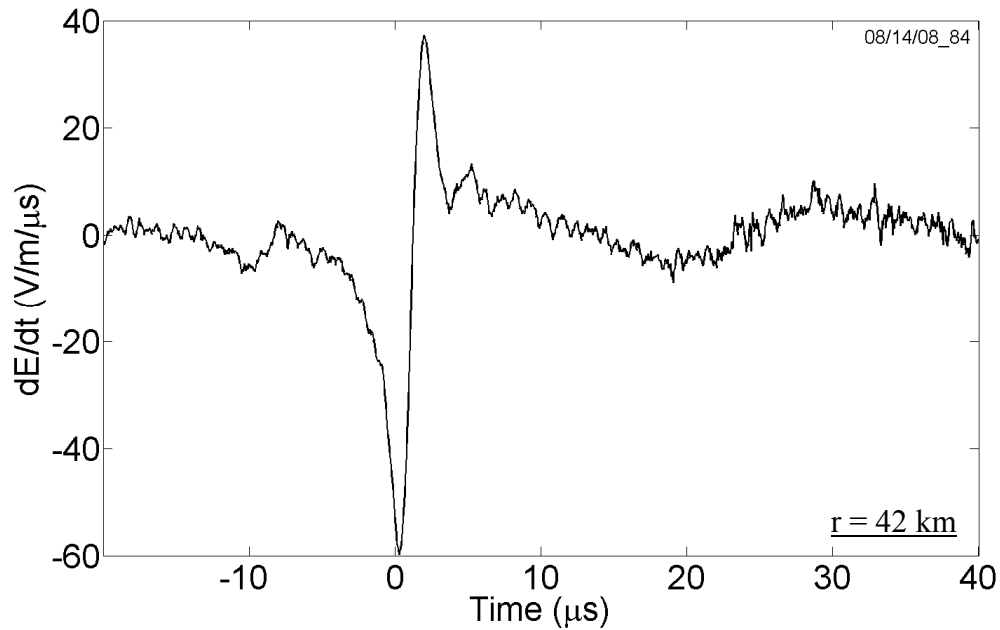


Figure B-19. Electric field derivative waveform of a positive return stroke that occurred on August 14, 2008, at 12:52:06 (UTC) at a distance of 42 km, shown on a 60- μ s time scale.

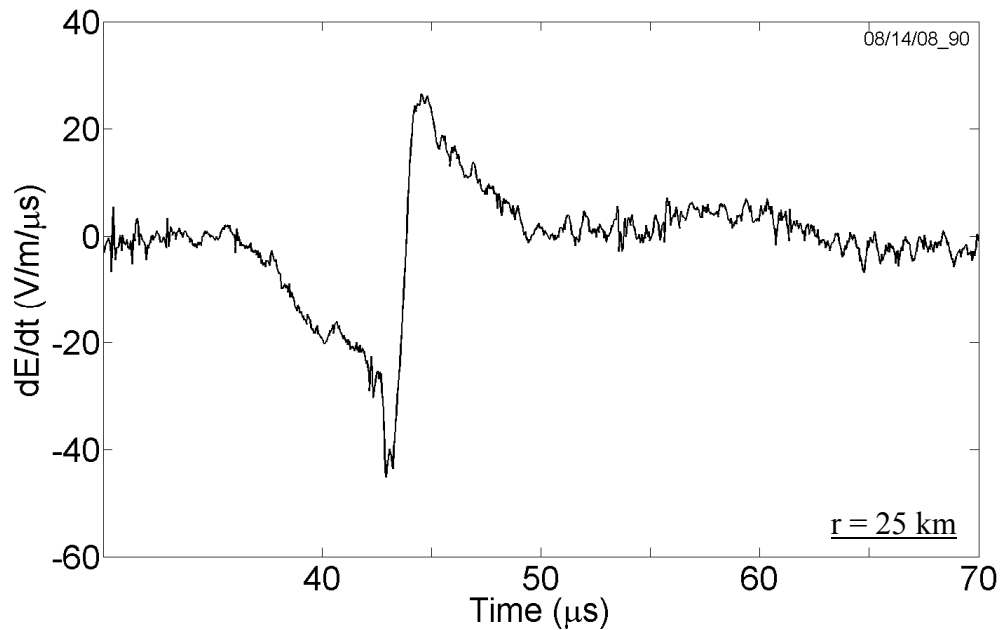


Figure B-20. Electric field derivative waveform of a positive return stroke that occurred on August 14, 2008, at 13:27:12 (UTC) at a distance of 25 km, shown on a 40- μ s time scale.

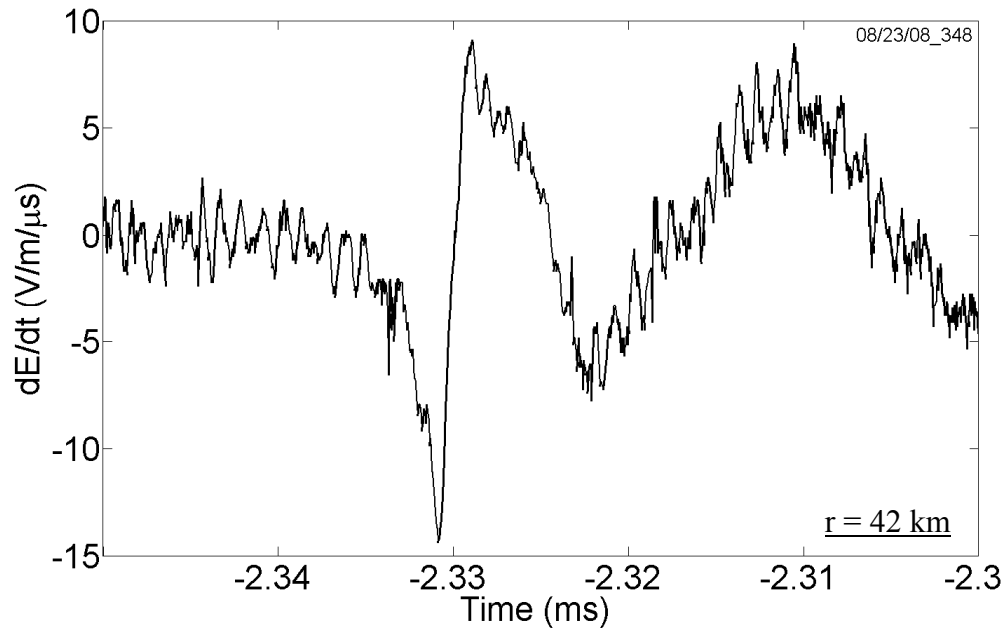


Figure B-21. Electric field derivative waveform of a positive return stroke that occurred on August 23, 2008, at 20:47:43 (UTC) at a distance of 42 km, shown on a 50- μ s time scale.

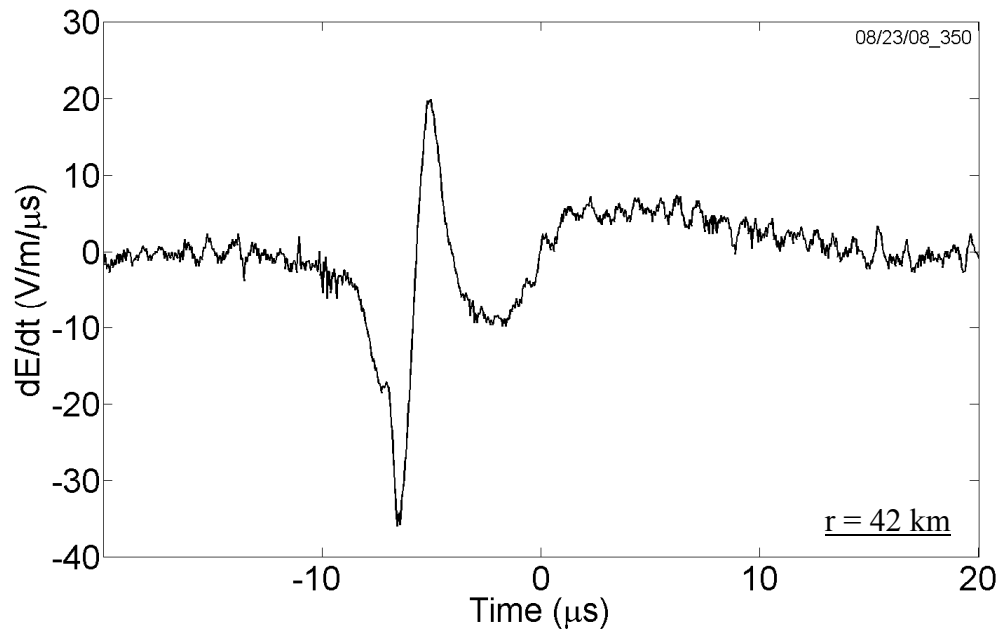


Figure B-22. Electric field derivative waveform of a positive return stroke that occurred on August 23, 2008, at 21:01:46 (UTC) at a distance of 42 km, shown on a 40- μ s time scale.

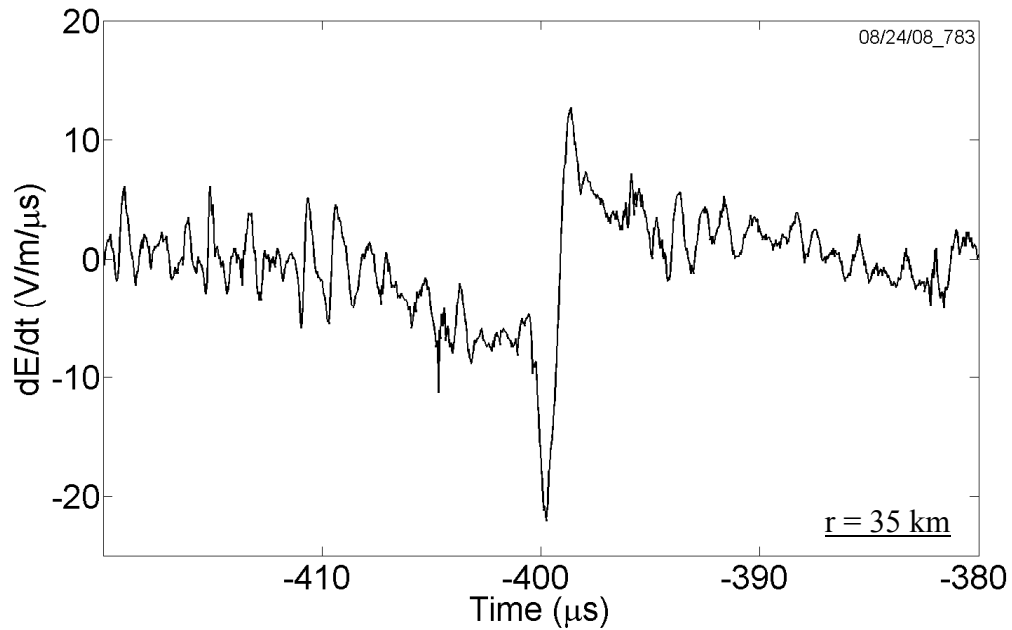


Figure B-23. Electric field derivative waveform of a positive return stroke that occurred on August 24, 2008, at 21:53:34 (UTC) at a distance of 35 km, shown on a 40- μ s time scale.

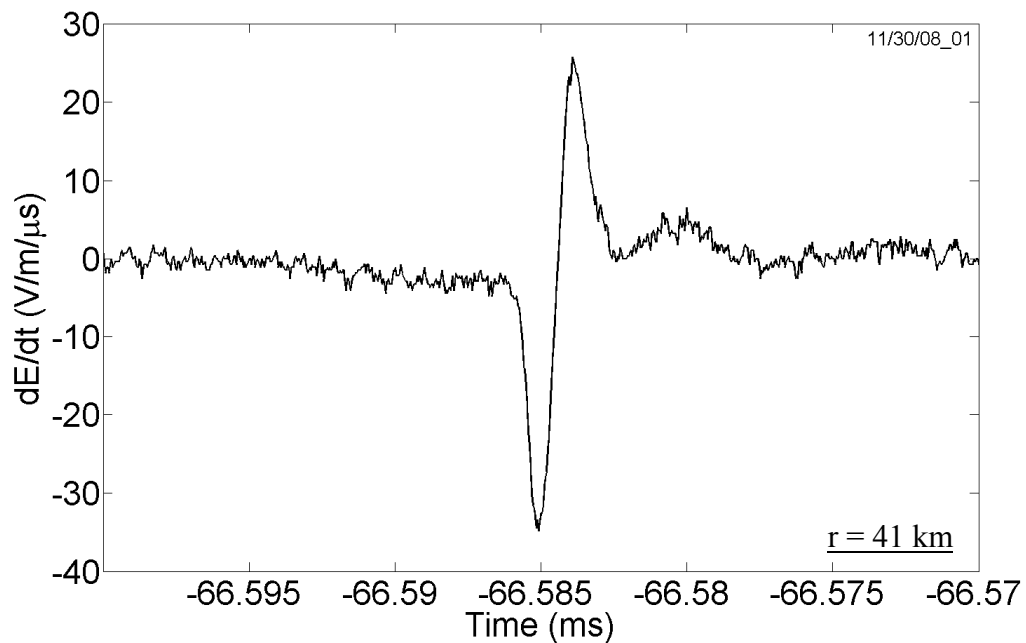


Figure B-24a. Electric field derivative waveform of the first return stroke (of a two-stroke positive flash), that occurred on November 30, 2008, at 16:03:52 (UTC) at a distance of 41 km, shown on a 30- μ s time scale.

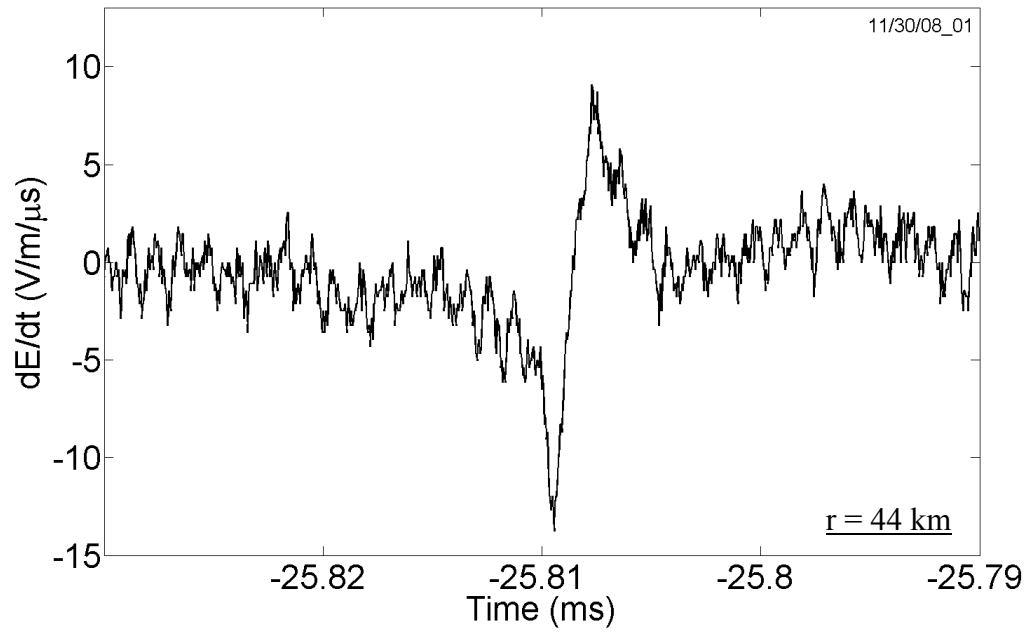


Figure B-24b. Electric field derivative waveform of the second return stroke (of a two-stroke positive flash), that occurred on November 30, 2008, at 16:03:52 (UTC) at a distance of 44 km, shown on a 40- μ s time scale.

APPENDIX C
NLDN RESPONSES TO ROCKET-TRIGGERED LIGHTNING AT CAMP BLANDING,
FLORIDA, IN 2004, 2005, AND 2007

C.1 Introduction

The U.S. National Lightning Detection Network (NLDN) data are used in Chapters 4, 6, and 7 of this dissertation. The NLDN has been providing real-time, continental-scale lightning data since 1989. The NLDN data consists of, among other things, information about lightning type (cloud or ground), time of occurrence with nanosecond resolution, peak currents, number of detecting sensors, and location information including associated uncertainties. The most recent network-wide NLDN upgrade that was completed in 2004 is described by *Cummins and Murphy* [2009]. Prior to the upgrade, the NLDN consisted of 106 sensors, including 63 LPATS III sensors, which provided only time of arrival information, and 43 IMPACT sensors, which provided both time of arrival and azimuth information. During the upgrade, all sensors in the NLDN were replaced with IMPACT-ESP sensors having improved analog front-end circuitry, higher speed processor, and configurable waveform criteria. The post-upgrade status of the network has been reported by Cummins et al. [2006]. *Jerauld et al.* [2005] examined the performance characteristics of the NLDN for the 2001-2003 period using rocket triggered lightning data acquired at Camp Blanding, Florida. Note that 2003 was essentially a post-upgrade year for the Florida region. The NLDN propagation model, which is part of the NLDN field to current conversion procedure, was modified on July 1, 2004 to provide a better match with Camp Blanding ground-truth data used in the evaluation performed by *Jerauld et al.* [2005]. In this Chapter, we use new rocket triggered lightning data obtained at Camp Blanding during the years 2004, 2005, and 2007 (there was no lightning triggering in 2006) to estimate the performance characteristics of the NLDN.

C.2 Data and Methodology

During the summers of 2004, 2005, and 2007, a total of 18 negative flashes were triggered at the ICLRT. Of these 18, 12 flashes contained a total of 28 leader/return stroke sequences and 6 flashes consisted of initial stage only. The latter 6 are not considered in this study. A summary of

Table C-1. Summary of flashes and strokes recorded at Camp Blanding during summers of 2004, 2005, and 2007, along with the corresponding NLDN detection efficiencies.

Year (Period)	Number of Flashes Triggered	Number of NLDN Detected Flashes	NLDN Flash Detection Efficiency	Number of Strokes	Number of NLDN Detected Strokes	NLDN Stroke Detection Efficiency
2004 (Pre- July 1, 2004)	2	2	100%	11	7	64%
2004, 2005 and 2007 (Post-July 1, 2004)	10	8	80%	17	11	65%
2004, 2005, and 2007	12	10	84%	28	18	64%

the flashes and strokes recorded at Camp Blanding during the three years is given in Table C-1.

During the 2004 and 2007 seasons, an 11-meter tower launcher was used, while in 2005 an 8-meter tall mobile launcher was used in addition to the tower launcher. Position of each launcher is known within a few meters. Lightning current was directly measured at the base of either launcher with a non-inductive current measuring resistor (shunt). Different shunts were used in different years, but in all cases, the bandwidth of the shunt exceeded 8 MHz. Lightning currents were transmitted to Yokogawa and LeCroy digitizing oscilloscopes via fiber optic links. The Yokogawa oscilloscopes sampled at 2 MHz (-3 dB low pass filtered at 500 kHz) and the LeCroy oscilloscopes sampled at 20 MHz (-3 dB filtered at 5 MHz). Of the 12 triggered flashes considered here, 2 flashes (containing 11 strokes) were triggered before July 1, 2004 (when the NLDN propagation model was modified) and 10 flashes (containing 17 strokes) were triggered

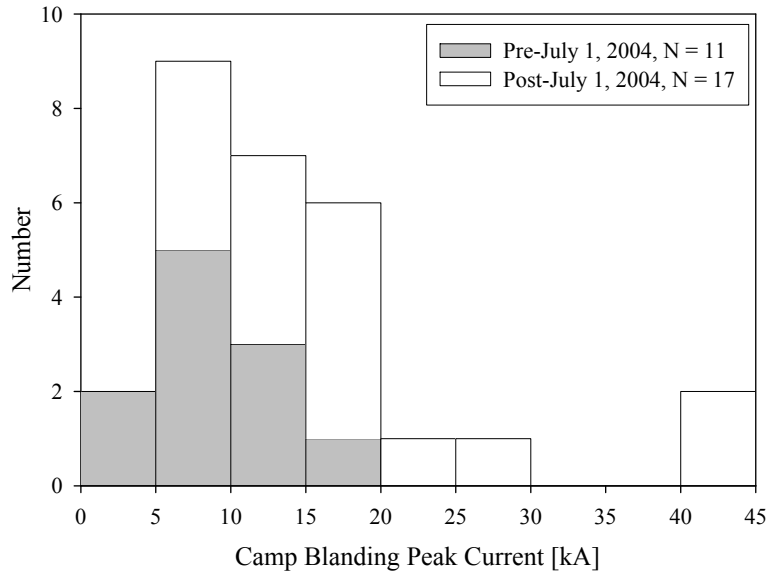
after that date. Although the propagation model modification does not affect flash or stroke detection efficiency, nor location errors, all the results are presented here for each of the two periods separately and for all data combined. The peak current distribution for all strokes recorded during 2004, 2005 and 2007 is given in Figure C-1. This distribution includes both strokes detected by the NLDN and those that were not. The arithmetic mean (AM) and median peak currents are 14.1 kA and 11.3 kA, respectively and the minimum and maximum peak currents are 3.3 kA and 44.9 kA, respectively. Note that the distribution resembles a lognormal one, for which the median is thought to be better characteristic than the AM.

Camp Blanding and NLDN events were correlated using GPS (Global Positioning System) time stamps. The following NLDN performance characteristics were determined: (1) flash detection efficiency, (2) stroke detection efficiency, (3) location errors, and (4) errors in peak current estimates.

C.3 Results and Discussion

C.3.1 Flash and Stroke Detection Efficiencies

Table C-1 summarizes the NLDN flash and stroke detection efficiencies for 2004, 2005, and 2007. For all flashes triggered during this period, the flash detection efficiency was 84 % (10 out of 12), which is the same as reported by *Jerauld et al.* [2005] for 2001-2003. Note that, all strokes in “classical” triggered flashes are similar to subsequent strokes in natural lightning and hence the flash detection efficiency reported here is likely to be an underestimate of the true value for natural negative lightning flashes, since first strokes typically have larger peak currents than subsequent ones. The stroke detection efficiency was 64% (18 out of 28) versus 60% reported by *Jerauld et al.* [2005]. The average stroke multiplicity for 2004, 2005, and 2007 (defined as the total number of strokes divided by the number of flashes triggered) at Camp Blanding was 2.3, versus 4.3 for 2001-2003. Figure C-2 gives the NLDN stroke detection



	Pre-July 1, 2004	Post-July 1, 2004	2004, 2005, and 2007
AM, kA	9.1	17.4	14.1
SD, kA	3.9	10.7	9.6
GM, kA	8.2	14.8	11.7
Median, kA	8.4	15.3	11.3
SD(log ₁₀ I)	0.20	0.25	0.26
Min, kA	3.3	5.8	3.3
Max, kA	17.3	44.9	44.9
N	11	17	28

Figure C-1. Histogram of Camp Blanding triggered lightning return-stroke peak currents, I , for 2004, 2005, and 2007. Statistics given are the arithmetic mean (AM), standard deviation (SD), geometric mean (GM), median, standard deviation of the \log_{10} of the parameter ($SD(\log_{10}I)$), minimum value (min), and maximum value (max) of peak currents for periods before and after July 1, 2004 and for all data combined.

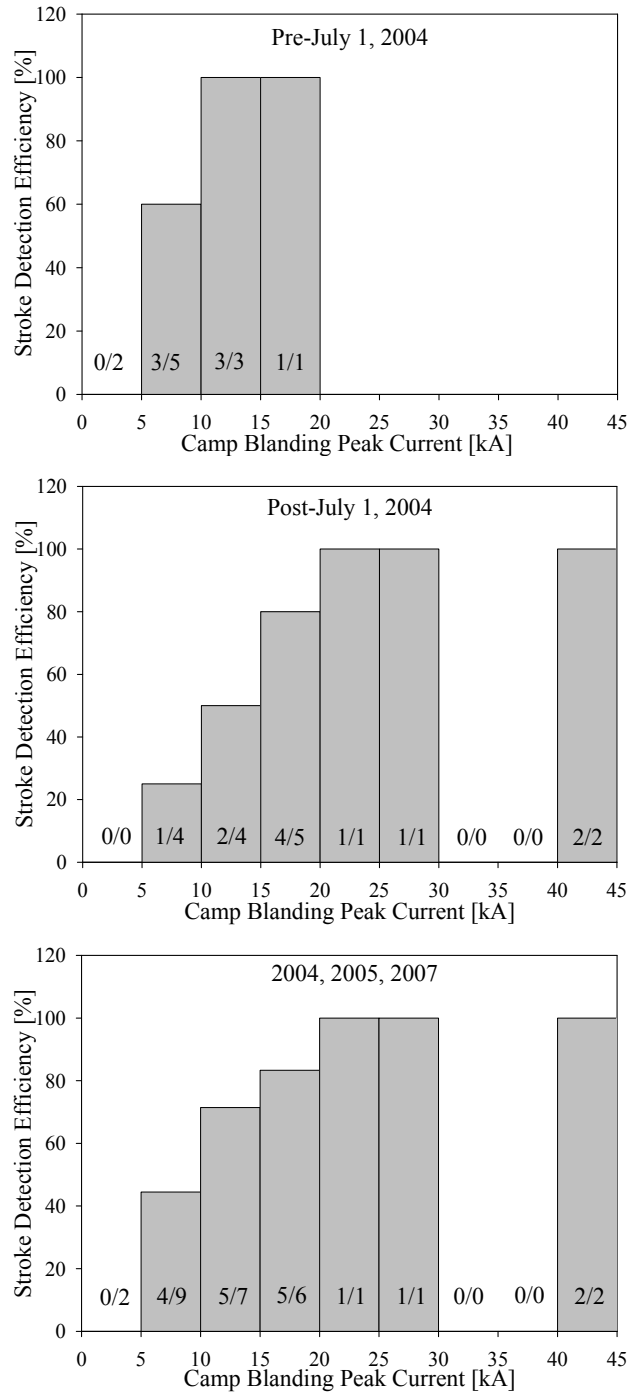
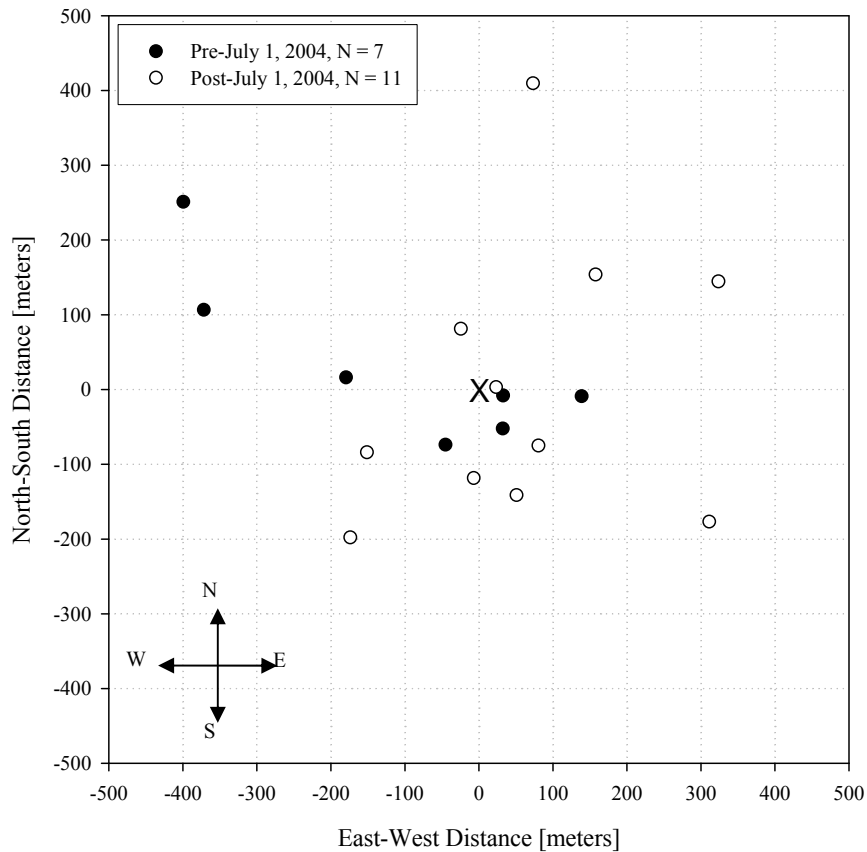


Figure C-2. NLDN stroke detection efficiency as a function of peak current measured at Camp Blanding. For each peak current range (bin size of 5 kA), the ratio given inside the column indicates the number of strokes detected by the NLDN (numerator) and the number of strokes recorded at Camp Blanding (denominator), for that peak current range. The total number of strokes whose currents were measured at Camp Blanding is 28, of which 18 were detected by the NLDN.

efficiency as a function of peak current measured at Camp Blanding. For all data combined the stroke detection efficiency is 100% for strokes above 20 kA, although the sample size (four strokes) is rather small. As the peak current decreases from 20 kA to 5 kA, the stroke detection efficiency decreases from 100 to 69%. Neither of the two strokes having peak currents less than 5 kA was detected by the NLDN. Similarly, for the 2001-2003 data set examined by *Jerauld et al.* [2005], all six strokes having peak currents less than 5 kA were missed by the NLDN.

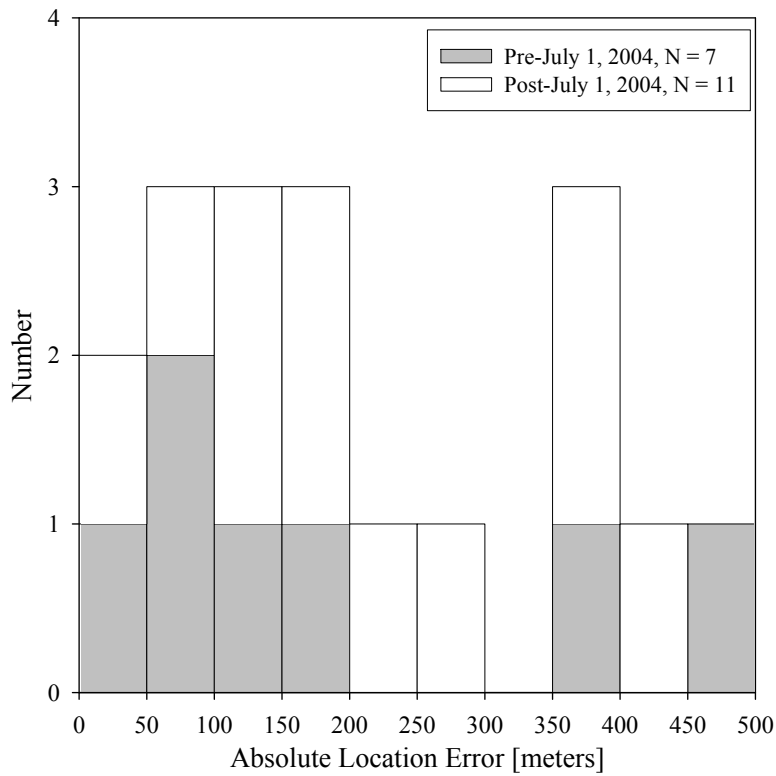
C.3.2 Location Accuracy

Figure C-3 shows a spatial distribution of NLDN stroke locations for 18 strokes in 10 flashes triggered at Camp Blanding during 2004, 2005, and 2007. The origin (marked X) corresponds to the actual strike location that was known within a few meters, so that the horizontal and vertical axes correspond to the east-west (east being positive) and north-south (north being positive) location error components, respectively. The AM and median north-south location errors are 12.7 m and -8.5 m, respectively, while the AM and median east-west location errors are -7.1 m and -27.8 m, respectively. Figure C-4 shows the histogram of NLDN absolute stroke location errors for the 18 strokes shown in Figure C-3. The median absolute location error was 162 m with the largest error being 472 m. This is better than a median absolute location error of 600 m and a maximum of 11 km reported by *Jerauld et al.* [2005] for 95 Camp Blanding strokes located by the NLDN in 2001-2003. Figure C-5 shows the NLDN absolute location error plotted versus the peak current measured at Camp Blanding. Largest location errors (> 300 m) correspond to strokes with peak currents less than 20 kA, although many strokes in this peak current range were located with considerably smaller errors. Figure C-6 shows the NLDN absolute location error plotted versus the number of NLDN sensors which were involved in the location solution. The number of reporting sensors ranges from 3 to 12. In general, location



	Pre- July 1, 2004	Post- July 1, 2004	2004, 2005, and 2007
N-S AM, m	32.9	-0.138	12.7
N-S SD, m	104	175	152
N-S Median, m	-8.1	-75.0	-8.5
E-W AM, m	-113.1	60.4	-7.1
E-W SD, m	194	152	190
E-W Median, m	-45.1	50.9	27.8
N	7	11	18

Figure C-3. Plot of NLDN stroke locations for 18 strokes in 10 flashes triggered during 2004, 2005, and 2007 at Camp Blanding. The origin (marked X) corresponds to the actual stroke location (lightning triggering location). The horizontal axis corresponds to the east-west component of the location error, with positive values corresponding to east. The vertical axis corresponds to the north-south component of the location error, with positive values corresponding to north. Statistics given are arithmetic mean (AM), median, and standard deviation (SD), for each location error component.



	Pre-July 1, 2004	Post- July 1, 2004	2004, 2005, and 2007
AM, m	194.2	206.6	201.8
SD, m	156.8	121.3	136.4
GM, m	135.1	162.3	151.2
Median, m	139.2	173.1	161.6
Min, m	33.7	23.4	23.4
Max, m	471.6	416.0	471.6
N	7	11	18

Figure C-4. Histogram of the NLDN absolute location errors. Corresponding statistics are also given.

errors seem to decrease as the number of reporting sensors increases, although the dependence is characterized by a large scatter.

The NLDN 50% error ellipse, calculated for each stroke location, is defined as a confidence region for which there is a 50% probability that the actual stroke location lies within the area circumscribed by the ellipse, with the center of the ellipse being the most-probable (reported) stroke location. Hence the semi-major axis of the 50% ellipse is usually viewed as the median (50%) location error. Corresponding error ellipses for any probability level (e.g., 90%) can be derived by multiplying the semi-major and semi-minor axes of the 50% ellipse by an appropriate scaling factor. The two-dimensional Gaussian distribution of errors in latitude and longitude is based on the assumption that the random errors in sensor time and angle measurements are uncorrelated and their distributions are approximately Gaussian [Cummins *et al.*, 1998]. Strokes located within a group of several sensors typically have relatively small, nearly circular error ellipses, whereas strokes detected by only two or three sensors typically have very large, elongated ellipses. A stroke detected by only two sensors, when that stroke is located near the line joining the two sensors (base line), typically has an elongated ellipse whose major axis is along the base line. Figure C-7 shows the NLDN 50% semi-major axis lengths plotted versus peak current, measured at Camp Blanding. A semi-major axis length of 0.4 km was reported for majority of the strokes (13 out of 18). The largest semi-major axis length was 1.1 km for a stroke having peak current 13.3 kA. Figure C-8 shows the NLDN absolute location error plotted versus NLDN 50% semi-major axis length. Strokes having absolute location errors less than 150 m are typically associated with a semi-major axis length of 0.4 km. The largest absolute location error is associated with a semi-major axis length of 0.6 km. The slanted solid line (slope = 1) in Figure C-8 is the locus of points for which the NLDN 50% semi-major axis

length and corresponding location error are equal, that is, represents the boundary of the 50% error ellipse. If the error ellipses are assumed to be nearly circular, then data points below this line correspond to strokes with ground-truth locations enclosed by the 50% error ellipse and data points above it to ground-truth locations outside the 50% error ellipse. Data points below the dashed line (slope = 1.82) in Figure C-8 correspond to strokes with ground-truth locations enclosed by the 90% error ellipse (assumed to be nearly circular). It is clear from Figure C-8 that all strokes had ground-truth locations enclosed by the 50% error ellipse, which means that location errors in 2004, 2005, and 2007 were considerably lower than predicted by the 50% and 90% NLDN error ellipses.

C.3.3 Peak Current Estimates

The NLDN-estimated peak current plotted versus peak current measured directly at Camp Blanding are shown in Figure C-9. The slanted solid line (slope = 1) is the locus of the points for which the NLDN peak currents and the Camp Blanding peak currents are equal. For both periods, that is before and after the propagation model was modified on July 1, 2004, there is a strong positive linear relationship between the measured and NLDN-estimated peak currents. As seen in Figure C-9, the linear relationship seems to be stronger for the data acquired prior to July 1, 2004 although the sample size and range of current variation are rather small. In fact, the mean values of the ratio I_{CB}/I_{NLDN} are about 1.0 and 1.2 for the data acquired prior to and after July 1, 2004, respectively. For all data combined, the mean ratio is about 1.1. This is to be compared to the mean I_{CB}/I_{NLDN} ratio of 1.2 found for 2001-2003 by *Jerauld et al.* [2005].

The AM and median Camp Blanding peak currents for all 18 strokes are 17.4 and 14.3 kA, respectively, versus 16.3 and 12.7, respectively, for NLDN-estimated peak currents. Figures C-10a and b, respectively, show the histograms for the signed and absolute values of NLDN peak

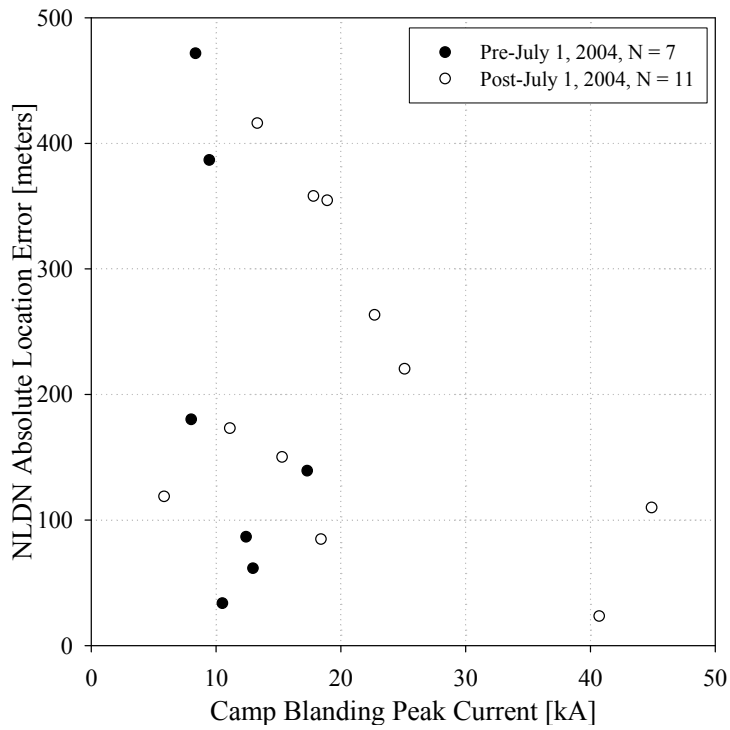


Figure C-5. NLDN absolute location error versus Camp Blanding peak current.

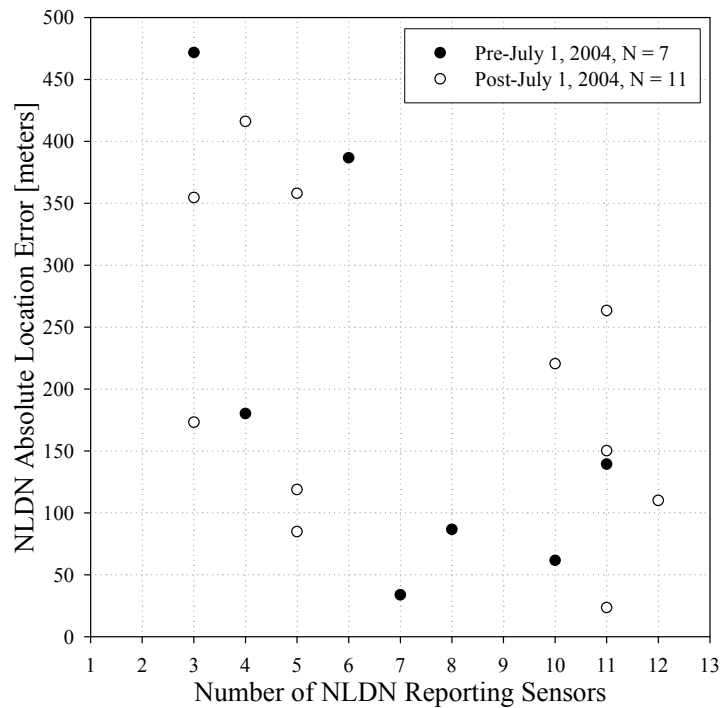


Figure C-6. NLDN absolute location error versus the number of reporting NLDN sensors.

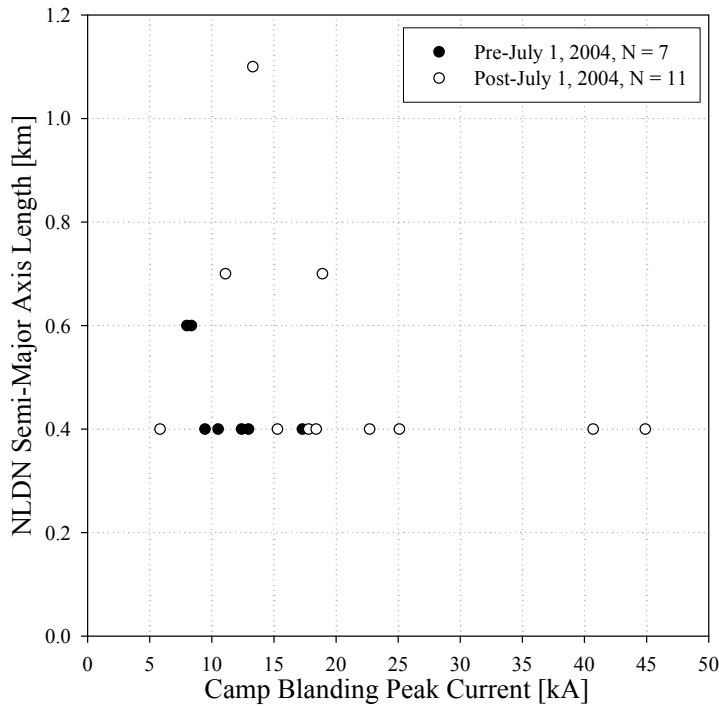


Figure C-7. NLDN 50% error ellipse semi-major axis length versus Camp Blanding peak current.

current estimation errors as a percent of Camp Blanding peak current ($\Delta I\% = 100\Delta I/I_{CB}$, where $\Delta I = I_{NLDN} - I_{CB}$). The AM values of $\Delta I\%$ for pre-July 1, 2004, post-July 1, 2004, and both periods combined are 2.8%, -10%, and -5.1%, respectively. The corresponding median values are 4.8%, -19%, and -1.2%. The AM and median NLDN-estimated peak current errors for all data combined are considerably lower (in absolute value) than the corresponding values of -15% and -18% reported by *Jerauld et al.* [2005].

For absolute value of $\Delta I\%$ (see Figure C-10b), the AM values are 12%, 24%, and 19%, for pre-July 1, 2004, post-July 1, 2004, and both periods combined, respectively. The corresponding median values are 11%, 29%, and 20%. *Jerauld et al.* [2005] reported a median absolute error of 20% for all 2001-2003 strokes combined. The percentage errors never exceeded in absolute value 41% for 2004, 2005 and 2007 versus 50% for 2001-2003.

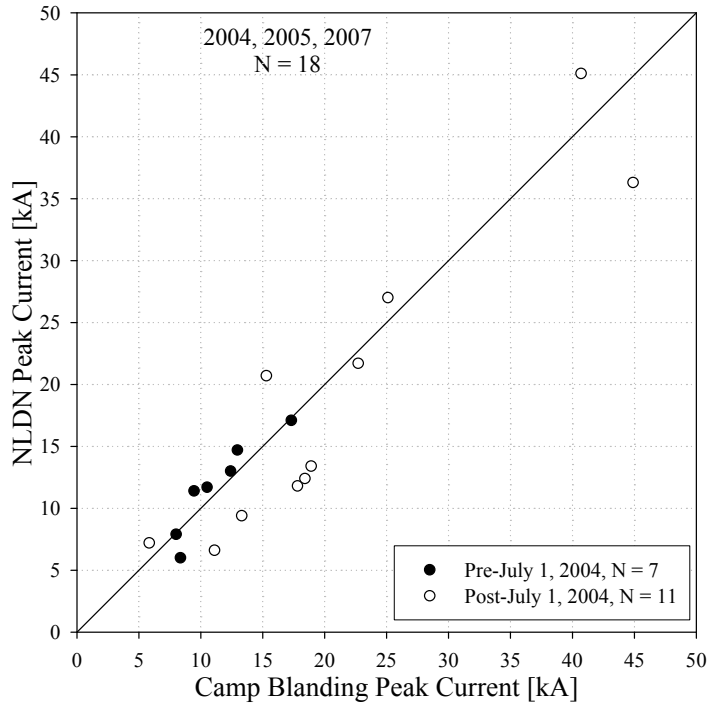


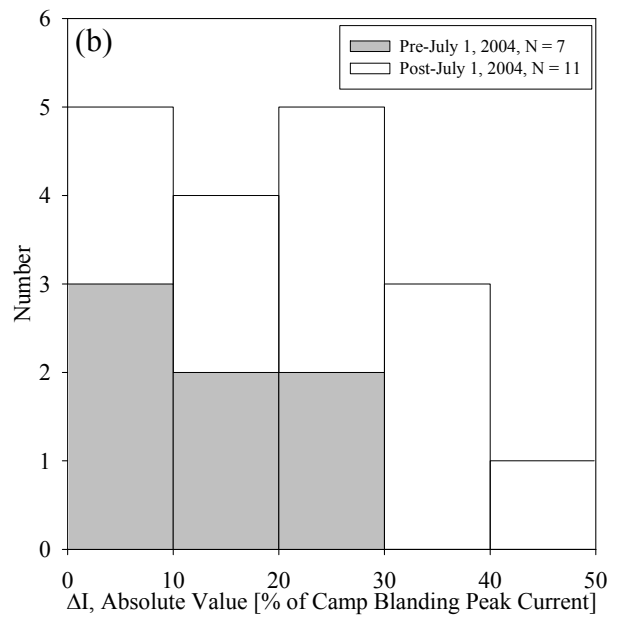
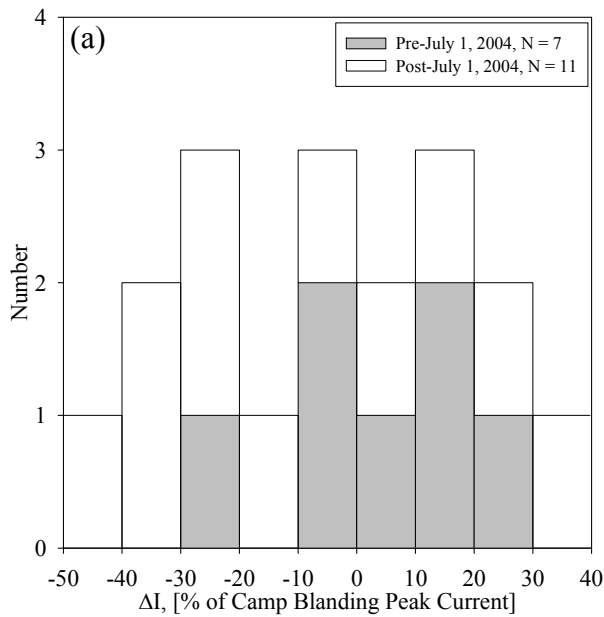
Figure C-9. NLDN-reported peak current versus peak current directly measured at Camp Blanding.

The number of NLDN reporting sensors plotted against Camp Blanding peak current for 23 strokes (18 analyzed above plus 5 reported by only one sensor and hence not located) is shown in Figure C-11. The 5 additional Camp Blanding strokes were detected by the NLDN sensor at Ocala, Florida, located 89 km from Camp Blanding. All these 5 strokes have peak currents less than 12 kA. Interestingly, 6 other Camp Blanding strokes which had peak currents less than 12 kA were detected by 3 to 7 NLDN sensors.

C.4 Summary

We evaluated performance characteristics of the U.S. National Lightning Detection Network (NLDN) using rocket-triggered lightning data acquired in 2004, 2005, and 2007 (there was no lightning triggering at Camp Blanding in 2006) at Camp Blanding, Florida as the ground-truth. Twelve flashes, containing a total of 28 negative strokes, were triggered at Camp Blanding during these three years. The NLDN recorded 18 Camp Blanding strokes in 10 flashes. The

resulting flash and stroke detection efficiencies are 84% and 64%, respectively. This is comparable to the results of *Jerauld et al.* [2005], who used triggered lightning data acquired in 2001-2003, also at Camp Blanding, Florida, and reported the same flash detection efficiency and a stroke detection efficiency of 60%. Note that, all strokes in “classical” triggered flashes are similar to subsequent strokes in natural lightning and hence the flash detection efficiency reported here is likely to be an underestimate of the true value for natural negative lightning flashes, since first strokes typically have larger peak currents than subsequent ones. The median absolute location error is 162 m and the largest error is 472 m which is better than a median absolute location error of 600 m and a maximum of 11 km reported by *Jerauld et al.* [2005] for 95 Camp Blanding strokes (2001-2003) located by the NLDN. The arithmetic mean and median NLDN-estimated peak current errors for the 18 negative strokes from 2004, 2005, and 2007 are about -5.1% and -1.2%, respectively, both being appreciably lower (in absolute value) than the corresponding values of -15% and -18% estimated by *Jerauld et al.* [2005]. The absolute value of median current estimation error in this study is 20%, which is the same as that in 2001-2003. The current estimation errors never exceeded in absolute value 50% in 2001-2003 and 41% in 2004, 2005, and 2007.



	Pre- July 1, 2004	Post- July 1, 2004	2004, 2005, and 2007
AM	2.8%	-10.1%	-5.1%
SD	14.6%	24.8%	22.4%
Median	4.8%	-19.2%	-1.2%
Min	-28.1%	-40.5%	-40.5%
Max	20.6%	35.4%	35.4%
N	7	11	18

	Pre- July 1, 2004	Post- July 1, 2004	2004, 2005, and 2007
AM	11.6%	24.2%	19.3%
SD	9.4%	11.6	12.4%
Median	11.4%	29.1%	19.9%
Min	1.2%	4.4%	1.2%
Max	28.1%	40.5%	40.5%
N	7	11	18

Figure C-10. Histograms of (a) signed and (b) absolute NLDN peak current estimation errors, given as a percentage of the directly measured Camp Blanding current ($\Delta I\% = 100\Delta I/I_{CB}$, where $\Delta I = I_{NLDN} - I_{CB}$). Corresponding statistics are given below each histogram.

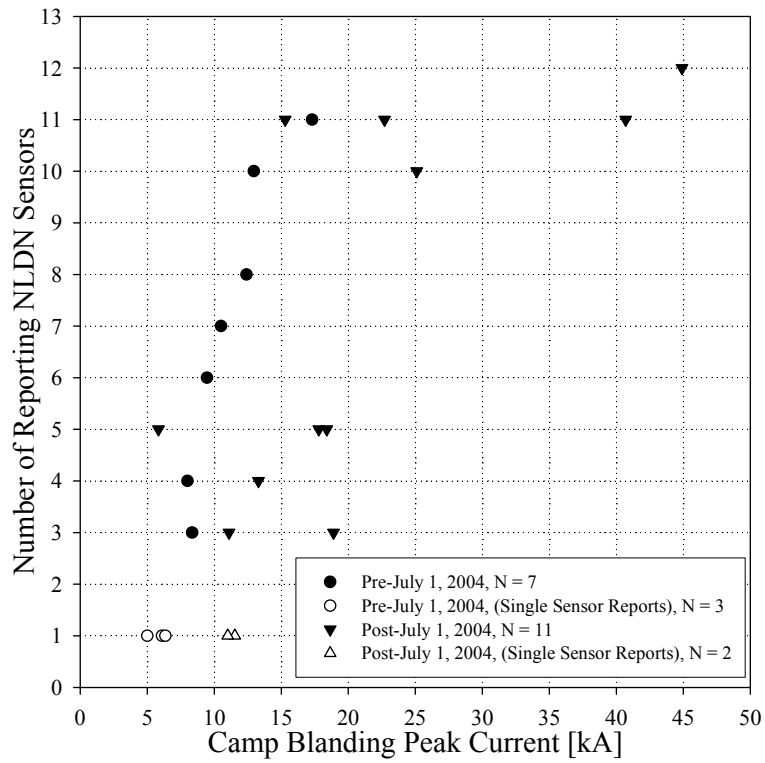


Figure C-11. Number of reporting NLDN sensors versus Camp Blanding peak current for 18 strokes detected by multiple sensors and 5 strokes detected by a single (Ocala) sensor.

LIST OF REFERENCES

- Anderson, R. B., and A. J. Eriksson (1980), Lightning parameters for engineering application, *Electra*, 69, 65–102.
- Baba, Y., and V. A. Rakov (2007), Electromagnetic fields at the top of a tall building associated with nearby lightning return strokes, *IEEE Trans. Electromagn. Compat.*, Vol. 49, No. 3, pp. 632–643, doi: 10.1109/TEMC.2007.902402.
- Baum, C. E. (2008), Measurement of closure position between downward and upward leaders: Return-stroke initiation position, in *Proceedings of XXIX General Assembly of the International Union of Radio Science*, edited by D. Erricolo, Union Radio Scientifique Internationale (URSI), paper no. 1038, Chicago, USA.
- Beasley, W. H., M. A. Uman, and P. L. Rustan (1982), Electric fields preceding cloud-to-ground lightning flashes, *J. Geophys. Res.*, 87, 4883–4902.
- Beasley, W. H., M. A. Uman, D. M. Jordan, and C. Ganesh (1983), Positive cloud to ground lightning return strokes, *J. Geophys. Res.*, 88(C13), 8475–8482.
- Berger, K. (1978), Blitzstrom-parameters von aufwärtsblitzen, *Bull. Schweiz. Elektrotech. Ver.*, 69, 353–360.
- Berger, K., R. B. Anderson, and H. Kroninger (1975), Parameters of lightning flashes, *Electra*, 80, 23–37.
- Biagi, C. J., K. L. Cummins, K. E. Kehoe, and E. P. Krider (2007), National Lightning Detection Network (NLDN) performance in southern Arizona, Texas, and Oklahoma in 2003–2004, *J. Geophys. Res.*, 112, D05208, doi:10.1029/2006JD007341.
- Boccippio, D.J., E.R. Williams, S.J. Heckman, W.A. Lyons, I.T. Baker, and R. Boldi (1995), Sprites, ELF transients, and positive ground strokes, *Science*, 269, 1088–91.
- Bodhika, J.P., M. Fernando, and V. Cooray (2006), Characteristics of cloud flashes inferred from measurements of electric fields over Sri Lanka a tropical country, *Proc. of 28th Intl. Conf. on Lightning Protection*, Kanazawa, Japan, 249–252.
- Bogacki, P., and L.F. Shampine (1989), A 3(2) pair of Runge–Kutta formulas, *Applied Mathematics Letters* 2 (4): 321–325, doi:10.1016/0893-9659(89)90079-7.
- Brook, M. (1992), Breakdown electric fields in winter storms, *Res. Lett. Atmos. Electr.*, 12, 47–52.
- Chalmers, J. A. (1967), *Atmospheric Electricity*, 2nd ed., pp. 515., New York, Pergamon Press.
- Chauzy, S., and S. Soula (1999), Contribution of the ground corona ions to the convective charging mechanism, *Atmos. Res.*, 51, 279–300.

- Chen, M., T. Watanabe, N. Takagi, Y. Du, D. Wang, and X. Liu (2003), Simultaneous observations of optical and electrical signals in altitude-triggered negative lightning flashes, *J. Geophys. Res.*, 108(D8), 4240, doi:10.1029/2002JD002676.
- Cheng, D. K. (1993), *Fundamentals of engineering electromagnetics*, Addison-Wesley Publishing Company, Inc., USA.
- Clarence, N. D., and D. J. Malan (1957), Preliminary discharge processes in lightning flashes to ground, *Q. J. R. Meteorol. Soc.*, 83, 161–172.
- Coleman, L.M., M. Stolzenburg, T.C. Marshall, and M. Stanley (2008), Horizontal lightning propagation, preliminary breakdown, and electric potential in New Mexico thunderstorms, *J. Geophys. Res.*, 113, D09208, doi: 10.1029/2007JD009459.
- Cooray, V. (1986a), A novel method to identify the radiation fields produced by positive return strokes and their submicrosecond structure, *J. Geophys. Res.*, 91, 7907–7911.
- Cooray, V. (1986b), Correction to: "A novel method to identify the radiation fields produced by positive return strokes and their submicrosecond structure, *J. Geophys. Res.*, 91, 13,318.
- Cooray, V. (1997), Energy dissipation in lightning flashes, *J. Geophys. Res.*, 102(D17), 21401–21410.
- Cooray, V., and K. P. S. C. Jayaratne (1994), Characteristics of lightning flashes observed in Sri Lanka in the tropics, *J. Geophys. Res.*, 99(D10), 21,051– 21,056, doi:10.1029/94JD01519.
- Cooray, V., and S. Lundquist (1982), On the characteristics of some radiation fields from lightning and their possible origin in possible origin in ground flashes, *J. Geophys. Res.*, 87, 11,203–11,214.
- Cooray, V., and H. Perez (1994), Some features of lightning flashes observed in Sweden, *J. Geophys. Res.*, 99(D5), 10,683–10,688, doi:10.1029/93JD02366.
- Cooray, V., and V. Scuka (1996), What attracts a lightning flash to ground?, *Proc. of the International Conference on Atmospheric Electricity*, pp. 256–259, Osaka , Japan.
- Cooray, V., M. Fernando, C. Gomes, T. Sorensen, V. Scuka, and A. Pedersen (1998), The fine structure of positive return stroke radiation fields: a collaborative study between researchers from Sweden and Denmark, *Proc. 24th Int. Conf. on Lightning Protection*, pp. 78-82, Staffordshire University, Birmingham, United Kingdom.
- Cooray, V., R. Montano, and V. Rakov (2004), A model to represent negative and positive lightning first strokes with connecting leaders, *J. Electrostatics*, 60, 97–109.
- Cummins, K. L., and M. J. Murphy (2009), An overview of lightning locating systems: history, techniques, and data uses, with an in-depth look at the U.S. NLDN, *IEEE Trans. Electromagn. Compat.*, Vol. 51, No. 3, pp. 499–518, doi: 10.1109/TEM.2009.2023450.

- Cummins, K. L., M. J. Murphy, E. A. Bardo, W. L. Hiscox, R. B. Pyle, and A. E. Pifer (1998), A combined TOA/MDF technology upgrade of the U.S. National Lightning Detection Network, *J. Geophys. Res.*, *103*(D8), 9035–9044.
- Cummins, K. L., J. A. Cramer, C. Biagi, E. P. Krider, J. Jerauld, M. A. Uman, and V. A. Rakov (2006), The U.S. National Lightning Detection Network: post-upgrade status, *Proc. of the Second Conference on Meteorological Applications of Lightning Data, 86th AMS Annual Meeting*, paper 6.1, American Meteorological Society, Atlanta, GA.
- Darrah, R.P. (1978), On the relationship of severe weather to radar tops, *Mon. Weather Rev.*, *106*, 1332–1339.
- De Conti, A., and S. Visacro (2007), Analytical representation of single- and double-peaked lightning current waveforms, *IEEE Trans. Electromagn. Compat.*, *Vol. 49*, No. 2, pp. 448–451, doi: 10.1109/TEMC.2007.897153.
- Defer, E., P. Blanchet, C. Thery, P. Laroche, J. Dye, and M. Venticinque (2001), Lightning activity for the July 10, 1996, storm during the Stratosphere-Troposphere Experiment: Radiation, Aerosol, and Ozone-A (STRAO-A) experiment, *J. Geophys. Res.*, *106*(D10), 10,151–10,172.
- Diendorfer, G., W. Schulz, and V. A. Rakov (1998), Lightning characteristics based on data from the Austrian Lightning Locating System, *IEEE Trans. Electromagn. Compat.*, *40*(4), 452–464, doi:10.1109/15.736206.
- Eack, K. B. (2004), Electrical characteristics of narrow bipolar events, *Geophys. Res. Lett.*, *31*, L20102, doi:10.1029/2004GL021117.
- Fisher, R. J., G. H. Schnetzer, R. Thottappillil, V. A. Rakov, M. A. Uman, and J. D. Goldberg (1993), Parameters of triggered-lightning flashes in Florida and Alabama, *J. Geophys. Res.*, *98*(D12), 22,887–22,902.
- Fleenor, S.A., C. J. Biagi, K.L. Cummins, E. P. Krider and X. M. Shao (2009), Characteristics of cloud-to-ground lightning in warm-season thunderstorms in the Central Great Plains, *Atmos. Res.*, *91*, doi:10.1016/j.atmosres.2008.08.011, 333–352.
- Frey, H. U., S. B. Mende, S. A. Cummer, A. B. Chen, R.-R. Hsu, H.-T. Su, Y.-S. Chang, T. Adachi, H. Fukunishi, and Y. Takahashi (2005), Beta-type stepped leader of elve-producing lightning, *Geophys. Res. Lett.*, *32*, L13824, doi: 10.1029/2005GL023080.
- Griffiths, R.F. and C.T. Phelps, (1976a), The effects of air pressure and water vapour content on the propagation of positive corona streamers, and their implications to lightning initiation. *Q. J. Roy. Meteor. Soc.* *102*, 419–426.
- Griffiths, R.F., and C.T. Phelps (1976b), A model of lightning initiation arising from positive corona streamer development. *J. Geophys. Res.*, *31*, 3671–3676.

- Gomes, C., and V. Cooray (1998), Radiation field pulses associated with the initiation of positive cloud to ground lightning flashes, *Proc. 24th Int. Conf. on Lightning Protection*, Birmingham, United Kingdom, Staffordshire University, pp. 365–370.
- Gomes, C., V. Cooray, and C. Jayaratne (1998), Comparison of preliminary breakdown pulses observed in Sweden and in Sri Lanka, *J. Atmos. Solar Terr. Phys.*, *60*, 975–979.
- Goto, Y., and K. Narita (1995), Electrical characteristics of winter lightning, *J. Atmos. Terr. Phys.*, *57*, 449–59.
- Gurevich, A.V., and K.P. Zybin (2004), High energy cosmic ray particles and the most powerful discharges in thunderstorm atmosphere, *Phys. Lett. A*, *329*, 341–347.
- Gurevich, A.V., K.P. Zybin, and R.A. Roussel-Dupre (1999), Lightning initiation by simultaneous effect of runaway breakdown and cosmic ray showers, *Phys. Lett. A*, *254*, 79–87.
- Gurevich, A.V., L.M. Duncan, Yu. V. Medvedev, and K.P. Zybin (2002), Radio emission due to simultaneous effect of runaway breakdown and extensive atmospheric showers, *Phys. Lett. A*, *301*, 320–6.
- Gurevich, A.V., L.M. Duncan, A.N. Karashtin, and K.P. Zybin (2003), Radio emission of lightning initiation, *Phys. Lett. A*, *312*: 228–237.
- Gurevich, A.V., Yu. V. Medvedev, and K.P. Zybin (2004), New type discharge generated in thunderclouds by joint action of runaway breakdown and extensive atmospheric shower, *Phys. Lett. A*, *329*, 348–361.
- Hamlin T., T. E. Light, X. M. Shao, K. B. Eack, and J. D. Harlin (2007), Estimating lightning channel characteristics of positive narrow bipolar events using intrachannel current reflection signatures, *J. Geophys. Res.*, *112*, D14108, doi:10.1029/2007JD008471.
- Hamlin, T., K. C. Wiens, A. R. Jacobson, T. E. L. Light, and K. B. Eack (2009), Space- and ground-based studies of lightning signatures, in *Lightning: Principles, Instruments and Applications*, edited by H. D. Betz, U. Schumann, and P. Laroche, New York: Springer-Verlag, pp. 287–307.
- Heavner, M. J., D. A. Smith, A. R. Jacobson, and R. J. Sheldon (2002), LF/VLF and VHF lightning fast-stepped leader observations, *J. Geophys. Res.*, *107*(D24), 4791, doi:10.1029/2001JD001290.
- Heidler, F. (1985), Travelling current source model for LEMP calculation, in *Proc. of 6th Intl. Symp. on Electromagnetic Compatibility*, Zurich, Switzerland, pp. 157–62.
- Heidler, F., F. Drumm, and C. Hopf (1998), Electric fields of positive earth flashes in near thunderstorms, *Proc. 24th Int. Conf. on Lightning Protection*, Birmingham, United Kingdom, Staffordshire University, pp. 42–47.

- Hojo, J., M. Ishii, T. Kawamura, F. Suzuki, and R. Funayama (1985), The fine structure in the field change produced by positive ground strokes, *J. Geophys. Res.*, *90*, 6139–6143.
- Idone, V. P., and R. E. Orville (1982), Lightning return stroke velocities in the Thunderstorm Research International Program (TRIP), *J. Geophys. Res.*, *87*(C7), 4903–4915, doi:10.1029/JC087iC07p04903.
- Ishii, M., and J. Hojo (1989), Statistics on fine structure of cloud-to-ground lightning field waveforms, *J. Geophys. Res.*, *94*, 13,267–13,274.
- Jacobson, A.R., and M.J. Heavner (2005), Comparison of narrow bipolar events with ordinary lightning as proxies for severe convection, *Mon. Weather Rev.*, *133*, 1144–1154.
- Janischewskyj, W., V. Shostak, A. M. Hussein, and B. Kordi (1999), A lightning flash containing strokes of opposite polarities, CIGRE SC 33.9 (COLL), *Int. Coun. on Large Electr. Syst.*, Paris, France.
- Jayakumar, V., V. A. Rakov, M. Miki, M. A. Uman, G. H. Schnetzer, and K. J. Rambo (2006), Estimation of input energy in rocket-triggered lightning, *Geophys. Res. Lett.*, *33*, L05702, doi:10.1029/2005GL025141.
- Jayarathne, E. R., C. P. R. Saunders, and J. Hallett (1983), Laboratory studies of the charging of soft-hail during ice crystal interactions, *Q. J. R. Meteor. Soc.*, *109*, 609–630.
- Jerauld, J. (2007), Properties of natural cloud-to-ground lightning inferred from multiple-station measurements of close electric and magnetic fields and field derivatives, PhD dissertation, University of Florida, Gainesville.
- Jerauld, J., M. A. Uman, V. A. Rakov, K. J. Rambo, and D. M. Jordan (2004), A triggered lightning flash containing both negative and positive strokes, *Geophys. Res. Lett.*, *31*, L08104, doi:10.1029/2004GL019457.
- Jerauld, J., V. A. Rakov, M. A. Uman, K. J. Rambo, D. M. Jordan, K. L. Cummins, and J. A. Cramer (2005), An evaluation of the performance characteristics of the U.S. National Lightning Detection Network in Florida using rocket-triggered lightning, *J. Geophys. Res.*, *110*, D19106, doi:10.1029/2005JD005924.
- Jerauld, J., M. A. Uman, V. A. Rakov, K. J. Rambo, and G. H. Schnetzer (2007), Insights into the ground attachment process of natural lightning gained from an unusual triggered-lightning stroke, *J. Geophys. Res.*, *112*, D13113, doi:10.1029/2006JD007682.
- Jerauld, J. E., M. A. Uman, V. A. Rakov, K. J. Rambo, D. M. Jordan, and G. H. Schnetzer (2009), Measured electric and magnetic fields from an unusual cloud-to-ground lightning flash containing two positive strokes followed by four negative strokes, *J. Geophys. Res.*, *114*, D19115, doi:10.1029/2008JD011660.
- Kitagawa, N. (1957), On the electric field change due to the leader processes and some of their discharge mechanism, *Pap. Meteor. Geophys.* (Tokyo), *7*, 414–7,424.

- Kitagawa, N., and M. Brook (1960), A comparison of intracloud and cloud-to-ground lightning discharges, *J. Geophys. Res.*, *65*, 1189–1201.
- Kitagawa, N., and M. Kobayashi (1959), Field changes and variations of luminosity due to lightning flashes, *Recent Advances in Atmospheric Electricity*, Oxford: Pergamon, 485–501.
- Kong, X., X. Qie, and Y. Zhao (2008), Characteristics of downward leader in a positive cloud-to-ground lightning flash observed by high-speed video camera and electric field changes, *Geophys. Res. Lett.*, *35*, L05816, doi:10.1029/2007GL032764.
- Krehbiel, P. R. (1986), *The Earth's Electrical Environment*, chap. The electrical structure of thunderstorms, pp. 90–113, National Academy Press, Washington, D.C.
- Krehbiel, P., W. Rison, R. J. Thomas, T. Hamlin, and J. Harlin (2003), Lightning modes in thunderstorms, *Eos Trans. AGU*, *84*(46), Fall Meet. Suppl., Abstract AE31A-06.
- Krehbiel, P. R., J. A. Rioussset, V. P. Pasko, R. J. Thomas, W. Rison, M. A. Stanley, and H. E. Edens (2008), Upward electrical discharges from thunderstorms, *Nature Geosci.*, *1*, 233–237, doi:10.1038/ngeo162.
- Krider, E., and C. Guo (1983), The peak electromagnetic power radiated by lightning return strokes, *J. Geophys. Res.*, *88*(C13), 8471–8474.
- Krider, E.P., and G.J. Radda (1975), Radiation field waveforms produced by lightning stepped leaders, *J. Geophys. Res.*, *80*, 2653–2657.
- Krider, E., G. Dawson, and M. Uman (1968), Peak power and energy dissipation in a single-stroke lightning flash, *J. Geophys. Res.*, *73*(10), 3335–3339.
- Krider, E., C. Weidman, and R. Noggle (1977), The electric fields produced by lightning stepped leaders, *J. Geophys. Res.*, *82*(6), 951–960.
- Krider, E. P., C. Leteinturier, and J. C. Willett (1996), Submicrosecond fields radiated during the onset of first return strokes in cloud-to-ground lightning, *J. Geophys. Res.*, *101*(D1), 1589–1597.
- Krider, E. P., C. J. Biagi, K. L. Cummins, S. Fleenor, and K. E. Kehoe (2007), Measurements of lightning parameters using video and NLDN data, paper presented at *13th International Conference on Atmospheric Electricity*, Int. Comm. on Atmos. Electr., Beijing.
- Lalande, P., A. Bondiou-Clergerie, P. Laroche, A. Eybert-Berard, J. P. Berlandis, B. Bador, A. Bonamy, M. A. Uman, and V. A. Rakov (1998), Leader properties determined with triggered lightning techniques, *J. Geophys. Res.*, *103*(D12), 14,109–14,115.
- Laroche, P., V. Idone, A. Eybert-Berard, and L. Barret (1991), Observations of bi-directional leader development in a triggered lightning flash, in *Pro. Int. Conf. on Lightning and Static Electricity*, pp. 57/1–10, Cocoa Beach, Florida.

- Le Vine, D. M. (1980), Sources of the strongest RF radiation from lightning, *J. Geophys. Res.*, *85*, 4091–4095.
- Light, T. E. L., and A. R. Jacobson (2002), Characteristics of impulsive VHF lightning signals observed by the FORTE satellite, *J. Geophys. Res.*, *107*(D24), 4756, doi:10.1029/2001JD001585.
- Lin, Y. T., M. A. Uman, J. A. Tiller, R. D. Brantley, W. H. Beasley, E. P. Krider, and C. D. Weidman (1979), Characterization of lightning return stroke electric and magnetic fields from simultaneous two-station measurements, *J. Geophys. Res.*, *84*, 6307–6314.
- Lin, Y. T., M. A. Uman, and R. B. Standler (1980), Lightning return stroke models, *J. Geophys. Res.*, *85*, 1571–1583.
- Maggio C. R., T. C. Marshall, M. Stolzenburg (2009), Estimations of charge transferred and energy released by lightning flashes, *J. Geophys. Res.*, *114*, D14203, doi:10.1029/2008JD011506.
- Makela, J. S., N. Porjo, A. Makela, T. Tuomi, and V. Cooray (2008), Properties of preliminary breakdown processes in Scandinavian lightning, *J. Atmos. Solar-Terrestrial Phys.*, *70*, 2041–2052.
- Maier, L., C. Lennon, P. Krehbiel, and M. Maier (1996), Lightning as observed by a four-dimensional lightning location system at Kennedy Space Center, *Proc. of the 10th International Conference on Atmospheric Electricity*, edited by E. P. Krider and E. R. Williams, pp. 280–283, Int. Comm. on Atmos. Electr., Osaka, Japan.
- Malan, D.J. (1952), Les décharges dans l’air et la charge inférieure positive d’un nuage orageuse, *Ann. Geophys.*, *8*, 385–401.
- Master, M. J., M. A. Uman, W. H. Beasley, and M. Darveniza (1984), Lightning induced voltages on power lines: Experiment, *IEEE Trans. PAS, PAS-103*, pp. 2519–2529.
- Miki, M., V. A. Rakov, T. Shindo, G. Diendorfer, M. Mair, F. Heidler, W. Zischank, M. A. Uman, R. Thottappillil, and D. Wang (2005), Initial stage in lightning initiated from tall objects and in rocket-triggered lightning, *J. Geophys. Res.*, *110*(D02109), doi:10.1029/2003JD004474.
- Moore, C. B., and B. Vonnegut (1977), The thundercloud, In *Lightning, Vol. 1, Physics of Lightning*, ed. R. H. Golde, pp. 51–98, New York, Academic Press.
- Nag, A. (2007), Microsecond- and submicrosecond-scale electric field pulses produced by cloud and ground lightning discharges, M. S. thesis, University of Florida, Gainesville.
- Nag, A., and V. A. Rakov (2008), Pulse trains that are characteristic of preliminary breakdown in cloud-to-ground lightning but are not followed by return stroke pulses, *J. Geophys. Res.*, *113*, D01102, doi:10.1029/2007JD008489.

- Nag, A., and V. A. Rakov (2009), Electric field pulse trains occurring prior to the first stroke in negative cloud-to-ground lightning, *IEEE Trans. Electromagn. Compat., Vol. 51*, No. 1, pp. 147 – 150, doi:10.1109/ TEMC.2008.2005488.
- Nag, A., J. Jerauld, V.A. Rakov, M.A. Uman, K.J. Rambo, D.M. Jordan, B.A. DeCarlo, J. Howard, K.L. Cummins, and J.A. Cramer (2008), NLDN responses to rocket-triggered lightning at Camp Blanding, Florida, in 2004 and 2005, *29th International Conference on Lightning Protection*, paper no. 2–05, Uppsala, Sweden.
- Nag, A., B. A. DeCarlo, and V. A. Rakov (2009), Analysis of microsecond- and submicrosecond-scale electric field pulses produced by cloud and ground lightning discharges, *Atmos. Res., 91*, doi:10.1016/j.atmosres.2008.01.014, 316–325.
- Nguyen, M.D., and S. Michnowski (1996), On the initiation of lightning discharge in a cloud 2. The lightning initiation on precipitation particles, *J. Geophys. Res., 101*, 26,675–26,680.
- Nucci, C. A., C. Mazzetti, F. Rachidi, and M. Ianoz (1988), On lightning return stroke models for LEMP calculations, in *Proc. 19th Int. Conf. Lightning Protection*, Graz, Austria.
- Ogawa, T. (1993), Initiation of Lightning in clouds, *J. Atmos. Electr., 13*, 121–132.
- Oliveira Filho, A., W. Schulz, M. M. F. Saba, O. Pinto Jr., and M. G. Ballarotti (2007), The relationship between first and subsequent stroke electric field peak in negative cloud-to-ground lightning, paper presented at *13th International Conference on Atmospheric Electricity*, Int. Comm. on Atmos. Electr., Beijing.
- Pavlick, A., D. E. Crawford, and V. A. Rakov (2002), Characteristics of distant lightning electric fields, paper presented at *7th International Conference on Probabilistic Methods Applied to Power Systems*, Assoc. per gli Studi sulla Qualita dell ‘Energia Elet., Naples, Italy.
- Pierce, E. T. (1974), Atmospheric electricity - some themes, *Bull. Am. Meteor. Soc.* 55, 1186–94.
- Qie, X., T. Zhang, C. Chen, G. Zhang, T. Zhang, and W. Wei (2005), The lower positive charge center and its effect on lightning discharges on the Tibetan plateau, *Geophys. Res. Lett., 32*, L05814, doi:10.1029/2004GL022162.
- Rakov, V.A. (1999), Lightning electric and magnetic fields. *Proc. 13th Int. Zurich Symp. on Electromagn. Compat.*, Zurich, Switzerland, 561–566.
- Rakov, V.A. (2003), A review of positive and bipolar lightning discharges, *Bull. Amer. Meteor. Soc.*, 84, 767–776.
- Rakov, V. A. (2005), Lightning flashes transporting both negative and positive charges to ground, in *Recent Progress in Lightning Physics*, edited by C. Pontikis, pp. 9-21, Research Signpost, Kerala, India.
- Rakov, V. A. (2006), Initiation of lightning in thunderclouds, *Proc. of SPIE, Vol. 5975*, 5975–12.

Rakov, V. A. (2008), Lightning electromagnetic environment: from continuing-current fields to x-rays, *Proc. of Intl. Conf. on Grounding and Earthing & 3rd Intl. Conf. on Lightning Phys. and Effects, Florianopolis, Brazil, November*, keynote speech.

Rakov, V. A., and B.A. DeCarlo (2005), Lightning initiation mechanisms: A review and new data on submicrosecond "lightning initiation pulses" , *Eos Trans. AGU*, 86(52), Fall Meeting Suppl., Abstract AE32A-06, 2005.

Rakov V. A., and A. A. Dulzon (1984), On latitudinal features of thunderstorm activity, *Meteor. Gidrol.*, 1, 52–57.

Rakov, V. A., and M. A. Uman (1990a), Long continuing current in negative lightning ground flashes, *J. Geophys. Res.*, 95(D5), 5455–5470, doi:10.1029/JD095iD05p05455.

Rakov, V. A., and M.A. Uman (1990b), Some properties of negative cloud-to-ground lightning flashes versus stroke order, *J. Geophys. Res.*, 95(D5), 5447–5453, doi:10.1029/JD095iD05p05447.

Rakov, V. A., and M.A. Uman (1998), Review and evaluation of lightning return stroke models including some aspects of their application, *IEEE Trans. on EMC*, vol. 40, No. 4, part II, Special Issue on Lightning, pp. 403–426.

Rakov, V. A., and M. A. Uman (2003), *Lightning: Physics and Effects*, Cambridge Univ. Press, New York.

Rakov, V. A., R. Thottappillil, and M. A. Uman (1992), On the empirical formula of Willett et al. relating lightning return-stroke peak current and peak electric field, *J. Geophys. Res.*, 97(D11), 11,527–11,533.

Rakov, V. A., M.A. Uman, and R. Thottappillil (1994), Review of lightning properties from electric field and TV observations", *J. Geophys. Res.*, 99, 10,745–10,750.

Rakov, V. A, M.A. Uman, G.R. Hoffman, M.W. Masters, and M. Brook (1996), Bursts of pulses in lightning electromagnetic radiation: observations and implications for lightning test standards, *IEEE Trans. on EMC*, 38, No. 2, 156–164.

Rakov, V. A., M. A. Uman, K. J. Rambo, M. I. Fernandez, R. J. Fisher, G. H. Schnetzer, R. Thottappillil, A. Eybert-Berard, J. P. Berlandis, P. Lalande, A. Bonamy, P. Laroche, and A. Bondiou-Clergerie (1998), New insights into lightning processes gained from triggered-lightning experiments in Florida and Alabama, *J. Geophys. Res.*, 103(D12), 14,117–14,130.

Reynolds, S. E., M. Brook, and M. F. Gourley (1957), Thunderstorm charge separation, *J. Meteor.*, 14, 426–36.

Rison, W., R. Thomas, P. Krehbiel, T. Hamlin, and J. Harlin (1999), A GPS-Based Three-Dimensional Lightning Mapping System: Initial Observations in Central New Mexico, *Geophys. Res. Lett.*, 26(23), 3573–3576.

- Romps, D.M., and Z. Kuang (2009), Overshooting convection in tropical cyclones, *Geophys. Res. Lett.*, *36*, L09804, doi: 10.1029/2009GL037396.
- Rust, W. D., D. R. MacGorman, and R. T. Arnold (1981), Positive cloud to ground lightning flashes in severe storms, *Geophys. Res. Lett.*, *8*, 791–794.
- Saba, M. M. F., O. Pinto Jr., N.N. Solorzano, A. Eybert-Berard (2005), Lightning current observation of an altitude-triggered flash, *Atmos. Res.*, *76* (1-4), 402–411.
- Saba, M. M. F., O. Pinto Jr., and M. G. Ballarotti (2006a), Relation between lightning return stroke peak current and following continuing current, *Geophys. Res. Lett.*, *33*, L23807, doi:10.1029/2006GL027455.
- Saba, M. M. F., M. G. Ballarotti, and O. Pinto Jr. (2006b), Negative cloud-to-ground lightning properties from high-speed video observations, *J. Geophys. Res.*, *111*, D03101, doi:10.1029/2005JD006415.
- Schonland, B. F. J., The lightning discharge (1956), *Handbuch der Physik*, *22*, edited by S. Flugge/Marburg, pp. 576–625, Springer-Verlag, New York.
- Schoene, J. D. (2007), Direct and nearby lightning interaction with test power distribution lines, PhD dissertation, University of Florida, Gainesville.
- Schoene J., M. A. Uman, V. A. Rakov, K. J. Rambo, J. Jerauld, G. H. Schnetzer (2003), Test of the transmission line model and the traveling current source model with triggered lightning return strokes at very close range, *J. Geophys. Res.*, *108* (D23), 4737, doi:10.1029/2003JD003683.
- Schoene, J. D., M. A. Uman, V. A. Rakov, K. J. Rambo, J. Jerauld, C. T. Mata, A. G. Mata, D. M. Jordan, G. H. Schnetzer (2009), Characterization of return-stroke currents in rocket-triggered lightning, *J. Geophys. Res.*, *114*, D03106, doi:10.1029/2008JD009873.
- Schulz, W., and G. Diendorfer (2006), Flash multiplicity and interstroke intervals in Austria, *Proc. 28th Intl. Conf. on Lightning Protection*, edited by C. Mazzetti and Z. Flisowski, pp. 402–404, Inst. of Electr. Installation Eng. of Jpn., Kanazawa, Japan.
- Schulz, W., S. Sindelar, A. Kafri, T. Gotschl, N. Theethayi, and R. Thottappillil (2008), The ratio between first and subsequent lightning return stroke electric field peaks in Sweden, paper presented at *29th International Conference on Lightning Protection*, Dep. of Eng. Sci., Uppsala Univ., Uppsala, Sweden.
- Shao, X., and P. Krehbiel (1996), The spatial and temporal development of intracloud lightning, *J. Geophys. Res.*, *101*(D21), 26641–26668.
- Shindo, T., and M. A. Uman (1989), Continuing current in negative cloud-to-ground lightning, *J. Geophys. Res.*, *94*(D4), 5189–5198, doi:10.1029/JD094iD04p05189.

- Simpson, G., and F. J. Scrase (1937), The distribution of electricity in thunderclouds, *Proc. Roy. Soc. London A*, *161*, 309–352.
- Smith, D. A. (1998), Compact Intracloud Discharges, PhD dissertation, University of Colorado, Boulder, CO.
- Smith D.A., K.B. Eack, J. Harlin, M.J. Heavner, A.R. Jacobson, R.S. Massey, X.M. Shao, and K.C. Wiens (2002), The Los Alamos Sferic Array: A research tool for lightning investigations, *J. Geophys. Res.*, *107* (D13), doi: 10.1029/2001JD000502.
- Smith, D. A., M. J. Heavener, A. R. Jacobson, X. M. Shao, R. S. Massey, R. J. Sheldon, and K. C. Wiens (2004), A method for determining intracloud lightning and ionospheric heights from VLF/LF electric field records, *Radio Sci.*, *39*, RS1010, doi:10.1029/2002RS002790.
- Smith, D. A., X. M. Shao, D. N. Holden, C. T. Rhodes, M. Brook, P. R. Krehbiel, M. Stanley, W. Rison, and R. J. Thomas (1999), A distinct class of isolated intracloud discharges and their associated radio emissions, *J. Geophys. Res.*, *104*, 4189–4212.
- Solomon, R., V. Schroeder, and M. B. Baker (2001), Lightning initiation-conventional and runaway-breakdown hypotheses, *Q. J. R. Meteorol. Soc.*, *127*, 2683–2704.
- Takahashi, T. (1978), Riming electrification as a charge generation mechanism in thunderstorms, *J. Atmos. Sci.*, *35*, 1536–48.
- Tessendorf, S. A., S. A. Rutledge, and K. C. Wiens (2007), Radar and lightning observations of normal and inverted polarity multicellular storms from STEPS, *Mon. Weather Rev.*, *135*, 3682–3706, doi:10.1175/2007MWR1954.1.
- Thomas, R., P. Krehbiel, W. Rison, T. Hamlin, J. Harlin, and D. Shown (2001), Observations of VHF Source Powers Radiated by Lightning, *Geophys. Res. Lett.*, *28*(1), 143–146.
- Thottappillil, R., V. A. Rakov, M. A. Uman, W. H. Beasley, M. J. Master, and D. V. Shelukhin (1992), Lightning subsequent-stroke electric field peak greater than the first stroke peak and multiple ground terminations, *J. Geophys. Res.*, *97*(D7), 7503–7505.
- Thottappillil, R., and M. A. Uman (1993), Comparison of return stroke models, *J. Geophys. Res.*, *98*(D12), 22,903–22,914.
- Tierney H. E., R. A. Roussel-Dupré, E. M. D. Symbalisty, W. H. Beasley (2005), Radio frequency emissions from a runaway electron avalanche model compared with intense, transient signals from thunderstorms, *J. Geophys. Res.*, *110*, D12109, doi:10.1029/2004JD005381.
- Uman, M. A. (1974), The earth and its atmosphere as a leaky spherical capacitor, *Am. J. Phys.*, *42*, 1033–1035.
- Uman, M. A. (1987), *The Lightning Discharge*, Dover Publications, Inc., Mineola, New York.

- Uman, M. A., and D. K. McLain (1969), Magnetic field of the lightning return stroke, *J. Geophys. Res.*, *74*, 6899–6910.
- Uman, M. A., D. K. McLain, and E. P. Krider (1975), The electromagnetic radiation from a finite antenna, *Am. J. Phys.*, *43*, 33–38.
- Ushio, T., Z.-I. Kawasaki, K. Matsu-ura, and D. Wang (1998), Electric fields of initial breakdown in positive ground flash, *J. Geophys. Res.*, *103*(D12), 14135–14139.
- Villanueva Y., V.A. Rakov, M.A. Uman, and M. Brook (1994), Microsecond-scale electric field pulses in cloud lightning discharges, *J. Geophys. Res.*, *99* (D7), 14,353–14,430.
- Visacro, S., A. Soares Jr., M. A. O. Schroeder, L. C. L. Cherchiglia, and V. J. Sousa (2004), Statistical analysis of lightning current parameters: Measurement at Morro do Cachimbo Station, *J. Geophys. Res.*, *109*, D01105, doi:10.1029/2003JD003662.
- Vonnegut, B. (1953), Possible mechanism for the formation of thunderstorm electricity, *Bull. Am. Meteor. Soc.*, *34*, 378–81.
- Vonnegut, B. (1994), The atmospheric electricity paradigm, *Bull. Am. Meteor. Soc.*, *75*, 53–61.
- Wang, D., N. Takagi, T. Watanabe, V. A. Rakov, M. A. Uman (1999), Observed leader and return stroke propagation characteristics in the bottom 400 m of the rocket triggered lightning channel, *J. Geophys. Res.*, *104*, 14,369–14,376.
- Watson, S. S., and T. C. Marshall (2007), Current propagation model for a narrow bipolar pulse, *Geophys. Res. Lett.*, *34*, L04816, doi:10.1029/2006GL027426.
- Weidman, C. D., and E. P. Krider (1978), The fine structure of lightning return stroke wave forms, *J. Geophys. Res.*, *83*(C12), 6239–6247.
- Weidman, C. D., and E.P. Krider (1979), The radiation field waveforms produced by intracloud lightning discharge processes, *J. Geophys. Res.*, *84*(C6), 3159–3164.
- Weidman, C. D., and E. P. Krider (1980), Submicrosecond risetimes in lightning return-stroke fields, *Geophys. Res. Lett.*, *7*, 955–958.
- Wiens K. C., T. Hamlin, J. Harlin, D. M. Suszcynsky (2008), Relationships among Narrow Bipolar Events, "total" lightning, and radar-inferred convective strength in Great Plains thunderstorms, *J. Geophys. Res.*, *113*, D05201, doi:10.1029/2007JD009400.
- Willett, J. C., V. P. Idone, R. E. Orville, C. Leteinturier, A. Eybert-Berard, L. Barret, and E. P. Krider (1988), An experimental test of the "transmission-line model" of electromagnetic radiation from triggered lightning return strokes, *J. Geophys. Res.*, *93*(D4), 3867–3878.
- Willett, J. C., J. C. Bailey, V. P. Idone, A. Eybert-Berard, and L. Barret (1989a), Submicrosecond intercomparison of radiation fields and currents in triggered lightning return strokes based on the transmission-line model, *J. Geophys. Res.*, *94*, 13,275–13,286.

Willett, J. C., J. C. Bailey, and E. P. Krider (1989b), A class of unusual lightning electric field waveforms with very strong high-frequency radiation, *J. Geophys. Res.*, *94*, 16,255–16,267.

Williams, E. R. (1989), The tripole structure of thunderstorms, *J. Geophys. Res.*, *94* (D11), 13,151–13,167.

Wilson, C. T. R. (1956), A theory of thundercloud electricity, *Proc. Roy. Soc. A*, *236*, 297–317.

BIOGRAPHICAL SKETCH

Amitabh Nag received the Bachelor of Technology in electronics and communication engineering from West Bengal University of Technology, Kolkata in June 2005. In August 2005, he was admitted to the Department of Electrical and Computer Engineering at the University of Florida as a Ph.D. student. He received the Master of Science and Ph.D. degrees in electrical engineering in May 2007 and May 2010, respectively, from the University of Florida, Gainesville. From 2005 to 2010, he was a Research Assistant at the International Center for Lightning Research and Testing, University of Florida, where he was in charge of the Lightning Observatory in Gainesville. He has authored or coauthored more than 25 papers and technical reports on various aspects of lightning, with 7 first-authored papers being published in reviewed journals. His current research interests include measurement, analysis, and modeling of electric and magnetic fields from cloud and ground lightning discharges, lightning detection and protection. He is a reviewer for various journals including the IEEE Transactions on EMC, Geophysical Research Letters, and Atmospheric Research and is a member of the Institute of Electrical and Electronic Engineers, American Geophysical Union, and American Meteorological Society.